NASA Conference Publication 3137

The Compton Observatory Science Workshop

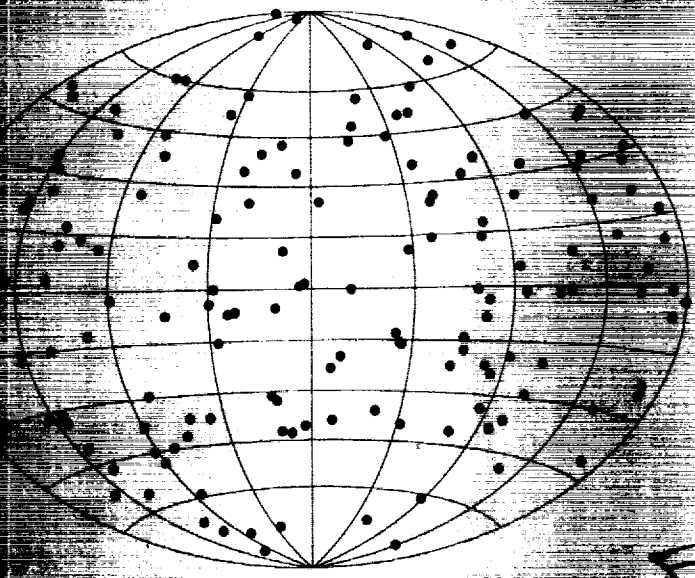

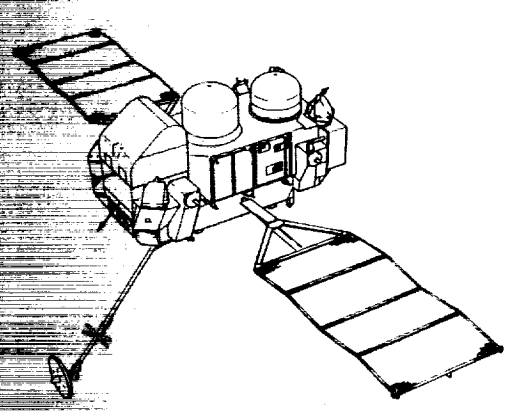

Proceedings of a workshop held in Annapolis, Maryland September 23–25, 1991

NASA

NASA Conference Publication 3137

The Compton Observatory Science Workshop

Edited by
Chris R. Shrader
Computer Sciences Corporation
Beltsville, Maryland

Neil Gehrels and Brian Dennis
NASA Goddard Space Flight Center
Greenbelt, Maryland

Proceedings of a workshop held in
Annapolis, Maryland
September 23–25, 1991

National Aeronautics and
Space Administration

Office of Management

Scientific and Technical
Information Program

1992

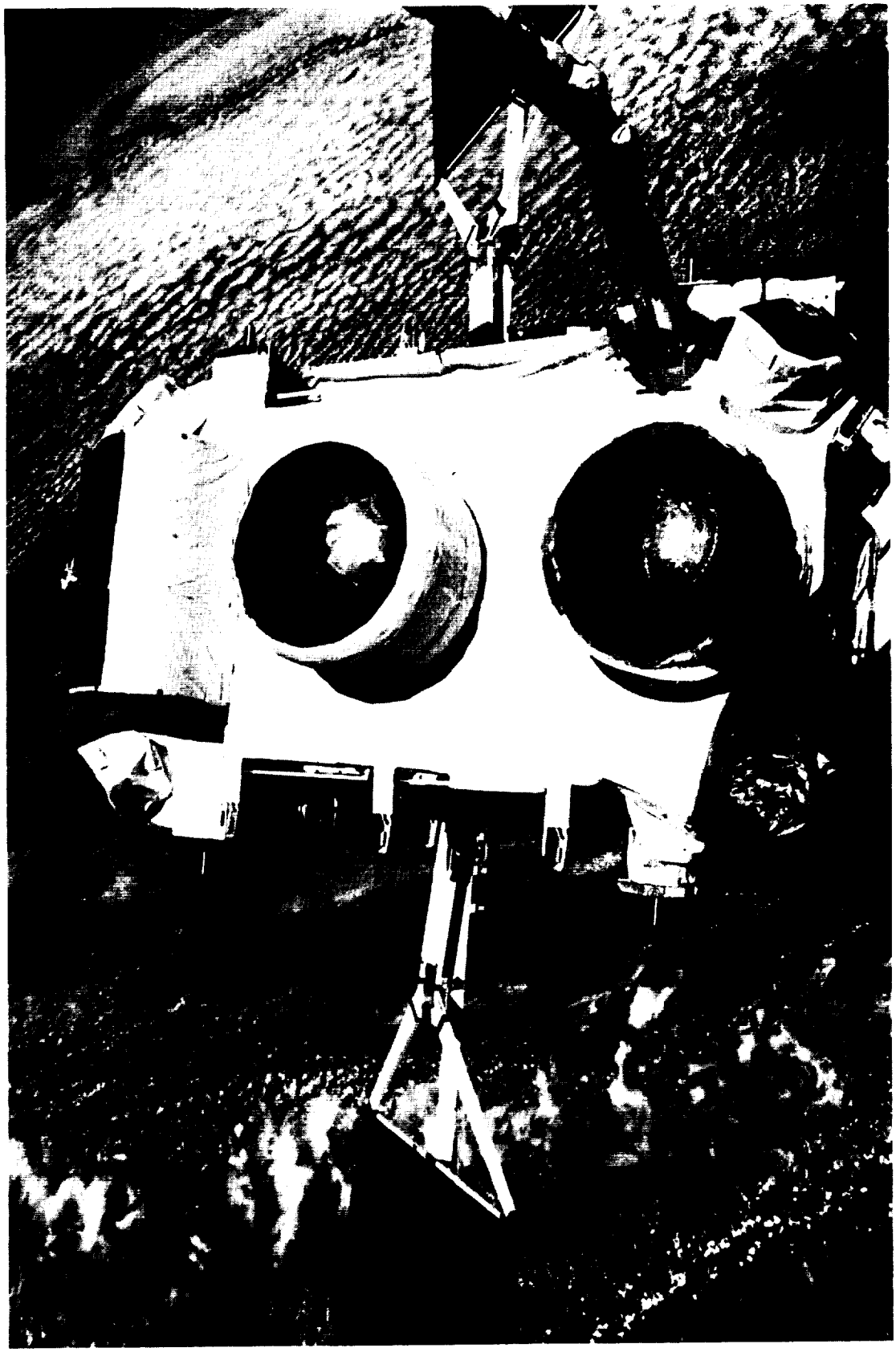

The Compton Observatory at the end of Atlantis' remote manipulator system just prior to its release.

COVER: Angular distribution in galactic coordinates of 153 gamma-ray bursts detected by BATSE.

Preface

This volume presents the proceedings of the *Compton Observatory Science Workshop*, held in Annapolis, Maryland on September 23-25 of 1991. The first 2 days of the workshop featured papers describing early scientific results from the four *Compton* instruments, as well as a series of technical papers describing instrument characteristics and in-flight performance. (The Compton Observatory was formerly the Gamma Ray Observatory or "GRO"; this name change was announced during the workshop.) The third day of the workshop focussed primarily on results from *Compton* solar observations along with related observational and theoretical work, with an emphasis on the exceptional flaring activity seen during June 1991. A general solicitation for contributed papers was issued, as well as select invitations for theoretical and review papers. The response was quite dramatic, particularly considering that the workshop occurred only 5 months subsequent to launch. In all, 77 papers covering a wide range of astrophysical topics were presented. This level of response reflects the great interest in the Compton Observatory from within the scientific community as well as the fact that the mission is widely perceived as an unqualified success thus far.

The scientific organization for the workshop was the responsibility of the Compton Gamma Ray Observatory Science Support Center, which is operated for Goddard Space Flight Center by Computer Sciences Corporation. We wish to acknowledge the efforts of Meta Hutchison-Frost for her assistance in organizing the workshop, and of Sandy Barnes and Luann Bindschadler for their assistance in preparation of the manuscript.

TABLE OF CONTENTS

3. PULSARS

4. GAMMA-RAY BURSTS

5. ACTIVE GALAXIES

1.
INSTRUMENTATION, ANALYSIS METHODS AND EARLY RESULTS

OPERATION AND PERFORMANCE OF THE OSSE INSTRUMENT

R.A. Cameron[1], J.D. Kurfess[2], W.N. Johnson[2], R.L. Kinzer[2], R.A. Kroeger[2], M.D. Leising[2,4], R.J. Murphy[2], G.H. Share[2], M.S. Strickman[2], J.E. Grove[2,5], G.V. Jung[1], D.A. Grabelsky[3], S.M. Matz[3], W.R. Purcell[3], M.P. Ulmer[3]

[1]Universities Space Research Association, Washington, DC
[2]E.O. Hulburt Center for Space Research, Naval Research Laboratory, Washington, DC
[3]Northwestern University, Evanston, IL
[4]Clemson University, Clemson, SC
[5]NRC/NRL Resident Research Associate

Abstract

The Oriented Scintillation Spectrometer Experiment (OSSE) on the Arthur Holly Compton Gamma Ray Observatory is described. An overview of the operation and control of the instrument is given, together with a discussion of typical observing strategies used with OSSE and basic data types produced by the instrument. Some performance measures for the instrument are presented, obtained from pre-launch and in-flight data. These include observing statistics, continuum and line sensitivity, and detector effective area and gain stability.

Introduction

The Oriented Scintillation Spectrometer Experiment (OSSE) is one of four scientific instruments on the Arthur Holly Compton Gamma Ray Observatory. Its primary capability is spectroscopy of astrophysical objects in the 0.05 to 10 MeV energy range. The instrument also has a number of secondary capabilities, including spectroscopy of gamma rays and neutrons with energies above 10 MeV; collection of timed-tagged spectral data for studies of pulsars and other variable sources; and collection of high-time resolution data in response to cosmic burst or solar flare triggers from the BATSE instrument on GRO.

Since the launch of GRO, the OSSE instrument has performed well, providing data on a large number of objects, including X-ray binary stars, pulsars, the Galactic Center and other galaxies and quasars. Analysis of the data collected by OSSE since launch has provided information on the in-flight performance of the instrument, particularly the background rates detected by the instrument and consequently the continuum and line sensitivity of the instrument. Some details of the in-flight performance of OSSE are presented, together with information on the instrument capabilities, operations, and a discussion of observing strategies applicable to OSSE. More detailed descriptions of OSSE and its associated data products are given in Johnson *et al.* (1989) and Strickman *et al.* (1989). Some details of the scientific objectives and methods of achieving these objectives for the OSSE instrument are given in Kurfess *et al.* (1989).

Instrument Description

The OSSE instrument (Figure 1) consists of four actively shielded NaI(Tl)-CsI(Na) phoswich detectors. Each detector has a 3.8° × 11.4° (FWHM) field of view, defined by a passive tungsten collimator. Each detector has an independent, single-axis orientation system which provides 192° of positioning in the GRO XZ plane, from 51° behind the +Z axis towards the −X axis to 51° below the +X axis towards the −Z axis. The long dimension of the collimator field of view is perpendicular to the XZ plane. The OSSE pointing system permits offset pointing from a target position for background measurements and also multiple target observations. Within the positioning range the four detectors are unobscured over 94° of position angle, from 6.5° behind the +Z axis to 2.5° above the +X axis. Beyond these angles the OSSE detectors block each other, and only either the upper or the lower detectors are unobscured.

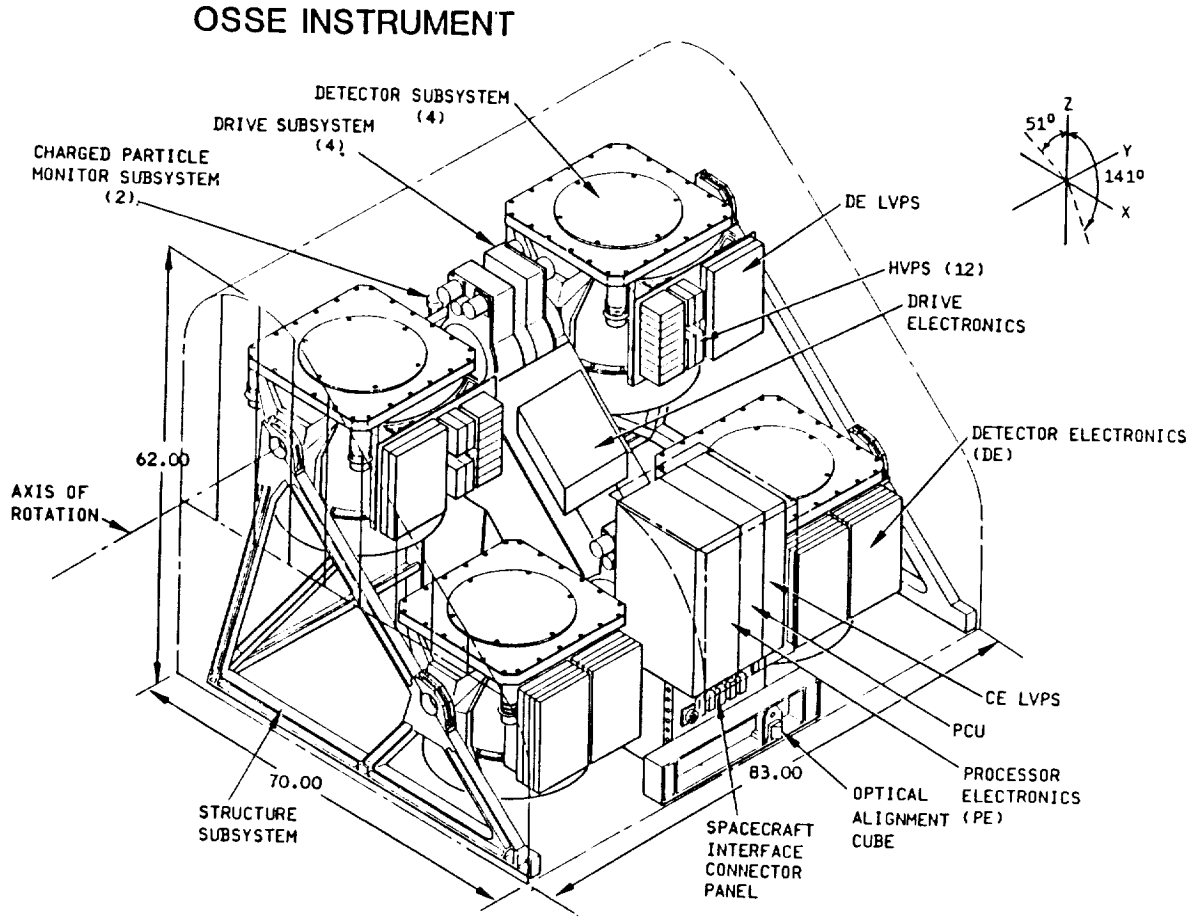

Figure 1: The OSSE Instrument

The detectors are controlled by a Central Electronics (CE) unit which coordinates the operation of the detectors, collects and formats data produced by the detectors, and provides the power, command and telemetry interface with the GRO spacecraft. A thermal shield consisting of multi-layer insulation covers the detectors and central electronics. A summary of the instrument characteristics is given in Table 1.

Figure 2 shows a single OSSE detector. The principal element of an OSSE detector is the 13-inch diameter phoswich scintillation crystal. The phoswich is 7 inches thick, viewed by 7 photomultiplier tubes, and fronted by the tungsten collimator. The phoswich and the collimator are surrounded by an annular anticoincidence shield, comprised of four NaI(Tl) scintillation segments. Each shield segment is viewed by 3 PMTs. The front of the detector is covered by a plastic scintillation detector sheet for charged particle detection, viewed by 4 PMTs.

In the phoswich, the 3-inch thick CsI crystal is optically coupled to the 4 inch thick NaI crystal, and provides active anticoincidence veto for the NaI crystal. Phoswich events from the PMTs are processed through three separate pulse-height and pulse-shape analysis systems, and the different scintillation decay time constants of the NaI and CsI crystals are used to select NaI events by pulse-shape discrimination. The three event analysis systems cover 0.05 – 1.5 MeV (Low), 1 – 10 MeV (Medium), and >10 MeV (High) energy ranges. The pulse-shape discrimination in the high energy range is also used to separate gamma ray and neutron events in the NaI portion of the phoswich, using the differing time characterstics of the secondaries produced by these interactions.

Table 1: OSSE Characteristics Summary

Detectors	
Type:	4 identical NaI-CsI phoswiches, actively-shielded, passively collimated
Aperture Area (total):	2620 cm^2
	1920 cm^2 at 0.511 MeV (photopeak)
Field-of-View:	$3.8° \times 11.4°$ FWHM
Energy Resolution:	8.2% at 0.661 MeV
	3.8% at 6.13 MeV
Time Resolution:	4 – 32 sec spectrum integrations
	0.125 or 1 msec in Pulsar EBE mode
	4 – 512 msec in Pulsar Rate mode
	4 – 32 msec in Burst mode
Experiment Sensitivities (500000 sec)	
0.05 – 10 MeV Line:	$\sim 3 - 8 \times 10^{-5}$ γ cm^{-2} s^{-1}
0.05 – 1 MeV Continuum:	$0.005 \times$ Crab
1 – 10 MeV Continuum:	$0.05 \times$ Crab
Gamma Ray Bursts:	1×10^{-7} erg cm^{-2}
Solar Flare Line (10^3 sec flare):	1×10^{-3} γ cm^{-2} s^{-1}
Solar Flare Neutrons (> 10 MeV):	5×10^{-3} n $cm^{-2}s^{-1}$
Pointing System	
Type:	Independent Single Axis
Range:	192° about the S/C Y-axis
Accuracy:	6 arcminutes
Speed:	2°/sec (max)
GRO – OSSE Interface	
Weight:	1820 kg
Power:	192 watts
Telemetry:	6492 bits/sec

Validated events from the phoswich must escape veto by the NaI annular shield and the plastic charged particle detector and pass pulse shape discrimination in the phoswich. The pulse height and pulse shape of each of these validated events are each digitized into 8 bits (256 channels) in each of the 3 energy ranges. The digitized pulse shapes are passed through energy-dependent pulse shape discrimination, for optimum rejection of events with energy loss shared between the NaI and the CsI in the phoswich.

The gain of each detector is controlled by an AGC system, which uses an LED flasher optically coupled to the phoswich. The high voltage applied to each PMT is controlled to keep the response to the LED flashes stable. The LED flashes are also monitored by a PIN diode light detector, with the PIN diode output used to control and stabilize the brightness of the LED. The gain of each detector is independently monitored with an internal ^{60}Co radioactive source, having an activity of 2 – 3 nanocuries.

A variety of data types are produced by the instrument, covering scientific spectral and timing data, calibration data and housekeeping data. Each detector independently accumulates spectra in the Low, Medium and High energy ranges for a selectable duration between 2 and 32 seconds. At the end of each accumulation the spectra are transferred to the CE and inserted into the OSSE telemetry stream. The Low and Medium spectra are 256 channels each, and the High range data consists of 16 channels of neutron data and 16 chan-

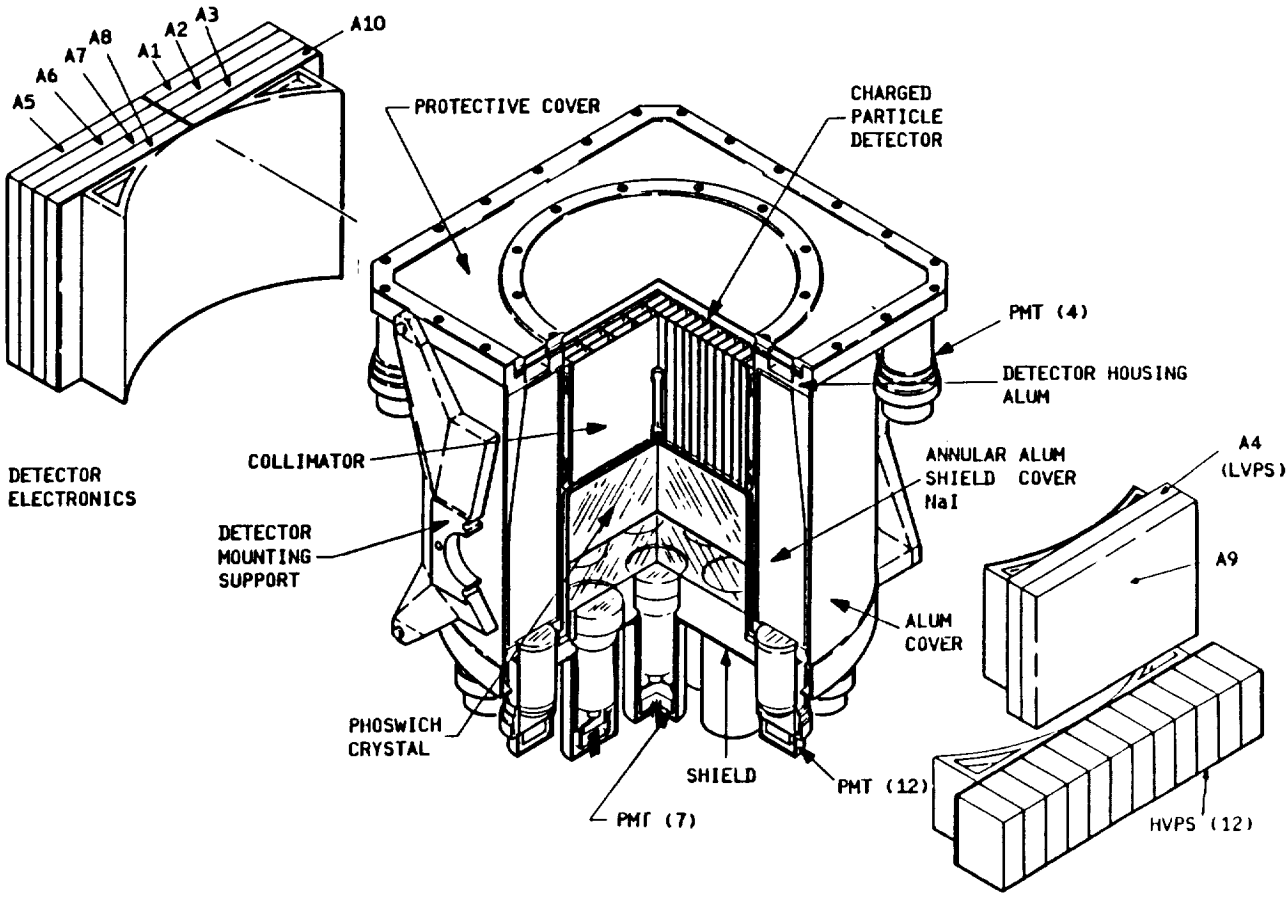

Figure 2: An OSSE Detector

nels of gamma-ray data. At standard gain the channels are nominally 6 keV wide in the Low energy range, 40 keV in the Medium range and 16 MeV in the High range.

OSSE supports a wide range of timing data types for variable sources. For pulsars and other rapidly variable sources, OSSE supports two pulsar data modes. Individual events may be time-tagged with a precision of either 0.125 or 1 milliseconds, in Event-by-Event (EBE) data. Alternatively, event count rates may be sampled over intervals from 4 to 512 milliseconds in Rate pulsar data. Corresponding energy information is also available for each of these pulsar data types. Either EBE or Rate pulsar data can saturate the OSSE telemetry capabilities, and so the event rate is restricted to events with energies in one of up to eight selectable energy range windows. EBE events are telemetered with the energy window identifier and 5 bits of energy information within the window energy range. Rate samples are identified by energy window only.

In addition to pulsar data obtained from phoswich events, OSSE can also respond to isolated events such as gamma ray bursts or solar flares by collecting 4096 samples of shield event rates at sample intervals of between 4 and 32 milliseconds, with shield events having energies between 0.1 and 8 MeV. This collection can be triggered by either OSSE shield rates or a trigger signal from BATSE. Operationally, only BATSE triggers have been used to initiate burst data collections.

Energy calibration spectra are collected in the Low and Medium energy ranges from tagged decay events in the internal ^{60}Co sources. Diagnostic information from each detector includes one dimensional energy spectra from a calibration pulse height analyzer, and two dimensional energy and pulse shape information from two separate pulse height analyzers. Diagnostic information may be collected from several different sources in

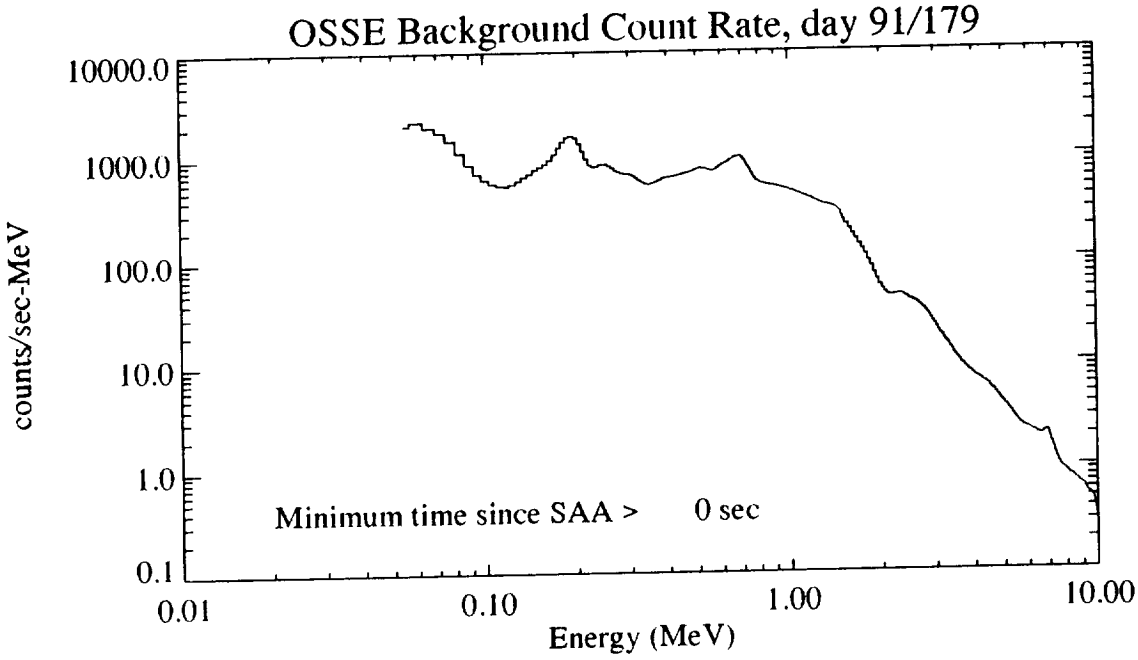

Figure 3: Typical OSSE Background Spectrum

each detector, including the phoswich, selected shield segments, the LED flasher, the PIN diode, and the Charged Particle Detector.

Instrument Capabilities and Performance

The performance and capabilities of OSSE were estimated before launch based on instrument calibration using a number of different radioactive sources and analysis of its expected response to the estimated orbital background flux by means of Monte Carlo simulations. However, the best measure of performance is provided by flight data. GRO was launched into a 28.5° inclination orbit, with an injected altitude of 462 km. As expected, the background rate in the detectors dominates the flux from most celestial gamma ray sources. The background is principally due to cosmic ray interactions and trapped particles in the detectors and the rest of the spacecraft. Figure 3 shows a typical background spectrum measured by OSSE, covering the Low and Medium energy ranges. A number of features are seen in the spectrum, identified with radioactive products resulting from energetic particle collisions in the spacecraft and detectors.

Figure 4 shows in summary form a number of features of the OSSE response. The plot shows a day of data from detector 3, for day 138 of 1991 (May 18), two days after the start of the first Phase I science observations by GRO. During this time OSSE observed the Crab Nebula and Pulsar as its primary target and the pulsar PSR 1957+20 as its secondary target (see below). The 24 hours of the day are marked horizontally across the plot. The count rate (counts/second) for fully validated phoswich events is shown in a number of different energy ranges. From the bottom to the top on the page the curves show the rates in the 0.05 – 0.1, 0.1 – 0.3, 0.3 – 0.8, 0.8 – 1.5, 1.5 – 3.0, 3.0 – 10.0 and >10 MeV energy ranges. Above these phoswich event rate curves, the event rates in the four shield segments of the detector are shown superimposed in a single plot. At the top of the page the calculated geomagnetic rigidity in GeV for the GRO position is shown.

A number of features are of interest in these plots. The 9 passages of GRO through the South Atlantic Anomaly for the day are readily apparent by the dropout of the count rates as the detector high voltages are turned off during these times. Approximately 12% of the day is spent in the SAA. The rates in the 0.1 – 3.0 MeV energy ranges show decays with a characteristic half-life of 25 minutes following the exit from

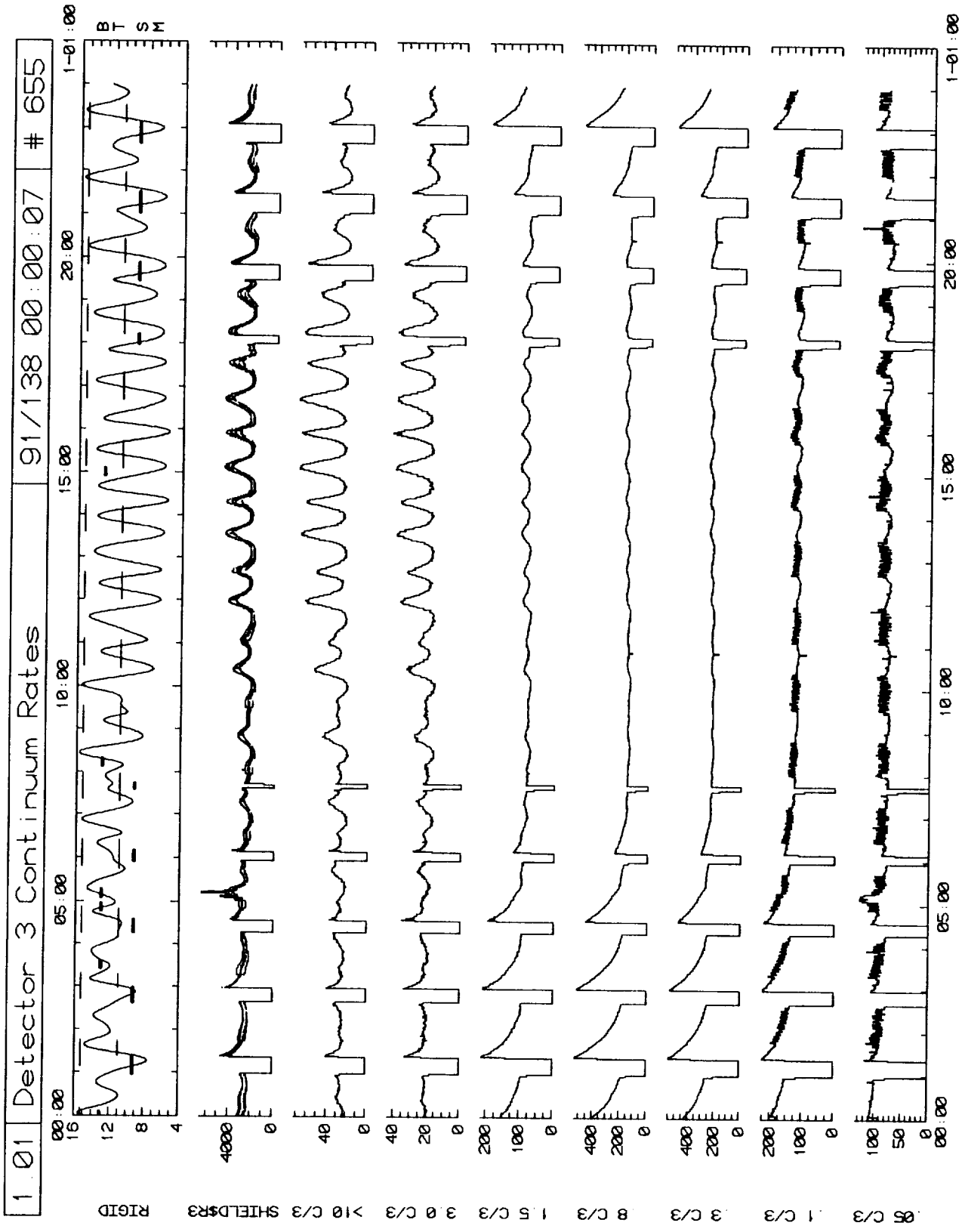

Figure 4: Daily Summary Plots for Detector 3, Day 138

each SAA passage. This is primarily produced by radioactive decay of ^{128}I produced in the phoswich from neutron capture on ^{127}I.

Geomagnetic modulation of the count rates is apparent at the higher energies, with the highest count rates occurring at the lowest cutoff energies. In the simplest geometry, the rigidity modulates at half the orbital period. This modulation reflects the cosmic-ray dependence of the local background and cosmic-ray related contribution to the internal background, and warns that measurement and subtraction of background from any celestial source observation must occur on a time scale fast enough to track the geomagnetic modulation of the background, or be dealt with by modelling and subtraction of rigidity effects in the data.

The lowest energy ranges also show some geomagnetic modulation of the measured rates. In the two lowest energy ranges, a more rapid modulation of the rates is also apparent, produced by alternating 2 minute observations of the Crab with 2 minute observations at offsets of 4.5° on either side of the Crab, to measure the local background spectra. This is the standard strategy for steady-state source observations, necessary to track the time-varying background. These rate plots show that the brightest object in the sky at these energies produces a small fraction of the events seen by the detector. However, the plots also show that the Crab is readily detectable by OSSE at energies up to 300 keV in a 2 minute observation. The Crab is seen at higher energies by OSSE, but its reduced flux at these energies requires longer integration times. The observations of the Crab alternate in each orbit with observations of PSR 1957+20, which is not readily apparent in the OSSE data.

Another feature in Figure 4 is the increase in the count rate in the lowest energy range and in the shield rates at about 05:10 UT. This was produced by an X2.8 class solar flare. While typical deadtimes for the detectors, produced by the anticoincidence systems and electronic processing times for events, are 10% in the Low energy range, 6% in the Medium range and 3% in the High range, very large solar flares such as those of June 1991 can increase deadtime to almost 100%.

Since the background flux detected by OSSE dominates any source flux except for transient events such as strong solar flares and gamma-ray bursts, the statistical significance of the measured background in any observing period dictates the corresponding sensitivity of the instrument in that period. Figure 5 shows the OSSE line sensitivity, for an integration time of 500000 seconds, corresponding roughly to the typical integration time on a target achievable in a two week period where OSSE observes two targets. The continuum sensitivity of OSSE for the same integration time is shown in Figure 6. The effective area for an OSSE detector, which is used in the calculations of both line and continuum sensitivity, is shown in Figure 7, reaching a peak of more than 500 cm^2 at 200 keV. An offset of 4.5° completely modulates the emission from a source on the boresight of the detector up to energies of about 400 keV. At higher energies, there is some flux leakage through the collimator, and the effective area is consequently reduced, primarily due to reduced detection efficiency.

The gain stability of each detector is an important aspect of the overall performance of the instrument, since rapid gain variations can degrade the energy resolution of the instrument and make the data reduction process more difficult. The performances of both the phoswich and the PMTs are sensitive to temperature variations, so that an essential factor of gain stability is temperature stability in the detectors. Figure 8 shows the temperature and gain variations of detector 4 in OSSE over a 15 day period. GRO was maneuvered for the start of a new observation period near the end of Truncated Julian Day 8449 (July 12), producing one of the largest changes in phoswich temperature and hence gain seen in the OSSE detectors since launch. Active heater control in each detector was designed to maintain the phoswich temperature at 20 C, and Figure 8 shows it comes within 0.5 C of this goal. Within a viewing period the solar illumination on GRO only slowly varies in direction, and temperature variations are less than 0.1 C. The corresponding gain changes in the detector, as measured from the Low energy range channel number of the 1.332 MeV line of the internal ^{60}Co source in the detector, are about $\pm$0.15% due to the maneuver and less than $\pm$0.1% over the rest of the viewing period.

Finally, the energy resolution of detector 3 is shown in Figure 9. Ground calibration data was used to measure

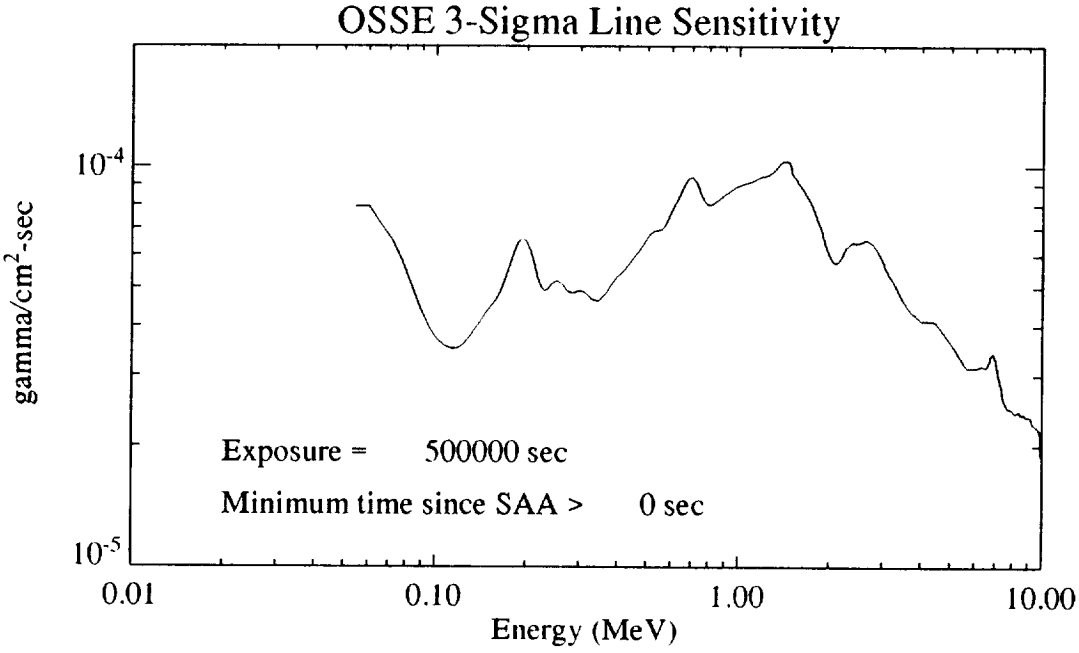

Figure 5: OSSE Line Sensitivity, Single Detector

the resolution at several energies, and an analytic curve fit to these data points is also shown.

Instrument Operations

Instrument operations cover the principal activities of carrying out an observation with OSSE and the initial processing of science and housekeeping data obtained from the instrument. Configuration control of the instrument itself and monitoring of its health and safety is carried out by a mission operations team at the Naval Research Laboratory.

With GRO in a low-earth orbit, a large fraction of the sky is blocked by the earth, and any object observed by OSSE has a high probability of being occulted by the earth. To improve the observing efficiency of OSSE, two targets are typically observed by OSSE in an orbit, with each target being observed while the other is occulted. Both targets must be on or near the 192 degree range in the XZ plane of GRO that is accessible to the OSSE detectors.

The relative integration times on each of these two targets is a function of their position with respect to each other and to the orbit of GRO. A target near the orbital pole may escape occultation by the earth and hence could be observed continuously, while a target in the orbital plane will be occulted for almost half of each orbit. Generally, there will be times in each orbit when both targets are visible simultaneously, and conversely times when both are occulted simultaneously. Depending on the relative scientific importance of the targets, useful observing time common to both targets may be allocated to one target or may be shared between the sources. Generally, one target will be designated the primary target and the other the secondary target, with the primary target having priority in relative observing time allocation.

OSSE supports up to four independent detector position sequences, stored in lookup tables, for different targets. This allows separation of confused sources and optimum observations of complex fields. Also a detector positioning table can be dedicated to the Sun when it is accessible to the OSSE detectors, so that the detectors can slew to the Sun when a BATSE solar flare signal is received by OSSE. If so configured, OSSE responds to a BATSE solar trigger within 3 seconds of the receipt of the trigger.

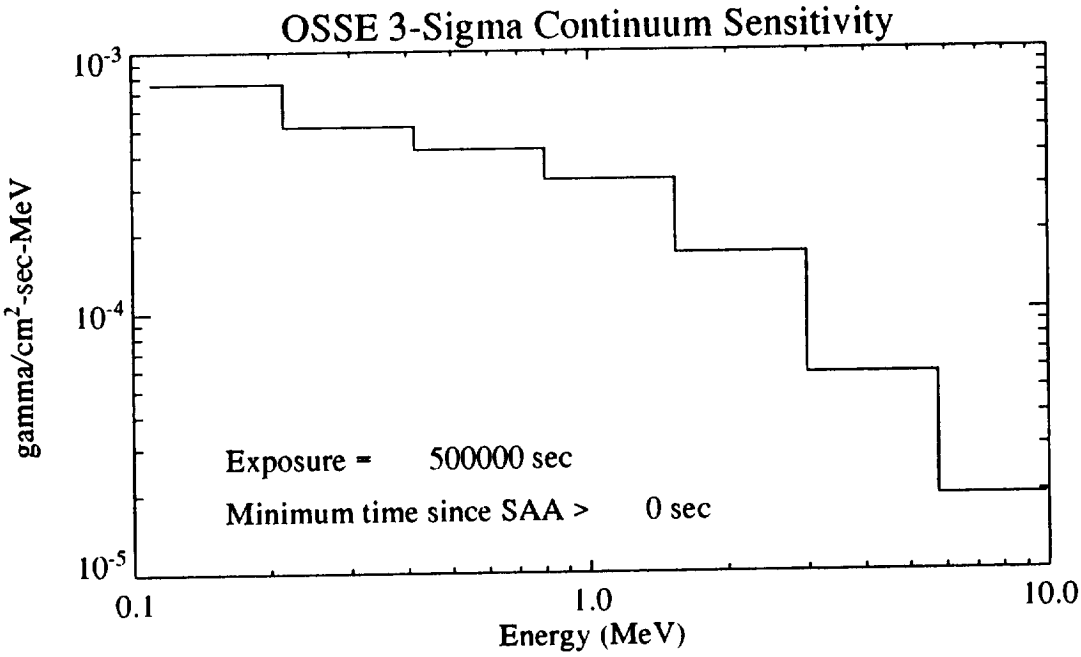

Figure 6: OSSE Continuum Sensitivity, Single Detector

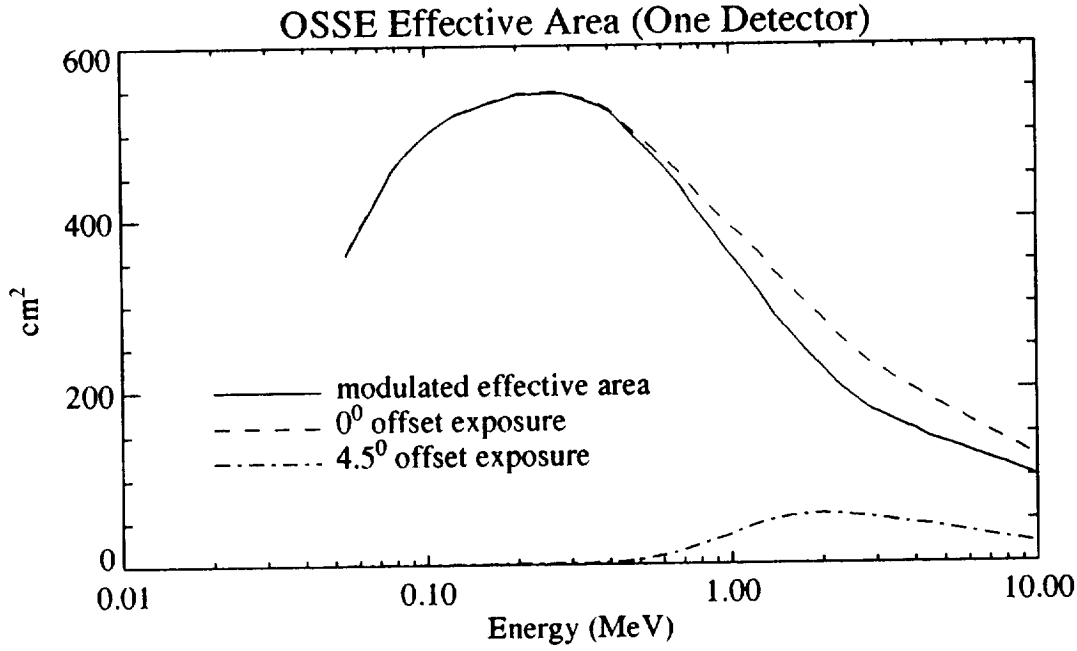

Figure 7: OSSE Effective Area

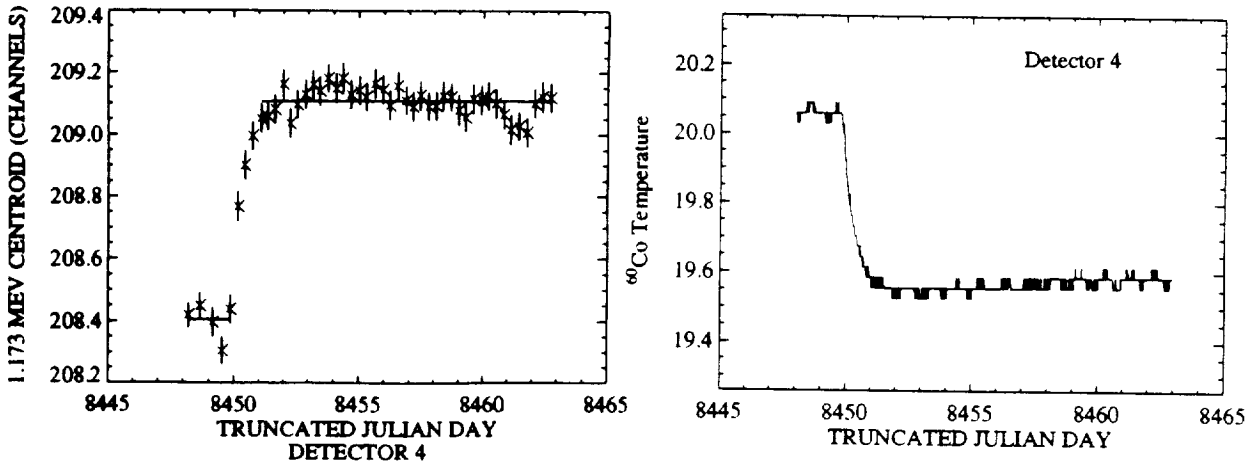

Figure 8: OSSE Temperature and Gain Stability

The mission operations team is responsible for converting the scientific objectives of an observation into a suitable instrument operating state, and the preparation of a command sequence to bring the instrument to that operating state. Very often there is some conflict between the scientific objectives of the primary and secondary target observations, so that some compromise in instrument configuration is required to best meet the objectives of both observations. In addition, a certain amount of customization of instrument configuration for each of these targets is possible. OSSE has the capability to execute internal command sequences when its detectors are commanded to a new target. These command sequences can provide limited instrument configuration changes such as redefinition of the pulsar data type to be collected from the target field. All instrument command sequences are verified for correctness before transmission to the instrument by the OSSE ground support equipment, which also preserves a complete history of OSSE configuration in a command state database.

The other prime function of instrument operations support is the receipt and processing of data from OSSE. After transmission of the data from GRO to the ground through TDRSS and processing through mission support facilities at Goddard Space Flight Center, OSSE data is electronically transmitted to NRL over the NASCOM X.25 network. OSSE data is received in three forms: Realtime, Quicklook and Production. Realtime data is transmitted with little processing from GRO during one or two 30 minute TDRSS contacts with GRO, and provides essentially instantaneous monitoring of the instrument. Quicklook data is minimally processed data from a single playback of a GRO tape recorder, and is received once per day, providing typically 3 hours of data. Production data is a fully processed 24 hour dataset, received once per day approximately 20–44 hours after being recorded on GRO.

Automatic processing of production data provides a standard set of daily data products, within approximately 8 hours of receipt of the production dataset. The principal data product is the set of spectra integrated for 2 minutes, for each offset pointing of each detector, and for all targets observed by OSSE on the day. Other data products include pulsar data, calibration data and diagnostic data. Most of the data are stored in a standard format consisting of Spectral Data Base (SDB) records, which are the basis of the OSSE data analysis system discussed in Purcell *et al.* (1991).

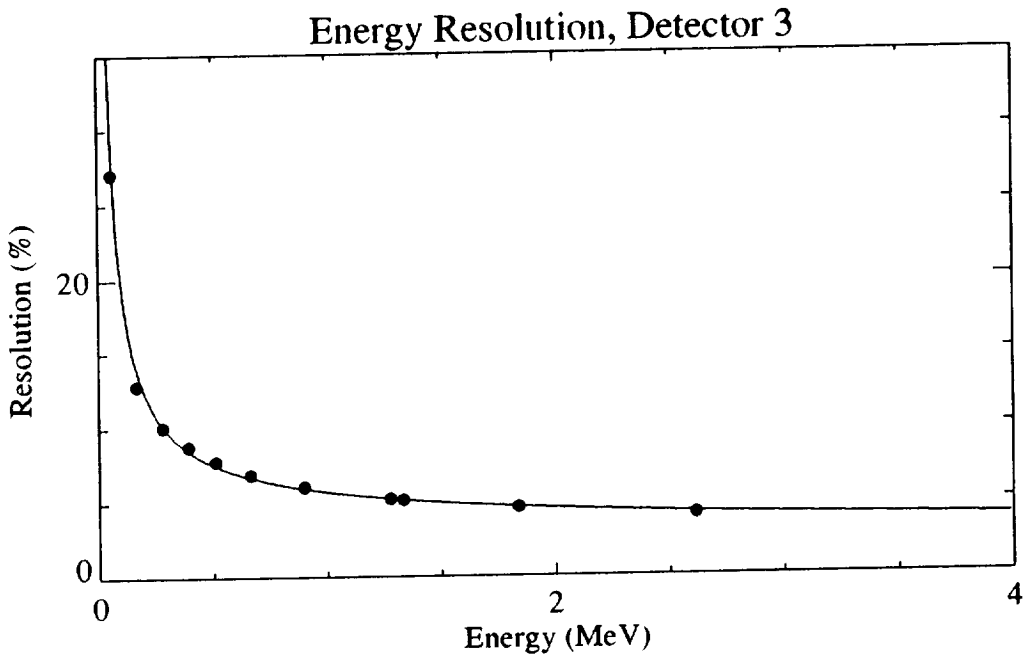

Figure 9: OSSE Energy Resolution

The basic data products obtained by processing a day of OSSE data are:

- OSSE telemetry, augmented with auxiliary data such as geomagnetic field and solar system barycenter vector.
- 2-minute Spectra (SDB), summed from raw OSSE spectra over each detector offset pointing, nominally 2 minutes long. Low, Medium and High energy spectra are included.
- Pulsar Data File, containing pulsar data plus OSSE pulsar mode and instrument configuration descriptors.
- ^{60}Co spectra (SDB), and associated line fit parameters. The ^{60}Co spectra are stored for both short (130 seconds) and long (1050 sec) integrations.
- Burst Data (SDB), containing the 4096 shield rate samples collected in response to a burst or solar flare trigger.
- 1-dimensional (energy) spectra and 2-dimensional (energy-shape) spectra (SDB) from selectable parts of each detector, through Calibration and Roving pulse height analyzers.
- Telemetry Scalar File, to record the time history of detector counting rates and other diagnostic and housekeeping information.
- Standard plot files, produced from the Telemetry Scalar File, for monitoring of instrument performance.
- Charged Particle Environment files, for tracking of spacecraft environment, used in analysis of instrumental background variations.
- Data quality information, observing statistics, database updates, etc.

Subsequent analysis of OSSE data is carried out asynchronously to receipt of the data and production of the above datasets. Combination of 2-minute spectra into longer periods of time is carried out using the higher level OSSE datasets such as background-subtracted spectra count and photon spectra that are derived from analysis of the above products.

Observing Strategies and Statistics

Given the wide range of the capabilities and data products of OSSE described in the previous sections, an overview of the considerations involved in the planning of observations for OSSE may be useful. Some major considerations are:

- Four programmable detector positioning tables are available, each providing up to 8 independent offset positions for each of the 4 detectors. The 8 offsets allow separate observations of closely spaced (a few degrees) sources or scanning observations of extended sources.
- Alignment of the collimator position angle may allow confusing sources to be separated, or enhance sensitivity for extended sources such as the galactic plane.
- Only the inner half of the detector scan range is accessible to four detectors. If a source is accessible with only two detectors, the other two may be used to observe another source simultaneously.
- Spectral data and pulsar data may be simultaneously collected from OSSE. However, because of limited telemetry bandwidth, larger amounts of pulsar data will require slower readout of spectral data. Typically, 16.384 second spectral accumulations allow a maximum pulsar EBE rate of 230 events/second.
- Eight energy windows are available for qualifying pulsar events, to restrict event rates. These windows may be shared between detectors, and in addition, pulsar data may be restricted to only on-target detectors, to prevent pulsar telemetry bandwidth being used for events from background offsets.
- The gain of the OSSE detectors may be varied. Observations have been carried out at double gain, to allow easier separation and measurement of spectral features at energies below 100 keV.
- OSSE provides a flexible response to BATSE triggers. In addition to collecting burst timing data, command sequences may be executed to provide additional responses to bursts or solar flares. For example, when the Sun is on or near the GRO XZ plane and accessible to the OSSE detectors, OSSE can be configured to slew the detectors to the Sun for a predefined duration, typically 1000 seconds, and to collect a variety of data products useful in studies of solar flares. Similarly, OSSE is configured to collect spectra from open shield segments in response to BATSE burst triggers, with the expectation that at least some of these spectra will capture the burst.

In conclusion, the configuration flexibility and multi-target capability of the OSSE instrument results in observing efficiencies of typically 70 - 100%, excluding time in the SAA. Therefore it is possible to achieve integration times of 500000 seconds per target in a 14 day observation.

References

Johnson, W.N., *et al.* 1989, "The Oriented Scintillation Spectrometer Experiment (OSSE) Instrument Description", in Proceedings of the GRO Science Workshop.

Kurfess, J.D., *et al.* 1989, "Scientific Objectives of the Oriented Scintillation Spectrometer Experiment", in Proceedings of the GRO Science Workshop.

Purcell, W.R., *et al.* 1991, "OSSE Spectral Analysis Methods and Techniques", in the Proceedings of the Second GRO Science Workshop.

Strickman, M.S., *et al.* 1989, "OSSE Data Flow and Analysis", in Proceedings of the GRO Science Workshop.

N92-21876

OSSE Spectral Analysis Techniques

W. R. Purcell*, K. M. Brown†, D. A. Grabelsky*, W. N. Johnson‡, G. V. Jung§
R. L. Kinzer‡, R. A. Kroeger‡, J. D. Kurfess‡, S. M. Matz*, M. S. Strickman‡, M. P. Ulmer*

ABSTRACT

Analysis of spectra from the Oriented Scintillation Spectrometer Experiment (OSSE) is complicated because of the typically low signal-to-noise ($\sim 0.1\%$) and the large background variability. The OSSE instrument was designed to address these difficulties by periodically offset-pointing the detectors from the source to perform background measurements. These background measurements are used to estimate the background during each of the source observations. The resulting background-subtracted spectra can then be accumulated and fitted for spectral lines and/or continua. Data selection based on various environmental parameters can be performed at several stages during the analysis procedure. In order to achieve the instrument's statistical sensitivity, however, it will be necessary for investigators to develop a detailed understanding of the instrument operation, data collection, and the background spectrum and its variability. A brief description of the major steps in the OSSE spectral analysis process will be described, including a discussion of the OSSE background spectrum and examples of several observation strategies.

INTRODUCTION

The OSSE instrument consists of four separate, nearly identical detectors. The primary detecting element of each detector is a large area NaI(Tl)-CsI(Na) phoswich crystal providing primary gamma-ray spectral capabilities over the energy range 0.05 – 10.0 MeV and secondary gamma-ray and neutron spectral capabilities at energies above 10 MeV. Passive tungsten collimators provide a field-of-view which is $3.8° \times 11.4°$ (FWHM), with the long direction of the collimators oriented parallel to the spacecraft Y-axis. Each detector has a separate elevation control system which provides independent positioning of the detectors about an axis parallel to the spacecraft Y-axis. During source observations, periodic background measurements are performed by offset-pointing the detectors from the source. Source and background measurements are typically alternated at two minute intervals, with backgrounds being sampled on each side of the source position along the instrument scan plane.

*Northwestern University, Evanston, IL
†George Mason University, Fairfax, VA
‡Naval Research Laboratory, Washington DC
§Universities Space Research Association, Washington DC

The primary data from the OSSE instrument consists of time-averaged energy loss spectra from the individual phoswich detectors. The time interval for these accumulations is in the range 4 – 32 seconds, depending on the operating mode of the instrument. After accumulation, these spectra are inserted into the spacecraft telemetry stream. As a part of the ground processing of the telemetry data, the OSSE spectra are summed into detector pointing intervals (typically two minutes) and stored in Spectrum Database (SDB) files. The SDB files are the primary medium for storage of all OSSE spectral data and related housekeeping and environmental information. These files typically contain: 1) an SDB header containing detailed information about the instrument configuration and environmental conditions during the spectral accumulation (e.g. detector position, temperature, geomagnetic cutoff rigidity, time since last SAA passage, data quality, etc.), 2) the spectral data and uncertainties, 3) PHA channel energies and widths, 4) calibration information (e.g. pulse-shape discrimination efficiencies), and 5) additional auxiliary information, as required. The spectra from each detector are accumulated and stored separately. A typical two-week observation of a single source consists of $\sim$ 20,000 spectra, requiring $\sim$ 40 MBytes of storage. A more detailed description of the OSSE data products can be found in Strickman *et al.* (1991). A detailed description of the OSSE instrument and its operation can be found in Johnson *et al.* (1989) and Cameron *et al.* (1992).

ANALYSIS SYSTEM

The primary OSSE data analysis system is the Interactive GRO/OSSE Reduction Environment (IGORE). The IGORE system was developed to provide an interactive scientific data analysis system for the reduction of OSSE data. The foundation of IGORE is the commercially available software package IDL (Interactive Data Language), which provides an interactive, programmable data manipulation language and application interface. Important additions to the native IDL capabilities include a simple interface mechanism for dynamically linking user written FORTRAN applications into the IGORE system and the support of IGORE structures which have been designed to minimize virtual memory requirements by allocating memory only as needed. IGORE also provides numerous applications to perform standard spectral analysis tasks. These applications are currently VAX/VMS FORTRAN specific and provide: 1) I/O access to OSSE data files, 2) access to OSSE Monte Carlo results and instrument response, and 3) the ability to move data between IGORE structures and local IDL variables. The IGORE system and applications were designed to retain the "look and feel" of IDL by providing similar command formats, interactive and batch programming capabilities, the ability to save/restore the analysis environment and associated data, and the option of journaling the user's analysis session. A more detailed description of the IGORE analysis system can be found in Grabelsky *et al.* (1991) and Strickman *et al.* (1991).

The primary method for manipulation of OSSE spectral data in IGORE is through an IGORE structure called a Spectral Data Record (SDR). The information in the SDR parallels that in the SDB file (e.g. SDB header, spectral data, uncertainties, channel

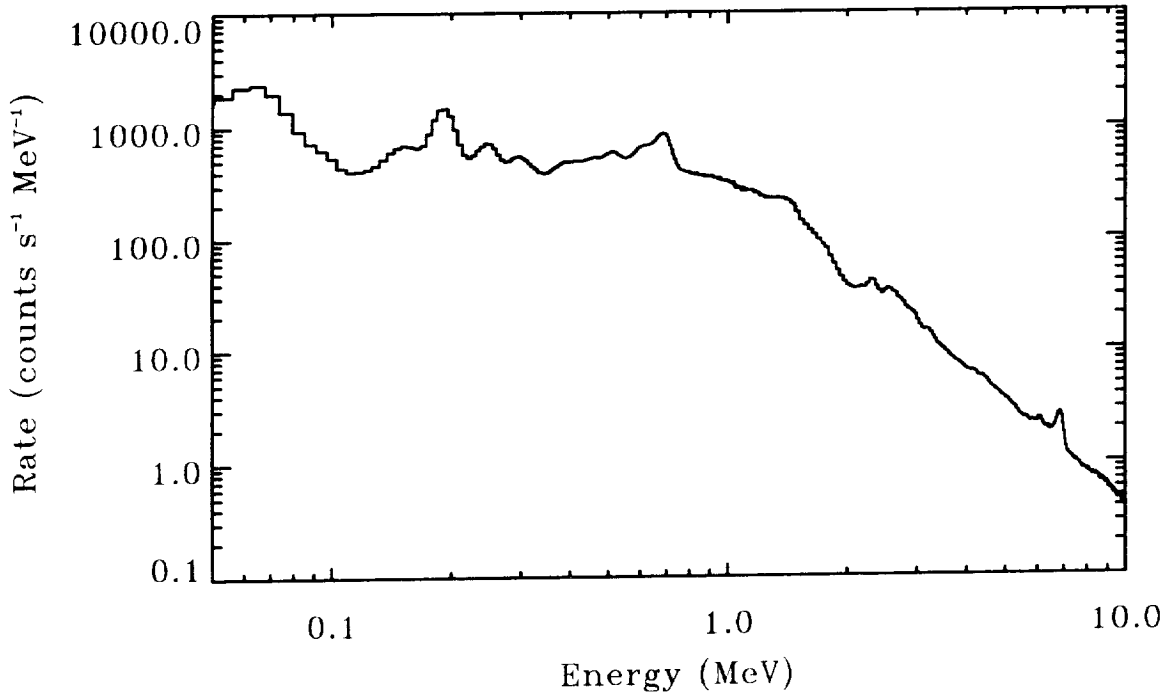

Figure 1: A typical OSSE background spectrum. The spectrum represents the average of all spectra accumulated on July 19, 1991 from a single detector. Both Low and Medium range spectral data are displayed, with overlap in the range 0.7 – 1.5 MeV.

energies, etc.). Because of the large amount of data which is typically required to perform spectral analysis, the SDR typically only contains a pointer to the data record in the associated SDB file; the data fields in the SDR are generally populated only as required during the analysis process. A brief outline of the major steps in the OSSE spectral analysis process is shown in Figure 5. These analysis tasks are all performed in IGORE and are designed to allow the user to analyze the data in an iterative fashion by returning to any of several earlier analysis steps and repeating the analysis with new parameters.

BACKGROUND SPECTRUM

Because OSSE samples the background by offset-pointing the detectors from the source, an understanding of the background spectrum and its variability is necessary to perform background estimation effectively. There are many sources of background line and continuum emission which affect space-borne gamma-ray detectors (see Dyer *et al.* 1980). An example of a typical OSSE background spectrum is shown in Figure 1. Numerous background lines and several continuum components are visible. Several aspects of the observed background spectrum, in particular the time variability of line and continuum components as it relates to OSSE background estimation, are discussed below. For a

detailed description and identification of background features in space-based gamma-ray scintillation detectors see Kurfess *et al.* (1989) and Share *et al.* (1989).

The dominant source of background is induced radioactivity resulting from particle interactions in the detector and surrounding material. Both cosmic-ray particles and particles trapped in the Earth's magnetic field contribute to the induced radioactivity. The dominant source of background from trapped particles is the passage of the spacecraft through the South Atlantic Anomaly (SAA), which occurs during $\sim 6 - 7$ orbits each day. The effects of cosmic-ray and SAA backgrounds vary over different time scales, depending on the modulation of the particles themselves and on the half-life of the induced radioactive species.

An example of the observed background time variability for two continuum window rates and for the background 511 keV line rate is shown in Figure 2. Also shown in this figure is the variation in the local vertical geomagnetic cutoff rigidity. Variation in the continuum rate at low energies is dominated by SAA induced radioactivities, as seen in the 1 – 2 MeV window rates. This is primarily due to the activation of ^{128}I in the phoswich crystal. The endpoint energy of the subsequent β-decay (half-life $\sim$ 25 minutes) is 2.1 MeV, producing a strong background continuum at lower energies. At energies above $\sim$ 2 MeV the relative amplitudes of the SAA and cosmic-ray induced components of the background continuum are similar, as seen in the 2 – 5 MeV window rates. These rates show a strong correlation with the local vertical geomagnetic cutoff rigidity. A similar correlation is seen in the fitted background 511 keV line rates.

The Earth's atmosphere and the spacecraft itself are also sources of gamma-rays, contributing to the background at energies above a few hundred keV because of the non-zero instrument response outside of the field-of-view at these energies. The offset-pointing method of background estimation may produce residual systematics at these energies because of the varying instrument response to the Earth's atmosphere during the source and background observations and because of the potential modulation of the spacecraft background due to the detector motion. The magnitudes of these effects have not yet been quantified.

OBSERVATION STRATEGIES

Before beginning to analyze OSSE spectral data, it is important to understand the positioning strategy which was used during the observation. The positioning strategy, which specifies the positioning of each detector separately, is defined by OSSE mission operations and uploaded into the instrument prior to the observation. The positioning strategy may consist of up to eight different observation positions for each detector.

An example of a simple OSSE pointing strategy is shown in Figure 3. In this example, background observations are located on each side of the source position and are separated

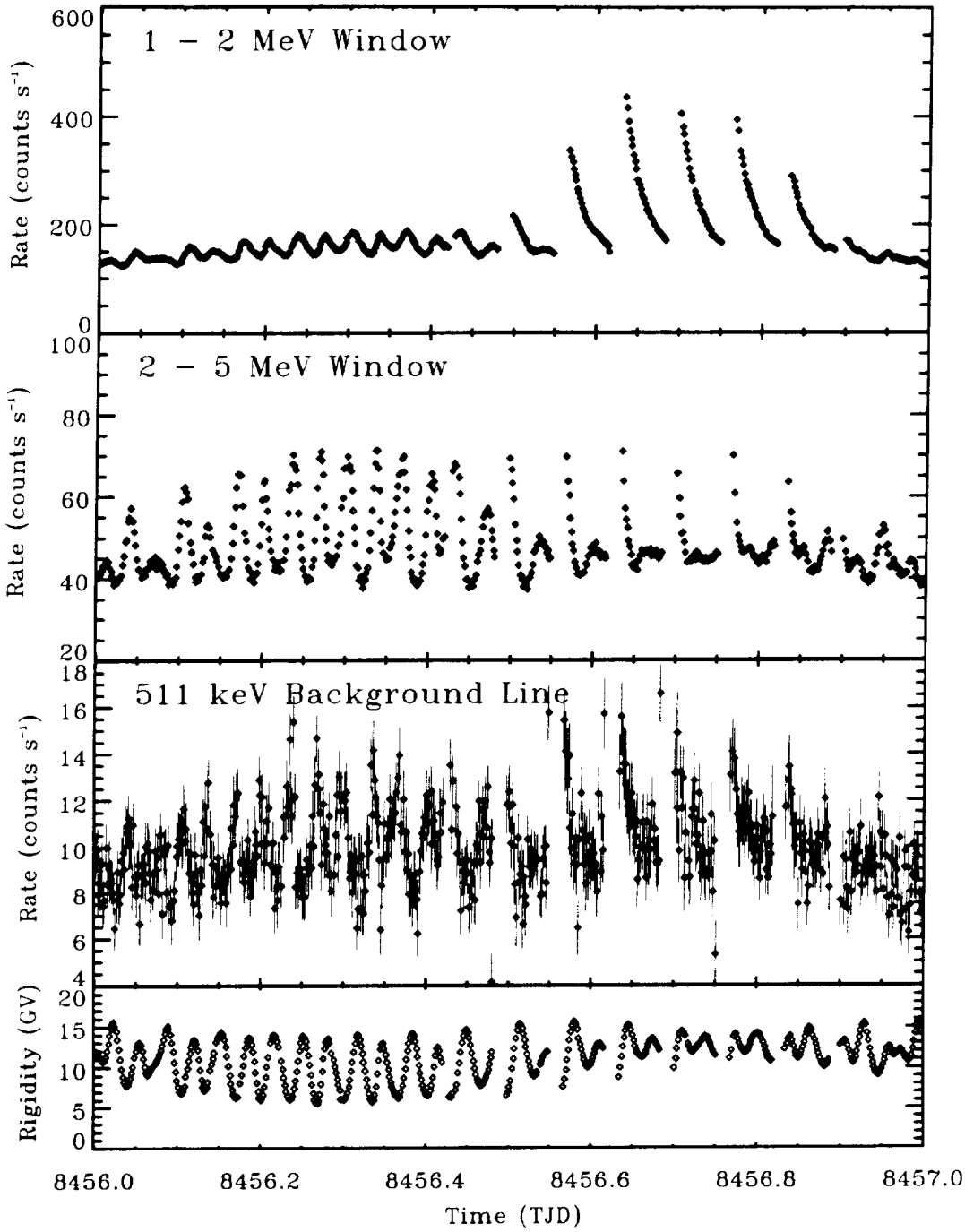

Figure 2: Observed temporal variations in background rates for two continuum windows and for the background 511 keV line. The data shown are from a single detector and were accumulated on July 19, 1991. Also shown is the variation of the local vertical geomagnetic cutoff rigidity. Missing data correspond to periods during which the spacecraft was passing through the SAA.

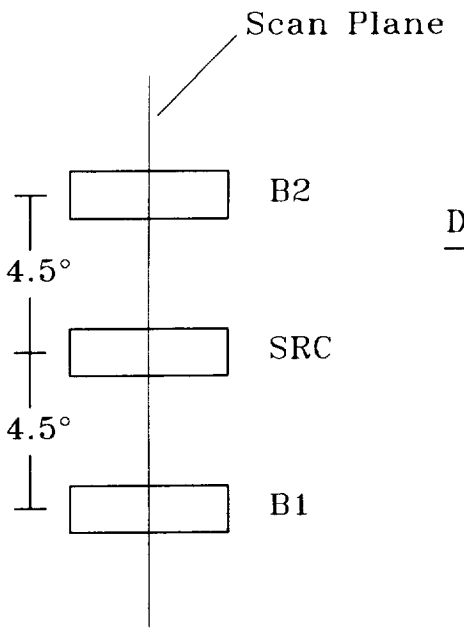

Observation Sequence

Det #1	Det #2	Det #3	Det #4
B1	B2	SRC	SRC
SRC	SRC	B2	B1
B2	B1	SRC	SRC
SRC	SRC	B1	B2

Figure 3: An example of a simple OSSE pointing strategy. The rectangles (not drawn to scale) represent the OSSE field-of-view for the source and background accumulations. The instrument scan plane corresponds to the spacecraft X–Z plane. A possible observation sequence for each detector is also given.

from the source position by 4.5°. This offset angle corresponds to the position of the first minimum of the angular response in the scan direction. Figure 3 also lists a typical observation sequence for each of the OSSE detectors. For each detector the accumulations alternate between source observations and background measurements. To reduce possible systematic effects, the sequencing of the source and background accumulations are different for each detector.

When performing observations in source-confused regions, or to generate a scan map of a region, a more complex pointing strategy may be required. An example of such a scan, used for an observation of the Galactic center region, is shown in Figure 4. In this example there are multiple source positions to provide a scan map of the region. The background observations are located on each side of the source positions and are separated from the central source position by 10° to minimize the possible residual response to diffuse emission. Figure 4 also lists one of the detector observation sequences used for this observation. For each detector the accumulations still alternate between source observations and background measurements, with the source position cycling between the central source position and one of the four outer source positions. As in the simple strategy described above, the sequencing of the source and background accumulations are different for each detector to

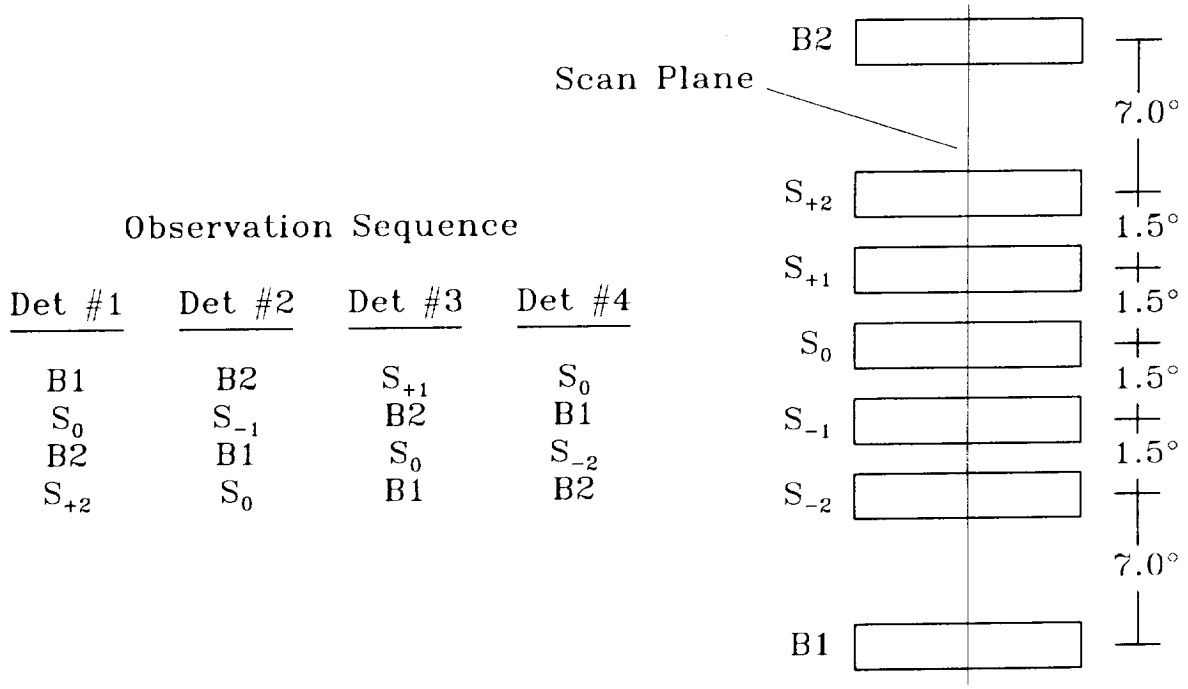

Figure 4: An example of a more complex OSSE pointing strategy. The rectangles (not drawn to scale) represent the OSSE field-of-view for the source and background accumulations. The instrument scan plane corresponds to the spacecraft X–Z plane. A possible observation sequence for each detector is also given.

reduce possible systematic effects.

While the two examples of observation strategies described above vary significantly in apparent complexity, the data collected from both may be analyzed in very similar ways. Much more complicated observation strategies may be constructed which use more than four of the eight possible detector positioning entries; however, care should be taken when constructing such strategies to ensure that the resulting data are analyzable.

SPECTRAL ANALYSIS

The OSSE spectral analysis is based on the concept of an Analyzable Unit (AU). An AU consists of a single source spectrum and a set of background spectra from one or more of the background offset positions. An AU may consist of spectra from a single detector only. The specified background spectra are used to estimate the background during the source observation. The number of background spectra required depends on the complexity of the background estimation model. In the simplest case (see Figure 3) an AU might consist of a source spectrum and two background spectra, one accumulated before and the other after

the source observation. The background estimation model in this case might merely be a linear interpolation in time between the two background spectra. Because the observations alternate between source and background measurements, the same background spectrum may be be used to estimate the background for more than one source observation.

The major steps required to analyze OSSE spectral data are shown in Figure 5. The entire analysis procedure is performed in IGORE and, in general, each step consists of only one or two IGORE commands. The first step consists of identifying the SDB files containing the data to be analyzed and determining the positioning strategy used for the observation. Initial data selection is then applied to these data. This selection is performed using the IDL WHERE function and is based on information stored in the SDB header associated with each spectrum. The initial selection criteria are generally constructed to exclude data having poor data quality (e.g. telemetry or positioning errors) or data accumulated during times in which the source was occulted by the Earth. Additional data selection criteria based on other SDB header variables (e.g. environmental parameters) may also be applied.

Next, the AU definition must be specified and applied to the spectra passing the initial data selection. Since the AU definition may restrict the types of background estimation models which can be applied, the background estimation model should be determined before specifying the AU definition. Both the AU definition and the spectra passing the initial data selection are input to an IGORE application which searches the spectra for valid AU's. The output of this application is an array of SDR's, one element for each valid AU, which contain pointers to the spectra making up each AU.

The SDR array containing the valid AU's is then input to an IGORE application which performs the background estimation and background subtraction. Background estimation and background subtraction is performed for each valid AU separately. The background estimation is assumed to be linear in the measured background spectra:

$$\tilde{B}(j) = \sum_{i=1}^{N_{spec}} A_i B_i(j) \tag{1}$$

where N_{spec} is the number of background spectra in the AU, i is the background spectrum number and j is the spectrum channel number. The coefficients A_i are determined by unweighted polynomial interpolation over one or more selected parameters, assuming no energy dependence. The currently supported interpolation parameters are time and detector step angle (scan angle). Interpolation including other parameters (e.g. rigidity, time from last SAA passage, etc.) may also be supported, as required. The resulting background-subtracted spectrum and uncertainties are written to an output SDB file. One background-subtracted spectrum is written for each valid AU. Also written to this SDB file is a set of pointers to the spectra forming the AU, the AU definition used to identify those spectra, the estimated background spectrum and uncertainties, the A_i coef-

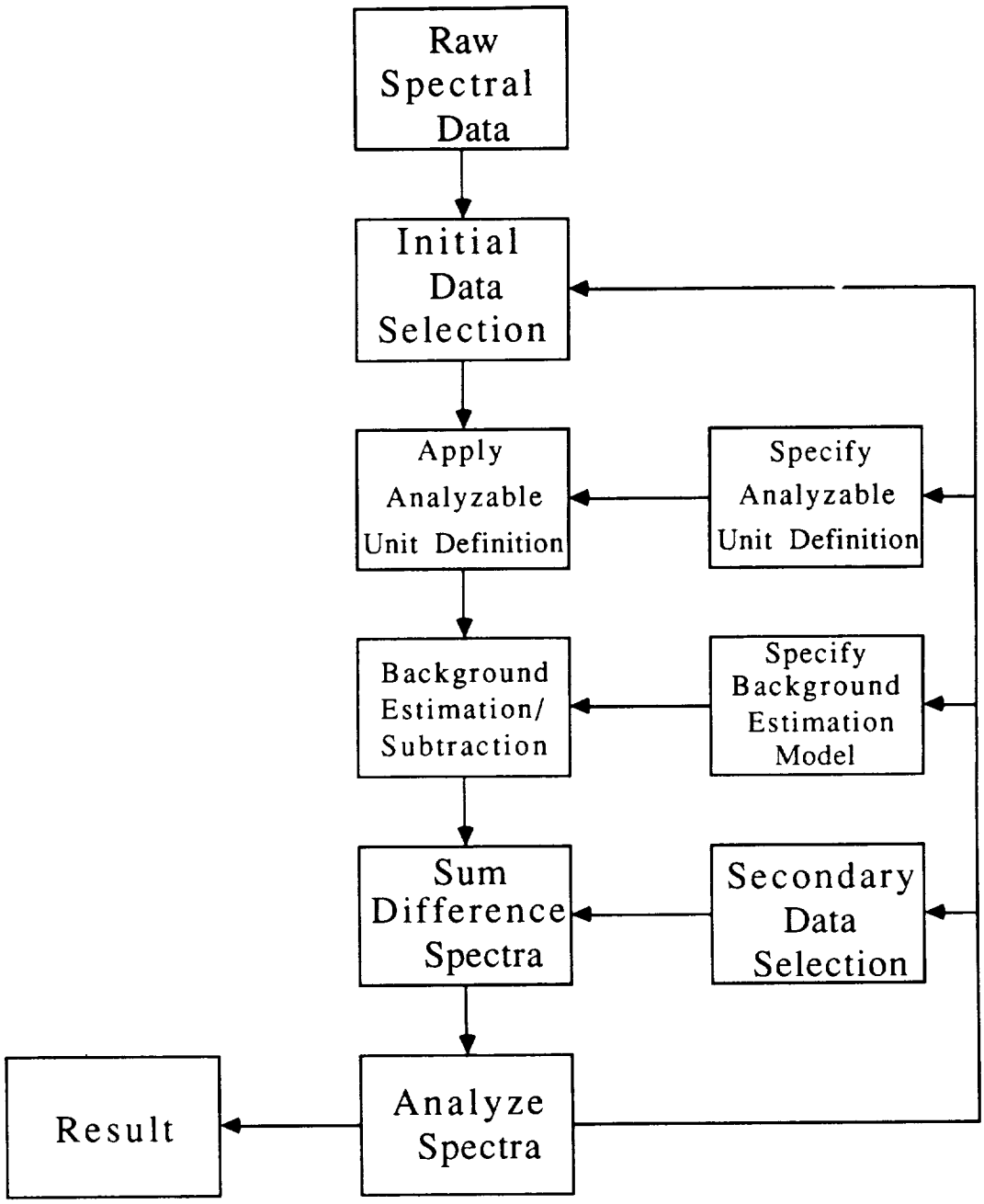

Figure 5: An outline of the major steps required to perform OSSE spectral analysis.

ficients used to estimate the background spectrum, and a complete SDB header containing the environmental parameters for the difference spectrum.

After the background subtraction has been performed, improved sensitivities are achieved by summing the individual difference spectra. Secondary data selection criteria may be applied to the difference spectra prior to summing. Like the initial data selection, the secondary data selection is performed in IGORE using the IDL WHERE function. The selection is again generally performed on SDB header variables, but the criteria are typically constructed to remove systematics in the spectrum caused by variations in the background which may not have been accurately modeled in the background estimation process. Typical secondary data selection criteria might impose limits on environmental parameters such as rigidity, time from last SAA passage, Earth zenith angle, and anti-coincidence shield rates. Difference spectra passing the secondary data selection criteria are then summed separately for each detector. The propagation of the uncertainties in the summed spectra includes the covariance caused by the multiple use of some background spectra. The A_i coefficients are also summed for use in generating the instrument response matrix.

An important aspect of the spectral analysis process is the identification and minimization of residual systematic features in the summed difference spectra. Residual features will be generated if there are systematic errors in the background estimation model. Such residual systematics may be reduced either by identifying and removing from the summed difference spectra those data accumulated during periods when the systematics in the background estimation model occur, or by developing new background estimation models. The current data analysis has typically been performed using a simple linear background estimation model which interpolates in time between two background spectra and with no environmental data selection. For standard two-week OSSE observations this method appears to produce relatively clean spectra with few residual background line features, though background continuum residuals are seen at energies below $\sim$ 2 MeV. Difference spectra produced over shorter periods (e.g. one-week intervals) appear to show stronger residual line features, suggesting that these background residuals may "average out" over a complete two-week observation during which many of the various orbital environmental conditions are sampled. Appropriate data selection on environmental parameters and/or more detailed background estimation models will likely reduce the residual line and continuum features significantly.

The summed difference spectra may then be fitted for spectral lines and/or continua. When fitting for the parameters of spectral lines alone, the summed difference spectra may be fitted directly. Fitting the spectrum for continua, however, requires spectral deconvolution. The only method of spectral deconvolution currently supported is forward-folding. Spectral deconvolution requires an instrument response matrix for each detector pointing position used in the AU. The instrument response matrices are generated from the results of Monte Carlo simulations of the OSSE detectors and the A_i coefficients associated with the summed difference spectrum. When using the forward-folding deconvolution

method, a model for the incident photon spectrum is selected and folded through the instrument response matrices. The resulting model spectrum is then compared with the data and the model parameters modified to achieve the best fit. The resulting estimate of the incident photon spectrum is model dependent, however.

CONCLUSION

OSSE spectral analysis is complicated because of the typically low signal-to-noise ($\sim 0.1\%$) and the large background variability. The OSSE instrument was designed to address these difficulties by offset-pointing the detectors from the source to perform periodic background measurements. In order to analyze OSSE spectral data effectively and achieve the statistical sensitivity, it will be necessary to develop a detailed understanding of the background spectrum and its variations. IGORE, the OSSE spectral analysis system, has been designed to provide the ability to perform detailed studies of the background spectrum and to use the OSSE offset-pointed observations to perform spectral analysis of astrophysical sources. New analysis methods may also be incorporated into the IGORE system, as required.

REFERENCES

Cameron, R. A., *et al.*, 1992, these proceedings.

Dyer, C. S., Trombka, J. I., Seltzer, S. M., and Evans, L. G., 1980, *Nucl. Instr. Meth.*, **173**, 585.

Grabelsky, D. A., *et al.*, 1991, in *Proceedings of the Fourth International Workshop on Data Analysis in Astronomy*, in press.

Johnson, W. N., *et al.*, 1989, in *Proc. of the GRO Science Workshop*, ed. W. N. Johnson, p. 2–22.

Kurfess, J. D., *et al.*, 1989, in *Proceedings of the Conference on High Energy Radiation Background in Space*, ed. A. C. Rester, Jr. and J. I. Trombka, (AIP Conference Proc. 186)(New York:AIP), p. 250.

Share, G. H., *et al.*, 1989, in *Proceedings of the Conference on High Energy Radiation Background in Space*, ed. A. C. Rester, Jr. and J. I. Trombka, (AIP Conference Proc. 186)(New York:AIP), p. 266.

Strickman, M. S., *et al.*, 1991, in *Proceedings of the Fourth International Workshop on Data Analysis in Astronomy*, in press.

The BATSE Experiment on the Compton Gamma Ray Observatory: Status and Some Early Results

G.J. Fishman, C.A. Meegan, R.B. Wilson,
NASA Marshall Space Flight Center

W.S. Paciesas, G.N. Pendleton
University of Alabama in Huntsville

for the BATSE Science Team

Abstract

The Burst and Transient Source Experiment (BATSE) on the Compton Gamma Ray Observatory is a sensitive all-sky detector system. It consists of eight uncollimated detectors at the corners of the spacecraft which have a total energy range of 15 keV to 100 Mev. The primary objective of BATSE is the detection, location and study of gamma-ray bursts and other transient sources. The instrument also has considerable capability for the study of pulsars, solar flares and other discrete high energy sources.

The experiment is now in full operation, detecting about one gamma-ray burst per day. A brief description of the on-orbit performance of BATSE is presented, along with examples of early results from some of the gamma-ray bursts observed.

Description and Scientific Objectives

The Burst and Transient Source Experiment (BATSE) consists of eight uncollimated detector modules arranged on the corners of the Compton Gamma Ray Observatory to provide the maximum unobstructed view of the celestial sphere. Each detector module contains a large-area detector (LAD), optimized for sensitivity and directional response, and a spectroscopy detector (SD) optimized for broad energy coverage and energy resolution. The eight planes of the large-area detectors are parallel to the faces of a regular octahedron. The three primary axes of the octahedron are parallel to the three principal axes of the spacecraft, as shown in figure 1. This provides nearly uniform sky coverage and produces an inherent symmetry in various aspects of the data analysis.

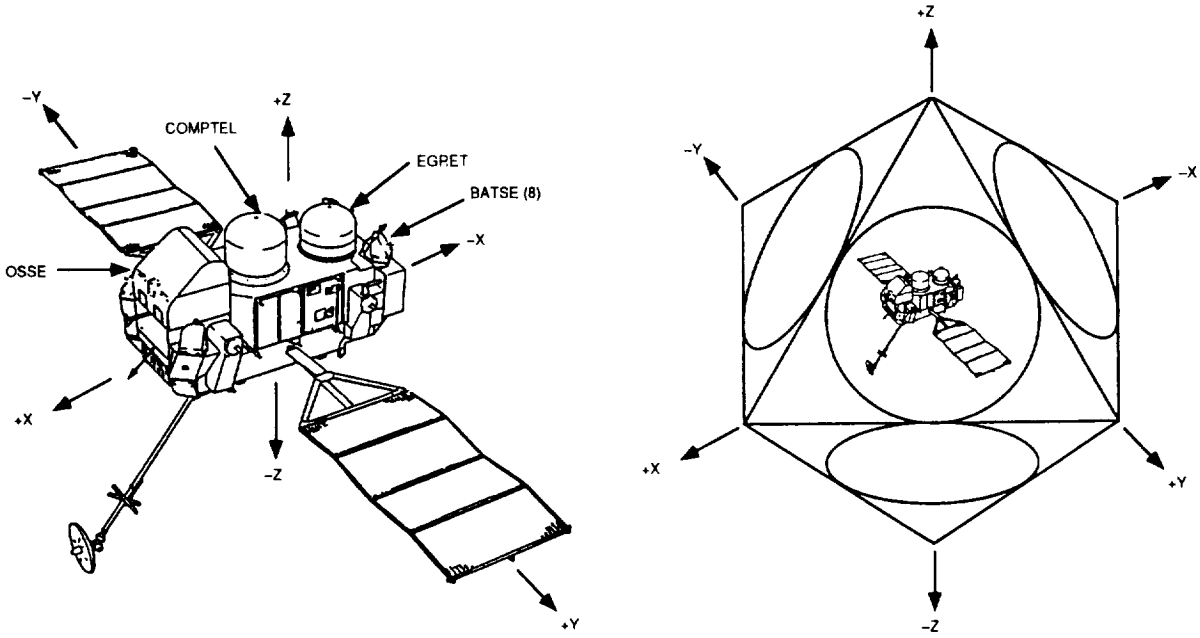

GAMMA RAY OBSERVATORY

BATSE DETECTOR ASPECT

Figure 1. The location and aspect of the eight BATSE detectors on the Compton Gamma Ray Observatory.

Table 1

	BATSE DETECTORS	
	LARGE AREA	SPECTROSCOPY
Material:	NaI(Tℓ)	NaI(Tℓ)
Frontal Area:	2,025 cm^2	127 cm^2
Thickness:	1.27 cm	7.62 cm
Energy Range:	30 – 1900 keV	15 keV – 110 MeV*
Energy Resol.:	27% @ 88 keV typ.	7.2% @ 662 keV typ.
		*Detector gain dependent

The basic characteristics of the two types of detectors are given in Table 1. A more comprehensive description of the instrument is given in several papers included in the first GRO Science Workshop (Fishman et al 1989a,b; Paciesas et al 1989; Pendleton

et al 1989), and in a recent report (Horack 1991). A detailed paper on instrumentation and calibration is currently in preparation (Fishman et al 1992). The BATSE data system is a versatile and complex system. Data from the detectors are sorted on-board into 14 data types with different temporal and spectral resolution. Some data types are continuously transmitted according to a preprogrammed schedule, while other, higher time resolution data are accumulated from on-board triggered gamma-ray bursts. The data recorded from a burst require the duration of the following orbit, about 93 minutes, to unload the experiment burst memory. A summary of the characteristics of the data types are contained in the references above.

BATSE is expected to provide the most sensitive observations of gamma-ray bursts yet obtained. The more significant features of BATSE include: the ability to obtain the locations of weak bursts; the ability to detect spectral features and rapid spectral variations in many bursts, and the ability to provide burst locations to the scientific community quicker than previously possible. The celestial distribution and intensity distribution of hundreds of weak gamma-ray bursts, unobtainable with previous instrumentation, may finally provide the distance scale for gamma-ray bursts. BATSE will also be able to provide long-term and frequent monitoring of hard x-ray and low energy gamma-ray emission from the stronger sources, including transients, pulsating sources and solar flares.

On-Orbit Performance

All eight detector modules have been operating well since the experiment high voltage was turned on April 24, 1991. Considerable progress has been made in the determination of the on-orbit energy calibration, atmospheric scattering contributions and the detector response matrices (Pendleton et al, 1992; these proceedings). The background in the large area detectors above 30 keV varies between approximately 3000 and 6000 counts/s per detector during most portions of the orbit. Often, usually above geographic latitudes of about 24 degrees, the spacecraft encounters regions of enhanced background radiation due to precipitating electrons. During these times, bremsstrahlung from these electrons increases the background considerably and many times produces false burst triggers (Horack and Fishman 1991). The BATSE operations team has been successful in eliminating many of these false triggers by pre-determining the regions of high background and disabling the on-board burst trigger system at the appropriate times. Other sources of false burst triggers include

solar flares and large increases in background radiation around the region of the South Atlantic Anomaly, especially during periods when the magnetosphere is disturbed.

During undisturbed times, the background radiation at energies between 30 keV and 100 keV is dominated by the diffuse x-ray background and discrete sources. Thus, the detector background is sensitive to the ratio of the earth/sky in the field of view, as well as which sources are in the field of view. At energies above 100 keV, the primary source of background is due to cosmic ray secondaries and is closely coupled to the geomagnetic latitude. The background shows an increase of approximately a factor of three twice per orbit at the high latitudes compared to that near the equator. At these energies, the counting rate is relatively insensitive to the detector aspect with respect to the earth.

Gamma-ray Burst Observations

The criteria for the on-board trigger of a gamma-ray burst are given in Table 2. During undisturbed times, the rate of gamma-ray bursts has averaged about one per day. The rate of false triggers increases to as much as six or eight per day during times of high solar activity or when the earth's magnetosphere is disturbed. During these times the apparent rate of real gamma-ray bursts decreases due to the reduction of the trigger efficiency, since the trigger threshold is increased until the burst data are read out over the next orbit.

Table 2

BATSE — Burst Trigger Criteria

- Trigger energy range : 60-300 keV
- 3 timescales tested : 64, 256, 1024 ms
- 5.5 σ increase above 17s background rate
- 2 or more detectors required to trigger

A few examples of the variety of gamma-ray bursts observed since launch are shown in Figures 2,3, and 4, and discussed in the captions. Detailed temporal and spectral analyses of gamma-ray bursts are underway. The results of these analyses will be presented in publications and presentations in the coming months.

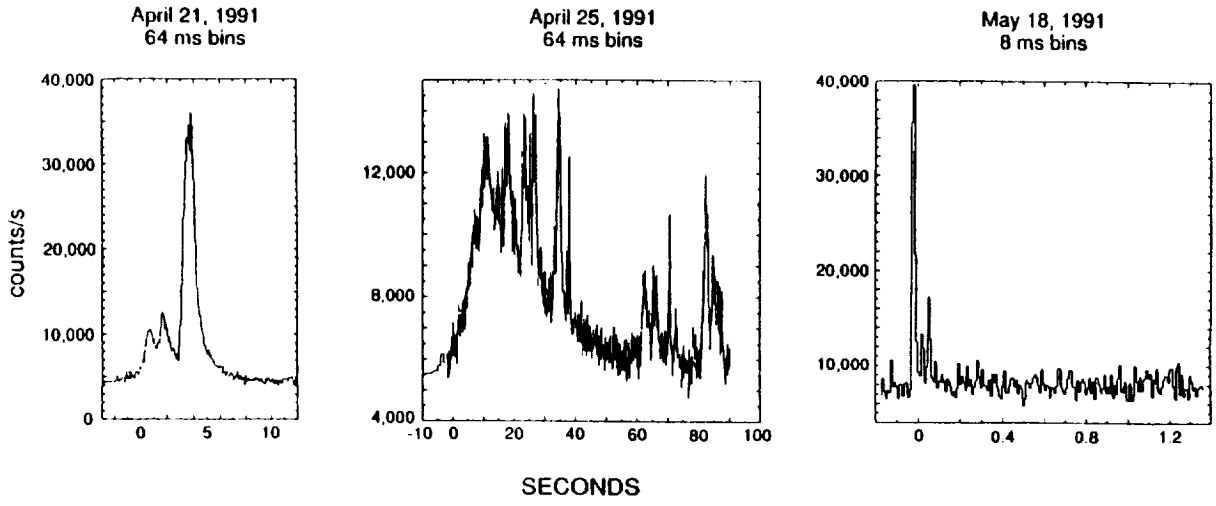

Figure 2. A sample of the wide variety of time profiles observed by BATSE. Burst durations have ranged from 8 ms to over 500 s. This figure illustrates three of the many types of time profiles that have been seen. The energy range of counts in these plots is 60 keV to 300 keV.

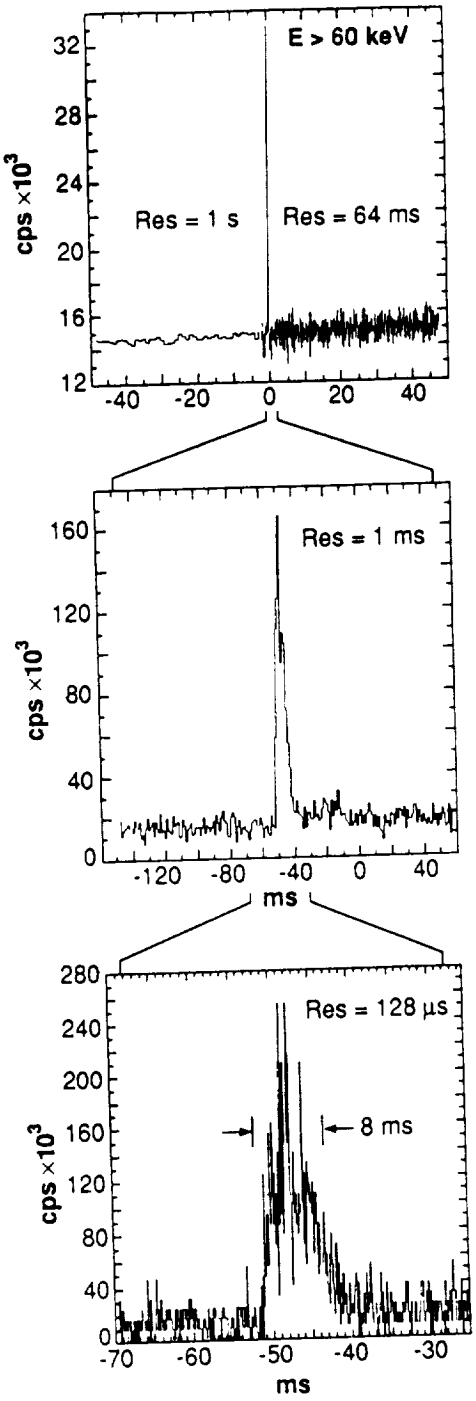

Figure 3. The shortest gamma-ray burst seen thus far (GRB 910711). The FWHM is 8 ms in this energy range. The burst is shown on three different time scales, with the time resolution indicated.

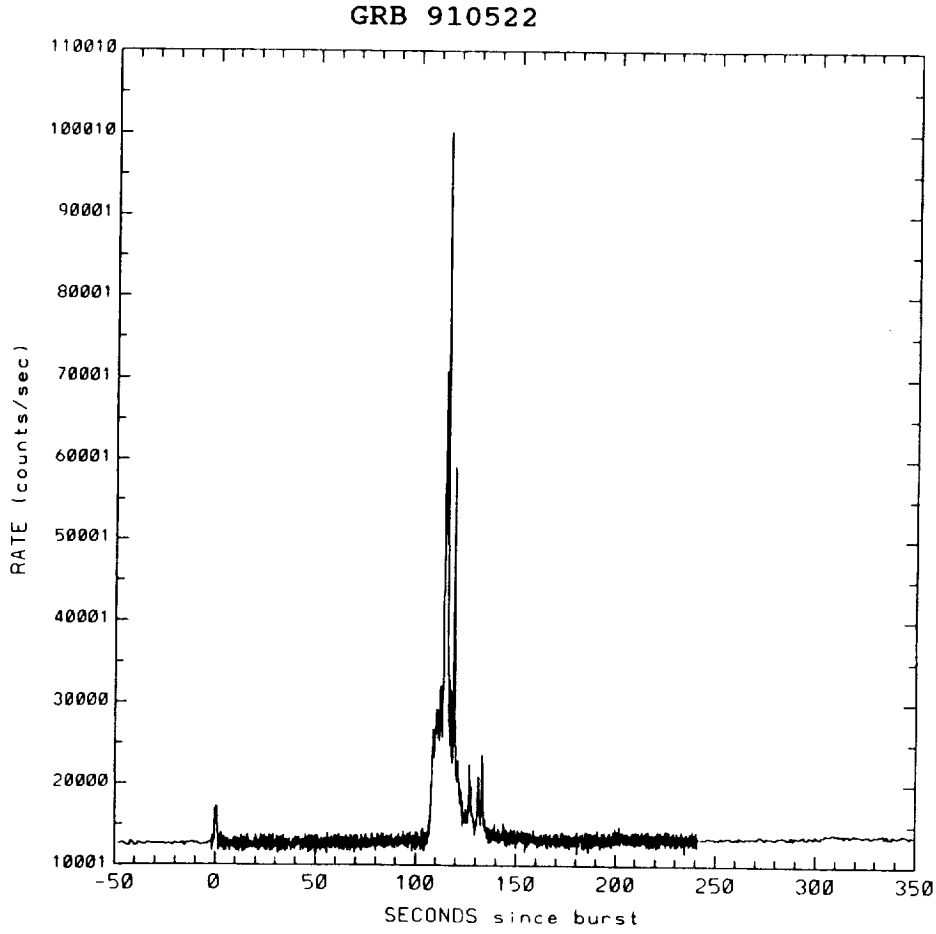

Figure 4. An unusual gamma-ray burst with a weak precursor occurring 110 s before the main part of the burst emission. Previous burst experiments would have missed this precursor or could not have determined that it was from the same location as the main part of the burst.

Perhaps the most dramatic and unexpected observation made by BATSE thus far is the isotropy of the distribution of gamma-ray bursts. From recent burst experiments on other spacecraft, as well as from the initial BATSE measurements of the frequency of gamma-ray bursts verses their intensity, it is apparent that the sources of gamma-ray bursts are spatially confined. The most widely assumed source of the confinement was thought to be the Galactic plane. The observed isotropy indicates that the gamma-ray bursts are not confined to the Galactic plane, and in

fact, may not be due to Galactic objects. The explanation of this observation is not presently known and is currently the subject of intense speculation. Two exciting possibilities are that: 1) The gamma-ray bursts are coming from objects, probably neutron stars, in an extremely large, and previously undetected, spherical Galactic halo, or 2) They are coming from some unknown objects at cosmological distances. These observations were reported in an IAU Circular (Meegan et al 1991), and at a gamma-ray burst Workshop in Huntsville in October. They will also be published soon in Nature (Meegan et al 1991).

Other Early Results

The analysis of early BATSE observations of hard x-ray pulsars, other discrete sources, and solar flares is proceeding well. The high sensitivity and all-sky viewing of the BATSE detectors is expected to provide new data on many of these objects. These GRO Workshop Proceedings contain a sample of some of these early results. The reader is referred to BATSE papers in these proceedings with the following lead authors: R.B. Wilson, B.A. Harmon, M. Finger, C. Kouveliotou, and R.A. Schwartz.

The BATSE experiment supports an active Guest Investigator Program. Several of the GRO Phase One Guest Investigators have been heavily involved with various aspects of BATSE data analysis. We look forward to continued collaborations with guest investigators in succeeding phases of the Compton Gamma Ray Observatory Guest Investigator Program.

References

Fishman, G.J., C.A. Meegan, R.B. Wilson, W.S. Paciesas, T.A. Parnell, R.W. Austin, J.R. Rehage, J.L. Matteson, B.J. Teegarden, T.L. Cline, B.E. Schaefer, G.N. Pendleton, F.A. Berry, Jr., J.M. Horack, S.D. Storey, M.N. Brock, and J.P. Lestrade"BATSE: The Burst and Transient Source Experiment on the Gamma Ray Observatory", GRO Science Workshop Proceedings, p.2-39, GSFC (1989a).

Fishman, G.J., C.A. Meegan, R.B. Wilson, W.S. Paciesas, T.A. Parnell, J.L. Matteson, B.J. Teegarden, T.L. Cline, G.N. Pendleton, and B.E. Schaefer, "The Burst and Transient Source Experiment (BATSE) Scientific Objectives and Capabilities", GRO Science Workshop Proceedings, p.3-47, GSFC (1989b).

Horack, J.M., "Development of the Burst and Transient Source Experiment (BATSE), NASA Reference Publication No. 1268 (1991).

Horack, J.M. and G.J. Fishman, "BATSE-GRO Observations of Bremsstrahlung from Electron Precipitation Events", NASA Tech. Memo. TM-103546 (1991).

Meegan, C.A., G.J. Fishman, R.B. Wilson, W.S. Paciesas, M.N. Brock, J.M. Horack, G.N. Pendleton, and C. Kouveliotou, "Gamma-ray Bursts", IAU Circular No. 5358, October 4 (1991).

Meegan, C.A., G.J. Fishman, R.B. Wilson, W.S. Paciesas, M.N. Brock, J.M. Horack, G.N. Pendleton, and C. Kouveliotou, "The Spatial Distribution of Gamma ray Bursts Observed by BATSE", Nature, submitted (1991).

Paciesas, W.S., G.N. Pendleton, G.J. Fishman, C.A. Meegan, R.B. Wilson, M.N. Brock, F.E. Roberts and B.E. Schaefer, "The BATSE Data Analysis System and Implementation of the Guest Investigator Program", GRO Science Workshop, p.2-89, Proceedings, GSFC (1989).

Pendleton, G.N., W.S. Paciesas, J.P. Lastrade, G.J. Fishman, R.B. Wilson, and C.A. Meegan,"The BATSE Detector Response Matrices", GRO Science Workshop Proceedings, p.4-547, GSFC (1989).

Long-term Source Monitoring with BATSE

R. B. Wilson,[1] B. A. Harmon,[1] M. H. Finger,[2]
G. J. Fishman,[1] C. A. Meegan,[1]
W. S. Paciesas[3]

ABSTRACT

The uncollimated BATSE large area detectors (LADs) are well suited to nearly continuous monitoring of the stronger hard x-ray sources, by use of Earth occultation for non-pulsed sources, and time series analysis for pulsars. An overview of the analysis techniques presently being applied to the data are discussed, including representative observations of the Crab Nebula, Crab pulsar, and summaries of the sources detected to date. Results of a search for variability in the Crab Pulsar pulse profile are presented.

1. Introduction

The full-sky, uncollimated field of view of the BATSE detectors, which is required to provide its burst observation and localization capabilities, also enables observations of objects with deterministic source variability, either due to intrinsic source periodicities, or via sampling of source intensity by Earth occultation. The pre-launch estimated sensitivity of both techniques may be found in Fishman *et al.* (1989). Although these sensitivities are much less than that of OSSE, the fact that these observations may be made frequently throughout the GRO mission are expected to add greatly to the understanding of the stronger low-mass and high-mass x-ray binaries, by determination of correlations between intensity states, $\dot{p}$ values, and pulse profile variations.

2. Occultation Method

The analysis method presently being applied to the BATSE data on a daily basis is as described by Fishman *et al.* (1989). The details of the method, with an evaluation of sensitivity currently being obtained, along with observations of an outburst from

[1]Space Science Laboratory, NASA/Marshall Space Flight Center
[2]Astronomy Programs,Computer Sciences Corporation
[3]Department of Physics and Center for Space Plasma and
Aeronomic Research, University of Alabama in Huntsville

Monitored Occultation Source Candidates

Source Name	Det.	Source Name	Det.
1E1024-57		Cen X-3	
3C279		Cyg X-1	*
4U0115+634		Gal. Ctr. Region	*
4U1700-37	*	GX301-2	*
A0535+26		GX339-4	*
Aql X-1		Her X-1	
Crab Nebula	*	Sco X-1	*
Cen A	*	Vela X-1	*

Table 1. Data have been routinely searched for the listed sources since the beginning of science operations. Emission has been detected from locations consistent with these source directions for those objects marked by an "*".

GX339-04 are presented in Harmon *et al.* (1991). Large Area Detector (LAD) data with 2.048 s time resolution and 16 energy channel resolution are always available for each detector (the CONT data type). A simple linear model of the background is applied at the known times of occultation of a candidate source, with the step amplitude determined by the fit.

2.1. Analysis Status

Two programs are run daily on the LAD CONT data type. Intensity and coarse spectral histories are being maintained on ~30 sources that are either measurable on that timescale, or are previously known transient sources which may be expected to flare during the lifetime of GRO. Table 1 lists a sample of the objects, with those that have exhibited significant fluxes identified. The association of the emission with the indicated objects is based on the consistent spectral indices obtained for them, the careful exclusion from the measurements of occultations when other sources are present elsewhere on the limb of the Earth, and observed source periodicities in some cases.

Additionally, a search is made for significant step-like features that occur at times different from the expected sources. To date, no new sources have been detected.

A measure of the systematic errors in these measurements is obtained by daily measurements of the Crab Nebula region. Figure 1 shows a time history of the source flux for an interval during which the GRO pointing was fixed. The BATSE values are within 10% of previous measurements (Jung, 1989) . The best fit to that data was a broken power law, while the present analysis uses a single power law over the indicated range. This is, in part, the reason why the BATSE measurement is somewhat higher. Additionally, atmospheric scattering is not presently a component of the detector response matrices that have been used. While the scattering geometry at times of source occultation is not the most severe

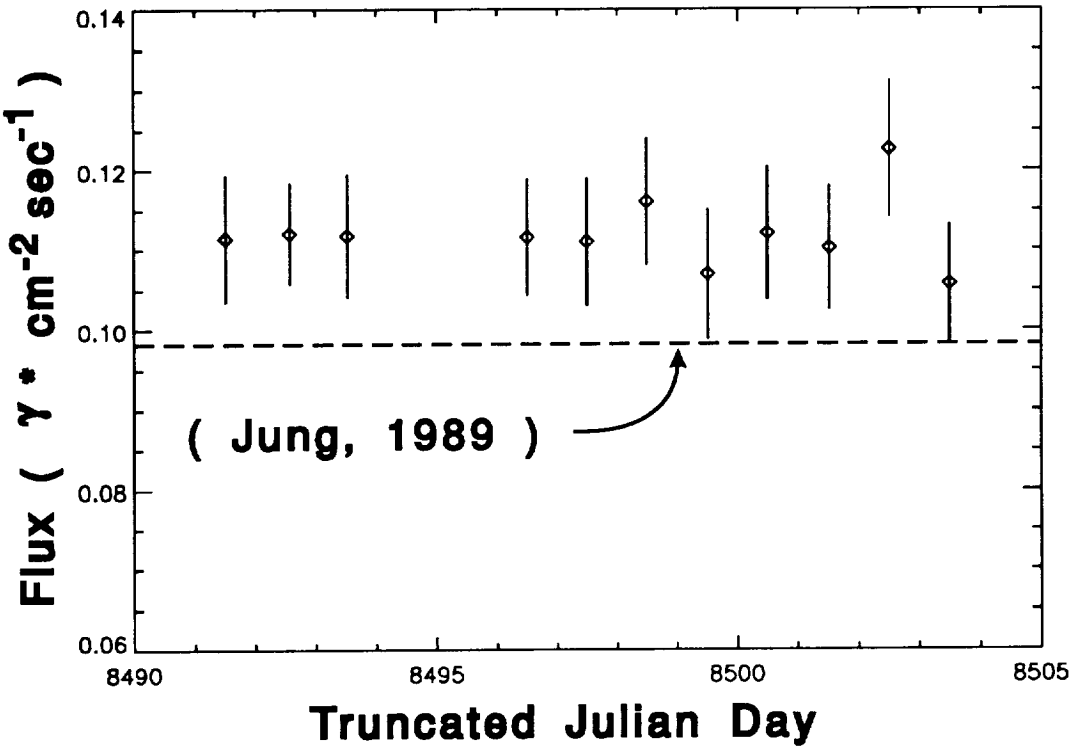

Figure 1. Time history of the Crab Nebula flux obtained using the occultation method. The photon flux has been computed by folding a single power law model spectrum through the BATSE LAD detector response matrices. The integrated spectrum of Jung *et al.* (1989) is shown for comparison.

case, it may produce a significant increase in the apparent source intensity.

With the present, simple model of the background, and the limited integration times used before and after the source emersion/immersion, a source ~10% as strong as the Crab Nebula is detectable in data summed over 1 day. Background modeling studies that are in progress are expected to permit much weaker sources to be monitored.

A representative Crab count spectrum obtain by the BATSE LADs for a 2 week GRO pointing is shown in Figure 2.

3. Pulsed Source Analyses

With the nearly 2π steradian viewing of each LAD, BATSE represents a significant resource for monitoring pulsating objects. The data types useful for this purpose are listed in Table 2. The integration times listed are principally limited by the solar and magnetospheric disturbances to the data on the day(s) to be utilized. During the present high solar activity, major portions of the dataset are undesirable, due to counting rate disturbances which would produce artifacts for any pulse profiles obtained.

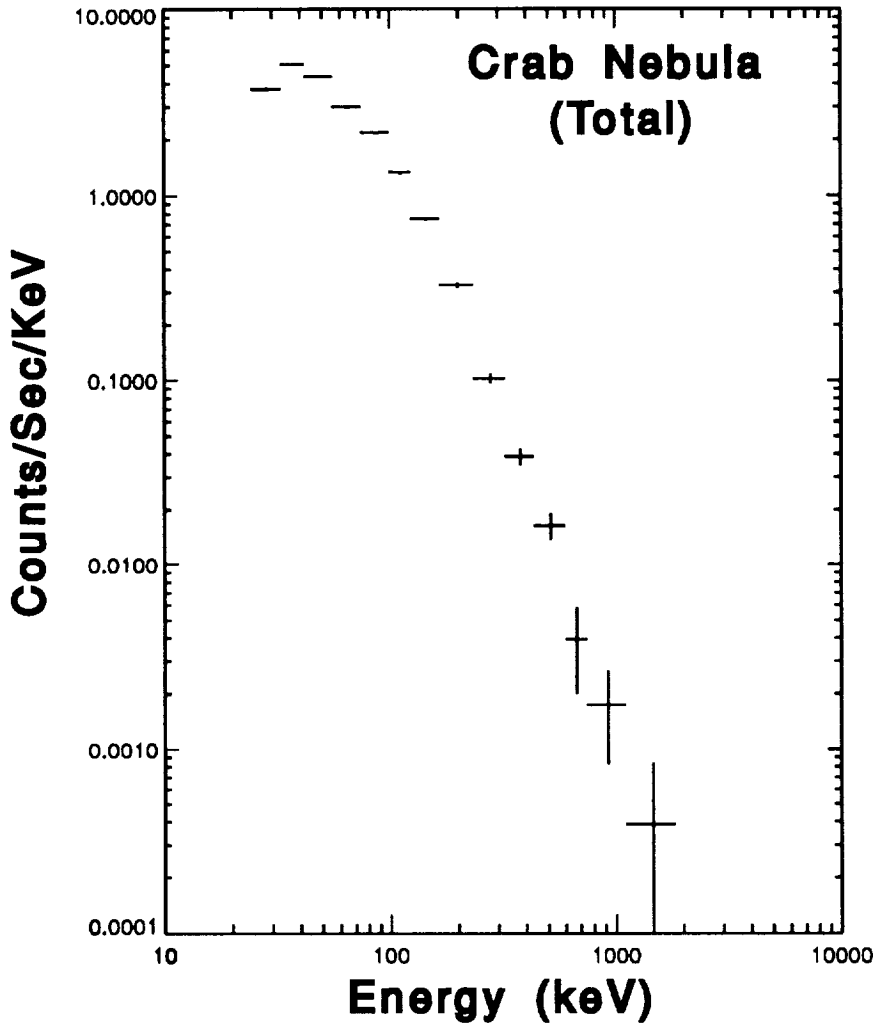

Figure 2. Count spectrum of the Crab Nebula total flux, for a single 2-week GRO viewing interval from Truncated Julian Day (TJD) 8490 to 8504.

3.1. Long-Period Sources

For pulsed sources which can be adequately measured using ~1s time resolution, the BATSE data are especially well suited. As indicated in Table 2, 4 energy channel data with 1.024s time resolution and 16 energy channel data with 2.048s time resolution are continously available for each LAD, except during the South Atlantic Anomaly. This makes it possible to search for periodic signals in the dataset without any need for advance planning.

Analysis tools based on oversampled FFT analysis of DISCLA data which have been filtered in both time and frequency domains are being developed by Guest Investigators T. Prince & J. Grunsfeld . Analysis is performed on each LAD detector individually, and also on appropriate combinations of detectors, to optimize viewing for all regions of the sky.

Pulsed Source Data Types			
Data Type	Time Bins	Energy Chls.	Daily Int. Time
DISCLA	1.024 s	4	50k - 80k s
CONT	2.048 s	16	50k - 80k s
PSRn	Period/64	16	10k - 20k s (Per Source)

Table 2. BATSE data types useful for pulsed source analysis. PSRn data types, which provide readouts of data folded on-board at the approximate period of interest, must be scheduled in advance. Present usage provides data for 4-6 objects per GRO viewing period.

To date, data for about 18 days have been processed as part of this software development effort. In that limited set of data, the following sources have been detected: Her X-1, 4U0115+63, Cen X-3, 4U1627-67, OAO1657-41, GX 1+4, Vela X-1, and GX301-2. Daily processing of the data with this tool has recently begun.

An independent analysis has been performed by Finger *et al.* (1991) of Cen X-3, using both DISCLA and on-board folded data.

The strongest x-ray binary objects are readily observed as signals with amplitudes several percent of the background counting rate in the raw telemetry data. For these objects, direct epoch-folding of the DISCLA or CONT data is a satisfactory analysis method if data from times of events with rapid time variations from unrelated processes are removed. These variations can be produced by gamma-ray bursts, electron precipitation events, solar flares, and phosphorescense events from high-Z cosmic ray interactions. To avoid artifacts in the pulse profiles from more subtle background variations, it is planned in the future to use data that have been "cleaned" as part of the FFT analysis mentioned in the previous section.

An observation of Vela X-1 during an ~8000 s long outburst is shown in Figure 3, demonstrating the BATSE capability to provide high-quality measurements of the emission state of moderate-to-bright sources on a *continuous* basis, except for times of Earth occultation.

3.2. Short-Period Sources

For periods that cannot be observed using the above data types, BATSE operates two controllers in its Central Electronics Unit (CEU), which can be scheduled to fold 16 energy channel data at the approximate observed period of an object, to the nearest microsecond, from a selectable subset of LADs or SDs. The sensitivity for the LADs is shown in Figure 4, based on an amount of data typical for a 2-week GRO pointing.

Since data from several detectors may be combined before on-board folding, it is necessary for the detector gains to be balanced (this need exists also for BATSE's burst location

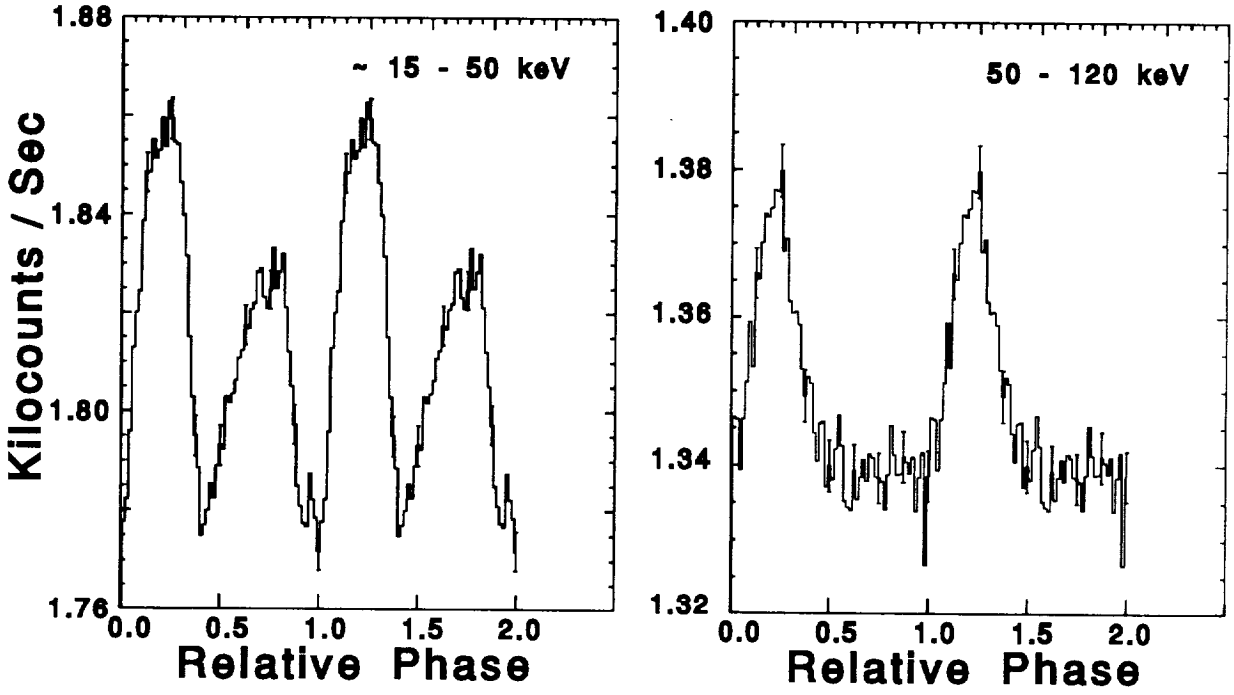

Figure 3. Pulse profile for Vela X-1, during a flaring episode on TJD 8432 for two different energy ranges.

technique). Gain is controlled on-board by locating the atmospheric 511 keV line in each LAD spectrum readout, typically obtained every 5 minutes. Individual detector gains are stable over 100 days or more to about 1%; gain balance is best near the calibration energy (within 2%), degrading to ~8% at 130 keV, still better than the intrinsic energy resolution at that of energy of about 30%.

3.2.1. Pulsar Hardware Usage

Since the sensitivity of BATSE is much less than that of OSSE for energies greater than OSSE's threshold energy of ~60 keV, it is not the best use of the BATSE on-board pulsar controller to search for γ-ray emission from candidate short-period radio pulsars. The ability of BATSE to perform such a search for any GRO orientation is not expected to be of benefit for this type of object, since they would not be expected to have strong amplitude variations over time. The most suitable usage is to frequently monitor the brighter objects, with sufficient exposure to provide spectral information for those sources. The on-board exposure obtained for Cen X-3, analyzed by Finger *et al.* (1991), is just sufficient for spectral analysis when the source is about 10% of the Crab pulsed flux. Thus, the number of objects which can be monitored with this data type is limited. Any object with a period suitably measured using the CONT data can obtain a much longer integration time with that data type. Table 3 lists the sources for which data have been collected to date. While it is

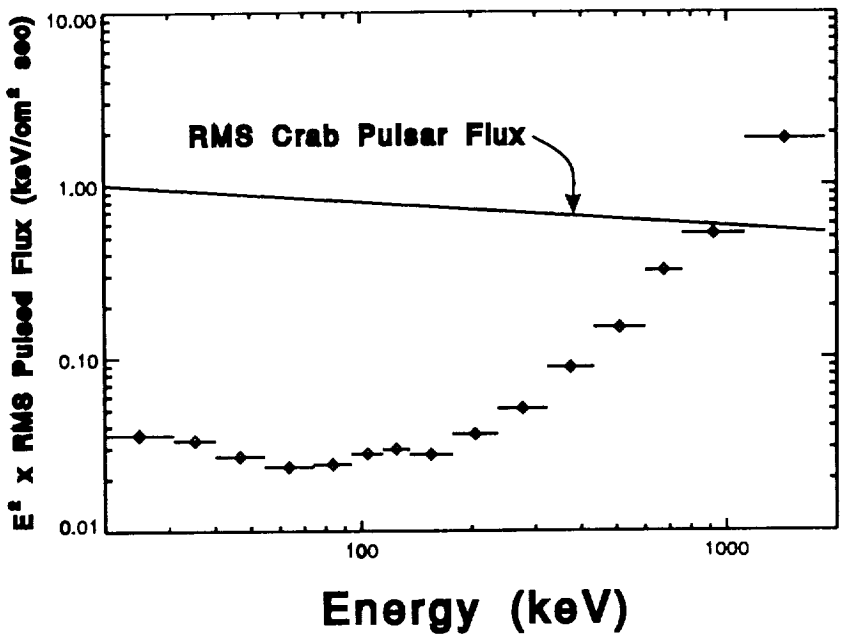

Figure 4. Pulsed source detection efficiency of the BATSE LADs for a 100,000 s exposure time. This sensitivity applies to both on-board and ground folded data, for a pulsar with a Crab-like pulse profile

possible to select the Spectroscopy Detectors (SDs) for on-board folding, it is usually more advantageous to utilize the LADs, due to their much larger area. The SDs have sensitivity above 1 MeV (Fishman *et al.* , 1989) just adequate to monitor a source as bright as the Crab pulsar.

4. Crab Pulsar Analysis

Data collected for the Crab pulsar consist of 8.192 s time integrations (243 folding periods, typically 33392 μs) for 16 energy channels, with 64 phase bin resolution. The start time of the accumulation is time-tagged using the on-board GRO clock, latched and stored to an accuracy of 1/64 ms. The absolute time specification for that clock is better than 0.1 ms. Using the JPL DE200 ephemeris and the GRO position (known to better than 30 km), the Solar system barycenter (SSB) arrival time of the midpoint of the accumulation is determined. Using the source ephemeris provided by Taylor *et al.* (1991), the phase is determined for each of the 64 bin boundaries, centered on the midpoint accumulation time (*i. e.* , the accumlated counts are treated as if they were all obtained during the central "fold"). The counts are then summed in 64 phase bins fixed in the SSB, with counts split linearly between those bins if the input bin phase edges span adjacent bins.

An example of the obtained pulse profile is shown in Figure 5, and is consistent with previous observations of the Crab, as found by Mahoney *et al.* (1984) and Wilson *et al.*

BATSE Pulsed Source Obseravations
Folded-on-Board Data Obtained

Source Name	Det.
Crab Pulsar	*
Vela Pulsar	
Cen X-3	*
SMC X-1	
Her X-1	*
(1957+20)	
(4U0115+63)	

Table 3. List of objects for which BATSE folded-on-board pulsar data has been obtained. Approximately equal exposures have been obtained for all sources except for those in parentheses, which were only present in the schedule for one viewing period. All objects are NOT viewed within every GRO viewing period.

(1983).

The first peak appears to be somewhat softer than the second. A counts spectrum for the two peaks is shown in Figure 6, and shows that this difference is only marginally significant.

4.1. Pulse Profile Variability Search

A search was made on a 0.25 day timescale for variations in the pulse profile of the Crab pulsar for all data obtained on that source from TJD 8370 - 8504. A 64-bin template was formed by minimizing χ^2 bin-by-bin over a large set of average-subtracted 0.25 day profiles, for 4 integrations over energy independently, since the pulse shape is not constant over energy. Since the energy edges of the 16 channels were changed on TJD 8405, and the radio ephemeris for the source was fit separately after that date, the analysis was done in two parts, divided at that date.

In a given energy channel, for the *kth* 0.25 day interval, phase bin i contains $C_k(i)$ counts. A χ^2 statistic, χ^2_E, is formed,

$$\chi^2_E = \sum_{k,i} (C_k(i) - M_k - \alpha_k \cdot T(i))^2 / \sigma^2_k(i) \equiv \sum_k \chi^2_k,$$

where M_k is the mean counting rate for interval k over all phase bins i, $T(i)$ is a template formed by minimizing χ_E for each bin i, obtaining in the process a set of amplitude coefficients, α_k.

Since the phase bins are not independent, due to the splitting of counts between bins, the χ^2 distribution is not that normally obtained. The mean value per degree of freedom (dof) is approximately 2/3. The distribution expected has been computed, taking this

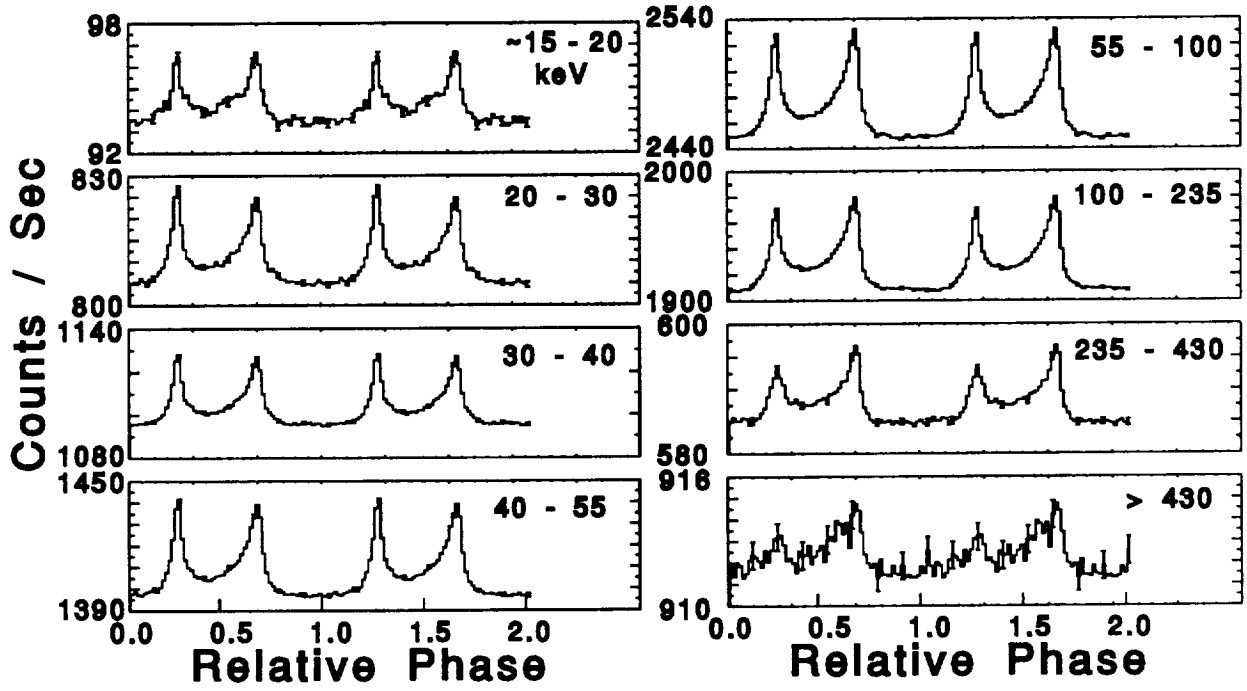

Figure 5. Pulse profile for the Crab Pulsar obtained for a 2-week GRO pointing from TJD 8490 to 8504, for the indicated energy ranges. The integration time for this exposure was 144,800 s. The data were combined on-board for two detectors, at angles of 34° and 54° from the detector normals.

into account. For data from TJD 8370 - 8405, no significant departures from the expected distribution are observed. Figure 7 shows a time history of the observed χ^2/dof for TJD 8406 - 8504. The histogram of these values is shown in Figure 8, along with the expected distribution. In each of the lower 3 energy intervals, there appear to be significant departures from the mean template. The contributions to χ^2_k are found to be primarily from the rising and falling edges of both peaks in the pulse profile.

Given the large viewing angle of the BATSE detectors, it is likely that atmospherically scattered contributions to the pulse shape are the cause of these variations. The time delay for source photons that scatter from as far away as the limb of the Earth are delayed by about 7 ms from those directly incident. While the observed falltime after the second pulse of about 1.5 ms demonstrates that scattering is not a large contributor to the signal, it may be sufficient to produce these small variations.

Data for the Crab are always obtained starting near the same point in inertial space, which represents different geometries relative to the Earth's atmosphere over the course of the precession period of about 52 days. The broad feature between TJD 8420 and 8470 may thus also be an indication of atmospheric scattering effects.

Another potential cause of pulse profile shape changes is the variety of exposure angles to the detectors used to observe the source over this interval. Since the spectral differences over phase for this source are not large, this is thought to be a less important contributor

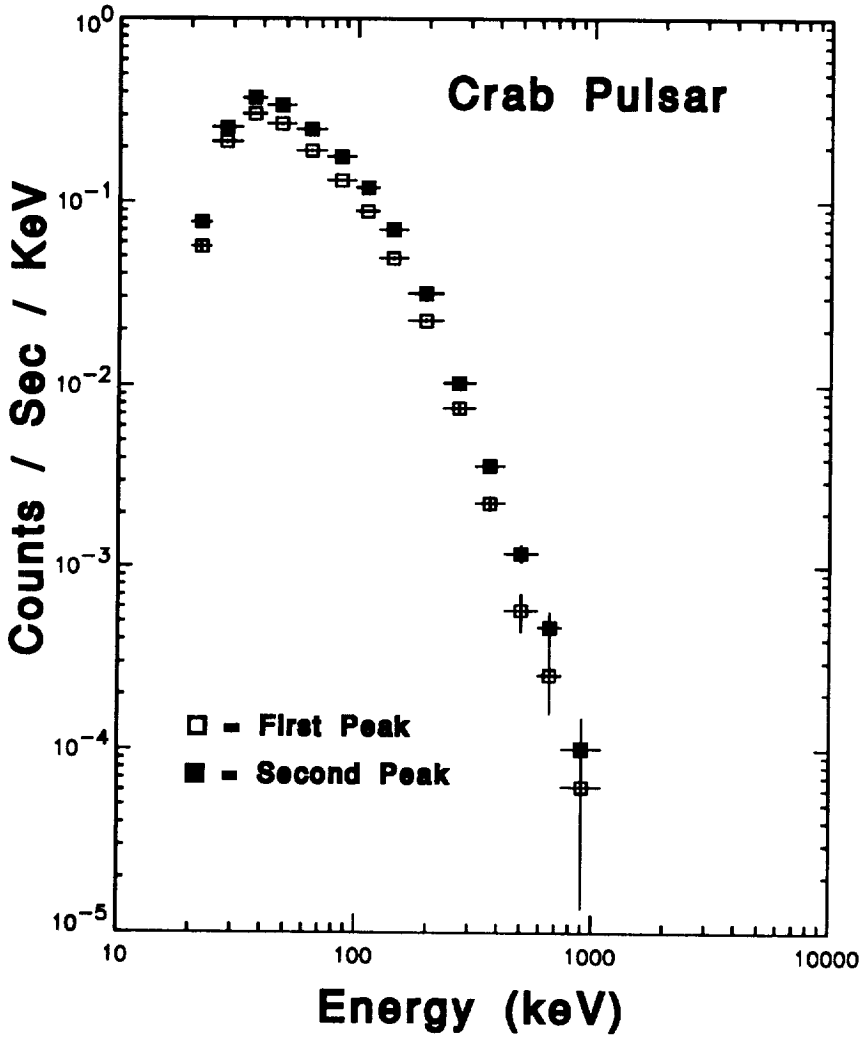

Figure 6. Count spectrum of the Crab pulsar for TJD 8490 to 8504. Peak 1 is defined as phases 0.19 to 0.38; peak 2 as phases 0.50 to 0.69, relative to zero phase as shown in Figure 5.

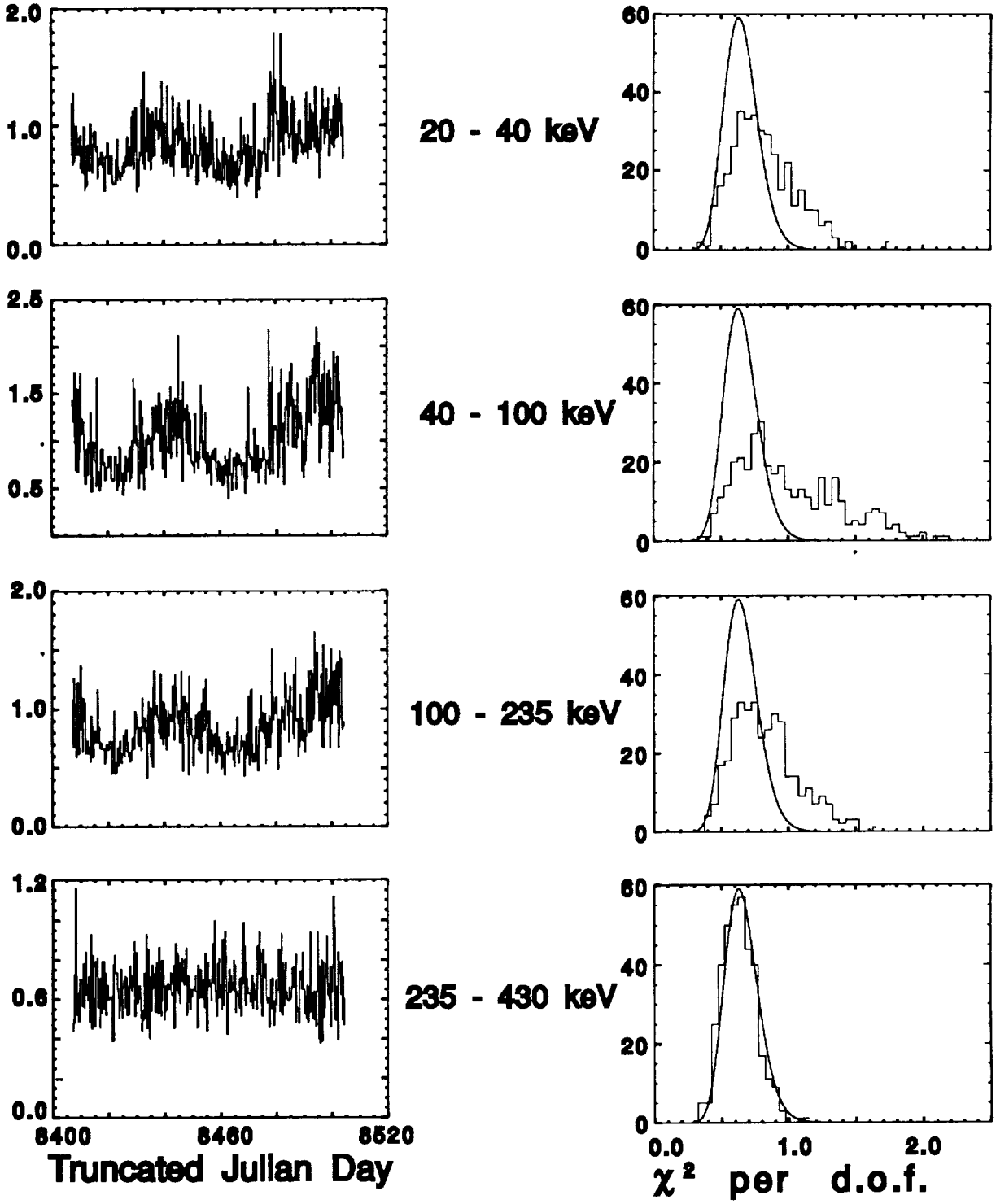

Figure 7. Time history of χ^2_k per dof for each 0.25 day interval, for departures from a best-fit template derived from the data. The abscissa is the χ^2 value.

Figure 8. Histogram of χ^2 per dof. The smooth curve is the expected distribution. The abscissa is the number of intervals with the indicated value of χ^2.

to the observed χ^2 behavior.

5. Summary

The measurements included here, along with those in Harmon *et al.* (1991) and Finger *et al.* (1991) , clearly demonstrate that BATSE represents a considerable resource for near-continuous monitoring of moderately strong hard X-ray sources. This capability is a useful complement to the more sensitive OSSE pointed observations, and has already been used to advantage in the decision to alter the GRO viewing schedule to observe GX339-4.

ACKNOWLEDGMENTS

The development and operation of the Burst and Transient Source Experiment is the result of the efforts of many people at the Marshall Space Flight Center and contractor facilities. We are especially grateful to the following individuals for dedicated support of the project: B. J. Schrick, J. D. Ellsworth, R. W. Austin, J. R. Rehage, F. A. Berry, Jr. , J. M. Horack, and S. D. Storey.

The software system used to archive and process the data also represents a large investment of effort by dedicated people. The work of K. Babine, M. N. Brock, L. Gibby, K. J. Hladky, R. Hunt, K. Majumdar, P. Moore, R. Newman, and G. Pendelton.

REFERENCES

Fishman, G. J. , Meegan, C. A. , Wilson, R. B. , Paciesas, W. S. , Parnell, T. A. , Matteson, J. L. , Teegarden, B. J. , Cline, T. L. , Pendelton, G. N. , and Schaefer, B. E. 1989 *Proceedings of the Gamma Ray Observeratory Science Workshop*, Goddard Space Flight Center, April 10-12 1989, Johnson, W. N. , ed., p.3-47.

Finger, M. H. , Wilson, R. B. , Meegan, C. A. , Paciesas, W. S. , and Fishman, G. J. 1991, *"Monitoring Cen X-3 with BATSE"*, these proceedings.

Harmon, B. A. , Wilson, R. B. , Finger, M. H. , Paciesas, W. S. ,

Fishman, G. J. , and Meegan, C. A. 1991, *" Occultation Analysis of BATSE Data - Operational Aspects"*, these proceedings.

Jung, G. V. 1989 *Ap. J*, **338**, 972.

Mahoney, W. A. , Ling, J. C. , and Jacobson, A. S. 1984 *Ap. J*, **278**, 784.

Taylor, J. H. 1991, private communication.

Wilson, R. B. , and Fishman, G. J. 1983, *Ap. J.*, **269**, 273.

PRELIMINARY CALIBRATION RESULTS FOR THE BATSE INSTRUMENT ON CGRO

G. N. Pendleton, W. S. Paciesas, G. J. Fishman, R. B. Wilson, C. A. Meegan,
F. E. Roberts, J. P. Lestrade, J. M. Horack, M. N. Brock, M. D. Flickinger
BATSE Science Team

ABSTRACT

Preliminary results pertaining to spectral reconstruction using BATSE Large Area Detector measurements of solar flares will be presented. These solar flare measurements are currently being used to fine tune the calibration of our data analysis software. The current status of the stability of spectral analysis given the systematic errors present in burst location at the time of the writing of this paper discussed. A brief description of enhancements to the input data for the atmospheric scattering algorithm that will be implemented in the data analysis software is presented.

SOLAR FLARE SPECTRAL MEASUREMENTS

Power law fits to a strong solar flare occurring May 30 th at 09:37 UT using large area detector continuous data are presented here in order to show the variability in spectral intensity encountered when coping with location errors of 5°. The current solar flare location accuracy averages about 5°. Spectra are calculated for a location on the sun and for a set of four locations around the sun about 5° away from the sun position. At each location the detector response matrices (DRM's) are evaluated for each of the three brightest detectors. The response depends primarily on the angle between the source direction and the detector normal. For this flare the angles between the sun direction and the first, second, and third detectors are 34.4°, 53.1°, and 61.43° respectively. These angles change for the locations offset from the sun by 5° hence the corresponding DRM's generated at these locations are different. The fits are performed for 6 continuous channels covering the energy range 63-203 keV. The channel to energy conversion is most reliable in this range currently and the flare intensity is significant here as well.

Figure 1 shows power law fits to the data in the brightest detector convolved through the detector response matrix for that detector evaluated at each of the five assumed source directions. The spread in spectral intensity of 13% is due to the differences in the DRM's. Figures 2 and 3 show the same set of fits to the second and third brightest detectors respectively. The spread in intensity for these fits is 27% for the second brightest detector and 27% for the third brightest detector.

Figure 4 shows power law fits to the three brightest detectors' data convolved through the DRM's simultaneously. This gives the best fit to the total data set for each assumed flare location. The spread in spectral intensity for these fits is 5%. These fits are subject to the least variability due to the fact that as one moves the apparent source location some detectors see the flare more directly while others see it less directly. For a set of three detectors these effects tend to cancel out resulting in a fairly stable measurement of the source intensity over a 5° range in assumed source direction. As systematic errors in the

detector response are identified and eliminated the errors on source location will decrease producing a corresponding decrease in the systematic errors in spectral analysis.

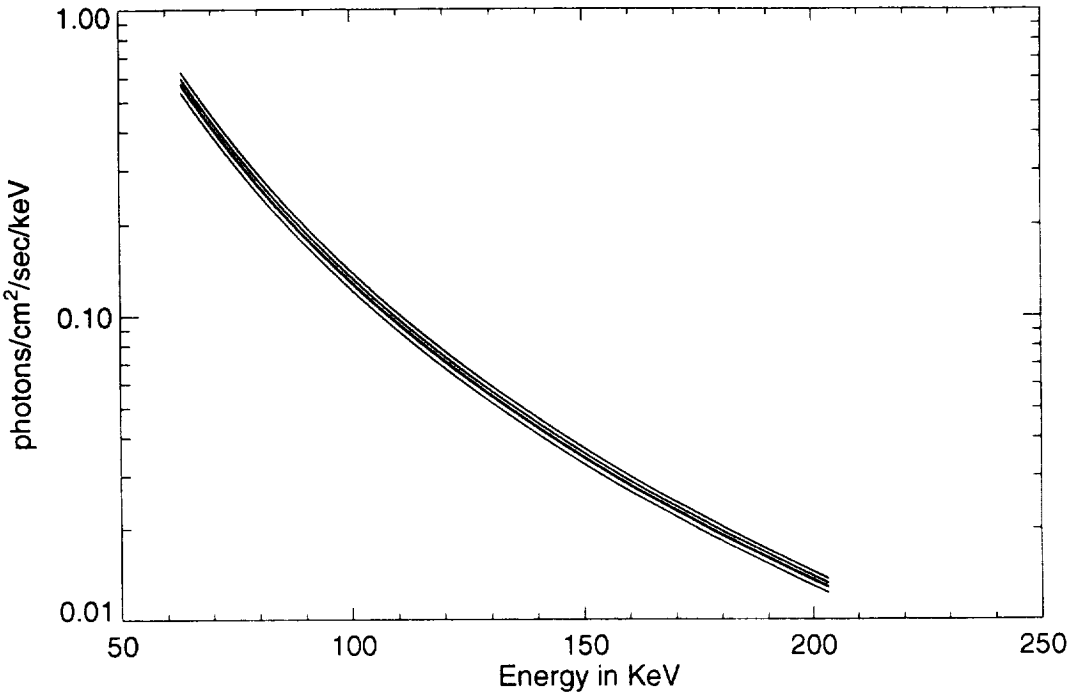

Figure 1: Power Law Fits to Brightest Detector

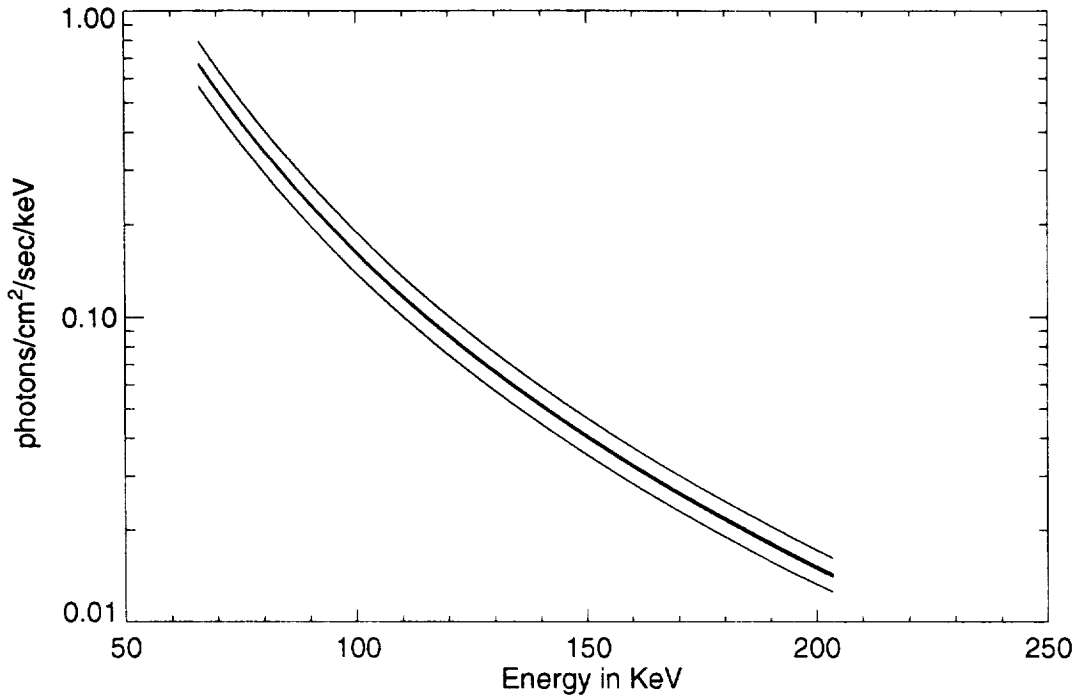

Figure 2: Power Law Fits to Second Brightest Detector

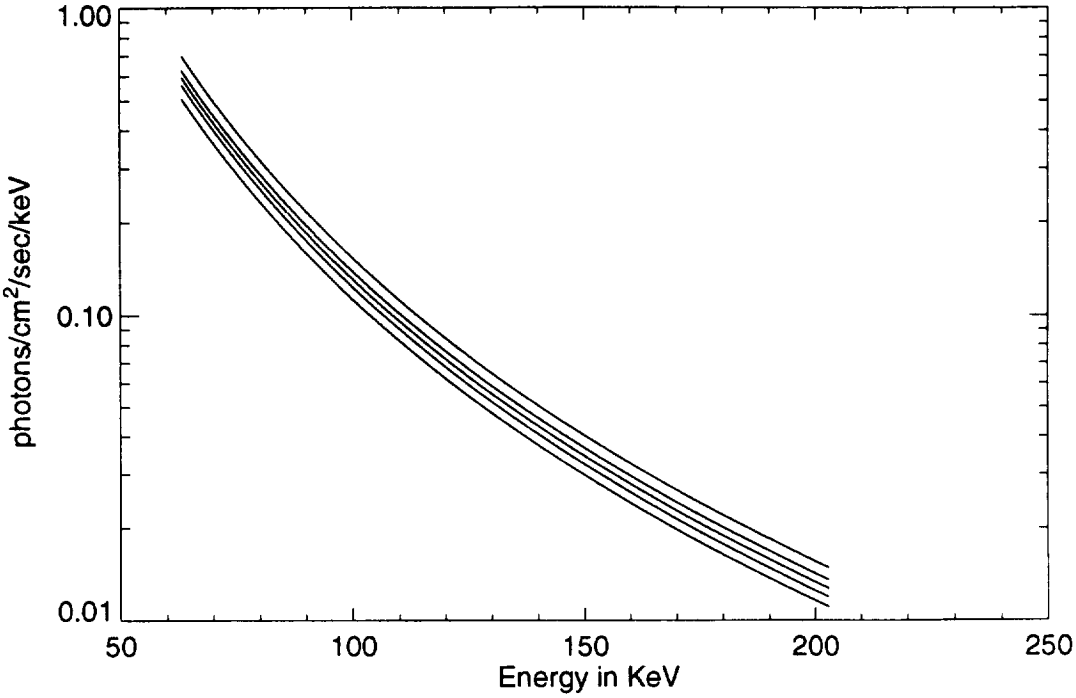

Figure 3: Power Law Fits to Third Brightest Detector

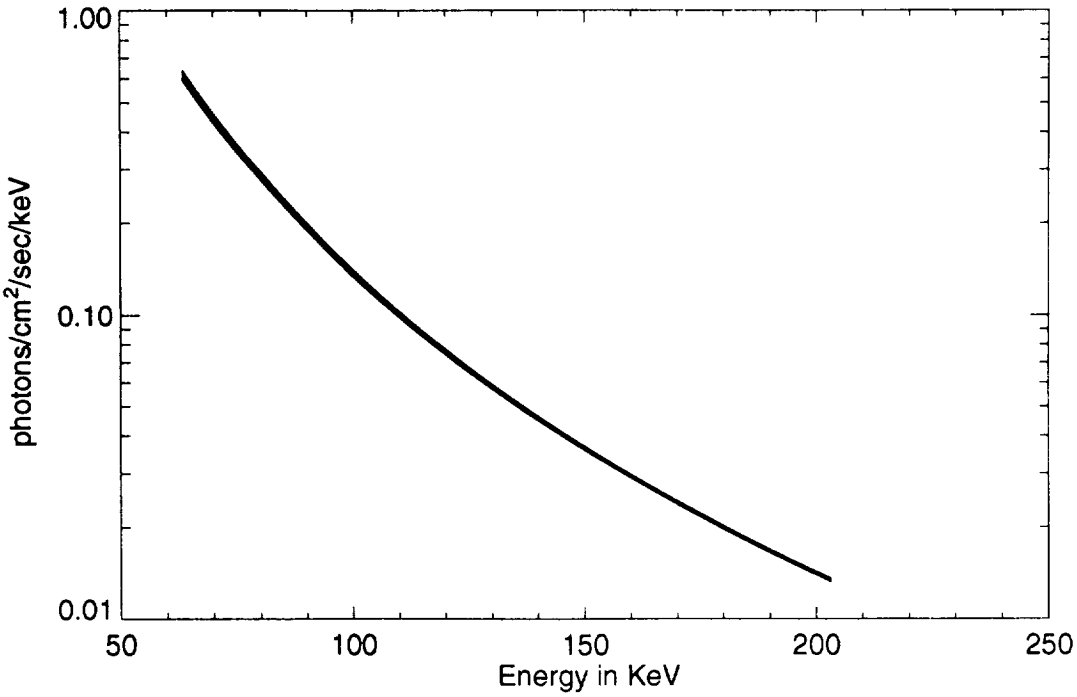

Figure 4: Power Law Fits to Three Brightest Detectors

ATMOSPHERIC SCATTERING

The atmospheric scattering algorithm currently employed in the burst location software calculates the scattered flux observed by a detector by numerically integrating an expression representing the single Compton scattering of photons off the earth into the detector. An atmospheric scattering algorithm has been created using the results of a Monte Carlo code that takes into account both single and multiple Compton scattering. This algorithm was used in the calculations performed above pertaining to solar flare intensity measurements. Figures 5 through 7 show spectra produced by the Monte Carlo code for monoenergetic plane waves of photons incident on the earth at a specific zenith angle of 60°. The spectra are for the photons collected at the spacecraft orbital altitude that have Compton scattered in the earth's atmosphere. Photoelectric absorption is also present in the simulation to account properly for the absorption of the lower energy photons. These figures show single scatter spectra for photons that have scattered only once in the atmosphere and multiple scatter spectra for photons that have scattered two or more times in the atmosphere before reaching orbital altitude. These results indicate that a significant number of the atmospherically scattered photons observed by the detectors have scattered two or more times in the atmosphere before hitting a detector.

At the time of the writing of this paper a data product incorporating these Monte Carlo results has been created and is ready for implementation into the burst location algorithm. The implementation of this algorithm should result in a significant decrease in the magnitude of our systematic errors.

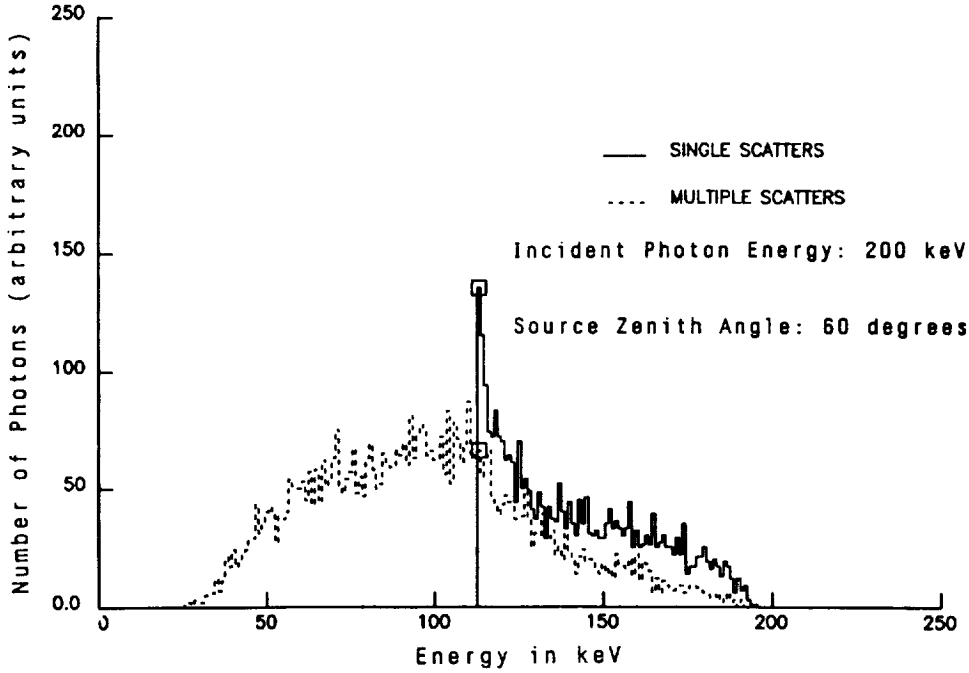

Figure 5: Energy Spectra of Collected Photons

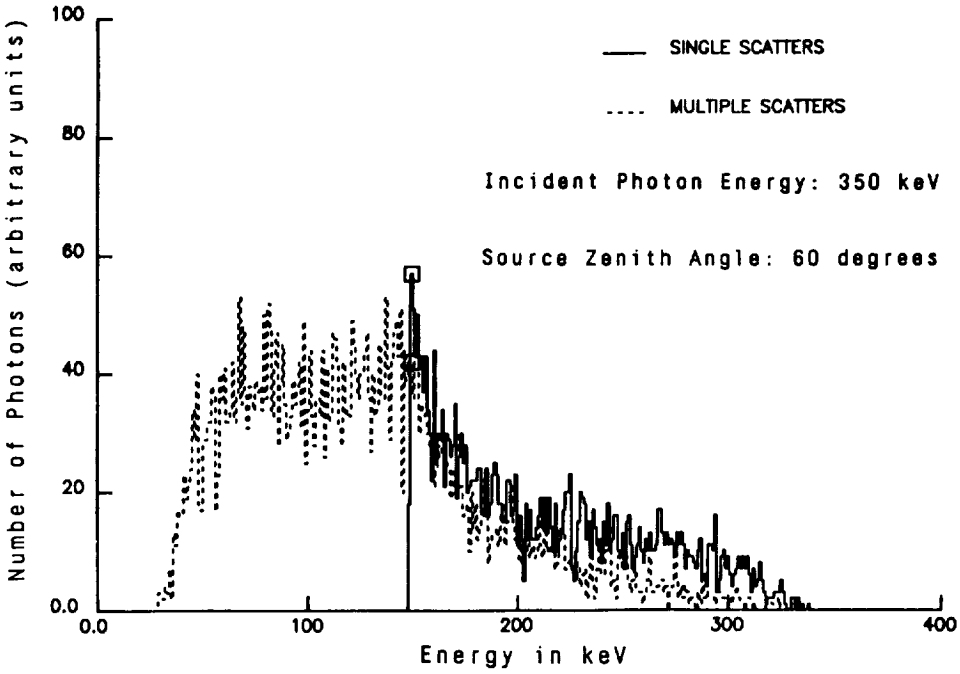

Figure 6: Energy Spectra of Collected Photons

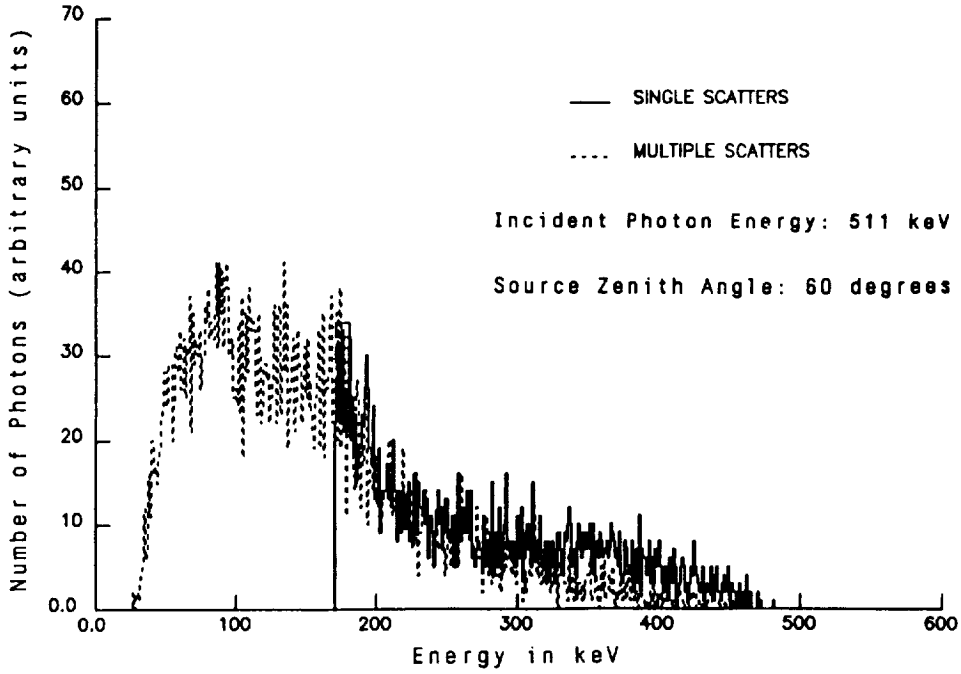

Figure 7: Energy Spectra of Collected Photons

REFERENCES

G. N. Pendleton, W. S. Paciesas, J. P. Lestrade, G. J. Fishman, R. B. Wilson, C. A. Meegan, (1989) The BATSE Detector Response Matrices, to be published in *Proceedings of the GRO Science Workshop*,p. 544-547, Greenbelt, Maryland, April 10-12

G. J. Fishman, C. A. Meegan, R. B. Wilson, W. S. Paciesas, T. A. Parnell, R. W. Austin, J. R. Rehage, J. L. Matteson, B. J. Teegarden, T. L. Cline, B. E. Schaefer, G. N. Pendleton, F. A. Berry, Jr., J. M. Horack, S. D. Storey, M. N. Brock, J. P. Lestrade, (1989) BATSE: The Burst and Transient Source Experiment on the Gamma Ray Observatory *Proceedings of the GRO Science Workshop*, p. 2-39, Greenbelt, Maryland, April 10-12

BATSE SPECTROSCOPY ANALYSIS SYSTEM

Bradley E. Schaefer[1], Sandhia Bansal[1], Anju Basu[1], Phil Brisco[1], Thomas L. Cline[1], Elliott Friend[1], Nancy Laubenthal[1], E. S. Panduranga[1], Nuru Parkar[1], Brad Rust[1], Teresa Sheets[1], Bonnard J. Teegarden[1], Gerald J. Fishman[2], Charles A. Meegan[2], Robert B. Wilson[2], William S. Paciesas[2], Geoff Pendleton[2], and James L. Matteson[3]

ABSTRACT

The BATSE Spectroscopy Analysis System (BSAS) is the software system which is the primary tool for analysis of spectral data from BATSE. As such, Guest Investigators and the community as a whole need to know its basic properties and capabilities. This paper describes the characteristics of the BATSE spectroscopy detectors and the BSAS.

INTRODUCTION

One of the primary goals of the BATSE is to obtain high quality spectra of gamma-ray bursts. The data returned from the Gamma Ray Observatory satellite will require considerable processing. In addition, a substantial bookkeeping system is needed to obtain ready access to the data. The BSAS is designed to handle the processing, analysis, and cataloging of the data. The BSAS was developed at the Goddard Space Flight Center and is now also in use at Marshall Space Flight Center and the University of California at San Diego.

BATSE SPECTROSCOPY DETECTORS

The eight detector modules of BATSE are positioned around the GRO spacecraft to provide a complete view of the entire sky including the Earth. The orientation of each module with respect to the satellite is the same as for the faces of a regular octahedron. This means that a burst from any region on the sky will directly illuminate four different detector modules. One of these four modules will be facing most directly at the burst and hence will have the highest count rate. During a burst, the on-board electronics chooses the four most brilliantly illuminated detectors (based on count rates) so that only data from these four detectors is transmitted to the ground. Frequently, the four chosen detectors will include one that is actually pointing away from the burst, but is nevertheless illuminated by the gamma rays reflected from the Earth's atmosphere.

Two types of detectors coexist inside each module; the Large Area Detectors (LADs) with high sensitivity and good time resolution, and the Spectroscopy Detectors (SDs) with good spectral resolution and a wide energy range. This paper will concentrate on the SDs due to their superior characteristics for spectral analysis.

The SDs each consist of a NaI(Tl) scintillator which has a round front face (127 cm^2 area) and is 7.6 cm thick. The energy range depends on the gain, with a range from roughly 60 keV to 11 MeV for high resolution channels at 1X gain. Some of the detectors have been operated at 0.4X gain, so that discriminator channels carry information for energies above 110 MeV. Currently, four detectors are being operated at 7X gain so as to get useful information as low as roughly 10 keV for the detection of cyclotron lines. The energy resolution is illustrated in Figure 1. The sensitivity for the detection of narrow lines is given by Figure 9 of Fishman et al. (1984).

The BATSE data can be sent to ground in a variety of data types or formats. These are summarized in Table 1. For spectral analysis, only three data types are used. The first is SHERB, which contains binned histograms (i.e., counts as a function of channel for some small time interval) for burst data. This data comes with a time resolution of 0.128 seconds or more depending on the brightness of the burst and on the detector. This data stream lasts typically for

[1]Goddard Space Flight Center, Greenbelt, MD 20771
[2]Marshall Space Flight Center, Huntsville, AL 35812
[3]University of California at San Diego, La Jolla, CA 92093

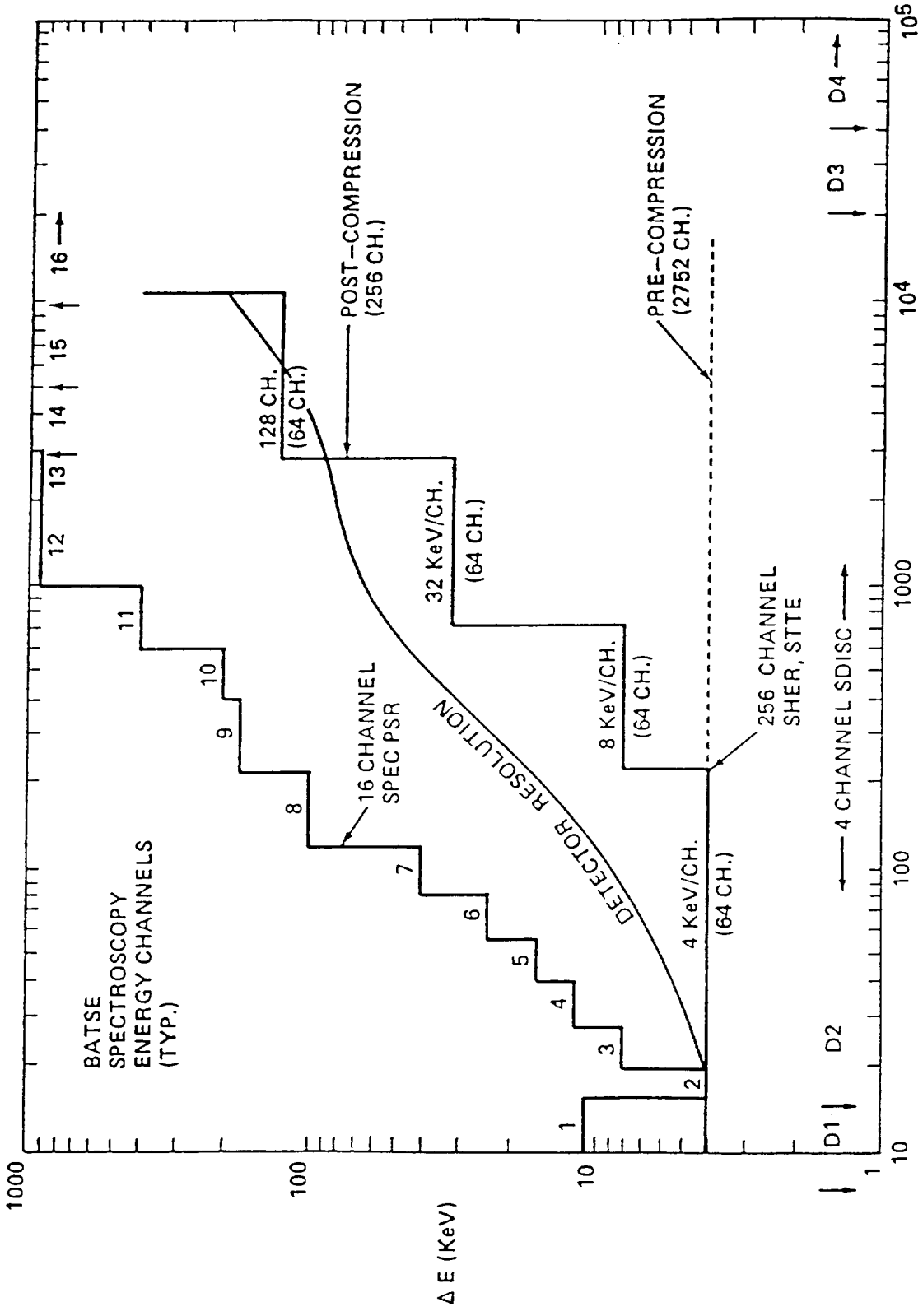

Figure 1. Energy resolution for the BATSE spectroscopy detectors.

TABLE 1. BATSE DATA TYPES

Mnemonic	Packet ID	# in Seq.	Detector	# of Channels	Mode	Burst Data?	Time Resolution
HER	20	8	LAD	128	binned	no	100-500 sec
HERB	32	128	LAD	128	binned	yes	N x 64 ms
MER	50-5F	32	LAD	16	binned†	yes	10-50 ms
CONT	*	*	LAD	16	binned	all	2.048 sec
TTE	33,34	128	LAD	4	time tag	yes	2 μs
TTS	41-44	128	LAD	4	spill time†	yes	typically ≈30μs
DISCSC	30	1	LAD	4	binned†	yes	64 ms
DISCLA	*	*	LAD	4	binned	all	1.024 sec
PREB	31	8	LAD	4	binned	yes	64 ms
SHER	21	16	SD	256	binned	no	200-1000 sec
SHERB	60-62	128	SD	256	binned	yes	Nx64 ms, $N \geq 2$
STTE	71-74	128	SD	256	time tag	yes	128 μs
DISCSP	*	*	SD	4	binned	all	2.048 sec
PSR16A	10	4	LAD¥	16	pulsar	no	64 phase bins
PSR16B	11	4	SD¥	16	pulsar	no	64 phase bins
PSRSELA	12	1	LAD¥	4	pulsar	no	64 phase bins
PSRSELB	13	1	SD¥	4	pulsar	no	64 phase bins
PSRSUMA	14	1	LAD¥	4	pulsar	no	64 phase bins
PSRSUMB	15	1	SD¥	4	pulsar	no	64 phase bins
PSRFULA	16	8	LAD¥	16	pulsar	no	64 phase bins
PSRFULB	17	8	SD¥	16	pulsar	no	64 phase bins
DUMP	00	1	-	-	-	-	-

*This data is contained in all packets.

†This data is summed over all triggered detectors.

¥Typically, memory A will be used for the LAD and memory B for the SD.

100 seconds after the trigger. The second burst data type is STTE, which contains a record of the channel and time (to within a 0.000128 second time bin) of every photon until the memory is filled up. This data type typically contains several seconds of pre-trigger data and 20 seconds of post-trigger data. SHERB data is partially redundant with the STTE data, where the STTE data should be used for the best time resolution. The SHER data type is for binned histograms of background data. The primary use of SHER data is to allow for the interpolation of the background spectrum at the time of the burst. The typical time resolution is five minutes. The total number of counts in the background spectra varies with the position of the satellite, with typical variations by a factor of two over one orbit (the counts are somewhat higher just after GRO passes through the South Atlantic Anomaly).

The calibration of the detector response matrix was achieved by detailed Monte Carlo calculations utilizing the precise geometry of the detector and spacecraft and confirmed with extensive ground-based testing of each module. The channel-to-energy conversion is based on ground-based testing, however there are currently some fine-tuning of the calibration in progress.

BSAS PROGRAMS

The BSAS embodies the traditional spectral deconvolution techniques as described in Loredo and Epstein (1989). That is, the deconvolution program (MODFIT) varies a set of model spectral parameters such that when the predicted spectrum is folded through the detector response matrix the predicted count spectrum is the best match to the observed spectrum in a chi-square sense. The output photon spectrum is then the predicted photon spectrum scaled by the ratio of the observed to predicted count spectra. The uncertainties in parameter values are found by searching through parameter space for the boundaries of the region for which the chi-square value is within some value of the minimum chi-square, as in Lampton, Margon, and Bowyer (1976). The minimization of chi-square is made with the CURFIT algorithm of Bevington (1969).

BSAS also contains a model-independent deconvolution technique (Schaefer 1988). Additional model-independent deconvolution techniques (including the Backus-Gilbert method of Loredo and Epstein) will be added sometime soon.

In support of these deconvolution programs, BSAS contains many programs which extract the histograms, plot the spectra, plot the time histories, search for lines, derive the detector response matrix, list the output, and so on. A list of these programs and a brief description of each is:

BCOUNT	-	Extracts count spectra for background data
BTIMES	-	Calculate times, rise times, and durations from light curves
CONF	-	Produce error bars for the fit parameters found by MODFIT
COUNT	-	Extract count spectra and background subtract
EXTMRG	-	Extract and merge data between the Inst.PDB and the User PDB
FLUENC	-	Calculates fluence from a spectrum
LSRCH	-	Search for spectral lines in a spectrum
MAXKEV	-	Find highest energy with significant flux in a spectrum
MATRIX	-	Calculate detector response matrix
MODFIT	-	Produce best fit parameters for specified models
PDBEDT	-	Modify or delete data stored in the PDB
PDBGEN	-	Create entry in the PDB and run initial analysis
PDBLST	-	List selected data from the PDB
PHOTON	-	Produce the photon spectrum using the results from MODFIT
PRBACK	-	Store background data from daily data set, and update catalog
PRBRST	-	Store burst data from daily data set, and update catalog
PRNTAR	-	Prints analysis results generated by PDBGEN
QFIT	-	Produce a model fit to a QPHOTN spectrum
QPHOTN	-	Produce a model-independent photon spectrum
RDCMAT	-	Utility to read coefficient matrices (for DRM generation) to file

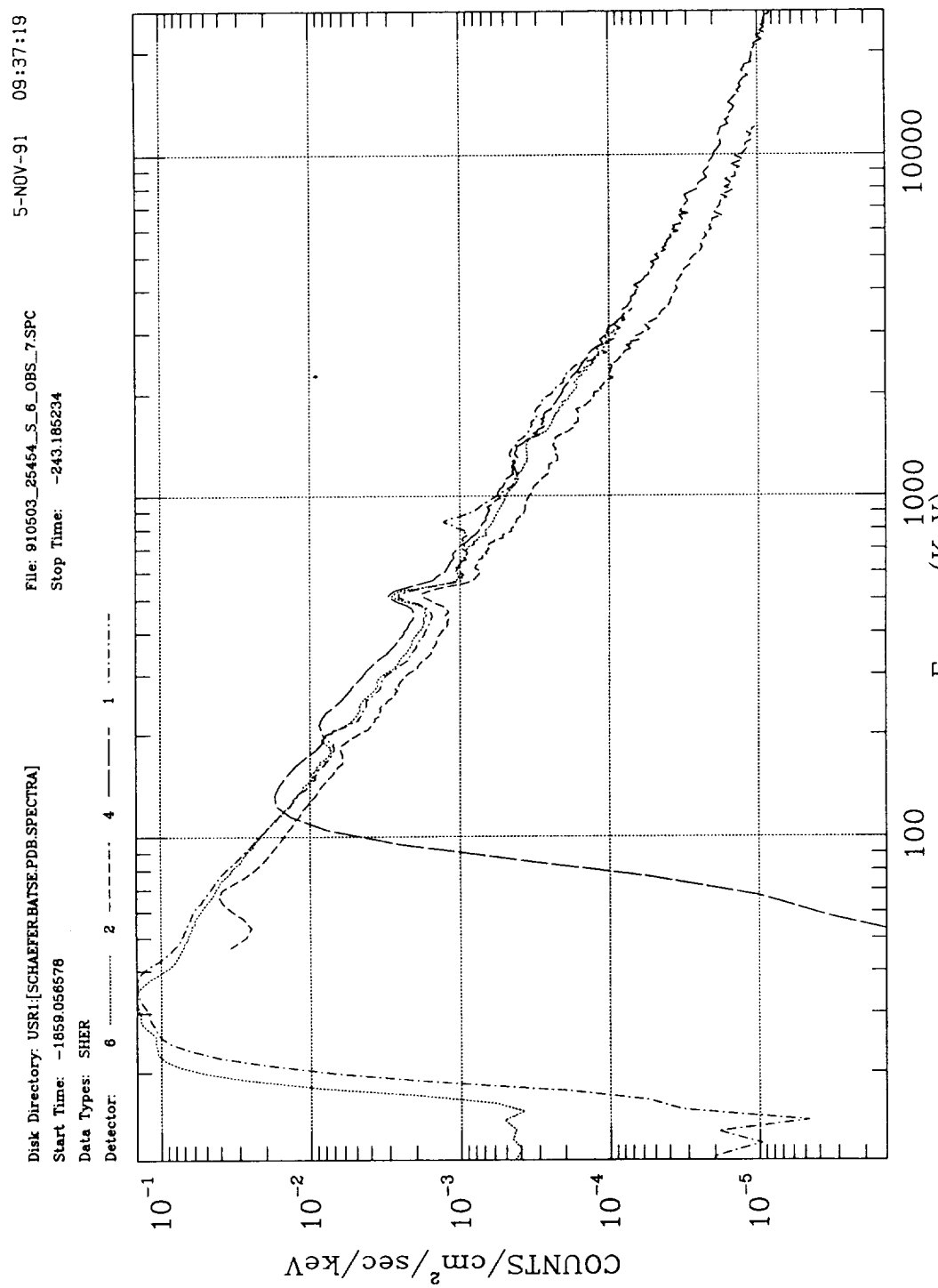

Figure 2. Background count spectra for four spectroscopy detectors.

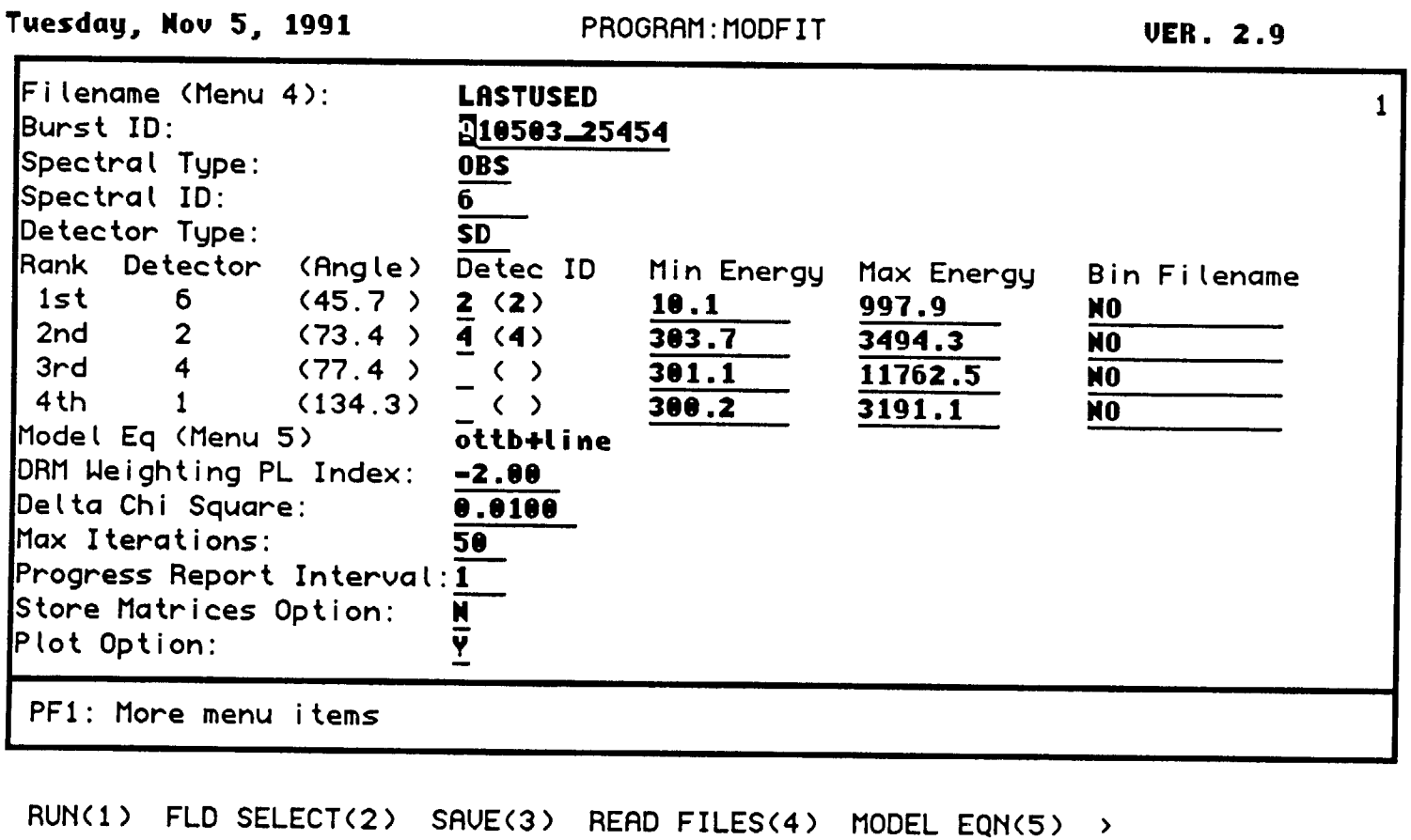

Figure 3. Parameter input screen for the MODFIT deconvolution program.

RDDRM	-	Utility to read full-resolution DRM to file and screen
RDIBDB	-	Utility to read nearly-raw spectral data in IBDB to file and screen
RDSPEC	-	Utility to read spectrum to file and screen
REDUCE	-	Menus for executing other programs
SETUP	-	Changes terminal and printer type for plotting programs
SPPLOT	-	Plot a spectrum and/or spectral fit on the terminal or printer
THGEN	-	Generate the time history (i.e., the light curve) of a burst
THPLOT	-	Plot the time history (i.e., the light curve) of a burst
VRANGE	-	Sets valid energy range for each burst

At the time of this writing, the programs LSRCH, BCOUNT, and BTIMES are not yet completed.

To give a general feel for the analysis procedure, let us describe the sequence of programs that should be run to obtain a photon spectrum for a new burst: (1) Create the Individual Burst Data Base from the daily dataset residing at Marshall Space Flight Center with PRBRST. (2) Create an entry in the Processed Data Base and perform some initial analysis with PDBGEN. (3) Enter the BSAS menu-driven analysis program with REDUCE. (4) Transfer the new burst entries to a personal Processed Data Base with EXTMRG. (5) Create the detector response matrices with MATRIX. (6) Accumulate background spectra for all four detectors with COUNT, as illustrated in Figure 2. (7) From these spectra, determine the energy range over which there is valid data, then enter these ranges with VRANGE. (8) Generate a time history file for some desired energy range with THGEN. (9) Plot the time history with THPLOT. (10) Accumulate the count spectra for the time interval of interest with COUNT. (11) Interpolate the background spectra to the time of the burst with COUNT. (12) Background subtract the observed count spectrum with COUNT. (13) Fit the background subtracted count spectrum to the spectral model of your choice with MODFIT. (14) Evaluate the error bars for the best fit model parameters with CONF. (15) Create the photon spectrum with PHOTON. (16) Plot the photon spectrum with SPPLOT.

The BSAS runs with menu driven inputs. The menus are created with the programs TAE and INGRES. A typical example of an input menu is shown in Figure 3 for the MODFIT program. A detailed and helpful user's guide is available from the BATSE team.

INSTALLATION

The BSAS is currently installed at Marshall Space Flight Center, Goddard Space Flight Center, and the University of California at San Diego. Guest Investigators may apply for support at any of these three BATSE institutions. This might imply a period of residence possibly combined with remote use of BATSE computers. A possible alternative would be for the Guest Investigator to port BSAS to their home institution.

The porting of BSAS is not a trivial task. First, the BSAS requires that the computer be a VAX running VMS. Second, it requires that the commercial programs FORTRAN, INGRES, TAE, and MONGO be installed. Third, our experience shows that minor differences in version numbers for these programs can lead to errors that can be difficult to track down. Fourth, the receiving system is likely to have some non-standard conditions that will also lead to errors. Thus, substantial help from an experienced system programmer will ease the problems of installation.

REFERENCES

Bevington, P. R. 1969, Data Reduction and Error Analysis for the Physical Sciences (New York: McGraw-Hill).

Fishman, G. J., Meegan, C. A., Parnell, T. A., Wilson, R. B., and Paciesas, W. 1984, in High Energy Transients in Astrophysics, ed. S. Woosley, American Institute of Physics Conf. Proc. No. 115 (New York: A. I. P.), p. 651.

Lampton, M., Margon, B.. and Bowyer, S.. 1976, Ap. J., 208, 177.

Loredo, T. J. and Epstein, R. I. 1989, Ap. J., 336, 896.

Schaefer, B. E. 1988, in Nuclear Spectroscopy of Astrophysical Sources, eds N. Gehrels & G. Share, American Institute of Physics Conf. Proc. No. 170 (New York: A. I. P.), p. 505.

N92-21881

GAMMA-RAY BURST SOURCE LOCATIONS WITH THE NEW INTERPLANETARY NETWORK

T. L. Cline*
NASA / Goddard Space Flight Center, Greenbelt, Maryland

Gerald Fishman*
NASA / Marshall Space Flight Center, Huntsville, Alabama

Kevin Hurley*
University of California, Berkeley, California

John Laros*
Los Alamos National Laboratory, Los Alamos, New Mexico

Neils Lund*
Danish Space Research Institute, Copenhagen, Denmark

Michael Sommer*
Max-Planck Institut fur Extraterrestrische Physik, Garching, Germany

The celestial source fields of gamma ray bursts can now be determined with precision considerably greater than that provided by earlier interplanetary networks. A new burst timing array consists of the *Ulysses* mission and the *Pioneer-Venus Orbiter* at great distances and the *Compton Observatory*, *Granat* and other burst-observing spacecraft near the Earth. With Ulysses providing a baseline approaching 5 astronomical units in its progress towards Jupiter, and given the timing resolution of the Compton Burst and Transient Source Experiment, source fields with dimensions as small as several arc seconds by less than one arc minute will be determined for many of the events to be studied with this network.

The Pioneer-Venus Orbiter will unfortunately enter the Venusian atmosphere during 1992, but an equivalent vertex in the interplanetary array will be created, perhaps less than a year later, with the *Mars Observer* and/or with the *Mars-94 Mission*. At present, various other near-Earth spacecraft with burst instrumentation may augment the coverage of this network; in a few years these will include *GGS-Wind* with its high-resolution transient gamma-ray spectrometer and its burst monitors, as well as *HETE* with its optical transient capability.

As of conference time, only three or four events had been observed with the long-baseline complement that can promise accurate results. The event rate implied may be deceptively low, however, due to the necessarily incomplete nature of the data scrutiny from some of the missions in the preliminary survey, thus far covering only a few months. The number of gamma ray bursts that are expected to provide optimum source precision with this network shall ultimately be ten to fifteen per year. These results will make possible a significant number of deep searches for the celestial source objects, especially in the high galactic latitude, low stellar density regions. Many more events per year will yield larger or irregularly shaped source fields; these will be useful for calibrations of BATSE source distributions. No final analyses are now available for presentation.

*Principal investigator from each institution; coauthors of these studies will vary.

Description of a subset of single events from the BATSE gamma-ray burst data

Chryssa Kouveliotou,
USRA/on leave from the University of Athens, Greece

William S. Paciesas,
University of Alabama in Huntsville

Gerald J. Fishman, Charles A. Meegan, and Robert B. Wilson
NASA/Marshall Space Flight Center

Abstract

About 15% of the gamma ray bursts in the BATSE data exhibit a simple light curve, consisting mainly of a single pulse without fine substructures. In 12 of the burst profiles the pulse shapes show a linear rise and decay. Three events have a distinct sharp rise followed by a long, almost exponential decay. Searches based only on a sharp rise selection criterion resulted in 5 more grbs with different profile complexities. In one case, we identify an envelope of fast oscillations with a long, softer tail lasting about 100 seconds.

The majority of the events were detectable at energies above 300 keV, with tentative estimates for fluences that vary between 4.0 x 10^{-8} and 5.4 x 10^{-6} ergs/cm^2. We describe here their general time characteristics (durations, rise-decay times) and their hardness ratios.

1. Introduction

Ever since its activation on April 21, 1991, the Burst and Transient Source Experiment (BATSE) on the Compton Gamma Ray Observatory (CGRO) has been detecting gamma ray bursts at an average rate of one event per day. A detailed description of BATSE is given elsewhere [1]. The data analyzed here have been collected with the Large Area Detectors (LADs). Each LAD has a 2000 cm^2 geometrical area affording very good photon statistics, unprecedented for very weak events. As a result, the majority of the GRB temporal structures emerge with clarity and high level of significance above background. This BATSE attribute has prompted us to devise a tentative morphological classification scheme along the lines of earlier attempts [2], [3], [4]. In general, we distinguish the following three wide groups of bursts:

COMPLEX: Events exhibiting long, multipeaked temporal profiles.
SINGLE: Single pulses without significant temporal substructures.
SPIKES: Very short (< 300 ms) vents that can either exhibit simple or complex profiles on the tens of ms timescale.

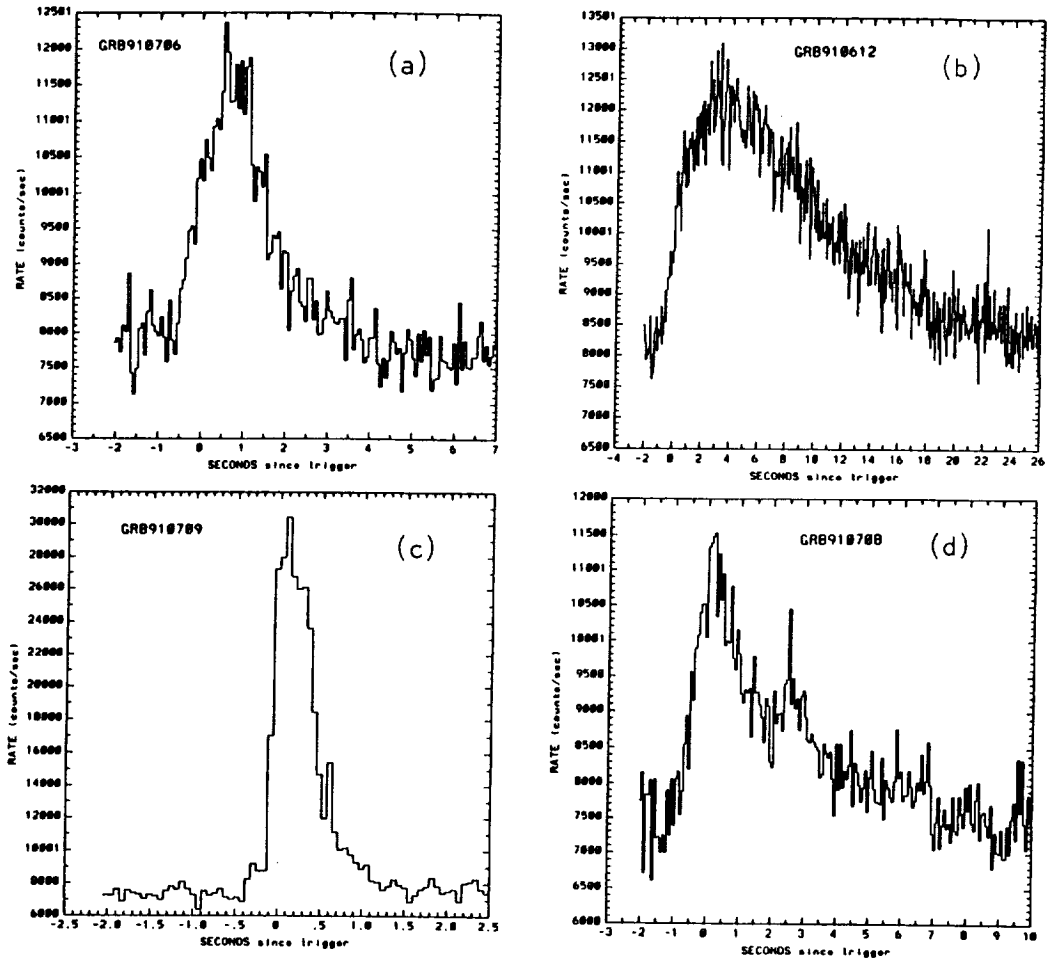

Figure 1. a-d) Typical time profiles of single, smooth grbs. Counts are collected from all 4 channels with 64 ms time resolution.

This classification is strictly morphological and should not be interpreted as reflecting any physical models on the origin of the events at this stage of GRB research. So far all three groups are distributed the same way (isotropically) on the sky [5]. It is rather a convenient division of the database into groups, that could be used to readily select events for different types of analyses, such as Fast Fourier Transforms for the complex events, calculations of rise- decay times for the single events, etc.

2. Data Analysis

(a) Temporal characteristics

In a period of 113 days, between April 21, 1991 and August 11, 1991, BATSE triggered on 100 GRBs. Among these, the subset of single events was selected for simple temporal analysis involving determination of rise-decay times and durations.

The majority of the single events selected had temporal profiles with gradual rises and decays; their shapes were best fitted with triangular-trapezoidal forms. Sometimes a "shoulder" appeared during the decay portion of the event, around 50% of peak level.

Figure 1 shows typical examples of single GRBs. Notice GRB910709 (Fig 1c), which has a peak intensity twice that of the others, an indication that intense events can appear single, countering the "tip of the iceberg" argument. Twelve such events were found in the database.

Several of the selected events had a uniquely characteristic profile with a very sharp rise (< 1 s), accompanied by a long, exponential-like decay (Fig 2a). We searched for more such GRBs in the BATSE data, using only this sharp-rise/exp-decay criterion, and we found a total of 8 events (including 3 single ones). They have been included in this study for completeness, and a progression of their profiles from single to multipeaked and extremely complex is shown in Figure 2 a-d. GRB910814 (Fig 2d) has very fast and non-periodic oscillations at its first part (lasting over 40 s), then it decays slowly for at least 50 more seconds. These events also range in peak intensities and are in general more intense than the first group.

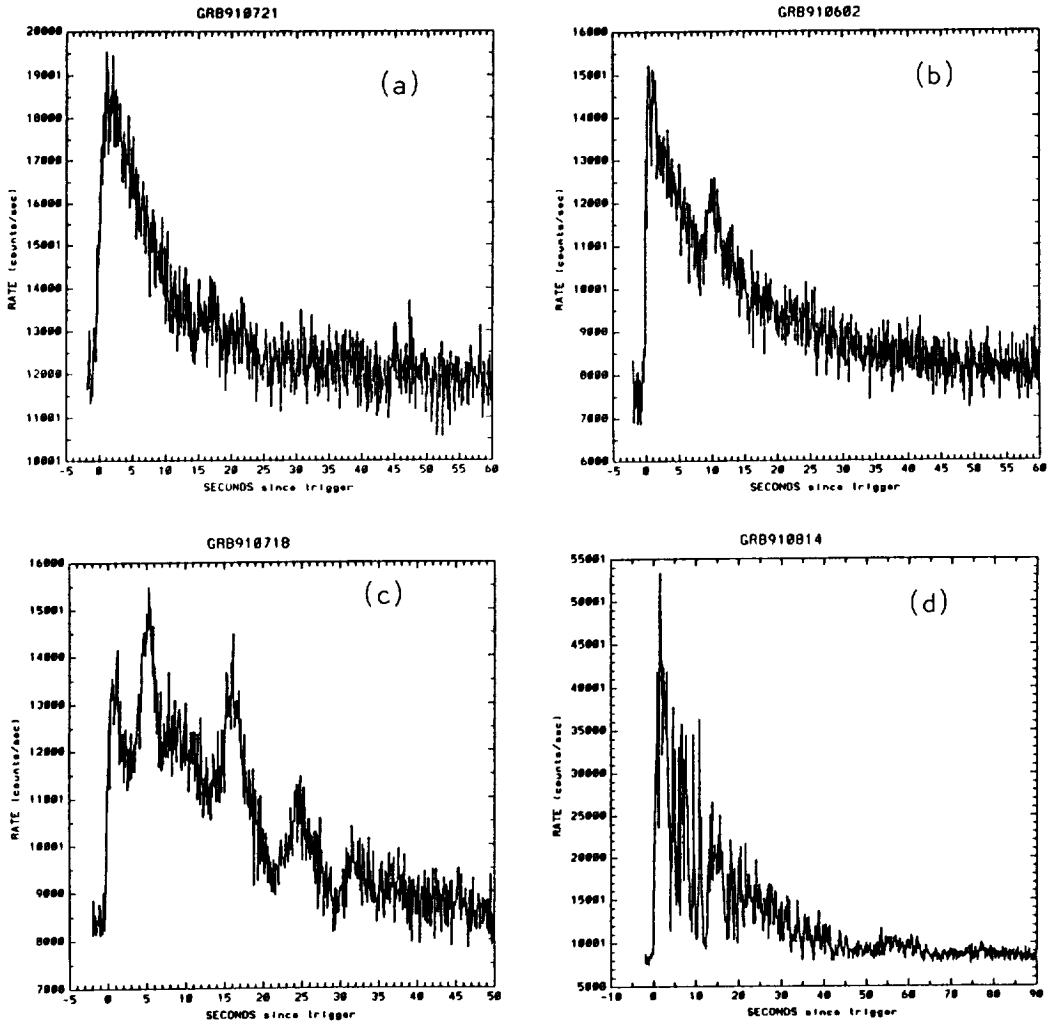

Figure 2. a-d) Examples of grbs with sharp rise, exponential decay time profiles. Notice the progression of the profiles from single (2a) to extremely complex (2d).

Table 1 shows the summary of the GRB temporal and spectral characteristics. We can see from the ratios of their rise times *vs* durations (fifth column) that the majority of the second group has values below 10%, while for the first, this number is above 20%.

We have plotted the rise *vs* decay times for both groups in Figure 3a. We use the cross sign (+) for the first group and the star sign (*) for the second , in all the subsequent plots. Note that the sharp-rise/exp-decay group has a limited range of rise times, below 1 s, as opposed to the wide range of their decay times. In Figure 3b we plot the rise times *vs* peak intensities in counts/s above background. As we mentioned, the second group contains more intense events, while in the first group, events usually peak below 10000 c/s.

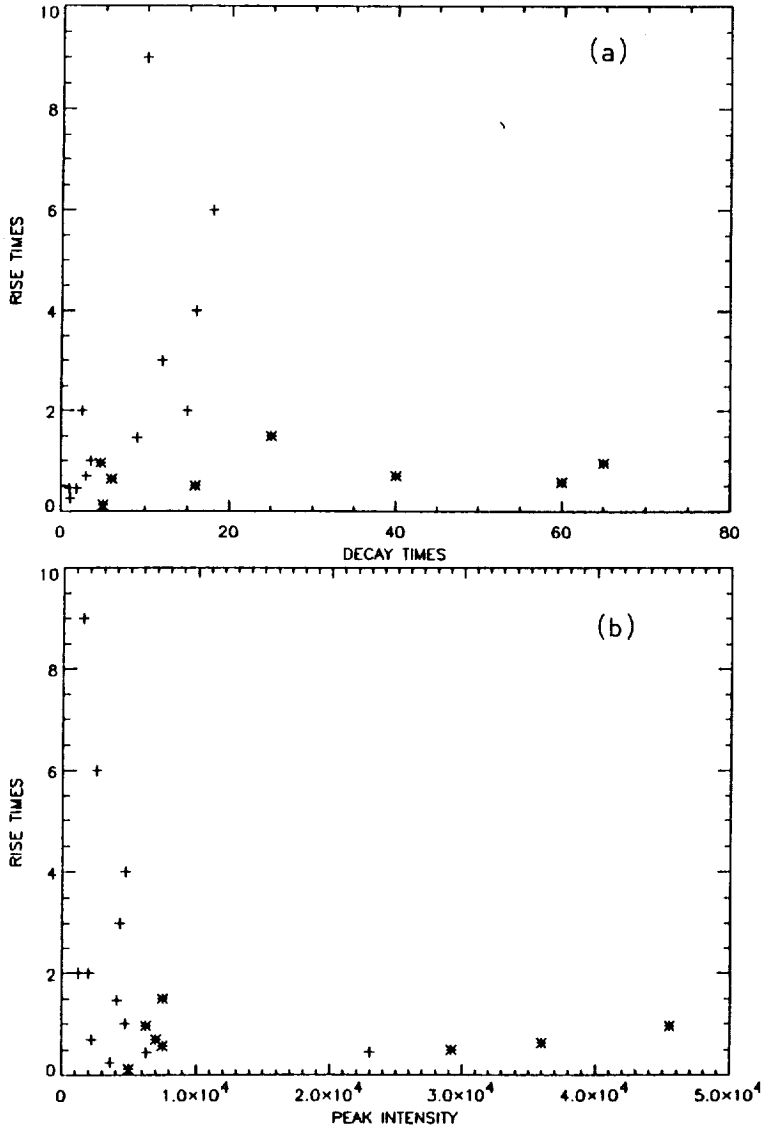

Figure 3. a) Rise *vs* decay times (in seconds) for all 20 grbs. Crosses (+) represent single, smooth events and stars (*) events with sharp rise exponential decay profiles. b) Rise times (in seconds) *vs* peak intensity (above background) summed over all energy channels.

(b) Spectral characteristics

As a first approach we examined the spectral behaviour of both groups in the four discriminator channels of the LADs. The channel energy ranges are defined approximately:

Channel 1 : 25 - 55 keV
Channel 2 : 55 - 100 keV
Channel 3 : 100 - 320 kev
Channel 4 : 320 - 1000 keV

We find that all the single events in the first group do not show any spectral evolution on timescales of 64-ms. Figure 4a shows the alignment of the pulse edge in the two extreme channels (low-high) for GRB910709. In contrast, Figure 4b shows the extreme spectral shift of about 1 s between the same channels observed in GRB910717. In general, spectral evolution is found only in the second group of GRBs.

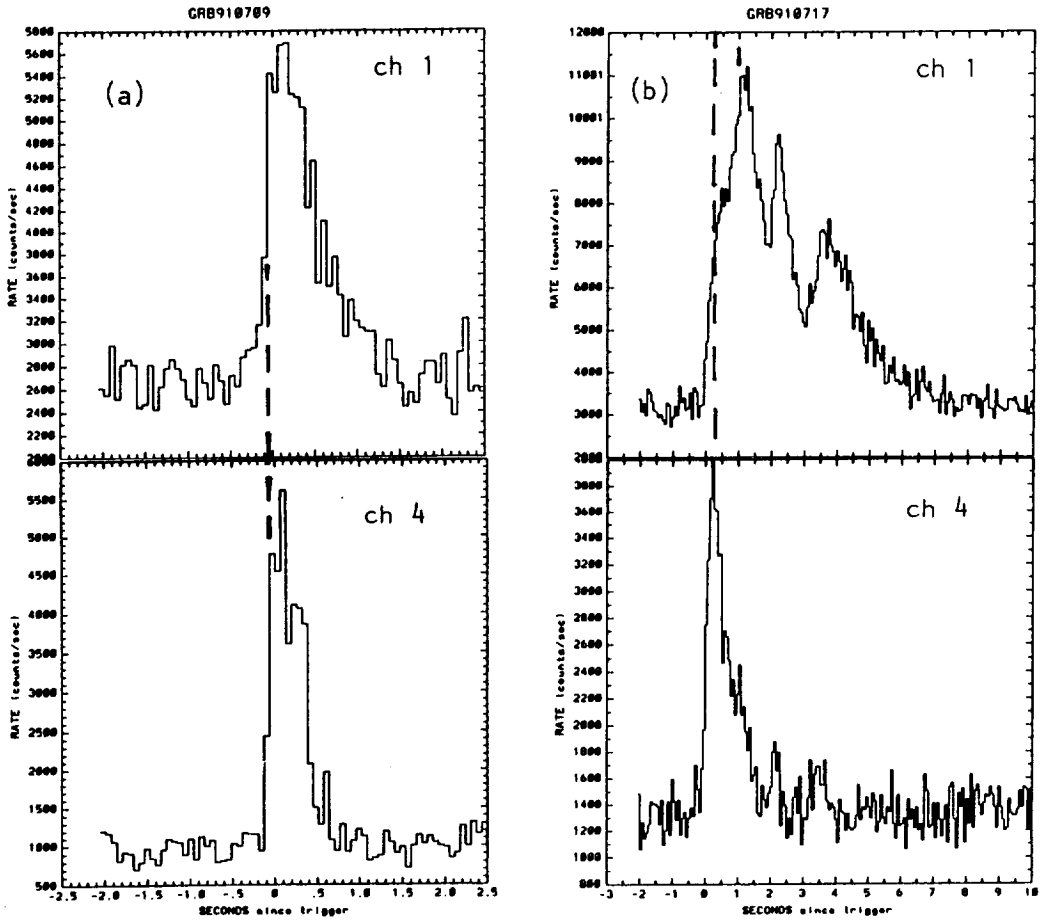

Figure 4. a) Time profile of a group 1 intense event in the two extreme energy channels (low-high). Notice the alignment of the pulse edge (indicated by the broken line) in both channels. b) Time profile of a group 2 intense event in the same energy channels, showing a large shift of about 1 s.

We have computed the hardness ratios (HRs) for all 20 events (see Table 1) by dividing R_3, the background-subtracted rate in channel 3 by R_2, the corresponding rate in channel 2, *i.e.*:

$$HR = \frac{R_3}{R_2}$$

The average HR for the first group is $\sim$ 1.0, while the second group has HRs with an average of 1.6, *i.e.*contains harder events. This result has been confirmed by [6], who estimated the hardness ratios for all BATSE events, and also found this particular group to be a harder subset.

Figure 5 shows the rise times *vs* the HRs. In general the two groups seem well separated in their main characteristics, *i.e.*events with short rise times have high HRs and events with longer rise times have lower HRs.

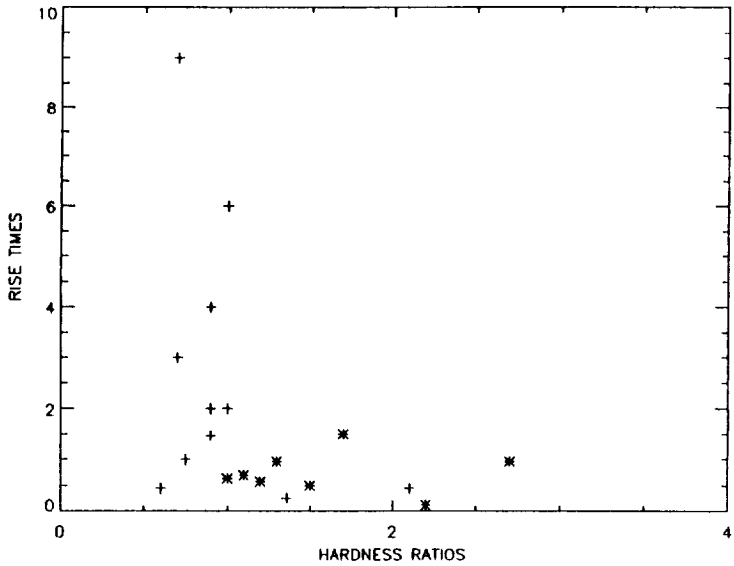

Figure 5. Rise times (in seconds) *vs* hardness ratios for all 20 events. Crosses and stars are the same as above.

3. Conclusions

Table 2 summarizes the statistics of the subset selected from the first 100 GRBs detected by BATSE. In the strictly single events detected, we identify in the majority smooth profiles with rise times usually lasting 25% of the total event duration. These events are usually weaker events, with very low hardness ratios and no evidence for spectral evolution.

In the same subset we identified another group of events with sharp rises and nearly exponential decays, which we then extended to encompass all different complexity time profiles. This group was found to have longer durations with rise times typically 5% of their durations. These events also had higher peak intensities and fluences. In some cases, they exhibited significant spectral evolution from hard to soft.

In summary, we conclude that the first group cannot yet be differentiated from other events in the GRB database on the basis of their spectral or temporal characteristics. We suggest that the second group has spectral and temporal properties distinguished from the majority of GRBs. More detailed spectral analysis is required to provide physical insight into this purely morphological classification.

References

[1] G. J. Fishman *et al.*, in *Proc. GRO Science Workshop,* ed. W. N. Johnson, NASA/Goddard Space Flight Center, 39, 1989.

[2] E. P. Mazets *et al.*, *Academy of Sciences of the USSR*, Report Nos. 630, 631, 632, 1979.

[3] U. D. Desai, *Ap. and Space Sci.,* **75,** 15, 1981.

[4] C. Kouveliotou, *Ph. D. Thesis,* Max-Planck Institute for Extraterrestrial Physics, 1981.

[5] J. Horack, personal communication.

[6] W. S. Paciesas, paper presented at the GRBs 1991 Workshop in Huntsville, AL., Oct 16-18, 1991.

Table 1. Summary of the GRB Temporal and Spectral Properties.

Group 1

Date	t_r s	t_d s	T s	R	Peak c/s	HR	Fluence[a] ergs/cm^2
GRB910709	0.45	1.50	2.00	28	23000	2.11	7.4×10^{-8}
GRB910708	1.47	9.00	10.47	14	4100	0.90	3.0×10^{-7}
GRB910612	4.00	16.00	20.00	20	4700	0.90	1.8×10^{-6}
GRB910715	0.45	1.90	2.40	19	6300	0.60	4.4×10^{-8}
GRB910809	3.00	12.00	15.00	20	4300	0.70	7.5×10^{-7}
GRB910725	6.00	18.00	24.00	25	2500	1.00	1.4×10^{-6}
GRB910629	2.00	2.50	4.50	44	1200	1.00	3.8×10^{-8}
GRB910805	9.00	10.00	19.00	47	1500	0.70	3.4×10^{-7}
GRB910718	0.70	3.00	3.70	19	2200	1.10	6.6×10^{-8}
GRB910521	0.30	1.00	1.30	19	3600	1.40	1.5×10^{-7}
GRB910706	1.00	3.50	4.50	22	4700	0.80	2.0×10^{-7}
GRB910702	2.00	15.00	17.00	12	2000	0.90	3.0×10^{-7}

Group 2

Date	t_r s	t_d s	T s	R	Peak c/s	HR	Fluence[a] ergs/cm^2
GRB910602	0.57	90.00	90.00	1	7500	1.20	1.1×10^{-6}
GRB910604	0.80	5.00	5.80	13	6300	1.30	1.7×10^{-7}
GRB910629	0.50	16.00	16.50	3	29200	1.50	9.6×10^{-7}
GRB910714	0.13	5.00	5.13	2	5000	2.20	2.3×10^{-7}
GRB910717	0.60	6.00	6.60	10	3600	1.00	2.0×10^{-6}
GRB910718	0.70	40.00	40.70	2	7000	1.10	4.0×10^{-6}
GRB910721	1.50	25.00	26.50	6	7500	1.70	2.5×10^{-6}
GRB910814	1.00	65.00	66.00	1	45500	2.70	1.5×10^{-5}

t_r = rise times, t_d = decay times, T = durations, R = $(t_r/T)*100$,
[a] = Fluences are estimated for the energy range between 60-320 keV

Table 2. Statistics of the analyzed GRB subset.

Total number of GRBs	100
Number of events in subset	20
Events with gradual shapes	12
Events with sharp rise/exp decay shapes	8
Range in durations	3.7 - 90 s
Range in fluences(ergs/cm^2)	4.0×10^{-8} - 1.5×10^{-5}
Range in hardness ratios	0.7 - 2.7
Range in peak intensities(c/s above background)	1200 - 45500

Occultation Analysis of BATSE Data- Operational Aspects

B. A. Harmon[1], M. H. Finger[2], B. Rubin[3]
R. Mallozzi[4], W. S. Paciesas[4], R. B. Wilson[1], G. J. Fishman[1],
M. Brock[1] and C. A. Meegan[1]

Abstract

The BATSE large area detectors are being used to monitor hard x-ray/gamma ray sources on a daily basis for evidence of transient behavior. Flux measurements are performed using a simple earth occultation technique. Daily searches are also performed to detect occultation steps of sources which are not being routinely monitored. Topics concerning the operational aspects of the occultation measurements are presented. Preliminary spectral results are also presented for several of the brighter sources.

I. Introduction

The Burst and Transient Source Experiment (BATSE) on the Compton Gamma Ray Observatory (CGRO) includes, as a part of its daily "quick-look" science analysis, hard x-ray/gamma-ray (20-2000 keV) source monitoring using the earth occultation technique. About 30 known source locations are checked for discontinuities in the detector background at times corresponding to the source rise or set at the earth's limb. This effort also includes searching for occultation steps of previously unknown sources or known sources which are not being monitored. The technique has already been used to detect transient behavior in two sources, GX339-4 and 4U1700-37, which have been monitored daily since the early part of the mission. No new sources have been found.

II. Procedure

The general method of earth occultation to measure gamma ray sources is especially suited to the near full-sky coverage of the BATSE detectors. Coupled with a hopefully long mission lifetime, the technique should eventually be a powerful observational tool for x-ray/gamma-ray source studies. Rigorous use of this technique and its ultimate sensitivity, however, will require a good understanding of the BATSE detector backgrounds in low

[1]Space Science Laboratory, NASA/Marshall Space Flight Center
[2]Computer Sciences Corporation
[3]Universities Space Research Association
[4]Department of Physics, University of Alabama in Huntsville

earth orbit. The process of characterizing the gamma ray background in the BATSE detectors is underway (see T. Skelton, *et al.*, these proceedings, where a model for the background is being assembled for use in measuring discrete source fluxes).

The current measuring technique uses a modified step function (background + step) to fit one to two minutes of background on each side of an occultation step feature. The short sampling interval allows the background variation to be treated as approximately linear. The current software uses only the medium energy resolution continuous data (2.048 sec time resolution, 16 energy channels) from the large area detectors (LADs). These eight detectors are gain-matched and employ automatic gain control so that data from different detectors pointing toward a given source can be combined for better statistics. A flux measurement is recorded daily in a history file, which represents the summed result of all available occultation steps for a single day. The sensitivity for a +-1 minute sample for combined data around 32 occultations is approximately 10% of the Crab nebula flux, being somewhat better when other sources are not interfering (i.e., another source along the earth's limb is occulted within the sampling period) with the source of interest.

The large area detector (LAD) data are also searched daily for step features from sources not routinely monitored by the previously described software. The procedure is to use a three-part test, again assuming a linear background, first checking for smoothness by comparison to a straight line, then application of the step model over the sampling interval, followed by a chi-square test on the step fit. This method yields the best time, step size, and brightest detector over the specified interval. Experience with this method has shown that the method is adequate for detecting step features reliably at about 25-40% of the Crab nebula flux in unfolded data. The primary drawback has been the presence of many non-statistical features, such as Vela X-1 pulses or short timescale flickering of Cyg X-1, which frequently produce variations in the background comparable in size to Crab occultation steps. While large background variations due to bursts, solar flares and other events are flagged each day and ignored in the search algorithm, it is still necessary to plot step significances in histogram or scatter plot form, and to examine the search results for recurrent steps in each orbit. Very large occultation steps have been observed from some sources, such as 4U1700-37 and Sco X-1. Occasional outbursts from these can exceed the Crab flux at low energies and vary greatly in intensity on the timescale of one orbit. The standard energy range for the search routine is 20-100 keV.

III. Preliminary Results of Flux Measurements

In this section, we present count spectra for several of the brighter sources, and the flux history for the QPO GX339-4. A count spectrum for the Crab nebula is presented in another contribution (R. B. Wilson, *et al.*, these proceedings), as well as a partial list of the sources which are being monitored. To date, about ten sources consistently exhibit significant fluxes summed over a one day period, with spectral shapes consistent with previous measurements. Complete confirmation of detection will require more thorough analysis of the count spectra convolved through the large area detector response matrices, and time series analyses to search for known periodicities. As yet, only power law fits have been performed to the count spectra.

In Fig. 1, we show sample spectra for Centaurus A, Cygnus X-1, 4U1700-37, and Scorpius X-1 obtained by the BATSE occultation analysis technique. Each spectrum has been time-averaged over a single pointing interval for the CGRO spacecraft to avoid systematic shifts due to the detector response; variability of the source flux has been ignored. The spectral indices obtained from a single power law folded through the LAD response and fit to the count spectra in Fig. 1 are given below:

Power Law Fits (see Fig. 1)

Cen A	(20-2000 keV)	-1.9 +-0.1
Cyg X-1	(20-2000 keV)	-1.9+-0.01
4U1700-37	(20- 230 keV)	-3.3 +-0.1
Sco X-1	(20- 100 keV)	-4.9 +-0.2

These spectral indices are consistent with earlier measurements of these sources over the given energy range [1-6].

The transition to the hard state of the QPO source GX339-4[7] was observed in late June through August 1991. The hard state is characterized[7,8] by hard x-ray emission to 200 keV. The soft state, however, has a very different spectrum, emitting 2-10 keV x-rays[9], and is not observable by BATSE. In Fig. 2, the daily average source flux estimated with a single power law fit over the energy range from 20-2000 keV with a fixed index of -2.0 is shown. In late September, GX339-4, which had reached a peak flux of approximately 300 mCrab, had dropped below the one-day sensitivity level. During the period of increasing flux (TJD 8430-8490) a power law fit gave an index of -2.0 and during the peak interval (TJD 8490-8520) softened somewhat to -2.4. The data gaps near 8465 and 8520 are due to the source's elevation with respect to the orbital plane becoming too great for occultations to occur (see discussion below).

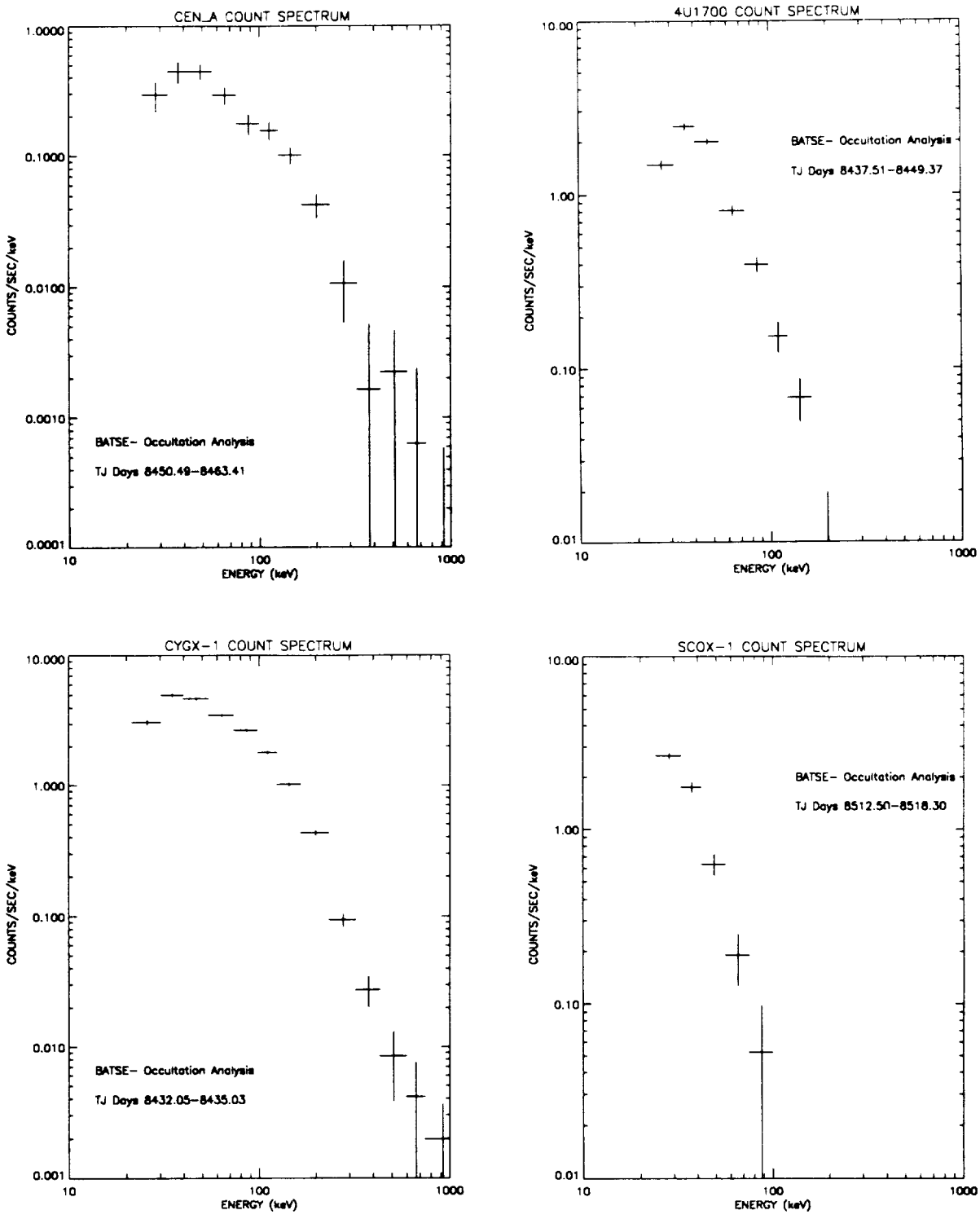

Fig. 1. Sample source spectra obtained with the BATSE occultation analysis averaged over the dates given (Truncated Julian Day=JD-2,440,000.5).

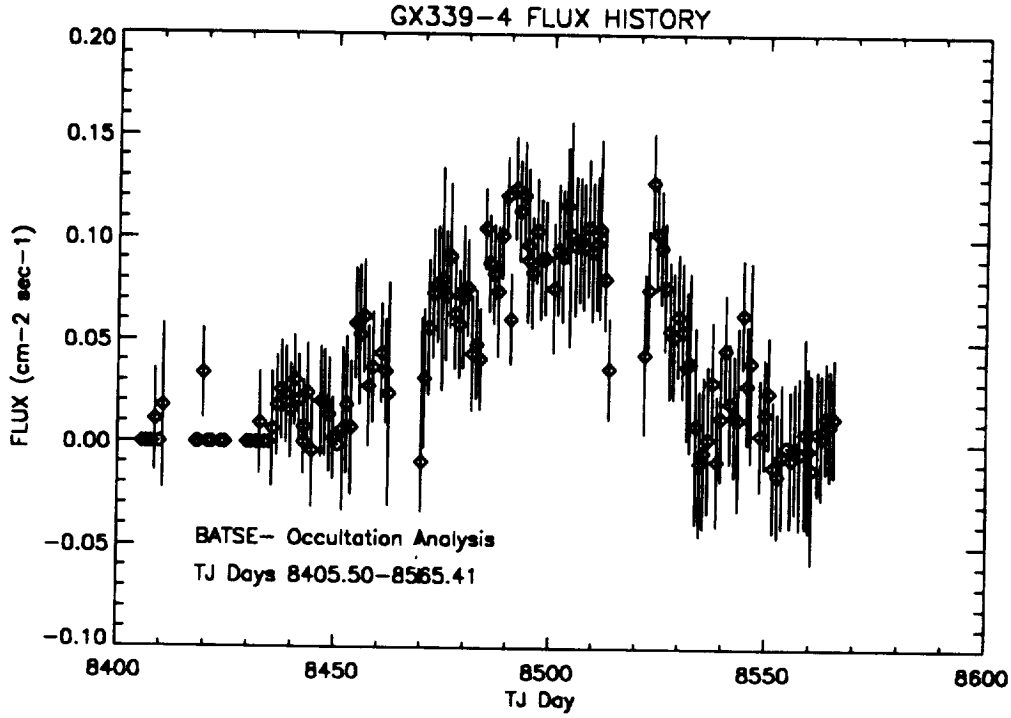

Fig. 2. Flux history for the QPO source GX339-4. TJ (Truncated Julian) Day 8405-8565 corresponds to the period May 29-Nov 2, 1991.

The identification of GX339-4 as a black hole candidate is disputed[8,10], as some quasi-periodic oscillations have been observed in the optical emission region[10].

IV. Improvements to the Occultation System

The BATSE mission operations occultation system has been automated since the early weeks of the mission. Both the source monitoring and the searching programs are now executed by the data operations team. Currently, additional software is being developed to examine processed data products from the occultation system, as well as direct improvements to the operations software.

The predicted times of earth occultation for given source locations are computed using spacecraft position data and an oblate earth+atmosphere model obtained from the Jet Propulsion Laboratory[11]. An occultation is defined to occur when the line-of-sight vector from the spacecraft to the source reaches a specific altitude above the earth's surface. This altitude has been set to 70 km, corresponding to 50% attenuation of 100 keV

gamma rays. The predicted times appear to be good to at least +- 5 secs from a statistical analysis of Crab and Cyg X-1 occultation profiles. This is consistent with an error in the spacecraft position of +- 30 km and allowance for statistical effects on the observed occultation profiles. This deviation appears not to significantly affect the measured count rates when averaged over a one day period.

The step model being used to fit LAD data has two parameters for the time and width of the occultation step, which are currently kept fixed at the time predicted for the 70 km occultation altitude and a width of 20 seconds. The effect of the angle of the source with respect to the orbital plane (beta angle) and the energy dependence of the gamma ray attenuation on the duration and time of the occultation, are being investigated. When the beta angle approaches 70°, the spacecraft-source line-of-sight vector is near the geometric limit for occultations to occur, and the step feature is significantly broadened. The data in Fig. 2, for example, show an artificial lowering of the flux estimate near the critical angle. It is planned to adjust the width parameter to allow for the slowly-varying beta angle as the orbit precesses.

A significant concern which will be dealt with explicitly in the enhanced system being developed (see T. Skelton, *et al.*, these proceedings) is the problem of interfering sources. Any source which is undergoing an occultation within the acceptance time interval for the occultation of a source of interest is a potential problem, and requires a model which incorporates multiple source fitting. While the operations system is designed only for the monitoring of transient behavior and generating crude flux estimates, it would be desirable to separate fluxes from a source which is near in the sky to a very bright source. Two instances where this occurs frequently are A0535+26 (about 4° from the Crab) and Cyg X-3 (about 10° from Cyg X-1); where we plan to use a simple two-source model with a linear or quadratic background.

Other improvements to the system will most likely move toward the goals of greater sensitivity and reducing the time required for identification of a transient source. Many factors can affect how well these can be accomplished, which includes optimizing the search routine, dealing with interfering sources, systematic effects due to detector background, and the effect of atmospheric scattering on the flux estimates.

References

1. H. Gursky and D. A. Schwartz, Ann. Rev. Astron.Astrophys. **15**, 541-68 (1977).

2. C. Montigny, Proc. of GRO Science Workshop, ed. by W. N. Johnson, Sec. 4, 30-35 (1989, Greenbelt, MD).

3. J. C. Ling and W. A. Wheaton, Proc. of GRO Science Workshop, ed. by W. N. Johnson, Sec. 4, 282-289 (1989, Greenbelt, MD).

4. M. Oda, Sp. Science Rev. **20**, 757 (1977).

5. J. F. Dolan, *et al.*, Ap. J. **238**, 238-243 (1980).

6. Lewin, W. H. G., *et al.*, Ap. J. **152**, L55 (1968).

7. P. L. Nolan, *et al.*, Ap. J. **262**, 727-731 (1982).

8. J. F. Dolan, *et al.*, Ap. J. **322**, 324-328 (1987).

9. K. Makishima, *et al.*, Ap. J. **308**, 635-643 (1986).

10. J. N. Imamura, *et al.*, Ap. J. **365**, 312-316 (1990).

11. W. A. Wheaton, private communication.

N92-21884

Scientific Objectives and First Results from COMPTEL

V. Schönfelder[1], K. Bennett[4], H. Bloemen[2], H. de Boer[2], M. Busetta[4], W. Collmar[1], A. Connors[3], R. Diehl[1], J. W. den Herder[2], W. Hermsen[2], M. Kippen[3], L. Kuiper[2], G.G. Lichti[1], J.A. Lockwood[3], J. Macri[3], M. McConnell[3], D. Morris[3], R. Much[1], J. Ryan[3], G. Stacy[3], H. Steinle[1], A. Strong[1], B.N. Swanenburg[2], B.G. Taylor[4], M. Varendorff[1], C. de Vries[2], W. Webber[3], C. Winkler[4]

[1] Max-Planck-Institut für extraterrestrische Physik, 8046 Garching, FRG;
[2] Laboratory for Space Research Leiden, 2333 AL Leiden, The Netherlands;
[3] University of New Hampshire, Space Science Center, Durham 03824, USA;
[4] Space Science Department of ESA, 2201-AZ Noordwijk, The Netherlands.

ABSTRACT

COMPTEL is the first imaging telescope in space to explore the MeV gamma-ray range. At present it is performing a complete sky survey. In later phases of the mission selected celestial objects will be studied in more detail. Targets of special interest in the COMPTEL energy range are radio pulsars, X-ray binaries, novae, supernova remnants, molecular clouds, and the interstellar medium within the Milky Way, as well as the nuclei of active galaxies, supernovae, and the diffuse cosmic background radiation in extragalactic space. The first four months of operation have demonstrated that COMPTEL basically performs as expected. The Crab is clearly seen at its proper position in the first images of the anticenter region of the Galaxy. The Crab pulsar lightcurve has been measured with unprecedented accuracy. The quasar 3C273 was seen for the first time at MeV-energies. Several cosmic bursts within the COMPTEL field-of-view could be located to an accuracy of about 1°. On June 9, 11, and 15, 1991 COMPTEL observed gamma-ray (continuum- and line-) emission from three solar flares. Neutrons were also detected from the June 9 flare. At the present state of analysis, COMPTEL achieves the prelaunch predictions of its sensitivtity within a factor of 2. Based on the present performance of COMPTEL, the team is confident that COMPTEL will fulfill its primary mission: to survey and explore the MeV-sky.

1. INTRODUCTION

COMPTEL covers the middle energy range of the four GRO-instruments - namely 1 to 30 MeV. This part of the electromagnetic spectrum belongs to the least explored ones in astronomy. So far only a few celestial objects have been observed in this energy band. With COMPTEL we have now the possibility to open this field. Since COMPTEL is an instrument with a wide field-of-view of about 1 steradian, about 8 % of the entire sky can be viewed in one single observation. Different sources within the field-of-view, which are separated by more than about 5° can be resolved - in this sense, COMPTEL is an imaging telescope. COMPTEL's sensitivity is about one order of magnitude better than that of any previous gamma-ray experiment at MeV energies. With its energy resolution of 5 % to 10 % FWHM COMPTEL is well suited to not only study continuum, but also line emission. The celestial targets which are of interest to COMPTEL are the following (not in order of importance, but with increasing distance from the Earth).

1) The Sun

The Sun is a bright gamma-ray source during major solar flares. COMPTEL is not only able to observe the gamma-ray emission (continuum and line-emission) during the flares, also solar neutrons can be measured by COMPTEL. During the one week in early June 1991, when GRO was pointed towards the Sun, three major flares (on June 9, 11, and 15) were observed by COMPTEL. Preliminary results from the June 9-flare are presented by Ryan et al. in these proceedings.

2) Galactic Gamma-Ray Sources

From COMPTEL we expect an answer to the question: "What kind of objects in the Galaxy do we see at MeV gamma-ray energies?" So far, only the Crab and Vela-pulsar and the Crab nebula have been observed as permanent gamma-ray sources in this energy range. Further, interesting objects are other radio pulsars, X-ray binaries containing neutron stars or black holes (especially Cyg X-1), the galactic center region, which contains a few variable hard X-ray sources (1E 1740-2942, GRS 1758-258, and GX 1+4), supernovae and their remnants, novae, the unidentified COS-B/SAS-2-sources (especially Geminga), and finally, dark clouds as extended sources.

3) Diffuse Galactic Gamma-Ray Emission

The interstellar medium is expected to be a strong source of continuum and line emission. From the continuum component we shall be able to derive conclusions about the flux, the spectral shape, and the spatial distribution of low energy cosmic ray electrons. From different gamma-ray line components we may be able to derive conclusions on nucleosynthesis sites. The mapping of the Galaxy in the light of the 1.8 MeV ^{26}Al-line will be one of the prime goals of COMPTEL.

4) Cosmic Gamma-Ray Bursts

The objects which are responsible for the cosmic gamma-ray bursts are not yet identified. According to the exciting BATSE results presented at this workshop, most of the sources have to be nearby if they are galactic, or very distant if they are extragalactic. COMPTEL is able to measure the energy spectra and time history of bursts in its single detector mode (0.1 to 10 MeV). It is also able to locate those bursts quite accurately (within 1° or less), that happen to occur in the field-of-view.

5) Extragalactic Objects

In the extragalactic sky the most interesting objects to be studied by COMPTEL are the nuclei of active galaxies (radio-galaxies, Seyfert-galaxies, and quasars). Some of them are expected to have their maximum of luminosity exactly in the COMPTEL energy range (see also later Fig. 8). Clusters of galaxies may be of interest as well, if they show non-thermal intra-cluster emission extending into the MeV-range.

6) The Cosmic Gamma-Ray Background

The question of the origin of the cosmic gamma-ray background radiation is of fundamental interest. COMPTEL will not only measure its absolute flux, its spectral shape and its spatial variations, it will also allow to estimate the contribution of active galactic nuclei to the background radiation.

This certainly is a very ambitious program, and it will take years until all questions raised above will find their proper answers. At the time of this workshop - four months after the start of the GRO sky survey - only first, still very preliminary results on a few selected topics can be presented.

2. COMPTEL IMAGE DECONVOLUTION

The COMPTEL team so far has concentrated on the scientific analysis of two sky regions: the anti-center region of the galaxy with the Crab as an expected strong source, and the galactic pole region with 3C273 as an expected weak source. The data from these observations are being used to optimize our data analysis tools, to study the instrumental background characteristics, and to exercise the image reconstruction.

In addition, we were lucky enough to observe a few transient events (solar flares and cosmic bursts) within the COMPTEL field-of-view in the early part of the mission. These events did not only contain interesting science, they also provided very powerful tools to study the inflight telescope performance under practically background-free conditions.

The image reconstruction from COMPTEL data requires the knowledge of the COMPTEL Point Spread Function. The telescope response to a gamma-ray point source can be described in the simplest way in a three-dimensional data space, defined by the scatter direction (χ, ψ) and the Compton scatter angle $\bar{\varphi}$. Each detected photon is represented by one point in this three-dimensional data space. In the idealised case, in which the scattered gamma ray is totally absorbed in the lower detector, the distribution of all data points resulting from a point source with coordinates (χ_o, ψ_o) lies on a cone in the (χ, ψ, $\bar{\varphi}$)-space, where the cone apex is at (χ_o, ψ_o), and the cone semi-angle is 45°. This idealised cone mantle is actually blurred due to measurement uncertainties and especially due to incomplete absorption in the lower detector.

At present, three different approaches are used by the COMPTEL team for the image reconstruction. The first one is the maximum entropy method, which searches for an input sky, which - after convolution with the response of the telescope - yields an acceptable match to the data and at the same time fulfills the entropy criterion. The second one is the likelihood method, in which the likelihood of a model-sky with and without a point source are compared. Again, the model-sky has to be convolved with the response in order to make the comparison between model and data.

The third approach - in contrast to the previous two methods - does not require the detailed knowledge of the three-dimensional response. It simply determines the one-dimensional ARM-distributions at different trial source positions. (The term "ARM-distribution" is explained in the paper of den Herder et al., in these proceedings. In terms of Figure 1 an ARM-distribution is the one-dimensional projection of all data points in the three-dimensional data space along the ideal cone mantle). If a trial source position coincides with a real one, the ARM distribution will have a maximum around $\bar{\varphi}$-φ_{geo} = zero.

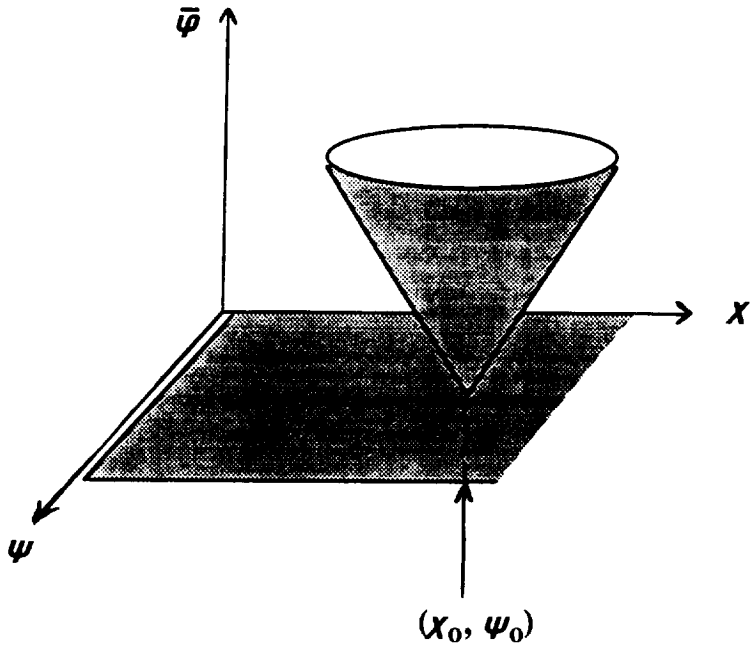

Fig. 1. Illustration of the COMPTEL response to a gamma-ray point source at $(\chi_o\ \psi_o)$.

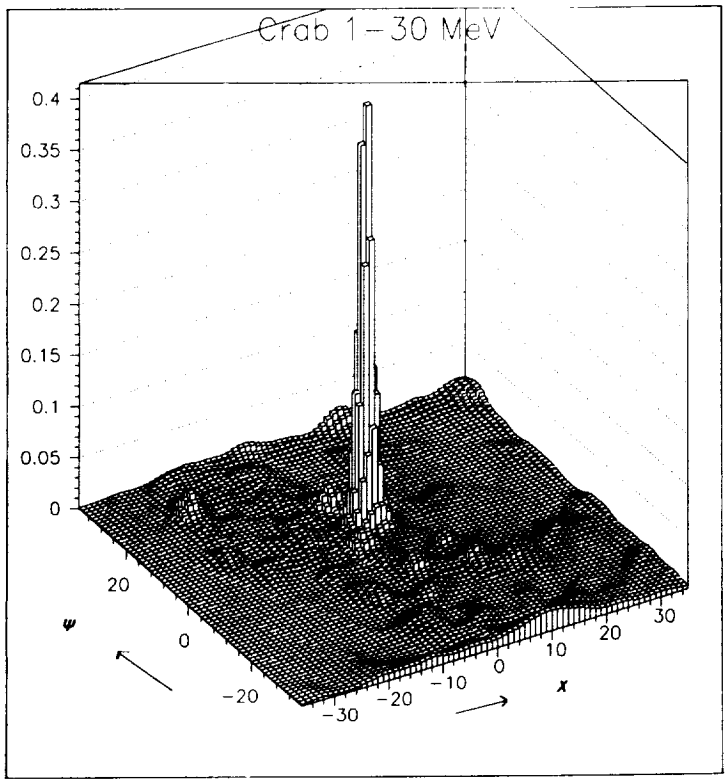

Fig. 2. Maximum Entropy image of the Anticenter region showing the Crab. Coordinates are in the telescope system. Crab is at $\chi = 0.1$, $\psi = 6.4$. The position of Geminga is at $\chi = 8.2$, $\psi = 5.6$.

3. FIRST RESULTS

3.1 The Anticenter region of the Galaxy. Figure 2 contains the maximum entropy image of the anticenter region of the galaxy as derived from 14 days of COMPTEL data in the 1 to 30 MeV range. Within the wide field-of-view of about 50° x 50°, the Crab stands out clearly as the only gamma-ray source. The derived position of the Crab agrees within 18 arcminutes with its known position. The structure around the Crab needs more investigations. At present, the instrumental background is not yet completely understood and, therefore, it is not possible to draw any conclusion about the structure around the Crab. On the other hand, it is already evident from this analysis that gamma-ray emission of Geminga in this energy region is significant smaller than that of the Crab.

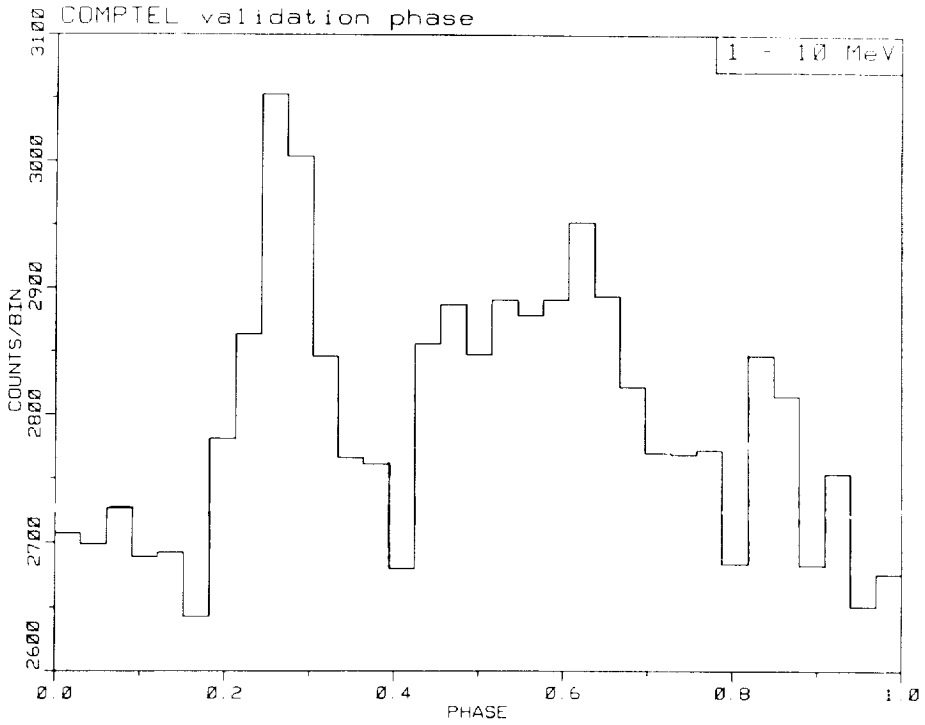

Fig. 3. Crab pulsar light curve from 10 days of data during the GRO verification phase.

The lightcurve from the Crab pulsar analysis of the first 10 days of observation is shown in Figure 3 for the energy interval 1 to 10 MeV. The two peaks of the light curve stand out at the 22 σ confidence level. There is a clear interpulse emission between the two main pulses similarly as in the several hundred keV-band (see Ulmer et al., these proceedings). The analysis of Crab pulsar data from 20 additional days of observation is in progress. There are hints for time variability of the shape of the pulsar light curve over this time interval. However, further analysis is needed before any firm conclusions can be derived.

3.2 Gamma-Ray Emission from 3C273. The quasar 3C273 was in the COMPTEL field-of-view when GRO pointed towards the target-of-opportunity SN 1991T from June 15 to June 28, 1991. 3C273 has always been a promising candidate source for COMPTEL, since its expected flux at MeV-energies - as estimated from an interpolation between X-ray and COS-B high energy gamma-ray measurements - was expected to be larger than the COMPTEL sensitivity limit (see also later Fig. 8).

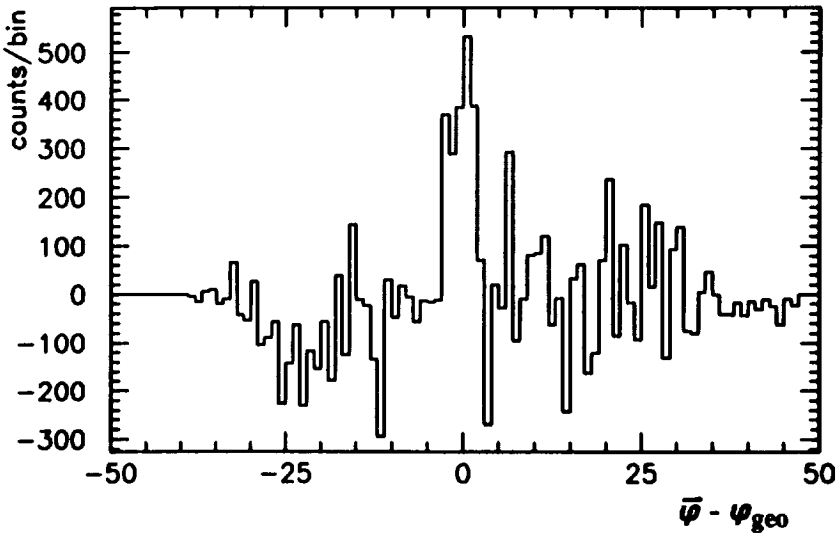

Fig. 4. The background-subtracted ARM-distribution at the position of 3C273 displays a detection of this quasar.

In Figure 4 the background subtracted ARM distribution centered at the position of 3C273 is plotted from 14 days of data in the energy range 0.7 to 20 MeV. There is a clear excess at $\bar{\varphi}$-φ_{geo} = zero, the width of this excess is consistent with that expected from a point source (4° to 5° FWHM). The statistical significance of the excess (using single count rate statistics) is about 6 σ. In principle a contribution to the excess from SN 1991T cannot be excluded (it is only 1.3° apart from 3C273). The strength of the source is about 15 % of that of the total Crab-emission.

It should be noted that no excess is found at the position of the quasar 3C279, which appeared in the EGRET observations at several 100 MeV, nearly as bright as the Crab (Fichtel et al., these proceedings). In the COMPTEL energy range its emission must be at least a factor of 2 below that of 3C273.

3.3. COMPTEL Observations of Cosmic Gamma-Ray Bursts. Apart from cosmic gamma-ray bursts, which were detected in the COMPTEL single detector mode, four bursts (on April 25, May 3, June 1, and August 14) were observed in the COMPTEL field-of-view. Here preliminary results from the May 3 and June 1 bursts are presented.

In Figure 5 the time profile of the May 3 bursts as measured in the telescope mode is plotted. The profile shows two main peaks of a few seconds duration each, separated by about 50 secs. Because on average no more than 20 events per second can be transmitted in the COMPTEL telescope mode, there are gaps in the time profile at the peaks due to dead-time effects, which, however, can be corrected for using internal scalar rates, transmitted during this interval. As the burst happened to occur in the field-of-view, it could be located on the sky.

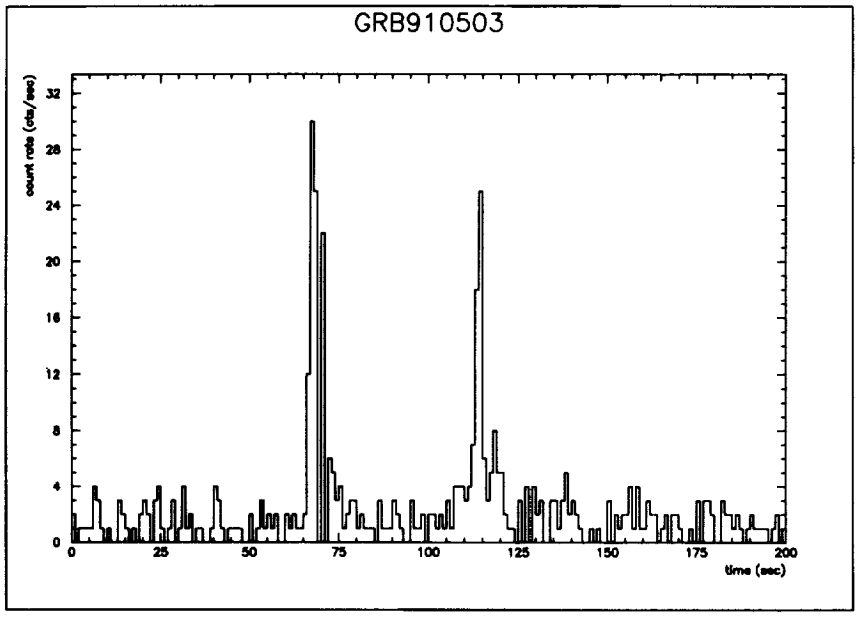

Fig. 5. Time Profile of GRB 910503 as measured in the COMPTEL telescope mode (1-20 MeV).

Figure 6 contains the maximum entropy image of that burst. The best position of the burst source is at l = 171°, b = 7°. The uncertainty of the position is about 1°. This position coincides with a one-dimensional location by triangulation using COMPTEL and Ulysses arrival times of this burst.

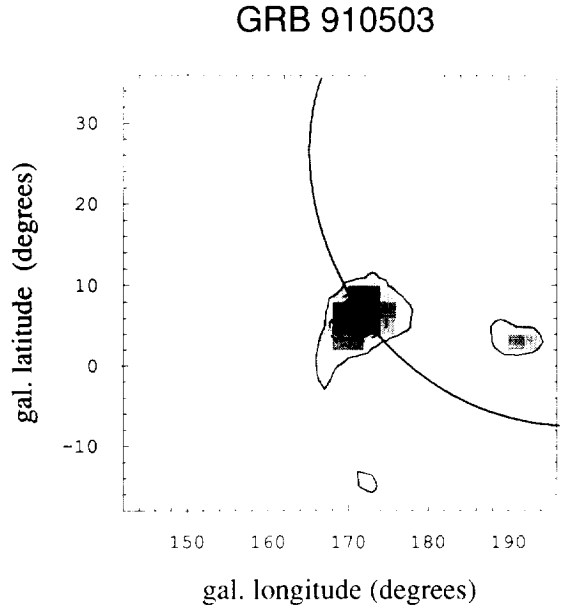

Fig. 6. (1 to 20 MeV) COMPTEL image of GRB 910503 in comparison with the triangulation circle from COMPTEL / Ulysses arrival times.

Similarly, the COMPTEL maximum entropy image of GRB 910601 and the COMPTEL / Ulysses triangulation circle of this burst are shown in Figure 7. Here the best position of the burst is l = 72.5°, b = -5°, again with an uncertainty of about 1 degree. This burst consisted of one spike of 2 sec duration, only.

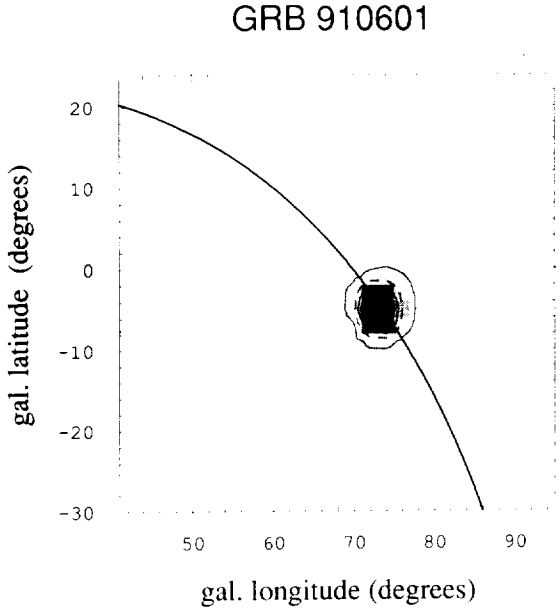

Fig. 7. (1 to 20 MeV) COMPTEL image of GRB 910601 in comparison with the triangulation circle from COMPTEL / Ulysses arrival times.

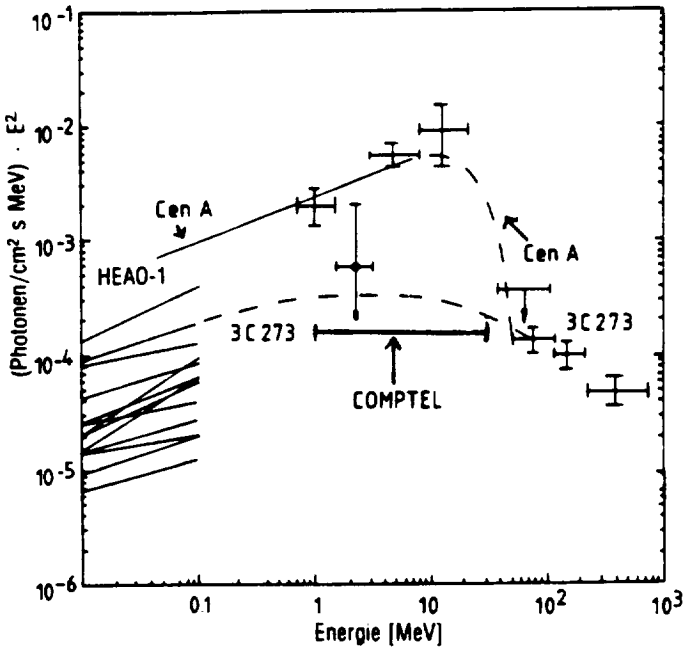

Fig. 8. 3 σ-COMPTEL point source continuum sensitivity for a 14 days observation period.

3.4 COMPTEL Point Source Sensitivity. Based on the first results from COMPTEL in the anti-center and north-galactic pole region of the Galaxy we are able to recalculate the COMPTEL point source sensitivity.

The sensitivity is mainly determined by the background count rate. This was one of the great unknown of COMPTEL, because all experience with Compton telescopes prior to the launch of GRO was based on balloon flights. Nobody really knew, how COMPTEL would perform in orbit.

The background count rate can be influenced in a very sensitive way by application of certain event selection criteria. A preliminary set of event selection criteria has been defined to optimise the signal-to-noise ratio. With this set the COMPTEL point source sensitivity to continuum-emission was recalculated.

The result of this calculation is shown in Figure 8 for an observation time of 2 weeks. The blockage of the field-of-view by the Earth during part of the time is taken into account. The 3 σ sensitivity is compared with the X-ray spectra of 12 active galactic nuclei below 100 keV. The presently achieved sensitivity approaches our predicted sensitivity within a factor of 2 and might be further improved after a more detailed study of the background and the instrument response.

4. CONCLUSION

COMPTEL performs to our full satisfaction. Based on the early results presented in this paper, we are confident that COMPTEL will fulfill its primary mission: to survey and explore the MeV-sky.

5. ACKNOWLEDGMENT

We are grateful to the Ulysses Team for providing us the Ulysses arrival times of GRB 910503 and GRB 910601.

COMPTEL: instrument description and performance

J.W. den Herder[2], H. Aarts[2], K. Bennett[4], H. de Boer[2], M. Busetta[4], W. Collmar[1], A. Connors[3], R. Diehl[1], W. Hermsen[2], J. Ryan[3], M. Kippen[3], L. Kuiper[2], G. Lichti[1], J. Lockwood[3], J. Macri[3], M. McConnell[3], D. Morris[3], R. Much[1], V. Schoenfelder[1], G. Stacy[3], H. Steinle[1], A. Strong[1], B. Swanenburg[2], B.G. Taylor[4], M. Varendorff[1], C. de Vries[2], C. Winkler[4]

[1] Max-Planck Institut fuer extraterrestrische Physik, D-8046 Garching, FRG
[2] Laboratory for Space Research Leiden, POB 9504, 2300 RA Leiden, The Netherlands
[3] University of New Hampshire, Institute for the Studies of Earth, Ocean and Space, Durham NH 03824, USA
[4] Astrophysics Division, Space Science Department of ESA/ESTEC, NL-2000 AG Noordwijk, The Netherlands

Abstract

The imaging Comtpon telescope, COMPTEL, is one of the four gamma-ray detectors onboard of the Compton Gamma-Ray Observatory (GRO). COMPTEL is sensitive to gamma-rays from 800 keV to 30 MeV with a field of view of approximately 1 sr. Its angular resolution (1 σ) ranges between 1° and 2° depending on the energy and incident angle. The energy resolution of better than 10% FWHM enables COMPTEL to provide spectral resolution in the regime of astrophysical nuclear lines. The effective area (for normal incidence) varies typically between 10 and 50 cm^2 depending on the energy and event selections made. In its telescope mode COMPTEL is able to study a wide variety of objects, pointlike as well as extended in space. With 0.125 msec timing resolution, pulsed emission can be studied. In single detector mode COMPTEL uses two of its detectors to study the temporal spectral evolution of strong gamma-ray bursts or transients.

A short description of the intrument, its characteristics as deduced from calibration measurements and simulations, and some first results on the inflight performance are presented.

Introduction

The exploration of the sky for gamma-ray energies between 1 and 30 MeV lags far behind the exploration in the X-ray band and at higher gamma-ray energies. Apart from a limited number of balloon flights, this energy range has hardly been explored. In this energy region an important interaction mechanism is Compton scattering. The photo-electric absorption cross section falls above 100 keV while pair production becomes significant above about 40 MeV. Photons between 1 and 30 MeV, including that part of the spectrum which is rich in nuclear lines, are very penetrating and can propagate over large distances in the universe carrying information about their origin. At the same time, this property makes it very hard to detect and measure them. In addition the showering activity of photons and electrons as well as de-excitation of atomic nuclei, cause a very high background in this energy band explaining its rather unexplored nature.

Inevitably, an imaging detector covering this energy range may rely on the Compton interaction. In this type of detector two detector layers are used. In the first layer (D1) the incoming gamma ray is subject to a Compton interaction and the scattered gamma is, idealistically, completely absorbed in the second layer (D2). In this case the Compton scatter kinematics (eq. 1) yield the scatter angle ($\bar{\phi}$) of the incoming gamma ray and thus defines, combined with the location of the interactions in both detectors, a circle at the sky.

$$\bar{\phi} = \arccos(1 - E_e/E_2 + E_e/(E_1+E_2)) \qquad (1)$$

where $E_\tau = E_1 + E_2$ is the energy of the incoming gamma ray, E_1 and E_2 are the energy deposits in the upper and lower detectors respectively and $E_e = m_e c^2$.

In figure 1 a schematic drawing of COMPTEL is given showing the main detector components (some of the key parameters are listed in table 1, see also reference 1). The upper detector consists of 7 liquid scintillators (NE 213A), the lower detector of 14 NaI scintillators. Each detector is monitored by a number of photo multiplier tubes (PMT). Time-of-flight measurement allows to discriminate forward moving gamma rays from backward moving gamma rays, reducing the background significantly. Each detector plane is surrounded by two anticoincidence shields rejecting charged particles. Neutrons, not detected by the anticoincidence shields, are rejected using pulse shape discrimination techniques in the D1 detector. Finally the figure shows clearly some of the mechanical structure around the D1 and above the D2.

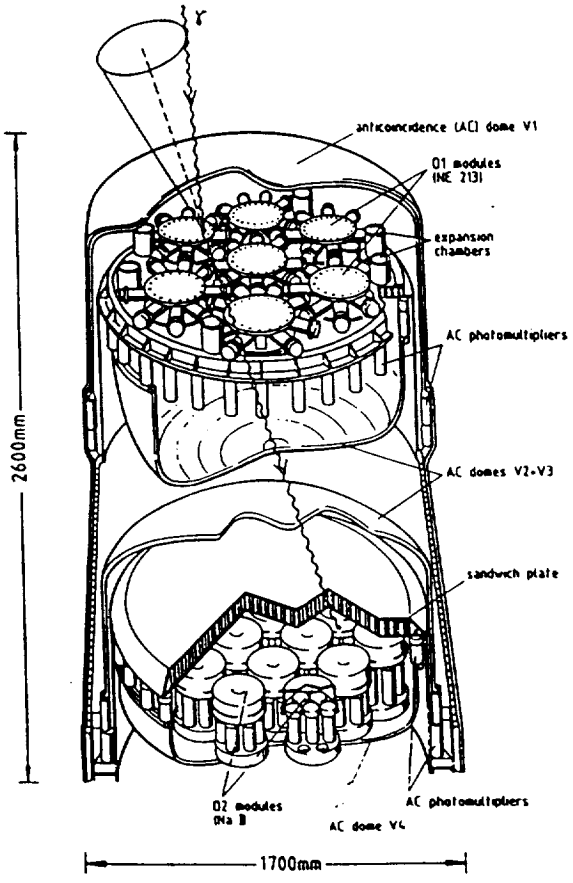

fig. 1 Cut away schematic of COMPTEL.

For each gamma-ray event, which is electronically defined by a delayed coincidence between the upper and lower detector in absence of a veto signal from the anti-coincidence shields the following quantities are available:

Table 1 Some key parameters

D1	: NE 213A, 4188 cm^2
D1 energy	: 50 keV - 20 MeV
D2	: NaI, 8620 cm^2
D2 energy	: 500 keV - 30 MeV
Energy	: 0.720 - 30 MeV, resolution 5-8% (FWHM)
$\bar{\phi}$	: angular resolution 1.7° - 4.4°
A_{eff}	: 20 - 50 cm^2
FoV	: 1 sr
timing	: 1/8 msec

- energy deposit in the upper detector
- location in the upper detector
- pulse shape in the upper detector
- energy deposit in the lower detector
- location in the lower detector
- time-of-flight between the upper and the lower detector
- the absolute time of the event

The pulse-shape and time-of-flight information are used to optimize the signal to noise ratio. The two interaction locations define, together with the pointing of the instrument a point at the sky and the two energy deposits can be converted into the Compton scattering angle ($\bar{\phi}$). This relation (see also eq. 1) is visualized in fig. 2. As a function of the energy deposit in the D1 and the D2 lines of equal E_τ and of equal $\bar{\phi}$ are drawn. The field of view is limited by the hardware energy thresholds: the E_1 threshold determines the lower range in $\bar{\phi}$ and the E_2 defines the upper range.

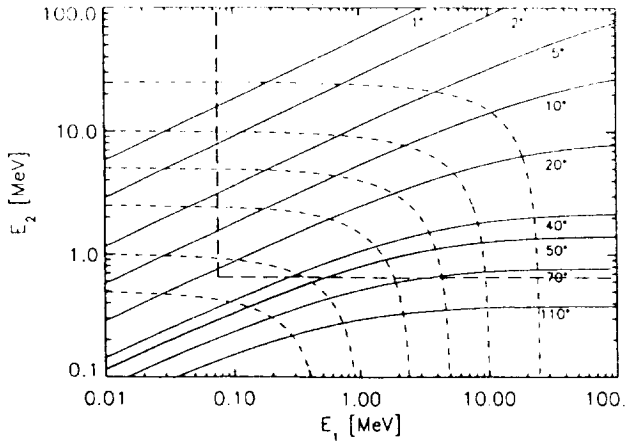

fig. 2 Relation between E_τ, E_1, E_2 and $\bar{\phi}$ for totally absorbed events.

In fig. 3 the Compton scattering cross section according to the Klein-Nishina formula is given for different energies. The probability for a Compton scatter decreases with increasing energy. The relative probability for a Compton scatter angle of less than 50° is indicated. This corresponds roughly to the applied selection in the present analysis (see also fig. 2). As can be noticed about half of the events have a scattering angle of less than 50°.

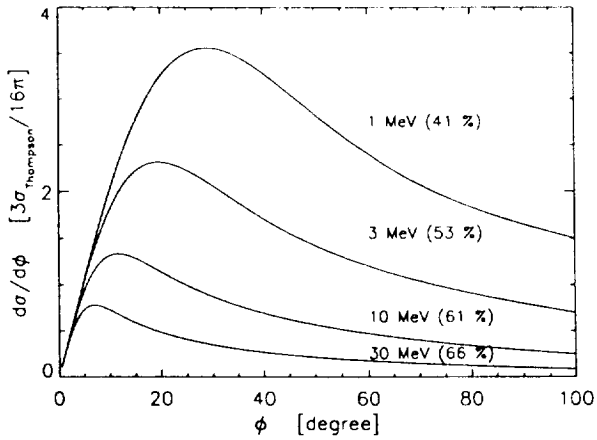

fig. 3 Klein-Nishina cross section for different energies (the relative probability for a scatter angle of < 50° is indicated between brackets).

The COMPTEL response is characterized by a cone with half-opening angle of 45° (see fig. 4) and a distribution along the cone given by the Klein-Nishina formula. The width of the response cone is given by the limited energy and interaction location resolution within the detector modules. Incompletely absorbed events in the D2 populate the inner part of the cone (see Diehl et al., these proceedings).

The width of the cone is a measure for the angular resolution of COMPTEL. In fig. 5 this is shown in a 2-dimensional representation. When no background is present all source events should be concentrated around $\bar{\phi} - \phi_{geo} = 0$ where ϕ_{geo} is the true scattering angle knowing the position of the (calibration) source. This quantity is referred to as Angular Resolution Measure (ARM=$\bar{\phi} - \phi_{geo}$). Partially absorbed events in the D2 will shift to larger $\bar{\phi} - \phi_{geo}$ values. In flight, however, the distribution will be dominated by background events and only strong sources will be identified by a clear signature in the ARM distribution.

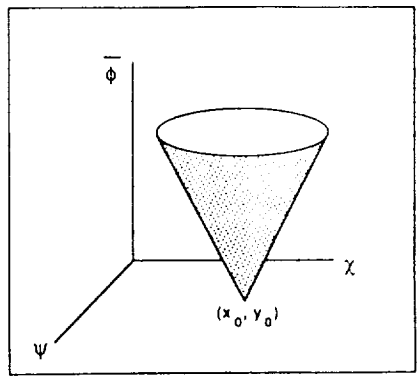

fig. 4 Schemical response of COMPTEL to a point source at position (x_0, y_0).

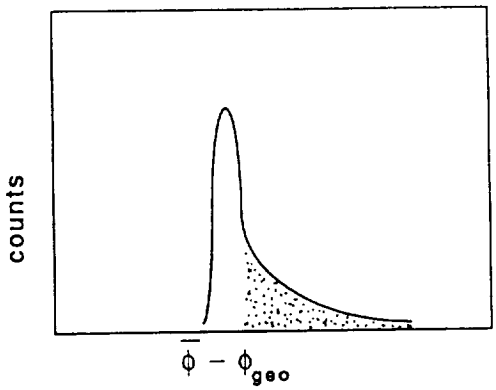

fig. 5 Schematical ARM distributions for a source at a know position (the shaded area indicates not fully absorbed events in the D2)

Main detector elements

The material used for the D1 is a liquid organic scintillator, NE 213A, with low density and low Z in order to maximize the probability of a single Compton interaction. The energy response of this detector is well described by a single Gaussian ($1\sigma = 1.10E^{0.57}$ where the energy is in keV) covering an energy range from 50 keV to 20 MeV. Each D1 detector is monitored by 8 PMTs. Using the Anger camera principle and a neural-net method[2] a spatial resolution of 2.3 cm (1σ) is obtained. The total geometric area for the 7 D1 modules is 4188 cm^2. The D1 also displays pulse shape discrimination properties. This allows to discriminate the slower rise times of proton ionization tracks, caused by neutron scattering on hydrogen, from the short rise times caused by electrons and other minimum ionizing particles. This pulse shape discrimination (PSD)

capability is shown in fig. 6 where the neutrons can be clearly separated from the gammas (note that the curved energy/PSD relation is made linear in the analysis). Alternatively this capability to distinguish neutrons and gammas can be used to measure neutrons created in solar flares (see Ryan et. al., these proceedings).

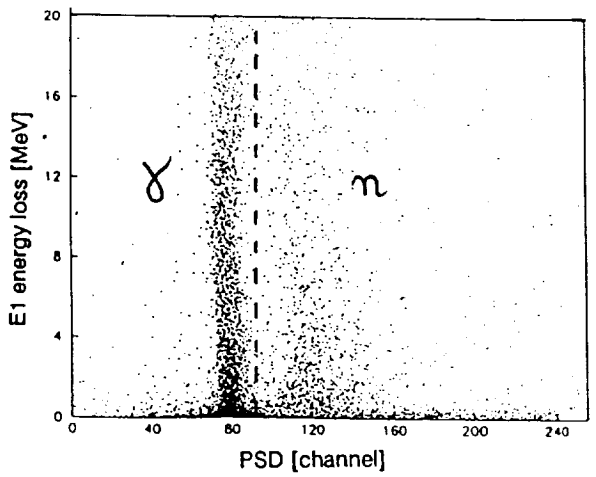

fig. 6 Pulse shape discrimination capability of COMPTEL.

For the D2 detectors NaI was selected to optimize photopeak efficiency. A typical spectrum is shown in fig. 7 where the different components (photo-peak, 1st and 2nd escape peaks and Compton edge) are clearly indicated. The energy resolution, up to 6.1 MeV, is well described by the square-root law ($=1.719E^{0.5}$ - 11.8, E in keV). Above this energy the photopeak signature in the data is not evident anymore. These detectors cover roughly an energy range from 0.6 to 30 MeV.

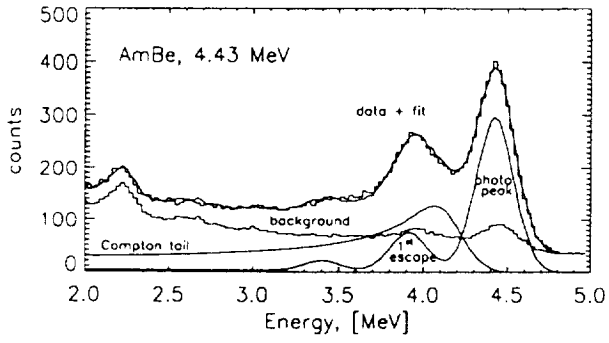

fig. 7 A D2 energy spectrum for AmBe (4.43 MeV). The various components are all indicated.

Each D2 detector is monitored from underneath by 7 PMT's. Using the Anger camera principle, the typical spatial resolution is 2.4 cm. In fig. 8 the spatial resolution for a single module is shown. The total geometrical area is 8620 cm^2.

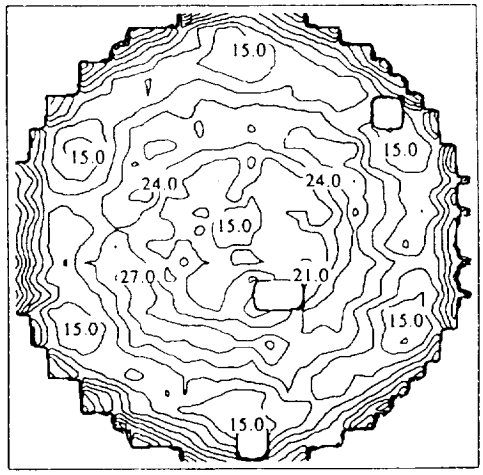

fig. 8 A D2 1-σ event location contour map for a single module (resolution in mm, radius ~ 140 mm).

Apart from the double scatter mode, two D2 modules are operated in single detector mode upon receiving a trigger from BATSE (the Burst and Transient Experiment onboard GRO)[3]. The electronics of these two modules are optmized to cover two different energy regions (0.1 - 1.1 MeV and 1 - 10 MeV respectively) and the time evolution of burst events can be recorded.

Other main detector features include:
- time-of-flight measurement between the upper and lower detector planes (separated by 1.58 m). The time-of-flight is measured with a 3 ns accuracy;
- the rejection of charged particles by the anti-coincidence shields (>99.9 % for each anti-coincidence shield);
- two ^{60}Co doped scintillators, mounted halfway between the D1 and the D2 (CAL units). ^{60}Co emits simultaneously 2 gamma rays (1.17 MeV and 1.33 MeV). These gamma rays are used to monitor the PMT gains and to determine the appropriate corrections;
- accurate measurement of the arrival time of each gamma (0.125 msec accuracy) allows for timing analysis of fast pulsars.

Instrument characteristics

For an imaging telescope the critical parameter is the point spread function which has been determined using different methods, namely[4]:
- measurement of the telescope response using a number of known calibration sources at different orientations with respect to COMPTEL;
- measurement of the single detector responses and calculating the telescope response using this single detector response and the known properties of the Compton scatter interaction;
- Monte Carlo simulation of the response for a given source position and input spectrum.
In figure 9 the measured response is shown for three energies.

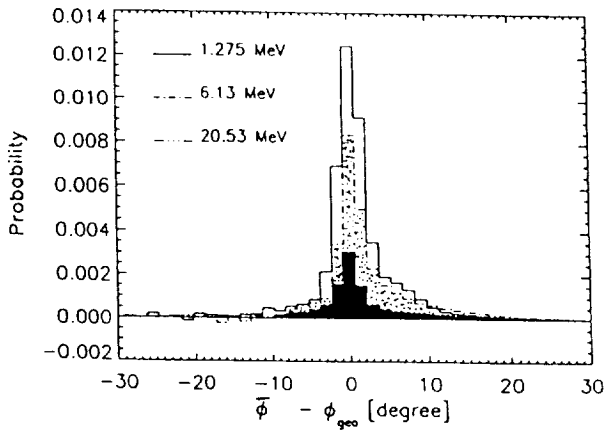

fig. 9 ARM distribution for three different input energies (black area = 20.52 MeV, dotted area = 6.13 MeV, empty area = 1.275 MeV).

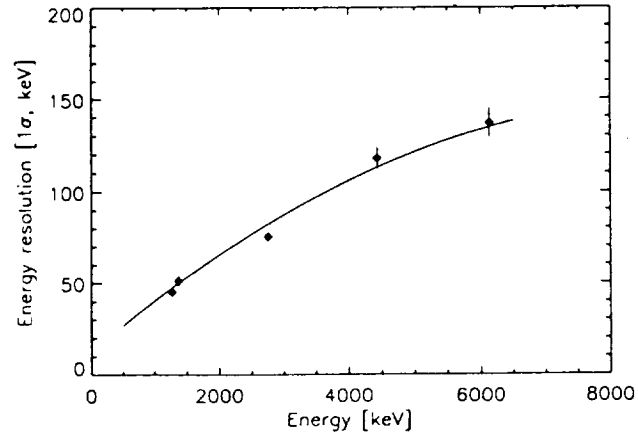

fig. 10 Telescope energy resolution based on calibration measurements (data) and on Monte Carlo simulations (line).

In figure 10 the energy resolution as a function of energy is shown. An energy resolution of better than 10% FWHM enables COMPTEL to provide spectral resolution in the regime of nuclear lines.

In fig. 11 the angular resolution is given. At energies above about 2 MeV the angular resolution is dominated by the D1 and D2 location uncertainty while, at lower energies, the energy resolution predominantly determines the angular resolution per the Compton scatter formula.

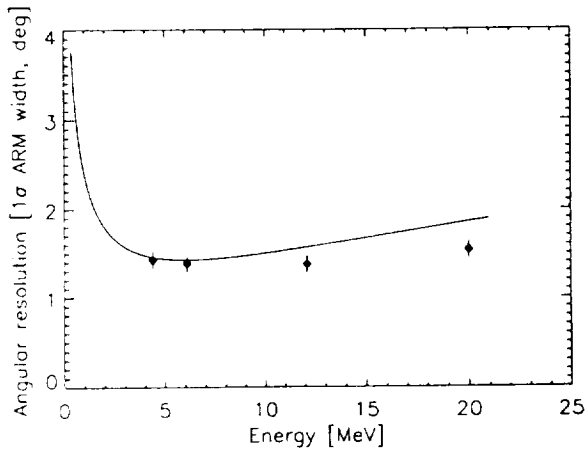

fig. 11 Telescope angular resolution as determined for calibration measurements (data) and from Monte Carlo simulations (line).

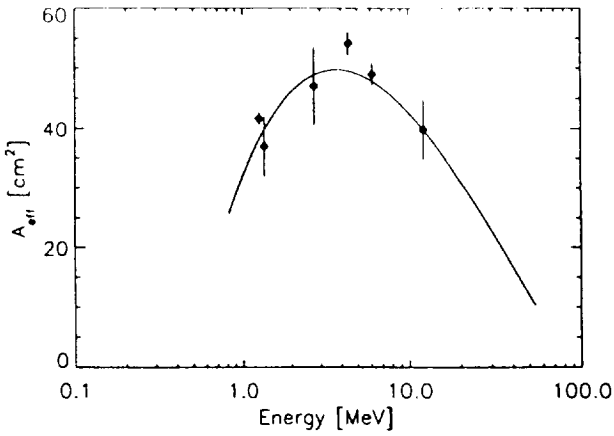

fig. 12 Effective detection area for normal incidence as deduced from calibration measurements (data) and Monte Carlo simulations (line).

In figure 12 the effective sensitive area of the telescope is given for vertical incidence as deduced from the calibration measurements. These results include the effects of the time-of-flight and PSD

selections as well as energy thresholds in the D1 and D2 of 50 and 500 keV, respectively (somewhat lower than the present in flight values). Further selections on the data (such as selection of photo-peak events only) typically reduce the effective area by a factor 2.

Obviously, the effective area depends on the incidence angle as well. This is demonstrated in figure 13 for 1.275 MeV. At higher energies the fall off is somewhat steeper than at 1.275 MeV.

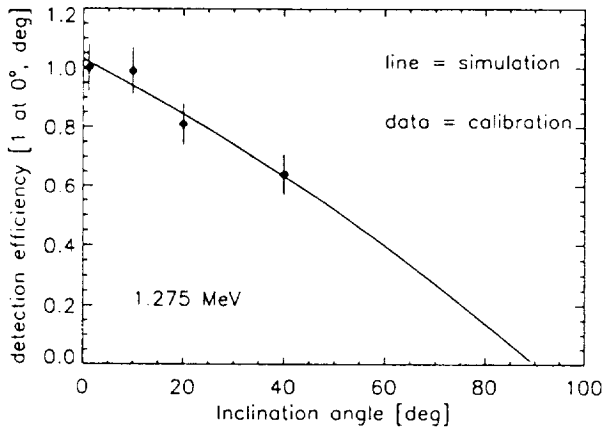

fig. 13 Detection efficiency as a function of inclination angle.

The energy response of the burst modules was calibrated separately before and after integration of COMPTEL on the Observatory. This was required since the response of these modules, which are in principle 4π sensitive, depends heavily on the position of the burst due to the large differences in absorbing material on the spacecraft. For this reason, the burst response decreases dramatically for incidence angles larger than 60°.

Operational modes

The main operational modes include the following:

Double scatter telescope mode:
In this mode a gamma event is defined by a coincidence between the upper and the lower detector in the absence of a signal in the anti-coincidence shields. The onboard selection includes a time-of-flight selection and energy threshold selections. Events with a time-of-flight value between - 7ns and +8 ns with respect to forward scattered gamma events and D1 and D2 energies larger than 65 keV and 600 keV, respectively, are selected (the gamma-1 class). In addition a subset of events with lower energies (larger than 35 and 440 keV respectively) or a less strict window on the time-of-flight (-23 ns to 20 ns) are selected for background studies (gamma-2 class). The available telemetry is first used to transmit gamma-1 events and any remaining capacity is used to transfer the gamma-2 events.

Single detector mode (burst mode):
The burst mode of the two D2 modules is triggered by the BATSE instrument onboard GRO. In absence of a BATSE trigger background spectra are accumulated (2-512 sec telecommandable integration time). After receipt of a BATSE trigger 6 high time-resolution burst spectra are recorded (0.1-25.6 sec telecommandable integration time). Following these 6 burst spectra up to 255 'tail' spectra can be collected (2-512 sec integration time) before the electronics return to the background mode. Gamma-ray bursts, occurring in the field of view and of sufficient strength are, of course, also recorded in the 'double scatter mode'. Then these bursts can be located on the sky with a typical accuracy of less than 2°, using the imaging capability of COMPTEL.

Solar neutron mode:
When BATSE records a burst in the direction of the sun, COMPTEL will switch to the 'solar neutron mode'. In this operational mode events continue to be recorded in the double scatter telescope mode. In addition the 'single detector mode' is enabled to record the evolution of the gamma-ray spectra. Finnally the selections of the gamma-2 channel, usually used for background monitoring, are optimized for the detection of neutrons by shifting the onboard time-of-flight selection to -10 to +33 ns. This enables the recording of neutrons down to about 10 MeV.

Special modes:
There are a number of special modes which support the routine operations. These include the 'proton mode' (no anti-coincidence with the veto shields), the 'D1 single mode' (no coincidence with a D2 trigger), the 'D2 single mode' (no coincidence with a D1 trigger), the 'SAA mode' (a high rate for the light emitting diodes which are attached to each detector module) and an 'atmospheric neutron mode' (settings optimized to detect atmospheric neutrons).

Inflight performance

Since the launch of GRO on April 5th, 1991, and the subsequent checkout and tuning of the instruments COMPTEL has behaved rather stably with two exceptions:
- Module D2-14 appeared to have a noisy PMT since May 24th, 1991, and had to be turned off for that reason;
- Module D1-4 showed high voltage loading problems since July 3rd, 1991, and is also turned off.
Effectively this reduces the telescope efficiency to about 80%. Unfortunately module D2-14 served also as the low-energy burst detector and thus only the high-energy burst detector remains operational.

Each day COMPTEL experiences up to 9 passages through the South Atlantic Anomaly (SAA) during which the high voltages are switched off (about 10% of the observation time). As a consequence of the fixed pointing at the sky during a two week observation the effective viewing time is further reduced to about 30% by the earth blocking the field of view. During each day about 600.000 gamma-1 events are recorded. In the standard analysis about 2/3 is rejected based on the time-of-flight values, the pulse shape information and the energy threshold of the modules. Of the remaining events about 20% is rejected since the scatter angle is larger than 50° and about 40% of the then remaining events are coming from the earth. Finally about 80.000 events remain for further analysis. This number includes events from gamma-ray sources, from the galactic and extra-galactic background, but also includes a substantial contribution from the instrumental background.

In figure 14 orbital variations for a number of characteristic parameters are displayed. On the top panel the high voltage (HV) of the D1-1 module is shown. The different SAA passages can be clearly identified. At the second panel the gamma-1 + gamma-2 rate is given. During SAA passages these rates drop to zero. In addition there are large fluctuations correlated with the cut-off rigidity (given at the bottom). The third panel displays the gamma-1 rate and the fourth panel the high-range burst detector rate, both correlate with rigidity. In the second lowest panel the veto rates are shown.

As stated, the instrumental background varies heavily as a function of geomagnetic latitude. This is demonstrated in figure 15 where the gamma-1 rate is plotted versus cut-off rigidity. The two branches in this correlation plot correspond to the time the earth is in the field of view (top branch) and the time COMPTEL is looking to the sky (lower branch). Even when looking to the sky the variations in the instrumental background vary by at least a factor 2 over the orbit.

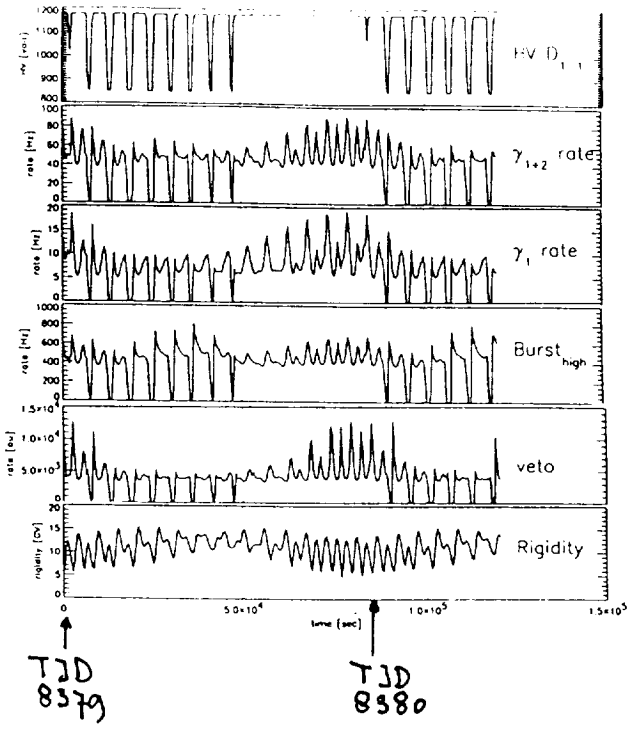

fig. 14 Typical orbital variations (see text for more details).

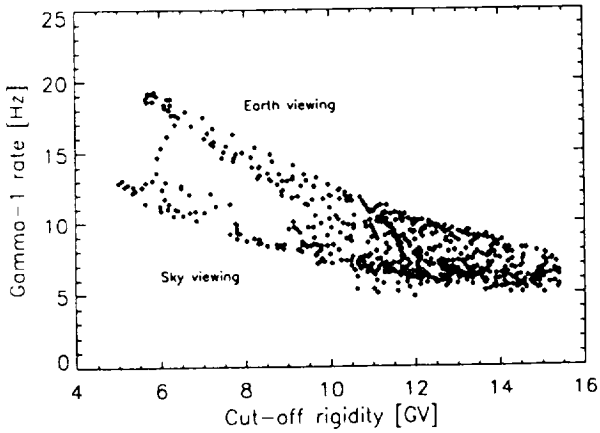

fig. 15 Gamma-1 rate as a function of rigidity.

In figure 16 a time-of-flight spectrum is shown, integrated over a full day and selecting periods of the orbit when the earth is not in the field of view. As expected the relative number of forward scattered events decreases if earth-viewing parts of the orbit are rejected (since the earth is a very strong source of gamma-rays). In the bottom panel of fig. 16 ϕ distributions for three typical time-of-flight selections are shown. The central lower panel corresponds to forward scattered events and could, in first order, be compared with the Klein-Nishina distributions shown in fig. 3. The two other panels show the ϕ distributions of background components. The left panel contains events with lower time-of-flight values. These so-called 'cascade' events are produced by the interaction of energetic cosmic rays with the spacecraft. The right panel is illustrative for the level of accidental coincidences and the $\bar{\phi}$ distribution is very similar to the interaction probability as determined by the geometry of COMPTEL.

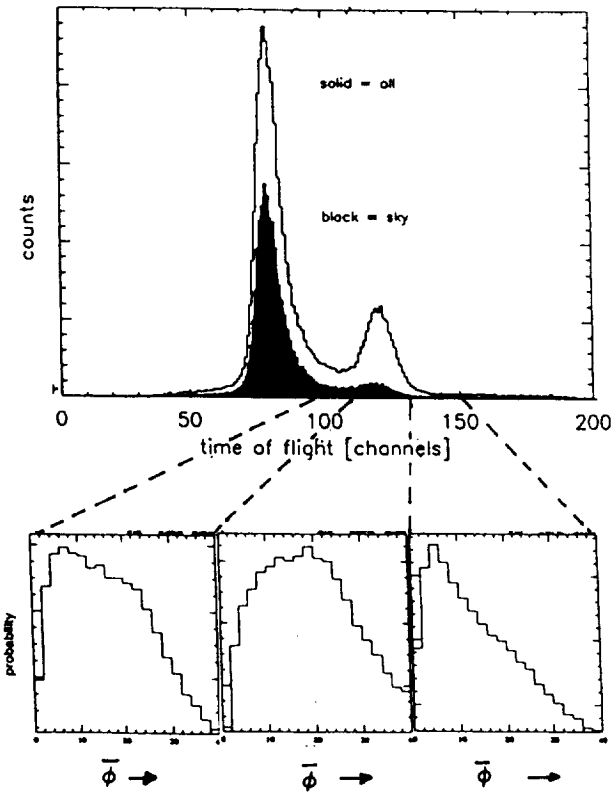

fig. 16 Time-of-flight distributions for a full day (line) and for the earth-viewing part of the orbit (solid). $\bar{\phi}$ distributions for different ToF windows are given.

As part of the in flight tuning the energy thresholds were set, since these directly affect the field of view.

In fig. 17 and 18 the thresholds for two D1 and two D2 modules are shown. The setting of thresholds is performed in three steps:

- onboard, a hardware threshold is set below which no trigger is accepted. This threshold can be set individually for each module (in the D1) or in pairs (in the D2). Due to different gains the corresponding energy of each hardware threshold differs.
- a software threshold is set as part of the onboard selection of gamma-1 events. Only one software threshold is available for the entire D1 and one for the entire D2 and these are applied on the raw data before these are corrected for gain fluctuations in the PMT s.
- finally in the analysis a software threshold is applied to the events after corrections have been applied for fluctuations in the PMT gains. This threshold is the same for all D1 and all D2 modules. It should be set sufficiently high to exclude variations in the effective area due to fluctuations in the gains.

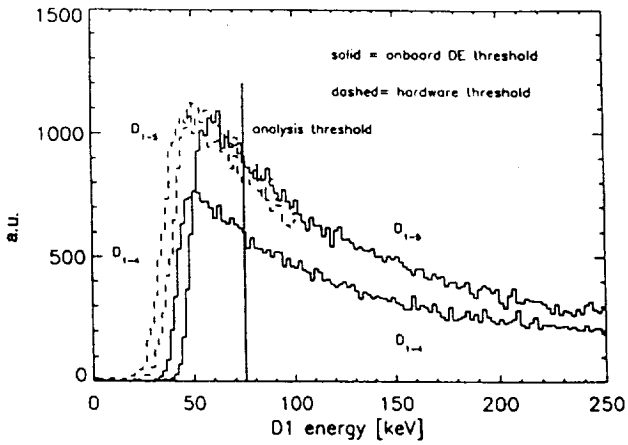

fig. 17 D1 energy thresholds for two modules. The dashed curve represents the effect of the onboard hardware threshold, the solid curve represents the effect of the onboard set software threshold and the straight line is illustrative for the threshold set during analysis of the data.

The onboard threshold and the analysis threshold of the D2 was set to about 580 keV and 650 keV respectively in order to reduce the very strong instrumental 511 keV line due to β^+ decay of the activated ^{11}C in the D1 detectors. A remainder of this 511 line can still be seen in the hardware threshold curve in fig. 18.

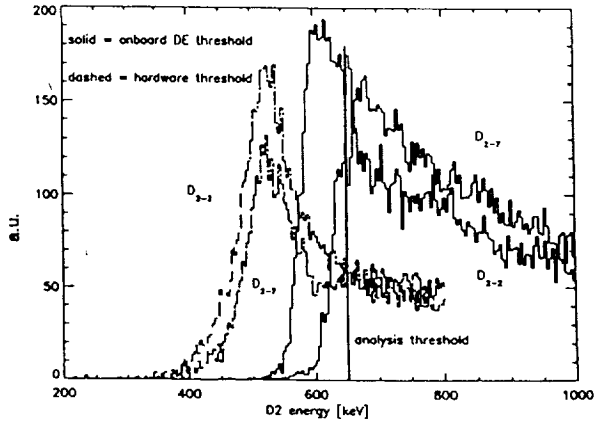

fig. 18 D2 energy threshold (for caption see fig. 16).

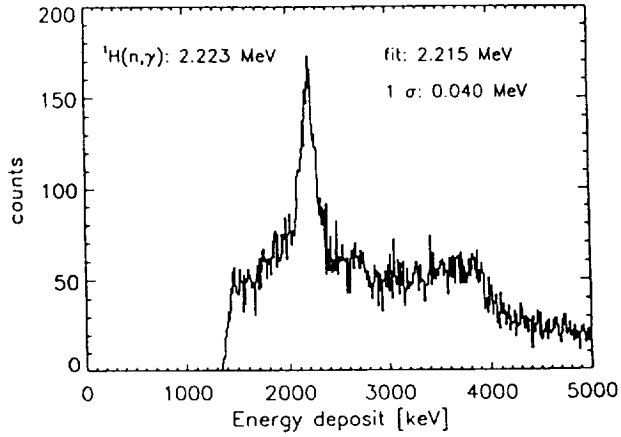

fig. 19 Total energy spectrum of the 2.223 MeV instrumental background line.

The in-flight energy calibration depends heavily on the corrections made for the gain fluctuations in the PMTs. These gains may fluctuate up to 40% for an individual PMT and, although not systematically, show largest fluctuations immediately after a SAA. On average the gains increased by about 10% compared to the pre-flight calibration measurements. While the D2 energy calibration and gain corrections could easily be verified by the photopeak signatures of the 1.17 and 1.33 MeV gamma rays from the two ^{60}Co doped calibration units, this is less straight forward for the D1 modules since these show only a broad Compton distribution for these events. The D1 energy calibration could, however, be checked independently using the neutron capture line of 2.223 MeV in hydrogen. In fig. 19 the result of this check is demonstrated and there is excellent agreement.

Finally the inflight performance of COMPTEL was evaluated during the initial period in orbit by pointing towards the Crab Nebula. In figure 20 the ARM distribution for a one day pointing is shown and the source signature is clearly seen on top of the background. The fact that it is nicely concentrated around 0° is a demonstration of the correct in-flight energy calibration. The estimated systematic error on the position is less than 0.5°. The in-flight sensitivities will be reported elsewhere in these proceedings (see Schoenfelder et al., these proceedings).

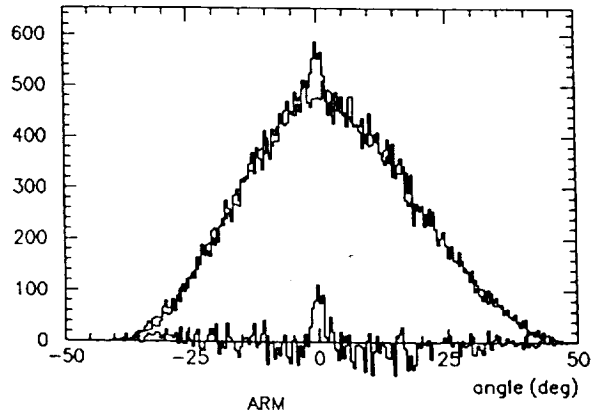

fig. 20 ARM distribution for a one day observation on the Crab Nebula. The lower histogram displayes the difference between the ARM distribution for the Crab Nebula and the background estimate for that observation.

Conclusion

It has been demonstrated that COMPTEL performs well in orbit and that most orbital variations in the data are under control which reduces systematic uncertainties in the data to a minimum. Nevertheless the results of COMPTEL will depend heavily on our detailed understanding of the background and this work could only start after launch (see Diehl et al., these proceedings).

References

[1] V. Schoenfelder et al., IEEE Trans on Nucl. Sci., NS-31, No 1, 766-770, (1984)

[2] A. Connors et al., Neural net approaches for event location in the detector modules, in Data Analysis in Astronomy IV, Erice, Italy 1991, in print

[3] C. Winkler et al., Observing cosmic gamma-ray bursts with COMPTEL, in proceedings of GRO science workshop, Greenbelt MD, USA, 1989

[4] R. Diehl et al., Response Determinations of COMPTEL from Calibration measurements, Models and Simulations, in Data Analysis in Astronomy IV, Erice, Italy 1991, in print

Data Analysis of the COMPTEL Instrument on the NASA Gamma Ray Observatory

R. Diehl[1,*], K. Bennett[4], W. Collmar[1], A. Connors[3], J.W. den Herder[2], W. Hermsen[2], G.G. Lichti[1], J.A. Lockwood[3], J. Macri[3], M. McConnell[3], D. Morris[3], J. Ryan[3], V. Schönfelder[1], H. Steinle[1], A.W. Strong[1], B.N. Swanenburg[2], C. de Vries[2], C. Winkler[4],

[1] *Max Planck Institut für Extraterrestrische Physik D-8046 Garching, FRG*
[2] *Space Research Leiden, Huygens Laboratorium, NL-2333 Leiden, The Netherlands*
[3] *Space Science Center of University of New Hampshire Durham, NH , USA*
[4] *ESA/ESTEC Space Science Departement NL-2200 Noordwijk, The Netherlands*

(*) on behalf of the COMPTEL Collaboration

ABSTRACT

The imaging Compton telescope COMPTEL on the NASA Gamma Ray Observatory is a wide field-of-view instrument. The coincidence measurement technique in two scintillation detector layers requires specific analysis methods. Straightforward event projection onto the sky is impossible. Therefore detector events are analyzed in a multi-dimensional dataspace using a gamma-ray sky hypothesis convolved with the point spread function of the instrument in this dataspace. Background suppression and analysis techniques have important implications on the gamma ray source results for this background limited telescope.
The COMPTEL collaboration applies a software system of analysis utilities, organized around a database management system. The use of this system for assistance of guest investigators at the various collaboration sites and external sites is foreseen and allows different detail levels of cooperation with the COMPTEL institutes, dependent on the type of data to be studied.

INTRODUCTION

The COMPTEL instrument as part of the NASA Gamma Ray Observatory, and its instrumental characteristics, have been described in detail by Schönfelder *et al.*, 1984. Instrumental performance and characteristics are presented by den Herder *et al.* (this volume). For details of calibrations and application of the instrumental response see Diehl *et al.*, 1991. The processing and analysis software environment COMPASS is described by den Herder *et al.*, 1991.
COMPTEL data analysis proceeds in three major steps:
1. Calibration processing of raw data
2. Response and background determination
3. Scientific Analysis

The raw data processing translates the raw telemetry data into normalized

and sorted databases (e.g. attitude data, housekeeping rates, event messages with calibrated and normalized parameters). After this step, the resultant data products (called 'level I data products') can be interpreted without particular knowledge of the data recording characteristics and stability performance of the instrument.

The second step is the analysis of the normalized event messages in terms of the instrumental response. Here a study of the signatures in the data is performed, the results are compared to prelaunch calibration data and other prior instrumental knowledge. Correlation studies of features in the dataspace spanned by all measured parameters of the events (e.g. signal pulse shape and time-of-flight) and instrument background environment (e.g. veto detector rates, cutoff rigidity) are performed on the flight data to establish models for the instrumental background. Here symmetry characteristics of the instrument are exploited to extract and smooth the background model. During this analysis the selection criteria for event messages are optimized. The resulting data products (response, background) constitute the second set of 'low level' data ('level IIa') needed for analysis.

The third step of analysis then combines the event data with these response and background matrices. Initially, a 'generic' skymap without specific astrophysical model assumptions is generated (via the Maximum Entropy Method). Hopefully this map gives indications of interesting regions, and the real in-depth scientific analysis begins: astrophysical models and their specific parameters are tested against the COMPTEL data, and parameter significance limits are derived. Maximum Likelihood based testing of the source models is applied in this dataspace to determine significances of the detected features and their parameters. In the course of these activities, selection criteria may be further optimized to improve the signal-to-background ratio for a specific topic under study; this leads back to the previous steps of re-generating applicable response and background matrices. The COMPTEL collaboration will assess the overall consistency of analysis steps, methods and selection criteria, before releasing the baseline set of results and data products (skymap; result parameter table; filtered event set; selection criteria; background matrices; response matrices) to the scientific community.

RESPONSE CHARACTERISTICS and ANALYSIS METHODS

The COMPTEL instrument operates in the range of MeV photons. Here the main photon interaction with matter is the Compton scattering process, thus dominating the response of the instrument. But this regime is also the domain of de-excitation radiation of atomic nuclei; this results in substantial contamination of the measured data with instrumental background events which do not originate in a Compton scatter interaction as quantified by the instrument response.

The interpretation of the telescope event messages is complicated further by the nature of the instrument response to photons from within the field of view:

For energies of about 1-2 MeV, the interactions in the instrument are mainly a single Compton scatter in the upper detector plane, followed by absorption of the scattered photon in the lower detector plane. This results in a fairly narrow 'source cone' signature of measured event parameters (see figure 1). However the Compton tail of the response of the scintillation detector results in event scatter angle measurements larger than the true scatter angle, forming a

'halo' in the inner part of the 'source cone' signature. At higher energies, the single Compton scattering competes with pair production as first interaction, resulting in a halo around the source cone in all directions. Similar halo events are produced at higher photon energies also by the increasing probability that the Compton scattered electron may produce bremsstrahlung photons, or may escape the scintillator. These response characteristics of the instrument are handled appropriately with the analysis methods operating in the full dataspace shown in figure 1; 'event circle' methods which just explore the main cone feature of the response can be used to confirm the more complex deconvolution method results, but only for strong, widely separated sources.

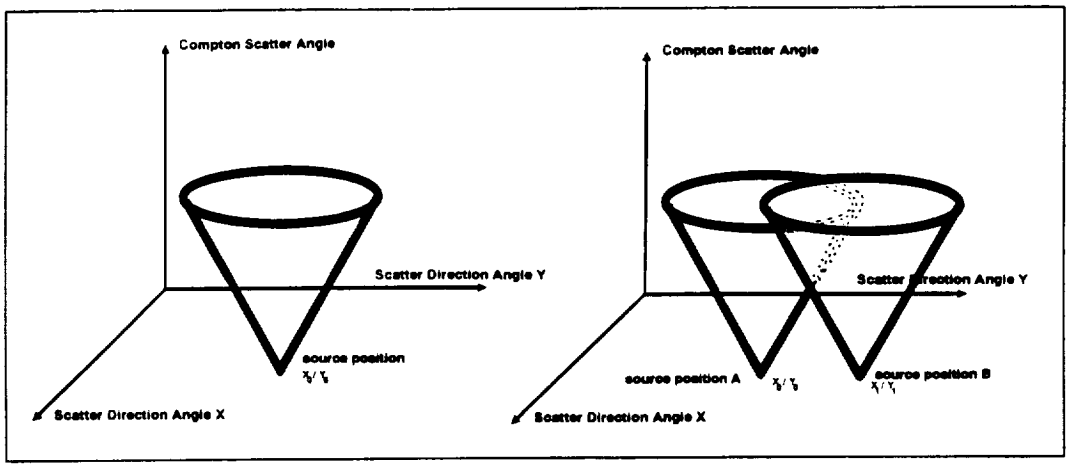

Fig.1 (left): *Dataspace for imaging analysis of COMPTEL data. The first order signature of a source is shown*
Fig.2 (right): *Overlapping measurement signatures from widely separated sources*

The azimuthally undetermined arrival directions of photons along a source cone also imply that source photons from very different directions in the sky may produce identical measured event parameters (see figure 2). Therefore the results of analysis of a particular sky region depend on the source assumptions in sky regions which are tens of degrees away. The standard analysis method should always involve a complete model for the entire instrument field of view.

ANALYSIS ILLUSTRATIONS

In the initial phase of the GRO mission, several cosmic gamma ray bursts were observed within the field of view of COMPTEL. Figure 3 displays the events from a burst (June 1, 1991) as distributed in the measured dataspace; the cone pattern can be traced in the form of rings of increasing diameter in the different slices of the (vertical) scatter angle axis. (Note that the large gamma-ray flux of cosmic bursts provides virtually background-free data, so that instrumental response features show up in the data with little contamination.) Figure 4 shows

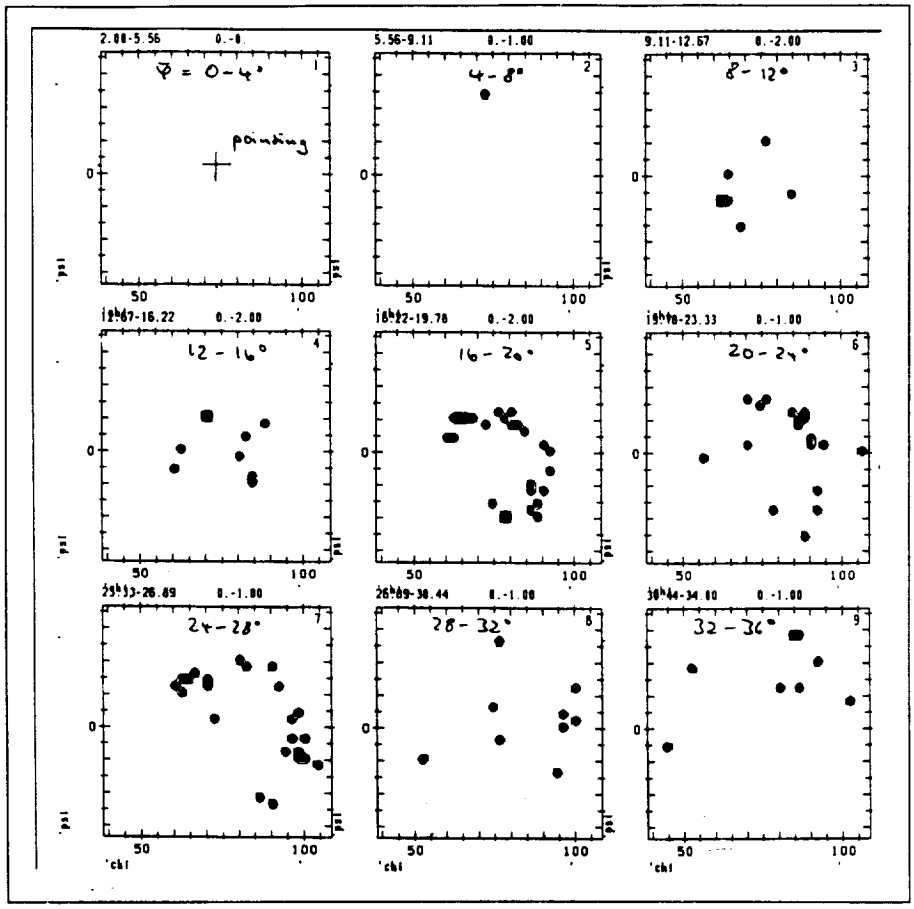

Fig.3: *Measured signatures from a cosmic burst (count diagrams in scatter directions are shown for different scatter angle slices). The cone signature is visible as a set of (inhomogeneously exposed) rings*

the projected raw event messages displayed as 'event circles' of possible arrival directions on the sky. These circles assume a Compton scatter interaction in the upper detector, and a total absorption of the scattered photon in the lower COMPTEL detector. Clumping of the event circle intersections can be seen at l=170, b=10 degrees. The Maximum Entropy deconvolved skymap using the full response detail (shown in figure 5) clearly shows that the sky is dominated by a single point source. Note that for these burst data any instrumental background is negligible.

In the normal case of imaging a complex sky region with the presence of substantial instrumental background, the analysis procedure is more complicated. Figure 6 shows a skymap generated with the same procedure as the burst skymap, namely ignoring background suppression and modelling. If no background knowledge is used at all, the skymap shows a wide range of structures; specifically a large extended structure is seen at longitudes 165-170 degrees. However, if the measurement of the time-of-flight is exploited to establish a background model via selection of events with time-of-flight values outside the

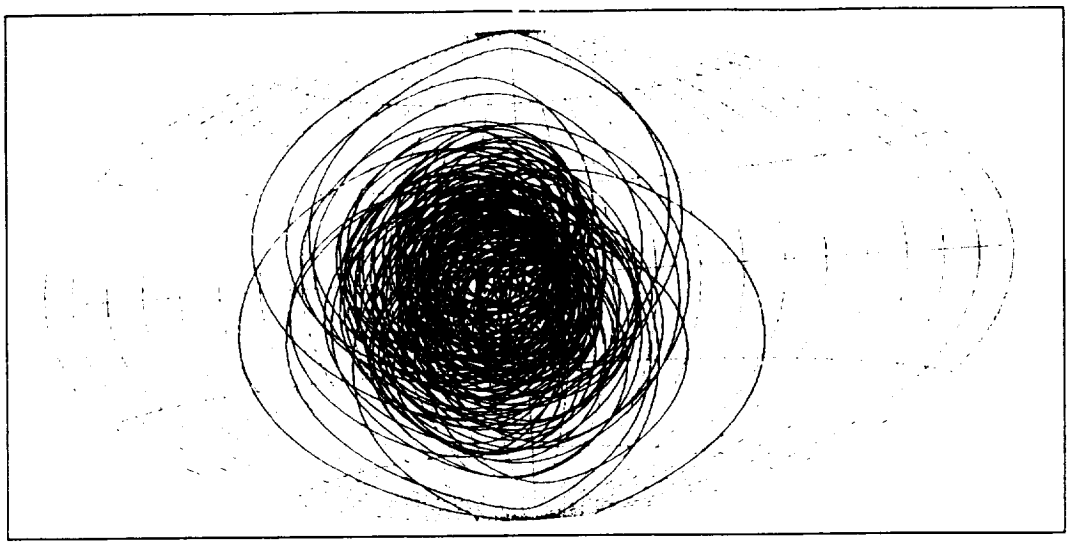

Fig.4: *Projected event circles measured from the cosmic burst 3 May 1991. Clumping of event circle intersections at the position of the burst is barely visible*

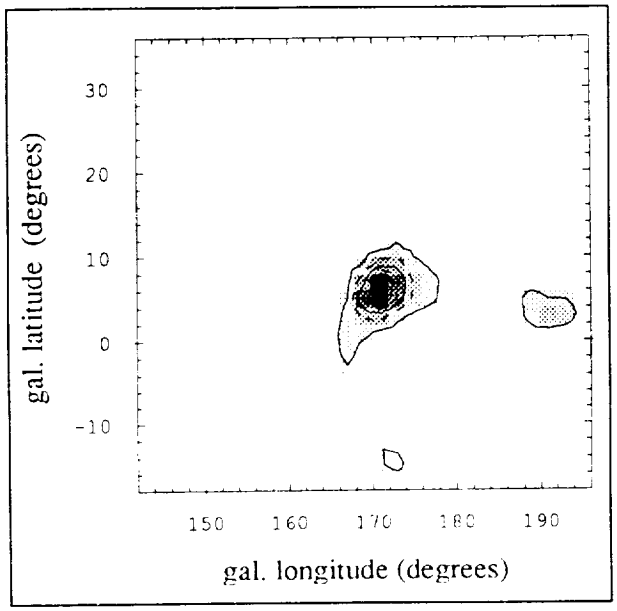

Fig.5: *Maximum Entropy deconvolved skymap from the cosmic burst 3 May 1991 using full response details*

normal values for forward scattering, this model can be applied in the analysis; the skymap in figure 6b is determined using this (crude) background information; obviously the large extended feature dissappears completely, while the dominating feature associated with the Crab nebula/pulsar remains.

Some detailed impacts of the response accuracy can also be demonstrated in the anticenter region (see figure 7). The COMPTEL point spread function can be determined in 3 different ways: via detailed calibration of the detecor

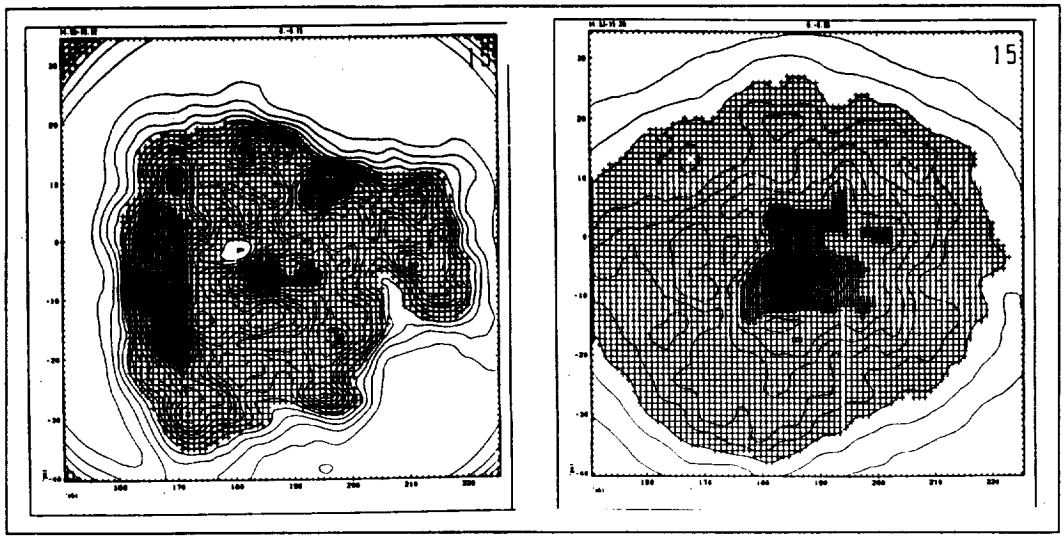

Fig.6: *Deconvolved skymaps from the anticenter region, illustrating the effect of background model inclusion. Without background modelling (a), left), and with inclusion of a coarse background model only, where the false feature dissappears (b, right)*

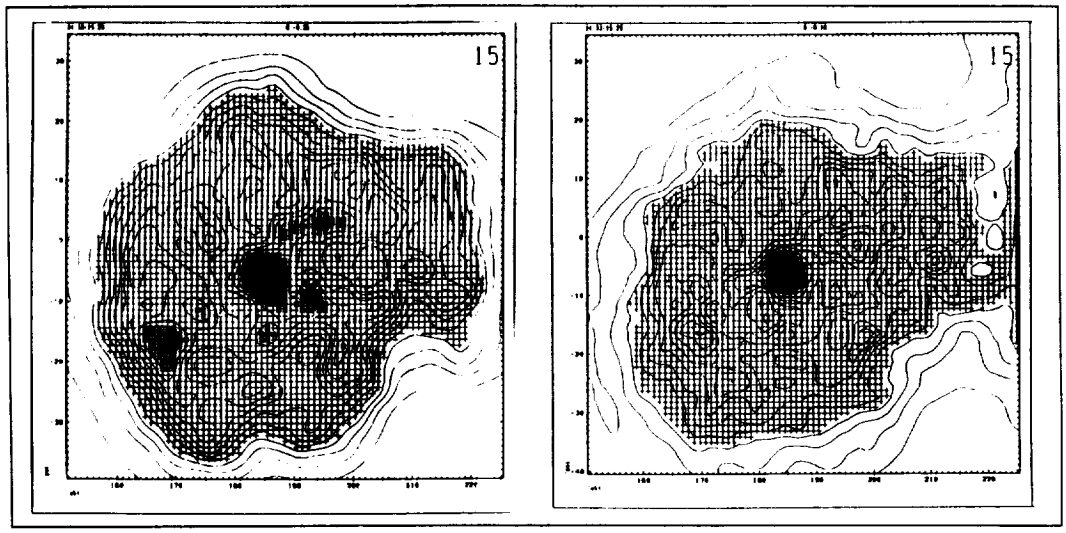

Fig.7: *Deconvolved skymaps from the anticenter region, illustrating the effect of different point spread functions. (Details see text)*

components and an analytical response calculation based on these detector characteristics, via sample calibration within the entire instrument field of view, or via simulations of the entire instrument. The analysis of the first observations (Crab at different aspect angles) will help determine which method actually describes the in-flight response most accurately. Figure 7 shows how the 2 different calibrated responses modify details of the skymap: The PSF used in the lefthand picture is based on accurate calibrations of the 21 COMPTEL detector modules, and on an analytical response calculation; this may ignore unknown secondary features of the true response. The PSF used in the righthand picture

is based on a few calibrations of the entire COMPTEL telescope field of view; this may include calibration contaminations due to the accelerator radiation environment and the non-parallel calibration photon beam. Clearly care must be applied in astrophysical interpretation of the small scale features: these could possibly be artifacts produced by interference of instrumental background and response imperfections as compounded in the complex deconvolution process. The COMPTEL collaboration analyzes details of the Crab image from different aspects, and exploits burst data, in order to optimize response and background treatment in the analysis, so that generation of such artifacts will be largely eliminated.

SUMMARY

The COMPTEL instrument aboard the NASA Compton Gamma Ray Observatory provides a unique opportunity for astrophysicists to enhance our present information about the gamma ray sky and about objects traceable via MeV gamma radiation. The large field of view of the imaging instrument, its operation in a high background environment, and its multiple-interaction based detection principle, necessitate sophisticated data analysis methods and procedures. First analysis results demonstrate the complexity of the analysis approach. Nevertheless the powerful analysis tools and methods established by the COMPTEL collaboration succeed in imaging the MeV sky, demonstrated with the 3 May 1991 cosmic gamma ray burst, and the Galactic anticenter region.

COMPTEL data products will be made available to the scientific community via the GRO Science Support Center. The complexity of the analysis requires care in the interpretation of these products and suggests that scientists should work in close association with the COMPTEL collaboration to benefit from our acquired expertise. Different levels of involvement are proposed and supported (for details see Diehl *et al.*, 1989 (1. GRO Science Workshop).

REFERENCES

— Diehl R., Aarts H., Bennett K., Collmar W., deBoer H., Deerenberg A.J.M., denHerder J.W., deVries C., Hermsen W., Kippen M., Knödlseder J., Kuiper L., Lichti G., Lockwood J.A., Macri J., McConnell M., Much R., Morris D., Ryan J., Schönfelder V., Simpson G., Steinle H., Strong A.W., Swanenburg B.N., vanSant T., Webber W.R., Winkler C., in: Data Analysis in Astronomy IV , edited by V. diGesu et al. , Plenum Press New York, (1991) (*to be published*)

— den Herder J.W., Aarts H., Bennett K., Diehl R., Hermsen W., Johnson M., McConnell M., Ryan J., Schönfelder V., Simpson G., Steinle H., Strong A.W., Swanenburg B.N., deVries C., Winkler C., Wood I., in: Data Analysis in Astronomy IV , edited by V. diGesu et al. , Plenum Press New York, (1991) (*to be published*)

— Strong A.W., Diehl R., in: Data Analysis in Astronomy III , edited by V. diGesu et al., Plenum Press New York, 55-66 (1989)

— Schönfelder V., Diehl R., Lichti G., Steinle H., Swanenburg B.N., Deerenberg A.J.M., Aarts H., Lockwood J., Webber W., Macri J., Ryan J., Simpson G., Taylor B.G., Bennett K., Snelling M., IEEE Trans. on Nucl. Sci., **NS-31** , No. 1, 766-770,(1984)

Neutron Induced Background in the COMPTEL Detector on the Gamma Ray Observatory

D.J. Morris[3], H. Aarts[2], K. Bennett[4], M. Busetta[4], R. Byrd[5], W. Collmar[1], A. Connors[3], R. Diehl[1], G. Eymann[4], C. Foster[5], J.W. den Herder[2], W. Hermsen[2], M. Kippen[3], L. Kuiper[2], J. Lockwood[3], J. Macri[3], M. McConnell[3], R. Much[1], J. Ryan[3], V. Schönfelder[1], G. Simpson[3], M. Snelling[4], G. Stacy[3], H. Steinle[1], A. Strong[1], B. Swanenburg[2], B.G. Taylor[4], T. Taddeucci[5], M. Varendorff[1], C. de Vries, and C. Winkler[4]

[1]*Max-Planck Institut für extraterrestrische Physik, Garching, FRG*
[2]*Laboratory for Space Research Leiden, Leiden, The Netherlands*
[3]*Space Science Center, University of New Hampshire, Durham NH 03824, USA*
[4]*Space Science Department, ESTEC, Noordwijk, The Netherlands*
[5]*Indiana University Cyclotron Facility, Bloomington IN 47504, USA*

Abstract

Interactions of neutrons in a prototype of the Comptel gamma-ray detector for the Gamma Ray Observatory were studied at the Indiana University Cyclotron Facility (IUCF) both to determine Comptel's sensitivity as a neutron telescope and to estimate the gamma-ray background resulting from neutron interactions. The IUCF provided a pulsed neutron beam at five different energies between 18 and 200 MeV. These measurements showed that the gamma-ray background from neutron interactions is greater than previously expected. It was thought that most such events would be due to interactions in the upper (D1) detector modules of Comptel and could be distinguished by pulse-shape discrimination. Rather, the bulk of the gamma-ray background appears to be due to interactions in passive material, primarily aluminum, surrounding the D1 modules. In a considerable fraction of these interactions two or more gamma-rays are produced simultaneously, with one interacting in a D1 module and another interacting in a module of the lower (D2) detector; if the neutron interacts near the D1 module, the D1-D2 time-of-flight cannot distinguish such an event from a true gamma-ray event. In order to assess the significance of this background the flux of neutrons in orbit has been estimated based on observed events with neutron pulse-shape signature in D1. The strength of the neutron-induced background is estimated. This is compared with the rate expected from the isotropic cosmic gamma-ray flux.

1. INTRODUCTION

One of the greatest difficulties in the medium energy γ-ray range (1-30 MeV) studied by Comptel [1] on the Arthur Holly Compton Gamma Ray Observatory is the large instrumental backgrounds from which astronomical γ-ray emission must be distinguished. While Comptel employs several effective strategies to reduce background [2], it is still a serious problem, particularly for observations of diffuse astronomical radiation. This problem is greatest for the apparently isotropic cosmic background radiation.

An important component of the instrumental background – prompt events produced by neutron interactions within the instrument – is the subject of this paper. This background was studied on the ground by exposing an advanced prototype of the Comptel experiment (referred to as Science Model III or SM3) to a pulsed neutron beam. These measurements showed that the prompt neutron-induced background was much larger than expected. Most of these background events are attributed to interactions of neutrons in passive material near the upper (D1) detector modules.

In order to judge the impact of this background on the sensitivity of Comptel, the neutron flux incident on the D1 detector in the Gamma Ray Observatory orbit must be known. This flux

has been estimated from measurements made with the Comptel instrument in a special mode, using one of the D1 modules as an isotropic neutron detector. The in-flight neutron flux is smaller than that observed by balloon experiments at similar latitudes [3], but appears to have a harder spectrum. Combining the estimated in-flight flux with the SM3 results produces an estimate of the rate of prompt neutron-induced γ-like events. This rate is a large fraction of the rate expected for cosmic-diffuse events.

2. SCIENCE MODEL III NEUTRON CALIBRATION

The SM3 instrument consisted of two D1 modules and three of the lower modules (D2) identical to those in the flight instrument [1]. The D1 and D2 modules were mounted separately on two circular aluminum plates reinforced with aluminum beams, similar to those in the flight model. These plates in turn were mounted on a framework of aluminum beams together with one ^{60}Co calibration unit and an anticoincidence detector, consisting of a square plate of plastic scintillator viewed by eight photomultiplier tubes, placed behind one of the D1 modules. Electronics boxes were mounted on top of the aluminum framework. The lines of sight between D1 and D2 modules were unobstructed, except by the anticoincidence detector. The six D1-D2 pairs (referred to as minitelescopes) provided a variety of γ-ray scattering angles, ranging from 1.8° to 30.2° for normal incidence.

The SM3 instrument was exposed to a tagged neutron beam at the Indiana University Cyclotron Facility. Pulses of protons were directed at a ^{7}Li target to produce neutrons via the reaction $^{7}Li(p,n)^{7}Be$. Energy loss by the protons in the target reduced the mean energy of the neutrons below that of the incident proton beam and introduced an energy spread which was greater at low energies. The neutron beam was directed at the SM3 instrument located in a hut 46 m from the ^{7}Li target, behind a Styrofoam filled window; at that distance the beam width was about 1.5 m. At normal incidence, data were obtained with five mean neutron energies: 18.5, 35.7, 77.0, 132.1, and 198.1 MeV. At the four higher energies data were obtained for incidence angles of 45° and 135°; at 35.7 and 132.1 MeV data were also obtained at 90° incidence.

Quantities measured for each event in the Comptel detector include energy deposits in the D1 and D2 detectors, a D1-D2 time of flight (TOF), and a D1 pulse shape (PSD). A neutron time-of-flight from the ^{7}Li target was also recorded for each SM3 event, allowing selection of events coincident with the neutron pulse. Several additional requirements were set for prompt γ-like events in SM3. Only events having a PSD value consistent with a scattered photon were selected. Threshold energies of 200 keV and 500 keV were set for the D1 and D2 detectors, respectively; for D1 energies below 200 keV the PSD is ambiguous. A 5 ns wide TOF window was chosen for each minitelescope. Events coincident with an anticoincidence signal were not accepted, which is consistent with the requirements for γ-like events in Comptel. Finally, the Compton scatter angle inferred from the D1 and D2 energy deposits had to be less than 30°.

Based on measurements with the simpler Double Compton Telescope (DCT) of Schönfelder and Daugherty [4], it was assumed that most neutron-induced γ-like events were the result of $^{12}C(n,\gamma)$ interactions in the NE213 liquid scintillator in the D1 modules (Fig. 1a); most other interactions in the scintillator will produce a proton or alpha particle, and can be distinguished by the PSD. Taking into account differences between the DCT and SM3 detectors, the probability for a neutron entering D1 to produce a γ-like event was expected to be a factor of 15 smaller in a single SM3 minitelescope than in DCT. Surprisingly, analysis of data from one SM3 minitelescope with event selections similar to those used for DCT showed the probabilities in the two cases to be nearly the same!

This discrepancy between the response of the DCT and Comptel detectors is resolved if most of the γ-like events in SM3 actually resulted from neutron interactions in passive material surrounding the D1 detectors, most of which is aluminum. The neutron interaction leaves an excited nucleus which promptly decays via a gamma cascade, emitting two or more photons (Fig.

1b). One of these photons scatters in a D1 module, providing a photon pulse shape; another interacts in D2, providing a γ-TOF. For neutron energies above 100 MeV the scattered neutron may also reach D2 quickly enough to provide a γ-TOF (Fig. 1c). In the DCT detector there were few such events because the mass of the D1 housing was much smaller than in SM3 (1.2 kg vs. 3.4 kg), and the DCT experiment used a collimated neutron beam with dimensions slightly smaller than those of the DCT D1 detector.

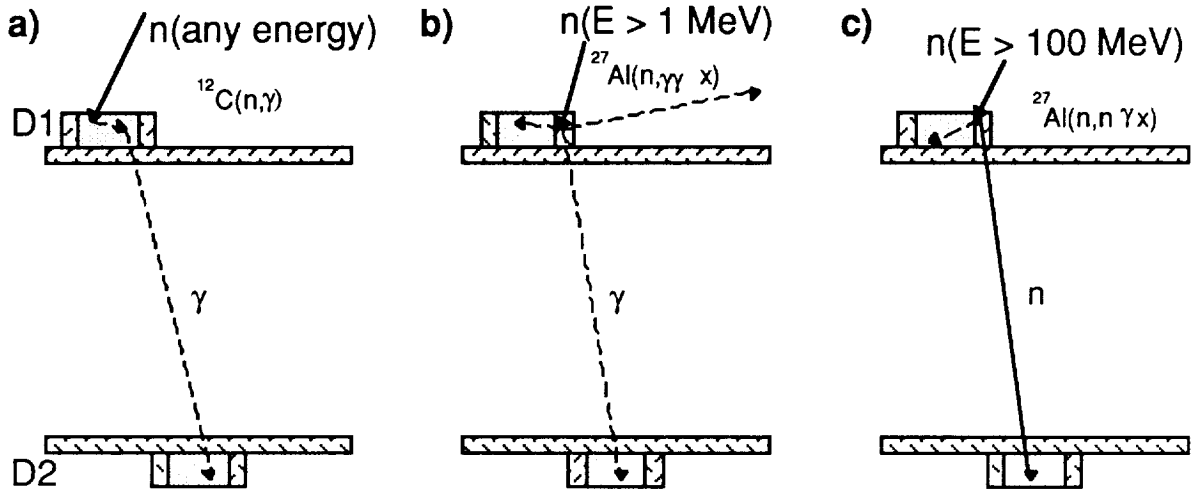

Figure 1: a)*The $^{12}C(n,\gamma)$ reaction formerly thought to be most important in producing prompt neutron-induced background;* (b) *and* (c) *illustrate the interactions occurring in passive material near the D1 modules which the SM3 measurements suggest are much more important.*

Published non-elastic $^{26}Al(n)$ cross-sections, which are available for neutron energies up to 100 MeV or more [5-9], can be used to demonstrate the plausibility of this explanation of the SM3 results. Unfortunately, photon multiplicity distributions for such interactions, which are needed to prove or disprove this hypothesis, are not available. An experiment similar to SM3, but varying the passive mass near D1, could provide more convincing evidence for this hypothesis. To show that the SM3 results are consistent with the published cross sections, the cross-section for a neutron to produce a γ-like event in one minitelescope, referred to here as σ_{SM3}, has been determined from the measurements. This quantity can be related to the non-elastic $^{26}Al(n)$ cross-section, σ_{non}, and the cascade photon multiplicity, m:

$$\sigma_{SM3} = [0.33\langle m\rangle + \langle m(m-1)\rangle]\ \sigma_{non}$$

Pointed brackets in this expression indicate the mean of the enclosed quantities. The first term within the square brackets accounts for events in which a single photon scatters from D1 to D2, while the second accounts for two-photon events of the type illustrated in Fig. 1b. Figure 2 compares σ_{SM3}, as measured in a single minitelescope with normally incident neutrons, to published cross-sections. At neutron energies from 18 to 77 MeV the ratio $\sigma_{non}/\sigma_{SM3}$ is about 4, consistent with a mean photon multiplicity $\langle m\rangle$ of 2.4 or less; at energies 15 to 50 MeV $\langle m\rangle$ is in the range 1.7 to 2 [9]. Above 100 MeV $\sigma_{non}/\sigma_{SM3}$ increases, probably due to high-energy neutrons scattering to D2, as in Fig. 1c; such interactions are not included in the expression for σ_{SM3} above.

The plausibility of this hypothesis can also be demonstrated by the presence of features in the D2 energy spectrum, where a strong line should produce a visible photopeak. The sum of D2 spectra in all three modules for the 35.7 MeV-135° runs shows such a feature at 1.5-2.0 MeV, consistent with a line at 1.81 MeV produced from the reaction $^{27}Al(n,d\gamma)^{26}Mg$. The statistics of the 18.5 MeV data were not sufficient to pick out such a feature; at higher neutron energies such features are weaker relative to the continuum [10].

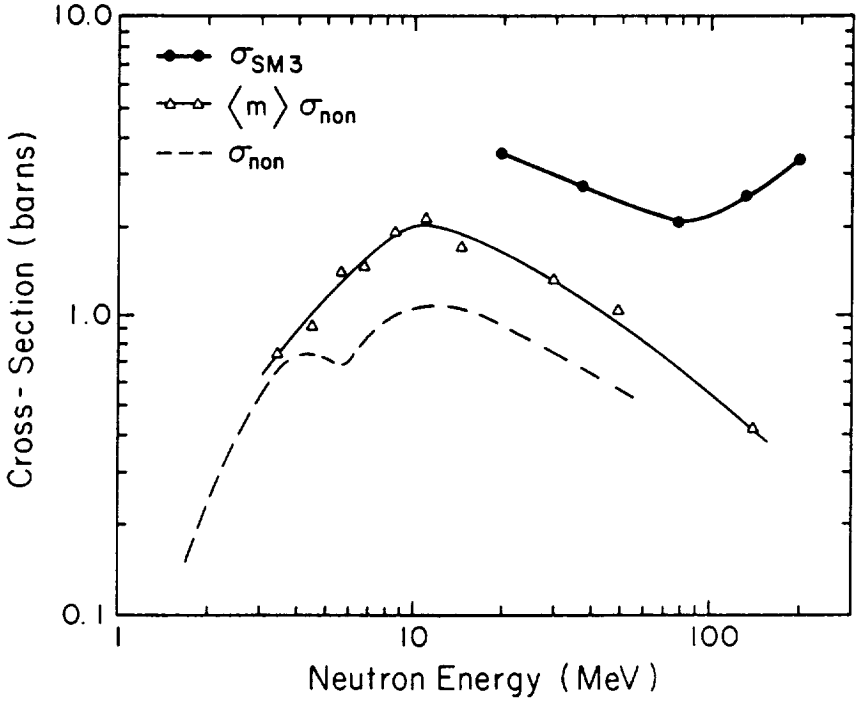

Figure 2: *Comparison of the quantity σ_{SM3}, estimated from events in a single SM3 minitelescope, with published non-elastic $^{27}Al(n)$ cross-sections (σ_{non}, refs. 5-7) and with the non-elastic cross section multiplied by the mean photon multiplicity ($<m>\sigma_{non}$, refs. 8 and 9).*

The probability that an incident neutron produces a γ-like event, as a function of the measured event energy, incident neutron energy, and incidence angle, was evaluated separately for each SM3 minitelescope. The probabilities varied considerably between minitelescopes but most of this variation could be attributed to the differences in D1-D2 distance for each minitelescope; the remaining discrepancies were on the order of 20% averaged over neutron energy and angle. Variations with incidence angle were relatively small. The results for individual minitelescopes were multiplied by a factor to correct the D1-D2 distance to that of a 'mean' Comptel minitelescope and then averaged. The cross section for a neutron to produce a γ-like event in the mean minitelescope, integrated over event energy, is in the range 0.008-0.014 cm^2. The cross section is greatest at 18.5 MeV incident energy and appears to have a minimum near 100 MeV, as in Fig. 2. As a function of the event energy measured in SM3 (as opposed to the incident neutron energy), the cross section falls slowly over the range 1 to 5 MeV, very steeply beyond that; few events with energies above 10 MeV were seen, and then only with incident neutrons above 100 MeV.

The lack of SM3 data for neutron energies above 200 MeV introduces large uncertainties in the γ-like background estimate, especially at higher event energies. While the SM3 cross section

increases above neutron energy 100 MeV, this increase probably stops at some point where most scattered neutrons have enough energy to reach D2 and produce a γ-TOF. At some energy self-veto effects with the full anticoincidence system may also become important in Comptel, hence reducing the cross section for γ-like events.

3. ORBITAL NEUTRON FLUX

The neutron flux incident on the D1 detectors in flight has been estimated from a special 26 minute measurement made during earth occultation on 8 July 1991. All D2 modules and all but one D1 module were turned off. The one remaining D1 module was operated with a very high threshold, 8 MeV. In this 'singles' mode, a coincidence with a D2 module is not required, although events can still be vetoed by signals from the anticoincidence domes. The event rate in this configuration was 30-100% of the telemetry capacity; lowering the threshold or using additional modules would lead to deadtime uncertainties without appreciably increasing the event rate.

The neutron sensitivity of a D1 module in the singles mode was calculated as a function of the neutron energy and D1 threshold by Byrd [11]. The orbital observations cannot be easily deconvolved to produce a definitive value for the neutron flux or a shape for the energy spectrum. Instead, some possible energy spectra have been folded with the sensitivity to predict a neutron detection rate; these predicted rates are compared with those observed to determine whether the flux is greater or less than that expected, and/or whether the spectrum is harder or softer.

The D1-singles events are divided into two groups based on energy: above and below 20 MeV, the highest energy at which the D1 energy and PSD were calibrated. For events outside the calibrated range (above 20 MeV) the energy can only be considered a lower limit, but neutron events can still be distinguished by their PSD signatures. It is also useful to divide the events into two periods based on the cosmic-ray vertical cutoff rigidities due to the geomagnetic field. During the first 16 minutes of the measurement the cutoff rigidity was high and nearly constant, in the range 10.5-12.5 GV. During the remaining 10 minutes the cutoff rigidity dropped rapidly from 10.5 GV to ~5 GV. About 58% of the neutron events occurred during the shorter low cutoff rigidity period.

TABLE I
D1 NEUTRON SINGLES EVENT RATES

Event Energies (MeV)	Event Rates (Hz)			
	High Vertical Cutoff Rigidity (10.5-12.5 GV)	Low Vertical Cutoff Rigidity (~5-10.5 GV)	Balloon Flight[1]	$E^{-1.3}$ Energy Spectrum
< 8.	0.07	0.18	—	—
8. - 20.	0.78	1.80	2.70	2.08
>20.	0.78	1.58	1.30	1.86
All	1.63	3.56	4.00	3.94

[1]Ait-Ouamer [10]

Table 1 lists the rates of neutron-singles events in both high and low cutoff rigidity periods in three D1 energy ranges. About 10% of the events below 20 MeV also fall below the nominal 8 MeV threshold after the events are corrected for photomultiplier gain variations. Also shown in this table are the rates expected for a neutron flux such as that seen by Ait-Ouamer [3] at balloon altitudes at a vertical cutoff rigidity of 8.5 GV, with a neutron energy spectrum having a

power law index of −1.61. The last column shows the rates for a power-law spectrum of index -1.3 and with the total flux above 10 MeV normalized to that seen by Ait-Ouamer.

While the Ait-Ouamer neutron energy spectrum is much softer than that inferred from the D1 singles data, the $E^{-1.3}$ spectrum is consistent with the D1 singles data in the low cutoff rigidity range. Simulations with a preliminary mass model indicate that the neutrons produced in the spacecraft have a harder spectrum than those from the atmosphere [12], though perhaps not as hard as $E^{-1.3}$. The total count rate at low rigidity is about 10% lower than that expected from the Ait-Ouamer measurements. This difference is well within the uncertainties in the calculated D1 singles neutron sensitivity.

4. ESTIMATED STRENGTH OF THE NEUTRON-INDUCED BACKGROUND

By folding the cross sections derived for SM3 (section 2) with an estimated neutron flux and energy spectrum into D1 (section 3), the strength of the neutron-induced background can be estimated. However, the cross sections for the mean SM3 minitelescope must first be multiplied by two factors to account for differences between SM3 and Comptel: a factor of 98 to include all the Comptel minitelescopes, and a factor of 1.5 to account for the greater amount of passive material near the D1 modules in Comptel. The latter factor is very uncertain; a better estimate may be obtained by comparing the 18.5 MeV SM3 data with calibration data for the Comptel flight model obtained using a 17 MeV neutron beam.

TABLE II
EXPECTED RATES OF NEUTRON-INDUCED GAMMA-LIKE EVENTS (Hz)

	Event Energy (MeV)				
Neutron Spectrum	1.0-3.0	3.0-5.0	5.0-10.0	10.0-30.0	0.0-50.0
10-250 MeV Neutrons					
Ait-Ouamer	0.08	0.05	0.030	0.0007	0.1578
$E^{-1.3}$	0.05	0.03	0.019	0.0007	0.0986
>10 MeV Neutrons					
Ait-Ouamer	0.09	0.06	0.035	0.0022	0.1828
$E^{-1.3}$	0.08	0.05	0.029	0.0045	0.1596
Isotropic Cosmic Flux	0.10	0.09	0.023	0.0060	

Expected rates of neutron-induced γ-like events for two different incident neutron spectra are presented in Table II. The two neutron spectra are Ait-Ouamer's spectrum, and the $E^{-1.3}$ spectrum with a total fluence above 10 MeV 10% lower than Ait-Ouamer's. Two rate estimates are given for each neutron spectrum: one for incident neutrons in the energy range 10-250 MeV only, and one for all incident neutrons above 10 MeV. For this second estimate the SM3 probabilities for 198.1 MeV neutrons are used for the incident neutrons above 250 MeV. These results imply that the high-energy neutrons are very important for event energies above 10 MeV; with the harder neutron spectrum they may also be important for the lower event energies. Thus there is a large uncertainty in the neutron-induced background rate, especially in the upper part of the Comptel energy range, depending on how the SM3 results are extrapolated to higher neutron energies. These background estimates are compared with the rate of events expected from an isotropic cosmic γ-ray flux, based on previous spacecraft observations [13] which were folded with the Comptel sensitivity; this sensitivity was determined from simulations with a mass model of Comptel, using the same event selections as in the SM3 analysis.

A comparison of the neutron-induced γ-like background rates with the expected rate of cosmic diffuse events, shows that this instrumental background may be a large fraction of the event rate from the isotropic cosmic γ-ray flux at all event energies. At high cutoff rigidities, the

background rates will be reduced by about a factor of two, but that level is still quite significant. It should be noted that both the neutron-induced background rates and the cosmic-diffuse rates depend on the event selections imposed; in particular, the high D1 threshold used in the SM3 analysis reduces the cosmic diffuse rate in the 1-3 MeV range by about a factor of three relative to the standard Comptel selections. A carefully chosen set of selections may increase the rate of events from the isotropic cosmic γ-ray flux relative to the instrumental background.

5. CONCLUSIONS

It is clear that the instrumental backgrounds in the Comptel γ-ray telescope, and indeed in all instruments operating in this γ-ray energy range, must be carefully accounted for in order to determine a reliable flux for the cosmic-diffuse radiation. An analysis such as that presented here is a necessary part of that process. The neutron-induced γ-like background is an important part of the instrumental background, perhaps the dominant part at certain event energies. This analysis may be improved in a number of ways: a) by further in-flight neutron singles measurements to better estimate the neutron flux into D1 as a function of rigidity, and to look for dependence on spacecraft orientation; b) by more accurate calculation of the D1 neutron singles sensitivity; c) by optimizing the event selection parameters and reanalysis of the SM3 data with the optimal selections; and (d) by analysis of the 17 MeV neutron calibration data to allow more reliable application of SM3 results to Comptel.

Other approaches will certainly be important in a full background analysis. In particular correlations must be sought between the gamma event rate, as a function of energy and direction within the field-of-view, and such quantities as magnetic rigidity and spacecraft orientation. However extrapolation from those measurements to infinite rigidity will still depend on laboratory measurements such as SM3, and their interpretation.

References

1. Schönfelder, V. *et al.*, *IEEE Trans. Nucl. Sci.* **NS-31**:766, 1984.
2. den Herder, J.W., *et al.*, these proceedings.
3. Ait-Ouamer, F., Atmospheric Neutrons at 8.5 GV Cutoff, M.S. thesis, University of California at Riverside, 1987.
4. Schönfelder, V.S. and J. Daugherty, *Space Sci. Instrum.* **3**:423, 1977.
5. Pal, B., A. Chatterjee, and A.M. Ghose, *Nucl. Instrum. Meth.* **171**:347, 1980.
6. Zanelli, C.I., P.P. Urone, J.L. Romero, F.P. Brady, M.L. Johnson, G.A. Needham, J.L. Ullmann, and D.L. Johnson, *Phys. Rev. C* **23**:1015, 1981.
7. Allen, R.C., R.E. Carter, and H.L. Taylor in Fast Neutron Physics, Part II: Experiments and Theory (eds. J.B. Marion & J.L. Fowler), Interscience Publishers, New York, 1963, p. 1429.
8. Orphan, V.J. *et al.*, Nucl. Sci. Eng. **42**:352, 1970.
9. Shima, Y. and R.G. Alsmiller, *Nucl. Sci. Eng.* **41**:47, 1970.
10. Sugiyama, K., in Proceedings of the International Conference on Nuclear Cross Sections for Technology, NBS Special Publication SP-594 (eds. J.L. Fowler, C.H. Johnson, & C.D. Bowman), p. 397, 1980.
11. Byrd, R.C., C.C. Foster, and T.N. Taddeucci, IUCF Research Report, 1985.
12. Cooper, J., private communication (Comptel document COM-RP-MPE-K70-040), 1985.
13. Fichtel, C.E., and J.I. Trombka, Gamma Ray Astrophysics, NASA SP-453, Washington DC, 1981, p. 207.

COMPTEL Neutron Response at 17 MeV

Terrence J. O'Neill*, Farid Ait-Ouamer, Joann Morris,
O. Tumay Tumer, R. Stephen White, Allen D. Zych

Institute of Geophysics and Planetary Physics
University of California, Riverside
*also at Riverside Community College

ABSTRACT

The COMPTEL instrument was exposed to 17 MeV d,t neutrons prior to launch. These data have been analyzed and are compared with Monte Carlo calculations using the MCNP(LANL) code. Energy and angular resolutions are compared and absolute efficiencies are calculated at 0 and 30 degrees incident angle. The COMPTEL neutron responses at 17 MeV and higher energies are needed to understand solar flare neutron data.

I. Introduction

The COMPTEL instrument on the Gamma Ray Observatory is sensitive to neutrons with energies above about 10 MeV. It has optimum sensitivity in the energy range expected for solar flare neutrons. These neutrons can be detected in the double scatter mode where the incident neutrons first elastically scatter from hydrogen in one of the 7 D1 liquid scintillator modules and then are detected in one of the 14 D2 NaI(Tℓ) scintillator modules. The neutron's incident energy and direction are determined in much the same way as they are for an incident gamma ray. The incident neutron energy, E_n, is the sum of the recoil proton energy loss in D1, E_p, and the scattered neutron energy, $E_{n'}$. This latter energy is determined from the time-of-flight from D1 to D2. The n-p scatter angle, θ_{np}, is calculated using $\tan(\theta_{np}) = E_p/E_{n'}$ (non-rel.). With the locations of the interactions in D1 and D2, the incident direction is determined to a cone in space containing the source direction (see Fig. 1).

The COMPTEL instrument is unique in that it can detect solar flare gamma rays and neutrons simultaneously and distinguish between these two different radiations. While the solar gamma ray arrival time histories duplicate their production time histories at the sun, this is not true for the neutrons which travel at different speeds. Thus, COMPTEL's independent determination of the neutron's energy also provides the time of production at the sun's surface.

COMPTEL's neutron response is complicated by the inclusion of neutron-carbon interactions in the D1 organic scintillator material (NE 213A). At neutron energies below 20 MeV, carbon elastic scattering can account for large direction changes for neutrons in D1 with minimal neutron energy loss. Above 20 MeV, inelastic carbon interactions which produce both a secondary charged particle and a neutron are important (e.g., C(n,n'p)B).

The pulse shape discrimination feature of COMPTEL's D1 scintillation detectors allows proton-producing events to be selected. The time-of-flight measurement selects events with neutrons moving from D1 to D2. These together with the requirement that the event cone include the solar direction should provide relatively clean selection criteria for solar neutron elastic n-p double scatter events.

Preliminary results will be presented here for COMPTEL's neutron response at 17 MeV. Calibration results are compared with Monte Carlo calculations.

II. Calibration Description

The complete COMPTEL instrument was extensively calibrated during the summer of 1987 at the GSF Van De Graaff accelerator facility at Neuherberg (Germany). As part of this calibration, the COMPTEL instrument was exposed to 17 MeV d,t neutrons. The calibration setup is shown in Figure 1. The telescope-target distance was 8.4 m. Data for nominal incident angles of 0° and 30° were obtained. Using a deuteron incident energy of 2.5 MeV, neutrons produced at 55.3° w.r.t. to the beam line have an energy of 17.2 MeV. The spread in neutron energy over the COMPTEL D1 area was 0.3 MeV.

Processed double scatter calibration event files consist of D1 and D2 interaction locations and pulse heights (in units of keV electron-equivalent energy loss), the D1 pulse shape parameter (PSD channel no.) and the D1-D2 time-of-flight (TOF channel no.). The separation of neutron and gamma ray events with time-of-flight (TOF) and pulse shape (PSD) is shown in the scatter plot in Figure 2. Only events with TOF > 170 are shown here. The forward gamma ray TOF peak is nominally at ch. 120. In our analysis of COMPTEL neutron data, only events with TOF > 200 and PSD > 100 are considered.

III. Monte Carlo Simulation

The simulation code MCNP (Forster et al. 1990 and references therein) -- Monte Carlo Neutron Photon -- is used to predict COMPTEL's neutron response. This code is a general-purpose continuous-energy Monte Carlo code developed as part of the Los Alamos Radiation Transport Code System. The physics of time-dependent neutron and photon transport and interactions are modeled in detail using the latest available cross-section data. Problems with neutrons, photons and electrons either as single particles or coupled particles can be calculated. Neutron cross-sections cover the energy range from 10^{-5} eV to 20 MeV while the range for photon transport is 1 keV to 100 MeV.

Another part of this transport code system is "LAHET" which is used with MCNP to extend the neutron range to in excess of 10 GeV. A third part of this system is "SABRINA" which is a graphics code to interactively set up three-dimensional models with a color display of geometries and particle tracks.

Currently, we are running MCNP with older neutron cross-section files which do not include Iodine-127. Barium-137 has been used instead along with Sodium-23 for the D2 NaI(Tℓ) scintillator material. New files available soon include iodine.

Table 1 lists the 1-sigma Gaussian resolutions which were incorporated into the analysis of simulated events.

Table 1. Simulation Resolutions (1 sigma)

D1 spatial: 2.5 cm	D1 Energy: 0.058 MeV at 1 MeV($E^{1/2}$)
D2 spatial: 2.5 cm	D2 Energy: 0.041 MeV at 1 MeV($E^{1/2}$)
Time of flight: 1 ns	

COMPTEL instrument electron-equivalent energy loss thresholds of 50 keV and 500 keV were imposed for D1 and D2, respectively. For D1 this corresponds to a 500 keV proton energy loss. At energies below 20 MeV, neutrons incident on the D2 NaI(Tℓ) modules produce a trigger almost exclusively by nuclear excitation followed by fast gamma emission (n,n'γ) and subsequent electron detection. Plural elastic scattering with the scintillator nuclei occurs as the neutron tends to bounce around the module. In general, more than one ionizing electron are produced. The interaction time and x,y location of the largest electron energy loss are used and the summed ionization energy loss in D2 is used for the threshold trigger. This extended time-of-flight produces a mean energy reduction of about 0.2 MeV for the scattered neutron. A few events ($\sim$8%) have energy reductions greater than 1 MeV. A maximum D2-D2 time-of-flight of 40.7 ns is used.

Our COMPTEL model includes the four anti-coincidence veto domes of plastic scintillator surrounding the D1 and D2 modules. With electron/proton energy loss thresholds of 250 keV/1 MeV, about 19% of neutron-induced double scatter events also trigger the veto domes for 20 MeV incident neutrons.

IV. Results

A. D1 Pulse Height Response to Protons

The D1 modules are calibrated for electron energy loss at various known gamma ray energies. It is well known that proton energy loss in organic scintillator material has reduced light output due to the much larger ionization energy loss (dE/dx) of stopping protons. This non-linear response has been measured for the liquid scintillator NE-213 by Cecil et al. (1979). The COMPTEL D1 material is NE-213A, an improved scintillator also with pulse shape discrimination properties.

For single elastic n,p scattering in the D1 modules, the recoil proton energy loss can be calculated directly from the difference of the known incident neutron energy, E_n, and the measured scattered neutron energy, $E_{n'}$, from time-of-flight. Figure 3 compares the electron equivalent energy losses determined from the measured pulse heights with the calculated recoil proton energies. The range of recoil proton energies allowed by the COMPTEL geometry for 30° incident neutrons is about 1-9 MeV.

The general agreement of the data with the relationship of Cecil et al. (1979) is shown in Figure 3. There is also considerable broadening due primarily to the uncertainty in time-of-flight distance resulting from the thicknesses of the D1 and D2 modules. Further analysis of calibration data is needed to confirm this agreement. For the remaining analyses below, the energy loss relationship of Cecil et al. will be used to interpret the pulse height in terms of proton energy loss.

B. COMPTEL Neutron Energy and Angular Resolutions

Both the 0° and 30° incident angle data sets have been analyzed to determine the energy and angular resolutions for 17 MeV neutrons. These results are directly compared with MCNP simulation results. Figure 4 shows the results for 30° incident angle. In Figure 4a, the solid curve represents the calculated n,p scatter angle distribution with only the previously discussed PSD (>100) and TOF (>200) cuts applied to the data. The large excess at 10-15° is due to gamma ray events with TOF and PSD values in the tails of the gamma ray PSD and TOF distributions which exceed the cuts. By requiring that the event cone for each event be within 3° of the true source (target) direction, this excess

is eliminated. This is shown by the dashed curve in Figure 4a. Figure 4b gives the scatter angle distribution from the Monte Carlo simulation. Note the agreements in the maximum and minimum scatter angles and the general shape of the distributions in these two figures.

The COMPTEL energy resolution for 17 MeV neutrons is found from the energy distribution of those neutron events with event cones again within 3° of the true source direction. This is a realistic restriction to apply to solar neutron data when the sun is within COMPTEL's field-of-view. Figure 4c shows such a distribution for the calibration data with Figure 4d providing the simulation distribution. The measured peak energy for 17.2 MeV incident neutrons at 30° is 16.7 MeV with a FWHM of 2.6 MeV or 16% energy resolution. The Monte Carlo simulation does not include the 0.3 MeV actual incident energy variation discussed in Part II.

The angular resolution is measured by comparing the true or geometric scatter angle with the calculated scatter angle. In Figure 1 the ARM (angular resolution measurement) angle (θ_{sp} - θ_g) is the angular distance between the event cone and the target direction measured from the D1 interaction. Figure 4e shows the ARM angle distribution for 17.2 MeV calibration neutrons incident at 30°. Only events with total energies within 2 MeV of the peak energy are included. The corresponding simulation ARM angle distribution is shown in Figure 4f. Table 2 summarizes the energy and angular distribution parameters for both 0° and 30° incident angles. Both calibration and simulation results are given.

Table 2. COMPTEL 17.2 MeV Neutron Energy and Angle Resolutions

Incident Angle	0°, Cal.	0°, Sim.	30°, Cal.	30°, Sim.
Peak Energy	17.0 MeV	17.0 MeV	16.7 MeV	17.1 MeV
ΔE, FWHM*	3.7 MeV (22%)	2.9 MeV (17%)	2.6 MeV (16%)	2.4 MeV (14%)
Peak ARM Angle	0.0°	+0.1°	-0.4°	+0.15°
$\Delta\theta$, 1-sigma†	2.3°	2.2°	2.2°	2.2°

*Only events with event cones within 3° of the target direction are included.
†Only events with energies within 2 MeV of the peak energy are included.

There is excellent agreement between the predicted and measured angular resolutions. Thus, at energies below 20 MeV, 1-sigma angular resolutions of 2.2-2.3° can be expected with negligible systematic effects.

Two discrepancies in the comparison of energy distribution parameters are evident. At 30°, the calibration peak energy is approximately 0.5 MeV below the nominal 17.2 MeV value and at 0°, the calibration energy distribution full-width is broader than expected by about 0.8 MeV. The sources of these differences are not understood at present. A 0.2 MeV decrease can be explained as discussed in Part III.

C. Efficiencies and Effective Areas at 17 MeV

Figures 5 and 6 present the COMPTEL calculated absolute detection efficiencies and effective areas for 17.2 MeV neutrons incident at 0° to 45° w.r.t. the telescope zenith direction. For the Monte Carlo simulation calculations, parallel beams of incident neutrons were used, as were D1 proton energy

thresholds of 500 keV and D2 energy thresholds of 500 keV (electron loss). In these simulations, no special restrictions were placed on the energy or ARM angle measurements. Neutron time-of-flights were cut off at 40.7 ns and induced gamma ray and backscatter neutron events were eliminated. The effective area is calculated from the efficiency, the D1 area and the incident angle. A maximum efficiency of 0.26% corresponding to an effective area of 11.5 cm^2 occurs at 0° incident angle. The efficiency decreases to 0.15% at 45° with an effective area of about 5 cm^2. As yet, a comparison of calculated and measured efficiencies has not been made. Beam monitor data for the 17 MeV runs will be analyzed in the near future.

V. Future Analyses

Additional neutron calibration data with a science model of COMPTEL are available and will be analyzed. The COMPTEL science model, consisting of two D1 modules and three D2 modules, was exposed to neutrons at four nominal energies from 20 to 135 MeV. The results of these data need to be compared critically with the simulation results of MCNP and LAHET. As more confidence in MCNP's ability to model the neutron response of COMPTEL over the full range of neutron energies expected from solar flares is gained, MCNP can be used as a data analysis tool for interpreting individual solar neutron events.

VI. Acknowledgements

The authors wish to acknowledge the full support and cooperation of the COMPTEL instrument team at the Space Science Center, University of New Hampshire, Durham, New Hampshire. Special thanks are due Drs. James Ryan and Mark McConnell for providing us with the calibration data files and calibration parameters. This work has been performed as part of our Phase 1 NASA GRO Guest Investigator Program grant No. NAG 5-1493.

REFERENCES

Cecil et al. (1979) Nuc. Inst. and Meth., 161, 439.

Forster et al. (1990) IEEE Trans. Nuc. Sci. 37, 1378.

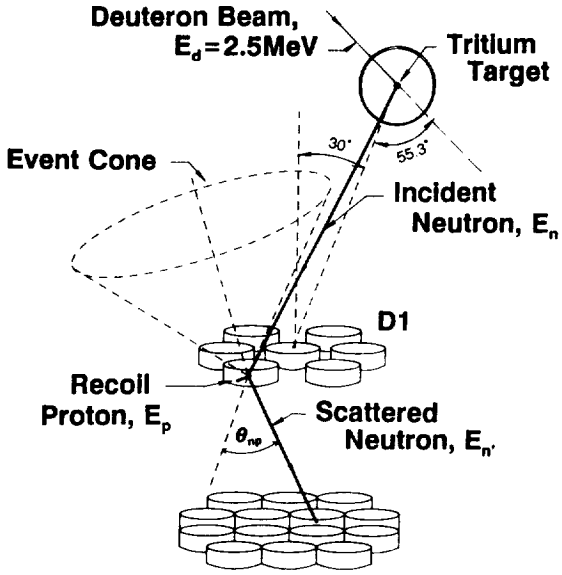

Fig. 1 Calibration Setup

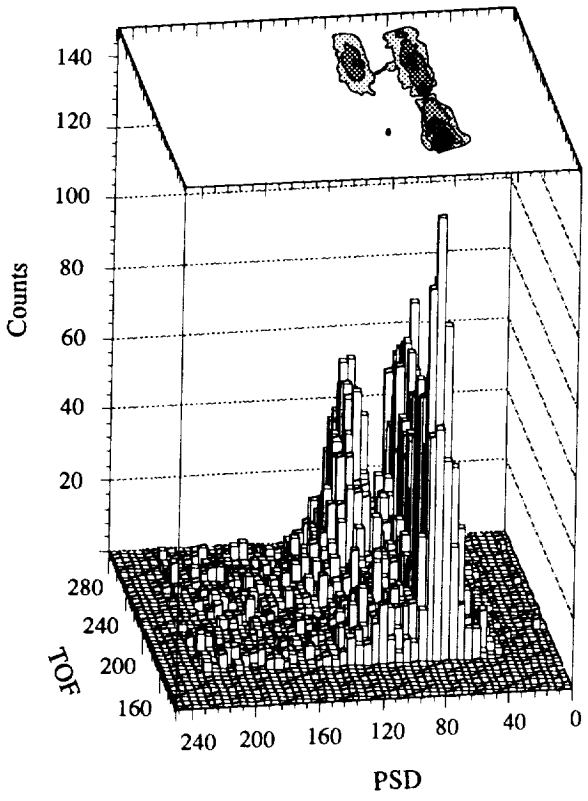

Fig. 2 Counts versus PSD and TOF parameters for 17 MeV neutrons incident at 30°.

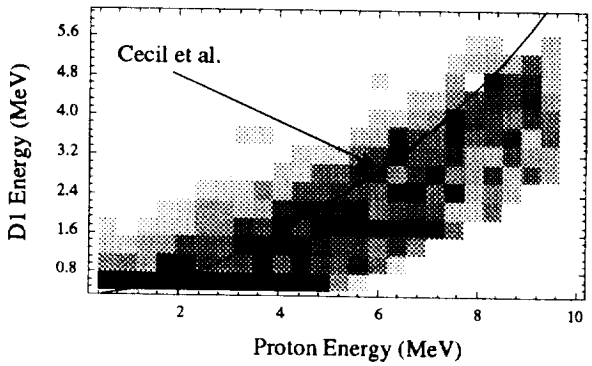

Fig. 3 Electron equivalent energy loss versus proton energy for 17 MeV incident neutrons at 30°.

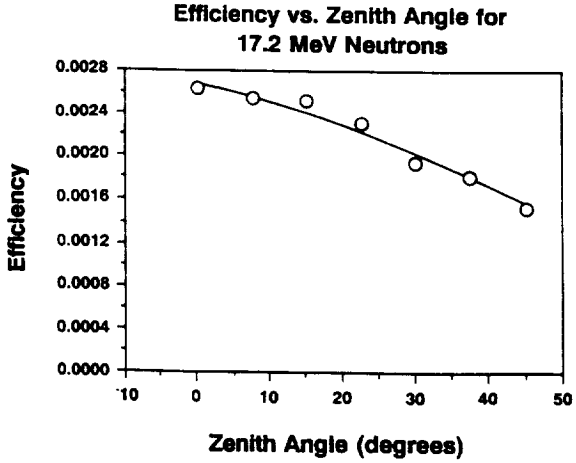

Fig. 5 COMPTEL Monte Carlo Efficiencies at 17.1 MeV as a function of incident angle.

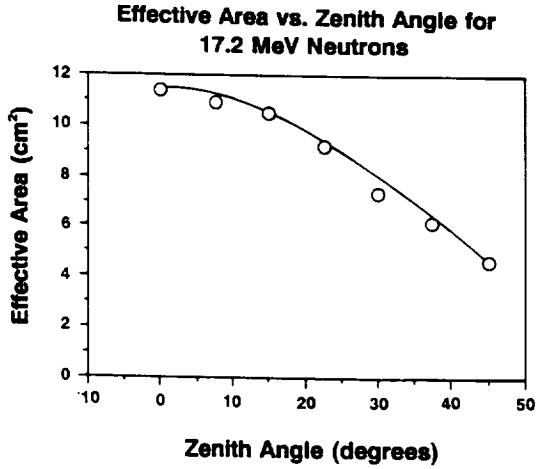

Fig. 6 COMPTEL Monte Carlo Effective Areas at 17.2 MeV as a function of incident angle.

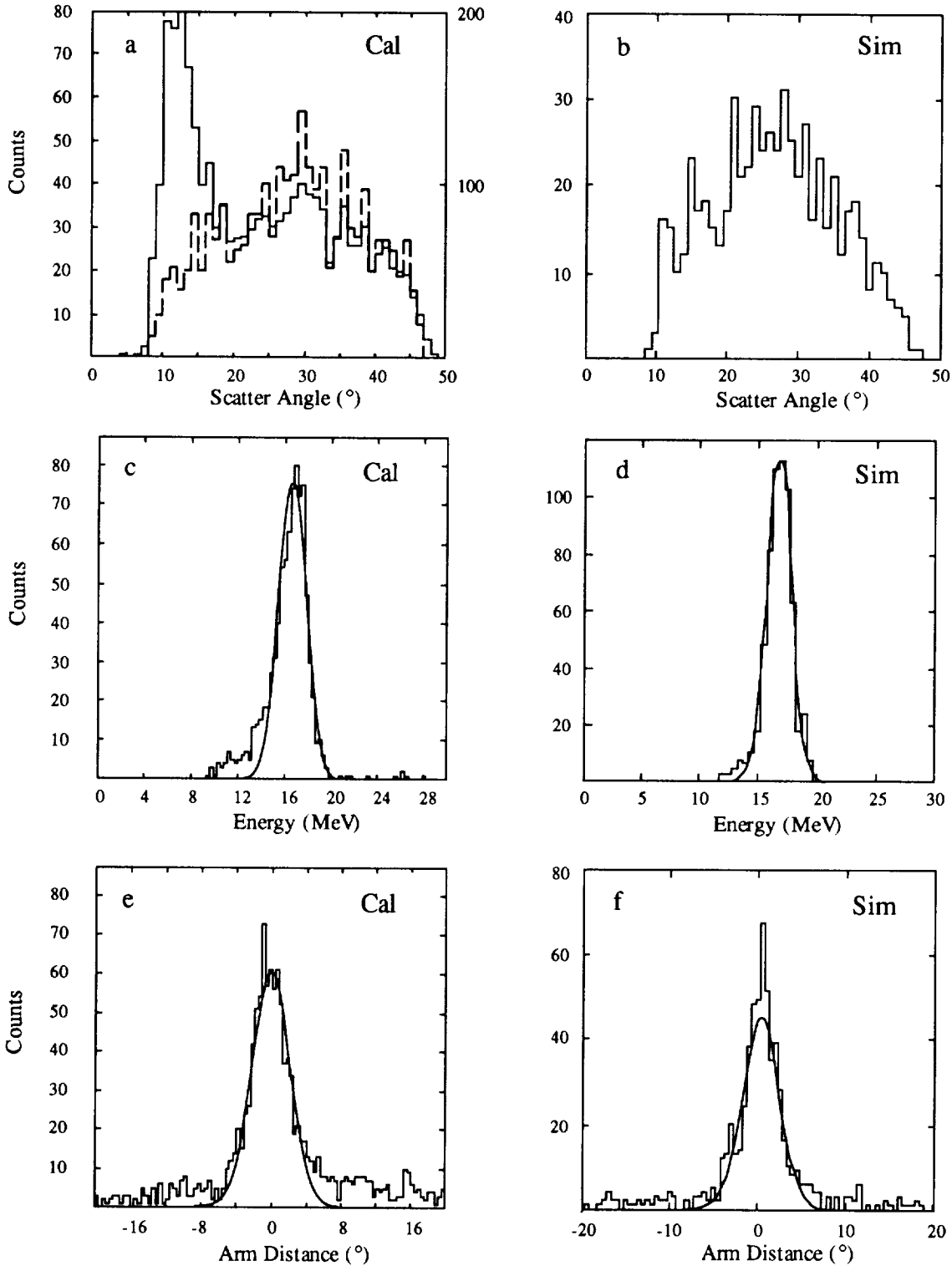

Fig. 4 Scatter angle, energy and angular distributions for 17 MeV incident neutrons at 30°. See text for discussion.

THE EGRET HIGH ENERGY GAMMA RAY TELESCOPE

R. C. HARTMAN[1], D. L. BERTSCH[1], C. E. FICHTEL[1], S. D. HUNTER[1], G. KANBACH[2], D. A. KNIFFEN[8], P. W. KWOK[1,3], Y. C. LIN[4], J. R. MATTOX[1,5], H. A. MAYER-HASSELWANDER[2], P. F. MICHELSON[4], C. VON MONTIGNY[2], P. L. NOLAN[4], K. PINKAU[2], H. ROTHERMEL[2], E. SCHNEID[6], M. SOMMER[2], P. SREEKUMAR[1,7], AND D. J. THOMPSON[1]

[1]NASA/Goddard Space Flight Center
[2]Max-Planck Institut fur Extraterrestrische Physik
[3]NAS/NRC Postdoctoral Research Associate
[4]Hansen Experimental Physics Laboratory, Stanford University
[5]Astronomy Programs, Computer Sciences Corporation
[6]Grumman Aerospace Corporation
[7]Universities Space Research Association
[8]Hampden-Sydney College

ABSTRACT

The Energetic Gamma Ray Experiment Telescope (EGRET) on the Compton Gamma Ray Observatory is sensitive in the energy range from about 20 MeV to about 30,000 MeV. Electron-positron pair production by incident gamma ray photons is utilized as the detection mechanism. The pair production occurs in tantalum foils interleaved with the layers of a digital spark chamber system; the spark chamber records the tracks of the electron and positron, allowing the reconstruction of the arrival direction of the gamma ray. If there is no signal from the charged-particle anticoincidence detector which surrounds the upper part of the detector, the spark chamber array is triggered by two hodoscopes of plastic scintillators; a time-of-flight requirement is included to reject events moving backward through the telescope. The energy of the gamma ray is primarily determined by absorption of the energies of the electron and positron in a 20 cm deep NaI(Tl) scintillator. The Compton Observatory was placed in orbit on April 6, 1991; EGRET completed activation and on-orbit testing and calibration on May 16, 1991, at which time it began a 15-month full sky survey.

1. Introduction

Although the SAS-2 and COS-B gamma ray telescopes (Derdeyn et al., 1972; Fichtel et al., 1975; Bignami et al., 1975; Scarsi et al., 1977) provided the first maps of the high energy (~100 MeV) gamma ray sky, those observations covered only about 70% of the celestial sphere. Furthermore, the small size of the instruments limited the statistical weight of many of the observations, leaving a wide variety of important astrophysical questions only partially explored. The EGRET telescope on the Compton Gamma Ray Observatory was designed to provide at least an order of magnitude improvement in sensitivity over the earlier instruments, as well as better angular and energy resolution and a very broad energy range. EGRET was developed by a collaboration of 4

institutions: NASA/Goddard Space Flight Center (Co-PI, Dr. C. Fichtel), Max-Planck Institut fur Extraterrestrische Physik (Co-PI, Prof. K. Pinkau), Stanford University (Co-PI, Prof. R. Hofstadter, deceased), and the Grumman Aerospace Corporation.

2. The EGRET Instrument

Since the EGRET instrument has been described in detail previously (Kanbach et al. 1988, 1989), only an outline of EGRET operation is provided here. Photons in the energy range covered by EGRET (20 MeV to about 30 GeV), interact almost exclusively via electron-positron pair production; thus that process is the basis for gamma ray detection in EGRET. As illustrated in Figure 1, the gamma ray photons enter through a dome of plastic scintillator. Having no electric charge, the gamma rays produce no signal in the scintillator. Charged cosmic ray particles, which outnumber the gamma rays by a factor of $10^3$to 10^4, do produce signals in the dome. These signals are used to veto the triggering of the instrument by the charged particles, and therefore prevent them from saturating the instrument telemetry. The conversion of the gamma rays to electron-positron pairs takes place within a series of 27 tantalum foils which are interleaved with digital spark chambers. If the pair particles satisfy the proper coincidence criteria in two layers of plastic scintillation counters, including a correct time-of-flight between the scintillator layers, the spark chambers are triggered to produce an image of the tracks of the electron and positron. In addition to providing a unique means of identify gamma ray events, this image also defines the direction from which the gamma ray arrived. Except at the lowest energies, the energy of the gamma ray is determined primarily from the energy deposited by the electron and positron in a large array of NaI(Tl) scintillator blocks (designated the Total Absorption Shower Counter, or TASC) below the triggering scintillator array. At energies below about 100 MeV, scattering measurements in the spark chamber and corrections for energy losses in the tantalum foils are of increasing importance in the energy determination. Since the efficiency of the spark chamber image formation degrades slowly with time (believed to be due to the action of sparks on the ethane quench gas in the neon/argon mixture), EGRET carries a gas supply sufficient for 5 refills.

In addition to providing energy information on events which trigger the spark chamber, the TASC subsystem has independent modes of operation in which it records spectra of all events which deposit energy between 1 and about 190 MeV in the NaI. Under quiescent conditions, these spectra are recorded over 32.768 second time intervals; this mode is appropriate for recording spectra of gamma rays from solar flares, and is therefore designated the Solar Mode. When the TASC subsystem receives a signal from the Burst and Transient Source Experiment (BATSE) indicating that a gamma ray burst (GRB) has been detected, the TASC electronics switches to a Burst Mode in which spectra are recorded during 4 previously commanded time intervals. The commandable range for each of the 4 intervals is 0.125 second to 15.875 seconds; normally the intervals are set to 1.0, 2.0, 4.0 and 15.875 seconds. Because the threshold of the TASC spectral measurements (~1 MeV) is considerably higher than that of the BATSE instrument (~20 keV), EGRET obtains spectral information on only 2-3% of the events for which BATSE sends a burst trigger signal. In the Solar and Burst Modes, the TASC has essentially omnidirectional response. However, because of intervening material in the spacecraft, the spectra recorded can be strongly influenced by the direction from which the flare or burst gamma rays arrive. A relatively detailed Mass Model of the CGRO spacecraft will

soon be available which can be used in generating instrument response functions for specific burst or solar arrival directions.

3. EGRET On-Orbit Operations

Since completion of activation, EGRET operation has been essentially nominal. A period of several weeks following initial activation was spent in optimizing the operating conditions with regard to triggering requirements, anticoincidence threshold, Earth occultation and South Atlantic Anomaly (SAA) response. Since that time, the instrument operation has been essentially stable. The two significant exceptions are a slow gain drift in the TASC, for which software corrections are being routinely made based on weekly on-orbit calibrations, and the expected slow degradation of the spark chamber gas noted above. The primary effect of the latter is that the number of events for which manual graphic analysis is required has increased by about 25%. Smaller corrections will probably be required to the instrument sensitivity due to loss of gamma ray event recognition efficiency; this correction will be made on the basis of repeated observations on regions of diffuse flux, which do not change with time.

The EGRET coincidence system has an option to require a signal from the TASC above a specified threshold (1, 2.5, 6 or 13 MeV) in order to trigger the spark chamber. During the initial on-orbit testing of EGRET, it was confirmed that requiring the TASC 2.5 MeV signal in the coincidence reduced the overall triggering rate of the spark chamber; since this is expected to result in a correspondingly increased gas lifetime, and therefore the instrument time available to Guest Investigators, the TASC-in-coincidence mode is the normal mode of operation. As shown below, the TASC-in-coincidence requirement slightly raises the instrument energy threshold and slightly reduces its sensitivity, especially to wide-angle events.

Based on the experience from the first six months of operation, the expected lifetime of a single gas fill is expected to be at least 7-8 months, and the total lifetime of the spark chamber subsystem is therefore expected to be at least 3.5-4 years, roughly twice the 2-year design lifetime. Thus EGRET is expected to be fully operational well into the period during which a major share of its time is available to Guest Investigators. An option which will be considered for the latter part of the EGRET lifetime (e.g., after the last gas refill has been made) is the possible disabling of the spark chamber trigger except during observations of high priority targets, or for important time variation measurements.

4. EGRET Performance Characteristics

Table I (from Appendix G of the NASA Research Announcement for Phase 2 of the GRO Guest Investigator Program, NRA 91-OSSA-22) shows the scientific capabilities of the principal (spark chamber triggered) mode of EGRET operation, based on prelaunch calibrations as well as preliminary analysis of on-orbit testing and calibration. The values for effective area are still considered preliminary. Note that for parameters which are significantly affected by the TASC-in-coincidence requirement, values are shown both with and without that requirement. The parameter values without the TASC requirement are generally quite close to those presented in earlier instrument descriptions (Kanbach et al. 1988, 1989).

Table II (also from Appendix G of NRA 91-OSSA-22) shows the preliminary angular accuracy of EGRET for various energies. For data analysis by Guest Investigators, point spread functions will be provided for a set of standard energy intervals.

Since the GRO spacecraft is not repointed during Earth occultations, and additionally because the photomultiplier tubes are turned off during SAA passage, the fraction of time usable for spark chamber triggered operation is typically 40-45%. With the roughly 85% livetime fraction typically observed, the effective livetime during a viewing period is found to be 35-40% of real time.

5. Preliminary Scientific Results from the Initial Observations

A normal GRO observing period is 2 weeks in length. With the ~0.5 sr EGRET field of view, this allows completion of a full-sky survey in the first 16 months of operation (GRO Phase 1). The first few observation periods were devoted to regions of high scientific interest which could also provide various types of on-orbit calibration.

By combining the "tune-up" period with a normal 2-week observation and a solar target-of-opportunity during which the sun was in the galactic anticenter, EGRET obtained very early in the mission about a month of exposure to that region. Two bright sources, the Crab pulsar and the enigmatic source known as Geminga, are seen in that region, for which contour plots in two energy ranges are shown in Figure 2. An obvious difference in spectrum is apparent in that figure; in the lower energy plot, the Crab pulsar is considerably brighter than Geminga, while at the higher energies the situation is reversed. Clearly, the Geminga spectrum is significantly harder than that of the Crab.

Figure 3 shows the phase histogram of the Crab pulsar; for comparison, that of the Vela pulsar is shown in Figure 4. These two pulsars show much more similarity in gamma rays than they do in the radio, optical or X-ray bands. Nevertheless, some differences are apparent. While the first (main) pulse of each is quite sharp, the secondary pulse of the Crab is much broader than that of Vela. Furthermore, the Vela pulsar shows significant emission in the interpulse region, while the Crab pulsar shows little or none.

The most surprising observation by EGRET during the early portion of the GRO mission is the discovery of strong gamma ray emission by the quasar 3C279. During the latter half of June 1991, 3C279 was nearly as bright as Geminga; it was not detected in the SAS-2 observations in the early 1970's (Fichtel et al. 1978), and at the times of the COS-B observations (Mayer-Hasselwander et al. 1985) was at least a factor of 10 less intense than during the EGRET observations (Hartman et al. 1991). Over the energy range 70 MeV to 10,000 MeV the photon spectrum of 3C279 fits well to a power law with index -2.0. If the object radiates gamma rays isotropically, its luminosity at the time of the EGRET observation was about 10^{48} ergs/second. Furthermore, EGRET saw statistically significant evidence for time variations on time scales of a few days.

In contrast with the increased emission from 3C279 since the 1970's, quasar 3C273 was found by EGRET to be roughly a factor of 4 less intense than at the time of the COS-B observations.

EGRET has observed gamma radiation to at least 100 MeV from both solar flares and cosmic gamma ray bursts. In addition to detection in the independent TASC mode, 6

gamma rays were observed in its spark chamber mode from the GRB on 3 May, 1991. The burst direction obtained from a centroid of the directions of the 6 individual gamma rays is l = 171.9± 1.3 degrees, b = 5.3± 1.1 degrees.

EGRET has made observations of several regions of the galactic plane. Although structure is seen in the galactic ridge, the separation of diffuse emission from that of point sources will require detailed comparison of the gamma ray observations with models of the gas and cosmic ray content of the galaxy.

6. Summary

The EGRET high energy gamma ray telescope on the Compton Gamma Ray Observatory is successfully carrying out significant observations on a wide variety of astronomical phenomena, including solar flares, gamma ray bursts, pulsars, galactic structure and active galactic nuclei. Within 17 months after launch, it is expected to complete a survey of the full sky, 30% of which has never been observed in high energy gamma rays previously.

We wish to acknowledge the essential contributions to the EGRET program over many years by Drs. Robert Hofstadter and E. Barrie Hughes until their deaths shortly before the GRO launch.

REFERENCES

Fichtel, C. E., Hartman, R. C., Kniffen, D. A., Thompson, D. J., Ogelman, K. B., Tumer, T., & Ozel, M. E. 1978, NASA Technical Memorandum 79650, Tabulated Data from the SAS-2 High Energy Gamma Ray Telescope

Hartman, R. C., et al. 1992, ApJ (in press)

Kanbach, G., et al. 1988, Space Science Reviews, 49, 69

Kanbach, G., et al. 1989, Gamma Ray Observatory Science Workshop Proc., p.2-1

Mayer-Hasselwander, H., et al. 1985, Proc. 19th ICRC, La Jolla, 3, 383

Table I - EGRET CAPABILITIES

Energy Range	20 MeV to about 30 GeV (TASC not in coinc.)
	35 MeV to about 30 GeV (TASC in coinc.)
Energy Resolution:	approx. 22% FWHM over central part of energy range

Effective Area (cm^2)

Energy(MeV)	TASC not in coinc.	TASC in coinc.
35	400	70 ??
100	1100	900
200	1400	1200
500	1600	1400
3000	1200	1200
10000	700	700

Point Source Sensitivity (E > 100 MeV) (for optimum conditions; varies with location and spectrum)	6×10^{-8} cm^{-2} s^{-1}
Point Source Location (for optimum conditions; varies with intensity, location and spectrum)	5-10 arcminutes
Field of View	Roughly gaussian in shape, ~40 degrees FWHM
Timing Accuracy	0.1 ms absolute

Table II - Preliminary EGRET Point Spread Function (degrees)

Energy (MeV)	projected rms (degrees)
35 - 70	4.3
70 - 150	2.6
150 - 500	1.4
500 - 2000	0.8
2000 - 30000	0.4

FIGURE CAPTIONS

Figure 1 - Schematic diagram of the EGRET telescope.

Figure 2 - Contour plot of gamma ray intensity in the general direction of the galactic anticenter, for two different energy intervals.

Figure 3 - Phase histogram for the Crab pulsar, 89 bins per period (1 ms/bin), for the energy range 100-150 MeV.

Figure 4 - Phase histogram for the Vela pulsar, 99 bins per period (0.3 ms/bin), for the energy range 100-150 MeV.

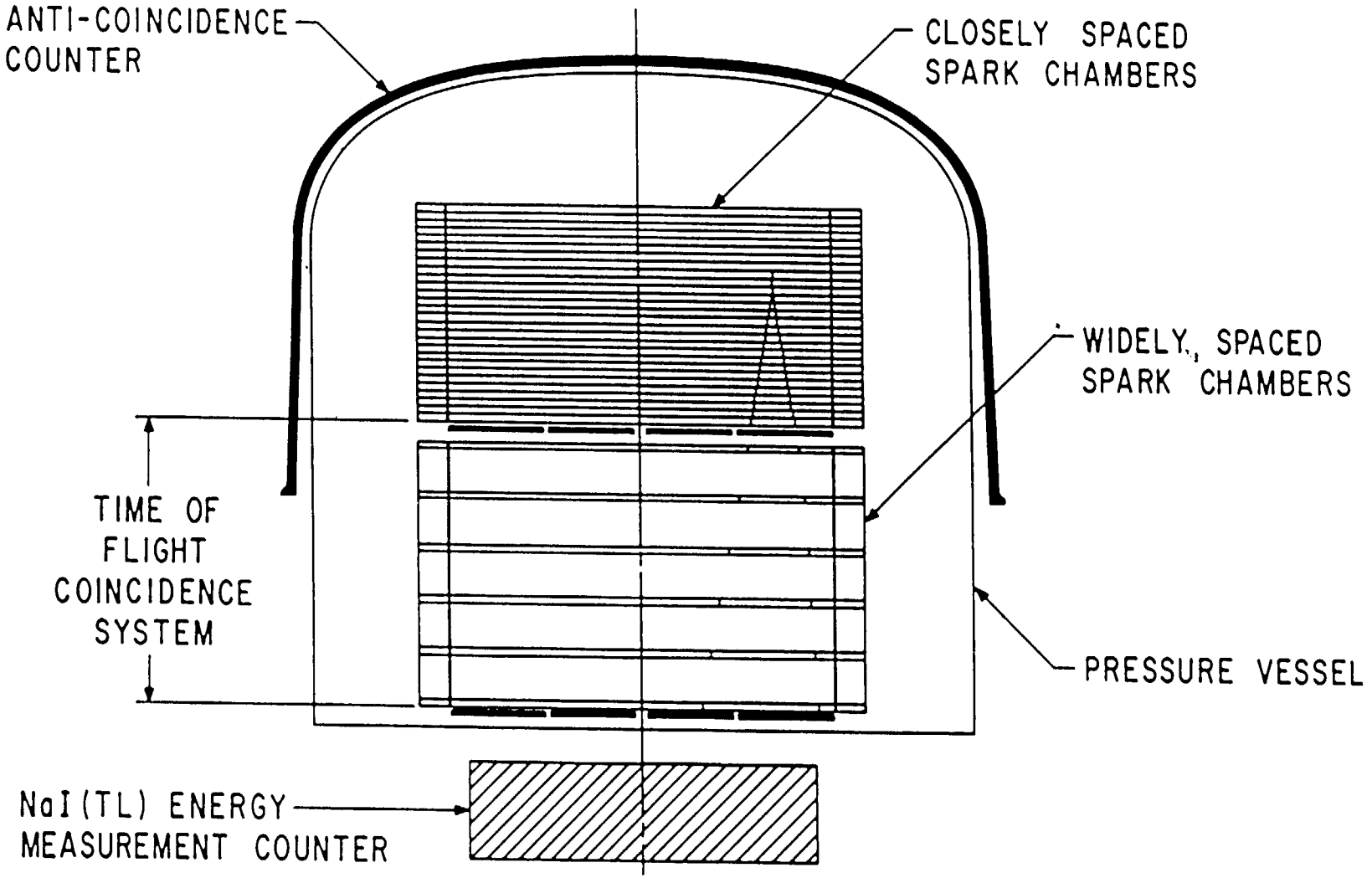
ANTI-COINCIDENCE COUNTER
CLOSELY SPACED SPARK CHAMBERS
WIDELY SPACED SPARK CHAMBERS
TIME OF FLIGHT COINCIDENCE SYSTEM
PRESSURE VESSEL
NaI(TL) ENERGY MEASUREMENT COUNTER

Figure 1

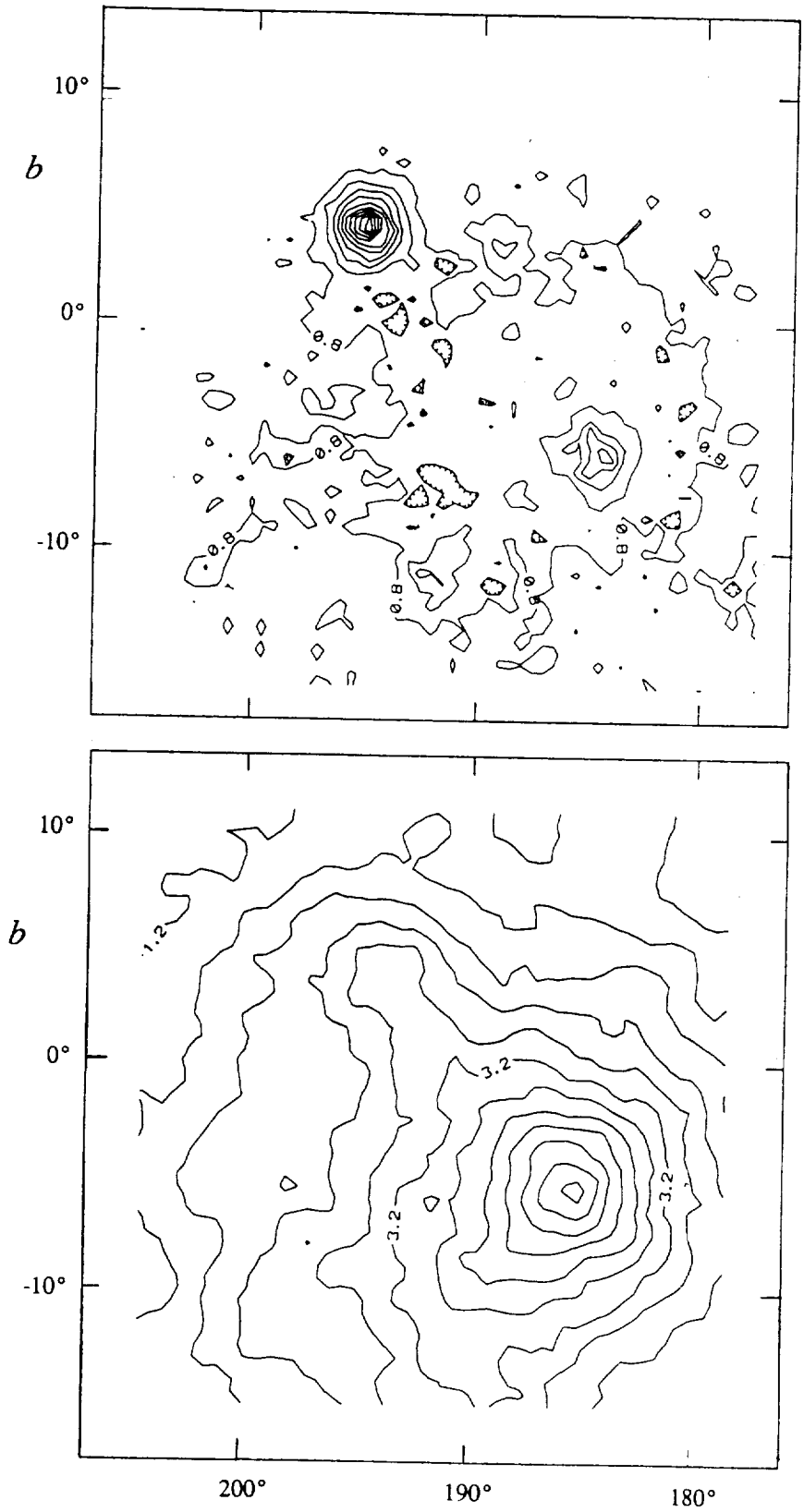
10°
b
0°
-10°
0.8
500 - 1000 MeV
Geminga
10°
b
0°
-10°
1.2
3.2
3.2
3.2
50 - 100 MeV
Crab
200°
190°
180°

Figure 2

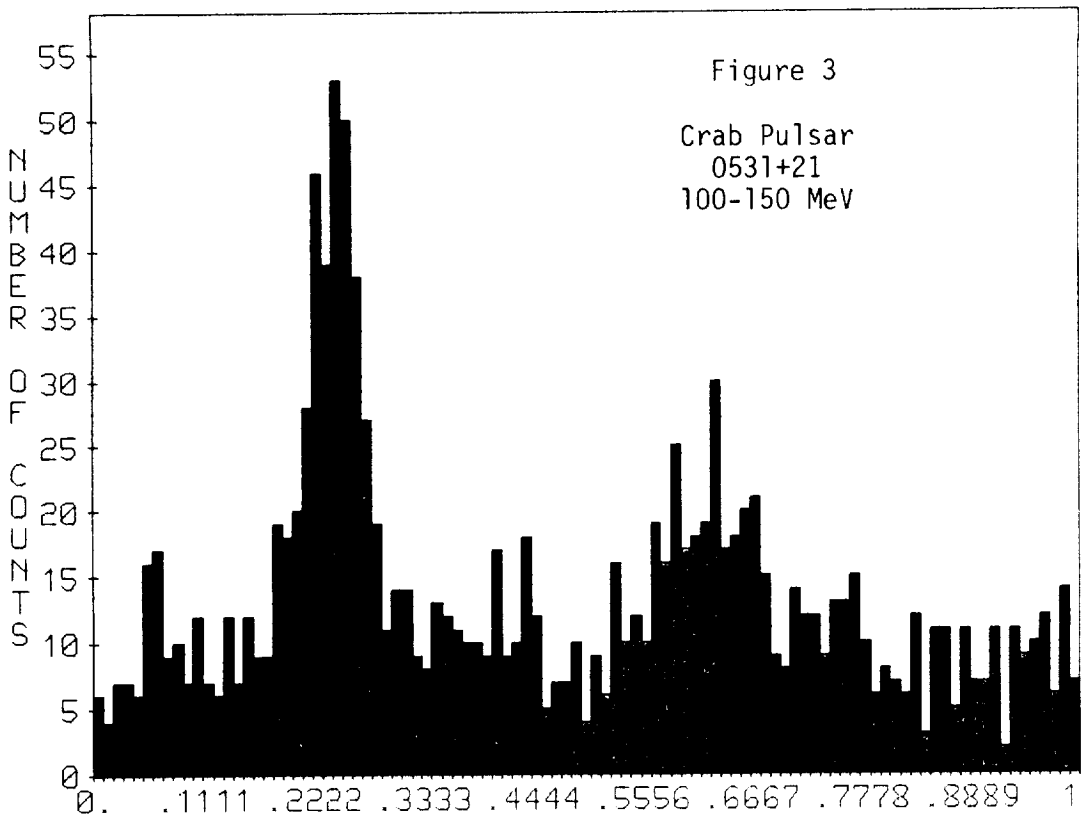
Figure 3
Crab Pulsar
0531+21
100-150 MeV
NUMBER OF COUNTS
55
50
45
40
35
30
25
20
15
10
5
0
0.
.1111
.2222
.3333
.4444
.5556
.6667
.7778
.8889
1.

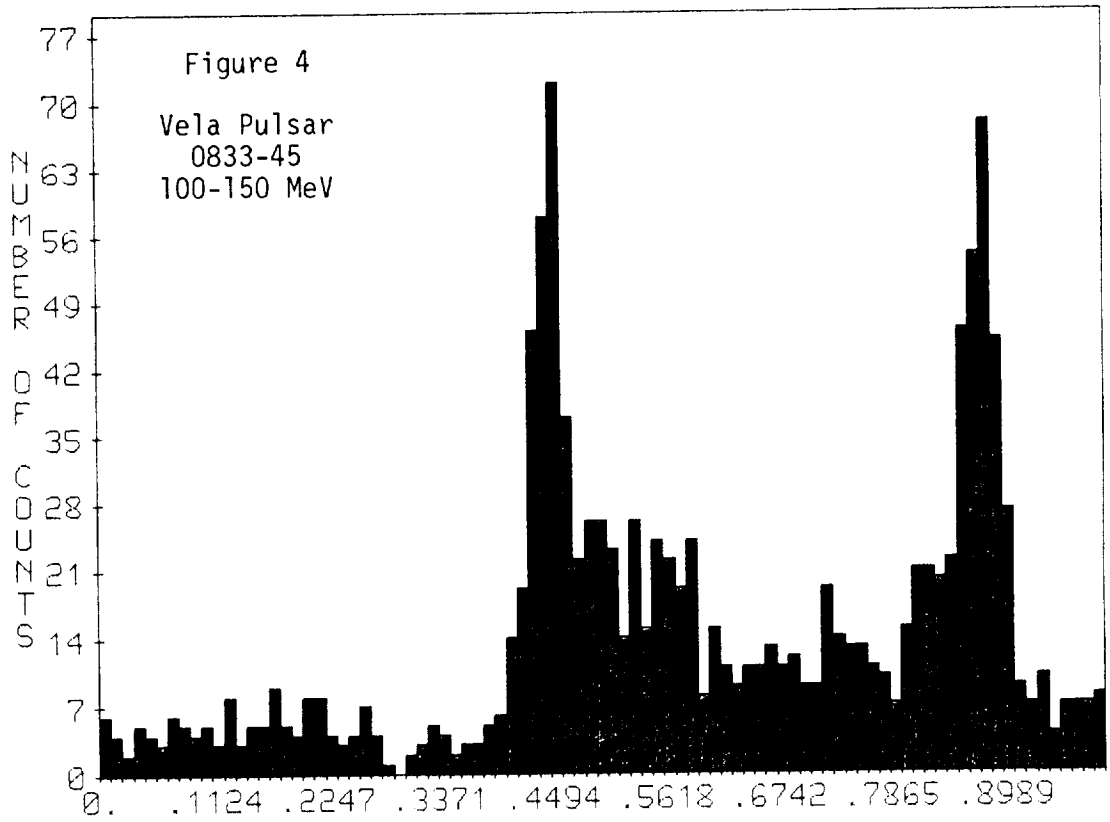
Figure 4
Vela Pulsar
0833-45
100-150 MeV
NUMBER OF COUNTS
77
70
63
56
49
42
35
28
21
14
7
0
0.
.1124
.2247
.3371
.4494
.5618
.6742
.7865
.8989

THE EGRET DATA PRODUCTS

J. R. Mattox[1,6], D. L. Bertsch[1], C. E. Fichtel[1], R. C. Hartman[1], S. D. Hunter[1], G. Kanbach[2], D. A. Kniffen[4], P.W. Kwok[1,8], Y. C. Lin[3], H. A. Mayer-Hasselwander[2], P. F. Michelson[3], C. von Montigny[2], P. L. Nolan[3], K. Pinkau[2], H. D. Radecke[2], H. Rothermel[2], E. Schneid[5], M. Sommer[2], P. Sreekumar[1,7], and D. J. Thompson[1]

[1]Code 662, NASA/Goddard Space Flight Center, Greenbelt, MD 20771
[2]Max Planck Institut für extraterrestrische Physik, W-8046, Garching, Germany
[3]Stanford University, Stanford, CA 94305
[4]Hampden-Sydney College, Hampden-Sydney, VA 23943
[5]Grumman Aerospace Corporation, Bethpage, NY, 11714
[6]*Compton* SSC, Computer Sciences Corp., Code 668.1, NASA/GSFC; Email: jrm@geminga.gsfc.nasa.gov
[7]Universities Space Research Association, NASA/GSFC
[8]NAS/NRC Research Associate

ABSTRACT

We describe the EGRET data products which we anticipate will suffice for virtually all guest and archival investigations. The production process, content, availability, format, and the associated software of each product is described. This paper also supplies sufficient detail for the archival researcher to do analysis which is not supported by extant software. Where published references don't exist, the EGRET team documentation is cited.

1. INTRODUCTION

The highest energy instrument aboard the Compton Observatory (formerly named GRO) is EGRET (Energetic Gamma Ray Experiment Telescope). The EGRET instrument is described by Kanbach *et al.* (1988, 1989) and Hartman *et al.* (1992). The scientific objectives of the EGRET mission are described by Kanbach *et al.* (1988) and Fichtel *et al.* (1989). On-orbit operation and initial EGRET scientific results are presented by Hartman *et al.* (1992) and Nolan *et al.* (1992).

The EGRET spark-chamber data should be useful for a wide variety of astrophysical investigations because of the high energy range (20 MeV $< E <$ 30 GeV), directional resolution ($\approx 1^\circ$ for individual gamma rays), large sensitive area ($\approx 10^3$ cm^2), good energy resolution ($\approx$20% $\Delta E/E$, for $E >$ 100 MeV where the TASC, Total Absorption Shower Counter is effective), and low background ($<$ 0.1 of the expected diffuse extragalactic gamma ray background).

The EGRET data analysis system has been previously described by Bertsch *et al.* (1989). Their description of the EGRET telemetry and low level data processing will not be repeated. This paper focuses on the current state of the EGRET data products, and expectations for the EGRET data products and associated software which are to be made available through the SSC (Arthur Holley Compton Gamma Ray Observatory Science Support Center; Chipman 1992) as specified by the GRO Project Data Management Plan (July 1990). Because of the intensive analysis and development in progress by the EGRET team and the SSC, it is expected that some of the details given here will soon be obsolete. Current information may be obtained by contacting the SSC or an EGRET team member.

These data products are shown in Table 1. The suffixes (for file types for which more than one file is anticipated) will correspond to entries in an on-line catalog to be maintained by the SSC. It is anticipated that virtually all scientific analyses may be performed using these products (including products specially prepared upon request in these formats by the SSC or the EGRET team). However, excerpts from the PDB (primary data base, Bertsch *et al.* 1989) will be made available if there are exceptions. The EGRET observations which have been completed are shown in Table 2. We intend to make the summary files, exposure history files, and the binned maps for each exposure public domain within 15 months of the end of the corresponding observation. However, if data product preparation for the EGRET team use requires more than 3 months (this appears unlikely at this time), the data products would be made available 12 months after they were prepared for the EGRET team use. GIs (Guest Investigators) who are awarded observation time will be furnished data products following preparation ($\approx$3 months).

The EGRET team will produce binary files which will be converted to FITS with SSC software. The GI (Guest Investigator) could be supplied with these binary files. However, FITS format is recommended since it provides portability and also is well documented via the ASCII header. The SSC will have subroutines available to read these data products using the FITSIO system of Fortran subroutines (Pence, 1991)[1]. FITSIO provides low-level routines for use with Unix, VMS, IBM main frame, or MSDOS operating systems.

Documentation of the techniques and algorithms used by the EGRET software exists in EGRET team documentation (normally the program's specification, program documentation, and user's guide). The EGRET PDB is currently maintained on an IBM MVS system at GSFC, and some of the EGRET team analysis is done on this IBM. The EXPHISTfiles are currently produced only on the IBM. However, all of the other data products are produced and used on a cluster of Sun workstations at GSFC. The Max Planck EGRET group produces and uses EGRET data products on an IBM CMS system (although they recently have acquired a Sun workstation). The Stanford EGRET group produces and uses EGRET data products on a cluster of Sun workstations. The EGRET software currently uses the TEMPLATE graphics system, but IDL is being used to an increasing extent.

Many of the EGRET team analysis capabilities will be ported to the SSC for use by GIs, and to some extent, for remote usage by the larger astrophysical community. The SSC bulletin board should be consulted for current status[2].

2. SUMMARY & SELECT GAMMA RAY DATA BASE

As described by Bertsch *et al.* (1989), the EGRET telemetry is processed by the program PDBGEN to produce the PDB, which contains $\approx$600 bytes per spark-chamber event. PDBGEN includes the SAGE (Search and Analysis of Gamma Ray Events) subroutine which structures the spark-chamber tracks before the gamma-ray directions and energies are ascertained. The information relevant to gamma-ray astronomy is extracted for the summary and select files. Also, the summary and select files contain only events which are judged (either automatically by SAGE or by human review (Nolan *et al.*, 1992; Bertsch *et al.* 1989) to be due to celestial[3] gamma rays. The format of the summary data base is shown in Table 3. Many of the details in the PDB are not included[4] in the summary database.

---

[1] Email: pence@tetra.gsfc.nasa.gov or LHEAVX::PENCE

[2] Telnet to grossc.gsfc.nasa.gov (or set host to GROSSC), and login as gronews. The same information may be obtained by calling the SSC (301)286-6257.

[3] Events within an energy dependent angle of the earth horizon (and thus probably due to cosmic ray induced atmospheric albedo gamma rays) will not be included in the summary and select files. The energy dependent angle is currently TBD (to be determined).

[4] The following are in the PDB, but not in the summary files or EXPHISTfiles: spark chamber data, trigger-telecope time of flight, TASC PHA timing measurements, various count rates, analysis program version numbers, editor identification, structuring summary parameters, scattering energy estimate and uncertainty, TASC PHA energy, and housekeeping data. Complete content and format details are available in EGRET team documentation (EGRET/GSFC/DLB/NAL/FORMATS).

Table 1. The EGRET Data Products

Name	Description	Format	Size	Numeration
Low level	processed products			
SUMMARYpppp	Summary of events	binary table FITS	≈10 Mbytes/2 weeks[1]	by Obs.
SELECTFxxxx	Subset of SUMMARY files	binary table FITS	≈100 Kbytes[1]	SSC catalog
TIMELINfile	EGRET Timeline	ASCII table FITS	≈10 Kbytes	1 expected
EXPHISTpppp	Exposure history	ASCII table FITS	≈350 Kbytes/2 weeks	by Obs.
SENHISTxxxx	Sensitivity history	ASCII table FITS	≈50 Kbytes/2 weeks	SSC catalog
BURSTCSxxxx	Burst mode counts spectra	binary table FITS	≈100 Kbytes[2]	SSC catalog
SOLARCSxxxx	Solar mode counts spectra	binary table FITS	≈100 Kbytes[2]	SSC catalog
BKGNDCSxxxx	Background counts spectra	binary table FITS	≈100 Kbytes[2]	SSC catalog
High level	processed products			
PSFFILExxxx	Point spread function tables	binary table FITS	16.3 Mbyte	SSC catalog
EDPFILExxxx	Energy dispersion tables	binary table FITS	16.3 Mbyte	SSC catalog
SARFILExxxx	Sensitive area tables	binary table FITS	160 Kbyte	SSC catalog
SARVARYfile	Sensitivity time dependence	ASCII table FITS	≈10 Kbyte	1 expected
BURSTRMxxxx	Burst Response matrices	binary table FITS	≈40 Kbytes/matrix	SSC catalog
CNTSMAPnnnn	Binned event counts maps	FITS format	≈400 Kbytes/Obs.[3]	by Obs.[4]
EXPOMAPnnnn	Binned exposure maps	FITS format	≈400 Kbytes/Obs.[3]	by Obs.[4]
INTSMAPnnnn	Binned intensity maps	FITS format	≈400 Kbytes/Obs.[3]	by Obs.[4]
DIFFMAPnnnn	Diffuse prediction maps	FITS format	≈400 Kbytes	SSC catalog
SRCECATfile	Source catalog	FITS format	≈10 Kbyte	1 expected
HESPECTxxxx	High energy spectra	FITS format	≈10 Kbyte	SSC catalog
HELTCRVxxxx	High energy light curves	FITS format	≈10 Kbyte	SSC catalog
BURSCATfile	Burst catalog	FITS format	≈10 Kbyte	1 expected
BURSTPSxxxx	Burst photon spectra	FITS format	≈10 Kbyte	SSC catalog
BULTCRVxxxx	Burst light curves	FITS format	≈10 Kbyte	SSC catalog
SOLRCATfile	Solar flare catalog	FITS format	≈10 Kbyte	SSC catalog
SOLARPSxxxx	Solar flare photon spectra	FITS format	≈10 Kbyte	1 expected
SOLTCRVxxxx	Solar flare light curves	FITS format	≈10 Kbyte	SSC catalog
EGRETPBfile	EGRET publication catalog	ASCII table FITS	≈10 Kbyte	1 expected

[1]Header plus 130 bytes/event, see table 3 for format; also called time-ordered gamma-ray event lists.

[2]Header plus 1230 bytes/spectrum

[3]For fourteen images each 60°×60°maps with 1/2° binning; one map for each of the following tentative energy selections; first ten narrow bands (which will be appropriate for spectroscopy): 30 < E < 50 MeV, 50 < E < 70 MeV, 70 < E < 100 MeV, 100 < E < 150 MeV, 150 < E < 300 MeV, 300 < E < 500 MeV, 500 < E < 1000 MeV, 1000 < E < 2000 MeV, 2000 < E < 5000 MeV, 5000 < E < 30000 MeV; and then four integral bands (which will be appropriate for source detection and position determination, and extended emission distribution studies): E > 30 MeV, E > 100 MeV, E > 300 MeV, E > 1000 MeV.

[4]Normally nnnn will be the Observation period number ×10. However multi-pointing maps (with number suffix _xxx) will be available and will be cataloged on line by the SSC.

Table 2. Completed Phase I EGRET Observations

Obs. period	Target name	Begin	End
0.2	CRAB 3° (L=186, B= −3)	22 APR 1991	28 APR 1991
0.3	CRAB 9° (L=193, B= −4)	28 APR 1991	1 MAY 1991
0.4	CRAB 9° (L=193, B= −4)	1 MAY 1991	4 MAY 1991
0.5	CRAB 0° (L=184, B= −6)	4 MAY 1991	7 MAY 1991
0.6	GALACTIC HOLE (L=150, B=53)	7 MAY 1991	10 MAY 1991
0.7	VELA (L=266, B=1)	10 MAY 1991	16 MAY 199
1.0	CRAB[a]	16 MAY 1991	30 MAY 1991
2.0	CYGNUS	30 MAY 1991	8 JUN 1991
2.1	SUN	8 JUN 1991	15 JUN 1991
3.0	SN 1991T	15 JUN 1991	28 JUN 1991
4.0	NGC 4151	28 JUN 1991	12 JUL 1991
5.0	GAL CENTER	12 JUL 1991	26 JUL 1991
6.0	SN 1987A	26 JUL 1991	8 AUG 1991
7.1	CYGNUS	8 AUG 1991	15 AUG 1991
7.2	GAL PLANE 25	15 AUG 1991	22 AUG 1991
8.0	VELA	22 AUG 1991	5 SEP 1991
9.1	GAL SOUTH POLE	5 SEP 1991	12 SEP 1991
9.2	HERCULES	12 SEP 1991	19 SEP 1991
10.0	FAIRALL 9	19 SEP 1991	3 OCT 1991
11.0	3C 273	3 OCT 1991	17 OCT 1991
12.0	CEN A	17 OCT 1991	31 OCT 1991
13.1	GAL PLANE 25	31 OCT 1991	7 NOV 1991
13.2 — 33.0	SUBSEQUENT OBS.[b]	7 NOV 1991	20 AUG 1992

[a] More details about these observations are given by Chipman (1992).
[b] A tentative schedule for the subsequent observations is given by Chipman (1992).

For investigators using SSC or EGRET team software, the detail given in Tables 3 & 4 will not be required. The software will be designed to operate correctly without user involvement in the details of the data products. The details are included in anticipation of the eventual creation of new software for archival analysis of summary data. The details given in Table 3 & 4 should suffice for this. The parameters documented only in EGRET team software are not anticipated to be useful.

The investigation of a specific source uses gamma rays from a radius corresponding to the extent of the PSF (point spread function), typically ≈5°. Since EGRET simultaneously observes a cone of radius ≈30°, only a small fraction of the events in a SUMMARYfile will be useful for an investigation of a specific source. The SELECTFiles will contain subsets of the SUMMARYfiles for the purposes of specific source investigations.

SELECTFiles will be produced at the SSC or by the EGRET team using the SELECT program. Events are chosen which meet user specified criteria[5]. The events which meet the criteria are written

[5] Direction within a specified region (either inside or outside of a circle, or a square; in either galactic or celestial coordinates); gamma-ray direction less than a specified maximum from the detector axis; gamma-ray earth zenith angle less than a specified maximum; gamma-ray energy between specified minimum and maximum; energy class: either A, A+B+C, A+C, B, or C (see Table 3, footnote 12); energy deposition in TASC above 6.5 MeV; specific Compton Observatory position (by earth latitude and longitude, or by rigidity); specific packet error flag conditions; specific analysis return code conditions.

to the SELECTFile in the same format as the SUMMARYfile.

The SSC or the EGRET team will provide the GI with the use of the following software which will analyze SELECTFiles: the PULSAR program constructs a binned light curve from the events in the SELECTFile for a specific pulsar ephemeris (correction may also be done for a binary orbit); the SEARCH program performs an epoch folding search in period for significant periodicity; the MAPGEN program constructs a binned counts map (also may use a SUMMARYfile); the QIKLOOK program allows for examination of individual records, and also allows easy installation of code for specific analyses. The SSC will make available the Fortran code for the QIKLOOK program.

An example of a special SELECTFile to be made available by the SSC is that containing the gamma-ray spark-chamber events associated with the May 3 gamma-ray burst (Schneid *et al.* 1991).

3. EGRET EXPOSURE

The calculation of the EGRET exposure is complicated because of measures taken to limit the rate of events due to cosmic-ray induced atmospheric-albedo gamma rays. The 32 scintillator tiles of the time-of-flight spark-chamber-trigger system form 96 recognized pairs which are grouped into 9 sub-telescope directions (Bertsch *et al.* 1989, fig. 4): vertical, and the 8 cardinal directions (for convenience designated E, NE, N, NW, W, SW, S, SE; see Table 3, footnote 3). These sub-telescope directions are individually commanded off by the Compton Observatory computer when their center is within 22° of the earth's atmosphere. The 9 sub-telescope directions can combine to form 74 possible combinations or sub-telescope modes. The EGRET sensitive area is different for each of these modes. However, some albedo gamma-ray events still cause events despite this measure. Therefore, the event by event earth zenith selection offered by the SELECT program is normally required, and must be accounted for when calculating exposure.

The TIMELINfile is a short file describing the beginning and ending time, and times for which data is to be excluded for various reasons from analysis. The first step in determining the EGRET exposure is the construction of the EXPHISTfile (exposure history) for each observation period from the TIMELINfile and the PDB with the EXPHST program (currently running only at GSFC on the IBM MVS system). The format of the EXPHISTfile is shown in Table 4. A new record is written to the file each time the EGRET operation mode changes, along with the integral of the live-time (dead time is created by event readout, and anticoincidence-dome interactions) for that time period.

The EXPHISTfile and the instrument response tables (section 5) are used by the INTMAP program to produce a binned map of exposure (EXPOMAPfiles). A CNTSMAPfile is used as a template for the binning and energy range selection. Thus the INTMAP program creates an EXPOMAPfile which corresponds exactly to a specific CNTSMAPfile. The INTMAP program simultaneously produces an intensity or flux map (INTSMAPfile) by dividing the CNTSMAP by the EXPOMAP.

The PNTEXPOS program (tentative name) uses the EXPHISTfile and the instrument response files to produce a table of instrument sensitive areas as a function of time for a specific direction and energy range (tentative data product name, SENHISTxxxx) which may subsequently be used to analyze source variability.

4. BINNED MAPS

The binned counts maps (CNTSMAPfiles) are produced from SELECTFiles or SUMMARYfiles with the MAPGEN program either in celestial or galactic coordinates. The exposure map (EXPOMAPfile) and intensity map (INTSMAPfile) are produced by the INTMAP program.

Table 3. EGRET Summary & Select Data Base Content

Content of each 130 byte record	Type	Start byte
Time in milliseconds of day[1]	I*4	1
Additional microseconds	I*2	5
Integer value of Modified Julian Date, (JD - 2440000.5)	I*2	7
Compton Observatory X position (J2000 earth centered inertial coordinate in km)	R*4	9
Compton Observatory Y position (J2000 earth centered inertial coordinate in km)	R*4	13
Compton Observatory Z position (J2000 earth centered inertial coordinate in km)	R*4	17
Trigger-telescope hits[2]	I*4	21
Trigger-telescope directions and types enabled[3]	I*2	25
Packet error flags[4]	I*2	27
TASC pulse height analyzer #1 flags[5]	Byte	29
TASC pulse height analyzer #2 flags[5]	Byte	30
Spare	I*2	31
Gamma-ray projected direction X-Z (radians)	R*4	33
Gamma-ray projected direction Y-Z (radians)	R*4	37
Gamma-ray Earth Zenith (radians)	R*4	41
Gamma-ray Earth Azimuth (radians from North toward East)	R*4	45

continued on the next page

[1]This is the time from the beginning of the Modified Julian Day to the event in milliseconds. Thus the time of the event may be obtained from the first three integers in the record. The absolute timing accuracy is ≈50 microseconds. The relative accuracy is 8 microseconds.

[2]The 32 bits in this integer indicate (1 means a hit) the state of each scintillator tile in the upper (B) plane, and lower (C) plane of the time-of-flight spark-chamber-trigger hodoscope (Hunter 1991; Bertsch *et al.* 1989, fig. 4). The tile order is (from low to high bit): C11, C12, C13, C14, C21, C22, C23, C24, C31, C32, C33, C34, C41, C42, C43, C44, B11, B12, B13, B14, B21, B22, B23, B24, B31, B32, B33, B34, B41, B42, B43, B44. The first index increases with increasing X. The second index increases with increasing Y.

[3]The first 15 bits in this integer indicate which trigger telescope directions and tile combination types (Bertsch *et al.* 1989) were enabled at the time of the event. The order is (from low to high bit; 1 means enabled): T1 (vertical central), T2 (vertical edge), T3 , T4, T5, T6, T7, D1=E, D2=NE, D3=N, D4=NW, D5=W, D6=SW, D7=S, D8=SE, unused. North is in the direction of the EGRET positive Y axis, and East is the direction of the EGRET positive X axis. The EGRET axes are aligned with the Compton Obervatory axes. The types are the combinations of tiles with similar expected background. The definitions may be found in EGRET team documentation (EGRET/GSFC/DLB/85/AUG/15). Types T1 and T2 are also the on-axis direction. All EGRET observations to date (except for several hours during instrument activation) have been made with all types enabled. However T1 and T2 are turned off if the earth limb is within 22° of the center of their direction (just as directions D1-D8).

[4]These flags indicate problems with the integrity of the telemetry. They are explained in EGRET team documentation (EGRET/GSFC/DLB/NAL/FORMATS). Generally, significant periods of problematic telemetry are removed by exclusion entries in the TIMELINfile.

[5]The 8 bits in this byte contain the TASC PHA (pulse height analyzer) flags. The order is (from low to high, 1 means yes): unused, ADC Busy At MET (master event trigger), timer OK at MET (TMOK), energy underflow (RNDN-C), energy overflow, zero cross overflow, rundown time overflow (PHA delay overflow), and zero cross hazard. The meanings of these flags are described in EGRET team documentation (EGRET/SU/PLN/87/OCT/9). The zero cross overflow bit will be 1 if less than 6.5 MeV was deposited in the TASC. This is important since the normal "TASC in coincidence" calibration files (section 5) pertain to a selection of events with at least 6.5 MeV energy deposition in the TASC. There is one byte for each TASC PHA.

Table 3. continued

Content	Type	Start byte
Gamma-ray Right Ascension (radians, J2000)	R*4	49
Gamma-ray Declination (radians, J2000)	R*4	53
Gamma-ray Galactic Latitude (radians, BII)	R*4	57
Gamma-ray Galactic Longitude (radians, LII)	R*4	61
Gamma-ray energy (MeV)	R*4	65
Gamma-ray energy uncertainty (MeV)	R*4	69
Spares	2I*4	73
Time correction to Barycenter[6]	R*8	81
Binary orbit phase at the time of the event (values 0 to 1)	R*4	89
Pulsar phase at the time of the event (values 0 to 1)	R*4	93
Pulsar Right Ascension (J2000, radians)	R*4	97
Pulsar Declination (J2000, radians)	R*4	101
Barycenter position X (J2000 earth centered inertial coord. in light microseconds)	I*4	105
Barycenter position Y (J2000 earth centered inertial coord. in light microseconds)	I*4	109
Barycenter position Z (J2000 earth centered inertial coord. in light microseconds)	I*4	113
Structure Analysis processing return code[7]	Byte	117
SINGLE subroutine return code[8]	Byte	118
SAGE subroutine return code[9]	Byte	119
Structure Flags[10]	2 Bytes	120
SCATTERING subroutine return code[11]	Byte	122
ENERGY subroutine return code[12]	Byte	123
DIRECTION subroutine return code[13]	Byte	124
Spares	3I*2	125

[6]The time correction to the solar system barycenter, T_C, can be used to calculate the arrival time at the barycenter for the pulsar direction specified in bytes 97–104. The barycentric arrival time is: Modified Julian Date = $IMJD + T_C + 0.5$; or full Julian Date = $IMJD + T_C + 2440001.$, where $IMJD$ is the integer value at byte 7. This and the next seven numbers are written to SELECTFiles by the PULSAR program. SUMMARYfiles will also contain the Barycenter vector for the time of each event.

[7]The Structure Analysis bit meanings are: bit 0, event disposition (1=Editor Last Set Disposition); bit 1, Two Tracks In X-View (1=yes); bit 2, Two Tracks In Y-View (1=yes); bits 3-4, Track Correlation Method (0 = Spark Density/Track Length, 1 = Gap Method, 2 = 45 Degree Grid Method); 5-7, Unused.

[8]The SINGLE return code also characterizes the presence of single or multiple tracks in the XZ and YZ projections. A detailed description is in the header of the SINGLE subroutine Fortran code.

[9]The SAGE return code characterizes the overall SAGE event structuring. A detailed description is in EGRET team documentation (The SAGE Document, chapter V).

[10]The 16 structure flags further characterize the SAGE structuring of the spark chamber events. The meanings of these flags are described in EGRET team documentation (The SAGE Document, chapter IX).

[11]The SCATTERING return code characterizes the determination of the energy of the lepton for each track from the extent of Coulomb scattering. A detailed description is in the header of the SCATTERING subroutine Fortran code.

[12]The ENERGY return code characterizes the assessment of the gamma-ray energy. Bits 0&1 describe the event class: 0, Class A – Best events for spectroscopy (all tracks hit TASC and both TASC PHAs are above threshold); 1, Class B – Lesser quality events because tracks show that much of the energy is not measured by TASC; 2, Class C – Like class A, but below PHA threshold. Energy is low, but estimate very uncertain; 3, No energy assigned – bits 3-7 give reason(s) for not assigning an energy. See the header of the ENERGY subroutine Fortran code for details.

[13]The DIRECTION return code characterizes the gamma-ray direction determination from an energy weighted average of the track directions. A detailed description is in the header of the DIRECTION subroutine Fortran code.

The exposure maps have units of cm^2 second steradian, where the solid angle is that of the specific bin. Thus, the intensity maps have units of cm^{-2} $second^{-1}$ $steradian^{-1}$. A point source flux (units, cm^{-2} $second^{-1}$) is the integral of the intensity over the solid angle into which it is dispersed by the EGRET PSF. However, because of diffuse gamma-ray emission, a simple integral is not appropriate.

The SSC or the EGRET team sites will provide the GI with the use of the following software which will analyze binned maps: the SKYMAP program produces a color display of a binned map (using X11 interactive graphics on a workstation) which may also be printed; the SHOW program provides for map evaluation. The following functions are available: display pixel values for specified coordinates; display in order of decreasing value for a region; make a one dimensional profile of a region of the map by integrating over the other dimension; integrate pixel values for a rectangular or circular region. The SOURCE program evaluates the likelihood of the existence of a source at a specific point. For a significant indication of a source, it provides an estimate of the number of source counts and the uncertainty of that estimate. The exposure from the appropriate EXPOMAPfile is then used to obtain the point-source flux. The SPECTRAL program tentatively uses SOURCE to obtain an estimate of the number of source counts in each of many energy selection bands (e.g. the 10 bands of footnote 3 of Table 1), and then uses the EXPHISTfile, and the instrument response files for a forward-folding chi-squared-minimization estimate of the source photon spectrum.

Binned maps of counts, exposure, and intensity will be available 15 months after data are acquired for a 60° by 60° square region centered on the Z axis for each observation with a separate image for each of the 14 gamma-ray energy selections given in footnote 3 of Table 1. Special maps will eventually be available of all extant data in specific directions of interest. For example, maps will be made available ($\approx$9/92) of the $\approx$5 weeks of exposure obtained between April and June of the Crab/Geminga region. Also, binned maps will eventually be available ($\approx$11/93) for the entire galactic plane (tentatively $|b| < 20°$), and the full sky (probably as a binned Aitoff projection). Also binned maps of the EGRET team estimate of galactic and extragalactic diffuse gamma-ray emission (DIFFMAPfiles) will eventually be available (see section 7).

5. CALIBRATION RESULTS

The SLAC (Stanford Linear Accelerator Center) calibration data have been analyzed at GSFC with software equivalent to that used to analyze flight data. The resulting gamma-ray energies and directions have been analyzed by the Max Planck EGRET group with program CALAN to obtain the response tables. A description of these results is in preparation (Thompson *et al.* 1992). The SLAC data have been analyzed to determine the EGRET response for each of the 74 sub-telescope modes (discussed in section 3). The response tables are SARFILEfiles (Sensitive area), PSFFILEfiles (Point spread function), and EDPFILEfiles (Energy dispersion). The suffix of these files correspond to EGRET operation conditions[6].

The sensitive area tables consist of a four byte floating number for twenty different true gamma ray energies[7] in each record. There are 1998 records: 74 sub-telescope modes × 3 azimuths (0°, 22.5°, 45°, with respect to the X axis) × 9 inclinations (0°,5°,10°,15°,20°,25°,30°,35°, 40°, with respect to the Z axis).

[6] The currently assigned suffixes are: suffix 01, event classes (A+B+C) & TASC not in coincidence; suffix 02, event classes (C) & TASC not in coincidence; suffix 03, event classes (A+C) & TASC not in coincidence; suffix 04, event classes (A) & TASC not in coincidence; suffix 05, event classes (B) & TASC not in coincidence; suffix 06, event classes (A+B+C) & TASC in coincidence at 6.5 MeV; suffix 07, event classes (A) & TASC in coincidence at 6.5 MeV; suffix 08, event classes (B) & TASC in coincidence at 6.5 MeV; suffix 09, event classes (C) & TASC in coincidence at 6.5 MeV; suffix 10, event classes (A+C) & TASC in coincidence at 6.5 MeV.

[7] True energies (in MeV): 15, 20, 30, 35, 50, 60, 70, 100, 150, 200, 300, 500, 700, 1000, 2000, 3000, 4000, 6000, 7000, 10000.

Table 4. EGRET Exposure History File Content

Content	format	Column
Comment indicator ('*' means entire record is a comment)	A1	1
Integer value of Modified Julian Date, (JD - 2440000.5)	I6	2
Time in milliseconds of day[1]	I9	18
Spare	L1	17
SAA Flag, 'T' when the Compton Observatory is in the SAA	L1	18
Pointing deviation flag ('T' if *Compton* pointing deviation > 0.5°)	L1	19
Exclusion flag ('T' if interval excluded by TIMELINfile during calibration, etc.)	L1	20
Spare	Z1	21
Hexadecimal value of hodoscope directions and types enabled[2]	Z4	22
Spare	Z1	26
Hexadecimal value of the event coincidence requirement[3]	Z1	27
Spare	Z1	28
Hexadecimal value of the TASC #1 coincidence energy deposition requirement [4]	Z1	29
Spare	Z1	30
Hexadecimal value of the TASC #2 coincidence energy deposition requirement [4]	Z1	31
Compton Observatory Z axis Right Ascension (J2000, radians)	F8.4	32
Compton Observatory Z axis Declination (J2000, radians)	F8.4	40
Compton Observatory X axis Right Ascension (J2000, radians)	F8.4	48
Compton Observatory X axis Declination (J2000, radians)	F8.4	56
Integrated live-time for this exposure record (seconds)	F7.1	64
Elapsed time for this exposure record (seconds)	F10.3	71
Earth center Right Ascension at beginning of record (J2000, radians)	F8.4	81
Earth center Declination at beginning of record (J2000, radians)	F8.4	89
Earth center Right Ascension at end of record (J2000, radians)	F8.4	97
Earth center Declination at end of record (J2000, radians)	F8.4	105

[1]This is the time from the beginning of the Modified Julian Date to the event in milliseconds. Thus the time for the beginning of the exposure record may be obtained from the first two integers in the record.

[2]The bits in this integer indicate (1 means enabled) which trigger hodoscope directions and tile combination types were enabled for the duration of this exposure history record (beginning at the time specified in the first two integers, and ending the Elapsed time later). The order is (from low to high bit): T1 (vertical central), T2 (vertical edge), T3 , T4, T5, T6, T7, D1=E, D2=NE, D3=N, D4=NW, D5=W, D6=SW, D7=S, D8=SE, unused. See table 3, footnote 3 for more information. Two important values are 7FFF for unocculted observation, and 007C for complete occultation.

[3]A bit value of 1 means the subsystem signal is included in the coincidence logic requirement. Bit 0, unused; bit 1, Anti-coincidence dome requirement; bit 2, TASC energy deposition requirement; and bit 3, trigger time-of-flight requirement.

[4] This integer represents the minimum energy deposition required in the specific TASC PHA for a spark-chamber event to occur. The levels corresponding to the hexadecimal values are: 0, 1.0 MeV; 4, 2.6 MeV; 8, 5.7 MeV; C, 13. MeV. Flight operation to date has been with a minimum TASC energy deposition of 2.6 MeV required.

It is observed that the EGRET sensitive area decreases as the spark-chamber gas ages. After the gas replacement (the first of five replacements is planned for December 2, 1991), it is expected that the sensitivity will return to the pre-deployment condition. The result will be a saw-tooth variation of sensitivity with time. This variation will be described by the SARVARYfile. The format is not yet determined.

The point spread function tables consist of a four byte floating number for 100 angles — 0.1°, 0.3°, ...19.9° (the first four bytes of the record is a flag, and the last four indicate the overflow, the point spread probability which extends beyond 19.9°) in each record. More specific documentation may be found in the FITS format header for these files. There are 39960 records: 74 sub-telescope modes × 3 azimuths × 9 inclinations × 20 true gamma ray energies[7].

The energy dispersion tables consist of a four byte floating number for 100 energies — fractions of 0,.02,...1.98 of the true energy (the first four bytes of the record is a flag, and the last four indicate the overflow, the energy dispersion probability which extends beyond 1.98 of the true energy), in each record. There are 39960 records as for the point spread function tables.

The SSC will be able to supply Fortran subroutines to access and interpolate these tables.

6. TASC SOLAR & BURST MODES

In addition to its primary role of providing energy resolution for gamma rays recorded by the spark chamber, the TASC also functions independently as a spectrometer for gamma rays between 1 and 190 MeV. Also, four TASC rates (for energy thresholds 1., 2.5, 7., and 20 MeV) are obtained in 2.048 second intervals; and the anticoincidence-dome rate (energy thresholds ≈20 keV) is obtained in 0.256 second intervals. The large mass of NaI(Tl) (400 kg) provides omni-directional sensitivity for high energy gamma rays. However, there is no charged particle veto, and there is considerable mass in front of the crystal in most directions (minimum 0.6 radiation lengths along the instrument axis).

There are two modes of TASC spectroscopy, Solar and Burst (Nolan *et al.*, 1992; Hartman *et al.*, 1992). The Solar spectra are continuously accumulated for intervals of 32.768 seconds. The Burst spectra are obtained over 4 preset intervals following a BATSE trigger. Both spectral modes have a common format. The logarithmic channel compression of the 256 channels is given by Bertsch *et al.*(1989, Table II). However, the energy to channel conversion varies with the TASC PMT gains — which have been drifting during the mission. (This effect is corrected by the ENERGY subroutine of the PDBGEN program for spark-chamber events.) These spectra are extracted from the PDB by the program TBURST. Each spectrum forms a 1230 byte record (see EGRET/GSFC/DLB/NAL/FORMATS for the format). The SSC plans to make some of these spectra available in binary table FITS format.

The BATSE-triggered counts-spectra will form the BURSTCSfiles. These tentatively will be made available for the BATSE bursts which are apparent in TASC, or for specifically requested BATSE bursts. The Solar-mode counts-spectra will form the SOLARCSfiles. These tentatively will be made available for solar flares which are apparent in TASC, or specifically requested intervals. The BKGNDCSfiles will offer a collection of spectra which can be used to estimate the TASC background for an event at a specific Compton Observatory orbital position and orientation. The BURSTRMfiles will contain TASC energy-dispersion matrices obtained for specific directions (in Compton Observatory reference frame) with the Compton Observatory Mass Model (Hartman *et al.*, 1992). These matrices are used to obtain the photon spectra (BURSTPSfiles and SOLARPSfiles).

7. OTHER HIGH LEVEL DATA PRODUCTS

In addition to the calibration results, and the binned maps which have already been discussed, the following EGRET high level data products will tentatively be produced. The exact formats for these products is currently uncertain. ASCII table FITS will be used. This will allow the product to be well documented. The ASCII information will be accessible for perusal via some texteditors (ASCII table FITS files have

2880 byte records). Also, the products may be read with software which is easily created (e.g., the FITSIO system) for high level analysis.

The SRCECATfile will be a catalog of sources detected with the EGRET spark chamber. The information given for each source will tentatively include: position, positional uncertainty, intensity above several different energies, intensity uncertainties, spectral information (either a spectral index, or a spectral parameter — the ratio of flux for different energy selections), the spectral uncertainty, and (possible) identification. The HESPECTfiles will give the spectra for sources detected with the EGRET spark chamber which are sufficiently intense. Spectra of the diffuse gamma-ray radiation by sky region will also be available as HESPECTfiles. The HELTCRVfiles will provide the light curves for sources detected with the EGRET spark chamber which are sufficiently intense. For pulsars or other periodic sources, the data will be epoch folded.

The BURSCATfile will contain a catalog of the BATSE bursts apparent in the TASC Burst mode. The contents are currently uncertain. The BURSTPSfiles will give the TASC photon spectra for BATSE bursts apparent in the TASC Burst mode. The BULTCRVfiles will give the TASC and anticoincidence-dome light curves for BATSE bursts apparent in the TASC Burst mode. The SOLRCATfile will contain a catalog of solar flares apparent in the TASC Solar mode. The SOLARPSfiles will give the TASC photon spectra for solar flares apparent in the TASC solar mode. The SOLTCRVfiles will give the TASC and anticoincidence-dome light curves for solar flares apparent in the TASC solar mode. For gamma-ray bursts, or solar flares where gamma rays are detected with the EGRET spark chamber, SELECTFiles will be available containing the spark-chamber events. This will be noted in BURSCATfile or SOLRCATfile.

The DIFFMAPfiles will be binned FITS formats which contain the results of the EGRET team diffuse emission studies. The galactic plane result will be a separate file. The format of the high galactic latitude maps is currently not certain (i.e. either an Aitoff projection, or regional maps). It is expected that DIFFMAPfiles will be made available in different resolutions. The highest resolution possible will be the resolution of the radio surveys used.

The EGRETPBfile will be an annotated list of publications by the EGRET team and GIs resulting from EGRET data.

References

Bertsch, D. *et al.* 1989, *Proceedings of the Gamma Ray Observatory Science Workshop*, Goddard Space Flight Center, April 10-12, 2-52

Chipman, E. 1992, *These Proceedings*

Fichtel, C.E. *et al.* 1989, *Proceedings of the Gamma Ray Observatory Science Workshop*, Goddard Space Flight Center, April 10-12, 3-1

Hartman, R.C. *et al.* 1992, *These Proceedings*

Hunter, S.D. 1991 1991, *Nucl. Instrum. Meth.* , **A307**, 520

Kanbach, G. *et al.* 1988, *Space Sci. Rev.* , **49**, 69

Kanbach, G. *et al.* 1989, *Proceedings of the Gamma Ray Observatory Science Workshop*, Goddard Space Flight Center, April 10-12, 2-1

Nolan, P.L. *et al.* 1992, *IEEE Transactions*, submitted.

Pence, W.D 1991, *Bulletin of the American Astronomical Society*, Vol 23, No. 2, p. 936

Schneid, E. *et al.* 1991 *Astron. Astrop.* in preparation

Thompson, D.J. *et al.* 1992 *Ap. J. Supp.* or *Journ. Exp. Astron.* in preparation

NEURAL NETWORK CLASSIFICATION OF "QUESTIONABLE" EGRET EVENTS

C. A. Meetre[1] and J. P. Norris[2]
NASA/Goddard Space Flight Center
Greenbelt, MD 20771

ABSTRACT

High-energy gamma rays (> 20 MeV) pair producing in the spark chamber of EGRET give rise to a characteristic but highly variable 3-D locus of spark sites, which must be processed to decide whether the event is to be included in the database. A significant fraction (~15%: 10^4 events / day) of the candidate events cannot be categorized (accept / reject) by an automated rule-based procedure, are therefore tagged, and must be examined and classified manually by a team of expert analysts. We describe a feed-forward, back-propagation neural network approach to the classification of the questionable events. The algorithm computes a set of coefficients using representative exemplars drawn from the preclassified set of questionable events. These coefficients map a given input event into a decision vector that, ideally, describes the correct disposition of the event. The net's accuracy is then tested using a different subset of preclassified events. Preliminary results demonstrate the net's ability to correctly classify a large proportion of the events for some categories of questionables. Current work includes the use of much larger training sets to improve the accuracy of the net.

INTRODUCTION

The Energetic Gamma Ray Experiment Telescope (EGRET) on the Compton Gamma Ray Observatory is sensitive to high-energy gamma rays in the regime 20 MeV to 30 GeV. Two vertically stacked spark chambers comprise the primary detector. A photon is detected when it interacts in one of several thin tantalum plates in the upper spark chamber, producing trajectories which, propagating downward, are revealed by sparks where the leptons interact in a series of decks (interleaved with the tantalum plates). Each deck contains two orthogonal, horizontal grids of closely spaced wires with a high voltage differential. A magnetic core readout system is used to determine the spark positions. An anti-coincidence scintillator dome surrounding the upper portion of the telescope and a directional time-of-flight coincidence system in the lower portion discriminate against cosmic rays and Earth albedo. Details of the EGRET instrument and its scientific objectives are described in Kanbach *et al.* (1989) and Fichtel *et al.* (1989), respectively.

A complex ruled-based program, Search and Analysis of Gamma Ray Events (SAGE), definitively processes a large proportion of candidate events. SAGE eliminates virtually all cosmic-ray events, and categorizes apparent gamma-ray events as either 'acceptable' or 'questionable'. About 15% of all events are questionables. These are examined visually and classified by a team of expert analysts. For both SAGE-accepted events and questionables which are accepted by analysts, SAGE characterizes the photon arrival direction and energy using the spark positions and the energy deposition measured by a large NaI(TP) scintillation crystal below the lower plastic scintillator.

[1] STX, Code 690.2 ; [2] Code 668

Although the manual processing task for questionable events is quite tractable, it is labor intensive, and - given the large data volumes - expensive and time consuming. In addition, human analysts are prone to variable performance. Rule-based and expert system approaches have been thoroughly investigated over the years and have not yielded satisfactory results on the set of questionables.

We have explored neural networks for processing some categories of EGRET questionable events. The fact that a trained human recognizes events as 'accepts' or 'rejects' implies that a neural network trained on a set of events categorized by analysts could perform the same feat. Because the EGRET data set is so large, the up-front effort involved in developing the network can be amortized to yield a very cost-effective solution. A network can process in minutes what an analyst can do in several months.

NEURAL NETWORKS

Neural networks are an artificial intelligence technique that applies an algorithm modeled on the way the human brain learns to discriminate among patterns perceived by the senses. In general, the brain receives sensory information (its input data) and produces an estimate of the classification of the pattern (its decision vector). This estimate is corrected by some training agent, by comparison with the ideal answer (its target vector), and the estimate is reinforced if correct. Over many repetitions the brain comes to recognize, for example, a picture of a horse as a horse, and can then extend this to other pictures of horses, provided the original sample of pictures showed a wide enough variety of horses and orientations.

It is clear that the human brain, when recognizing patterns, does not usually use a rule-based system. The brain's cycle time is relatively slow, and rule-based 'if-then-else' systems are inherently serial in nature. The number of decisions necessary to apply an 'if-then-else' algorithm to visual pattern recognition would vastly overrun the actual 0.5-s response time of the brain. Thus, pattern recognition is accomplished by the brain in a massively parallel manner using many processors, many connections, and few cycles. Recognition knowledge appears to be embedded into the brain by the amplification or attenuation of the pathways over which the signals travel between successive neurons. Not surprisingly, this type of learning behavior can be simulated by an electronic circuit. And, more importantly for our purposes, it can be simulated by a computer.

This simulation requires the algorithm shown graphically in Figure 1. Vectors are used to represent the input to and output from neurons. Neurons are simulated using the sigmoid function, $f(x) = 1/(1 + \exp[-x])$, where $f(x)$ is the output from a neuron whose collective input is x. This function models closely the response and thresholding activity of a neuron. A weight, or coefficient, is associated with each connection among the neurons and it is this coefficient that amplifies or attenuates the information associated with the connection. These coefficients 'store' the knowledge of the net in a non-explicit form and are changed by small increments to allow the net to converge to a correct outcome.

A network is trained using an appropriately sized set of exemplars which previously have been classified. The size of this set will depend on the complexity of the pattern to be classified. The selection of patterns must cover the possible range of input data. Once the training is completed, the network can be used to classify new patterns drawn from the range of training patterns.

The selection of exemplars is a major part of the up-front effort required to use a neural network and means that networks are practical in application only where considerable amounts of data are to be processed. In addition, it should be noted that there is no physical information embedded in

A Simple Three-Layer Neural Network

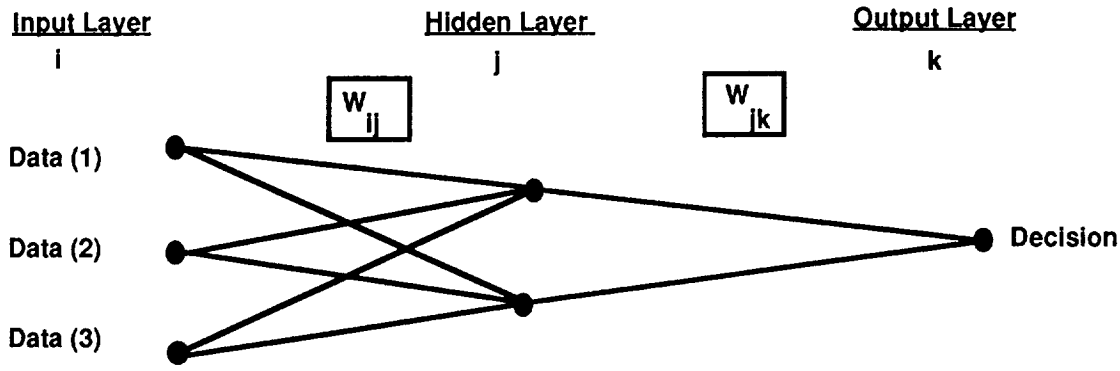

The Activation Function

$$x_j = \Sigma\, data_i \cdot w_{i,j}$$

$$f(x_j) = \frac{1}{1 + e^{-x_j}}$$

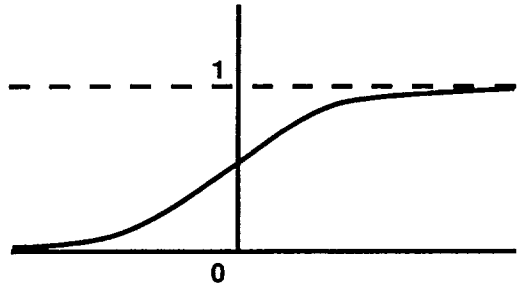

This function acts as a processor, and produces an output between 0 and 1.

Fig. 1– Connectivity of a small neural network with one layer of hidden nodes. The activation function closely models the threshold response of a biological neuron.

the coefficients. The network is simply a classifier and gives no analytical information about physical processes.

Because the function used is general, although variable in the number of terms it contains, the software used to train the network is reusable for any problem. It is surprisingly uncomplicated, and, in this application, was implemented in Fortran on a VAX 3100. In a rule-based system, the program must be written uniquely for each problem. Even with expert systems, an explicit knowledge base must be developed for each problem, though the software that handles the knowledge is reusable.

A neural network is a non-linear least-squares fit to a very general function (h) in which the independent variable is an array of experimental data (X), and the dependent variable is an array of characteristics (D) often called the decision vector – the classification. During training, the decision vector is compared to a target vector (T) which contains the correct classification for the event. The error vector thus generated (E) can be used to calculate the relative contribution to this outcome of all the coefficients (a vector W) in the network, and to effect a small change ΔW in a direction that will minimize the error. The relationships are, therefore:

$$h(X) = D$$

$$\text{or} \quad h(x_1,x_2,x.....x_n) = (d_1,d_2,...d_n) \ ,$$

$$E = |(T - D)| \quad \text{and} \quad \Delta W = g(E) \ .$$

A value of $d_i \cong 1$ indicates the presence of characteristic *i*. Conversely, a value of $d_i \cong 0$ indicates its absence. The order and number of characteristics is fixed in the formulation of the problem and remains constant. Note that the sigmoid function is applied many times in h(X).

The fitting process determines an optimal value for the coefficients of the function h(X). After the coefficients are determined and inserted in the function, it can be evaluated for a given array of data. The value of the output array is an estimate of the characteristics of the data.

PREPROCESSING EVENTS AND TRAINING THE NETWORKS

The added advantage of human analysts over an automated, rule-based system is the capability of visual pattern recognition. An expert analyst can immediately see which sparks are extraneous to the expected gamma-ray signature, whereas rule-based decision-making sometimes misses the obvious. In reviewing questionable events, analysts continue to apply the rules that SAGE demands for event acceptance. The analyst's role reduces both pattern recognition and respect for SAGE rules to one final decision: accept or reject. We utilize the analysts' decisions on questionable events as input to train the network. Clearly, the network can perform, on average, only as well as the analysts.

The most frequently encountered signature of pair production in the EGRET is an upsidedown 'y' (miniscule): When the gamma ray converts to a pair, both leptons continue practically undeviated until one of them undergoes a major Coulomb collision in a tantalum plate. The two paths diverge at that point (the vertex), forming the two arms of the 'y', the undeviated path above the vertex forming the leg of the 'y' (see Figure 2). Additional scatterings may occur, and therefore the paths near the vertex are required to have straight segments of minimum length so that the event may be characterized. If neither lepton scatters, the signature is a single, undeviated track.

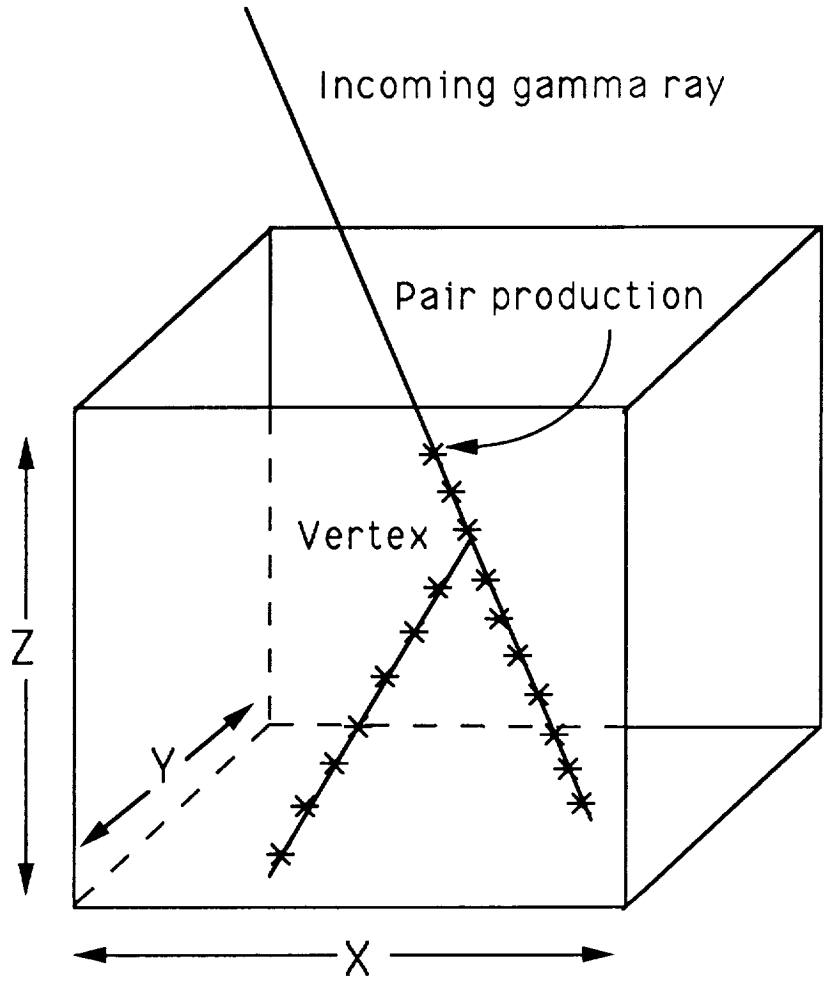

Fig. 2– Schematic of characteristic signature of pair production in the EGRET spark chamber. One lepton usually undergoes a major Coulomb scattering, resulting in a characteristic locus of sparks resembling an upsidedown 'y'.

EGRET data is best represented visually to an analyst as a sparse, large, 3-D matrix shown graphically in two views, X and Y (the XZ and YZ planes). But a more compact representation is necessary for a feasible neural network. Data representation is complicated by the fact that a given deck may have any number of sparks, including none. Furthermore, a spark in the X view cannot unambiguously be associated with a spark in the Y view, unless the spark is the only one on a deck.

Spark information was utilized from 34 decks (stacked in the Z direction) of the upper and lower spark chambers. In both the X and Y directions, there are 992 cores; cores which are 'on' (e.g., 'fired') indicate the paths of the leptons. Usually several adjacent cores fire on each deck when a lepton passes. A string of adjacent fired cores on a deck is called a spark. Two strings of fired cores with an interjacent gap of up to three unfired cores were treated as one spark. The central core of such a string of cores and gaps was then adopted as the X or Y coordinate of the spark.

In the majority of questionable events the recorded pattern has missing sparks and/or extraneous sparks. This kind of 'fuzziness' is difficult for rule-based systems to handle, whereas analysts and neural networks can more easily recognize a good event in the presence of flawed information.

Because a parsimonious representation is desirable, and because the network requires a constant number of independent variables, we retain exactly two sparks per deck. Some information is therefore lost when three or more sparks are present. The rules for retention of sparks per deck are: (1) If no spark is present, zero-fill both positions. (2) If only one spark is present, duplicate its position. (3) If there are two sparks, fill the respective positions with the spark coordinates. (4) If there are more than two sparks, retain the two sparks closest to the {1 spark, 2 sparks, or center} of the preceding (higher) deck. Since one spark per deck is usually present after pair production and before scattering, the duplicated portion of the trajectory may be thought of as representing the paths of the two unscattered leptons.

A single network was trained to recognize the existence of the following states, each of which corresponds to a SAGE rejection criterion: (1) an event appears to enter through a spark chamber wall rather than through the instrument aperture; (2) an event has too few sparks, thus the spark pattern is not sufficiently well-defined; (3) the event separation vertex appears to be on different decks in the X and Y views (thus compromising the characterization of event attributes). Hence, in experiments to date a network was trained with four output nodes: {accept, too few sparks, wall, or different decks}. In future experiments, we plan to train one network for each rejection criterion (e.g., only two output targets per network: accept or reject), and to be accepted an event will have to pass each network in succession.

Both the X and Y views are reviewed simultaneously by the analysts. However, the flaw in a pattern which leads SAGE to question an event may be present in only one view, in which case only the flawed view is used in the training set. Including the apparently acceptable view would introduce contradictory information and tend to influence the net in the wrong direction. For example, a wall event is usually apparent in only one view. In the recognition phase, both views would be required to pass muster (serially) for the event to be accepted by the network. In order to keep the number of input nodes small, we present the two views separately.

In addition to the rejection criteria, three classes of events are distinguished, and each must be processed with a different network. Events which exhibit the characteristic 'y' pattern in both views are called 'doubles'. Events for which SAGE cannot characterize both arms of the 'y' in both views are referred to as 'single-doubles' – apparently single in one view, double in the other. For very high energy gamma rays no separation may occur, or the separation angle may be negligible. These events are 'singles'. For inflight data, about 40% of the questionable events are singles, and the vast majority of these are rejected by analysts. Thus, a solution to the singles problem alone would be very useful. Since very few accepts are found among singles – none in ground-based calibration data, and very few in source-free inflight data – we have not yet been able to train a network to recognize singles. However, this problem seems eminently tractable since it is basically a task of recognizing well-formed straight lines. About 30% of questionables fall in the single-double category. Most of these events are in fact double in both views; however,

because of missing and extraneous sparks, SAGE could not identify the scattered track in one view. The remaining 30% of questionables appear double in both views. Most of our experiments have concentrated on this class. The single-double category should be more easily addressed when more experiments with doubles have been performed.

We utilized ground-based calibration data for the experiments reported here. A large group of doubles was submitted serially to the training portion of the software; network training was iterated ~ 5000 times until the network was able to classify correctly all the events in the training set. The coefficients which resulted from the training were then incorporated into the function h(X). Events not included in the training set were used to evaluate h(X) for each event. The extent to which agreement was obtained between the evaluation of the test case and the ideal target values for that case gave an empirical measure of success.

EXPERIMENTS AND RESULTS TO DATE

Several fruitful experiments with events which appear double in both views have been performed. The best results have been obtained when 3 reject targets are supplied. These reject targets reflect how SAGE perceived the event: (1) too few sparks in the event locus; (2) wall event in the X or Y view; and/or (3) separation vertex on different decks in the two views. It appears that several reject targets give the net better definition of the reject criteria.

Results for a typical 4-target run are shown in the table below, where the numbers are occurrences/bin expressed as a percentage of the total number of events; e.g., 74% of events with too few sparks were correctly classified at the highest level of reliability, while 86% were correctly indicated.

1.0 <= Correct					||			Incorrect => 0.0		Target
74.	5.	7.	0.	0.	2.	0.	0.	0.	12.	Too few
60.	3.	2.	1.	0.	1.	0.	2.	0.	31.	Wall
53.	2.	1.	1.	1.	0.	1.	1.	2.	37.	Vertex
43.	1.	1.	14.	0.	0.	12.	3.	1.	22.	Accepts

The net usually tends to drive the decision on an event to one extreme or the other (closeness to 1.0 means more confidence in the decision). In the case of the accept target, two additional peaks in the distribution are seen. These peaks appear to reflect the net's inability to converge on unknown subclasses of events, prompting us to consider in future experiments the use of serially applied networks, each of which has only one reject target and one accept target. Because the rejects are divided up between 3 reject targets, the number of events per target is small (in fact, to obtain equal training, the target with the least number of examples determines how many events must be used for all the targets).

From the current level of success in experiments with doubles, we may extrapolate that a large proportion (perhaps > 90%) of rejects may be ultimately recognizable by a sequence of trained nets for the various reject targets, from a decision based on one view. Basing the decision on the combined outcome from views should result in only a few percent false accepts. This is a primary measure of success since the goal is to minimize inclusion of incorrectly characterized gamma-ray events in the EGRET database.

Currently, doubles are correctly recognized as accepts in about 60% of the cases; thus about 40% of accepts are falsely rejected, and would still require examination by human analysts. Since only exploratory experiments have been carried out, we expect some improvements as experience is gained in understanding how to present spark pictures to the nets.

FUTURE EXPERIMENTS

We also expect results to improve when larger inflight datasets are used to train the net. From the number of degrees of freedom in the problem, {2-D aperture, angle of incidence, vertex deck, and gamma-ray energy - related to vertex separation angle}, we estimate that it will be necessary to use many thousands each of accept and reject targets in order to train the networks sufficiently well. The distribution of energies for ground-based and inflight data is different. Thus, well-characterized experiments await sets of questionable events from the inflight database that have been processed by human analysts. Only datasets with weak sources or no source in the field-of-view are usable since sources tend to bias the associated incidence angles.

In a source-free field of view, much less than 1% of questionables are acceptable singles. Since questionables account for about 15% of the EGRET database, in order to find ~ 1000 good singles - a minimum requirement to train a network for any given target - we would have to search through a few million events of inflight data. However, the singles problem may very well be soluble by simulating acceptable singles - straight lines - using appropriate numbers of extraneous and missing sparks, as well as small deviations from straightness which occur as a result of electron scattering suffered by the pair. A simulation program for acceptable singles is currently in development.

Several improvements are under consideration. Once the 'double in both views' networks are optimized, it should be straightforward to address the 'single/double view' problem by making appropriate changes in some accept and reject targets. An efficient way to account for left/right symmetry may be to train networks using both an event and its mirror image about the Z-axis. The reject category which involves the separation vertex apparently being on different decks in the two views may require combining the X and Y views. Finally, additional rejection criteria have been identified in the inflight dataset which may be accommodated by adding one reject target.

REFERENCES

Fichtel, C. E. *et al.*, 1989, Proc. GRO Science Workshop, ed. W. N. Johnson (Greenbelt, MD: NASA/GSFC), p. 3-1.

Kanbach, G. *et al.*, 1989, Proc. GRO Science Workshop, ed. W. N. Johnson (Greenbelt, MD: NASA/GSFC), p. 2-1.

SUGGESTED READING ON NEURAL NETWORKS

Parallel Distributed Processing, eds. D. E. Rumelhart, J. L. McCelland, and The PDP Research Group, MIT Press, Cambridge, MA, 1986.

Fahlman, S. E., and Hinton, G. E., Connectionist Architectures for Artificial Intelligence, IEEE Computer, 1987.

Lippman, R. P., An Introduction to Computing with Neural Nets, IEEE ASSP Magazine, April 1987, p. 4.

NEW OBSERVATIONS WITH THE GAMMA-RAY IMAGER SIGMA

J.P. Roques and G. Vedrenne

CESR, 9 av. du Colonel Roche - BP4346 - 31029 Toulouse Cedex - France

Since its launch in December 1989, the gamma-ray telescope SIGMA on board the soviet satellite GRANAT works nominally. For the first time a gamma-ray telescope (35 keV - 1.3 MeV) observes the sky with the ability to localise sources with an accuracy of a few arc minutes. Figure 1 presents in galactic coordinates the different sky regions on which the telescope has been pointed since its launch. It can be noticed that a large fraction of the time has been devoted to the central regions of our Galaxy. Figure 2 shows the position of the sources detected by SIGMA in a region of 10° x 10° around the Galactic Center. All these sources exhibit a large variability on all time scales above 35 keV ; these important characteristics revealed by SIGMA must be taken into account for future planned missions.

After a brief description of the SIGMA telescope we will concentrate on some new and exciting results concerning either Galactic and Extragalactic observations.

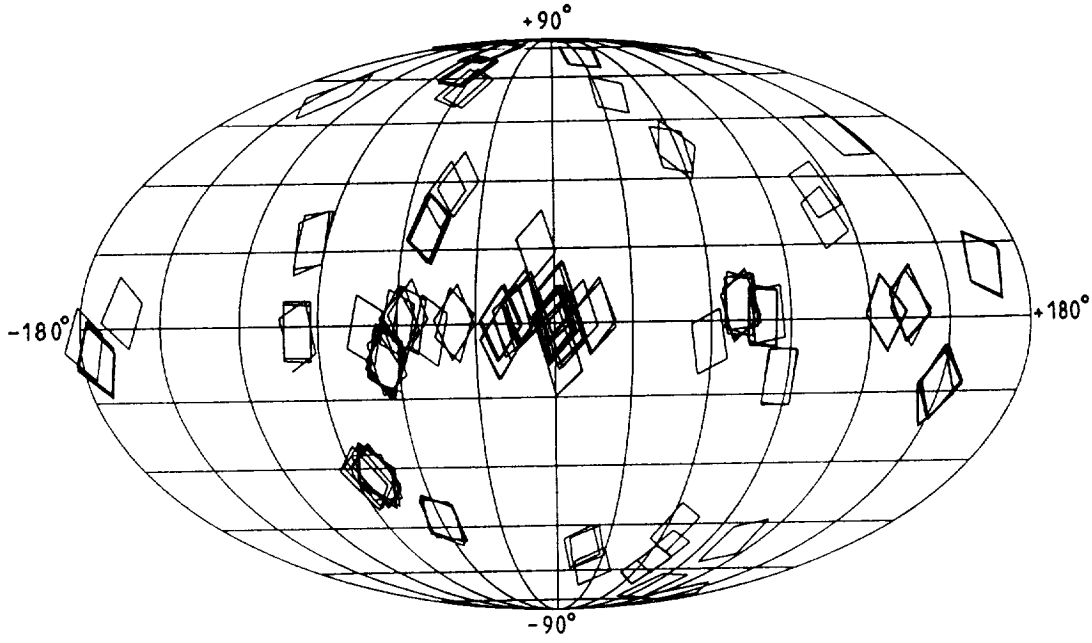

Figure 1 : Sky regions observed by SIGMA, the half sensitivity field of view (11° x 10°) is drawn for each observation.

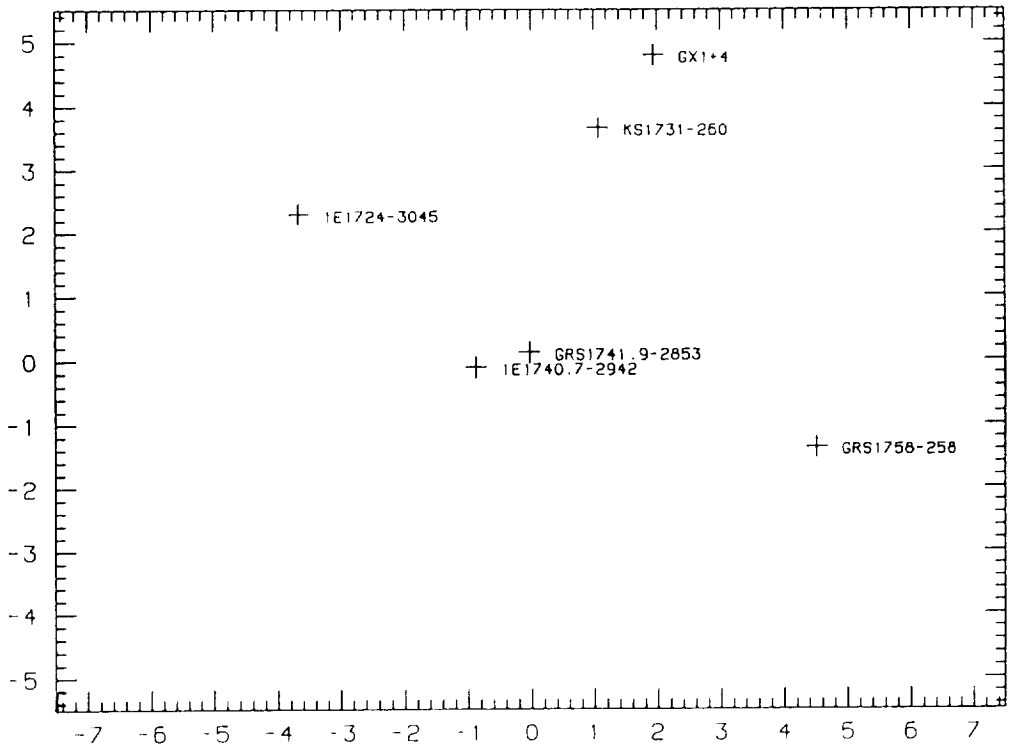

Figure 2 : Galactic center sources observed by SIGMA.

1. Brief description of the SIGMA experiment

SIGMA has been designed by two french laboratories : the Centre d'Etude Spatiale des Rayonnements in Toulouse, and the Service d'Astrophysique in Saclay. It has been realized in the framework of the French-Soviet cooperation under CNES contract and support.

SIGMA operates between 35 keV and 1.3 MeV and provides high resolution images of the sky in this energy range. The imaging capabilities of the instrument are obtained thanks to the association of a coded mask (based on a 31 x 29 URA pattern) and a position sensitive detector (based on the Anger Camera principle). This camera consists of a 1.25 cm thick NaI crystal analyzed by 61 photomultipliers. This detector is surrounded by a large CsI anticoïncidence.

The imaging properties of the instrument are : a 4°45′ x 4°20′ totally coded field of view ; a half sensitivity field of view of 11°20′ x 10°30′ ; a pixel size for high resolution images of 1.6 arc minutes.

A complete description of SIGMA can be found in Ref. 1 .

2. The Galactic Center region

This region was observed by SIGMA in 1990 during 288 hours of useful time. During this period, it has been unambiguously demonstrated that the Einstein source 1E1740.7-2942 is the most luminous object above 40 keV. This object, located 48 arc minutes away from the radiosource Sgr A, was discovered during the Einstein observatory IPC survey of the galactic plane (Ref. 2). Further observations at higher energy (3-30 keV) made with a coded mask imaging instrument (Ref. 3) showed that in this energy range 1E1740 was the strongest source within a 6 x 6 degree square around the Galactic Center.

The hard nature of the source was demonstrated by GRIP (Ref. 31) and by SIGMA during 1990 observations (Ref. 4 and 5). Figure 3 shows the energy spectrum of the source as observed during March/April observations. This spectrum is well fitted by a comptonization disk model (Ref. 6) with an electron temperature KT= 32 keV. In fact during the March, April and September 1990 observations this spectrum remained quite stable. It is interesting to notice that it is almost identical to the CYG X-1 spectrum in low state (Ref. 7).

During the October 13-14 observations of this region a spectacular event occurred : a large bump between 300 and 800 keV appeared in the spectrum of 1E1740.7-2942. This spectral feature, which lasted between 18 and 70 hours, is centered around 500 keV with a clear cut-off close to 700 keV (figure 4).

This shape immediately suggests an electron-positron annihilation process in the vicinity of the source, associated with a hot pair plasma. In the framework of the Ramaty and Mézaros model (Ref. 8). The width of the spectral feature suggests a plasma temperature of 5.10^8 K. The results of the different fits performed on this quite new type of spectrum are given in Table I and discussed in detail in Ref. 9.

Although the bump is not at the same energy, such a structure can be compared to the γ_1 state of Cygnus X-1, but in this precise case a noticeable decrease of the emission under 400 keV has been observed while the spectrum of 1E1740.7-2942 below 200 keV doesn't change.

Very recently Mattesson et al. (1991) reported the same kind of feature (Ref. 10).

During the 1991 observations of the Galactic Center, the picture was drastically different : the observations of Spring 1991 (Ref. 5) showed a decrease by a factor 4 of the 1E1740 flux as well as a change in the spectral shape : the spectral index was $\alpha \approx 3$ (figure 3).

Moreover in the observations performed in August the source was definitely absent from the SIGMA images.

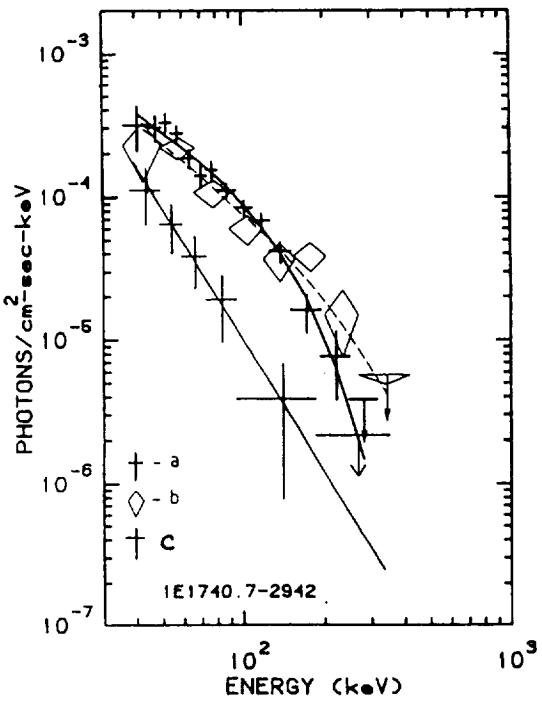

Figure 3 : Spectrum of 1E1740.7 observed in : a) Spring 1990 ; b) October 10th 1990 ; c) Spring 1991

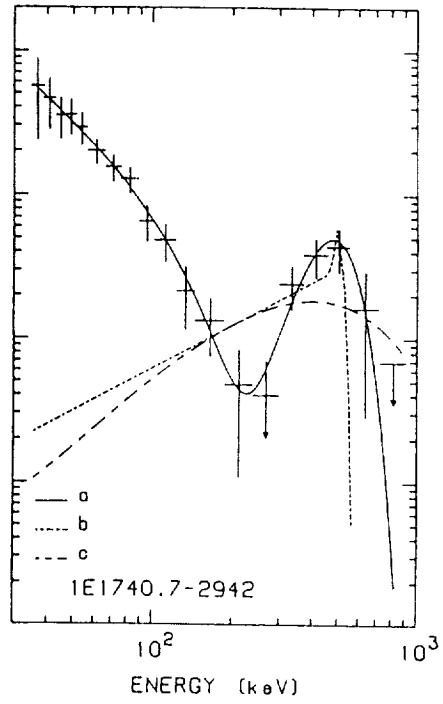

Figure 4 : Spectrum of 1E1740.7 observed on October 13th 1991. The hot pair plasma + comptonization model (a), the positronium model (b), the high temperature comptonization model (c) are reported for comparison.

OCTOBER 13 - 14, 1990					
TWO TEMPERATURE COMPTONIZED DISK		**COMPTONIZED DISK PLUS GAUSSIAN LAW**		**COMPTONIZED DISK PLUS POSITRONIUM**	
kT_1 (keV)	20 (+5, -4)	kT (keV)	27 (+8, -7)	kT (keV)	20 (± 3)
τ_1	2.5 (+2.7, -1.0)	τ	1.6 (+1.0, -0.5)	τ	2.5 (± 0.4)
kT_2 (keV)	201 (+139, -72)	Line center (keV)	480 (+96, -72)	Orthopositronium flux (ph/cm^2. s)	0.9 (± 0.3) x 10^{-2}
τ_2	36 (+8, -11)	FHWM (KeV)	240 (+101, -94)	RED χ2	0.86
RED χ2	0.90	Flux (ph/cm^2. s)	1.3 x 10^{-2}	degrees of freedom	87
degrees of freedom	85	RED χ2	0.78		
		degrees of freedom	85		

Table 1 : Model fit parameters for 1E1740.7.

A recent suggestion made by Bally and Leventhal (Ref. 11) explains the variable nature of this gamma emitter : this source can be a black hole situated in a dense molecular cloud (10^5 M_O) which has been observed on the line of sight of 1E1740.7 (see also Ref. 12). The accretion flow might be unsteady providing time variability but can it explain a long extinction of the source as observed last month ?

The 1990 Galactic Center survey by SIGMA led to another important result : the discovery of a new hard source GRS1758-258 (spectral index of ≈ 2) near the position of GX5-1. Its spectrum extends up to 300 keV (Ref. 4).

3. Transient sources observed by SIGMA

GRS 1724-308

Hard X-ray emission at 35-200 keV has been detected in the direction of the globular Cluster Terzan II (Ref. 13 and 14). A possible association with the source X1724-308 has then been proposed.

The observation of X-ray bursts from this source (Ref. 15) indicates the presence of a neutron star. Thus, if this association is real, such a source might be a low mass X-ray binary with a neutron star as the compact object.

In figure 5 are displayed : the spectrum observed by SIGMA, well fitted by a power law of index α = 1.65 (+0.4,-0.6) and the spectrum below 10 keV observed by Exosat in April 1985 (Ref. 16).

Although the variable nature of the source prevents a direct comparison of the two spectra, these observations immediately suggest a two component spectrum.

This transient source might be considered to belong to the class of soft X-ray transients (SFXT) in which we find for example Cen X-4. These transients would be accreting neutron stars in low mass binary systems (Ref. 19).

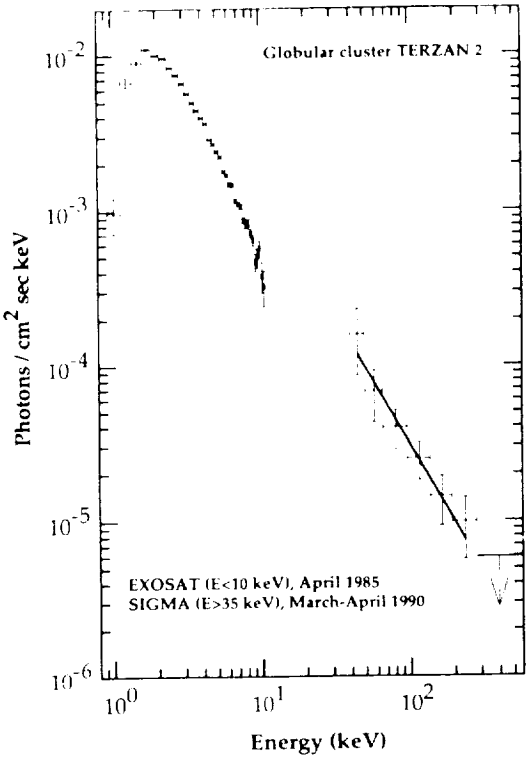

Figure 5 : Spectra of Terzan II region.

Moreover, it is worth noting that a two components spectrum suggested by KS1731 (Ref. 18) and Terzan II observation is quite comparable to the Cen X-4 spectrum measured during May 1979 outburst by the French Signe II MP experiment aboard the Prognoz 7 satellite (Ref. 20). To illustrate this point, the figures 6 and 7 give the light curve of the outburst and the spectra observed at different times during the first peak of this outburst between 13 and 163 keV.

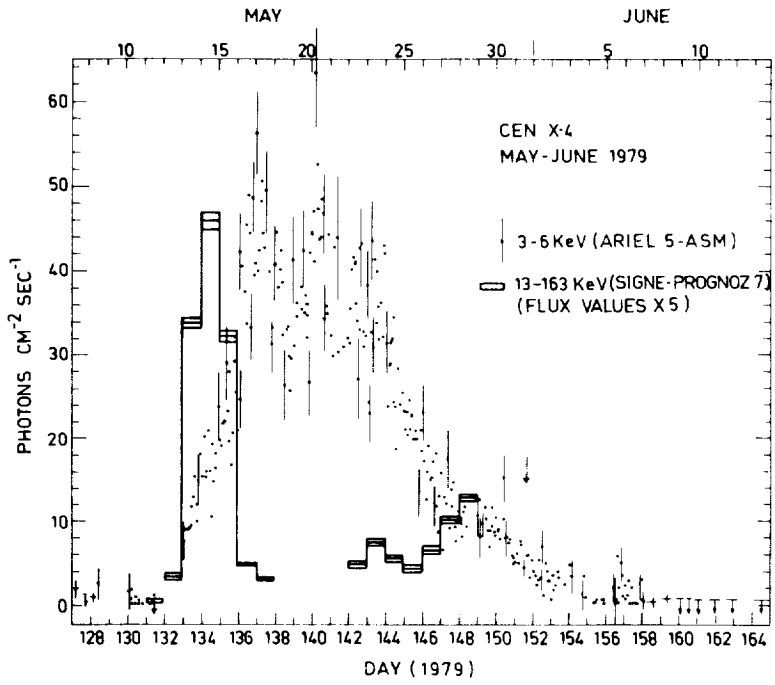

Figure 6 :

Light curve of CEN X-4 as observed by Ariel V and Signe II.

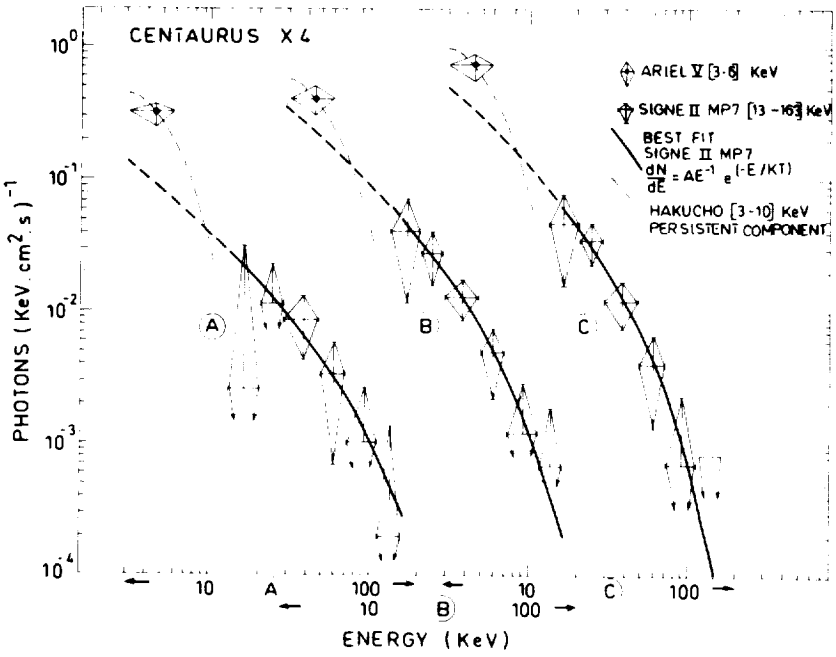

Figure 7 :

CEN X-4 spectra observed during the 1979 outburst.

This idea of possible two component spectra for these transients can be strengthened with another example : the source ASM2000+25 observed by MIR Kvant in the 4-300 keV energy range (Ref. 21). A break in the spectrum is observed between 10-20 keV with a high energy tail above.

Another example of hard X-ray emission for these SFXT is given by the observation on August 1990 of the TRA X-1 transient by SIGMA (IAU Circular no.5104).

Now we will consider the case of Nova Muscae discovered by Watch on Granat and then observed by Ginga and SIGMA. Here we also will find almost the same behaviour.

4. Nova Muscae

A new X-ray nova was discovered in the MUSCA constellation by the Watch X-ray detector and at the same time by GINGA all sky monitor (IAU Circular no. 5161).

The source named GRS 1124-684 was discovered on the 9th February 1991. At this time SIGMA was looking at GX301-2 and the nova was just at the limit of its field of view, despite the low sensitivity of the telescope in this configuration, an image was done showing a great excess compatible with the nova position.

Reorientation of the satellite in the direction of this new source allowed observations on January 16th, 17th, 20th and during five days in February.

During all these observations the source was detected up to at least 300 keV with high significance level. An extensive analysis of these observations can be found in Ref. 22 and 23, while the SIGMA data are reported on IAU circular no.5176, 5201, 5310, 5329.

Figure 8 presents the counting rate in the 41-77 keV energy range for the different observations and Figure 9 shows the evolution of the hardness ratio in the 77-160 keV and 41-77 keV energy ranges. During the first two days it remains stable but after, an anticorrelation appears between the hardness ratio and the counting rate. As it has been observed for the outburst of Cen X-4, the high energy intensity increased and reached a maximum before the low energies (E_x < 30 keV) detected for instance by Watch.

Moreover, during the observation of the 20-21st January, the energy spectrum exhibited a clear excess at 480 keV (figure 10). In the same spectrum a strong feature around 170 keV is present. This energy corresponds to the minimum energy obtainable in a single downscattering of 511 keV photons. Even if the line is not observed at 511 keV and is visible only during 13 hours, we should ask the following question : what might be the contribution of such transient sources in the production of lines in the Galaxy ?

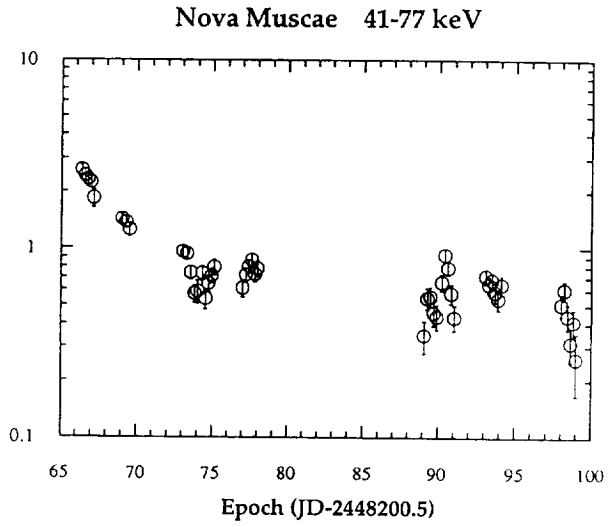

Figure 8 : Light curve of Nova Muscae as observed by SIGMA.

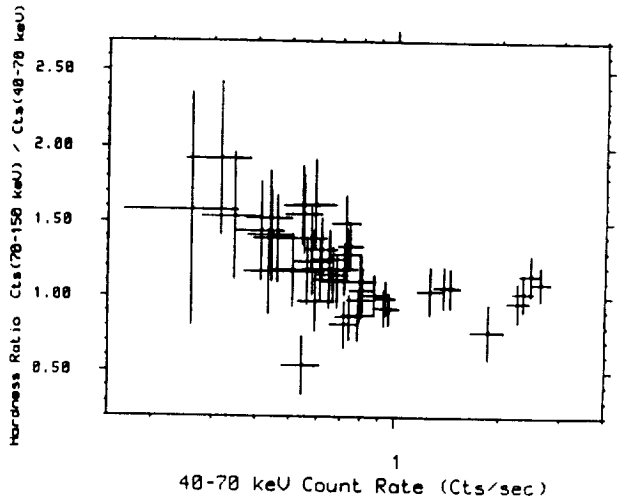

Figure 9 : Evolution of the hardness ratio of Nova Muscae spectrum.

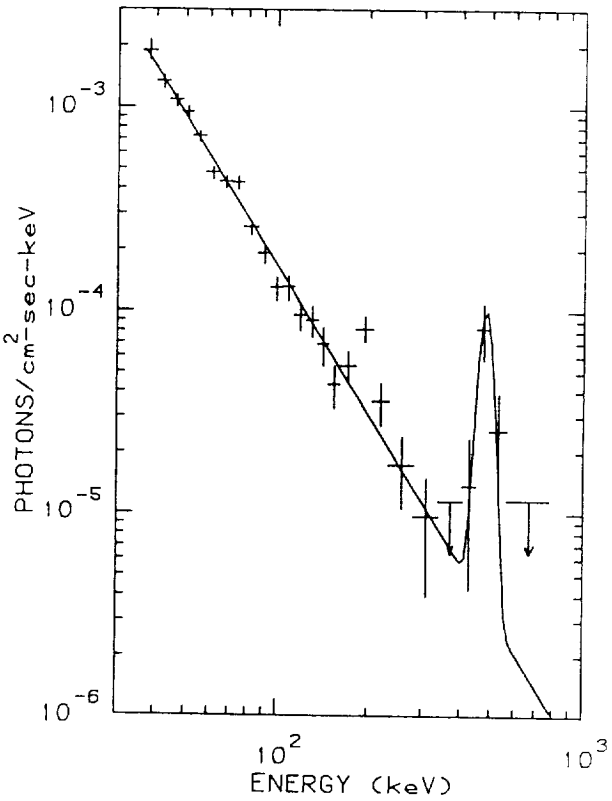

Figure 10 : Spectrum of Nova Muscae, observed during 13 hours on January 20th 1991.

Another point concerns the combined spectrum obtained with Art-P and SIGMA instruments (Ref. 23) : again a break around 10 keV appears clearly putting naturally this object in the class of SFXT as the previous sources reported in this paper.

In fact, even if we have more work to do on the spectral characteristics of these objects, the presence of two component spectra seems to be a common characteristic of SFXTs when they are active at high energy (E > 30 keV).

5. Extragalactic sources

a) NGC4151

This AGN was observed by SIGMA during 82 hours. Figure 11 shows the unambiguous identification at 6σ level (Ref. 24).

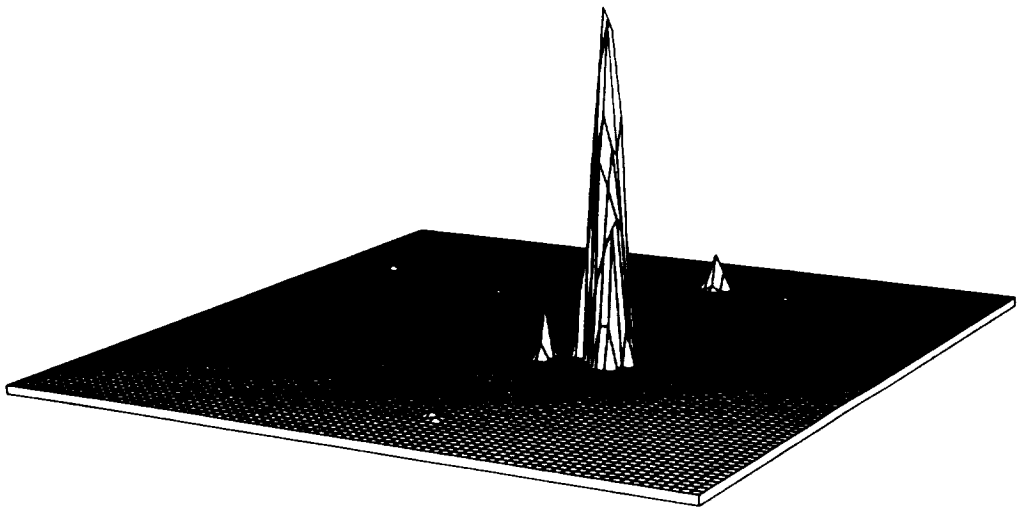

Figure 11 : Map of NGC 4151 region observed by SIGMA. The value below 2.5σ are suppressed.

Figure 12 gives the average photon spectrum obtained combining all the data : it is unusually steep and only marginally compatible with the mean value $\alpha = 0.5$ reported at soft and hard X-ray energies (Ref. 25).

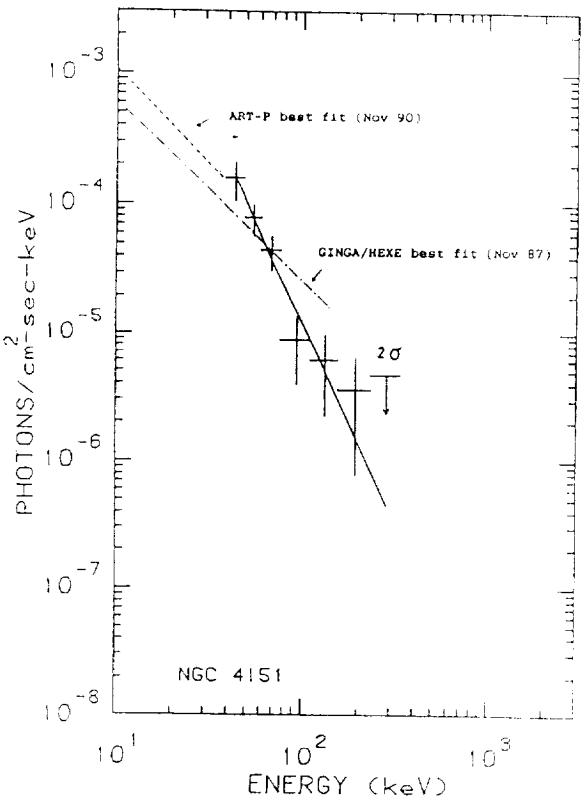

Figure 12 : Spectrum of NGC 4151 in 1990 as observed by SIGMA.

If we consider the Art-P data below 30 keV (Ref. 26) and the SIGMA spectrum a break is visible around 50 keV.

Thus the canonical single power law from a few keV to a few hundred keV is not observable. This kind of spectrum is in good agreement with the observation of NGC4151 made in June 78 by HEAO-A4 (Ref. 27). Even if this spectral behaviour is not permanent and perhaps rare it is worth noting that it is well explained by recent models including compton reprocessing by cold optically thick material very close to the central engine. In fact, first suggested by Guilbert and Rees (Ref. 28), this idea was revived by Zdiadsky et al. (Ref. 29) : γ-rays are absorbed via photon-photon collisions producing non thermal pairs which in turn radiate further X-rays. If a substantial fraction of this radiation interact with cold material, the Compton reflection leads to a composite spectrum which predicts a spectral break around a few tens of keV.

This result on NGC4151 is also interesting for its implications on the contribution of the Seyfert Galaxies to the cosmic diffuse background which also presents a break at 60 keV. If AGNs have steep spectra for some fraction of the time the previous estimate of the AGN contribution to the CDB might have been overestimated at energies greater than 50 keV (Ref. 24).

b) 3C273

A total exposure time of 62 hours cumulating three pointings was devoted to this quasar in 1990 (June, July, November). In the two first pointings the source was clearly detected, the combined spectrum obtained is displayed in figure 13. It is compatible with a power law $\phi_E = (2.4 \pm 0.6)\ 10^{-5} \left(\frac{E}{100}\right)^{-(1.5 \pm 0.5)}$ ph/cm^2.s.keV (these errors are at 1σ for joint variation of the parameters). The interval between these two observations was 40 days and the 56-120 keV counting rate indicated a variability of a factor 2 at a confidence level of 2.5σ. These data are interesting as they infer a variability on a timescale as short as 40 days.

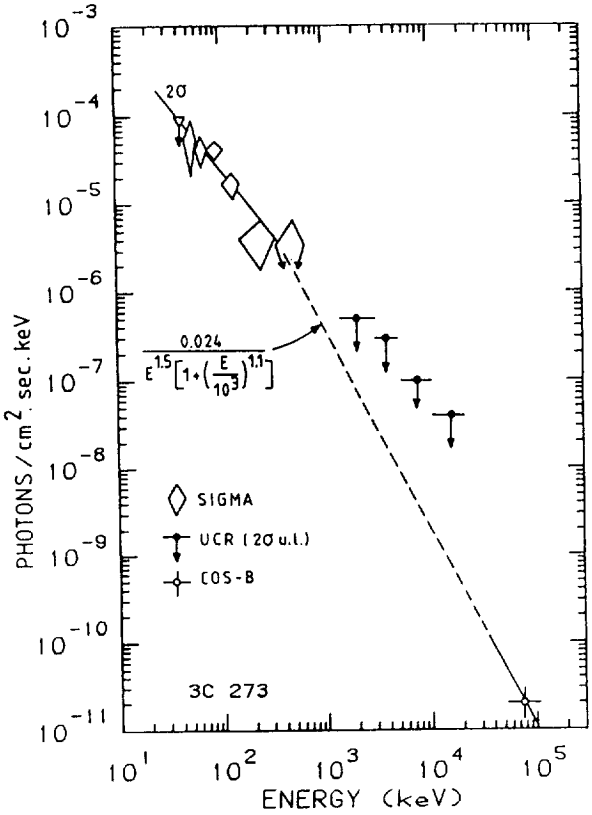

Figure 13 : Spectrum of 3C 273 observed in June/July 1990 observations.

For the observation made in November SIGMA, data show a marginal detection. More details are given in Ref. 30. Another interesting result was also obtained during the November observation of 3C273. SIGMA images revealed a 5.5σ excess in a location (1950) RA = 12h27mn21s Dec = 02°29'12" with an associated error circle of ± 5'. This source tentatively named GR1227+0229 is situated 15' away from 3C273 and could explain naturally some strange results on 3C273 : for instance the detection of a half day flare by Ariel V. Even if the presence of the source requires confirmation it clearly demonstrates the need for imaging system in the hard X-ray domain.

Conclusion

This review demonstrates that SIGMA has obtained very exciting results :

- The identification and extensive study of sources contributing to the emission of the Galactic center region above 30 keV.

- The observed strong line at 480 keV from Nova Muscae which may be interpreted as an annihilation line with a redshift due to the presence of a compact object. In this case the contribution of such transients in the 511 keV production should be considered.

- The soft γ-ray tails observed by SIGMA from some transient sources already identified as soft X-ray transients might be a common characteristic of these objects and has to be explained.

- The unusual spectrum of NGC4151 with a break around 50 keV can characterize a particular state of this kind of objects. If it is the case it has interesting implications on the origin of the Cosmic Diffuse Background.

For the near future, as SIGMA works nominally, simultaneous observations of the Galactic Center region with SIGMA and OSSE will be performed. They can be very useful to understand completely the origin of the 511 keV emission from this region ; SIGMA being able to identify the sources which are in hard state during the observations. This is a crucial point, as we have shown that the sources in this region are all highly variable.

This large variability is a common feature clearly demonstrated by SIGMA : if we except the Crab, all sources are variable, some of them disappearing during long periods. Perhaps this large variability is a permanent feature of high energy sources in the soft γ-ray domain. In fact this is not so strange, as a very quiet and common star like the Sun produced recently very high energy gamma-rays during solar flares !

Definitively, such a variability shows the absolute necessity for future missions to associate imaging systems with fine spectroscopic instruments as it is now planned for Integral.

REFERENCES

1. Paul, J., et al. 1990-a, *Adv. Space Res.. ,* 11, 8, 289
2. Hertz, P., and Grindlay, J.E. 1984, *Ap.J.*, 278, 137.
3. Skinner, G.K., et al. 1987, *Nature*, 330, 554.
4. Sunyaev, R., et al. 1991, *Astron. & Astrophys.*, 247, L29.
5. Bouchet, L., et al., 1991, *ICRC proc.*, OG 3.3.8
6. Sunyaev, R., and Titartchuk, L.G. 1980, *Astron. & Astrophys. ,* 86, 121.
7. Ling, J.C., et al., 1987, *Ap.J. (Letters)*, 321, L117.
8. Ramaty, R., and Mészaros, P. 1981, *Ap.J.*, 250, 384.
9. Bouchet, L., et al., *Ap.J. Lett.*, in press, Dec 1991.
10. Briggs, M.S., et al., 1991, ICRC, OG 7.1.6.
11. Bally, J., and Leventhal, M., 1991, *Nature*, 353, 234.
12. Mirabel, et al., 1991, *Astron. & Astrophys.*, in press.
13. Barret, D., et al., 1991, *Ap.J. Lett.*, 379, L21.
14. Barret, D., et al., 1991, *ICRC Proc.*, OG 3.3.5.
15. Grindlay, J.E., et al., 1980, *Ap.J.*, 240, L21.
16. Parmar, A.N., et al., 1989, *Astron. & Astrophys.*, 222, 96.
17. Sunyaev, R., et al., 1989, *23rd ESLAB Symposium*, Italy, p 641.
18. Barret, D., et al., 1991, submitted to *Ap.J.*
19. White, et al., 1984, *AIP n° 115*, Santa Cruz.
20. Bouchacourt, et al., 1984, *Ap.J. Lett.*, 285, L67.
21. Borisov, N.V., 1989, *23rd ESLAB Symposium*, Italy, p. 305.
22. Goldwurm, A., et al., 1991, *Nova Muscae workshop*, Lingby, Denmark.
23. Sunyaev, et al., 1991, *Nova Muscae workshop*, Lingby, Denmark.
24. Jourdain, E., et al., 1991, *ICRC proc.*, 0G 3.3.12
25. Yaqoob, T., et al., 1991, *MNRAS*, 248, 773.
26. Apalkov, Yu., et al., 1991 *Proc. of 28th Yamada Conference on Frontiers of X-ray Astronomy*, in press.
27. Baity, W.A., et al., 1984, *Ap.J.*, 279, 555.
28. Guilbert, P.W. and Rees, M.J, 1988, MNRAS 233, 475.
29. Zdiarsky, et al., 1990, *Ap.J. Lett.*, 363, L1.
30. Bassani L., et al., 1991, *ICRC Proc.*, O.G. 3.3.
31. Cook, W.R., et al., 1989, Proc. of I.A.U. Symposium, 581, 1989.

N92-21893

Optical Monitoring of GRO Phase 1 Objects

Bernard McNamara, Jack Burns, William Webber

New Mexico State University

Abstract

This paper presents a brief overview of the three phases of our GRO/optical monitoring program: 1) the acquisition of simultaneous GRO/optical data on targeted OSSE objects, 2) the collection of noncoincident observations of suspected GRO gamma-ray emitters to determine their current level of activity, and 3) the optical imaging of burst fields in an attempt to identify the burst source. Finally a table of future simultaneous optical observations of Phase I GRO targets is presented along with plans for the rapid optical imaging of gamma-ray burst fields.

Introduction

This paper describes our optical monitoring program as of mid-September 1991. Results are presented in four sections:
1) a discussion and graphical presentation of the optical behavior of Cyg X-1 and 3C273 during the time these sources were observed by GRO/OSSE,
2) noncoincident database measurements of the targeted GRO/OSSE discrete sources Sco X-1 and NGC 4151,
3) an example of the optical image of a recently detected GRO burst field, and
4) plans to optically observe other targeted GRO objects and burst sources at the NMSU Blue Mesa Observatory and ARC Apache Point Observatory.

Coincident Ground Based Observations of Cyg X-1 and 3C273

Cyg X-1 was originally targeted to be observed by GRO/OSSE from 30 May 1991 to 13 June 1991. Observations of this object were interrupted when the spacecraft was redirected to a target of opportunity. It was therefore not possible to obtain as much coincident data as was originally planned. Our photoelectric data was obtained using the 24-inch reflecting telescope and unfiltered single channel high speed photometer at the New Mexico

State University Blue Mesa Observatory. Cyg X-1 optical measurements were obtained on the nights (U.T.) of:

May 29, 1991
May 30, 1991
May 31, 1991
June 1, 1991
June 3, 1991
June 4, 1991
June 5, 1991
June 6, 1991
June 7, 1991
June 8, 1991

Data reduction is continuing. Some results are presented in Figure 1 in the form of a light curve. Typically Cyg X-1 was observed using an integration interval of 0.1 second. To reduce scintillation noise, measurements have been collected into 5 second bins. A power spectrum of the partially reduced data does not indicate any short term periodicity. Since Cyg X-1 is a HMXB, the high energy source would have had to produce a significant optical flux in order to be detectable against the primary 09.7 Iab star.

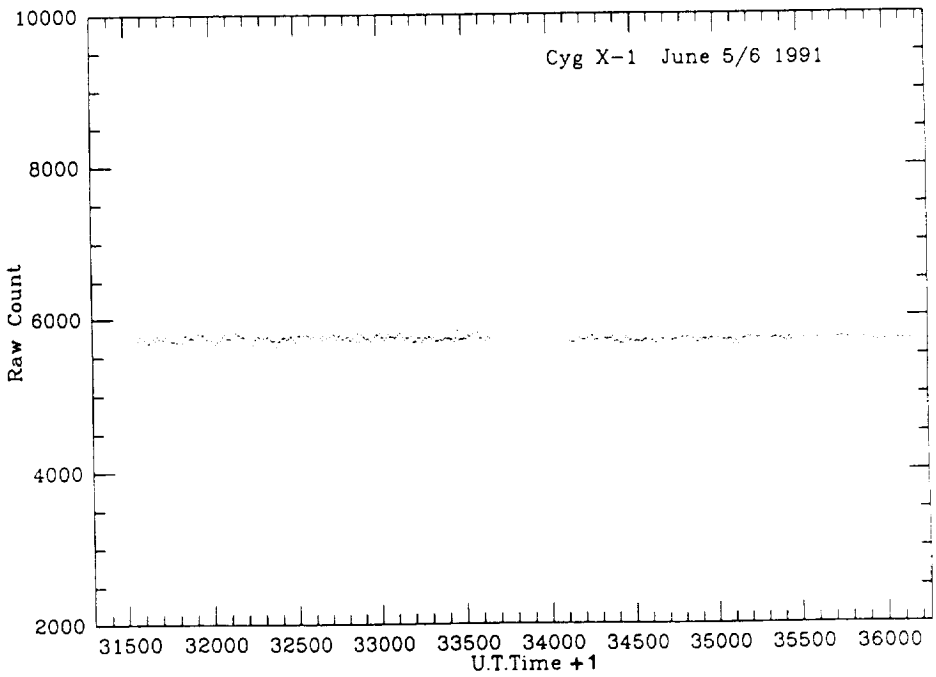

FIGURE 1 - Example of a partial light curve for Cyg X-1 obtained during June 6, 1991 U.T. using the NMSU Blue Mesa Observatory 24 inch telescope and a high speed photometer. The Y axis represents unfiltered, normalized raw counts. The X axis is U.T. + 1 hour.

Once the spacecraft was redirected, GRO/OSSE obtained observations of 3C273. We had already collected some baseline data on this target and once notified of the scheduling change, it was placed back on our observing list. Unfiltered photoelectric measurements of 3C273 were thus acquired on the nights (U.T.) of:

May 30, 1991
June 1, 1991
June 4, 1991
June 16, 1991
June 17, 1991
June 18, 1991
June 19, 1991

No erratic optical behavior from this source was detected.

Noncoincident Database Measurements of Targeted GRO/OSSE Discrete Sources

As time permitted, other noncoincident optical measurements at Blue Mesa were obtained of two other GRO/OSSE targets: Sco X-1 and NGC 4151. The intent of these observations was to provide an activity baseline which could be useful in the interpretation of upcoming GRO/OSSE observations. The U.T. dates of these optical observations and an example of the activity seen in Sco X-1 are given below and in Figure 2.

NGC 4151	Sco X-1
May 31, 1991	June 1, 1991
June 3, 1991	June 4, 1991
June 7, 1991	June 6, 1991
	June 8, 1991
	June 16, 1991
	June 18, 1991

Future NMSU Optical GRO Support

with J. Ryan and G. Fishman

A) Upcoming Simultaneous Optical Observations of GRO/OSSE Targeted Fields

Our plan is to obtain high time resolution coincident photoelectric measurements of the following GRO/OSSE objects to search to periodicities or correlated gamma-ray/optical transient events.

GRO Run 15	28 Nov. 1991 - 12 Dec. 1991	NGC 1275 and Cyg X-1
GRO Run 19	23 Jan. 1992 - 06 Feb. 1992	M82

B) NMSU Attempts at Locating the Optical Counterparts of Gamma-Ray Burst Sources

Despite many attempts to detect the optical counterpart of a gamma-ray burst, we still lack a positive source identification. The optical detection of a gamma-ray burst source would therefore be of great interest.

We have begun to experiment with a scheme which utilizes the fast response time of the ARC (Astrophysical Research Consortium) telescope located at Apache Point, NM to search for the optical counterparts of these transient events. Our plan is to obtain deep CCD images of localized (<10 arcmin) GRO burst fields in an attempt to identify the source. Each burst field would be imaged using 4 CCD frames. Observations would be obtained in both the visual and red and then repeated as part of a continuing monitoring program. The CCD images will then be examined for unusual stellar objects, colors, or variability. We anticipate that the entire exposure sequence could be obtained using less than one hour of telescope time. Below is a reproduction of an ARC telescope (using its temporary 1.8 meter mirror) 15 minute CCD R image of a burst field detected by GRO on June 1, 1991. Coordinates were kindly provided to us by J. Ryan (UNH). This image was compared to the Palomar Sky Survey R print. No peculiar object or obvious differences between the stars seen on the PSS and the CCD frame are apparent. The image presented here is primarily intended to demonstrate our current optical capability. We anticipate further improvements in this process in the near future.

Summary

As of the end of mid-September 1991 coincident optical observations have been obtained for two targeted GRO/OSSE objects: 3C273 and Cyg X-1. No unusual photometric activity was noted from either of these sources. Additional observations of the activity present in NGC 4151 and Sco X-1 were obtained. One newly discovered GRO burst field has been imaged. No obvious burst candidate was found but only the central region of the gamma-ray error box was examined. As smaller error boxes become available due to refinements in GRO data analysis and/or additional information becomes available from other satellites this effort will be expanded.

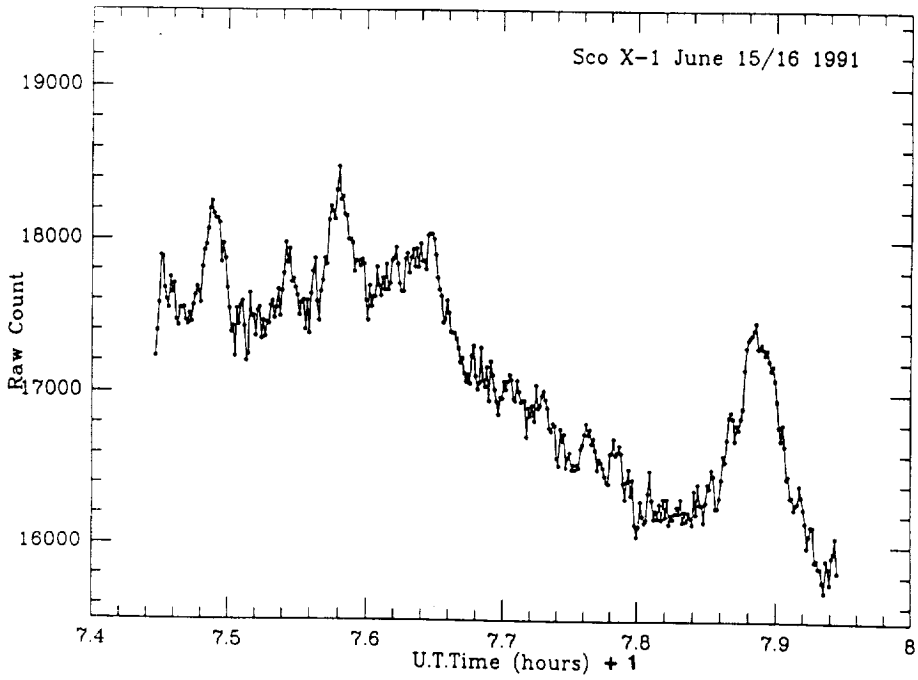

FIGURE 2 - Example of a partial light curve for Sco X-1 obtained on June 16, 1991 U.T. The Y axis represents an unfiltered, normalized raw count and the Y axis is U.T. + 1 hour. Both flickering and flaring activity is evident.

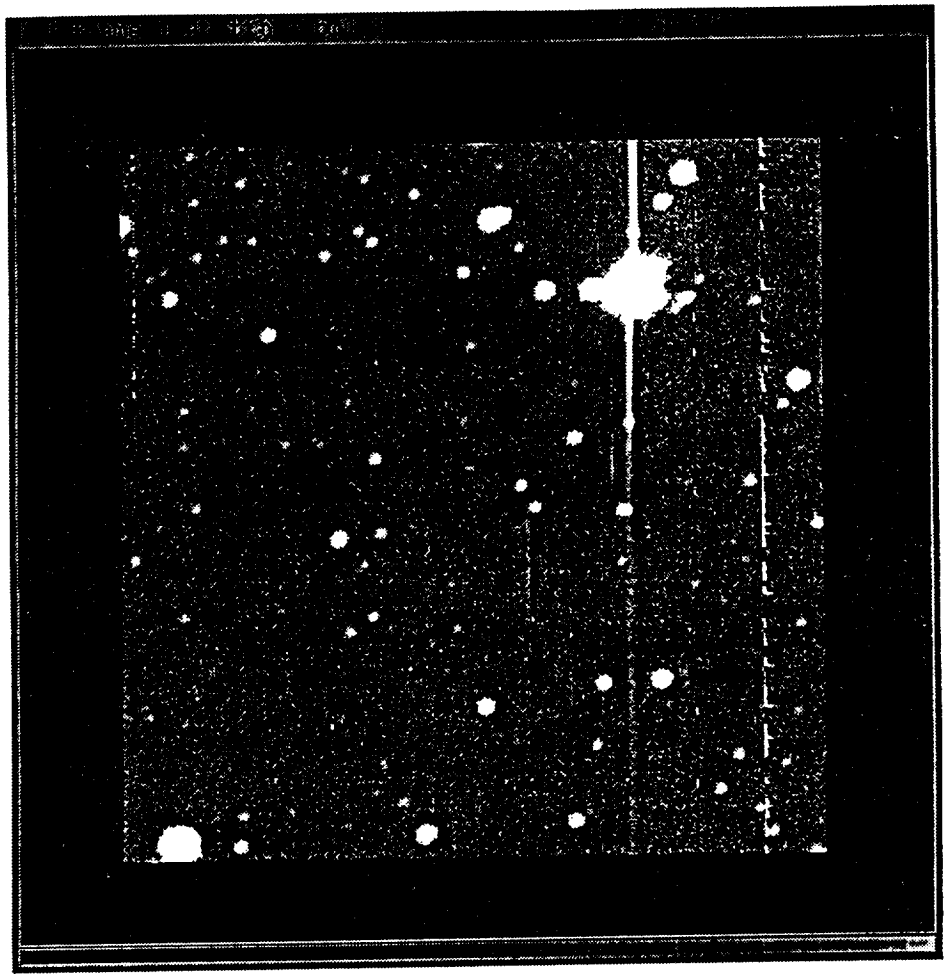

FIGURE 3 - CCD R image of the central region of the June 1, 1991 GRO burst error box. The 15 minute CCD image was obtained using the ARC 1.8m telescope. The imaged area is ~3'x3'. The telescope coordinates where $\alpha(2000) = 20^h\ 36^m\ 53^s.9$, $\delta(2000) = 30^\circ\ 47'31".28$.

The Phase 2 NRA

Eric Chipman

Compton Observatory Science Support Center, NASA Goddard Space Flight Center, Greenbelt, Maryland
and
Astronomy Programs, Computer Sciences Corporation, Greenbelt, Maryland

ABSTRACT

We present points of special interest to potential proposers for the Compton Observatory Phase 2 Guest Investigator Program. A general summary of some of the most important details of the Phase 2 NRA is followed by an enumeration of the modes of participation and proposal types available to GI proposers. Finally, the method which is planned for selection of the Phase 2 Guest Investigations in parallel with the development of a preliminary Phase 2 observing timeline is outlined. The ways in which the selection of targets by GIs could be affected by the Phase 2 timeline development procedure is described.

1. Overview of the Phase 2 NRA

The NASA Research Announcement (NRA) for the Gamma Ray Observatory (now Compton Gamma Ray Observatory [CGRO]) Phase 2 Guest Investigator Program has now been released. Some key dates for this NRA are:

NRA Release	September 16, 1991
Proposals Due	December 20, 1991
Selections Announced	April 1992
Start of Observing Period	August 20, 1992
End of Observing Period	August 20, 1993

Note that an addendum to the NRA was issued soon after the original NRA release on September 16. This addendum calls particular attention to the opportunity to propose theoretical and correlative investigations aimed at understanding the early Compton Observatory observations as well as anticipated later Compton observations.

In order to submit a proposal in response to the NRA, it is essential to have not only the NRA itself and the Appendices therein, but also appendices F (Science Plan), G (The Gamma Ray Observatory as a Guest Investigator Facility) and H (Project Data Management Plan). These appendices contain details of data products, science capabilities of the instruments, and in-flight performance of the instruments which would be used in developing a Guest Investigator proposal.

The Phase 2 NRA, unlike the earlier Phase 1 NRA, permits Guest Investigators to propose their own independent observations of gamma-ray sources. At the same time, all the modes of GI participation previously available are still possible.

2. Modes of Participation by Guest Investigators

The Phase 2 NRA enumerates two modes of participation by GIs, and six types of Phase 2 proposals. In this instance, modes of participation refer to the degree of collaboration between GIs and the Instrument Teams, and proposal types refer to the amount of processing and data reduction which has been done to the data before it is given to the Guest Investigator. The primary modes of participation are:

1. A Guest Investigator may propose to work closely with one or more Instrument Scientists, or with an Instrument Specialist who is a member of the Compton Observatory Science Support Center but is co-located with the Instrument Team. This mode of participation is appropriate where the GI's data analysis plans require extensive use of software developed for CGRO data analysis by the Instrument Teams, such as low-level data might call for.
2. An alternative mode is to have a Guest Investigator work independently, with only occasional support for data retrieval or processing activities from the Science Support Center personnel or from Instrument Team members. This is most appropriate where higher-level data products are being analyzed so that the details of the hardware and software performance of the CGRO instruments are not critical to the data analysis.

As extensions of these two modes, a continuum of other degrees of collaboration between GIs and Instrument Team members is possible. Proposers should be careful to indicate in their proposals the degree of support from and collaboration with Instrument Team members or Instrument Specialists that is anticipated.

Proposal types are categorized as follows:

Type 1: Proposals for analysis or use of existing low-level processed CGRO data; this includes both archival data and new data.
Type 2: Proposals for analysis or use of existing high-level processed CGRO data; this includes both archival data and new data.
Type 3: Proposals for guest observing time in which the Investigator plans to work with low-level processed CGRO data.
Type 4: Proposals for guest observing time in which the Investigator plans to work with high-level processed CGRO data.
Type 5: Proposals for theoretical or correlative investigations in direct support of the CGRO observing program. Note that there are limitations as to which aspects of correlative observing programs can be supported.
Type 6: Proposals for new observations from CGRO Instrument Teams. This category is intended to provide for follow-up observations during Phase 2 of sources detected during Phase 1 after the NRA release.

A new subcategory of proposal included within types 1 and 2 is the use of archival data. All CGRO data will be archived and made available to all users approximately 12 months after it is made available to the Instrument Team members for analysis. Hence the start of the archiving of Phase 1 data will occur during Phase 2.

The proposal forms included in the NRA provide for an indication of the proposal type. In general, high-level processed data consists of images, spectra, source locations, or light

curves in physical units with a minimum of remaining instrumental artifacts, suitable for direct analysis or for further processing with a general-purpose data analysis language such as IDL or IRAF. Low-level data may be raw spectra before background subtraction, or photon event lists, etc.

3. Target Selection

In proposing Phase 2 Guest Investigations, proposers must be aware of how their choice of proposed targets will affect their chances of being selected. A careful reading of the NRA shows that there are several different classes of targets, each class with its own advantages and disadvantages with respect to GI selection. Of course, the most important single criterion in target selection by a proposer must always be the scientific objectives; other things being equal, each proposal should propose those targets best suited for the planned scientific investigation. The categories of targets could be broken out as follows:

1. Topics or Sources Reserved for the Instrument Teams.....Page C-7 of the NRA lists a set of specific sources (e.g., galactic supernovae) and general areas (e.g., sky surveys) that are reserved for the respective Instrument Teams. Independent or collaborative Guest Investigations in these areas are not solicited by the NRA, except for the OSSE team where Guest Investigators are welcome to propose to participate in the OSSE scientific teams working on these topics. If Guest Investigators are selected to join the OSSE teams on these topics, it is expected that the observing time for each scientific team will be allocated between GI time and Instrument Team time in proportion to the number of Instrument Team members and GIs on the scientific team.
2. High Priority Instrument Team Targets.....Part 1 of Tables 3 and 4 in Appendix D of the NRA lists those targets which the EGRET, COMPTEL and OSSE Teams have designated as their high priority observational objectives for Phase 2. If these targets can be observed within the 70% of observing time allocated to the Instrument Teams, then the Instrument Teams have priority over independent GI investigations of these targets. However, GIs may propose to collaborate with the Instrument Teams in investigations of these targets. All such collaborations should be arranged before the proposal is submitted. In addition, it is quite possible that not all of the targets listed in part 1 of Tables 3 and 4 can be scheduled during the allocated Instrument Team portion of the Phase 2 timeline, or that some targets may be observed, according to an optimized Phase 2 timeline, for longer periods than the Instrument Teams have specified in Tables 3 and 4. In those cases, GI proposals for these targets may be selected by the Peer Review Panel.
3. Low Priority Instrument Team Targets.....Part 2 of Tables 3 and 4 in Appendix D of the NRA lists targets which the Instrument Teams would observe as second priority during Phase 2. These targets would be observed by the Instrument Teams if observing time or opportunities are available, but GIs are free to propose observations of these targets and GIs may be awarded proprietary rights to observations of these targets by the Peer Review Panel.

4. All other targets are open for GI proposals.....It should be noted that the Instrument Teams are permitted to submit proposals of their own for other targets (type 6 proposals), due on December 20, 1991, which would be reviewed in competition with the GI proposals. This was done to allow follow-up observations by the Instrument Teams of interesting sources detected or marginally detected in Phase 1. In anticipation of this, the EGRET/COMPTEL list of high priority sources in Table 3, part 1, leaves a significant fraction of the Phase 2 observing time as pointing TBD (item I). In addition some other special target cases still deserve separate mention. The following sections describe these cases.
5. Burst sources, such as cosmic and solar bursts.....BATSE will make available 30% of randomly selected bursts (excluding the largest burst of each month) and 50% of solar flares to GIs. COMPTEL, EGRET and OSSE will also make available 30% of their burst data. Whenever possible, GIs would receive data from the same burst from multiple instruments. In some cases, different GIs could be given access to overlapping or identical datasets of burst data, if their science objectives allowed for this.
6. BATSE non-burst targets.....Besides the burst sources just described, on page D-12 of the NRA are listed 17 sources whose temporal variability the BATSE Team intends to study during Phase 2, using occultation and periodic variability search techniques. GIs may propose collaborative investigations of these sources with BATSE team members. For sources not listed, GIs may propose either independent or collaborative investigations.
7 Targets of Opportunity.....As stated on page D-13 of the NRA, the Instrument Teams will have priority for observations of nearby supernovae or galactic novae. For all other targets of opportunity Guest Investigators may propose without restrictions. However, it must be noted that only a few Targets of Opportunity can be accommodated during each year of the mission.
8. OSSE and COMPTEL science teams.....In addition to the target types listed above, GIs may propose to join the OSSE science teams working in the areas of a galactic plane survey, a comprehensive sky survey, and solar flares. Also, proposers who are interested in working with the COMPTEL Team on targets listed in Part 1 of Table 3 may contact the COMPTEL PI to see if a collaboration can be arranged.

Given these categories, it can be seen that there are some ways in which a GI-proposed target could have a good chance of being observable in the Phase 2 schedule, strictly based on timeline considerations. For example, targets which are within the fields of view specified in Table 3, Part 1 for EGRET-COMPTEL high priority pointings will very likely be observed, so a GI proposal for such a target would be unlikely to be rejected because of scheduling problems. Such targets would be observed in parallel with the high priority EGRET-COMPTEL targets, and the observation of these GI targets would not count against the 30% of spacecraft pointing time allocated to GIs, although it would of course count against total GI time. The other way in which GI observations can be done "in parallel" is to observe multiple GI targets for different GIs at one pointing where the pointing is not driven by an Instrument Team target, but by one or more GI targets. If a proposer had reason to believe that other GI proposers were planning to propose targets in one particular region of the sky not included within a high priority Instrument Team region, it might be advantageous to propose targets in this region rather than in an isolated part of the sky near few other objects of interest. Finally, it may be useful to list two or three targets which could be observed as alternates to optimize the chances that at least one would be

schedulable, as long as the alternates are of nearly equivalent scientific value for the investigation. Listing too many alternate choices would probably be counter-productive, however, as the scheduling problem becomes very poorly defined at some point.

Other target selection criteria result from the spacecraft constraints on the position of the Sun relative to the Compton Observatory z-axis. An inspection of Table 4, Part 1 of the OSSE high priority targets will show that most of these targets are in or near the galactic plane, and often close to the galactic center. For technical reasons, it turns out that it is difficult to schedule many OSSE targets in the galactic plane and very few outside it, while always observing a primary and a secondary OSSE target for each spacecraft orientation. Thus an attempt to observe as many as possible of the high priority OSSE targets may leave opportunities for additional targets outside of the galactic plane. So given a choice, it could be advantageous to propose GI OSSE targets outside the galactic plane, or far from the galactic center. Of course, many classes of targets are virtually all found either inside or outside of the galactic plane region, so this choice may not often present itself.

A proposer should, of course, also study the observing program as completed so far and as planned for the remainder of Phase 1 of the mission (see Table 1, below). This shows individual OSSE targets, and the locations of EGRET/COMPTEL pointings, each of which has a sizable field of view.

4. Planned Phase 2 Scheduling Method (EGRET,COMPTEL, OSSE)

The strong interaction between the observing constraints of the EGRET/COMPTEL instruments, the primary and secondary OSSE targets, the possibilities for parallel observations of multiple targets by EGRET and COMPTEL, and the spacecraft constraints means that it would be very inefficient to simply select a preset number of target-weeks for Phase 2 GI proposals and then to attempt to schedule these targets, as is done for most other missions with GI programs. Instead, it is planned to do the Guest Investigator selection as a two-stage process. First, the Peer Review Panel will rank all of the GI proposals, then a preliminary schedule timeline will be developed taking into consideration the rankings and the other scheduling constraints. The final selection of Guest Investigations would be announced after the preliminary timeline is complete for the entire year, and would reflect the feasibility of actually observing the targets in the selected proposals. While the preliminary timeline would cover the year, it is quite possible that changes would occur during the course of the year, either to accommodate targets of opportunity, or for changes in target priorities by the Instrument Teams. For this reason NASA may choose to slightly overselect the GI proposals beyond those which can be scheduled on any given timeline, to have a few proposals as alternates.

The development of the preliminary timeline will be done using software tools currently available to compute the observing constraints for any combination of spacecraft attitude, primary and secondary OSSE target, and observing week of the year. The timeline will be assembled usually in two-week segments (occasionally one-week observations will be done), at each step scheduling the highest priority candidates currently available, from the following list of targets, in roughly descending order of priority:

- High priority EGRET/COMPTEL and OSSE Instrument Team targets from part 1 of Tables 3 and 4 in the NRA.
- Highly rated Guest Investigator proposal targets.
- Instrument Team supplementary targets (submitted on December 20 and in part 2 of

Table 1

GRO PHASE 1 VIEWING PLAN AS OF OCTOBER 7, 1991

VIEW		+Z-AXIS*	GRO Z-AXIS*		GRO Z-AXIS* GALACTIC		GRO X-AXIS*		OSSE PRIMARY TARGET			OSSE SECONDARY TARGET		
PER.	START	TARGET	RA	DEC	LONG	LAT	RA	DEC	TARGET	RA	DEC	TARGET	RA	DEC
1	5/16/91	CRAB PULSAR	88.07	17.14	190.92	-4.74	339.12	46.48	CRAB PULSAR	83.52	22.02	PSR 1957+20	299.84	20.81
2	5/30/91	CYG X-1	301.39	36.58	73.28	2.56	60.31	33.09	CYG X-1	299.59	35.21	SUN	-	-
2.1	6/8/91	SUN	87.83	12.47	194.86	-7.29	338.68	56.03	SUN	-	-	CYG X-1	299.59	35.21
3	6/15/91	SN 1991T	191.54	2.62	299.76	65.46	101.49	1.04	SN 1991T	188.54	2.66	QSO 0736+016	114.82	1.62
4	6/28/91	NGC 4151	179.84	41.52	156.19	72.08	57.38	31.23	NGC 4151	182.63	39.41	3C 111	64.59	38.02
5	7/12/91	G CENTER	270.39	-30.96	0.00	-4.00	196.56	24.91	G CENTER	266.40	-28.94	MRK 421	166.11	38.21
6	7/26/91	SN 1987A	91.28	-67.97	278.00	-29.32	153.97	10.52	SN 1987A	83.86	-69.27	MRK 421	166.11	38.21
7.1	8/8/91	CYG X-3	310.05	28.06	70.44	-8.31	143.74	61.25	CYG X-3	308.10	40.96	M 82	148.96	69.67
7.2	8/15/91	GAL 025-14	291.98	-13.27	25.00	-14.00	208.11	24.38	G PLANE 25	279.22	-7.05	NGC 5548	214.50	25.13
8	8/22/91	VELA PULSAR	124.96	-46.35	262.94	-5.67	198.99	14.71	VELA PULSAR	128.92	-45.18	SN 1991T	188.54	2.66
9.1	9/5/91	GAL 339-84	8.34	-32.31	338.94	-83.50	244.20	-41.58	GX 339-4	255.71	-48.79	NGC 253	11.89	-25.29
9.2	9/12/91	HER X-1	251.28	36.89	59.67	40.28	142.05	23.69	HER X-1	254.46	35.34	MRK 421	166.11	38.21
10	9/19/91	FAIRALL 9	30.91	-60.66	287.85	-54.31	190.28	-27.75	NOVA MUSCAE	171.61	-68.68	3C 279	194.05	-5.79
11	10/3/91	3C 273	189.02	1.06	294.25	63.67	278.42	-29.71	3C 273	187.28	2.05	G CENTER	266.40	-28.94
12	10/17/91	CEN A	202.29	-40.09	310.71	22.21	221.48	48.29	CEN A	201.38	-43.01	3C 390.3	280.56	79.76
13.1	10/31/91	GAL 025-14	291.98	-13.27	25.00	-14.00	208.11	24.38	G PLANE 25	279.22	-7.05	NGC 5548	214.50	25.13
13.2	11/7/91	GAL 339-84	8.34	-32.31	338.94	-83.50	244.20	-41.58	GX 339-4	255.71	-48.79	ESO 141-55	290.31	-58.67
14	11/14/91	ETA CAR	156.83	-58.51	285.04	-0.74	274.30	-15.78	G CENTER	266.40	-28.94	ETA CAR	161.95	-59.98
15	11/27/91	NGC 1275	52.00	40.24	152.63	-13.44	293.36	29.53	NGC 1275	49.96	41.51	CYG X-1	299.59	35.21
16	12/12/91	SCO X-1	248.36	-17.20	0.00	20.29	351.62	-36.55	G CENTER	266.40	-28.94	SCO X-1	244.97	-15.63
17	12/27/91	SN 1987A	83.48	-72.27	283.21	-31.62	266.22	-17.72	SN 1987A	83.86	-69.27	G CENTER	266.40	-28.94
18	1/10/92	M 82	154.59	72.04	137.47	40.48	292.51	13.52	M 82	148.96	69.67	PSR 1929+10	293.05	10.99
19	1/23/92	GAL 058-43	331.41	-1.93	58.15	-43.00	242.82	36.31	G PLANE 58.1	294.98	22.28	-		
20	2/6/92	SS 433	285.28	6.37	39.70	0.76	12.01	-27.04	SS 433	287.95	4.99	-		
21	2/20/92	NGC 1068	39.09	-1.24	171.52	-53.90	308.14	-37.66	G CENTER	266.40	-28.94	NGC 1068	40.67	-0.01
22	3/5/92	MRK 279	209.76	71.24	115.35	44.88	13.43	18.05	MRK 279	208.24	69.31	M 31	10.69	41.27
23	3/19/92	CIR X-1	227.43	-54.62	322.14	3.01	11.72	-29.97	CIR X-1	230.23	-57.18	-		
24	4/2/92	MRK 335	1.59	20.21	108.77	-41.42	76.46	-35.33	MRK 335	1.59	20.21	VELA X-1	135.53	-40.56
25	4/16/92	GAL 009+57	223.34	11.03	9.53	57.15	358.02	74.51	4U 0115+634	19.86	62.49	-		
26	4/30/92	MCG +8-11-11	84.37	46.61	164.06	7.90	353.16	1.14	MCG +8-11-11	88.73	46.44	III ZW 2	2.63	10.97
27	5/14/92	GAL 224-40	68.97	-25.09	224.00	-40.00	53.03	64.04	3C 390.3	280.56	79.76	SN 1987A	83.86	-69.27
28	5/28/92	CAS A	345.77	57.49	108.75	-2.37	100.24	14.79	CAS A	350.87	58.81	GEMINGA	98.48	17.77
29	6/11/92	NGC 2992	149.50	-14.73	252.41	30.65	61.41	7.23	NGC 2992	146.43	-14.33	3C 120	68.29	5.35
30	6/25/92	ESO 141-55	287.12	-61.21	335.10	-25.56	144.33	-23.64	ESO 141-55	290.31	-58.67	MCG -5-23-16	146.92	-30.96
31	7/9/92	GAL 225+02	110.40	-10.22	225.46	1.95	197.74	14.42	M 87	187.71	12.39	-		
32	7/23/92	PKS 2155-304	330.74	-33.09	13.11	-53.32	121.56	-53.26	PKS 2155-304	329.72	-30.22	SMC X-1	19.18	-73.44
33	8/6/92	MCG +5-23-16	142.06	30.03	196.66	45.66	186.75	-50.89	MCG +5-23-16	143.56	27.33	NGC 3783	174.76	-37.74

* Z-axis is pointing direction for COMPTEL and EGRET. OSSE points in X-Z plane. RA and DEC are J2000.

Tables 3 and 4) that were highly rated by the peer review in competition with GI proposals to observe the same objects.
- Guest Investigator targets from lower-rated GI proposals.
- Instrument Team low-priority targets (from Tables 3 and 4, part 2) not proposed in any GI proposals.
- Other Instrument Team targets

As the timeline is developed, the overall 70%-30% division of Instrument Team time versus GI time will be kept in mind so that the final timeline will reflect this split as accurately as possible.

The scheduling of BATSE observations is not affected by this timeline procedure. For BATSE, the limit on the number of GI proposals selected will be based on the rankings of the proposals, the general 70%-30% split of data between the Instrument Team and GIs, the limit on the number of special-format observations (e.g. pulsars) which can be done per week, and the funding limitations of the Guest Investigator program.

2.
X-RAY BINARIES

SOFT GAMMA RAYS FROM BLACK HOLES VERSUS NEUTRON STARS

Edison P. Liang
Department of Space Physics and Astronomy, Rice University, Houston, TX 77251

ABSTRACT

The recent launches of GRANAT and GRO provide unprecedented opportunities to study compact collapsed objects from their hard x-ray and gamma ray emissions. The spectral range above 100 keV can now be explored with much higher sensitivity and time resolution than before. Here we review the soft gamma ray spectral data of black holes and neutron stars, radiation and particle energization mechanisms and potentially distinguishing gamma ray signatures. These may include soft x-ray excesses versus deficiencies, thermal versus nonthermal processes, transient gamma ray bumps versus power law tails, lines and periodicities. We also outline some of the highest priority future observations that will shed much light on such systems.

I. INTRODUCTION

Gamma ray observations of compact objects likely provide the most penetrating probe and diagnostics of neutron star and black hole systems. The recent launches of GRANAT and GRO provide new opportunities to study these objects above 100 keV with unprecedented spatial and time resolutions. In particular, gamma ray observations hold the promise of being able to distinguish between black holes and neutron stars based on their spectral and temporal behaviors. In this paper we will review the current status of observational data, radiation and particle energization mechanisms, astrophysical models for soft gamma ray emission, and summarize the potential distinguishing signatures of neutron stars and black holes. For the present discussions we will define soft gamma rays as the spectral range from ~100 keV to ~100 MeV.

Recent observations suggest that the most prominent soft gamma ray sources in the sky fall into 4 main categories: a) Galactic black hole candidates including both steady x-ray sources such as Cyg X-1 and transient sources (x-ray novae) such as A0620, GS2000+25, novae Muscae etc; b) AGN sources; c) young pulsars such as Crab and Vela and d) gamma ray bursters. The power per decade spectra (νF_ν) of these sources are sketched in Fig. 1. It is widely believed that the former two groups are associated with black holes while the latter two groups are associated with neutron stars. Another popular view is that black holes are thermal gamma ray sources while neutron stars are nonthermal gamma ray sources. However, the persistent power law gamma ray tails observed in many AGN sources suggest that if they are indeed black holes, then either black hole can also emit nonthermally, or the power laws are produced elsewhere such as in a jet rather than in the accretion disk itself. Since both pulsars and gamma ray bursters are popularly associated with isolated, non accreting neutron stars (see e.g. Liang and Petrosian 1986 for review), some authors also believe that accreting neutron stars (e.g. x-ray pulsars, x-ray bursters, LMXBs etc) cannot be strong soft gamma ray emitters (Sunyaev et al 1991). However recent detection of gamma rays from an increasing number of accreting neutron stars: GX1+4 (X-ray pulsar), GX354+0 (x-ray burster) etc casts such segregational themes in doubt. Only systematic long term observations leading to much broader databases can clarify such issues.

We first review the spectral data in Section II. In Section III we briefly list the radiative and particle energization processes relevant to soft gamma ray emission. In Section IV we discuss astrophysical models of black hole and neutron star gamma ray

sources. Section V is devoted to speculative potentially distinguishing signatures of black holes and neutron stars.

II. REVIEW OF SPECTRAL DATA

Figure 2 gives some sample spectra of black hole candidates while Figure 3 gives sample spectra of pulsars and gamma ray bursters. A characteristic of nonthermal neutron star emission is a persistent power law tail of index 2 - 2.5 extending out to > 10 MeV with possible low energy turnover (x-ray deficiency) in the case of Vela pulsar and gamma ray bursters. On the other hand black hole candidates seem to show strong variability both at the soft x-rays below 10 keV as well as gamma rays above a few hundred keV. During the quiescent state the spectrum is a power law of index 1.5-2 from ~ kev to ~ hundreds of keV followed by an exponential cutoff suggestive of thermal emission. During the gamma ray high state of Cyg X-1(Ling et al 1987), 1E1740.7-2942 (Paul et al 1991) and the Briggs source (Briggs 1991), the continuum exhibits a bump at 400 keV - 2 MeV with a sharp cutoff at high energies, again suggestive of thermal origins.

Spectra of x-ray novae evolve with time (Fig. 2), with the early phase resembling the soft x-ray high state of Cyg X-1 or GX339-4, and the late time spectra resembling the quiescent (low) state of Cyg X-1. It is this similarity in spectral behavior and the high orbital mass of A0620, the prototype of this class of transient sources, that prompt most authors to associate x-ray novae with black hole candidates (Sunyaev et al 1991). Crab and Vela represent the prototype of nonthermal gamma ray sources driven by strong fields. The low energy cutoff appears a measure of their age. It is interesting that the typical GRB spectrum falls in between the Crab and Vela.

AGN spectra (e.g. Cen A, NGC4151) seem to contain signatures of both Galactic black hole candidates as well as those of neutron stars. In the low gamma ray state (Fig.4) the spectrum is typically a power law with exponential cutoff at a few hundred keV - MeV, similar to Galactic black hole candidates in their quiescent state. But in the high gamma ray state (Fig.4) it often has a nonthermal power law tail extending out to very high energy. It is possible that this nonthermal power law comes from a separate component, e.g. a jet, rather than the black hole accretion disk itself.

III. RADIATION AND PARTICLE ENERGIZATION PROCESSES

Table 1 summarizes the most important continuum radiation processes in the gamma ray regime. We note that inverse Compton is the most popular mechanism for quiescent black hole emission (e.g. Sunyaev and Trumper 1979) while pair-dominated emission might be relevant to their gamma ray high states (Liang and Dermer 1988). Figure 5 illustrates the two regimes in the B versus (n, n_γ) plane where n is particle density and n is photon density. In the low density high field regime, nonthermal synchrotron, curvature, resonant Compton and 1-photon pair processes dominate. In the opposite regime, thermal bremsstrahlung, Compton and two-photon pair processes dominate. It is likely that the former regime is relevant to high-field neutron star emission while the latter regime is relevant to black hole candidates.

It is known from early days of accretion disk theory (Thorne and Price 1975) that the only way a black hole accretion disk can become hot enough to radiate hard x-rays is to become optically thin. Moreover, how hot an optically thin disk gets depends on i) how many soft photons, both internal and external, are cooling the system (Shapiro et al 1976) and ii) how efficient is the coupling between the ions which form the heat reservoir and the electrons and pairs which are the cooling agents. The question of the abundance of soft photons will be addressed in the next section.

For a plasma to remain thermal, i.e. Maxwellian, the thermalization (or randomization) time must be shorter than the cooling time due to radiative processes. Such thermalization time is usually associated with the Coulomb coupling time between ions and electrons, which imply a high particle density. At very low density so that the plasma is collisionless, under special conditions thermalization may be achieved via collective processes on plasma oscillation time scales (e.g Max 1982, Begelman and Chiueh 1988). However, even at high particle density there is a limit to the maximum electron temperature of a Coulomb plasma (Dermer 1989). Since the ion virial temperature cannot exceed ~ 100 MeV around a nonrotating black hole, electron temperature is estimated not to exceed ~ 3.5 MeV via Coulomb heating by the ions. So thermal plasmas around black holes cannot produce many gamma rays above ~ 10 MeV.

Table 1. Radiation Processes

A. Optically Thin Limit:
- lepton-lepton: bremsstrahlung, 2-γ pair annihilation
- lepton-ion: bremsstrahlung
- lepton-photon: Compton, double Compton, resonant scattering
- lepton-B: synchrotron, curvature, 1-γ pair annihilation
- photon-photon: 2-γ pair production
- photon-B: 1-γ pair production
- ion-ion, ion-photon: π_o decay

B. Optically Thick Limit:
- $\tau_{absorb} >> \tau_{sc} > 1$: true blackbody
- $\tau_{sc} >> \tau_{absorb} > 1$: modified blackbody
- $\tau_{sc} >> 1 > \tau_{absorb}$: Wien
- $\tau_{\gamma\gamma}, \tau_{sc} > 1 > \tau_{absorb}$, and ℓ(dimensionless compactness) > 1: pair-dominated spectrum

For nonthermal processes, whether it is operating around a black hole or neutron star, we should distinguish between thick target and thin target distributions. Table 2 summarizes the different particle acceleration mechanisms and relations between particle and photon indices.

Table 2. Nonthermal Processes

A. Direct Acceleration of Electrons and Problems
1. shocks & turbulence: difficult to get -2 power law, too slow
2. waves: hard to get in phase with particle
3. neutral line current sheets: act on too few particles
4. macroscopic $E_{//}$: easy to short out

B. Acceleration of Ions: less radiative loss
1. Ion couples to electrons via Coulomb or collective processes
2. Ion-Ion collisions: pion production and decay
3. Ion-Photon collisions: photon pion production

C. Relation between Power Law Indices : $f(\gamma) \propto \gamma^{\delta}$ ----> $N_\nu \propto \nu^{-n}$
1. thin target (steady distribution): $t_{accel} << t_{cool}$: $n=(\delta+1)/2$
2. thick target (cooling distribution): $t_{accel} >> t_{cool}$: $n=(\delta/2)+1$

IV. ASTROPHYSICAL MODELS

How do compact objects emit gamma rays? We will first consider thermal scenarios for accreting black holes and nonthermal scenarios for nonaccreting neutron stars. But we will also speculate on alternative scenarios.

A. Thermal Models for Black Holes:

Within the context of thermal accreting disks around black holes, it has been suggested that there are at least 3 phases with increasing temperature (Fig.6, Wandel and Liang 1991):

a) optically thick, physically thin disks emitting blackbody radiation of UV to soft X-ray temperatures (Shakura and Sunyaev 1973); b) disks with optically thin inner region cooled by inverse Comptonization of soft photons (external or synchrotron,Thorne and Price 1975, Shapiro et al 1976); c) disks where the soft photon source is completely quenched in the inner optically thin region; such regions can only cool inefficiently via bremsstrahlung and could heat up to relativistic temperatures, leading to copious production of e+e- pairs and possibly the dominance of the pairs (Svensson 1984, Zdziarski 1984, White and Lightman 1989, Kusunose and Takahara 1988). The pair-balance emission of such regions give rise to a bump in the 400 keV - ~ MeV region (Ramaty and Meszaros 1981, Liang and Dermer 1988). The escape of some of the pairs to annihilate in the cool circumstellar or interstellar medium will likely lead to correlated appearance of a narrow 511 keV line (Lingenfelter and Ramaty 1989, Dermer and Liang 1989).

Once we accept this kind of scenario for gamma ray emission from black holes, then a number of consequences can be predicted that can be confronted with observational data. For a nonrotating hole we expect that: i) the fluence of the narrow 511 keV line, coming out of escaped pairs from the gamma ray emitting source in this picture, should be correlated with the fluence of the gamma ray bump and its value can be computed dependent on the geometry of the disk model (Dermer and Liang 1989); ii) the mass of the black hole can be constrained as a function of the disk Keplerianess parameter from the gamma ray bump color temperature and the ratio of gamma ray flux to total (x-ray plus gamma ray) flux (Liang 1990); iii) the gamma ray bump should be correlated with pion decay continuum emission below ~ 70 MeV whose intensity can be calculated (Dermer 1989); iv) a globally average viscosity parameter can be estimated for the pair cloud as a whole (Liang 1991); v) upper limit on the magnetic field of the emission region can be obtained from the hardness of the gamma ray spectrum via the lack of synchrotron soft x-rays (Dermer and Liang 1989). In particular, ii) can be used to check the overall self-consistency of the pair cloud black hole accretion model when we have multiple data points for a single object, i.e. many episodes of gamma ray flaring in which both the x-ray and gamma ray spectra are obtained.

B. Nonthermal Models for Neutron Stars:

Conventional ideas of nonthermal gamma ray emission from isolated neutron stars center around the acceleration of electrons and pairs by macroscopic electric fields parallel to magnetic fields. The hardness of the power law (photon index ~ 2) and the rapid time scales (down to ms) make it difficult, if not unlikely, for acceleration by shocks, waves and turbulences. In both young radio pulsars and gamma ray bursters (if they are indeed associated with strong field neutron stars), it is yet unclear if the emission is from near the surface or the outer magnetosphere (Fig. 7). If it is surface emission then the gamma rays must be strongly beamed. The origin of the accelerator in the pulsar case is of course stellar spin ($\mathbf{V} \times \mathbf{B}$), but the origin in the gamma ray burst case is far from clear. But the similarity of the GRB spectra to pulsar spectra is striking, with most spectral shapes lying between Crab and Vela. In fact, in many bursts the spectrum starts out hard with a total lack of x-rays similar to the Vela spectrum and evolves towards more x-rays at late times similar to Crab.

Even though we still have no satisfactory model of gamma ray emission from GRBs, it is likely that the emission will involve a combination of synchrotron and curvature radiation and resonant Compton scattering together with some form of pair cascade, similar to pulsars. In the model of Ruderman and Cheng (1988) for young pulsars, they predict a limiting luminosity of ~ 5×10^{36} erg/s (Fig. 8). Note that this is considerably below that observed for typical black hole candidates ($10^{37\text{-}38}$ erg/s). This may be used as a discriminant between pulsar and black hole gamma ray sources.

C. Alternative Scenarios:

What about nonthermal black hole models and thermal neutron star gamma rays? Despite the popularity of thermal disk models for black holes there is no compelling

reason to exclude nonthermal models. In particular for rapidly rotating black holes which can sustain a macroscopic ordered B-field nonthermal accelerations seems likely (e.g. Begelman et al 198). Even for nonrotating holes the shearing motion can in principle also lead to equipartition fields up to 10^{6-7}G whose reconnection can provide plenty of free energy for particle acceleration (Galeev et al 1979). However, such fields will also unavoidably lead to copious production of soft synchrotron photons which will cool the plasma, making it hard to pump most energy into gamma rays.

Similarly, accreting neutron stars will have an abundance of soft photons, both from blackbody emission from its surface and synchrotron soft photons from the inner magnetosphere. Hence it might be difficult to sustain a hot thermal pair cloud near the star emitting gamma ray bumps or even nonthermal accelerators. It has therefore been a popular belief (e.g. Sunyaev et al 1991) that accreting neutron stars cannot be strong gamma ray emitters above ~ 100 keV. However, recent results on GX1+4 (Fontera et al 1989, Sunyaev et al 1991) and GX354+0 (Cook et al 1991) as well as the possible association of a source in Terzian 2 (Barret et al 1991) with an x-ray burster, plus the possibility that Cyg X-3 (Meegan et al 1979) is an accreting neutron star all suggest that accreting neutron stars may be occasional strong emitter of soft gamma rays.

Recent works by the Columbia group (Kluzniak et al 1988, Cheng and Ruderman 1991) suggest that the disk-neutron star magnetospheric boundary may be the site of an efficient accelerator leading to emission of gamma rays. However, the soft x-rays will remain a problem for any such model. Also in the case of GX1+4 the gamma ray luminosity can become a good fraction of Eddington luminosity, making it unlikely that the gamma ray emitting region can be too far from the star due to energetic requirements.

D. Lines and Periodicities:

The presence of redshifted annihilation line and cyclotron lines in the 10's of keV had been considered telltale signs of neutron star emission, while narrow unredshifted 511 keV line (e.g. Leventhal et al 1989, Riegler et al 1985, Ling and Wheaton 1989) may be associated with black holes. However, recently discovered narrow gamma ray bumps from the 1E source and the Briggs source both may be peaking redward of 511 keV. If these are indeed black holes then the above discriminant may be in trouble. Moreover, if the B-field is weak enough so that the cyclotron line shifts into the few keV range then it can no longer be distinguished from, say Fe K lines or edges, which are observed from black hole candidates (Ebisawa 1991). However, if more than one well-defined harmonic (e.g. Ginga GRBs, Murikami et al 1988) is found then the case for neutron star is still strong.

Lack of (spin) period has always been a prerequisite for black hole candidacy. On the other hand, the case with QPOs is less clear cut. The fast QPOs (10's of ms period) is currently associated with neutron stars in most models (see e.g. Lamb 1990 for review), but the slow QPOs (~ few Hz) may well be associated with the accretion flow itself rather than the stellar spin, so it could arise in black hole systems as well as neutron star systems. Disk seismology is still in its infant stage and observations of QPOs in hard x-rays and gamma rays are still lacking.

V. POTENTIAL DISTINCTIONS

In Table 3 we list some of the gamma ray signatures currently associated with black holes and neutron stars. Whether they will stand up as universal signatures only time will tell. It is clear that spectrally, both black holes and neutron stars are capable of producing power law spectra in the mid-energy range from 10's of keV to few hundred keV. Their distinctions come in their variability in soft x-rays and gamma rays above a few hundred keV. Black hole candidates seem to have soft x-ray excesses at least episodically, whereas nonaccreting neutron stars often seem to have x-ray deficiencies. Black hole candidates

emit thermal gamma ray bumps episodically, whereas neutron stars have persistent power law spectra of photon index ~2. In addition to periodicity and QPOs, the distinction between black holes and neutron stars may also lie in the redshift and width of the annihilation line and its correlation with the continuum. Details of such distinctions remain to be worked out theoretically.

We believe the current observations with GRANAT and GRO will shed much light on the origin of gamma rays from both classes of systems. This work is partially supported by NASA NAG51515 and NAG51547.

Table 3. Potentially Observable Signatures of Black Holes versus Neutron Stars

	Black Holes	Neutron Stars
1. Continuum Shape in Quiescent State	1.5-2 power law with exponential cutoff above few hundred keV	2-2.5 power law with low energy flattening or turnover
2. Soft X-Rays	episodic excess with soft spectrum below 10 keV	x-ray deficiency, no excess
3. Gamma Rays	transient Bump at ~400 - 2000 keV	power law may vary, no bump
4. Periodicity	no fast period or QPO, may have slow QPO	period or QPO
5. Variability	long term transients	X and Gamma Ray Bursts
6. Lines	unredshifted 511 keV line Fe lines below 10 keV	redshifted 511 keV line cyclotron lines 10's of keV

VI. REFERENCES

Baity, W. et al. 1981, Ap. J. 244, 429.
Barret, D. et al. 1991, Ap. J. Lett. in press.
Begelman, M et al 198 , Rev. Mod. Phys.
Begelman, M. and Chieuh, T. 1988, Ap. J. 332, 872.
Briggs, M. 1991, U. of Calif. San Diego Ph.D. Thesis.
Cheng, K. et al. 1986, Ap. J. 300, 522.
Cheng, K.S. and Ruderman, M. 1991, Ap. J. in press.
Cook, W.R. et al. 1991, Ap. J. Lett. 372, L75.
Coe, M. et al. 1976, Nature 259, 544.
Dermer, C.1989, in Proc. 14th Texas Symp. Rel. Ap.,ed. E. Fenyves, p.513 (Ann. NYAS, NY).
Dermer, C. and Liang, E. 1989, AIP Conf. Proc. No.170, ed. N. Gehrels & G. Share, p.326 (AIP, NY).
Ebisawa, K. 1991, U. of Toyko Ph.D. Thesis.
Fontera, F. et al. 1989, Proc. 23rd ESLAB Symp. ed. N. White p.57 (ESA Pub. SP-296).
Galeev, A. et al. 1979, Ap. J. 229, 318.
Golenetskii, S. et al. 1984, Nature 307, 41.
Ho, C. and Epstein, R. 1989, Ap. J. 343, 277.
Jourdain, E. et al. 1991, Proc. Dublin ICRC OG3.3.12.
Kluzniak, L. et al. 1988, Nature
Kusunose, M. and Takahara, F. 1988, PASJ 40, 435.
Lamb, F. 1990, in "Neutron Stars", ed. J. Ventura (Kluwer Acad., Holland).
Levernthal, M. et al. 1989, Nature 339, 36.
Liang, E. 1989, GRO Workshop Proc. p.4-397, ed. W. Johnson (NASA).
Liang, E. 1990, Ast. Ap. 227, 447.
Liang, E. 1991, Ap. J. 367. 470.
Liang, E. and Dermer, C. 1988, Ap. J. Lett. 325, L39.

Liang, E. and Dermer, C. 1991, Nature submitted.
Liang, E. and Petrosian, V. ed 1986, AIP Conf. Proc. No. 140 (AIP, NY).
Ling, J. et al. 1987, Ap. J. Lett. 321, L117.
Ling, J. and Wheaton, W. 1989, Ap. J. Lett. 321, L117.
Lingenfelter, R. and Ramaty, R. 1989, Ap. J. 343, 686.
Max, C. 1982, in "Laser Plasma Interactions", ed. R. Balian and J.C. Adam, p.302 (North Holland, Amsterdam).
Meegan, C. et al. 1979, Ap. J. Lett. 234, L123.
Murikami, T. et al. 1988, Nature 335, 234.
Paul, J. et al. 1991, in AIP Conf. Proc. No.232, ed. P. Durouchoux & N. Prantzos, p.17 (AIP, NY).
Ramaty, R. and Meszaros, P. 1981, Ap. J. 250, 389.
Ruderman, M. and Cheng, K.S. 1988, Ap. J. 335, 306.
Riegler, G. et al. 1985, Ap. J. Lett. 294, L13.
Shakura, N. and Sunyaev, R. 1973, Ast. Ap. 24, 337.
Shapiro, S. et al. 1976, Ap. J. 204, 187.
Svensson, R. 1984, MNRAS 209, 175.
Sunyaev, R. and Trumper, J. 1979, Nature 179, 506.
Sunyaev, et al. 1988, Sov. Ast. Lett. 14, 771.
Sunyaev, R. et al. 1991, in Proc. 28th Yamada Conf. on Front. X-ray Ast. (Nagoya, Japan).
Thorne, K. and Price, R. 1975, Ap. J. Lett. 195, L101.
Wandel, A. and Liang, E. 1991, Ap. J. 380, 84.
White, T. and Lightman, A. 1989, Ap. J. 340, 1024.
Zdziarski, A. 1984, Ap. J. 283, 842.

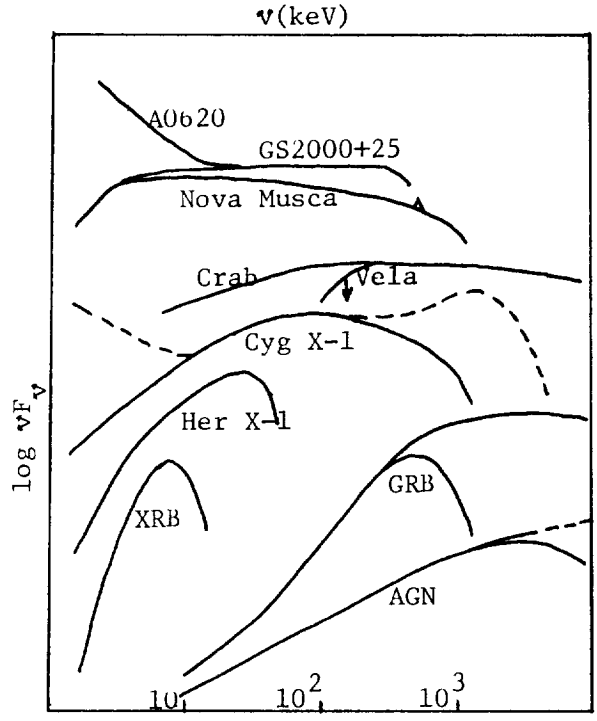

Fig.1 Power per decade spectra of 4 classes of soft gamma ray sources. For comparison we also sketch spectra of typical x-ray neutron star binaries. Vertical scale is arbitrary.

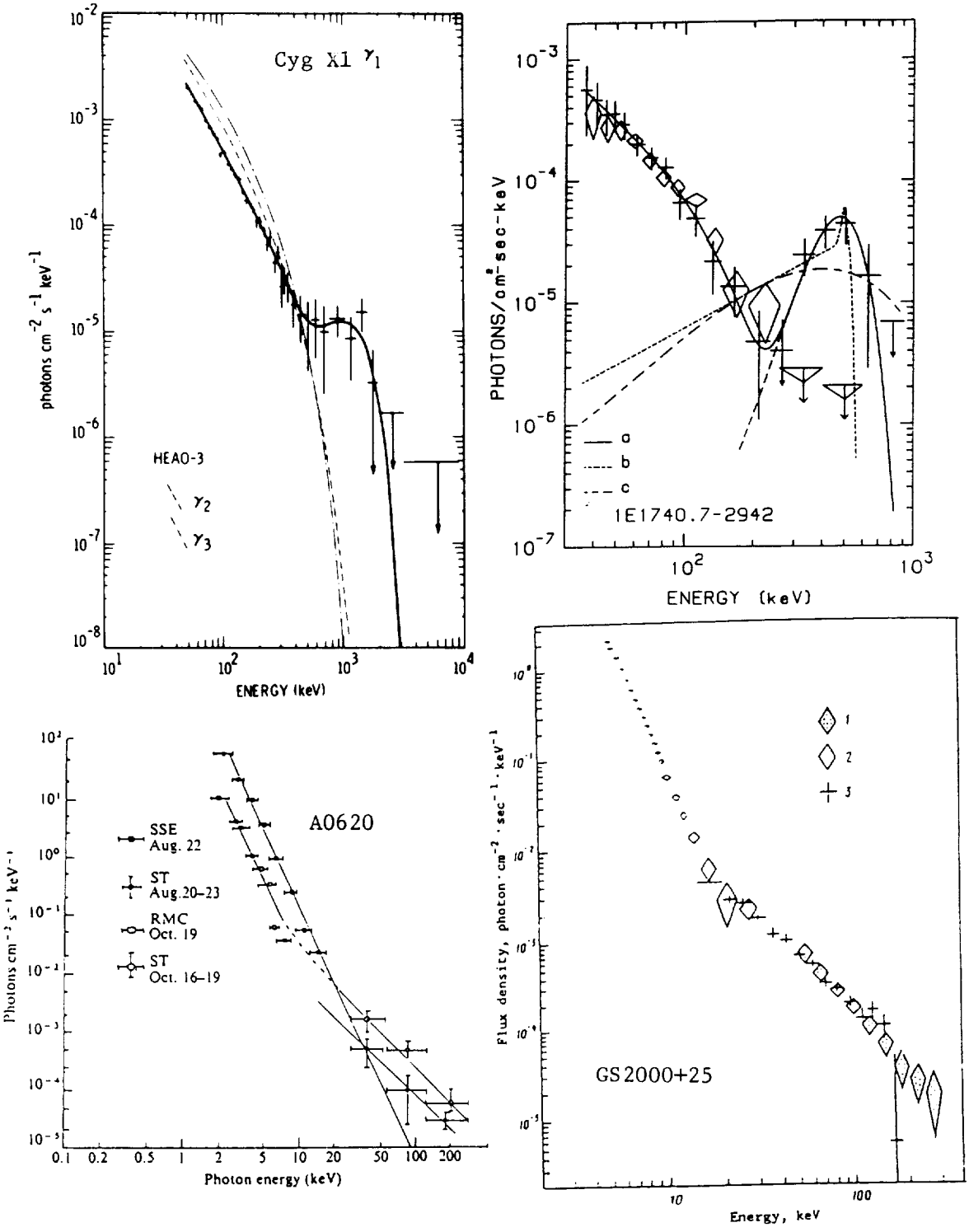

Fig. 2 Sample spectra of black hole candidates:Cyg X-1(Ling et al 1987), 1E (Paul et al 1991), A0620 (Coe et al 1976), GS2000+25 (Sunyaev et al 1988).

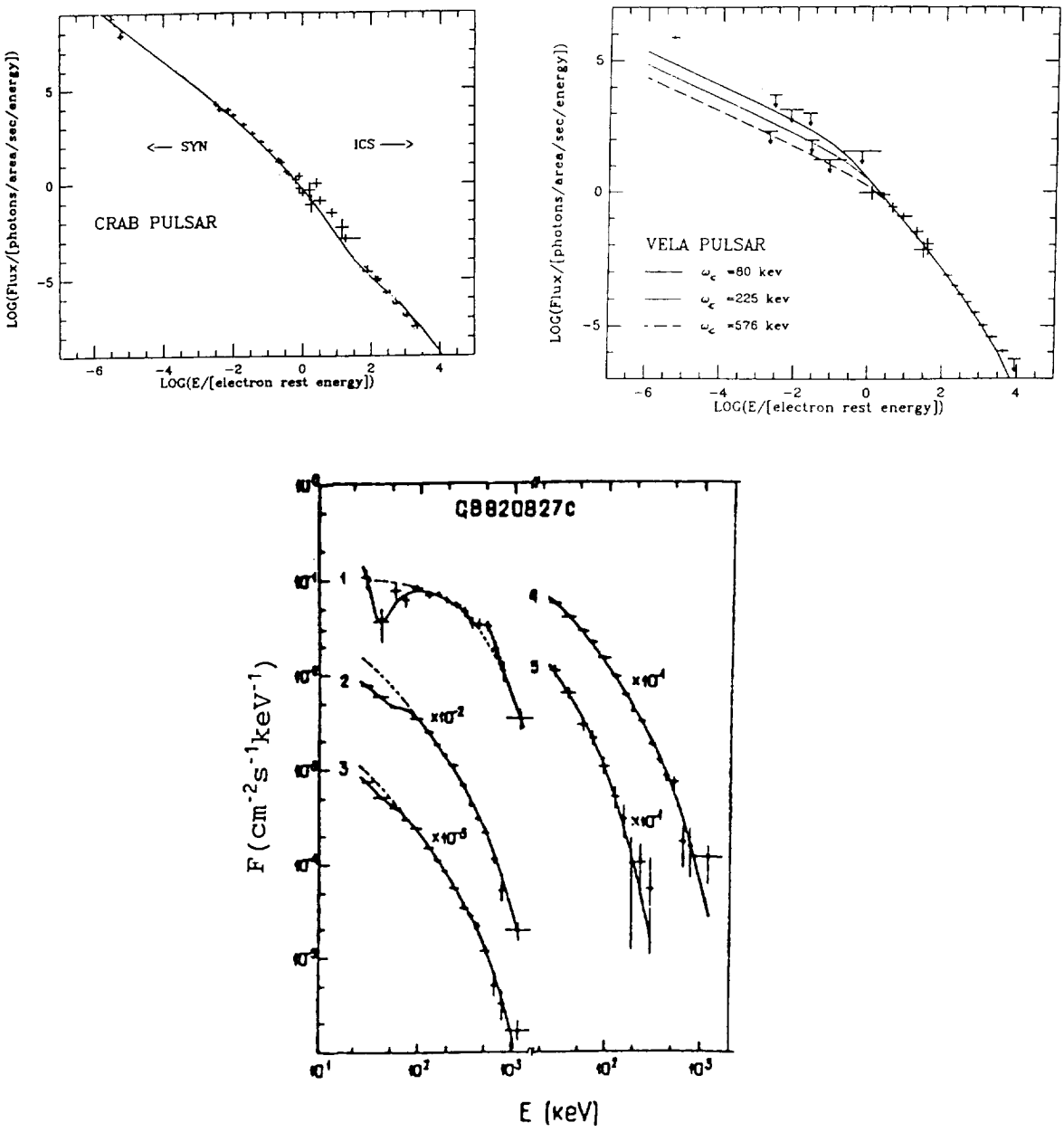

Fig. 3 Sample spectra of young pulsars and gamma ray bursters. Crab, Vela (from Cheng et al 1986), GB820827c (from Golenetskii et al 1984).

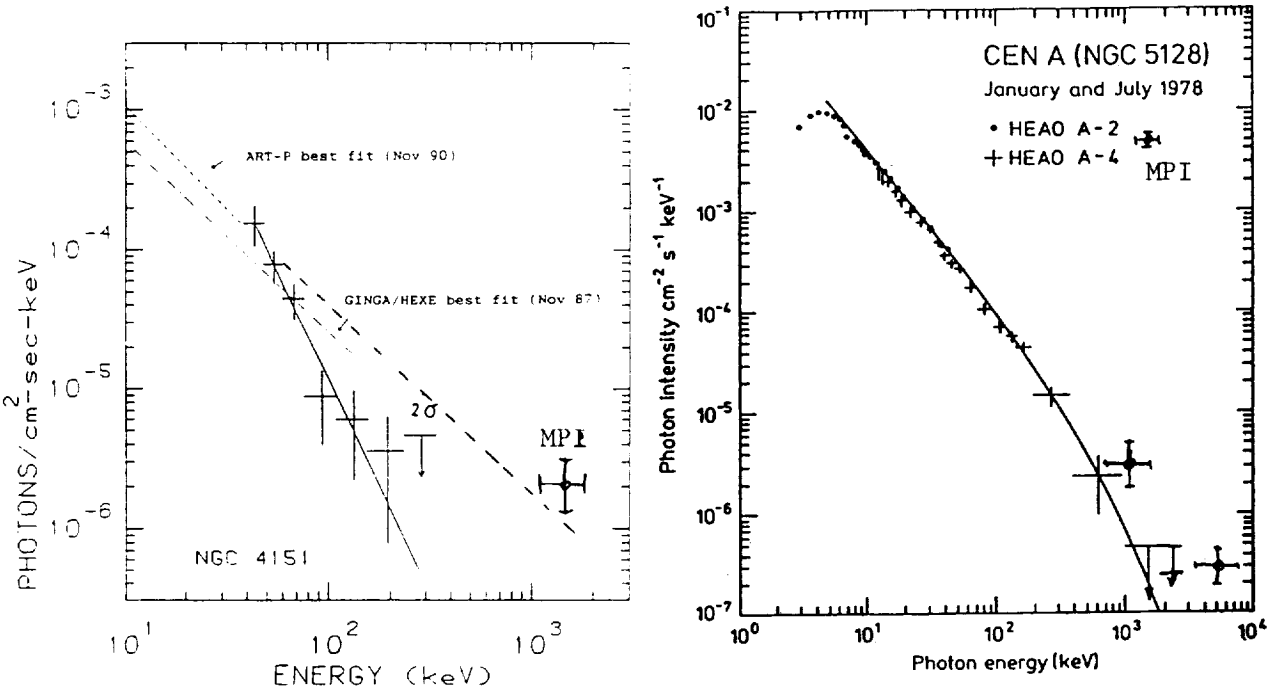

Fig. 4 Sample AGN spectra showing the variable high energy tails. NGC4151 (from Jourdain et al 1991), Cen A (from Baity et al 1981) adapted to include MPI data.

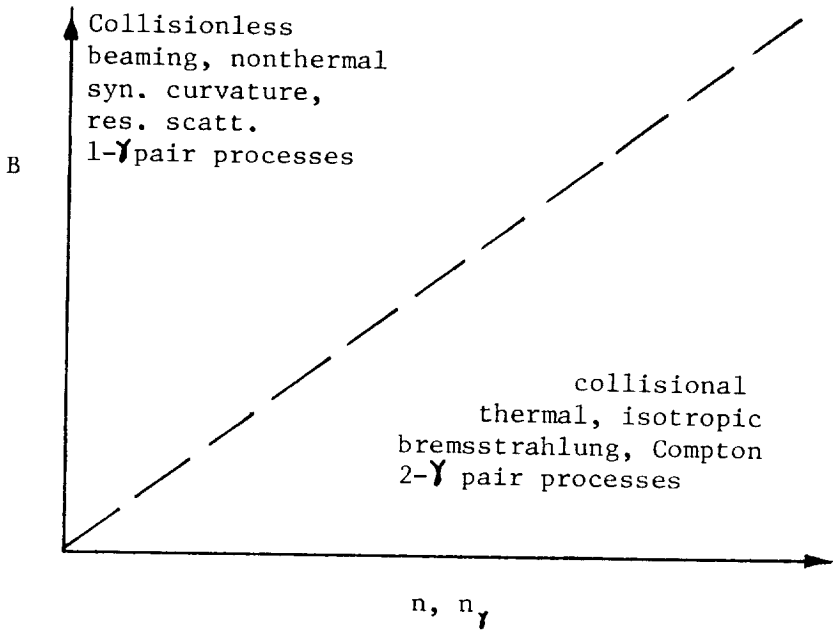

Fig. 5 Domains of B - n, n_γ plane showing the two regimes. The upper left is more relevant to neutron stars and the lower right is relevant to black holes.

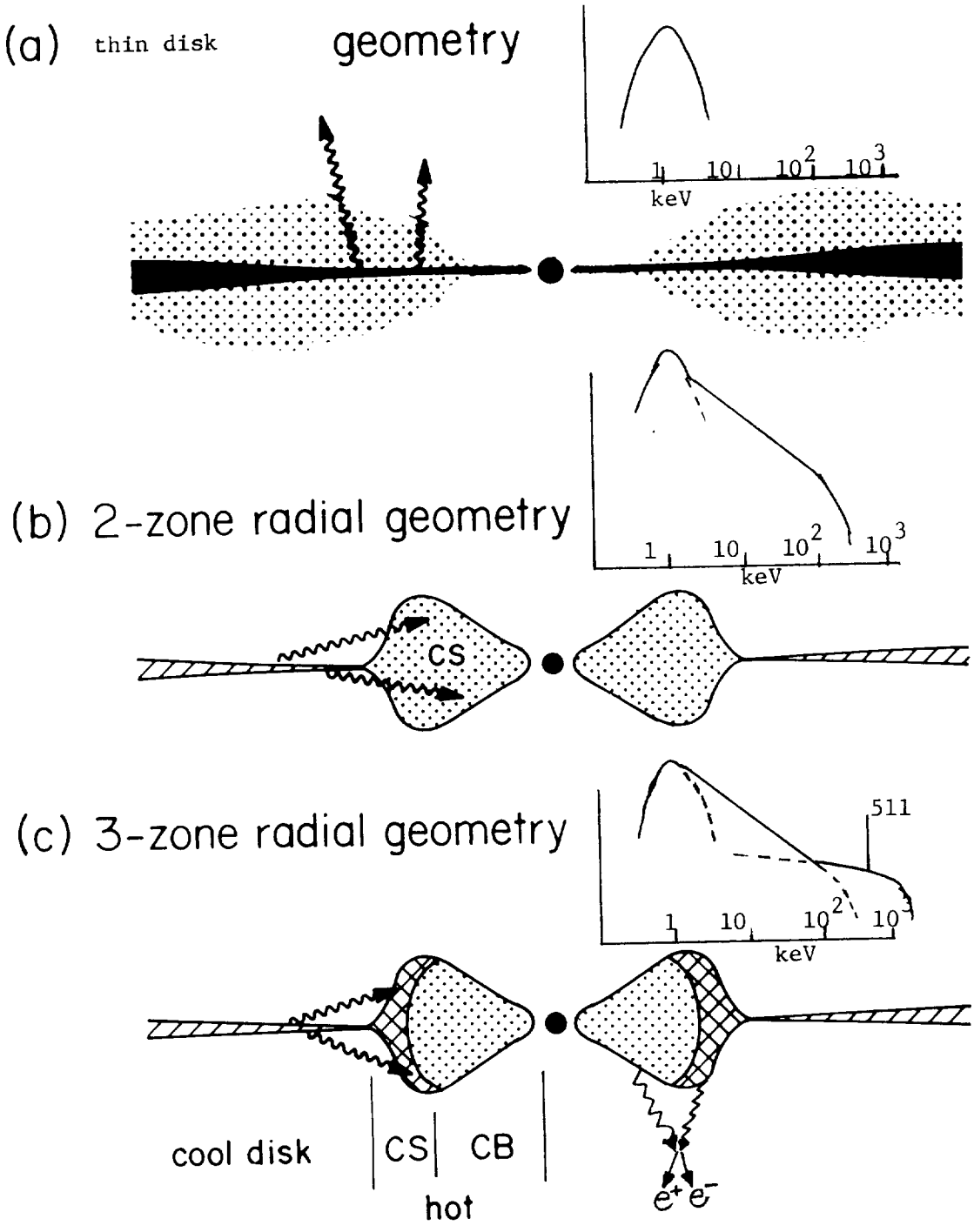

Fig. 6 Three phases of black hole accretion disks with their respective spectrum. CS= Comptonized Soft Photons. CB= Comptonized bremsstrahlung. Shaded area in (a) indicate a possible corona (adapted from Wandel and Liang 1991).

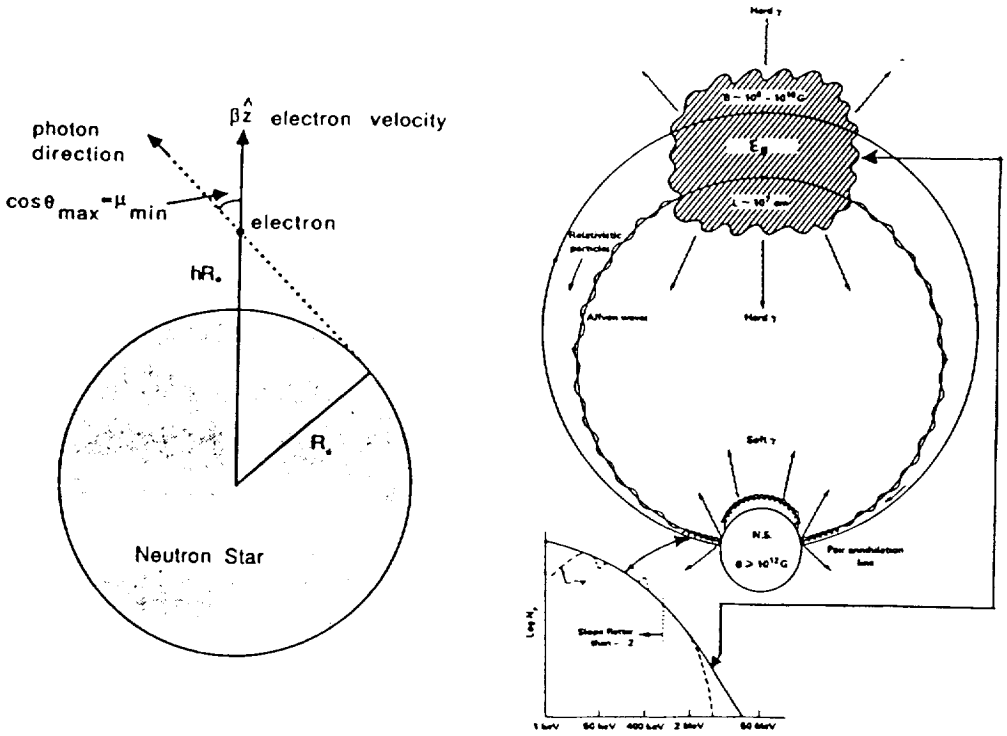

Fig. 7 Artist conception of two different scenarios of continuum spectra formation: (a) emissions by outwardly beamed electrons (pairs) near stellar surface (from Ho and Epstein 1989); (b) two component emission (from Liang 1989)

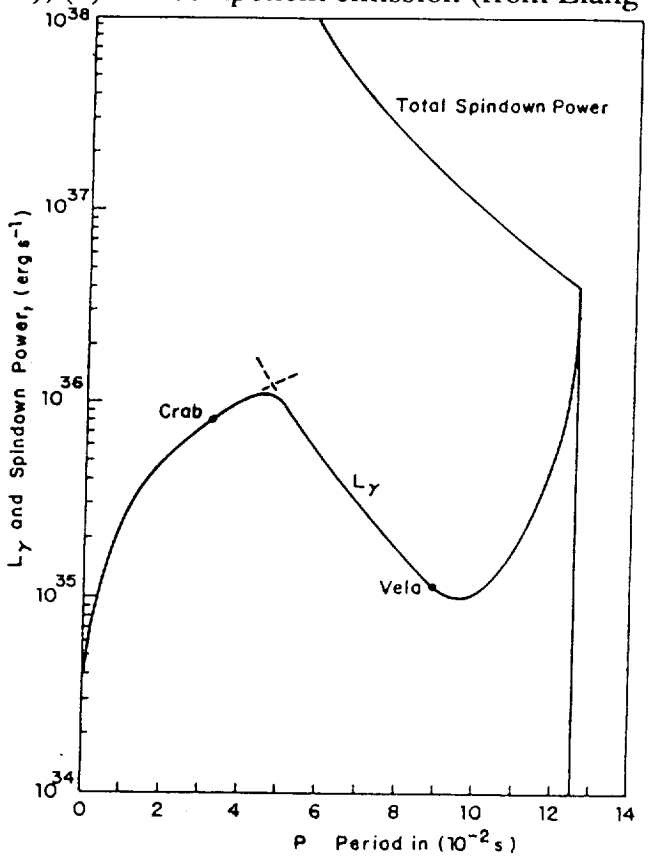

Fig. 8 Limit on gamma ray luminosity of pulsars based on the Ruderman and Cheng model (1988)

Monitoring Cen X-3 with BATSE

Mark H. Finger,[1] Robert B. Wilson,[2]
Charles A. Meegan[2], William S. Paciesas,[3] and Gerald J. Fishman

Abstract

The eight uncollimated BATSE Large Area Detectors (LAD's) provide the ability to monitor pulsed hard x-ray sources on a nearly continuous basis. Using data from the LAD's, the pulse timing and pulsed flux of the 4.8 second period binary x-ray pulsar Centaurus X-3 has been analysed over a two month period. The methods and initial results of this analysis, which includes both data folded on-board GRO and 1.024 second resolution discriminator rates folded on the ground, are presented.

1. Introduction

One of the objectives of the Compton Gamma ray Observatory's Burst and Transient Source Experiment (BATSE) is the long-term monitoring of x-ray pulsars. As a exploration of BATSE's pulsar monitoring capabilities, this paper presents the initial results of a timing analysis of the x-ray pulsar Centaurus X-3.

Pulsations from Cen X-3 with a period of 4.8 seconds were first observed in Uhuru data in 1971 [1]. Further analysis of the Uhuru data revealed that the source was a member of a binary system [2]. This was demonstrated both by 2.087 day period doppler signatures in the detected pulse period, and eclipses with the same period. Since that time a considerable body of observations has accumulated, including observations by Uhuru [3], Cos-B [4], SAS 3 [5], Heao 1 [6], Hakucho [7], Tenma [8], Ginga [9], Röntgen on Kvant [10], and Art-P on Granat [11]. To this body of observations BATSE promises to add a nearly continuous data set spanning several years.

BATSE has eight uncollimated Large Area Detectors (LAD's) placed on the corners of the Compton Gamma Ray Observatory spacecraft [12]. Cen X-3 (or any other source) is continuously viewed by four of these detectors during the portion of each orbit that it is unocculted by the Earth. Each LAD consists of a .5 inch thick by 20 inch diameter NaI(Tl) scintillator coupled by a light integration chamber to three 5 inch photo-multiplier tubes. The useful energy range of the LAD's is from 20 keV to 1 MeV. The data types from these detectors relevant to pulsar analysis are summarized in Table 1.

[1] Astronomy Programs, Computer Sciences Corporation
[2] Space Science Laboratory, NASA/Marshall Space Flight Center
[3] Department of Physics and Center for Space Plasma and Aeronomic Research, University of Alabama in Huntsville

Data Type	Energy Channels	Time Resolution	Accumulation Time per day
Folded On-Board	16	Period/64	5000-10000 sec
DISCLA	4	1.024 sec	50000-86400 sec
CONT	16	2.048 sec	50000-86400 sec

Table 1. Data from the BATSE LAD's that is useful for pulsar analysis.

The BATSE hardware can fold data on-board for periods specified in integral numbers of microseconds. The result of this folding is 64 phase resolved count spectra each with 16 energy channels. Due to scheduling competition with other pulsars, and due to telemetry competition with burst data, typically only 5000 to 10000 seconds of this data type is acquired per day for Cen X-3. The DISCLA data contains the four discriminator rates for each of the LADS with 1.024 second time resolution. The CONT data contains 16 channel count spectra for each of the LADS with 2.048 second time resolution. Useful data of each type is available at all times the source is visible, except for times of SAA passage, solar flares, and other interfering events.

In the analysis presented here we begin by studying the lowest DISCLA energy channel (20-60 keV). This data is used to establish the history of Cen X-3's intensity and rotational phase. High intensity portions of the folded on board data are then examined using the phase ephemeris developed from the DISCLA data. The CONT data, which contains additional spectral information, has not yet been analysed.

2. DISCLA Analysis

The DISCLA data used in this analysis consists of the counting rates from the eight BATSE LADS in the 20-60 keV energy deposit range sampled every 1.024 seconds. The data set analysed covers the period from Truncated Julian Date (TJD) 8369 to TJD 8433 (23rd April to 26th June 1991). These rates are typically between 1000 and 2000 counts per second. In this energy range the sky is brighter than the Earth's atmosphere. This contrast imposes a modulation at the spacecraft orbital period (5600 seconds) of 500-1000 counts per second. Excursions from these typical rates are caused by solar flares, gamma-ray bursts, and atmospheric electron events. And of course, buried in these rates is the few counts per second periodic signature of Cen X-3.

The first step taken in the DISCLA processing was to filter the data and form a linear combination of the rates from individual detectors. Data was rejected from periods when Cen X-3 was occulted by the Earth. Data was also rejected during periods when solar flares, gamma ray bursts, or other events caused rapid variations in the counting rates. The rates were then summed over the detectors exposed to Cen X-3, with a weighting for each detector given by the cosine of the angle between the detector's normal and the source direction. This weighting roughly mimics the detector response, and produces a linear combination that is fairly insensitive to reorientations of the Compton GRO spacecraft. In this first step of processing the time-tags associated with each rate

were reduced to the geocenter, thereby eliminating any further need for the spacecraft ephemeris.

The linearly combined rates were then "pulse folded" using a technique simular to that employed by Deeter et al. [13] in timing analyses of Vela X-1. The data were divided into segments 300 seconds long which were individually fit to models of the form:

$$R(t) = B_0 + B_1 t + B_2 t^2 + \sum_{k=1}^{3} [C_k \cos 2\pi k\phi + S_k \sin 2\pi k\phi] \quad (1)$$

where R is the model rate, the quadratic in time t represents the background rate, ϕ is a provisional model of the pulsar's rotational phase, and the pulsar light curve is parameterized by the first three harmonics of the observed pulse shape. Due to the 1.024 second resolution of the DISCLA rates, little additional information could be obtain by including higher harmonics. These χ^2 fits to this nine parameter model used variances calculated from the individual detector rates by assuming Poisson statistics. Data segments with a χ^2 per degree of freedom greater than 1.4 were rejected from further analysis. For the remaining segments sufficient information was recorded to allow the calculation of the χ^2 associated with the model in equation (1) for an arbitrary set of parameters.

A further step was then employed that resulted in a χ^2 fit to the remaining data over intervals of approximately 10000 seconds. The resulting fit was to a model of the form

$$R = B(t) + \sum_{k=1}^{3} [C_k \cos 2\pi k(\phi + \delta\phi) + S_k \sin 2\pi k(\phi + \delta\phi)] \quad (2)$$

where $B(t)$ is the background model and $\delta\phi$ is a correction to the model of the pulsar's rotational phase applied above. The pulsar light curve is assumed to be constant over each interval. For each 300 second segment within an interval the background was again modeled as a quadratic,

$$B(t) = B_0^i + B_1^i t + B_2^i t^2 \quad for \quad \tau^i < t < \tau^{i+1} \quad (3)$$

where τ^i are the segment boundaries. The model however was constrained to be continuous in value and slope at the boundaries of adjoining segments. These interval fits were obtained from the previous segment fits using a sequential estimation technique known as Square-Root Information Filtering (SRIF) [14]. Only the estimates of the pulsar light curve harmonic amplitudes and their associated errors were retained from these interval fits.

The parameterized light curves obtained from the interval fits were then correlated with a template to obtain a Cen X-3 pulse intensity and phase offset for each interval. The template used is shown in Figure 1. This resulted from folding data from TJD 8369.9 to 8370.5, subtracting the mean, and normalizing to obtain a mean square value of one.

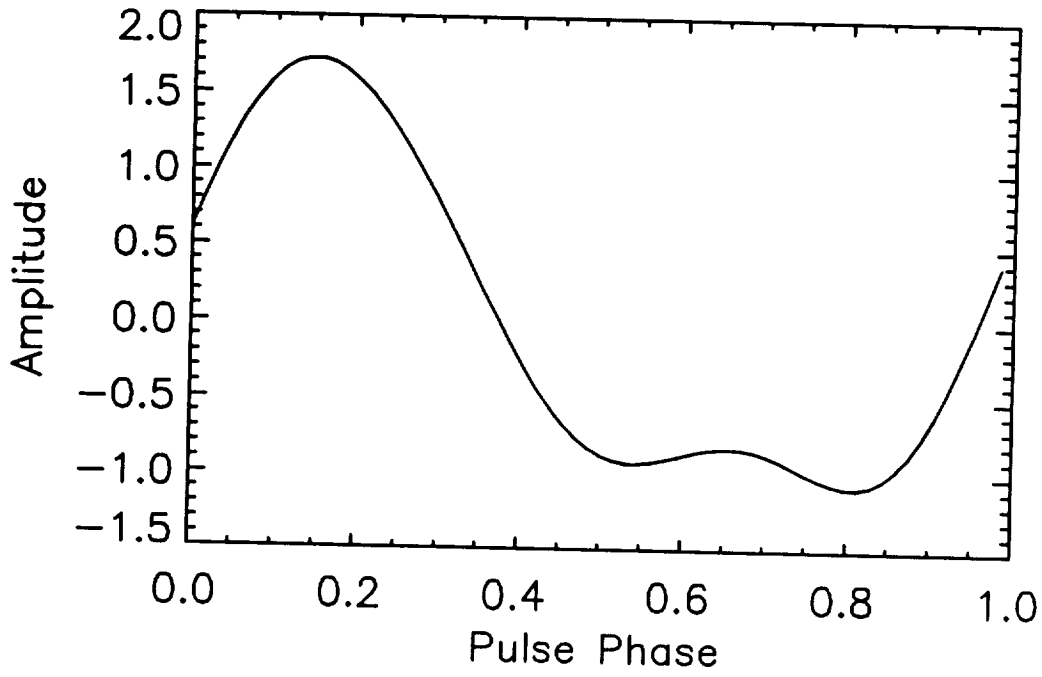

Figure 1. The pulse template used for Cen X-3 timing. This was derived from data in the interval TJD 8569-8574.

3. Results

In the calculation of pulsar phases for the folding of the DISCLA data the planetary ephemeris DE200 was used in conjunction with the Cen X-3 binary system ephemeris given in Table 2. This binary ephemeris was based on orbital elements found by Murakami et al. [7] and the orbital period derivative derive by Kelley et al. [5]. It was found necessary to make an adjustment to the orbital phase. This adjustment, which was consistent with the quoted ephemeris errors, was determined from data in the period TJD 8370-8374, and is reflected in the mid eclipse epoch given in Table 2.

Epoch of mid Eclipse	$t_{\pi/2}$ = JD 2448370.1470 ± .0005
Binary Period	P_{orb} = 2.0870686 days
Period rate of change	$\dot{P}_{orb}$ = -1.02·10^{-8}
Projected semi-major axis	x = 39.664 sec

Table 2. Cen X-3 binary ephemeris adopted from Murakami et al. and Kelly et al. with an adjustment in orbital phase.

The data was initially folded with a pulse frequency of 0.20747 Hz. Phase residuals from the template correlation were then fit and the interval fits recalculated. After several iterations the following total phase model was arrived at:

$$\phi + \delta\phi = -0.2350 + 17925.701442\Delta t - 0.03355982\Delta t^2 + 0.0003579274\Delta t^3 \qquad (4)$$

where Δt is the time elapsed in days since JD 2448370.5 in the pulsar timescale.

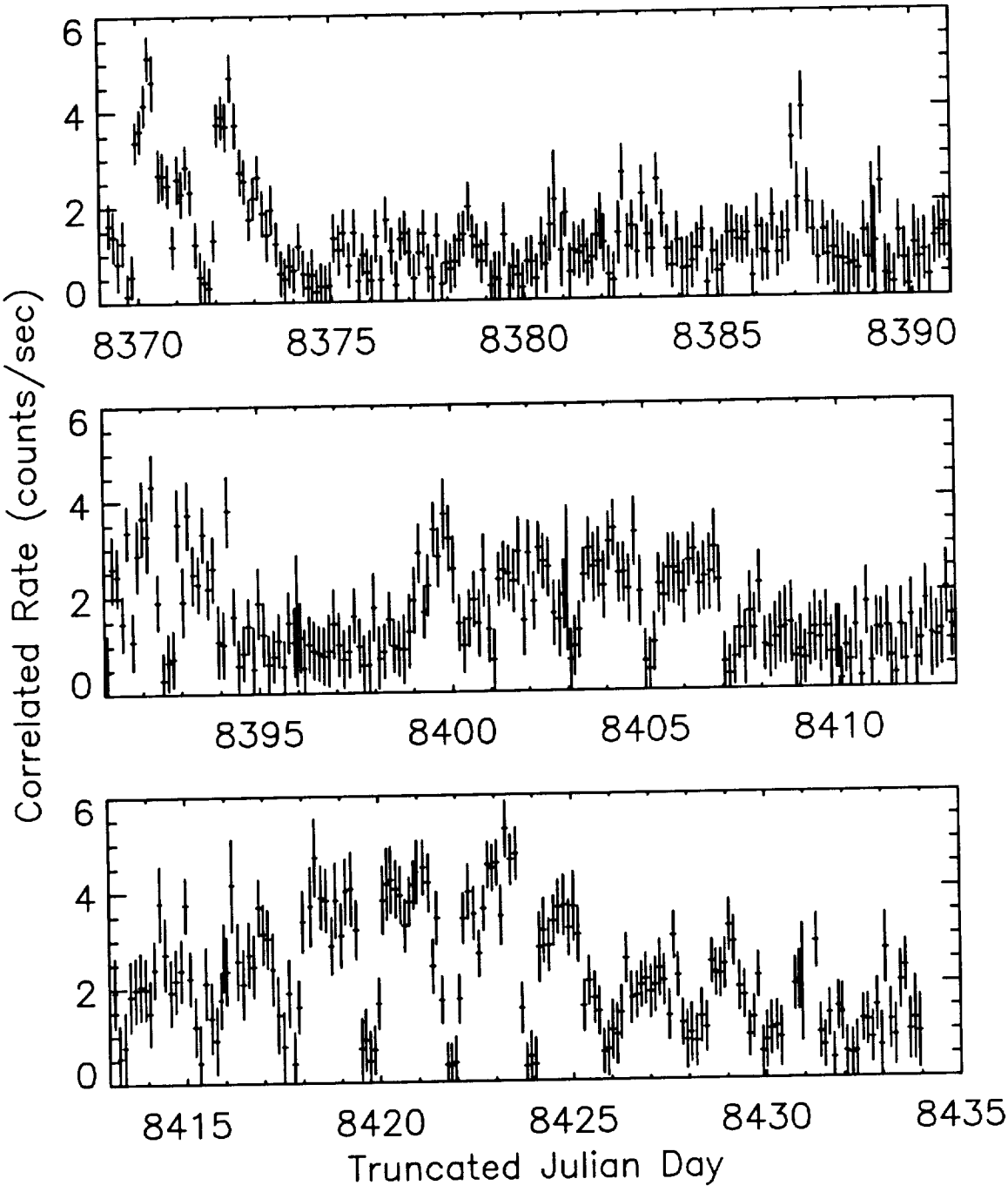

Figure 2. The Intensity history of Cen X-3 obtained by correlation of the folded rates with a pulse template.

The intensity history of Cen X-3, as determined from the 10000 second interval template correlations, is show in Figure 2. Several high intensity periods are visible, the most notable being from TJD 8369 to 8384, from TJD 8399 to 8407 and from TJD 8413 to TJD 8430. During these periods the eclipses are clearly visible. The phase residuals relative

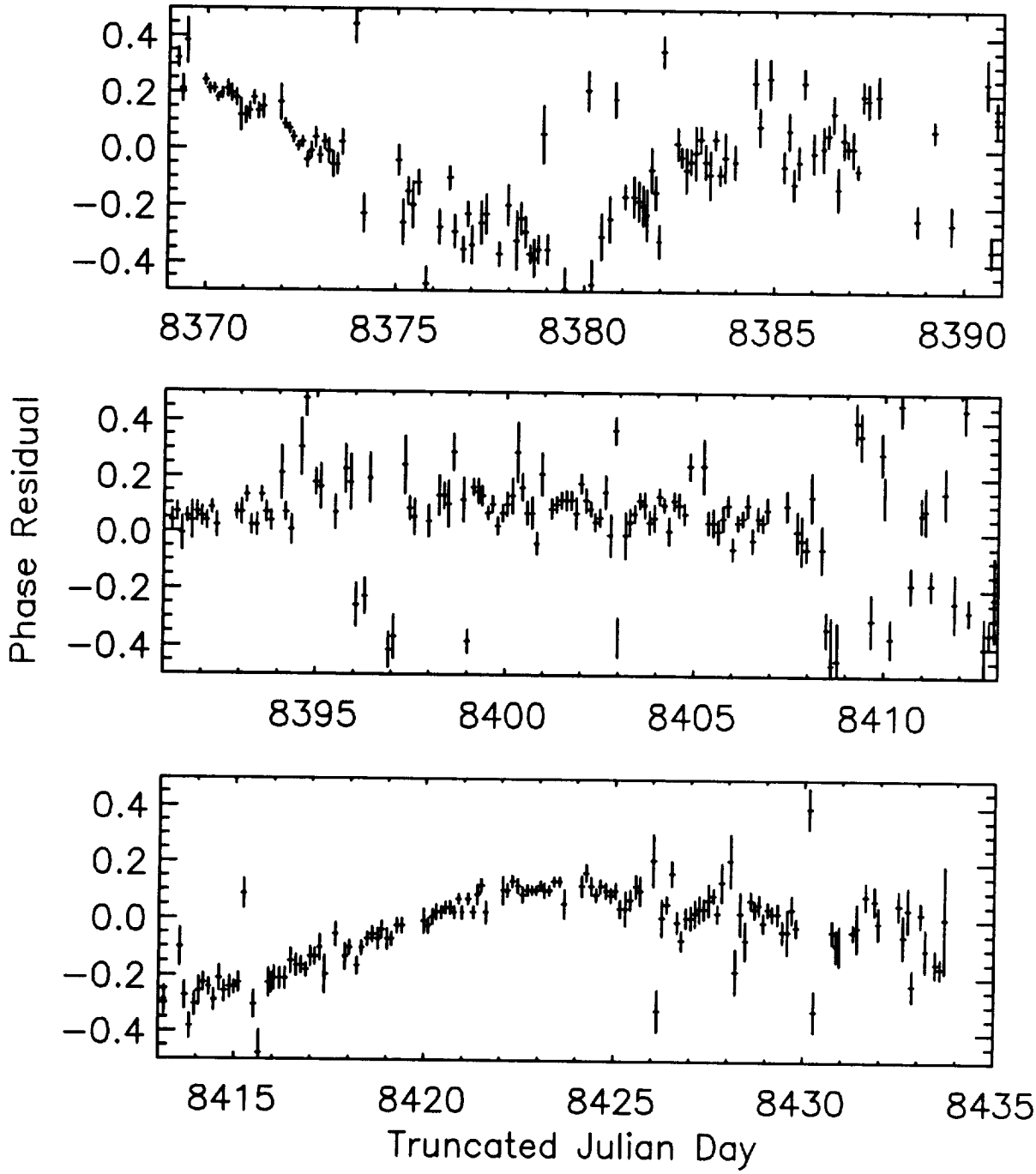

Figure 3. The phase residuals of Cen X-3 relative to the model given in equation (4) obtained by correlation of the folded rates with a pulse template.

to the model in equation (4) are shown in Figure 3. In order to eliminate the majority of intervals when no signal was detected, phase points are only shown if the intensity to intensity error ratios is greater than 1.5. The connectivity of the phase points is clear in the intervals of high intensity. In the intervals from TJD 8388 to 8390 and from TJD 8408 to 8413 however, it appear that no signal from Cen X-3 has been detected, and it is possible that the phase slips by a cycle. During the interval from TJD 8399 to 8407 the phase residuals appear to have a periodic signature which suggest a possible need for orbital parameter corrections. However the same signature is not present in the other intense intervals. A possible explanation that needs to be investigated is a variation of pulse shape with orbital phase within this or other intervals. The total observed phase in these three period of high intensity were fit with a quadratic model resulting in the periods and period derivatives given in Table 3.

Epoch (JD)	Period (sec)	Period Rate (10^{-10} sec/sec)
2448372.0	4.8199422(10)	2.06(29)
2448403.5	4.8201772(5)	−0.01(6)
2448421.0	4.8200583(3)	−1.00(3)

Table 3. Cen X-3 pulse period and derivative at selected epochs. Errors on the last digit are given in parentheses.

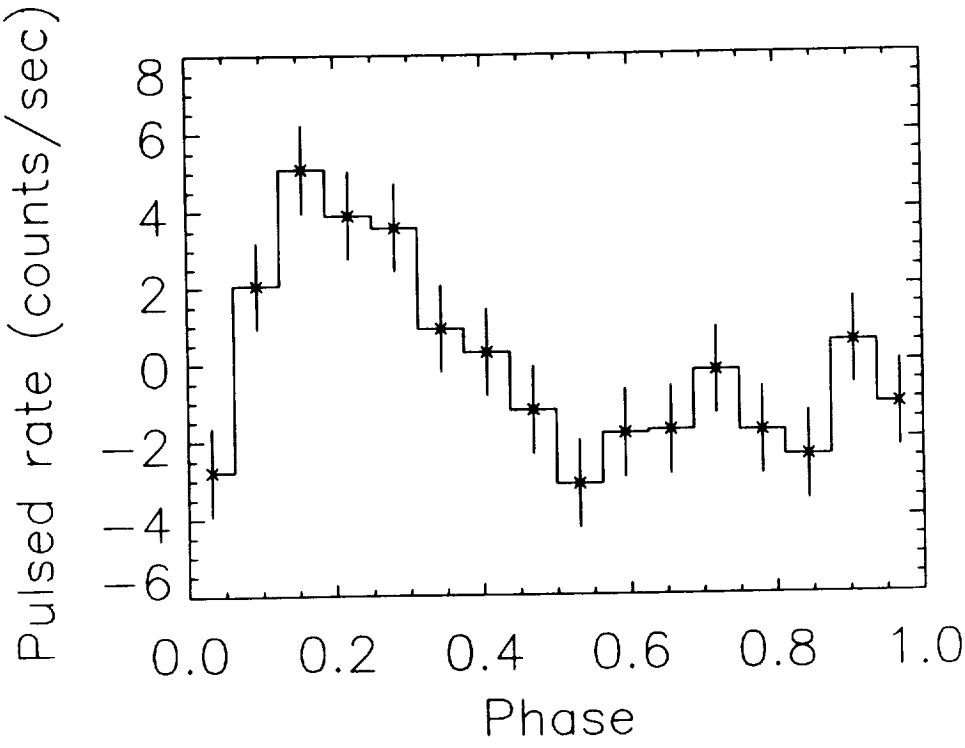

Figure 4. The light curve of Cen X-3 in the 20 to 60 keV energy band for the period TJD 8399-8407 based on folded-on-board data.

Folded-on-board Data Analysis

The folded-on-board data analysis is described by Wilson et al. in these proceedings. The analysis of the folded-on-board data from Cen X-3 is still in its early stages. An example of the light curves obtained from the folded on board data is shown in Figure 4. For this light curve data in the 20 to 60 keV range from the high intensity period from TJD 8399 to 8407 was folded using the period and period derivative given in Table 3. Data was included only for Cen X-3 orbital phases in the range from .1 to .9. The total accumulation time of the included data was 23369 seconds. Significantly greater pulse shape information is available in the folded-on-board data than in the DISCLA. However due to counting statistic the full hardware resolution of 64 phase bins is not useful and is not shown in the figure.

Conclusion

The uniqueness of BATSE from the standpoint of pulsar observation is its ability to view in all directions continuously. This ability makes BATSE an excellent instrument for the long term monitoring of x-ray pulsars. This is particularly true for the longer period pulsars which may be studied exclusively with the continuously available DISCLA and CONT data.

References

[1] R. Giacconi et al.,*Ap. J. (Letters),* **167,** L67, (1971).

[2] E. Schreier et al., *Ap. J. (Letters),* **172,** L79-L89, (1972).

[3] G. Fabbino and E. J. Schreier, *Ap. J.,* **214,** 235-244, (1977).

[4] M. van der Klis, J. M. Bonnet-Bidaud, and N. R. Robba, *Astron. Astrophys.,* **88,** 8-14, (1980).

[5] R. L. Kelly, S. Rappaport, G. W. Clark, and L. D. Petro, *Ap. J.,* **268,** 678-686, (1983).

[6] S. K. Howe et al., *Ap. J.,* **272,** 678-686, (1983).

[7] T. Murakami et al., *Ap. J.,* **264,** 563-567, (1983).

[8] F. Nagase et al., *Publ. Astron. Soc. Japan,* **36,** 667, (1984).

[9] H. Tsunemi, *Publ. Astron. Soc. Japan,* **42,** 456-460, (1989).

[10] M. Gil'fanov et al., *Pis'ma Astron. Zh.,* **15,** 675-685, (1989).

[11] M. Gil'fanov et al., *Pis'ma Astron. Zh.,* **17,** 108-115, (1990).

[12] G. J. Fishman et al., *GRO Science Workshop,* Goddard Space Flight Center, 1989.

[13] J. E. Deeter et al., *Ap. J.,* **93,** 877-889, (1987).

[14] Gerald J. Bierman, *Factorization Methods for Discrete Sequential Estimation,* Academic Press, San Diego, 1977.

144 SECOND PERIODIC FLUX VARIATIONS DURING X-RAY TURN-ON OF HERCULES X-1

D.A. Leahy[1], A. Yoshida[2], N. Kawai[2], M. Matsuoka[2]

[1]Dept. of Physics and Astronomy,
University of Calgary, Calgary, Canada T2N 1N4

[2]Institute of Physical and Chemical Research
Hirosawa, Wako, Saitama 351-01 Japan

ABSTRACT

Hercules X-1 is a well known bright binary X-ray pulsator. It has a 1.70-day orbital period, a pulsation period of 1.24 second, and a 35 day semi-periodic variability. Here we report the discovery of a new 144 second periodicity in the X-ray emission from Her X-1. The periodicity is seen in X-ray observations of Her X-1 by the LAC instrument on board the Ginga satellite during Aug.-Sept. 1988. The periodic flux variations occur during the time of X-ray turn-on at the beginning of a high-state of Her X-1, in the same time that a pre-eclipse dip also occurs. An analysis of the LAC spectra of Her X-1 during this period is also presented. Large changes in spectral shape occur associated with the dip.

1. INTRODUCTION

The 1.24 s X-ray pulsar Hercules X-1 was discovered by UHURU (Tananbaum et al. 1972). It is an eclipsing system with a 1.70-day orbit. The mass ratio and inclination have been determined by analysis of the optical pulsations (Middleditch and Nelson 1976). The orbital parameters have been accurately determined by analysis of arrival times of the X-ray pulses (e.g. see Deeter et al., 1991 and references therein). In addition the X-ray flux exhibits a regular variation with a 35 day period. This period is not well defined, but whether the variations are due to white noise acting on a precise period, or due to an inherent instability in the clock mechanism is not yet known (Ogelman, 1987).

Her X-1 has been studied in X rays with several previous satellite instruments. Pravdo et al. (1977) and Pravdo et al. (1978) study the OSO-8 high-state spectrum. Becker et al. (1977) find evidence in the OSO-8 spectra for variations in absorption during the turn-on, which are also seen in Tenma observations (Ohashi et al. 1984, Ushimaru et al. 1989). Soong et al. (1990)

report on HEAO-1 observations. Mihara et al. (1990) give unambiguous evidence for the cyclotron absorption feature near 35 keV. Mihara et al. (1991) study the low-state spectrum of Her X-1 and find a two component emission model is needed. Leahy et al. (1991) find a two component model is needed to represent the high state spectrum also.

We report a new periodic flux variation seen from Her X-1 during dipping periods. The results are based on analysis of observations by the GINGA satellite (Makino and the Astro-C Team, 1987) with the Large Area proportional Counter (LAC) instrument (Turner et al. 1989). We also report on variations in the spectrum of Her X-1 during the dipping period. The LAC had a total effective area of 4000 cm^2 and low intrinsic background, thus provided much superior data regarding the details of the X-ray time variability and spectrum of Her X-1 than previous experiments.

2. OBSERVATIONS AND ANALYSIS

The analysis presented here is based on observations of Her X-1 by the LAC on GINGA during the period 1988 Aug. 17 to Sept. 1. Her X-1 was in a low state during the Aug. 17 and 19 observations, and in the high state for the Aug. 28 and Sept. 1 observations. During the Aug. 28 observations extensive dipping behaviour was seen.

The LAC can observe in several data modes. We use modes MPC2h, which records 48 channel pulse-height spectra with 0.0625s time resolution and MPC3h, which records 12 channel pulse-height spectra with 0.0078s time resolution. The data were selected to pass several selection criteria. Then the detector background count rates in the different pulse height channels were determined using the method of Hayashida (Hayashida et al., 1989).

These background subtracted data were used to construct light curves in four energy bands and also a plot of softness ratio vs. time. The energy bands chosen were 0- 4,65 keV (low energy band), 4.65- 9.63 keV (iron line and iron edge band), 9.3- 14.0 keV (medium energy band), and 14.0- 37.2 keV (high energy band).

The light curves and softness ratio curves are shown in Figure 1 for the dipping state on Aug. 28. Light curves for parts of the low state data on Aug. 17 and of the high state data on Sept. 1 are shown in Figures 2a and 2b. The constancy of the count rates and of the softness ratio is apparent for the high state and low state data. This is in great contrast to the strong variability seen during the dipping period.

Inspection of Figure 1 suggests a regular variation of intensity. Visually there appears to be a period of about 70 s. The most significant variations are seen in the 0-4.65 and 4.65-9.3 keV energy bands. The entire data for Aug. 28 was combined and subjected to a period search using the epoch folding technique. This data spans the time period 16 hr 8 min 16.2 s to 19 hr 38 min 4.3 s UT (12588.1 s), with some large data gaps, giving a net observation time of 2383.5 s.

The resulting folded light curves from the epoch folding of the Aug. 28 data in the four energy bands are shown in Figure 3. The period of 143.6 seconds is highly significant- the reduced chisquared values for the four energy bands are 44.3, 53.1, 21.3 and 9.8, in order of low to high energy. There is a clear double peak in the folded light curves. The 143.6 s period is the period of maximum chisquared for both of the higher energy bands. For the two lower energy bands there is a nearby period (140.8 s) with slightly higher chisquared. However, the chisquared vs. period is affected by both the longer timescale dip modulation, and the presence of data gaps. The two higher energy bands are less affected by the dip modulation. The chisquared vs. period plots for these high energy bands more clearly indicate the correct period (see Figures 4a and b), giving strong evidence that the correct period for the flux variations is 143.6 s.

The data from the low state and from the high state were also epoch-folded. There were significant data gaps for the low-state and high-state data similar to those in the dipping-state data. There is no statistically significant period found for either the low-state or high state data. The chisquared vs. period curve for the low state data is shown in Figure 4c.

A spectral analysis for selected periods during the observation was also carried out. As reported by Leahy et al. (1991) only one two-continuum spectral model was found to adequately fit the data. The model consists of: an unabsorbed continuum (power-law-plus-cyclotron-absorption-line); an absorbed continuum of the same form; an iron emission line. The model has 10 parameters (P1 to P10):

POWL(1,2)*CYAB(3,4,5)*(1+P10*ABSM(6))+GAUS(7,8,9)

Here POWL and CYAB are given by:

$$POWL=P1\ E^{-P2}\quad CYAB=\exp\{-P3\ E^2/((E-P4)^2+P5^2)\}$$

CYAB is the function used to represent the cyclotron absorption feature seen in the spectrum of Her X-1 (Mihara et al. 1990, and references therein), however we use only the first cyclotron harmonic. ABSM is absorption by neutral gas of cosmic abundance with log of column density given by P6, and using the cross-section given by Morrison and McCammon (1983). GAUS is a Gaussian

function with area P7, center energy P8 and width (σ) P9. Figure 5 shows the results of fitting the two component model to the dip onset periods A, B and C of Figure 1.

3. DISCUSSION

The phenomenon of pre-eclipse dips for Her X-1 has been long established. The Ginga light curves, with their superior statistics, show the dipping phenomenon to be much more complex than apparent in previous observations. The well known dips correspond to periods B and C and period D and E in Figure 1, where the total count rate drops by factor of 4 or more, and lasting tens of minutes. However the Ginga data resolves new "minidips", which last about one minute. Two of these are clearly seen during period A, more are seen in periods G and H. Periods G and H also show that the dip can stay at an intermediate count rate for an extended period of time sometimes, in contrast to the sharp decrease seen in the transition between periods A and B.

A periodic flux variation has also been found in the Ginga data. Figure 3 shows this variation at the same 143.6 second period in all 4 energy bands. At this period a highly significant variation with a double peaked profile is seen, thus explaining the apparent 70 second period seen by visual inspection. The two maxima (and two minima) in the folded light curve are not separated by 0.5 in phase, consistent with the finding that there is no real 70 s period.

The 143.6 s periodicity occurs only during the dipping period and is not present in the other days' data. It is suggested here that the period is a Keplerian rotation period in the accretion disk and that the flux variation corresponds to periodic partial obscuration of the neutron star. For a 1.4 solar mass neutron star, this period corresponds to a distance of 5×10^9cm. This places the matter well within the Roche lobe of the neutron star, yet far outside the corotation radius or the Alfven radius. The reason that the disk matter would have an extent enough above the disk to obscure the neutron star at this particular radial distance is unclear.

Vrtilek and Halpern (1985) have reported a 108 s during dipping periods of Her X-1. We do not find any evidence of this phenomenon in the Ginga data, despite that the Ginga data should be more sensitive to such time variations.

The spectral analysis shows that, in contrast to previous work (except Mihara et al. 1991, Leahy et al, 1991), Her X-1 requires a two component spectral model to describe its X-ray spectrum. During the times when dips occur, the spectrum undergoes complex changes. However these can all be adequately modeled with the two-continuum model presented here. Figure 5 shows the spectra during onset of a major pre-eclipse dip (periods A, B and C of

Figure 1). The pre-dip spectrum (A) shows weak absorption. As the dip changes to its full decrease (from B to C) two changes occur: the unabsorbed component decreases in intensity and the amount of absorption of the absorbed component increases. Thus the dips are caused by thick cold matter and which is likely the same matter which has been detected in both the high-state and low-state spectra of Her X-1 (Leahy et al. 1991).

The pre-dip period A shows small dips which have not previously been reported, primarily due to the greatly increased sensitivity of the GINGA LAC compared to previous instruments. These "mini-dips" are very clear in the lowest energy light curve and in the plot of softness ratio (Band 1/ Band 3, Figure 1).

4. SUMMARY

The well known dips of Her X-1 have been shown to be more complex than apparent in previous observations. A new periodicity has been found which is only present during dipping periods.

The X-ray spectrum of Her X-1 has two continuum components- an unabsorbed component and a highly absorbed component. These two components are always present: during high, low and dipping states of Her X-1. The contribution of the absorbed and unabsorbed components and is highly variable during dips. The dips are caused by changes in the amount of unabsorbed continuum and in the amount of absorption.

REFERENCES

Becker, R. et al., 1977, Ap.J., 214, 879.
Deeter, J. et al., 1991, submitted.
Hayashida, K. et al., 1989, Publ. Astron.Soc.Japan, 41, 373.
Leahy, D., Matsuoka, M., Yoshida, A. and Kawai, N. 1991, to appear in Proceedings of the 22nd International Cosmic Ray Conference, Dublin, Aug. 11-23, 1991.
Middleditch, J. and Nelson, J. 1976, Ap.J., 208, 567.
Mihara, T. et al., 1991, to appear in Publ.Astron.Soc.Japan, Vol.43, no.3.
Mihara, T. et al., 1990, Nature, 346, 250.
Morrison,R and McCammon,D 1983, Ap.J., 270, 119.
Ohashi, T. et al., 1984, Publ.Astron.Soc.Japan, 36, 719.
Ogelman, H. 1987, Astron. Ap., 172, 79.
Pravdo,S., et al., 1977, Ap.J. Lett., 215, L61.
Pravdo,S., et al., 1978, Ap.J., 225, 988.
Soong, Y. et al., 1990, Ap.J., 348, 641.
Tananbaum, H., et al. 1972, Ap.J. Lett, 174, L143.
Ushimaru, N. et al. Publ.Astron.Soc.Japan, 41, 441.
Vrtilek, S. and Halpern, J. 1985, ApJ, 296, 606.

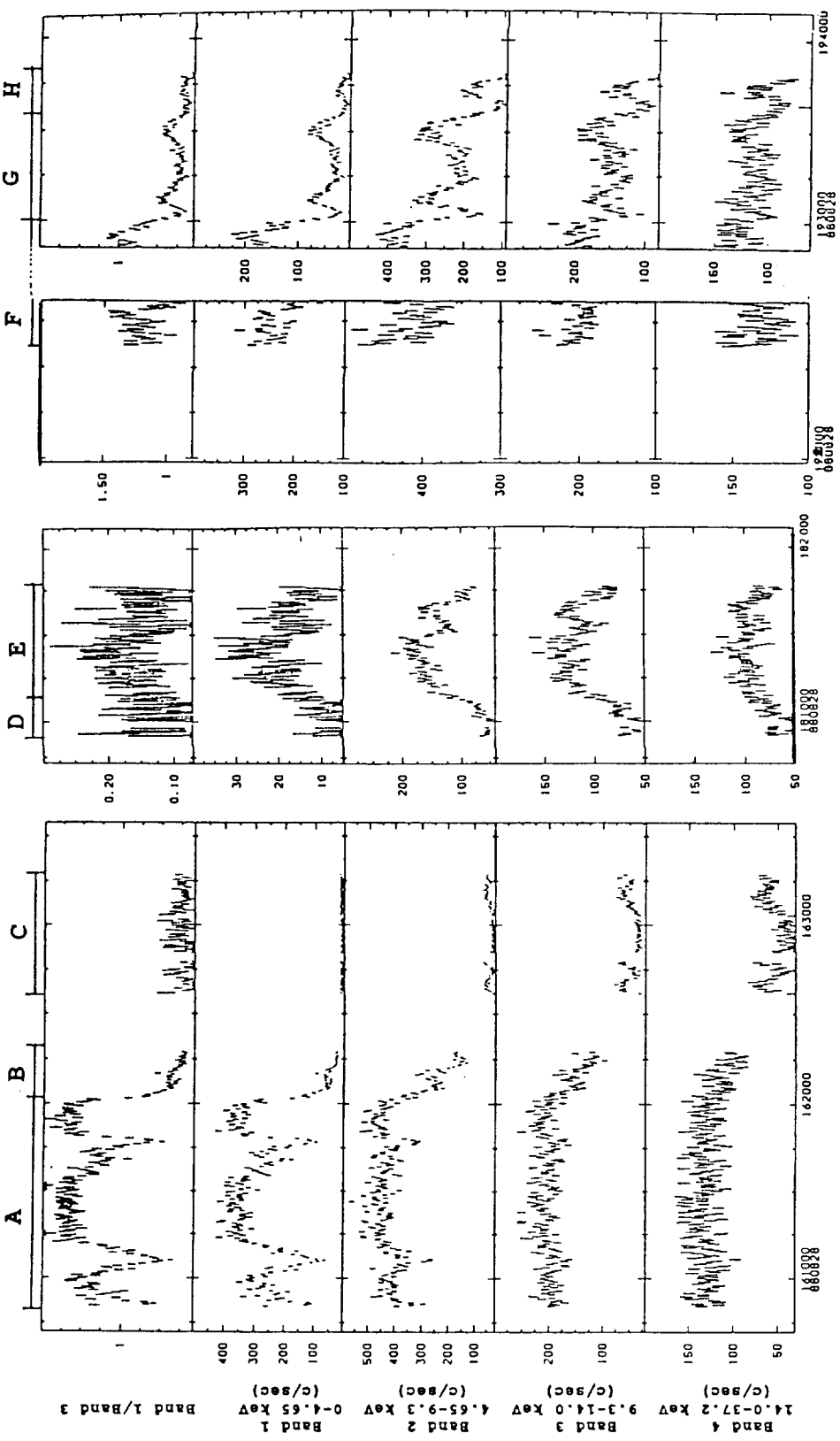

FIGURE 1. Light curves during the dipping state on 1988.08.28 in four energy bands.

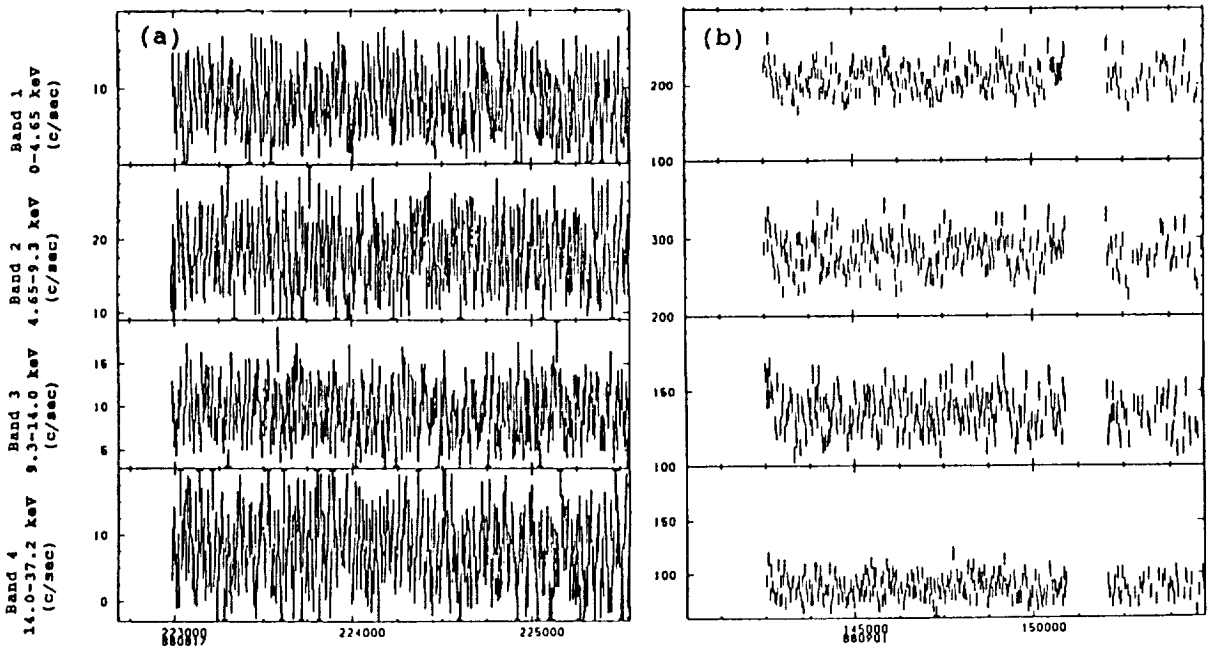

FIGURE 2. Sample light curves in four energy bands during: (a) the low state on 1988.08.17; (b) the high state on 1988.09.01.

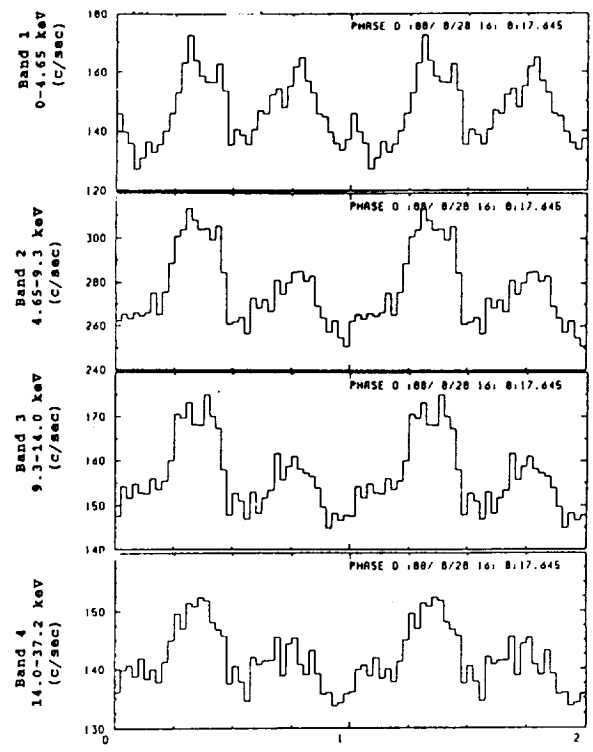

FIGURE 3. Folded light curve of 1988,08,28 data at the period of 143.6 s, in four energy bands.

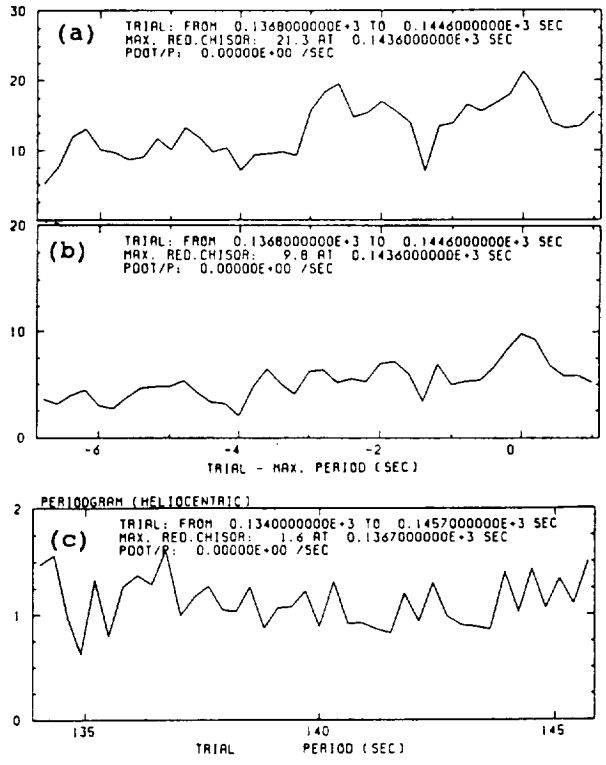

FIGURE 4. Chisquared vs. period for: (a) band 3 and (b) band 4 on 1988.0828; (c) for bands 1 and 2 on 1988.08.17.

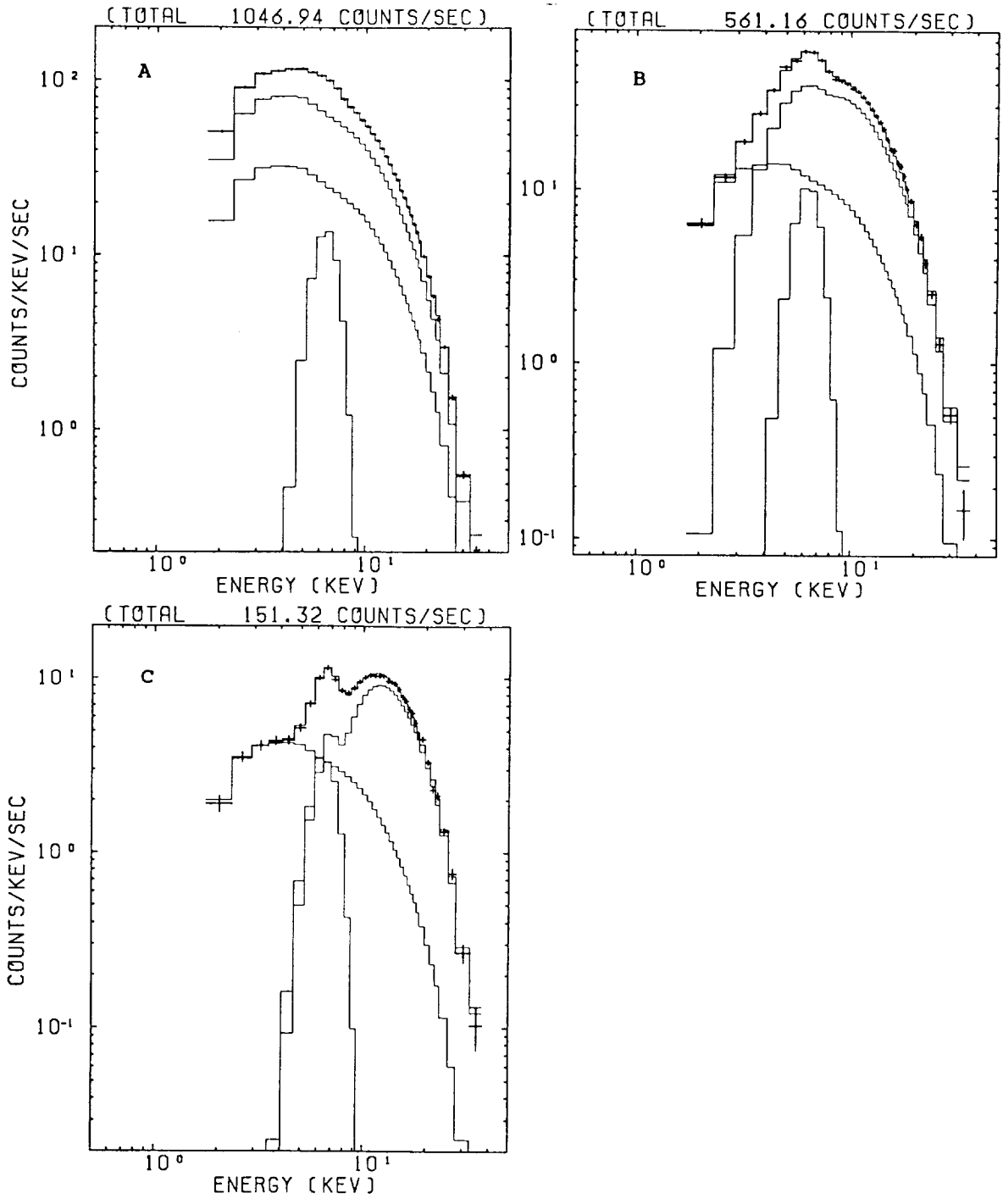

FIGURE 5. Pulse height spectra (right panel, crosses), with best-fit model spectra (histogram) for intervals A, B and C (see Figure 1).

COMPTON BACKSCATTERED ANNIHILATION LINE EMISSION A NEW DIAGNOSTIC OF ACCRETING COMPACT SOURCES

RICHARD E. LINGENFELTER
Center for Astrophysics and Space Sciences, University of California, San Diego,
La Jolla CA 92093 USA

AND

XIN-MIN HUA
Space Astrophysics Laboratory, Institute for Space and Terrestrial Science,
Concord, Ontario, L4K 3C8 Canada

ABSTRACT

We show that Compton scattering of 511 keV electron-positron annihilation radiation produces a line-like feature at $\sim$ 170 keV from backscattered photons. Assuming a simple model of an accretion disk around a compact source, we explore the spectrum of Compton scattered annihilation line emission for a range of observing angles and disk opacities and find that the line-like feature is produced under a wide range of conditions. We further show that such Compton backscattering of annihilation line emission from the inner edge of an accretion disk could account for the previously unidentified 170 keV line emission and high energy continuum observed[1-3] from a variable, compact source, or sources, of annihilation radiation near the Galactic Center. Identification of the observed 170 keV line as an annihilation line reflection feature provides strong new evidence that the source of the emission is an accreting compact object. Further study of these features in existing spectra and in forthcoming GRO observation of these and other sources can provide unique new diagnostics of the innermost regions of accretion disks around compact objects.

INTRODUCTION

Compton scattering of x-rays and gamma rays has been studied in a variety of astrophysical sources. Comptonization of x-rays by plasma clouds has been studied in compact sources[4]. Compton reflection of the hard x-ray and gamma-ray continuum has been studied in solar flares[5] and in accretion disks around compact objects[6]. Compton attenuation of gamma-ray line emission has been studied in solar flares[7] and in supernovae[8,9]. And Compton "tails" of gamma-ray lines have been studied as a diagnostic in solar flares[10], and as a continuum source in supernovae[8,11] and an alternative to orthopositronium emission in the variable annihilation radiation source in the direction of the Galactic center[12,13].

We have recently pointed out[14] the astrophysical importance of Compton backscattering of gamma-ray lines that can produce *line-like reflection features* at lower energies. These Compton backscattered features are well-known in the laboratory, but their astrophysical significance had not been discussed previously. We considered, by way of illustration, the Compton backscattering of the 511 keV electron-positron annihilation line which produces a line-like feature at $\sim$ 170 keV. We studied the Compton scattering of 511 keV photons because they are the most nearly ubiquitous of any astrophysical gamma-ray line photons, and because 170 keV line emission has, in fact, been observed[1-3] to accompany the intense 511 keV line emission from the direction of the Galactic center.

Here we briefly discuss the generation of line-like features by Compton backscattering of the 511 keV annihilation line in the context of an accreting black hole source of the variable annihilation line emission in the region near of the Galactic center.

COMPTON BACKSCATTERING OF THE ANNIHILATION LINE

The energy of the Compton-scattered photon relative to the initial photon energy is $r = E'_\gamma/E_\gamma = 1/(1+\alpha-\alpha\cos\phi)$, where $\alpha = E_\gamma/m_ec^2$ and ϕ is the scattering angle. The energy distribution of the Compton-scattered photons is

$$f(r) \propto \left[r - 1 + \frac{1}{r} + \frac{(\alpha r + r - 1)^2}{\alpha^2 r^2}\right]$$

for $1/(2\alpha+1) \leq r \leq 1$, corresponding to scattering angles $180° \geq \phi \geq 0°$, and $f(r) = 0$ for other values of r. This distribution, which rises steeply at the lowest energies and then cuts off sharply at the 180° backscattered energy of $r = 1/(2\alpha+1)$, produces a line-like feature just above the minimum energy. This feature can be seen in Figure 1, where we show the energy distribution of Compton scattered 511 keV annihilation radiation photons. For 511 keV photons $\alpha = 1$ and the scattered photons have energies $1/3 \leq r \leq 1$, or 170 keV $\leq E'_\gamma \leq$ 511 keV, so that the scattered photon energy distribution is simply $f(r) \propto (r + 3 - 3/r + 1/r^2)$. As can also be seen in Figure 1, the backscattered photons ($90° \leq \phi \leq 180°$) are compressed into a relatively narrow energy range of 1/6 of 511 kev, while the forward scattered photons are spread over an energy range of 1/2 of 511 keV, three times larger.

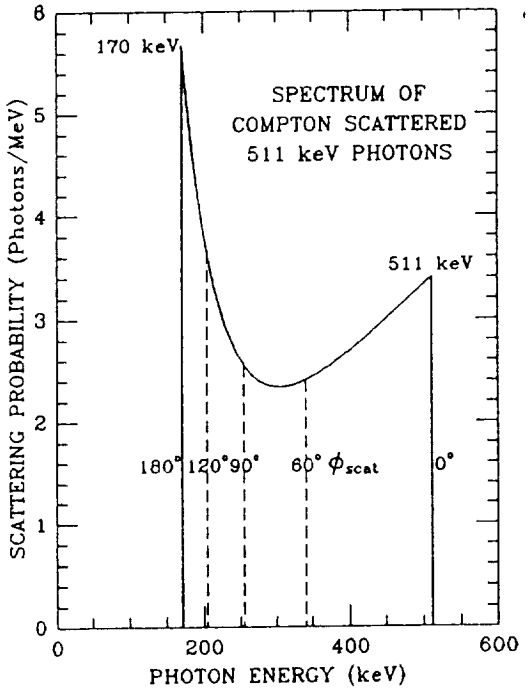

Figure 1. The spectrum of Compton scattered 511 keV photons as a function of the scattered photon energy and scattering angle, showing the line-like backscattered feature at 170 keV.

The Compton scattering distribution shown in Figure 1, of course, is only for singly scattered line photons and multiple scattering produces a broader spectrum extending down to much lower energies. To study the full spectrum resulting from multiple Compton scattering of line photons, we have made a series of Monte Carlo simulations. In all cases we assumed an isotropic, monoenergetic source of 511 keV annihilation line photons, and allowed them to Compton scatter on cold ($kT \ll m_ec^2$) electrons in a simple, uniform density, gaseous disk. In particular, we considered a disk in a cylindrical coordinate system with linear dimensions defined in terms of the Compton scattering optical depth τ at 511 keV, equivalent to 3.5×10^{24} electrons cm^{-2}. The disk was assumed to lie in a plane normal to the z axis with a thicknesses in the z direction equal to τ and a radius $\gg \tau$. In order to approximate the inner edge of an accretion disk around a compact object, we considered a cylindrical hole in the disk centered at the origin with its axis in the z direction normal to the plane of the disk. The size of the hole is defined by an opening angle θ_o which is the zenith angle of the inner edge of the disk measured with respect to the axis of the cylinder. Thus, the radius of the hole is equivalent to $\frac{1}{2}\tau\tan\theta_o$ and the limiting case of $\theta_o = 0°$ is simply the uniform disk without a hole. We have ignored disk rotation in this simple model. We also assumed for simplicity that the source of the 511 keV photons is located at the origin in the center of the hole. Thus the emerging unscattered 511 keV line intensity, as a function of μ the cosine of the observing angle θ, is equal to $1/2\pi$ for $\theta < \theta_o$, and

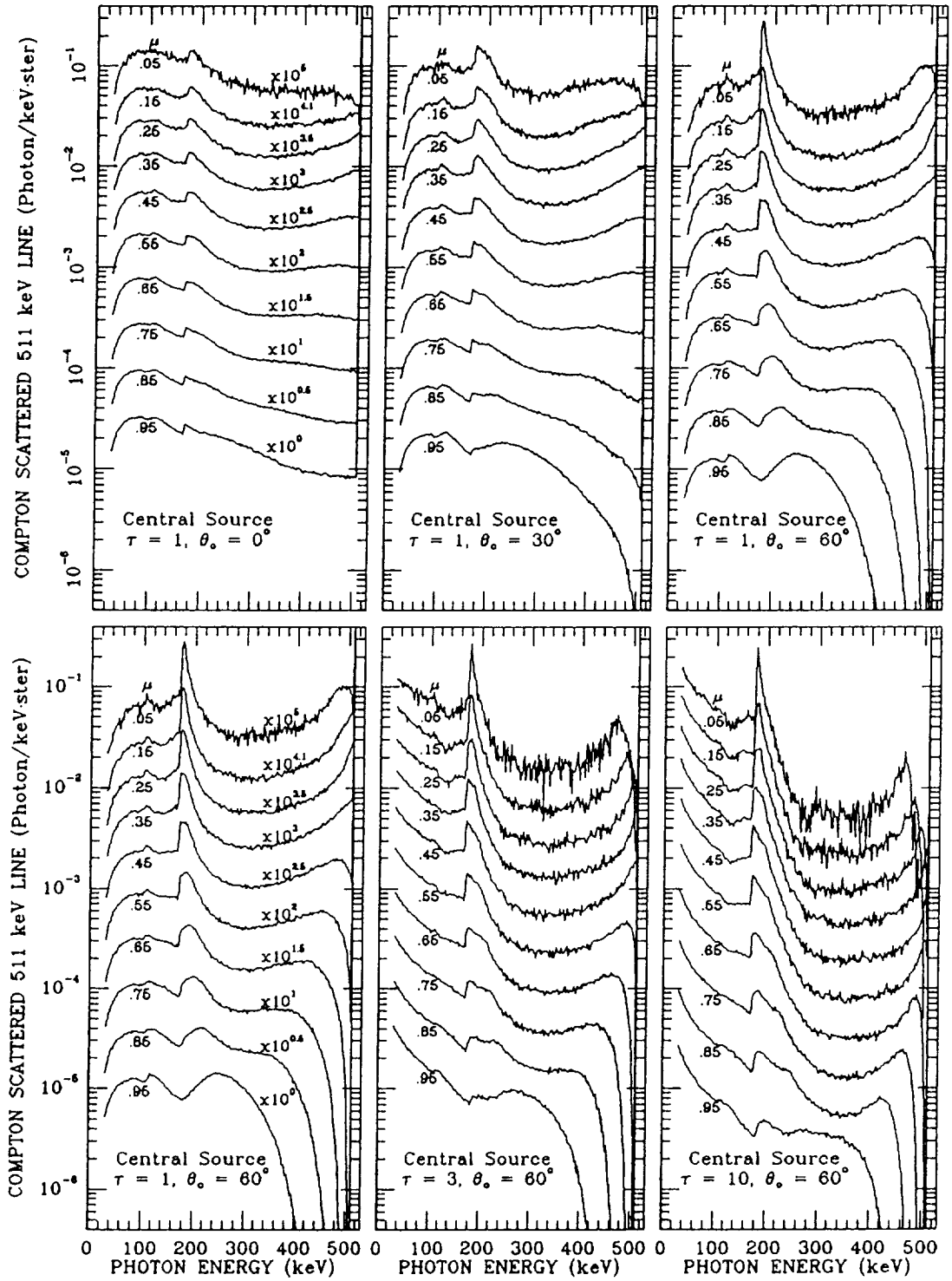

Figure 2. Monte Carlo spectra of the line-like reflection feature at 170 keV and the associated continuum from Compton scattered 511 keV photons in a uniform disk with varying opacities, τ, and central hole opening angles, θ_o, showing the effect of disk opacity and geometry. All of the spectra are normalized to one isotropically emitted 511 keV photon, and individual spectra are displaced from one another by a factor of $10^{0.5}$ or more for clarity.

$$f(\mu) = \frac{1}{2\pi} \exp\left[-\frac{\tau}{2}\left(\frac{1}{\mu} - \frac{\tan\theta_o}{(1-\mu^2)^{1/2}}\right)\right], \text{ for } \theta > \theta_o.$$

The resulting Compton scattered 511 keV line spectra determined for a range of opacities, τ, and opening angles, θ_o, are shown in Figure 2, as a function of μ the cosine of the observing angle. As can be seen, there is a significant singly backscattered line-like feature at 170 keV, or higher energies, in the Compton scattered 511 keV line spectra for each of the disk cases as seen from nearly any angle of observation. The strength, mean energy and shape of this feature all depend on the opacity and the geometry of the disk, i.e. the opening angle of the central hole, and the angle of observation with respect to the disk.

In particular, we see from the upper panels of Figure 2 for large observing angles (small μ), near the plane of the disk, that the 170 keV feature becomes more intense and narrower as the opening angle of the central hole increases. Because the reflecting matter behind the inner edge of the disk subtends a smaller solid angle from the source as the opening angle increases, the scattering angles for observable singly scattered photons are concentrated into a narrower band around 180° and the observable energy band above 170 keV is likewise narrower. Correspondingly at smaller observing angles (larger μ), as θ become less than θ_o, an increasing opening angle concentrates the reflecting matter more nearly perpendicular to the line of sight and there is no reflecting matter directly behind the source. Thus, the peak energy of the reflection feature is shifted up toward 255 keV as scattering angles around 90° dominate the observable singly scattered photon emission, and there is a significant depression in the observable spectrum around 170 keV. This shift in the energy of the peak of the reflection feature can serve as a diagnostic of the observing angle.

Considering the effect of disk opacity, we see from the lower panels of Figure 2, that for large observing angles the 170 keV feature also becomes narrower as the opacity of the disk increases, since that further enhances the singly backscattered photons by attenuating the flux of photons with scattering angles around 90° relative to those around 180°. Because the scattering probability for photons moving away from the observer is already close to unity for large observing angles, increasing the disk opacity can not further increase the peak intensity of the 170 keV feature. For small observing angles, however, increasing the disk opacity does attenuate the flux in the singly scattered feature around 255 keV from scattering around 90°.

In addition to the backscattered feature, we see that at higher energies, just below 511 keV, there is a conspicuous forward scattering peak, which is also a characteristic signature of Compton scattering. As we can see, especially in the lower panels of Figure 2, depending upon the angle of observation, the forward scattered emission does not always extend all the way up to 511 keV. This can happen either because there is no matter close to the line of sight to scatter the line photons, as is the situation for observing angles less than the opening angle of the central hole, or because there is so much scattering matter in the line of sight that the source is completely obscured, as is the situation for large observing angles, closest to the plane of the disk.

We compare these calculated spectra with the observations of the annihilation radiation and accompanying 170 keV line from the direction of the Galactic center.

THE 170 KEV LINE FROM THE GALACTIC CENTER REGION

Positron annihilation radiation in the 511 keV line and in the apparent three-photon orthopositronium continuum has been observed from the direction of the Galactic center since 1970. An analysis of these observations suggests[15] that there are two sources of the emission: a steady,

diffuse interstellar source with a broad distribution in galactic longitude, and a variable, compact source, quite possibly an accreting black hole near the Galactic center.

This emission was first measured by Haymes et al.[23] with low resolution NaI spectrometers in a series of three balloon flights in the early 1970s. However, it was not until the fall of 1977 that a narrow (FWHM < 3.2 keV) line was clearly identified at an energy of 510.7±0.5 keV together with an apparent orthopositronium continuum by Leventhal, MacCallum and Stang[1] with a balloon-borne high resolution Ge spectrometer.

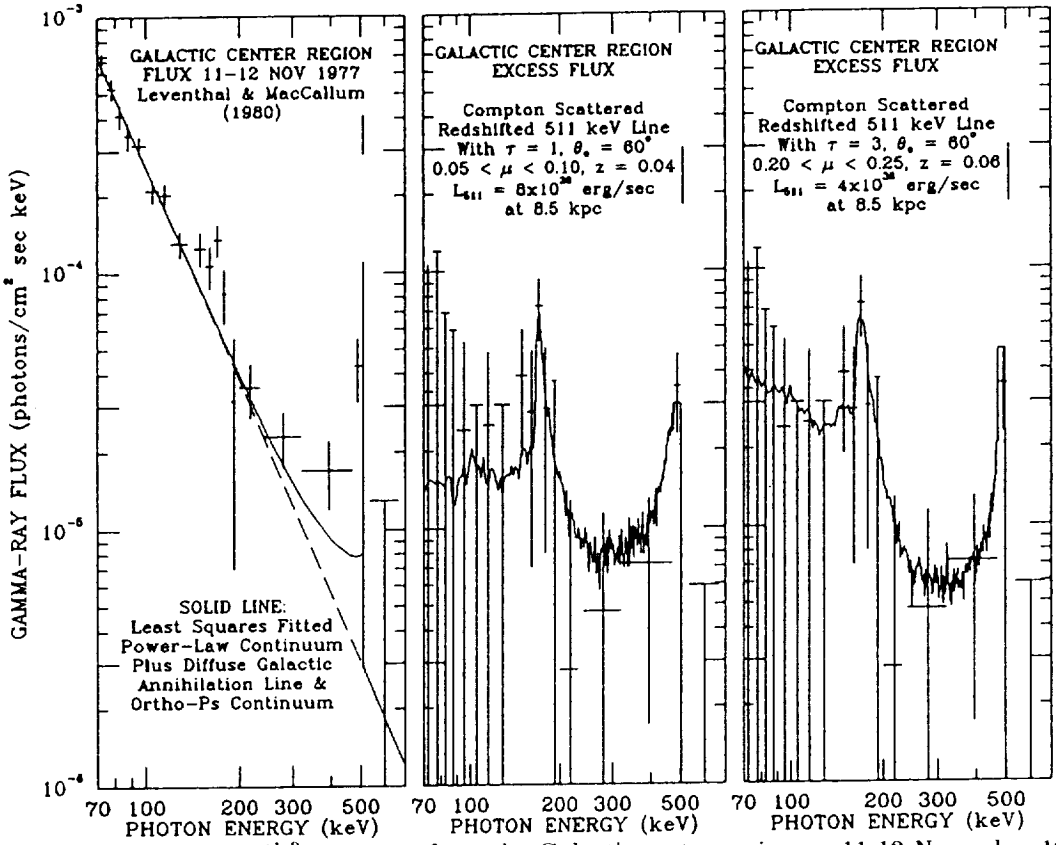

Figure 3. The observed[1,2] spectrum from the Galactic center region on 11-12 November 1977 (left panel), showing the 170 keV and 511 keV lines and other excess flux above a best-fit, low-energy power-law spectrum and the diffuse Galactic annihilation line and orthopositronium continuum flux expected for the detector field of view. This excess flux is also shown separately (central and right panels) with calculated spectra of Compton scattered, slightly-redshifted 511 keV line photons isotropically emitted in a hole of opening angle $\theta_o = 60°$ in a uniform disk. The calculated spectra are for disk opacities τ of 1 and 3, and observing angle cosines μ of 0.05–0.1 and 0.20–0.25, normalized to 511 keV annihilation line luminosities of 8×10^{38} and 4×10^{38} erg s^{-1}, redshifted by 0.04 and 0.06, respectively.

This observation was made during a period < 1977–1979 > when the annihilation line emission from the direction of the Galactic center was significantly higher than average and the variable, compact source was active. It was during this same observation that they[1,2] also detected an unidentified "candidate" line at 170 keV with a width (FWHM) of 12 keV and a flux of $(7.4 \pm 1.8) \times 10^{-4}$ photons cm^{-2} s^{-1} (see Figure 3, left panel). This 170 keV line flux was roughly 60% of that in the narrow 511 keV line, $(1.22 \pm 0.22) \times 10^{-3}$ photons cm^{-2} s^{-1}, seen at the same time. Although the 170 keV line was detected at the 4.1σ or 99.998% confidence level, and no similar negative (presumably spurious) features were found in the spectrum at $> 3.5\sigma$, two other positive

unidentified "candidate" lines were also detected at 1611 keV with a width of 10 keV and 3700 keV with a width of 500 keV at 4.9 and 3.9σ, respectively. Lacking a "reasonable identification" of any of these lines, Leventhal and MacCallum[2] cautioned against taking them seriously until they were confirmed by other observations.

We suggested[14] that a reasonable identification of the 170 keV line can be found in Compton backscattering of the 511 keV annihilation line. Moreover, there is now at least one confirming observation of such a line in spectra of the Galactic center region. Matteson et al.[3] observed a line-like feature at 170 keV at the several σ level of significance with a high resolution Ge spectrometer during a balloon flight in May of 1989. There are also suggestions of features in the range from 150 to 250 keV in other published[17–19] spectra. Clearly these and the future GRO observations of the Galactic center region should be reexamined for evidence of such a feature.

In order to identify the 170 keV line observed from the direction of the Galactic center as Compton backscattered annihilation radiation, however, it is necessary to assume a small gravitational redshift. Such a redshift should in fact be expected, if the backscattered feature arises from reflection near the inner edge of an accretion disk around a compact object. Moreover, it shows that the 170 keV line could not originate locally from Compton backscattered annihilation radiation in either the instrument or the earth's atmosphere.

The need to assume a redshift for a Compton backscattering identification of the line arises from the fact that a Gaussian fit to the observed[2] line was centered at 170 keV with a uncertainty of < 0.5 keV and a width (FWHM) of 12 keV, whereas the backscattered feature is cut off sharply below 170.3 keV and such a width would require the effective center of the feature to be shifted higher in energy by $\sim$ FWMH/2, or $\sim$ 6 keV. Thus, if the observed 170 keV line is Compton backscattered 511 keV line emission, the Compton spectrum and the annihilation line must be redshifted by that amount, which would correspond to a $z \sim 6/170 \sim 0.04$. Such a redshift can be produced gravitationally, if the source of the annihilation radiation is located at a distance of $\sim$ 12 Schwarzschild radii from a compact object, which would be consistent with emission and reflection near the inner edge of an accretion disk. This, of course, requires that any observable 511 keV annihilation line photons, coming directly from the source, would be redshifted down by $\sim$ 18 keV to an energy of $\sim$ 493 keV.

Thus, the observed narrow 511 keV line could not be the source of the backscattered photons, but as was previously pointed out[16,20] these photons could not have come from positron annihilation directly in the compact source. That is because the line center of 510.7$\pm$0.5 keV determined by Leventhal, MacCallum and Stang[1] only allowed a redshift of < 1.3 keV from the rest energy of 510.9991 keV at the 2σ level, and the subsequent measurement by Riegler et al.[21] in 1979 reduced that to < 0.6 keV. Therefore, even if the diffuse Galactic contribution to the observed line were centered exactly at the rest energy, the annihilation region in which the variable component of the narrow line originates could not be closer than $\sim$ 300 Schwarzschild radii from the compact object. Moreover, if the annihilation region is in a surrounding accretion disk, the observed[1,2] line width, FWHM < 3.2 keV, would not allow it to be closer than $\sim 10^5$ Schwarzschild radii from the compact object, because of Doppler broadening by the Keplerian velocities.

A redshifted annihilation line from the compact source at an energy of $\sim$ 493 keV would lie right in the middle of the data bin just below the 511 keV line in the spectrum of Leventhal, MacCallum and Stang[1,2], shown in Figure 3. The flux of $(1.4 \pm 0.4) \times 10^{-3}$ photons cm^{-2} s^{-1} in this band from 476 to 509 keV is actually larger than that in the narrow 511 keV line and it seems to be quite anomalous, as we shall discuss further below. This flux is also roughly twice that in the 170 keV feature. Such emission may also have contributed to the redshift of the annihilation

line observed by Haymes et al.[17] in their first two observations with a low resolution spectrometer.

As can be seen in the left panel of Figure 3, there is a strong power-law continuum underlying all of these features. However, the contribution of the variable source of annihilating positrons to this hard x-ray and gamma-ray continuum is not known, because there are also several highly variable hard x-ray sources[22-23] within the 15° instrumental field of view. But, since we are interested in the non-power-law components of the spectrum, we can simply subtract a best-fit power-law from the observed spectrum. We find that the least squares fit to the spectrum below 135 keV is a power law of $(2.6 \pm 0.1) \times 10^{-4}(E/100\text{keV})^{-2.8\pm0.2}$ photons cm^{-2} s^{-1} keV^{-1}. To this power-law continuum, we also add the diffuse galactic 511 keV line and orthopositronium continuum fluxes expected for the instrumental field of view of 15°, assuming a diffuse galactic 511 keV line flux of $(1.5 \pm 0.3) \times 10^{-3}$ photons cm^{-2} s^{-1} per radian of galactic longitude[15,24-25] and a diffuse galactic positronium annihilation fraction[26] of $0.89^{+0.10}_{-0.06}$.

Comparing the observed flux from the Galactic center region with the sum of the low energy power-law continuum and the diffuse galactic annihilation radiation, we clearly see that there is a significant excess flux not only around 170 keV and in the narrow 511 keV line already noted by Leventhal and MacCallum[2], but also in that seemingly anomalous energy band from 476 to 509 keV, which we suggest includes both redshifted 511 keV line and forward scattered photons from the compact source. The 33 keV width of this data band limits the thermal broadening of the redshifted 511 keV line to a temperature of $< 1.6 \times 10^7$ K, assuming direct annihilation with hot electrons[27].

The excess flux alone is shown in the central and right panels of Figure 3, with the additional uncertainties in both the low energy power-law and the diffuse annihilation radiation included in the error bars. Comparing this excess flux with the calculated Compton scattered 511 keV line spectra from the simple accretion disk model discussed above, we see that such emission can in fact account not just for the 170 keV line-like feature, but for all of the rest of the excess flux, as well. Although we do not attempt to explore the full range of possible spectral fitting here, because that is beyond the scope of this paper, these two examples clearly show that Compton scattered 511 keV line emission can in fact give a good fit to the observations. They also allow us to explore some of the constraints on the disk opacity, opening angle and viewing angle that can be set by the observations, and they give a measure of the gravitational redshift and 511 keV line luminosity that are required to fit the observations. We plan much more detailed studies of the observations with more realistic accretion disk models.

SUMMARY

We have shown that Compton scattering of 511 keV electron-positron annihilation radiation produces a line-like reflection feature at $\sim$ 170 keV from backscattered photons. We have further shown that such Compton backscattering of slightly redshifted annihilation line emission from the inner edge of an accretion disk can account for the 170 keV line emission and higher energy continuum observed[1,2] together with the 511 keV annihilation radiation from the direction of the Galactic center. Although the identification of the observed 170 keV line as Compton backscattered annihilation radiation requires a small redshift of 0.04 to 0.06, such a redshift should in fact be expected, if the backscattered feature arises from reflection near the inner edge of an accretion disk around a compact object. Moreover, such a redshift shows that the 170 keV line could not originate locally from Compton backscattering of annihilation radiation in either the instrument or the earth's atmosphere.

Identification of the 170 keV line as Compton backscattered 511 keV line emission provides direct new evidence for an accreting compact source in the direction of the Galactic center, because the diffuse Galactic line emission could not generate such a reflection feature at the observed intensity.

As this example clearly suggests, study of these features in existing spectra and in forthcoming GRO observation of these and other sources can provide unique new diagnostics of the innermost regions of accretion disks around compact objects. Moreover, line-like reflection features from Compton backscattering of other nuclear line emission as well, could also be an important new tool for studying high energy processes in many other astrophysical sources.

Acknowledgements. We thank NASA for financial support under grant NAGW 1970 and the Province of Ontario for support at ISTS. The calculations were carried out on a SUN at ISTS and a VAX at UCSD.

REFERENCES

1. M. Leventhal, C. J. MacCallum and P. D. Stang, *Ap. J. (Letters),* **225,** L11 (1978).
2. M. Leventhal and C. J. MacCallum, *Ann. N. Y. Acad. Sci.,* **336,** 248 (1980).
3. J. L. Matteson, et al. in *Gamma-Ray Line Astrophysics,* ed. P. Durouchoux and N. Prantzos, (New York: Am. Inst. Phys., 1991). p. 45
4. R. A. Sunyaev, and L. G. Titarchuk, *Astron. Ap.,* **86,** 121 (1980).
5. T. Bai and R. Ramaty, *Ap. J.,* **219,** 705 (1978).
6. T. R. White, A. P. Lightman, and A. A. Zdziarski, *Ap. J.,* **331,** 939 (1988).
7. X.-M. Hua and R. E. Lingenfelter, *Solar Phys.,* **107,** 351 (1987).
8. A. Burrows and L. S. The, *Ap. J.,* **360,** 626 (1990).
9. K. W. Chan and R. E. Lingenfelter, *Ap. J.,* **368,** 515 (1991).
10. W. T. Vestrand, *Ap. J.,* **352,** 353 (1990).
11. P. A. Pinto and S. E. Woosley, *Ap. J.,* **329,** 820 (1988).
12. D. J. Forrest, in *The Galactic Center,* ed. G. R. Riegler and R. D. Blandford (New York: Am. Inst. Phys., 1982) p. 160.
13. L. Bildsten and W. H. Zurek, *Ap. J.,* **329,** 212 (1988).
14. R. E. Lingenfelter and X. M. Hua, *Ap. J.,* **381,** in press (1991).
15. R. E. Lingenfelter and R. Ramaty, *Ap. J.,* **343,** 686 (1989).
16. R. E. Lingenfelter and R. Ramaty, in *The Galactic Center,* ed. G. R. Riegler and R. D. Blandford (New York: Am. Inst. Phys., 1982) p. 148.
17. R. C. Haymes, et al., *Ap. J.,* **201,** 593 (1975).
18. W. S. Paciesas, et al., *Ap. J. (Letters),* **260,** L7 (1982).
19. G. R. Riegler, et al., *Ap. J. (Letters),* **294,** L13 (1985).
20. R. E. Lingenfelter and R. Ramaty, in *The Center of the Galaxy,* ed. M. Morris, Dordrecht: Kluwer Academic, p. 587 (1989).
21. G. R. Riegler, et al., *Ap. J. (Letters),* **248,** L13 (1981).
22. J. L. Matteson, in *The Galactic Center,* ed. G. R. Riegler and R. D. Blandford, New York: Am. Inst. Phys., p. 109 (1982).
23. A. M. Levine, et al., *Ap. J., Supp.,* **54,** 581 (1984).
24. G. H. Share, et al., *Ap. J. (Letters),* **358,** L45 (1990).
25. G. H. Share, et al., *Ap. J.,* **326,** 717 (1988).
26. M. J. Harris, et al., *Ap. J.,* **362,** 135 (1990).
27. N. Guessoum, R. Ramaty and R. E. Lingenfelter, *Ap. J.,* **378,** 170 (1991).

DETECTION AND PERIOD MEASUREMENTS OF GX1+4 AT HARD X-RAY ENERGIES WITH THE SIGMA TELESCOPE

Ph Laurent, L. Salotti, F. Lebrun, J. Paul
Service d'Astrophysique, CEN Saclay, 91191 Gif sur Yvette Cedex, FRANCE
M. Denis, D. Barret, E. Jourdain, J.P. Roques
Centre d'Etude Spatiale des Rayonnements, 9 ave du colonel Roche, 31029 Toulouse Cedex, FRANCE
E. Churazov, M. Gilfanov, R. Sunyaev, A. Diachkov, N. Khavenson, B. Novickov, I. Chulkov, A. Kuznetzov
IKI, Space Research Institute, Profsoyouznaya, 84/32, Moscow, 117296, USSR

ABSTRACT

The galactic Low Mass X-ray Binary GX1+4 has been detected by the coded aperture hard X-ray/gamma-ray SIGMA telescope during the February/March/April 1991 observations of the galactic center regions. The source, whose emission varied during the survey of a factor greater than 40 %, reached a maximum luminosity in the 40-140 energy range of 1.03 10^{37} erg s^{-1} (D=8.5 kpc), thus approaching the emission level of the 1970-1980 high state. 2 minute flux pulsations have been detected on March 22 and on March 31/ April 1. Comparison with the last period measurements shows that the current spin-down phase of GX1+4 is ending. Concerning the proposed association of this source with the galactic center 511 keV annihilation emission, upper limits have been derived.

1 INTRODUCTION

GX1+4 is the X-ray pulsar nearest to the galactic center. It was discovered first at high energies (E>20 keV) by the MIT Balloon Group in 1970 [1] and later identified in the X-ray band (2-10 keV) with the source 4U1728-24 [2]. X-ray pulsations of about 2 minutes period were interpreted as the spin signature of a highly magnetized neutron star accreting matter from a normal companion. During all the 1970's GX1+4 maintained an average X-ray emission level of 100 mCrab that, for d=8 kpc, gives a typical luminosity of 10^{37}-10^{38} erg s^{-1}, while the pulsation period decreased steadily with a spin-up rate of dP/dt = -2.6 s yr^{-1}, the fastest among the known pulsars. As pointed out by the discoverer the energy spectrum stretches deeply to high energies (kT=30-50 keV for thermal bremmstrahlung models or, alternatively, α = -2.7 for a power law) making GX1+4 the hardest pulsar and one of the brightest sources of the galaxy also for E>30 keV.

In the early 1980's, however, GX1+4 faded away. Deep exposures performed by EXOSAT in 1983 and 1984 failed to reveal any signal down to an upper limit of 0.4 mCrab (2-7 keV band) [3]. It was only in 1987 that the source was again detected by

GINGA, but at the weak level of 3 mCrab [4]. GINGA and the X/gamma HEXE instrument onboard the MIR space station observed GX1+4 in 1987,1988 and 1989 [5][6][7][8] showing that, at X-ray energies, the source has brightened up to a level of about 15 mCrab and that the pulsation period had unambiguously reversed the spin up to a spin down at the quite steady rate of $dP/dt = +1.4$ s yr^{-1}. The HEXE luminosity in the 20-100 keV energy band was 1.0 10^{37} erg s^{-1} on October 31, 1987, assuming a distance of 10 kpc.

In 1990, SIGMA has detected the pulsation of GX1+4, confirming the spin down phase but at a slower rate ($dP/dt = +0.9$ s yr^{-1})[9].

McClintock and Leventhal [10] made the hypothesis that this source could be the compact source responsible for the variable positron/511 keV galactic center line [11][12]. However, no decisive argument was given to rule out another hard source, 1E1740-2942, and the authors deferred the final word to observations carried out by imaging/high resolution gamma ray instruments.

In this paper we discuss the observations of GX1+4 at hard X/soft gamma energies (0.035-1.3 MeV) performed by the coded aperture SIGMA telescope during the winter/spring 1991 survey of the galactic center.

2 THE SIGMA TELESCOPE

The CEA/CESR/CNES imaging telescope SIGMA is the main payload of the Soviet scientific satellite GRANAT in orbit since December 1989. The detector is an Anger camera which measure energies and interaction points of photons in the 0.035-1.3 MeV energy range. The optical system is provided by an URA coded mask placed 2.5 m in front of the detector.

This arrangement features a Full Sensitivity Field of View (FSFOV) of 4.7°x 4.3°. In a wider external zone (11.5°x10.9° at half sensitivity), named Partially Coded Field of View (PCFOV), the incomplete shadowing progressively reduces the instrument sensitivity to zero.

During a typical SIGMA observation, lasting approximately one day, the telescope records three series of 'spectral' images (124 x 116 3.30 arcmin pixels) in 95 energy channels which cover the entire energy range varying with the energy resolution. In addition, the total camera counts are stocked every 4 s in four energy bands. Dead time information is also known every 4 s.

More details about the instrument and the data collection modes can be found in Paul et al. [13] while the in-flight performances are described by Mandrou et al. [14].

3 OBSERVATIONS

Figure 1 shows the strong variability of the Galactic Center region during Spring 90, Winter 91, and Spring 91 [15]. Contour levels are drawn every 0.1 cts/s starting at 0.25 cts/s.

The first image shows the well known source 1E1740.7-29.42 and the source GRS 1758-258, discovered by GRANAT. GX1+4 is not visible.

In the second image taken in Winter 91, appears only the GRANAT source. 1E1740.7-29.42 has faded away and GX1+4 is not yet visible.

GX1+4 dominates the third image taken in March/April 91. 1E1740.7-29.42 is still below the SIGMA detection limit and GRS 1758-258 is detected at the same flux level as it was observed in Spring and Fall 1990.

In order to better determine the source position as detected by SIGMA, the Spring 91 observations in the range 43-77 keV have been fitted with the SIGMA/URA point spread function having as additional free parameters the amplitude and the background level. Best fit equatorial coordinates are :

α_{1950}=262.26 ± 0.06 deg.

δ_{1950}=-24.74 ± 0.06 deg.

where the errors indicate the 95% confidence level. This position is fully compatible with the optical position.

A simple χ^2 analysis performed including all positive and negative observations in the 40-77 keV range reveals that

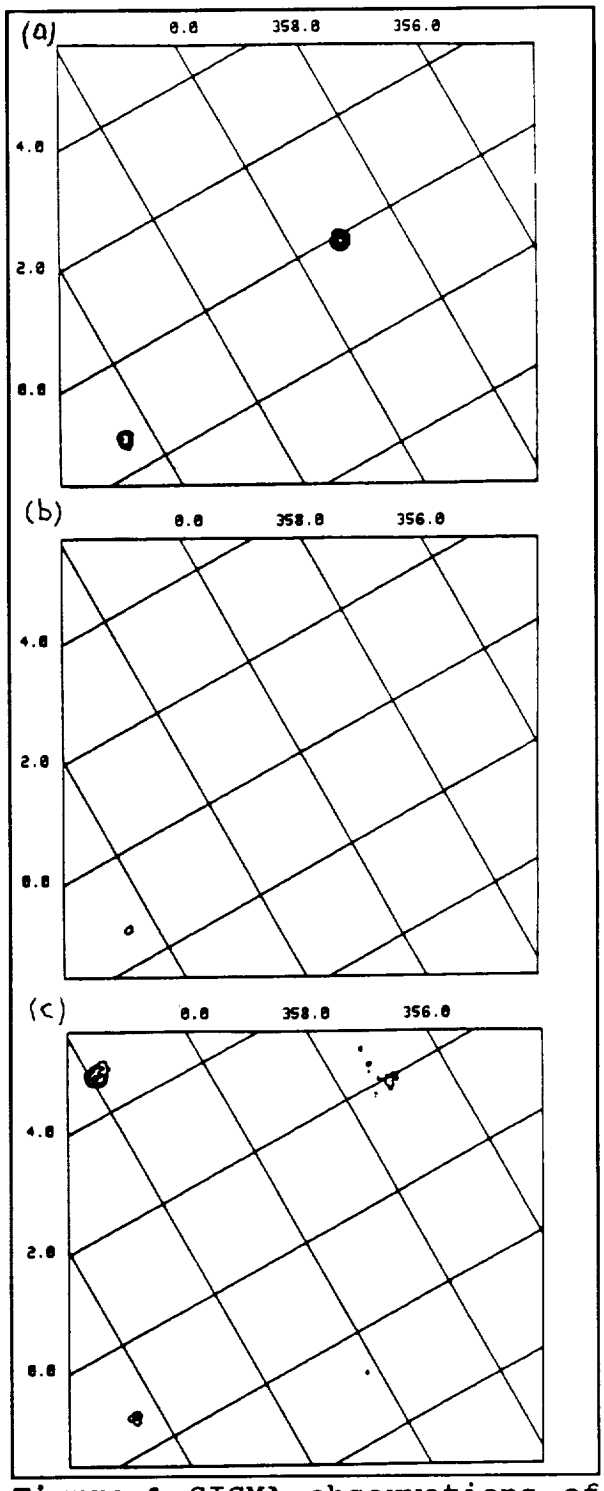

Figure 1 SIGMA observations of the Galactic Center region in the 40-110 keV energy band : (a) Spring 90. (b) Winter 91. (c) Spring 91.

during the Spring 91 survey the source was variable at a very high (99.95%) confidence level; taking into account only the positive observations the confidence drops to 95%. The mean positive count rate during the positive detections (0.27+/-0.03 cts/s) compared to the upper limits derived in the other cases suggests a variation of more than 40% of the hard flux.

An average raw energy spectrum of the source has been obtained regrouping the net source counts in 10 channels covering the band 40-140 keV. This spectrum has been fitted folding successively a power law and a thermal bremmstrahlung model with the detector response function [16]. The best fitting slope and electron temperature was -3.5 (-4.5:-2.8) and 28.4 (18.7:46.7) keV respectively. Errors are given at the one sigma confidence level.

The average flux in the 40-77 keV energy band was 125 mCrab on March/ April 1991. Assuming a distance of 8.5 kpc, the source luminosity reached on March 22 the level $L = 1.1 \pm 0.3\ 10^{37}$ erg s^{-1} in the 40-140 keV energy interval.

No statistically significant evidence of a peaked annihilation/511 keV emission has been found, at the source position, in individual observations of the survey nor in their sum which totals a dead-time corrected exposure time of about $2.3\ 10^5$ s. This enables to put an upper limit of $1.9\ 10^{-3}$ phot. cm^{-2} s^{-1} (90% confidence level) for a 511 keV emission from GX1+4.

4 THE PULSE PERIOD AND PROFILE

In order to measure the source pulsation we have used the epoch folding method applied on 4 s total camera counts computing the χ^2 statistic against the hypothesis of uniform distribution. The four accumulation energy bands have been held fixed at 40-77, 77-155, 155-290 and 290-630 keV throughout the whole survey.

As the spacing between statistically independent periods ($\Delta P = P^2/T_s$, T_s total time of observation) was, in all the cases, substantially greater than the period shift expected from the last measured period derivative [9] we have not used this term in the folding procedure.

We have detected the pulsation of GX1+4 in the first energy band, in two sets of observation.

The results are summarized in the following table :

Date	Time base T_s (10^4 s)	Epoch of observation (JD-2440000)	Period (s)
03/22/91	5.6	8338.59	115.06±0.03
03/31/91 & 04/01/91	19.6	8347.87	115.086±0.005

The light curve relative to the second period detection is traced in Fig. 2. It reveals a smooth profile with a broad single hump. The better defined March 31/ April 1 curve appears asymmetric about the peak position with a sharp drop on the right side. Contrary to previous detections [8][17] our results do not show any evidence of a double peak pulse confirming that the high energy profile is variable. The ratio of the modulated flux to the modulated+steady component for the March 22 observation was 0.54+/-0.15 while for the March 31/April 1 observation it was 0.67+/-0.14. These values indicate an highly modulated flux as already reported in the review of Frontera and Dal Fiume [18] at the same energies and by Kendziorra et al. [19].

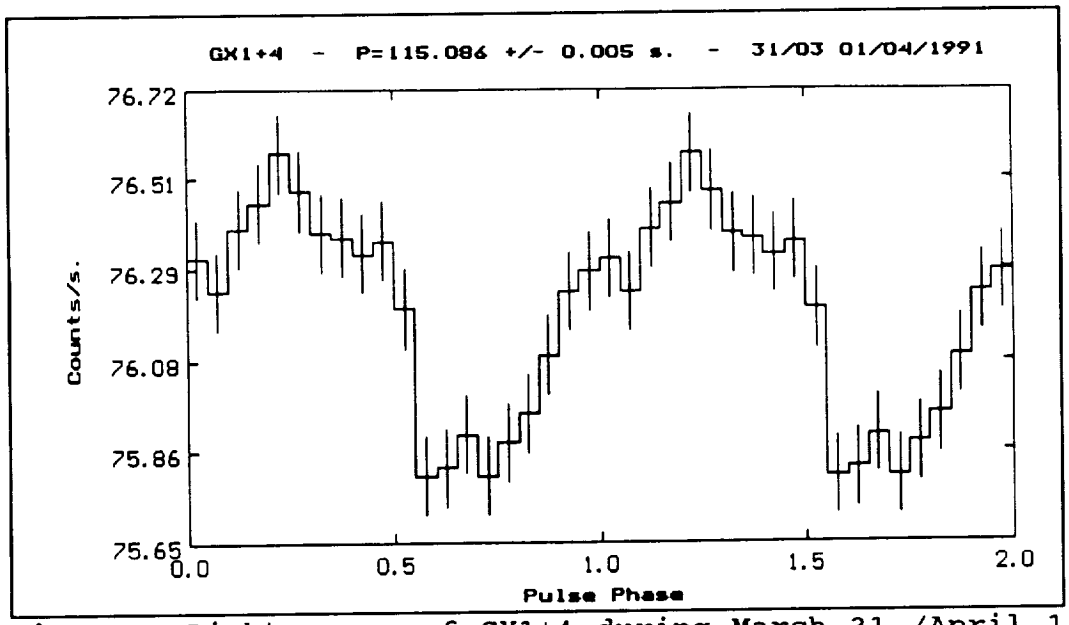

Figure 2 Light curve of GX1+4 during March 31 /April 1 observation.

It has been reported by some authors [20][21][22] that for E>20 keV there are significative differences between odd and even pulses and that the true pulsation has a period twice the 2 minute period. In this respect we have folded our data at the

double of the periods reported into 20 bin light curves. Then, the two halves of the light curves have been compared by means of a standard χ^2 Test. Reduced χ^2 (10 d.o.f.) values were 1.51 and 0.57 for the March 22 and the March 31/April 1 respectively, i.e. values compatible with the null hypothesis.

5 PERIOD HISTORY

Since 1986 GX1+4 has showed a clear spin down behavior. Taking into account the Ginga and the Kvant measurements in 1986-1989 an average spin down rate of $dP/dt = 4.5\ 10^{-8}$ s s^{-1} has been derived with little deviations from the linear trend [8]. However the two GRANAT points in 1990 and 1991 (Barret et al. [9], and this paper) have significantly changed the scenario showing that the spin down rate is unambiguously lowering. In fact, comparing our March 31/April 1 measurement with the point obtained by Barret et al. [9] on August, 27th 1990, an average spin down rate of $dP/dt = 2.6 +/- 0.3\ 10^{-8}$ s s^{-1} is deduced, a value which further lower the last dP/dt (3.1 10^{-8} s s-1) measured by Barret et al. [9]. The complete period history of GX1+4 is shown in Figure 3.

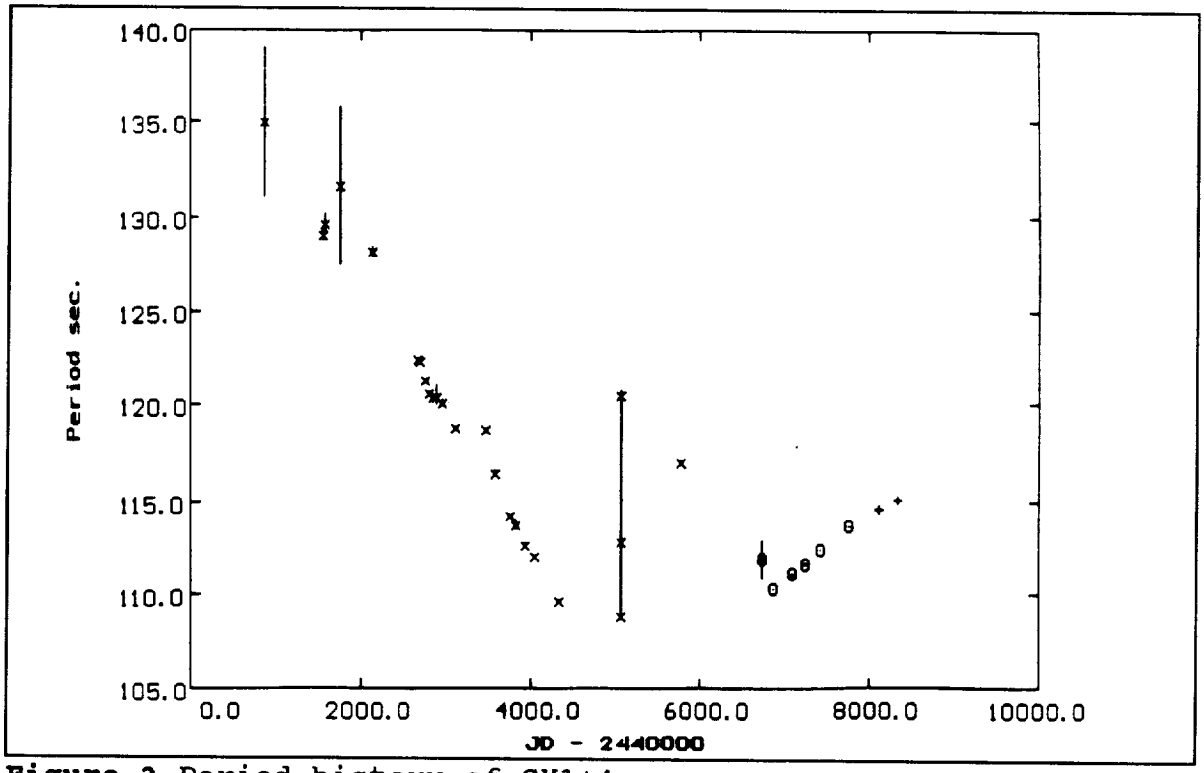

Figure 3 Period history of GX1+4.

6 CONCLUSIONS AND DISCUSSION

The winter/spring 1991 SIGMA survey has shown the strong variability of the Galactic Center region. For instance, the 40-77 keV flux from GX1+4 has varied by more than 40%. At maximum level the source luminosity reached 1.1 10^{37} erg s^{-1} (40-140 keV) assuming a distance of 8.5 kpc. Similar luminosity levels have been reported during the '70 when the source was in the high state.

The average energy spectrum has been found softer than expected and looks more similar to the steeply falling spectra typical of other known hard X-ray binaries (GX304-1, GX301-2, 4U1626-67) rather than to previously recorded spectra from GX1+4. Given the large error bars, our plasma temperature can be made consistent with the temperature of 41+/-8 keV measured by the AIT/MPI group [19] but a decrease is found if we compare our value with the more recent HEXE measurement [8].

We have obtained an upper limit for the annihilation emission coming from GX1+4 (1.9 10^{-3} phot cm^{-2} s^{-1}) that does not rule out this source as the compact galactic center annihilation emitter, since reliable 511 keV fluxes from the compact component lower than 10^{-3} phot cm^{-2} s^{-1} have been recorded [23][24][25][26]. A more compelling limit (0.6 10^{-3} phot cm^{-2} s^{-1}) was given by the OSSE instrument onboard the GRO satellite (this conference).

We have detected the 2 minute pulsation period in the 40-77 keV range on two occasions (considering the 03/31-04/01 observations as a single detection). Folded light curves reveal a broad single hump. There is no indication of the double peak structure previously detected at hard energies. Marginal evidence has been found concerning the differences between alternate pulses. Our result ($dP/dt = +0.8 \pm 0.09$ s yr^{-1}) confirms the spin down trend observed by GINGA and during the first SIGMA survey of the galactic center but at a slower rate [27][9]. The pulsation history clearly suggests that the current spin down phase of GX1+4 is ending.

The evolution we observed in GX 1+4 could be due to an increasing accretion rate as it is expected from a "fast rotator" with a magnetic field of $\approx 10^{12}$ Gauss [28]. As the luminosity of the source reaches the values obtained during the seventies, it seems reasonable to think that GX1+4 will end soon its spin down trend and perhaps go back to a spin up period.

7 REFERENCES

[1] Lewin W.H.G., Ricker G.R. and McClintock J.E., 1971, ApJ, L17.
[2] Forman W., Jones C., Cominsky L., et al., 1978, ApJS 38, 357.

[3] Mukai K., 1988, 1984 Low State of GX1+4, Mullard Space Laboratory internal report.
[4] Makishima K., Ohashi T., Sakao T., et al., 1988, Nat, 333, 746.
[5] Dotani T, Kii T., Makishima K., et al., 1989, PASJ, 41, 427.
[6] Gilfanov M., Sunyaev R., Churazov E., et al., 1989, Proc. of the 23th ESLAB Symposium "X-ray Binaries", Bologna, Italy, September 13-20, 71.
[7] Nagase F., 1989, Proc. of the 23th ESLAB Symposium "X-ray Binaries", Bologna, Italy, September 13-20, 45.
[8] Mony B., Kendziorra E., Maisack M., et al., 1991, A&A, in press.
[9] Barret D., Mereghetti S., Natalucci L., et al., 1991, Gamma Ray Line Astrophysics, AIP:NY, ed. Ph. Durouchoux, N. Prantzos, p42.
[10] McClintock J.E., and Leventhal M., 1989, ApJ, 346, 143.
[11] Ramaty R., and Lingenfelter R.E., 1987, The Galactic Center, ed. D.C. Becker, 51.
[12] Leventhal M., 1987, 13th Texas Symposium on Relativistic Astrophysics, ed. M.P. Ulmer, 382.
[13] Paul J., Mandrou P., Ballet J., et al., 1990, Proc. XXVIII COSPAR (The Hague), Adv. Space Res., in press.
[14] Mandrou P., Chabaud J.P., Ehanno M., et al., 1990, Proc. XXVIII COSPAR (The Hague), Adv. Space Res., in press.
[15] Cordier B., Ballet J., Goldwurm A, et al., 1991, Proc. of the IAU General Assembly, Buenos Aires, in press.
[16] Barret D. and Laurent Ph., 1991, NIM, in press.
[17] Greenhill J.G., Giles A.B., Sharma D.P., et al., 1989, A&A, 208, L1.
[18] Frontera F., and Dal Fiume D., 1989, Proc. of the 23th ESLAB Symposium "X-ray Binaries", Bologna, Italy, September 13-20, 1989, 57.
[19] Kendziorra E., Staubert R., Reppin R., et al., 1982, in Galactic X-ray Sources, ed. P. Sanford, P. Laskarides and J. Salton, 205.
[20] Koo J.W., and Haymes R.C., 1980, ApJ, 239, L57.
[21] Strickman M.S., Johnson W.N., and Kurfess J.D., 1980, ApJ, 240, L21.
[22] Manchanda R., Agrawal P., and Rao A., 1987, Proc. of the 20th I.C.R.C., Moscow, 1, 99.
[23] Haymes R., Walraven G., Meegan C.A., et al., 1975, ApJ, 201, 593.
[24] Riegler G., Ling J., Mahoney W., et al., 1981, ApJ, 248, L13.
[25] Leventhal M., MacCallum C.J., Barthelemy S., et al., 1989, Nat, 339, 36.
[26] Chapuis C.G.L., Wallyn P., Durouchoux Ph., et al., 1991, Gamma Ray Line Astrophysics, AIP:NY, ed. Ph. Durouchoux, N. Prantzos, p54.
[27] Sakao T., Kohmura Y., Makishima K., et al., 1990, MNRAS, 246, 11P.
[28] Ghosh P., and Lamb F.K., 1979, ApJ, 234, 296.

Hard X-Ray Observations of Vela X-1 and A0535+26 With HEXE: Discovery of Cyclotron Lines

E. Kendziorra[1], B. Mony[1], P. Kretschmar[1], M. Maisack[4], R. Staubert[1], S. Döbereiner[2], J. Englhauser[2], W. Pietsch[2], C. Reppin[2], J. Trümper[2], V. Efremov[3], S. Kaniovsky[3], R. Sunyaev[3]

[1] Astronomisches Institut der Universität Tübingen, Germany
[2] Max-Planck-Institut für Extraterrestrische Physik, Garching, Germany
[3] Space Research Institute, Moscow, USSR
[4] George Mason University, Fairfax, Virginia, USA

ABSTRACT

The X-ray pulsars Vela X-1 (4U 0900-40) and A0535+26 have been observed with the High Energy X-ray Experiment (HEXE) on board the Mir space station at energies above 20 keV.

The pulse profiles of Vela X-1 (P=283.22 s for JD 244 7486) and A0535+26 (P=103.27 s for JD 244 7626) have been measured up to at least 100 keV. The time averaged pulse profiles of the two sources both show a clear double peak structure with an asymmetric main pulse and a more symmetric secondary pulse. The spectrum of the main pulse is significantly harder than that of the secondary.

Pulse phase resolved spectra show absorption features at 54 keV and possibly 27 keV for Vela X-1 and around 100 keV for A0535+26. If we interpret these features as second and first harmonic (fundamental) cyclotron absorption lines we derive lower limits of $2.6 \cdot 10^{12}$ and $4.3 \cdot 10^{12}$ Gauss for the magnetic fields of the neutron stars in Vela X-1 and A0535+26, respectively.

3.
PULSARS

GAMMA-RAYS FROM THE CRAB AND VELA PULSARS

By

Cheng Ho
Los Alamos National Laboratory
Los Alamos, New Mexico 87545

Abstract

We will discuss gamma-ray pulsed emission from the Crab and Vela pulsars. Emphasis will be put on utilizing current and future GRO observations as diagnostics to examine and constrain theoretical models. Issues on the spectra and pulse profile will be discussed. Specifically, the absence and possibly significant time variability of pulsed emission below 10 MeV from the Vela pulsar represents a serious challenge to current models. Theoretical implication of this "peculiarity" will be addressed.

THE CRAB PULSAR LIGHT CURVE IN THE SOFT GAMMA RAY RANGE: FIGARO II RESULTS

E.Massaro[1], B. Agrinier[2], E. Barouch[2], R. Comte[2], E. Costa[3], G.C. Cusumano[4], G.Gerardi[5], D. Lemoine[2], P. Mandrou[6], J.L. Masnou[7], G. Matt[1], T. Mineo[4], M. Niel[6], J.F. Olive[6], B. Parlier[2], B. Sacco[4], M. Salvati[8] and L. Scarsi[4]

[1] Istituto Astronomico, Universitá "La Sapienza", Roma (Italy)

[2] Service d' Astrophysique, D.A.Ph.P.E., CEN, Saclay (France)

[3] Istituto di Astrofisica Spaziale, CNR, Frascati (Italy)

[4] Istituto di Fisica Cosmica e Appl. Inform., CNR, Palermo (Italy)

[5] Istituto di Fisica, Universitá di Palermo (Italy)

[6] CESR, Université P. Sabatier, Toulouse (France)

[7] UPR176 du CNRS, DARC, Observatoire de Paris, Meudon (France)

[8] Osservatorio Astrofisico di Arcetri, Firenze (Italy)

Abstract

The FIGARO II experiment - a large area, balloon borne, crystal scintillator detector working from 0.15 to 4.3 MeV - observed the Crab pulsar on 1990 July 9 for about seven hours. The study of the pulse profile confirms some structures detected with a lower significance during the shorter observation of 1986, and adds new important elements to the picture. In particular, between the two main peaks, two secondary peaks appear centered at phase values 0.1 and 0.3, in the energy range 0.38-0.49 MeV; in the same energy range, a spectral feature at 0.44 MeV, interpreted as a redshifted positron annihilation line, has been observed during the same balloon flight in the phase interval including the second main peak and the neighboring secondary peak. If the phase interval considered is extended to include also the other secondary peak, the significance of the spectral line appears to increase.

1. Introduction

The FIGARO II (French Italian GAmma Ray Observatory) experiment (Agnetta *et al.* 1989) was specifically designed to study sources with a well established time signature in the low energy γ rays. The Crab pulsar (PSR 0531+21) was observed by FIGARO II in the course of two transmediterranean balloon flights: on July 11 1986 for about two and a half hours (Agrinier et al. 1990) and on July 9 1990 for about seven hours. In this contribution we present some recent findings from the latter observation: we investigate the dependences of the light curve on the energy, and show that significant minor structures are present in the interpulse region between the two main peaks.

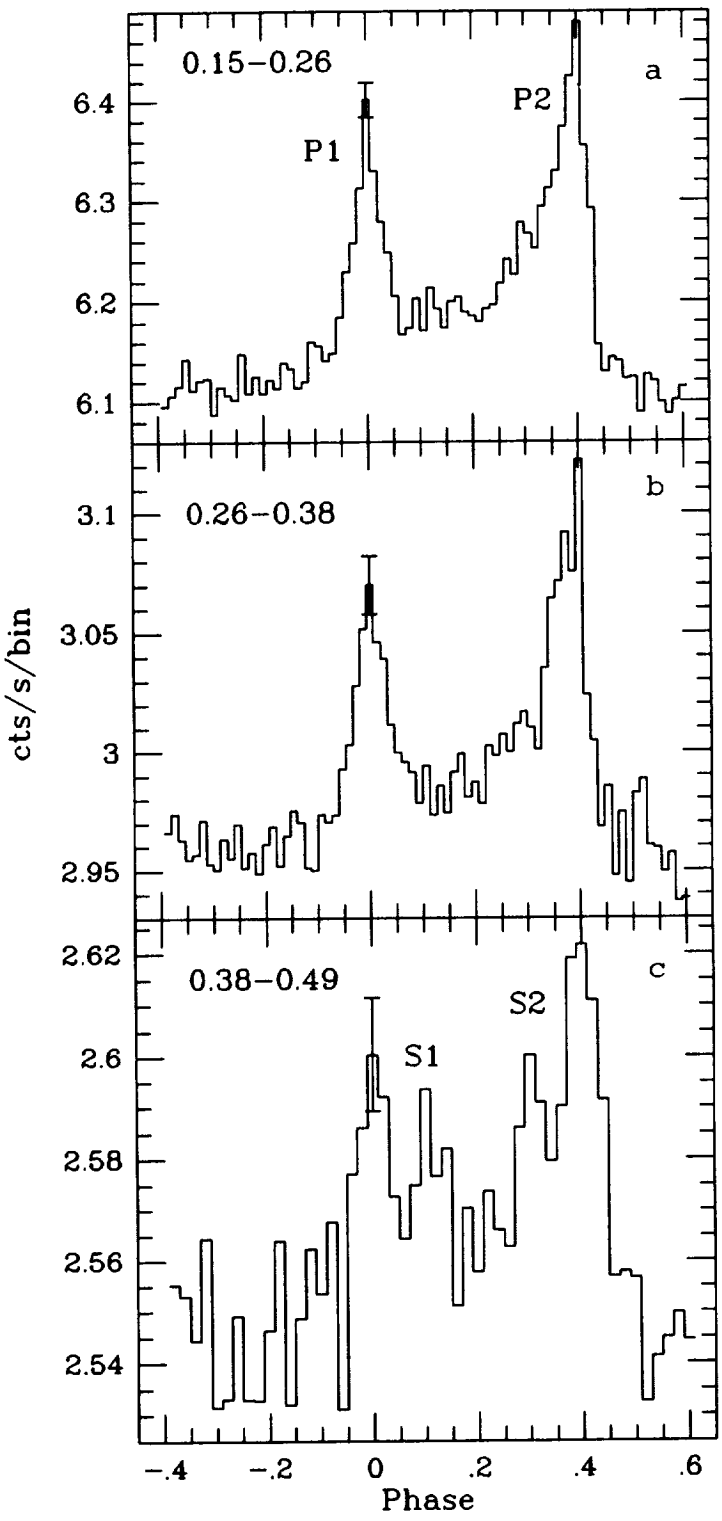

Fig. 1a,b,c - Phase histograms of PSR 0531+21 in different energy bands. The zero phase corresponds to the main radio peak. The energy ranges (in MeV) are reported in each panel.

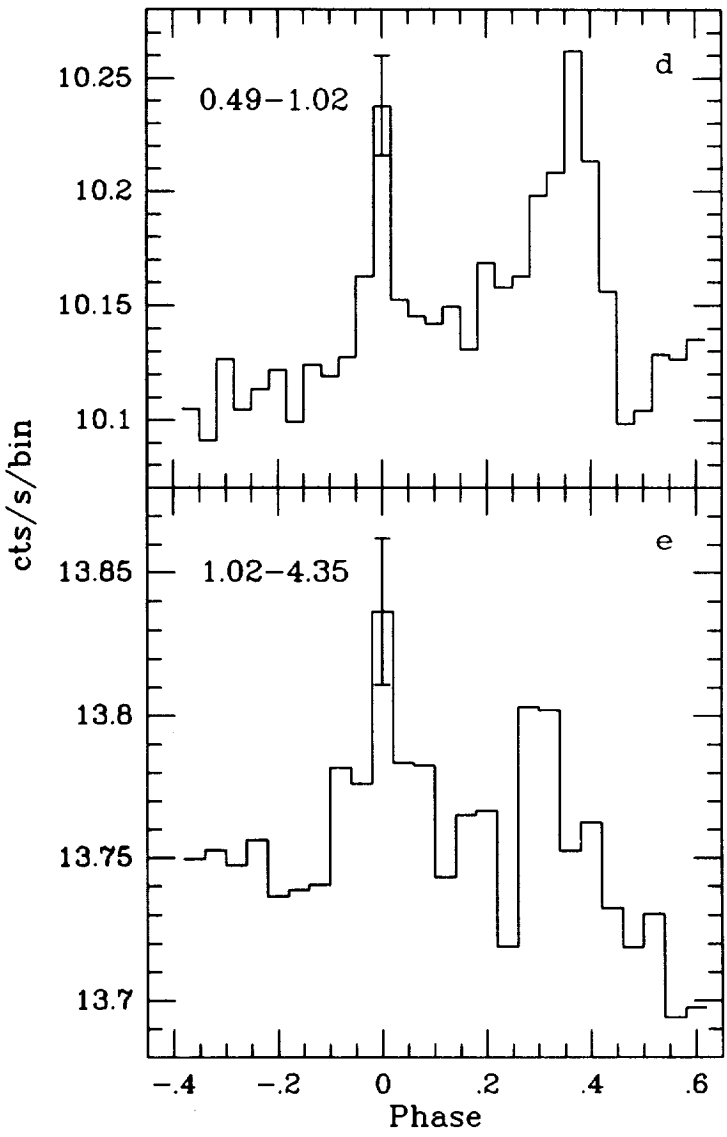

Fig. 1d,e - Phase histograms of PSR 0531+21 in different energy bands.

2. Data analysis and results

We computed the pulsed light curve of PSR 0531+21 by folding the arrival time (converted to the solar system barycenter by means of the JPL Ephemeris DE200) of each accepted event with the instantaneous radio period. The pulsar parameters at the reference epoch 2448081.5 JD were derived from the Jodrell Bank Crab Pulsar Monthly Ephemeris (Lyne and Pritchard, private communication): the adopted values of the frequency and frequency derivative were $\nu = 29.95871763685136$ Hz and $\nu' = -3.779343\ 10^{-10}\ s^{-2}$, respectively. The Crab was in the field of view of FIGARO II from 7:06 until 14:30 UT;

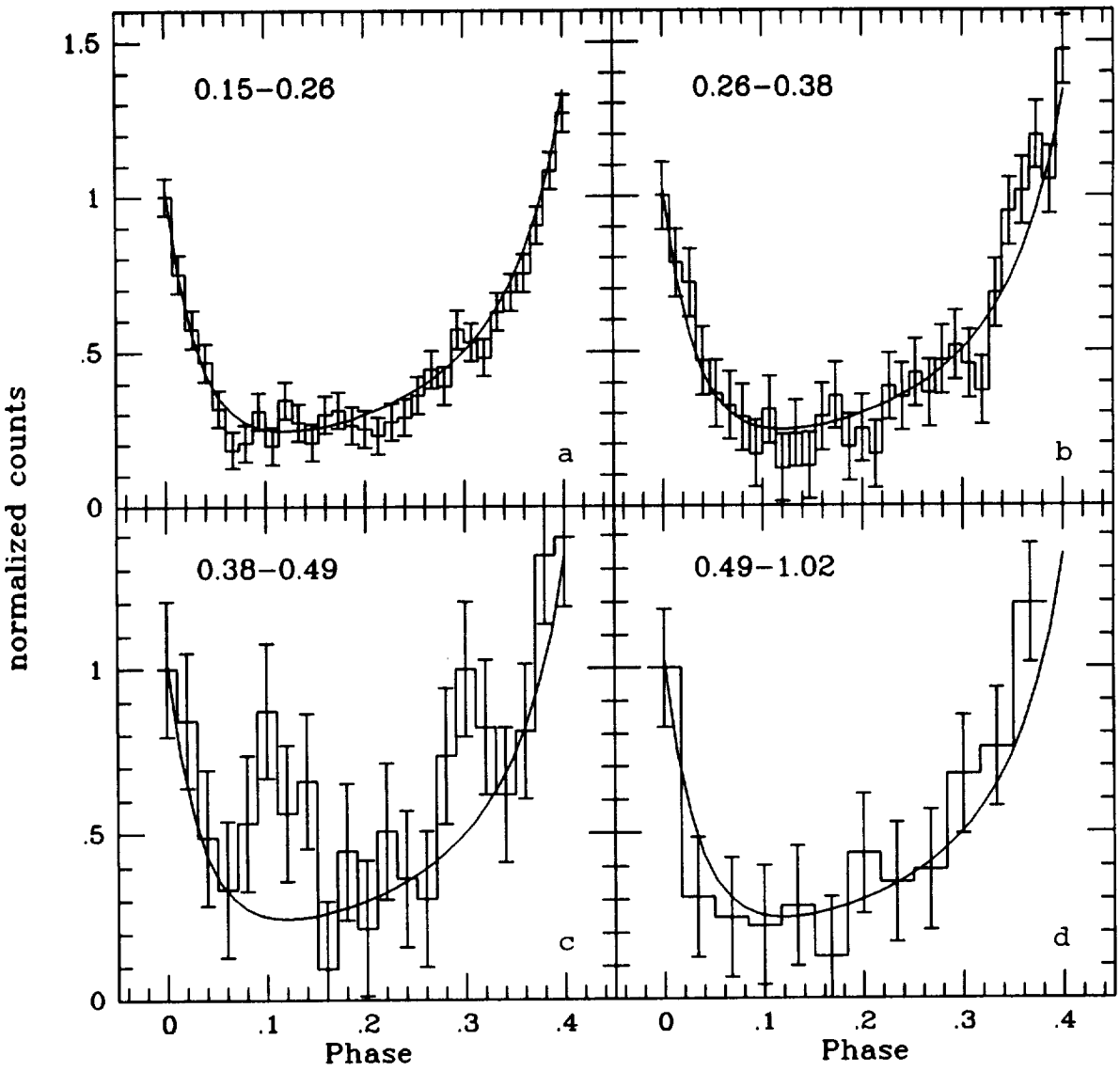

Fig. 2a,d - The Ip region in four energy bands: the nominal ranges (in MeV) are reported in each panel. The solid line represents the model template given in the text. The excesses corresponding to S1 and S2 are clearly evident in panel c.

the present analysis refers to the data acquired when the experiment parameters were nominal, for a total duration of 20,940 seconds. Following Agrinier et al.(1990), we take the zero phase at the position of the main radio peak.

In Fig. 1a-e the phase histograms for five photon energy ranges are plotted, corresponding to the nominal values (0.15-0.26), (0.26-0.38), (0.38-0.49), (0.49-1.02), and (1.02-4.35) MeV, after correction for the instrumental dead time in each individual bin. The double peaked profile is very evident throughout the experiment spectral range: P2 dominates over P1 in Figs. 1a to 1d, but above $\sim$ 1 MeV (Fig. 1e) the reverse is true, in accordance with the pattern already observed at hard γ-ray energies.

A new and unexpected result is shown in Fig. 1c, where in addition to the main peaks two extra structures are evident at phases close to 0.1 and 0.3 (S1 and S2). Note that the new features appear only in this energy interval and are not visible in the adjacent intervals. To be more confident on the reality of the extra features we analyzed anew the data of 1986, and found additional evidence of their existence. The energy binning of the two observations was different, so it is very unlikely that the new components are due to an instrumental effect.

3. The interpeak region

The pulse profile of the Crab pulsar is poorly known above ~ 0.3 MeV, and no acceptable template for the interpeak region is available. In order to build up our own template, we took the phase interval (0.0-0.4), i.e., from the maximum of P1 to that of P2. The phase histograms were then normalized by subtracting the average value of the off-pulse segment and by dividing the content of each bin by the maximum of P1. We found that the Ip region is very well described in all the three bands (0.15-0.26 MeV), (0.26-0.38 MeV) and (0.49-1.02 MeV) by the same formula

$$\frac{1}{|\phi+\phi_1|^m}+\frac{A}{|\phi-\phi_2|^n}$$

with $\phi_1 = 1.0044$, $\phi_2 = 0.47872$, $m = 31.002$, $n = 1.1964$ and $A = 0.06420$, respectively (Fig. 2a,d). The only exception to this model is the interval (0.38-0.49 MeV), where the excesses S1 and S2 with respect to the template profile are now clearly evident. A rough estimate of their statistical significance would be of about 3.9 and 2.8 standard deviations, respectively.

In the same energy interval, but at phases covering only S2 and P2 (0.27-0.47), Massaro *et al.* (1991) discovered a feature which was tentatively identified with a redshifted positron annihilation line. Fig. 3 shows the spectrum which is obtained by including also S1: the signal to noise ratio increases and the shape of the feature is better defined.

4. Conclusions

The presence of these additional structures could be relevant to the geometry of the emission pattern and to the physics of the inner magnetosphere. The Ip region, in fact, seems to exhibit an interesting activity not only in the Crab pulsar but also in Vela. We recall that above 50 MeV these two objects have quite similar pulse shapes (Kanbach et al. 1980), but in the optical Vela is characterized by two peaks at phases intermediate between the two γ-ray peaks (Manchester et al. 1980), rather close to the positions of S1 and S2 in Crab. Recent observations of the Vela pulsar above 100 MeV (Akimov et al. 1991) have shown that the interpeak region is variable in time and that structures can occasionally be detectable. Finally, we stress that the most recent observations of the Crab pulsar by GRO/OSSE (Ulmer et al. this workshop) indicate a variability of the Ip on a time scale of a few hours between 60 and 246 keV, and the largest changes are at the phases of S1 and S2. The Crab and Vela pulsars could be much more similar from a geometrical point of view than one would argue from their widely different energy spectra.

The present results show also that the occurrence of minor structures can be an energy dependent effect and therefore they can be related to spectral features. In conclusion we stress that wide-band high sensitivity observations of relatively short duration (typically

a few hours) are the only way to obtain a picture of the complex phenomenology of the Ip region in the soft γ ray range.

Acknowledgements. This research was financially supported by CNES and ASI. We are grateful to many persons from CESR, CNES, CEN, CNR and ASI who contributed to the payload and to the flight campaigns and particularly to A. Soubrier, to E. Myles-Standish Jr. for providing DE200 Ephemeris, and to A.G. Lyne for the Crab pulsar Ephemeris.

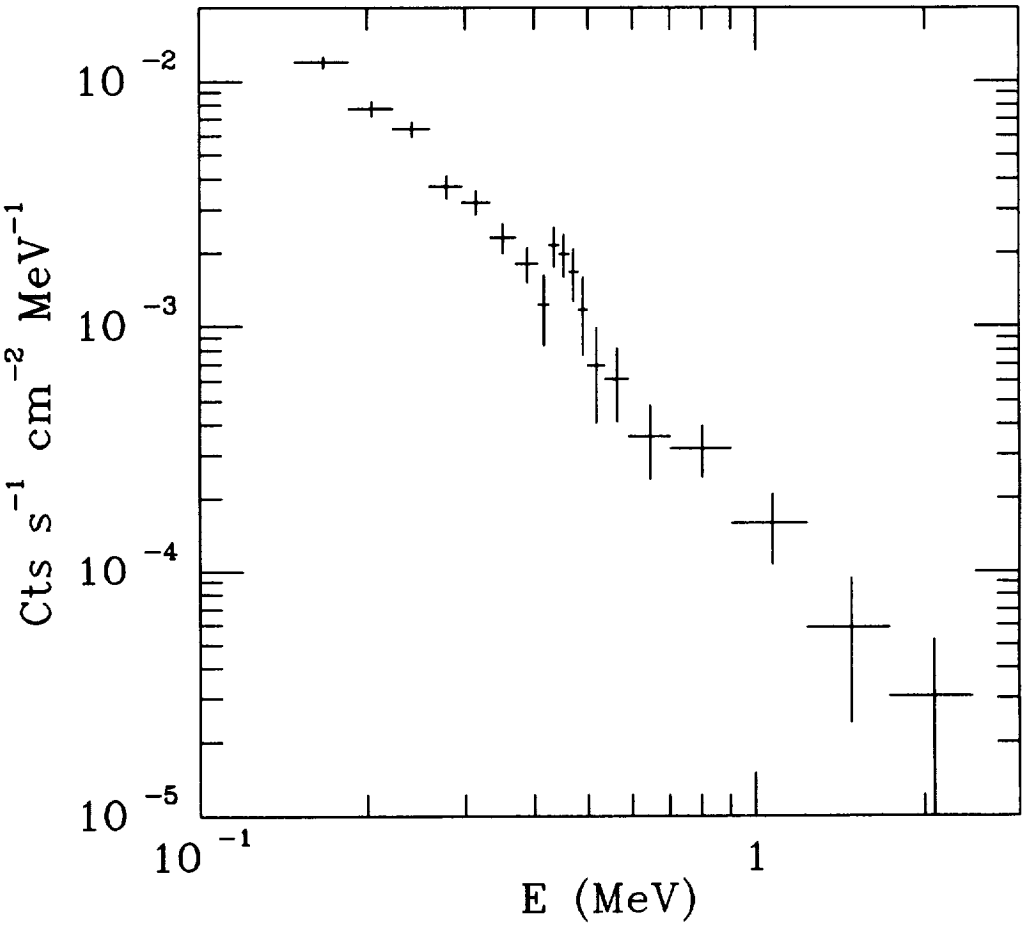

Fig. 3 - The spectrum of the phase regions S1+S2+P2. Note the four-channel excess at 0.44 MeV.

References

Agnetta, G., *et al.* 1989, *Nucl. Instr. Methods A*, **281**, 197.

Agrinier, B., *et al.* 1990, *Ap. J.*, **355**, 645.

Akimov, V.V. *et al.* 1991, *Proc. 22nd ICRC*, OG 3.3.1, in the press.

Kanbach, G., *et al.* 1980, *Astron. Astrophys.*, **90**, 163.

Manchester, R.N., *et al.* 1980, *MNRAS*, **190**, 9P.

Massaro, E., *et al.* 1991, *Ap. J. Letters*, **376**, L11.

GAMMA RAYS FROM 'HIDDEN' MILLISECOND PULSARS

Marco Tavani

University of California
Institute of Geophysics and Planetary Physics, LLNL, CA 94550
and
Astronomy Department, UC Berkeley, CA 94720

Abstract

We study the properties of a new class of gamma-ray sources consisting of millisecond pulsars totally or partially surrounded by evaporating material from irradiated companion stars. Hidden millisecond pulsars offer a unique possibility to study gamma-ray, optical and radio emission from vaporizing binaries. The relevance of this class of binaries for GRO observations and interpretation of COS-B data is emphasized.

1. Introduction

The missing link between low mass binaries (LMXBs) containing rapidly rotating neutron stars and binary millisecond pulsars has been provided by the discovery of pulsars in the process of vaporizing their very low-mass companion star. Two such systems are currently known: PSR 1957+20 with spin period $P = 1.6$ msec (Fruchter, Stinebring and Taylor, 1988) and PSR 1744-24A with $P = 11.6$ msec in the globular cluster Terzan 5 (Lyne et al., 1990; Nice *et al.*, 1990). PSR 1957+20 is the prototype of SVPs with stable eclipse properties (type I) whereas PSR 1744-24A shows a more erratic and sometimes intermittent behavior of radio-eclipses characteristics of a second class of SVPs (type II). In addition to these two SVP-classes, a third class of SVPs is expected on theoretical grounds (type III). The SVPs of type III are completely enshrouded by the evaporated material from the irradiated companion star, and they are therefore 'hidden' pulsars because their radio-emission may be completely blocked. However, they might be revealed by X-ray/gamma-ray emission produced by the interaction of the pulsar wind with evaporating material at the termination shock (Tavani, 1991b,c).

The existence of 'star-vaporizing pulsars' (SVPs) is in agreement with an evolutionary scenario of low-mass binaries containing compact stars whose energetic radiation (X-rays and γ-rays) illuminates their companion stars and drives a strong evaporative mass outflow during the LMXB and post-accretion evolutionary phases (Ruderman, Shaham and Tavani, 1989, hereafter RST; Tavani, 1989,1991a,b,c). Further 'vaporization' of the companion star in the post-accretion phase is caused by radiation produced by the interaction of the pulsar wind with the outflowing material from the companion. It is precisely this evolutionary phase that leads to the formation of a new class of γ-ray sources consisting of hidden millisecond pulsars. We follow here the discussion of hidden millisecond pulsars presented in Tavani (1991c), with emphasis on their gamma-ray emission (Tavani, 1991f).

2. Three Classes of Star-Vaporizing Pulsars

Pulsar emission in the form of a Poynting flux and a relativistic particle wind is possible if $r_{lc} < r_b$, with r_{lc} the light-cylinder radius $r_{lc} = c/\Omega = (4.77 \cdot 10^6 \text{ cm}) \cdot \text{P}_{-3}$, where $P_{-3} = P/(10^{-3}\,\text{sec})$, and r_b the distance from the pulsar at which the material outflowing from the companion star is stopped by radiation or magnetic pressure. For the cases considered in this paper, $r_b = a - R_s$, with a the orbital distance, and R_s the distance from the companion star at which the ram pressure of the outflowing gas is balanced by the radiation pressure from the pulsar. For SVPs, r_s is in the range $r_{lc} < r_s < a$, and satisfies the relation $L/(4\pi r_s^2 c) = \alpha \dot{m} v_g/(2\pi r'^2)$ with L the pulsar luminosity, r the distance from the pulsar, c the speed of light, $\dot{m} = |\dot{m}|_{rad}$ the mass loss from the irradiated companion star, $r' = a - r_s = R_s$ the distance from the companion, α a dimensionless quantity giving the hydrodynamical density enhancement near R_s relative to the density obtained from a $1/r'^2$ ideal dependence for constant wind velocity[1], and v_g the gas velocity. Since the wind velocity of radiation-driven mass outflows in SVPs and LMXBs is of the same order of magnitude of the escape velocity from the star v_e (Tavani and London, 1991) and since the Keplerian orbital velocities v_K of low-mass binaries with orbital periods $P_{orb} \lesssim 1$ day are comparable with v_e, we can write the pressure balance equation as follows

$$\mathcal{K} F[x] = \dot{m} \tag{1}$$

where we defined $x = r_s/a$, $\mathcal{K} = L\sqrt{a}/(2c\alpha\sqrt{GM_1}) \simeq (1.53 \cdot 10^{17}\, g\, s^{-1})\sqrt{a_{11}}\dot{P}_{-20} I_{45}/(\alpha P_{-3}^3)$, with $\dot{P}_{-20}$ given by $\dot{P} = 10^{-20}\,\dot{P}_{-20}\ \ s\ \ s^{-1}$, I_{45} the neutron star moment of inertia in units of 10^{45} g cm^2, $a = 10^{11}\, a_{11}$ cm, and M_1 the pulsar mass. The function $F[x]$ is given by

$$F[x] = (1 - x)^{3/2}\, x^{-2} \tag{2}$$

Eqs. (1) and (2) give the position of the shock radius as a function of $\dot{m}$, orbital (a_{11}, M_1), pulsar $(\dot{P}_{-20}, P_{-3})$ and hydrodynamics (α) parameters.

It is also useful to write the radiation-driven mass loss rate (in cgs units) as (RST) $\dot{m} = 10^{-17}\, f\, L\, \Delta = (3.95 \cdot 10^{16}\ \ g\ \ s^{-1})\, f\, \dot{P}_{-20} I_{45} \Delta_{-2}/P_{-3}^3$, where the quantity f depends on the net heating and hydrodynamics of the mass outflow near the companion star (Tavani 1989), and with $\Delta \equiv [R_*/(2a)]^2$ (and $\Delta = 10^{-2}\Delta_{-2}$) the solid angle subtended by the companion star to the primary where R_* is the companion radius. For typical fluxes irradiating SVP companions we have $f \sim 0.1\Upsilon$, where Υ is a dimensionless spectral 'quality' parameter which gives the efficiency of energy deposition. For the two energy bands which are effective in driving a strong wind, we obtain $\Upsilon \sim 10 - 100$ for soft X-rays and $\Upsilon \lesssim 0.2$ for hard X-rays and γ-rays (Tavani, 1989).

We can then rewrite the pressure balance condition Eq. (1) in a form which, in first approximation, is independent of the pulsar luminosity and depends upon the spectral 'quality' of the heating f as well as upon α and orbital parameters

$$F[x] = 0.258\, f\, \alpha \Delta_{-2} \sqrt{M_{1.4}}\, a_{11}^{-1/2} \tag{3}$$

[1]Results of a hydrodynamical calculation of the outflow in the case of PSR 1957+20 and PSR 1744-20A gives $1 \lesssim \alpha \lesssim 10$ (Tavani and Brookshaw, 1991).

Given the variety of pulsar luminosities and orbital parameters of low-mass binaries we can expect several types of SVPs characterized by different R_s's and shapes of the mass outflow influenced by the combined action of gravitational, radiation and Coriolis forces.

SVPs of type I are obtained when $\dot{m}$ is close to $\dot{m}_1 \equiv \mathcal{K}F[1 - R_*/a]$ *and* the Coriolis forces acting on the wind particles near R_s are not large enough to produce an appreciable tangential component of the gas pressure. The radio eclipses expected for type I SVPs are sharply defined and possibly symmetric (see Fig. 1). In the case of PSR 1957+20 (the prototype of type I SVPs) we obtain $\dot{m}_1 \simeq 10^{14}$ g s^{-1} for $R_*/a = 0.0353$. A lower limit for f in the case of PSR 1957+20 is obtained by equating $\dot{m}$ with $\dot{m}_1$, i.e., $f \gtrsim 0.213/\alpha$. The upper limit on f is obtained by the relation $f \lesssim (0.213/\alpha)(F[1-R_s/a]/F[1-R_*/a]) \sim 10/\alpha$, where we used the shock distance from the companion appropriate for PSR 1957+20 to be $R_s/a \simeq 1/5$ as suggested by hydrodynamical calculations of the mass outflow fitting the eclipse characteristics of PSR 1957+20 (Tavani and Brookshaw, 1991).

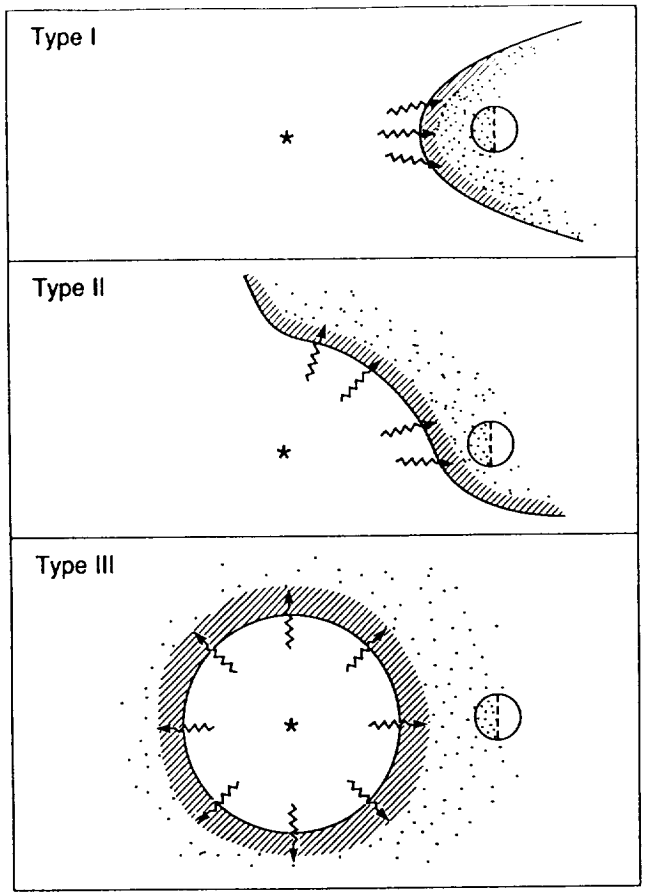

FIG. 1 - Schematic behavior of SVPs of different types (based on the hydrodynamical calculation of Tavani and Brookshaw (1991)). The asterisk denotes the position of the pulsar and the companion star is assumed to be rotating counterclockwise.

SVP's of type II and III are possible when $\dot{m}$ is larger than $\dot{m}_1$ *and* the Coriolis forces together with outflow velocities of order of Keplerian velocities are sufficiently large to produce a large tangential component of the gas pressure near R_s. This additional component of the gas pressure forces the gas to begin to surround the pulsar in the leading edge of the eclipsing region. The eclipses of type II SVPs are expected to be occasionally non-symmetric with a time variable leading edge of the eclipse (see Fig. 1).

A remarkable example of SVP of type II is offered by PSR 1744-20A which shows symmetric (Nice *et al.*, 1990), non-symmetric (Lyne *et al.*, 1990) and total eclipses. We obtain in this case $\dot{m}_1 \simeq (3.71 \cdot 10^{12}\ g\ s^{-1})\dot{P}_{-20}\Psi^2/\alpha$, where $\Psi = R/R_L \sim 1$ with R_L the Roche lobe radius, and $R_*/a \simeq 0.18\Psi$ (Lyne *et al.*, 1990). As in the case of PSR 1957+20 we obtain for PSR 1744-20A the possible range for f, $0.16/\alpha \lesssim f \lesssim 10/\alpha$, where the upper limit has been obtained by taking $R_S/a \sim 1/2$, as suggested by the hydrodynamical calculation of the outflow of PSR 1744-20A (Tavani and Brookshaw, 1991) .

3. Hidden Millisecond Pulsars

SVPs of type III are obtained if the material near R_s has sufficient tangential kinetic energy to overcome the pulsar radiation pressure and is able to surround the pulsar completely (see Fig. 1). Eq. (3) shows that this case may occur for a favorable combination of the quantities f, α, Δ, and a. PSR 1744-20A offers a good example of a SVP of type III during its 'radio-quiescent' mode observed several times in 1990 (Lyne *et al.*, 1990; Nice *et al.*, 1990). PSR 1744-20A is an example of a SVP which is able to switch between different eclipse modes, but SVPs which spend most of their time as type III SVPs may exist as well. In this case the central pulsar is completely surrounded by the wind material in the orbital plane that partly accumulates near R_s and partly escapes from the binary. This class of 'hidden' millisecond pulsars may have their radio emission completely quenched unless the wind material is confined in a thin disk. The shape of the enshrouding material in three dimensions depends on the interplay among gravitational, radiation and pressure forces, and a 'bubble' or a donut-shaped 'torus' can describe the gas configuration surrounding the pulsar. The hydrodynamics together with the stability and time dependent effects influencing the enshrouding material is the subject of intense research (Tavani, 1991c,f) and an account of the results is beyond the scope of this paper. Furthermore, even though the currently known SVPs and the related numerical modelling suggest the existence of a gas configuration enshrouding the pulsar which is optically thin to hard X-rays and gamma-rays (Tavani and Brookshaw, 1991), a more complex configuration may be possible. In the following we will address the main qualitative features concerning the emission of gamma-rays expected from hidden millisecond pulsars assuming that the evaporating material is optically thin to hard X-rays and γ-rays.

4. Gamma rays from shock acceleration

Rapidly rotating pulsars are believed to produce a radially expanding relativistic wind of ions and $e^{\pm}$pairs in addition to the comoving Poynting flux of electromagnetic energy in a MHD approximation (e.g., Kennel and Coroniti, 1984; Hoshino *et al.*, 1991). The

MHD pulsar wind is characterized by the Lorentz factor of particles and by the ratio σ of electromagnetic to kinetic energy of wind particles. We can express the Lorentz gamma factor γ_1 in terms of a parameter η which gives the efficiency of acceleration and pair production near the pulsar as

$$\gamma_1 = \eta(Ze\Phi_c)/(m_i c^2) \simeq 2.3 \cdot 10^6 \eta (Z/A)(\dot{P}_{-20}/P_{-3}^3)^{1/2}. \quad (4)$$

where $\Phi_c \sim (2\pi R_p/cP)^2(2\mu/R_p^3)R_p$ is the voltage across open field lines of a pulsar of magnetic moment μ, and Z/A is the average ratio of charge over mass number of the wind particles. The quantity σ is

$$\sigma = B^2/4\pi c^2[N_i m_i \gamma_i + (N_{e+} + N_{e-})m_e \gamma_{e\pm}] \quad (5)$$

where N_i, m_i, γ_i and $N_{e\pm}, m_e, \gamma_{e\pm}$ are the number densities, masses and relativistic Lorentz factors for the ions and $e^{\pm}$pairs, respectively. In the MHD approximation, $\gamma_{e\pm} = \gamma_i = \gamma_1$. Detailed models for the Crab nebula require $\sigma \sim 10^{-2} - 10^{-3}$ (Kennel and Coroniti, 1984), and $\eta \sim 0.3$ (Hoshino *et al.*, 1991) which implies a value of γ_1 between $10^{5.3}$ (fully stripped iron) and $10^{5.6}$ (protons).

The pulsar wind of relativistic particles and Poynting flux interacts with the inner boundary of the SVP 'bubble' or 'torus' of Fig. 1 and a relativistic shock ensues. For simplicity, we will assume that the region around the shock region is sufficiently dense that the e.m. waves and plasma in the pulsar wind do not penetrate the mass outflow, and that the magnetic field is transverse to the shock normal at r_s. Under these conditions, diffusive Fermi acceleration (e.g., Ellison *et al.*, 1990) is not applicable, and the shock is transverse. The characteristics of particle acceleration depend on the details of the relativistic shock and several models are currently being investigated (Tavani, 1991f).

One sufficiently developed model of shock acceleration based on resonant absorption of magnetosonic waves by positrons near the ion reflecting region has been recently applied to the study of gamma-ray emission from PSR 1957+20 (Arons and Tavani, 1991). The radiation spectrum emitted downstream depends on the physical processes regulating the efficiency of synchrotron, inverse Compton scattering and non-thermal emission of the relativistic shock. The typical synchrotron energy is of order $E_{syn} \simeq (10\ keV)\gamma_{e\pm,6}^2 B_P \sqrt{\sigma/(1+\sigma)}$, where $\gamma_{e\pm} = 10^6 \gamma_{e\pm,6}$ and B_P is equal to the magnetic field of an ideal Poynting flux assumed to carry all the spindown energy of the pulsar. Typically, $B_P = \mu/(r_{lc}^2 r) \simeq (440\ G)B_9/(P_{-3}^2 r_{s,11})$, with B_9 the surface magnetic field in units of 10^9 G, and $r_{s,11} = r_s/(10^{11}\ cm)$.

The radiation spectrum expected from the relativistic shock with ion-induced acceleration of positrons has been shown to have a photon index $s \sim 2$ (Hoshino *et al.*, 1991). The effective synchrotron emissivity of the shock is a power law $j_\epsilon^{(b)}/\epsilon \propto \epsilon^{-2}$ (in units of photons $\sec^{-1}$ cm^{-3}), extending from $\epsilon_1^{(b)}$ to $\epsilon_s^{(b)}$. By equating the radiation loss timescale with the ion-induced acceleration timescale we obtain a range for the upper energy cutoff 10 MeV $\lesssim \epsilon_s^{(b)} \lesssim$ 10 GeV for different choices of γ_1 and σ. As an example, an application to PSR 1957+20 of the ion-induced acceleration model with pulsar wind parameters for

the Crab nebula gives $\epsilon_s^{(b)} \sim 3$ MeV (Arons and Tavani, 1991). If ions contribute to a substantial part of the pulsar wind energy, the radiation spectrum is expected to be a power law of index s from a few keV to tens or hundreds of GeV. The corresponding heating on the surface of the irradiated companion yields $10^{-3} \lesssim f \lesssim 10^{-2}$. Alternately, if ions do not appreciably contribute to the pulsar wind kinetic energy and therefore are not effective in pair acceleration near r_s, most of the pulsar wind energy is expected to be radiated at lower energies peaked around E_{syn} (Hoshino *et al.*, 1991) unless an additional shock acceleration mechanism (such as shock-drift acceleration) operates. The corresponding spectrum is expected to be in the X-ray energy range and $1 \lesssim f \lesssim 0.1$. For energies below ϵ_1, the spectrum is cut off, since the emission comes from the low energy tail of the nonthermal part of the particle spectrum, and from the Maxwellian pairs at energies less than $\gamma_1 m_{\pm} c^2$, with $\epsilon j_\epsilon \propto \epsilon^{4/3}$ (e.g., Jones and Hardee, 1979).

5. Observational Consequences

Hidden millisecond pulsars produce a gamma-ray yield larger than in the case of isolated pulsars, and they are therefore interesting for interpreting galactic gamma-ray sources. The γ-ray flux from hidden millisecond pulsars at the distance D can be estimated for a power-law emission as follows (ε is the photon energy)

$$\frac{dN(E>\varepsilon)}{dt} \sim (3 \cdot 10^{-4} \text{ ph. cm}^{-2} \text{ s}^{-1}) \frac{L_{p,36}}{D_{kpc}^2} \frac{\tilde{\varepsilon}}{0.2} \frac{1\,\text{MeV}}{\varepsilon} \tag{6}$$

where $\tilde{\varepsilon}$ is the efficiency of conversion of pulsar wind energy into radiation (Hoshino *et al.*, 1991), $L_{p,36} = L_p/(10^{36} \text{ erg s}^{-1})$, and $D_{kpc} = D/(1 \text{ kpc})$.

The detectability of gamma-rays from a hidden millisecond pulsar depends crucially on the ratio $L_{p,36}/D_{kpc}^2$. In the case of GRO detectors, we notice that hidden pulsars would be detectable by OSSE, COMPTEL and EGRET for a normal pointing time of two weeks if $L_{p,36}/D_{kpc}^2$ were larger or equal to ~ 1, 0.2, and 0.01, respectively.

5.1 Hidden Pulsars with Main Sequence Companions

Low-mass X-ray binaries (LMXBs) are believed to be the most probable progenitor of binary millisecond pulsars (e.g., Tavani, 1991a). However, no galactic binary millisecond pulsar has yet been discovered with a main sequence companion (e.g., Tavani, 1991e) even though the majority of LMXBs have orbital periods proper to binaries with main sequence companions (e.g., Ritter, 1990). This might be due to the effect of Doppler spread of the radio signal in orbits with orbital periods $P_{orb} \lesssim 6$ hrs. However, millisecond pulsars with main sequence companions satisfy Eq. (3) with $\Delta_{-2} \gtrsim 1$, and they may be hidden SVPs. Hidden SVPs with main sequence companions may be revealed by the X-ray/γ-ray emission from the radio-obscuring 'bubble' and, possibly, by an optical modulation of the irradiated companion star if the inclination angle is favorable. The luminosity of the companion star reprocessing the secondary radiation from the pulsar wind is $L \simeq (4 \cdot 10^{33} \text{ erg s}^{-1}) \dot{P}_{-20} I_{45} \Delta_{-2} / P_{-3}^3$ with a photospheric temperature $T \simeq (1.5 \cdot 10^{4\,o} \text{ K}) \dot{P}_{-20}^{1/4} P_{-3}^{-3/4} a_{11}^{-1/2}$. Main sequence companion stars of millisecond pulsars

would appear brighter and 'bluer' compared to similar undisturbed stars.

5.2 Interpretation of COS-B sources

Even though the pulsed and unpulsed radio emission of hidden SVPs is probably completely blocked, they can be visible in the X-ray/γ-ray band and, indirectly, in the optical band because of irradiation of the companion star (see Sect. 5.1). The radiation spectrum originating from the 'bubble' surrounding a SVP can be a power-law extending to energies $\sim$ 10 GeV, and hidden SVPs can be important for the interpretation of X-ray and γ-ray sources already discovered by COS-B and/or to be discovered by the Gamma Ray Observatory (GRO). The association of an X-ray and/or γ-ray source with a 'blue' companion star possibly showing optical modulation provides a well defined signature for the existence of hidden SVPs (Tavani, 1991c). The detectability of this association depends on details such as the inclination angle, and the amount of shadowing of the optical emission. It is however worthwhile to search for optical modulations in the field of known γ-ray sources (e.g., unidentified COS-B sources , Swanenburg *et al.*, 1981).

Furthermore, again depending on the geometry, even the gamma-rays can be modulated with an orbital period by scattering and absorbing material related to either the companion star itself or to density enhancements in the bubble/ torus surrounding the pulsar. A well defined signature for a successful association of gamma-ray sources with binary systems is therefore the existence of modulations in the gamma-ray flux with periods of few hours. A search of orbital period modulations in the gamma-rays from COS-B-like sources has not been systematically attempted before, and a periodicity search of GRO and COS-B data is strongly urged. Folding gamma-ray data with given periodic patterns may significantly increase the signal to noise ratio.

5.3 Gamma rays from globular clusters

A relatively large number of single and binary millisecond pulsars ($\sim$ 25) has been discovered in globular clusters (e.g., Tavani, 1991e), possibly as a consequence of the high probability of stellar encounters in dense cluster cores. A remarkable example of a globular cluster which harbors many millisecond pulsars ($\sim$ 10) is 47 Tucanae (Manchester *et al.*, 1991). It is therefore natural to expect that a relatively large number of pulsars in globular clusters are hidden, and that a detectable gamma-ray or optical signal can be used to deduce their existence. We note here that a class of 'blue stragglers' as those discovered in NGC 6397 (Auriere, Ortolani and Lauzeral, 1990)and in 47 Tucanae (Paresce *et al.*, 1991) might contain millisecond pulsars whose irradiation alter the properties of their companions (Tavani, 1991b,d). The existence of pulsar-driven blue stragglers is particularly interesting in globular clusters where the majority of stars are main sequence (Tavani, 1991d).

We note that the gamma-ray flux from individual and not enshrouded pulsars in globular clusters is too low to be detected by current gamma-ray detectors. However, the shock acceleration mechanism of hidden powerful pulsars enhances the gamma-ray yield for each single source, and single (in the case of EGRET) or collective emission from hidden pulsars might be detected by GRO. A periodicity search in a range of a few hours

might enhance the discovery probability. We estimated the number of sources necessary to make globular clusters detectable by the GRO instruments. We assumed the photon flux from Eq. (6) and an average $L_{P,36} = 1$. For 47 Tucanae we obtain the minimum numbers (21, 4 , 1) for OSSE, COMPEL and EGRET, respectively. For Terzan 5 we obtain (50, 10, 3), and for the core collapsed cluster NGC 6397 we estimate the minimum numbers in the range (5, 1, 1).

Work was performed at IGPP-LLNL under the auspices of the U.S. DOE under contract W-7405-ENG-48 with NASA support, grants GRO-90-29 and GRO-PFP-91-23.

References

Arons, J., and Tavani, M., 1991, submitted to *Ap. J.*.

Auriere, M. Ortolani, S., and Lauzeral, C., 1990, *Nature*, **344**, 638.

Ellison, D.C., Jones, F.C., and Reynolds, S.P. 1990, *Ap.J.*, **360**, 702.

Fruchter, A.S., Stinebring, D.R., and Taylor, J.H., 1988, *Nature*, **333**, 237.

Hoshino, M., Arons, J., Gallant, Y.A., and Langdon, A.B., 1991, *Ap. J.*, in press.

Kennel, C.F., and Coroniti, F.V., 1984, *Ap.J.*, **283**, 694.

Jones, T.W., and Hardee, P.E., 1979, *Ap.J.*, **228**, 268.

Lyne, A.G., *et al.*, 1990, *Nature*, **347**, 650-652.

Manchester, R.N., et al., 1991, *Nature*, **352**, 219.

Nemec, J.M., and Harris, H.C., 1987, *Ap.J.*, **316**, 172.

Nice, D.J., *et al.*, 1990, *Ap.J.(Letters)*, **361**, L61.

Paresce, F., *et al.*, 1991, *Nature*, **352**, 297-301.

Ritter, H, *Astron. Astrophys. Suppl. Series*, **85**, 1179.

Ruderman, M., Shaham, J., Tavani, M., 1989, *Ap.J.*, **336**, 507 (RST).

Swanenburg, B.N., *et al.*, 1981, *Ap.J.(Letters)*, **243**, L69.

Tavani, M., 1989, in *Proceedings of the 23rd ESLAB Symposium on X-Ray Binaries*, Bologna 13-15 Sept. 1989, ed. N. White, ESA Publications Division, p. 241.

Tavani, M., 1991a, *Ap.J.(Letters)*, **366**, L27.

Tavani, M., 1991b, in *X-Ray Binaries and the Formation of Binary and Millisecond Radio Pulsars*, Santa Barbara, 21-25 January 1991, eds. E.P.J. van den Heuvel and S. Rappaport, (Dordrecht: Kluwer) .

Tavani, M., 1991c, *Ap.J.(Letters)*, **379**, L69-L73.

Tavani, M., 1991d, submitted to *Nature* .

Tavani, M., 1991e, in *Relativistic Experiments in Space*, Rome 10-14 September 1990, eds. M. Demianski and R. Ruffini (Singapore: World Scientific).

Tavani, M., 1991f, to be submitted to *Ap. J.*.

Tavani, M., and Brookshaw, L., 1991, *Ap.J.(Letters)*, **381**, L21.

Tavani, M., and London, R., 1991, to be submitted to *Ap. J.*.

Pulsar γ Rays from Polar Cap regions

James Chiang and Roger W. Romani

Dept. of Physics, Stanford University
Stanford, CA 94305-4060

Abstract

We investigate the production of pulsar gamma rays by energetic electrons flowing in the open-field region above pulsar polar caps. We have followed the propagation of curvature radiation from primary electrons, as well as hard synchrotron radiation generated by secondary pairs, through the pulsar magnetosphere for vacuum dipole open-field geometries. Using data from radio and optical observations we construct models for the specific geometries and viewing angles appropriate to particular pulsars. These detailed models produce normalized spectra above 10MeV, pulse profiles, beaming fractions and phase resolved spectra appropriate for direct comparison with COS-B and GRO data. Models are given for the Crab, Vela and other potentially detectable pulsars; general agreement with existing data is good, although perturbations to the simplified models are needed for close matches. We have also extended the calculations to the millisecond pulsar range, which allow us to produce predictions for the flux and spectra of populations of recycled pulsars and point to search strategies.

Introduction

Early observations of galactic γ-ray sources, culminating with the COS-B mission, showed that radio pulsars with high spin-down luminosities are the brightest sources in the sky and have provided substantial information on their pulse profiles and integrated spectra. Attempts to model the production of this radiation have concentrated on two scenarios: polar cap models with radiation generated by primaries accelerated over a pulsar polar cap surface (*e.g.* Daugherty and Harding, 1982) and "outer gap" models with acceleration occurring high in the open field zone (*e.g.* Cheng, Ho and Ruderman, 1986). Both of these pictures have had some success in reproducing global properties of the observed emission.

Recent developments suggest that improved versions of such calculations are now appropriate. Progress in polarization observations and modeling of radio pulsars (Lyne and Manchester, 1988; Rankin, 1990) have allowed the particular viewing geometries of individual objects to be determined in many cases. Further, with the advent of the GRO facility, it is likely that improved sensitivity on the brightest gamma ray pulsars will allow the observations of detailed pulse profiles and phase resolved spectra as well as the detection of several fainter objects. We are computing models for

these pulsars in both the 'Cap' and 'Gap' pictures which provide detailed spectral and pulse profile information that may be directly compared with these data. It appears that the phase resolved spectra, in particular, can provide a means of discriminating between these two classes of models. Further comparison of the models with the data should allow us to study perturbations to the basic magnetic field geometry and provide insights into the primary acceleration mechanisms.

A second arena in which improved calculations are now needed stems from the discovery of large numbers of recycled pulsars. These short period, low magnetic field objects have very long lifetimes and substantial spindown luminosities and thus have been proposed as possible gamma ray sources by several authors. However, no specific models for the luminosity and spectral behavior of recycled pulsars have been produced. We have computed such models for polar cap geometries. An important ingredient of these computations is a substantial coverage of the parameter space in pulsar period, magnetic field, and inclination which both highlight the differences in these scalings from those of the Crab-like pulsars and allows us to compute fluxes integrated over recycled pulsar populations.

Model Computations

In the present model, we confine origin of the outflowing relativistic primaries to the pulsar polar cap, as defined by the open field line region in the vacuum magnetic dipole model. When the inclination of the magnetic axis to the pulsar rotation axis $\alpha \neq 0$, then the locus of field lines defining the cap boundary will not, in general, be a circle. In addition, the line of sight swept out by the observer often lies at a substantial angle β with respect to the magnetic pole (*cf.* Figure 1).

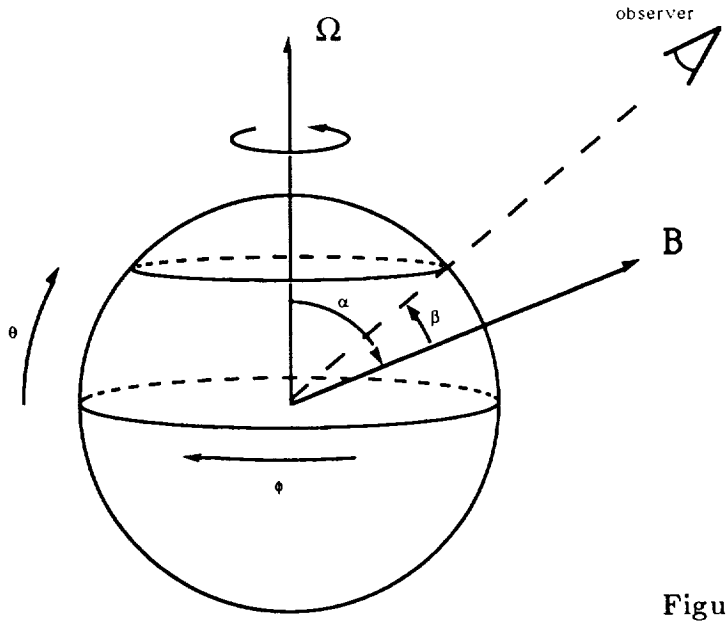

Figure 1. Magnetic Dipole Geometry

The model assumes that primary $e^{\pm}$ are accelerated in a small zone above the polar cap surface. In our simulation, $e^{\pm}$ are injected with $\Gamma \equiv E/m_e c^2$, distributed with the dipole field strength across the polar cap zone. Typically $\Gamma \sim 3 \times 10^7$ for these models, appropriate to the Ruderman and Sutherland (1975) model of the pulsar polar cap – different energies and allowance for an extended spectrum of primaries were shown to have a modest effect on the emergent γ radiation. In the spirit of Sturrock's (1971) pair cascade model and following the early computations of Harding (1981) and Daugherty and Harding (1982), we follow the curvature photons from these energetic primaries as they propagate through the rotating magnetosphere. Attenuation from magnetic pair production (Daugherty and Lerche, 1975) reduces the curvature spectrum, and for the chosen rays a Monte Carlo draw of the conversion points gives relativistic secondary pairs that synchrotron radiate in the strong magnetic field. Our computation evaluates this spectrum according to the distribution function of Erber (1966) in the frame co-moving with the e^+/e^-, discretizes and follows trajectories for the resultant photons as they propagate out of the pulsar magnetosphere.

Synchrotron photons of sufficient energy will further pair produce, and the propagation and attenuation of the resulting shower is followed to give γ spectra extending down to $\sim$ 10MeV in the observer's frame. Quantization of the synchrotron spectrum for very low pair energies has not been considered in detail, and may have some effect on the lowest energy bins in the final spectrum. By creating a new and substantially streamlined Monte Carlo code, we have been able to follow large numbers of primaries above the polar cap, allowing a calculation of the true spectra and pulse profile observed along a particular line of sight and comparison with the appearance of the pulsar from other directions for the model dipole geometry.

To compute the effective phases of the various photons (or, equivalently, the relative arrival times in the solar system barycenter) aberration of the photons from the rotating emission region has been treated. In addition, we consider the relative time delays in travel across the magnetosphere, which can amount to an appreciable fraction of the pulsar period, especially for curvature photons.

Individual Pulsar Models

Optical polarization data on the Crab (Kristian *et al.*, 1970) allow the geometry angles to be determined as $\alpha = 86°$, main pulse $\beta = -9.6°$, interpulse $\beta = 18°$. Similarly, radio data on Vela gives $\alpha = 90°$, $\beta = 6.4°$, where the statistical errors are small but certain systematic variations probably remain.

Since the dipole model for the pulse polarization sweep is generally successful, the radio emission should result from emission aberrated from the magnetic dipole axis. In figures 2-4 we indicate the phase of the center of the radio main pulse as a function of the height of the radio pulse production in the open field line zone (in units of r_{LC}, right scale). This phase is that at infinite radio frequency. Radio emission heights of several tenths of the light cylinder distance are suggested by some other observations and can explain the offset between the gamma emission and the radio pulse seen for the Crab.

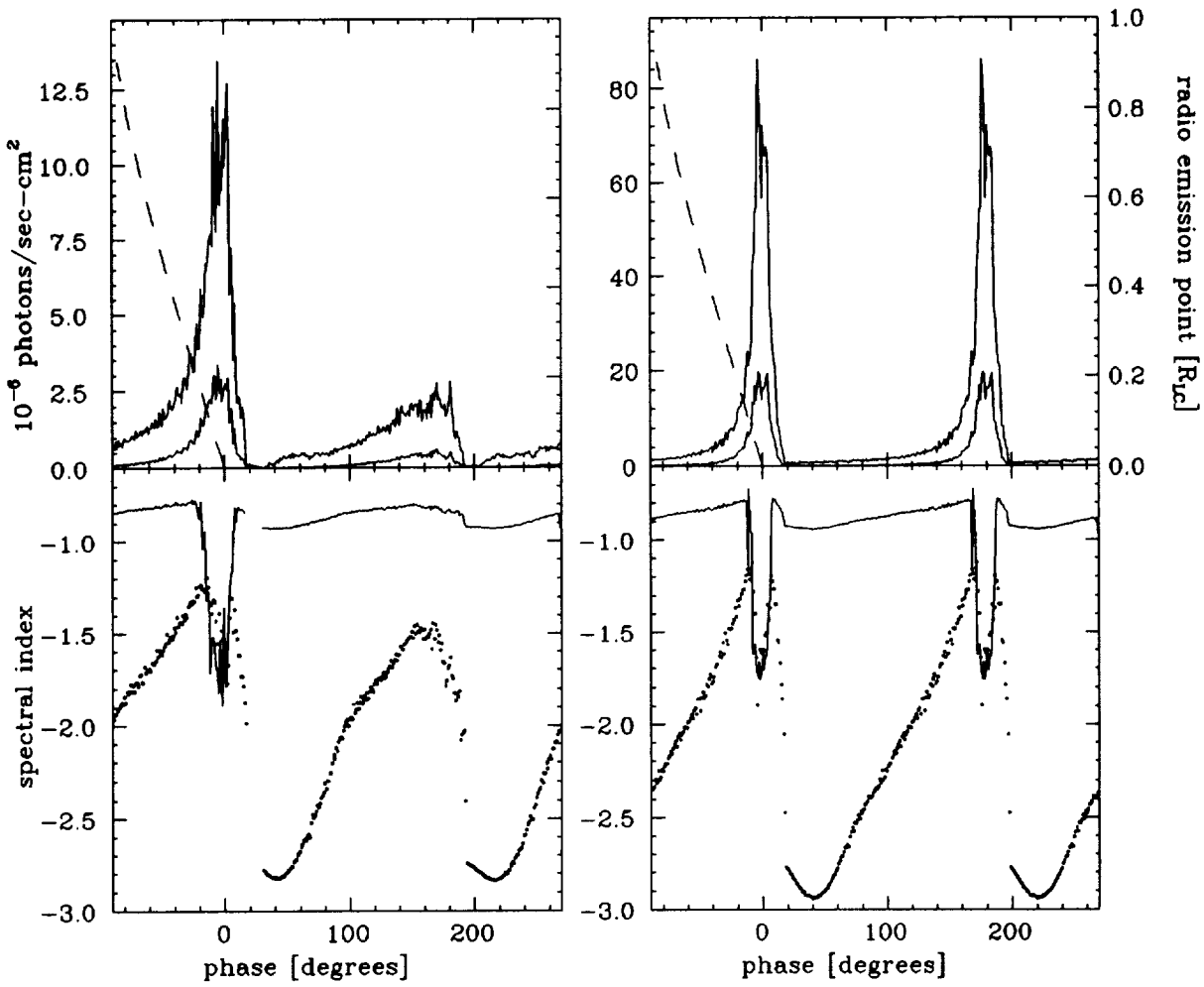

Figures 2,3. Light curves and spectral index variations for Crab(left) and Vela (right).

In figures 2 and 3, we show the results of polar cap calculations for Crab and Vela, respectively. In the upper panel pulse profiles are shown for energies above 100MeV and for energies above 500MeV. Fluxes are total count rates with the normalization determined by a corotation charge density of primaries flowing at the polar cap and by the pulsar distance. Note that the Crab interpulse does not cross the synchrotron core and so does not have a cusp due to the low energy emission; clearly perturbations to the simple dipole geometry are needed in this case. In the lower panels, we show the phase resolved spectral indices as determined from simple power law fits to the ranges 10MeV-100MeV (upper curve) and 100MeV-1GeV (lower points). Clearly a power law is a poor fit to the higher energy range, as the cut off of the curvature spectrum moves well below 1GeV off the center of the pulse, causing large variations in the fitted value. In the bright center of the pulse the spectral index approaches -2, but is typically much larger (harder spectrum) between the pulses and in the crab second pulse. Note that the inevitable admixture of residual background at these low count rates will bias all the spectral index values closer to -2.

In figure 4, we show the light curves predicted for three nearby pulsars which have been

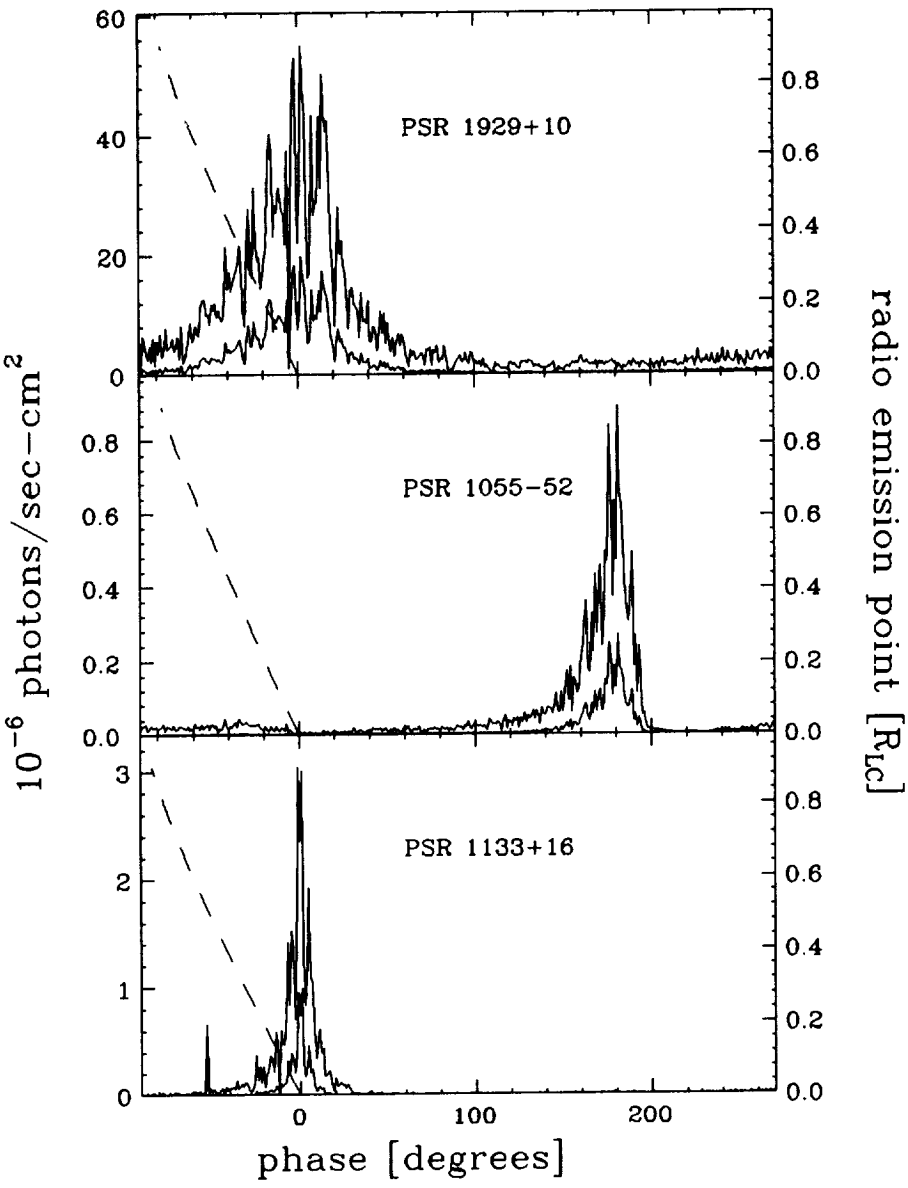

Figure 4. Some potentially bright pulsars.

suggested as candidates for detection by the EGRET experiment on GRO (Buccheri and Schoenfelder, 1989). The energy ranges and flux normalizations are as for Crab and Vela. PSR1055-52 is a nearly orthogonal rotator dominated by an interpulse, PSR1133+16 has $\alpha = 51.3°$, and PSR1929+10 is a nearly aligned rotator with a broad pulse. Emission geometries are determined from radio polarization and pulse-width data (Lyne and Manchester, 1988).

Integration along our model slice gives the expected time-average spectrum of the pulsar. In figure 5, we compare the results for Crab and Vela with the spectrum averaged over all viewing angles. There are significant differences for both models. In particular, a low-energy deficit for the

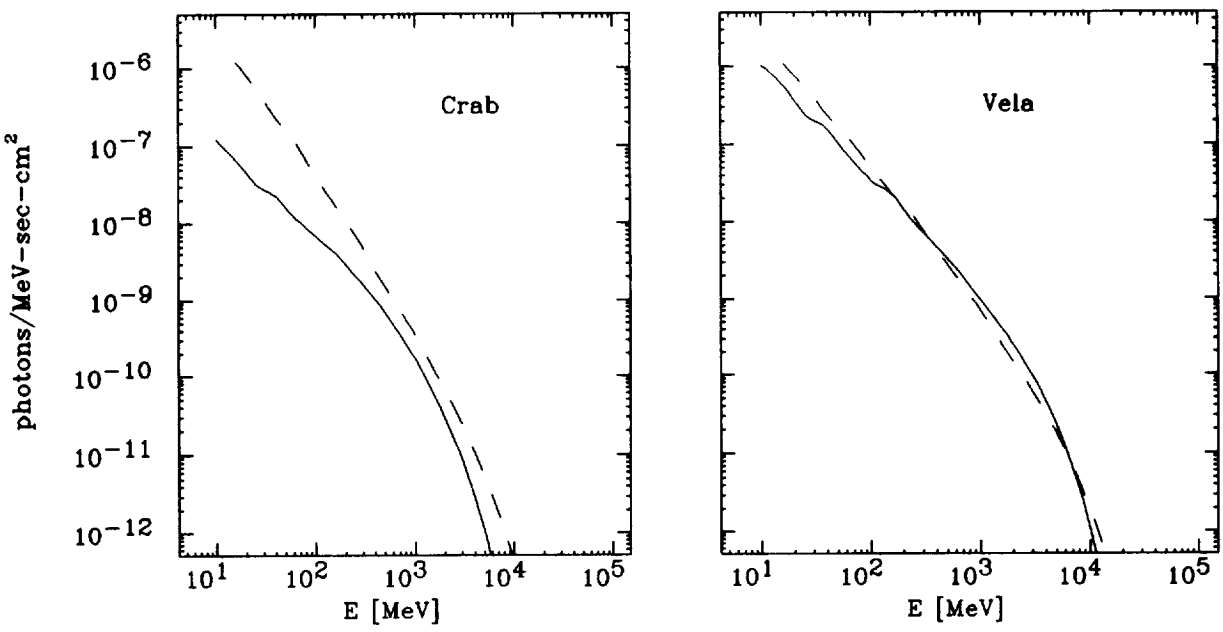

Figure 5. Phase (solid) and all-viewing-angle (dashed) averaged spectra for Crab and Vela.

Crab slice indicates that there should be perturbations from the simple dipole model that place the second pulse line of sight closer to the magnetic axis.

Scaling Laws for Recycled Pulsars

We have computed families of models to find the average emission of recycled pulsars and to compare the scalings of the integrated flux and the spectral indices with pulsar parameters with those found for high field (Crab-like) models. Typical recycled pulsar models have $B = 10^8 - 10^{10}$G and $P = 1 - 33$ms. The models show that except for the highest field recycled pulsars, synchrotron emission is unimportant. Also, with the very large open field line region of fast pulsars, most lines of sight see comparable integrated fluxes. The scaling with P of the luminosity and the spectral indices in two energy ranges is shown in figure 6.

With large opening angles, small radii of curvature and the dominance of curvature spectra we find that the total ($\geq$10MeV) luminosity scales as

$$F \sim 3.5 \times 10^{33} P_s^{-1.4} B_{12}^{0.95} \mathrm{erg/s}.$$

This is to be compared with the Crab-like objects for which

$$F \sim 6.4 \times 10^{32} P_s^{-2.2} B_{12}^{1.1} \mathrm{erg/s}.$$

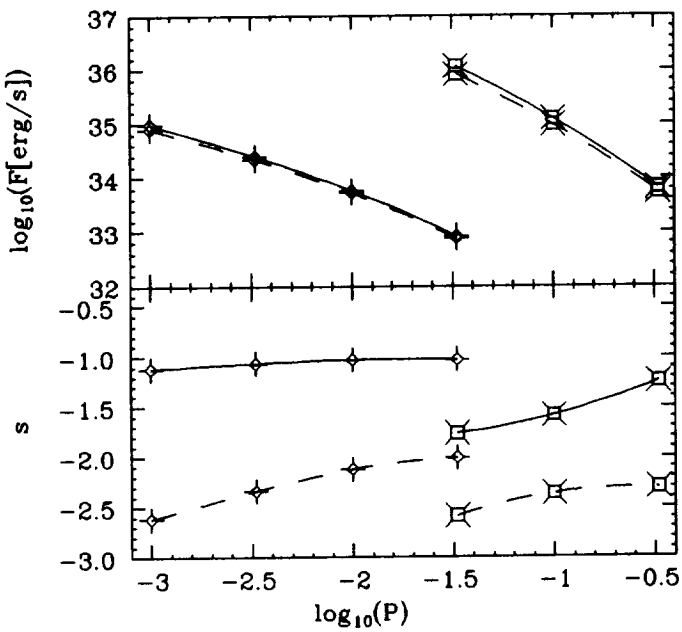

Figure 6. Period Dependence of Pulsar Fluxes and Spectral Indices

For low magnetic fields the spectral slopes in the low energy range (10MeV-1GeV) are relatively flat and do not strongly depend on P or B. This is as expected since pair attenuation of the curvature spectrum and the resultant synchrotron radiation is weak. For higher energies (1GeV-10GeV) the fitted spectral slope is sensitive to the curvature cut-off in the varying cap size, giving spectral indices $s \approx -1.59 - 0.08\log(B_{12}) + 0.4\log(P_s)$. Thus millisecond pulsars have substantially harder spectra than their high field cousins. At high energies the spectral cut-off depends fairly strongly on P.

Conclusions and Work in Progress

When normalized to a vacuum co-rotation charge density flowing through the cap surface, polar cap models reproduce the overall flux and spectrum of observed gamma ray pulsars at energies $\geq$10MeV quite well. These cap models produce beams of secondary synchrotron photons tightly collimated to the dipole axis. It is clear that models with lines-of-sight at large impact parameters to the field axis will not reproduce the cusp-like profiles of Crab and Vela. For the angles determined from low frequency observations the match of the models to observed profiles is reasonable at high (EGRET) energies, but does not fit in detail. The best hope for discrimination of these models arises from the phase resolved spectra: lowered fields off the pulse center cause harder curvature spectra, while simultaneously lowering the high energy cut-off.

For recycled pulsars the predicted fluxes and fairly hard spectral indices below 1GeV bode well for possible detections. The combined fluxes from groups of such objects, especially the known large populations of recycled pulsars in globular clusters, will also make interesting targets. We are presently integrating over populations of cluster pulsars to find the energy range most suitable for searches for such objects. As a test case, we are deriving upper limits from the COS-B data base and are using these data as a guide to appropriate search strategies.

The computations with specific geometries should be viewed as an interpretive tool for the refinement of acceleration and emission models. In this spirit, we are extending the calculation to a realization of the 'outer gap' picture, as described by Cheng, Ho and Ruderman. Inclusion of geometric effects will produce significant signatures in the pulse phase fluxes and spectra. Impending observations are likely to allow good discrimination among different models. An important feature of these computations is the production of normalized fluxes and energy ranges appropriate to particular GRO instruments. This should allow ready adoption and use by scientists working directly with the data.

References

Buccheri, R. and Schoenfelder, V. 1989, in *Timing Neutron Stars*, Oegelman and van den Huevel, eds. (Kluwer:Dordrecht), 419.

Cheng, K.S., Ho, C. and Ruderman, M. 1986, *Ap.J.*, **300**, 522.

Daugherty, J.K. and Harding, A.K. 1982, *Ap.J.*, **252**, 337.

Daugherty, J.K. and Lerche, I. 1975, *Ap. Sp. Sci.*, **38**, 437.

Erber, T. 1966, *Rev. Mod. Phys.*, **38**, 626.

Harding, A.K. 1981, *Ap.J.*, 245, 267.

Kristian, J., Visvanathan, N, Westphal, J.A. and Snellen, G.H. 1970, *Ap.J.*, **162**, 475.

Lynn, A. and Manchester, R.M. 1988, *MNRAS*, **234**, 477.

Rankin, J.M. 1990, *Ap.J.*, **352**, 247.

Ruderman, M.A. and Sutherland, P.G. 1975, *Ap.J.*, **196**, 51.

Sturrock, P.A. 1971,*Ap.J.*, **164**, 529.

TWO-PHOTON ANNIHILATION OF THERMAL PAIRS IN STRONG MAGNETIC FIELDS

MATTHEW G. BARING
Department of Physics
North Carolina State University
and
ALICE K. HARDING
Laboratory for High Energy Astrophysics
NASA/Goddard Space Flight Center

ABSTRACT

The annihilation spectrum of pairs with one-dimensional thermal distributions in the presence of a strong magnetic field is calculated. Numerical computations of the spectrum are performed for mildly relativistic temperatures and for different angles of emission with respect to field lines. Teragauss magnetic fields are assumed so that conditions are typical of gamma-ray burst and pulsar environments. The spectra at each viewing angle reveal asymmetric line profiles that are signatures of the magnetic broadening and redshifting of the line: these asymmetries are more prominent for small viewing angles. Thermal Doppler broadening tends to dominate in the right wing of the line and obscures the magnetic broadening more at high temperatures and smaller viewing angles. This angular dependence of the line asymmetry may prove a valuable observational diagnostic tool. For low temperatures and magnetic field strengths useful analytic expressions are presented for the line width, and also for the annihilation spectrum at zero viewing angle. The results presented find application in gamma-ray burst and pulsar models, and may prove very helpful in deducing field strengths and temperatures of the emission regions of these objects from line observations made by Compton/GRO and future missions.

INTRODUCTION

There is substantial observational motivation for detailed calculations of the annihilation spectrum of thermal pairs in the presence of a strong magnetic field. If the features observed around 400 keV in gamma-ray burst (GRB) spectra (see Mazets *et al.*, 1981) are interpreted as red-shifted 511 keV lines (for an extensive list of observations see Liang, 1986), then pair annihilation is taking place near a neutron star surface and will thus be influenced by a strong magnetic field. Further, recent observations (see Agrinier *et al.*, 1990) by the FIGARO II experiment of an emission feature at about 400 keV in the spectrum of the Crab pulsar are suggestive of a red-shifted annihilation line in this neutron star source. A study of the influence that a strong magnetic field has on the annihilation spectrum is therefore of significant interest to astrophysicists.

There are two important effects of the magnetic field on two-photon pair annihilation: (i) because of the very high cyclotron emission rates, the vast majority of pairs will annihi-

late from the ground Landau state with a one-dimensional (1D) momentum distribution, and (ii) since transverse momentum is not conserved in a strong magnetic field, there is an intrinsic broadening of the two-photon annihilation line due to an increased availability of phase space for this interaction. These effects become significant when the magnetic field exceeds about a few percent of the quantum critical field $B_c = m_e^2 c^3/(e\hbar) = 4.413 \times 10^{13}$ Gauss, which corresponds to conditions in neutron star environments. To a first approximation, it is reasonable to assume that the annihilating pairs have a 1D thermal distribution. The effects of the field on the shape of the thermal annihilation spectrum are potentially the most useful observational diagnostic tool: the total rate of annihilation is not altered much by the presence of the field when $B \lesssim 4 \times 10^{12}$ Gauss (Wunner, 1979).

Due to the intrinsic geometrical asymmetry imposed by the field, both the thermal and magnetic contributions to the width of the annihilation line will be very angle dependent. Intuitively, at viewing angles $\theta_1 \sim 0^0$ to the field, thermal Doppler broadening is expected to be a maximum while magnetic broadening is a minimum. For viewing angles $\theta_1 \sim 90^0$ to the field this situation is reversed so that the magnetic broadening should be more significant in comparison with the Doppler broadening. These expectations are borne out by the computational results that are presented here. The prediction that the width of observed lines at some angles could be due primarily to the magnetic field is observationally significant. Annihilation spectra produced by pairs with a 1D thermal distribution have been calculated by Kaminker *et al.* (1990), revealing significantly reduced Doppler broadening at $\theta_1 \sim 90^0$. However, they did not include the effects of magnetic broadening. In an earlier paper, Kaminker *et al.* (1987) presented spectra for the annihilation of pairs *at rest* in the presence of a field. Here we present the first calculation of two-photon annihilation spectra from a 1D thermal pair distribution, including full magnetic broadening effects using the QED second-order annihilation cross section of Daugherty and Bussard (1980, hereafter DB80). Of particular interest are the angle-dependent asymmetries of the line profiles introduced by field broadening, signatures that may be detectable by the *BATSE* instrument aboard the GRO mission and future high-resolution detectors (e.g. *TGRS* and *NAE*).

MAGNETIC TWO-PHOTON ANNIHILATION

It is convenient to use a simple dimensionless notation for various quantities in relativistic magnetized environments, in order to express analytic results more compactly. Hereafter, all magnetic fields will be expressed in units of the critical field B_c, and the parallel pair temperature parameter T will represent the quantity $k_B T_e/(m_e c^2)$, where k_B is Boltzmann's constant. All photon and particle energies and momenta will be scaled by $m_e c^2$ and $m_e c$, respectively.

The conservation relations for energy and also for momentum parallel to the magnetic field during pair annihilation can be simply written down. Let $p_- m_e c$ and $p_+ m_e c$ be the momenta of the annihilating electron and positron, oppositely directed along the field, and $\varepsilon_- m_e c^2$ and $\varepsilon_+ m_e c^2$ be their energies. The produced photons have energies $\omega_1 m_e c^2$ and $\omega_2 m_e c^2$, and propagate at angles θ_1 and θ_2 to the field. Using the abbreviated notation

$c_i = \cos\theta_i$, $s_i = \sin\theta_i$, $i = 1,2$, the conservation relations are

$$\begin{aligned} \varepsilon_- + \varepsilon_+ &= \omega_1 + \omega_2 \\ p_- - p_+ &= \omega_1 c_1 + \omega_2 c_2 \quad . \end{aligned} \tag{1}$$

Alternatively these relations can be expressed in terms of the solutions for the pair momenta $p_\pm$ (see DB80). The kinematical requirement that these momenta be real gives a restriction on the energy-angle phase space of the emitted photons:

$$\left|\omega_1 c_1 + \omega_2 c_2\right| \leq \sqrt{(\omega_1+\omega_2)^2 - 4} \quad . \tag{2}$$

For the annihilation of pairs with momenta $p_\pm m_e c$ along the field, the distribution function for the pairs that is needed for the computation of thermal annihilation spectra can be obtained from equation (23) of Harding (1986):

$$\eta_\pm(p_\pm) = \frac{1}{2K_1(1/T)} \exp\left\{-\frac{\varepsilon_\pm}{T}\right\} \quad , \tag{3}$$

where T is the dimensionless temperature of the pairs and K_1 is a modified Bessel function. The thermal annihilation spectrum can then be calculated by inserting this into the expression in eq. (24) of DB80, who performed the QED calculation for the annihilation cross-section from first principles. Their result is too small by a factor of two (c.f. Wunner, 1979), and also contains some minor typographical errors. The corrected annihilation spectrum taken from DB80 is then

$$R_{2\gamma}(\omega_1) = \int_{-\infty}^{\infty} \frac{dp_-}{\varepsilon_-} \int_{-\infty}^{\infty} \frac{dp_+}{\varepsilon_+} \int_0^{2\pi} d\phi_2 \, Q_{2\gamma} \tag{4a}$$

where

$$Q_{2\gamma} = \frac{n_+ n_- c}{4K_1^2(1/T)} \frac{\alpha_f^2 \lambda_c^2}{32\pi} \frac{\omega_1}{B} \exp\left\{-\frac{\omega_1^2 s_1^2 + \omega_2^2 s_2^2}{2B} - \frac{\varepsilon_- + \varepsilon_+}{T}\right\} \sum_{\text{pol}} |\mathcal{M}|^2 \quad . \tag{4b}$$

Here $\alpha_f \approx 1/137$ is the fine structure constant, $\lambda_c = \hbar/(m_e c)$ and $n_\pm$ are the particle number densities. The matrix element $\mathcal{M}$ can be obtained from the results of DB80. The sum is over the polarization states of the photons.

In obtaining eq. (4) a change of variables was performed: the energy ω_2 and angle θ_2 of the unobserved photon were expressed in terms of the momenta $p_\pm$ of the pairs via eq. (1). This transformation is convenient for both numerical and analytic computations, yielding simple integration limits: with it is associated a Jacobian given by $\omega_2 d\omega_2 \, dc_2 = |p_-\varepsilon_+ + p_+\varepsilon_-|/(\varepsilon_-\varepsilon_+)\, dp_- dp_+$. The azimuthal angle ϕ_2 of the second photon is the third integration variable. In the limit of small θ_1 , the dominant contribution to the annihilation spectrum occurs when the exponential factor in eq. (4b) is maximized.

NUMERICAL RESULTS

The results of numerical computations of the spectrum in eq. (4) are displayed in Figures 1–3. The principle magnetic effects are demonstrated in Fig. 1, where the pairs are assumed to be at rest, i.e. zero temperature. This corresponds to the case studied numerically by DB80 and Kaminker *et al.* (1987), and indeed the results presented in Fig. 1 are in close agreement with these earlier studies. With thermal broadening absent, Fig. 1 clearly illustrates the magnetic broadening effect in the left wing of the two-photon annihilation line. There are two prominent features to notice. First, the widths of the annihilation lines are dependent on the strength of the field and the angle of emission relative to field. These magnetic widths can be expressed approximately (for $B \ll 1$) as

$$(\Delta\omega_1)^B \sim \begin{cases} B/2\,, & s_1 < \sqrt{2B}\,, \\ s_1\sqrt{B/2}\,, & s_1 > \sqrt{2B}\,, \end{cases} \tag{5}$$

remembering that $s_1 = \sin\theta_1$. These estimates can be obtained from eq. (4) or from the results of Kaminker *et al.* (1987). Second, observe the appearance of angular-dependent kinematic cutoffs, eliminating the right (blue) wing of the line. These occur at

$$\omega_1 \;=\; \frac{2}{1+|c_1|} \quad , \tag{6}$$

as can be determined from eq. (2). Due to the presence of this kinematic cutoff at $\omega_1 > 1$, most of the broadening occurs on the left (red) side of the line at angles other than 90^0. Note that a summation of the spectra over emission angles removes the evidence of the line asymmetry and the kinematic cutoffs, producing a symmetric line profile.

The inclusion of thermal broadening for the case of finite T is illustrated in Figs. 2–3. The basic nature of Doppler broadening is similar to the 1D field-free case (Kaminker *et al.*, 1990), and the results show that the thermal contribution to the line broadening is greatest for small viewing angles. The first order contribution to the Doppler width is

$$(\Delta\omega_1)^D \;=\; c_1\sqrt{2T} \quad , \tag{7}$$

when $T \ll 1$. The thermal broadening smooths out the line profile, and dominates the blue wing of the line, but evidence of the magnetically-broadened left wing remains for larger viewing angles. A comparison of eqs. (5) and (7) reveals that magnetic broadening will dominate over first-order Doppler broadening when

$$T \;\lesssim\; \begin{cases} 0.25\,B\,s_1^2/c_1^2\,, & s_1 > \sqrt{2B}\,, \\ 0.125\,B^2/c_1^2\,, & s_1 < \sqrt{2B}\,, \end{cases} \tag{8}$$

confirming the numerical spectral results that the Doppler mechanism is more effective at broadening the line for small viewing angles.

The calculations performed here are for conditions expected to be typical of gamma-ray burst or pulsar environments. It is anticipated that pairs in the ground state are likely to be in relatively cool quasi-thermal distributions. Cyclotron resonant scattering can

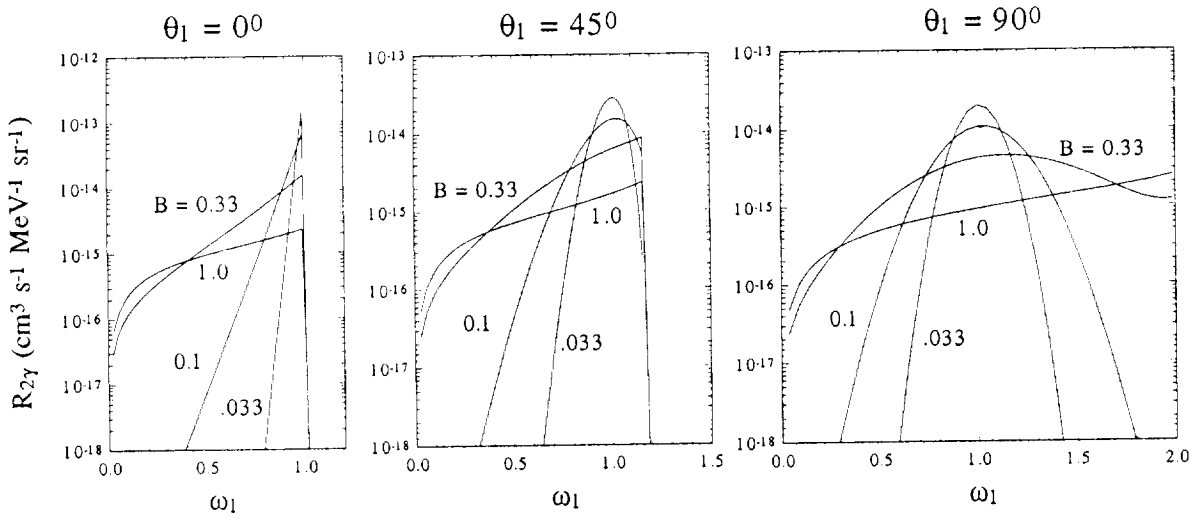

FIGURE 1 - Two-photon annihilation spectra for pairs at rest in the ground state, for different magnetic fields B and viewing angles θ_1 from numerical integration of the cross section over the energy ω_2 and angle θ_2 of the unobserved photon. The kinematic cutoffs occur when $|\cos\theta_2| = 1$ (cf. Eq. 6).

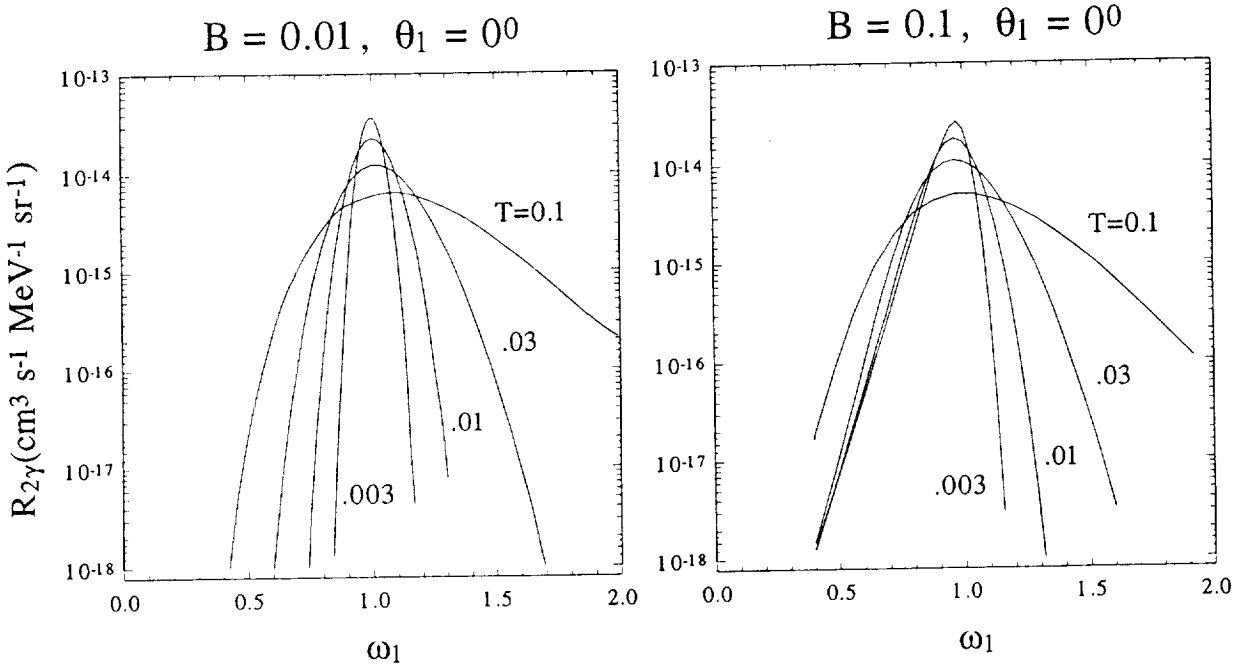

FIGURE 2 - Numerical annihilation spectra at an angle of 0^0 to the field direction for pairs in a 1D thermal distribution with parallel temperature T (in units of $m_e c^2$) at two different field strengths.

C-4

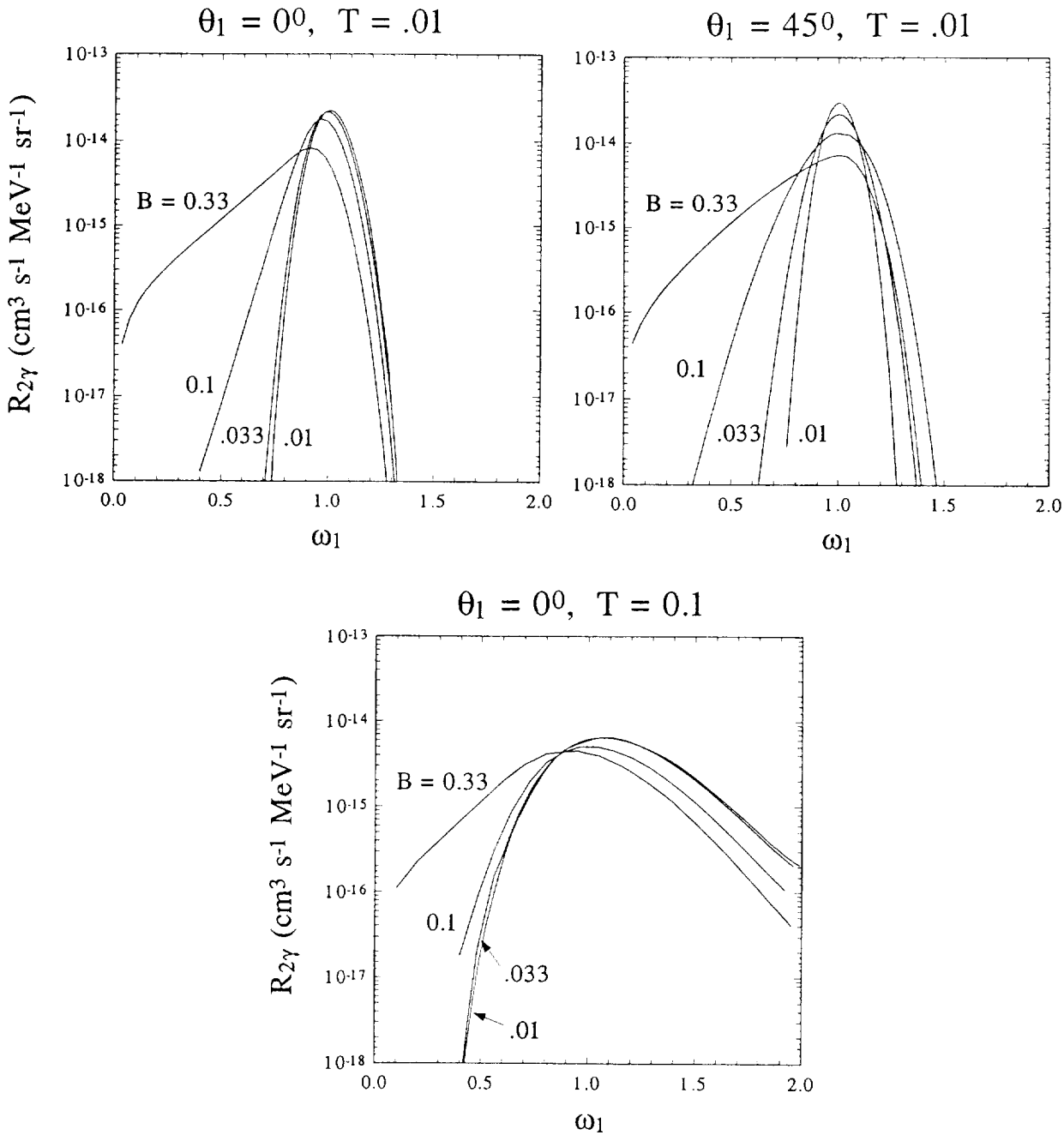

FIGURE 3 - Numerical annihilation spectra at different viewing angles θ_1 and parallel pair temperatures T, showing the effect of combined magnetic and thermal broadening.

cool pairs in the ground state before they annihilate (Preece and Harding, 1991) to temperatures $T \sim B/4$ (Lamb *et al.*, 1990). In this case magnetic broadening is dominant for $\tan^2 \theta_1 > 1$ or at viewing angles $\theta_1 > 45^0$. This angular effect shows significant potential as a spectral diagnostic for line observations in astrophysical sources.

ANALYTIC SPECTRAL FORMS

It is useful to develop analytic approximations to the annihilation spectrum. These can be simply obtained in the low T, low B limit, and when the viewing angle is small: $\theta_1 \approx 0^0$. The integrations in eq. (4) are then analytically tractable because of the effective restriction to the $\omega_2 - \cos\theta_2$ (or equivalently the $p_- - p_+$) phase space. For low T, we set $p_- = p_+ = 0$ in $\mathcal{M}$. Further, specializing to $s_1 \approx 0$ simplifies $\mathcal{M}$ dramatically (only one term of a series remains — see DB80 for details). In this case, $\mathcal{M} = \mathcal{N}^{(1)} + \mathcal{N}^{(2)}$, with

$$\begin{aligned} \mathcal{N}^{(1)} &= \frac{2}{B+\omega_1}\left\{\omega_1 c_1 \epsilon_+^{(2)}\epsilon_-^{(1)} + \omega_2 s_2 \epsilon_z^{(2)}\epsilon_-^{(1)}\, e^{i\phi_2}\right\} \\ \mathcal{N}^{(2)} &= \frac{2}{B+\omega_2}\left\{\omega_2 c_2 \epsilon_+^{(1)}\epsilon_-^{(2)} - \omega_2 s_2 \epsilon_z^{(2)}\epsilon_+^{(1)}\, e^{-i\phi_2}\right\} \quad , \end{aligned} \tag{9}$$

and the polarization vector components ϵ_z, $\epsilon_\pm$ are given in DB80. The integration over azimuthal angle turns out to be trivial, yielding

$$R_{2\gamma}(\omega_1) \approx \int_{-\infty}^{\infty}\frac{dp_-}{\varepsilon_-}\int_{-\infty}^{\infty}\frac{dp_+}{\varepsilon_+}\,\Lambda\,\exp\left\{-\frac{\omega_2^2 s_2^2}{2B} - \frac{\varepsilon_- + \varepsilon_+ - 2}{T}\right\} \quad , \tag{10a}$$

where

$$\Lambda = \frac{n_+ n_- c}{32\pi}\,\frac{\alpha_f^2\lambda_c^2}{TB}\,\omega_1 \sum_{\text{pol}}\left\{\left|\mathcal{N}^{(1)}\right|^2 + \left|\mathcal{N}^{(2)}\right|^2\right\} \quad . \tag{10b}$$

Since the pair temperature is low, the integrations over p_- and p_+ can be performed by the method of steepest descent. However it must be noted that there are two major regions of contribution to these integrals: in the neighbourhood of $p_- = -p_+ = 0$, corresponding to $c_2 = -\omega_1 c_1/\omega_2$ and $\omega_2 = 2 - \omega_1$, and also near $c_2 = -1$ and $\omega_2 = 1/\omega_1$. The total spectrum is, in general, well approximated by the sum of these two contributions.

The contribution $R_{\rm I}$ from $p_\pm \approx 0$ for $\theta_1 = 0^0$ occurs only in the left wing of the line. Evaluation of eq. (10) is then straightforward, resulting in

$$R_{\rm I}(\omega_1) \approx n_+ n_- c\,\alpha_f^2\lambda_c^2\,\frac{2\omega_1}{B}\,\frac{\omega_1^2 - 2\omega_1 + 2}{(B+\omega_1)^2}\,\exp\left\{-\frac{2(1-\omega_1)}{B}\right\} \quad , \quad \omega_1 < 1 \quad . \tag{11}$$

This contribution is magnetically broadened, and is generally the dominant contribution when $T \lesssim B^2$. It is consistent with the numerical plots, and reproduces the exact cold plasma, zero viewing angle approximation derived in eq. (14) of Kaminker *et al.* (1987). The second component $R_{\rm II}$, for $c_2 \approx -1$, $p_+ \approx 0$ and $p_- \approx \omega_1 - 1/\omega_1$, occurs in both wings of the line and is a Doppler broadened contribution. When $B \lesssim \sqrt{T}$, eq. (10) gives

$$R_{\rm II}(\omega_1) \approx n_+ n_- c\,\alpha_f^2\lambda_c^2\,\frac{\omega_1^{3/2}}{\sqrt{\pi T}}\,\exp\left\{-\frac{(\omega_1 - 1)^2}{T\omega_1}\right\} \quad , \tag{12}$$

which agrees with the $B = 0$, 1D thermal result in eq. (30) of Kaminker *et al.* (1990).

The results in equations (11) and (12), which can be extended to provide a more complicated approximation to the spectrum when $T \sim B^2$, indicate that the annihilation line is thermally broadened in the right wing ($\omega_1 > 1$), but both thermally and magnetically broadened in the left wing. This concurs with the numerical results plotted in the figures. The widths obtainable from eqs. (11) and (12) agree with those in eqs. (5) and (7), and from eq. (8) it can be deduced that when $B \ll 1$, small temperatures $T \lesssim B^2/8$ are necessary for magnetic broadening to be important when $\theta_1 \approx 0^0$. Work is in progress to extend these analytic results to the regime of larger angles θ_1.

CONCLUSIONS

The results presented in this paper show that two-photon annihilation of electrons and positrons with 1D thermal distributions can be significantly influenced by a strong magnetic field. Even for temperatures as high as $T = 0.1$, at large viewing angles to the field, magnetic broadening dominates for $B \gtrsim 10^{12}$ G. More specifically, in gamma-ray burst models where the cooling of pairs by cyclotron resonant scattering is important, the widths of annihilation features seen at viewing angles $\theta > 45^0$ will be determined primarily by the magnetic field. At most viewing angles, the magnetic field preferentially broadens the red side of the annihilation line. An integration over viewing angles removes this asymmetry. Analytic approximations for zero viewing angle are obtained: the spectrum is well-described by a simple sum of magnetically-broadened and Doppler-broadened contributions. For low T, the numerical computations are found to agree well with the cold annihilation results of Kaminker *et al.* (1987). The results presented in this paper have significant observational implications: the widths and spectral shapes of observed annihilation features in gamma-ray burst and pulsar spectra may provide diagnostics of both the magnetic field strength and viewing angle in these sources.

REFERENCES

Agrinier, B., *et al.*: 1990 *Astrophys. J.* **355**, 645

Daugherty, J. K., and Bussard, R. W.: 1980 *Astrophys. J.* **238**, 296 (DB80)

Harding, A. K.: 1986 *Astrophys. J.* **300**, 167 (Corr. 462)

Kaminker, A. D., Pavlov, G. G. and Mamradze, P. G.: 1987 *Astrophys. Sp. Sci.* **138**, 1

Kaminker, A. D., Pavlov, G. G. and Mamradze, P. G.: 1990 *Astrophys. Sp. Sci.* **174**, 241

Lamb, D. Q., Wang, J. C. L. and Wasserman, I.: 1990 *Astrophys. J.* **363**, 670

Liang, E. P.: 1986 *Astrophys. J.* **304**, 682

Mazets, E. P., *et al.*: 1981 *Nature* **290**, 378

Preece, R. D. and Harding, A. K.: 1991 *Astrophys. J.*, in press.

Wunner, G.: 1979 *Phys Rev. Lett.* **42**, 79

OSSE OBSERVATIONS OF THE CRAB PULSAR

M. P. Ulmer*, S. M. Matz*, R. A. Cameron†,
D. A. Grabelsky*, J. E. Grove‡, W. N. Johnson‡, G. V. Jung§,
R. L. Kinzer‡, J. D. Kurfess‡, M. D. Leising¶, W. R. Purcell*, M. S. Strickman†

ABSTRACT

We present preliminary results of the *Compton Gamma Ray Observatory* OSSE observations of the Crab pulsar. The pulsar energy spectra and light curves are in general agreement with previous observations, validating the OSSE pulsar data acquisition modes and data analysis algorithms. The data suggest that the spectrum of the pulsar varies throughout the light curve. The "interpulse" region has a slightly flatter spectrum in the $\sim$ 60–250 keV region and a slightly steeper spectrum at higher energies than the two main pulses. We find no evidence for any lines in the spectra with a typical sensitivity of about 10^{-4} photons cm^{-2} s^{-1}.

INTRODUCTION

The Oriented Scintillation Spectrometer Experiment (OSSE; Johnson *et al.* 1989) observed the Crab pulsar during instrument activation and also during observation period 1. In this paper we report on the preliminary analysis of the data acquired during viewing period 1 (17 May 1991 to 30 May 1991).

The OSSE pulsar data modes permit acquisition of time-tagged gamma-ray energy losses for the study of fast pulsars. The entire event stream for the detectors cannot be accommodated on an event-by-event basis in telemetry; consequently, the pulsar processing includes event selection and compression for telemetry formatting. The pulsar processing permits the definition of up to eight energy bands to be included in the transmitted pulsar data. These energy bands, as well as the rest of the pulsar data collection configuration, can be defined by OSSE mission operations activities and uploaded into the experiment via command. The pulsar data can therefore be optimized to the specific observing strategy and energy range of particular interest while limiting the event rate to that which can be handled in the OSSE telemetry.

*Northwestern University, Evanston, IL
†Naval Research Laboratory, Washington DC
‡NRC/NRL Resident Research Associate
§Universities Space Research Association, Washington DC
¶Clemson University, Clemson, SC

Table 1: Crab pulsar ephemeris

ν	$29.9493820573442\ s^{-1}$
$\dot{\nu}$	$-3.77660 \times 10^{-10}\ s^{-2}$
$\ddot{\nu}$	$7.45 \times 10^{-21}\ s^{-3}$
T0	8367.0 (TJD)
RA	$5^h34^m31\overset{s}{.}973$
Dec	$22°00'52\overset{''}{.}06$

Gamma-ray events qualified as being in one of these eight energy bands are then processed in one of two modes: (1) event-by-event mode, where selected events are time-tagged, and both energy loss and arrival time of the event are transmitted in the telemetry, or (2) rate mode, where high time resolution rate samples are taken in each of the eight energy bands.

The event-by-event mode of pulsar data provides the highest time resolution for the study of fast pulsars. This mode time-tags events accurate to 0.125 milliseconds at its highest resolution, and transmits the arrival times, detector identifications, and encoded energy losses. Depending on the OSSE telemetry format, a maximum of $\sim$ 290 events per second is supported in the event-by-event pulsar mode.

The pulsar rate mode can accommodate a much higher event rate but at the sacrifice of spectral resolution. This mode records the number of events in each of the defined energy bands at a specified sample frequency. The highest sample rate in this mode provides a resolution of 4 milliseconds. Sample times from 4 msec to 512 msec can be selected. In this mode OSSE can achieve its best sensitivity to a continuum flux.

The data presented here were collected in the 1 millisecond event-by-event (or EBE) mode, and various energy ranges were selected at different times for different detectors in order to cover nearly the entire 50 keV–10 MeV range with optimal energy resolution.

ANALYSIS METHOD

Using a version of TEMPO (Taylor and Weisberg 1989) and a position of the Crab pulsar based on an ephemeris provided by Taylor and Nice (private communication), we corrected the arrival time of the time-tagged photons to the solar system barycenter. Next, we epoch-folded the data using the relative phases of these events calculated from the ephemeris provided by Taylor and Nice (Table 1). The resulting light curve for the $\sim$ 60–246 keV energy range integrated over the observations made from TJD 8393.6 to 8399.5 is shown in Figure 1. In order to compare the phase of our pulse with that seen at radio frequencies, further phase corrections must be applied to the light curve (Taylor, private

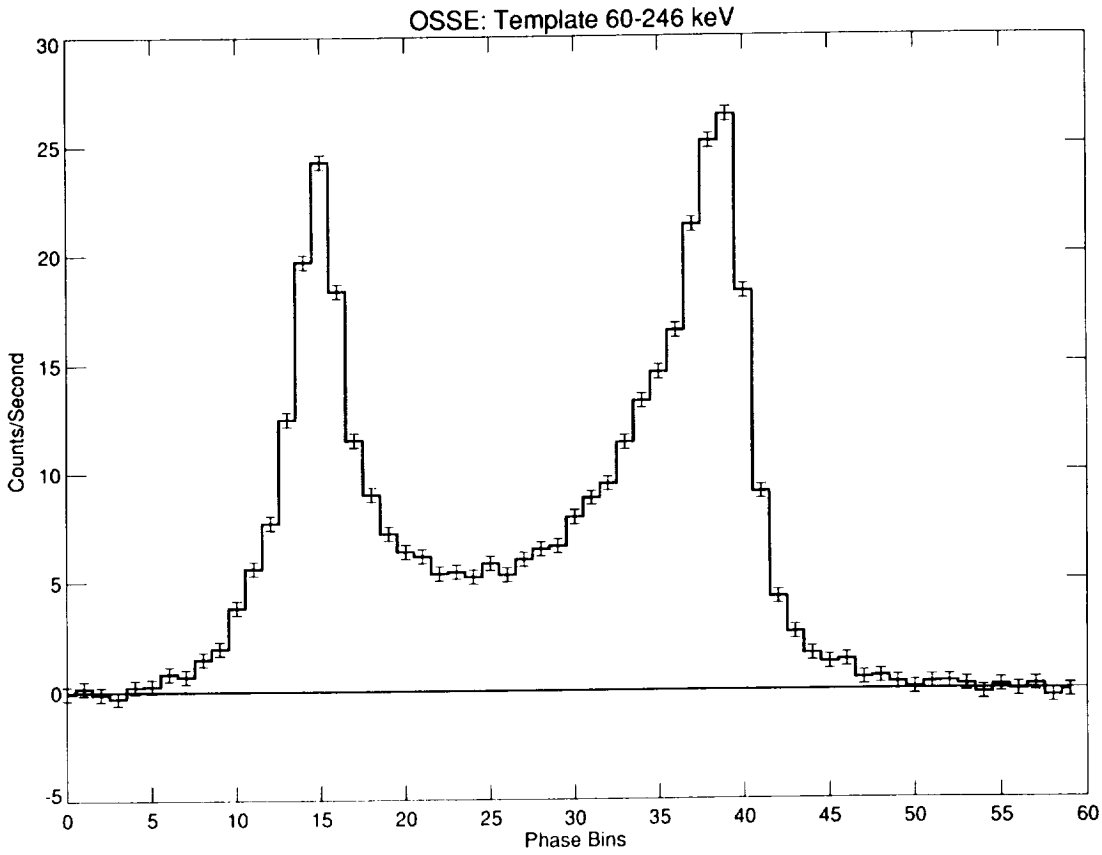

Figure 1: The average Crab pulsar light curve.

communication). However, even after applying these corrections, there is still a net offset of approximately 6 milliseconds between the two light curves. This offset is almost certainly not real, but is probably caused by insufficient accuracy in extrapolating the radio phase to infinite frequency. Further study of this problem is required.

PRELIMINARY RESULTS

In Figure 2 we show the light curves in several broad energy channels and in Figure 3 we show the hardness ratio as a function of phase. From these two figures we see that in the lower energy range, the spectrum of the interpulse region (phase bins 20 to 29) is flatter than the spectra of the pulse peaks (phase bins 14 to 19 and 35 to 41). This is in basic agreement with Knight (1982), Mahoney *et al.* (1984), and Agrinier *et al.* (1990). We have produced several preliminary spectra, but it is too early to report a detailed spectral comparison between the different regions.

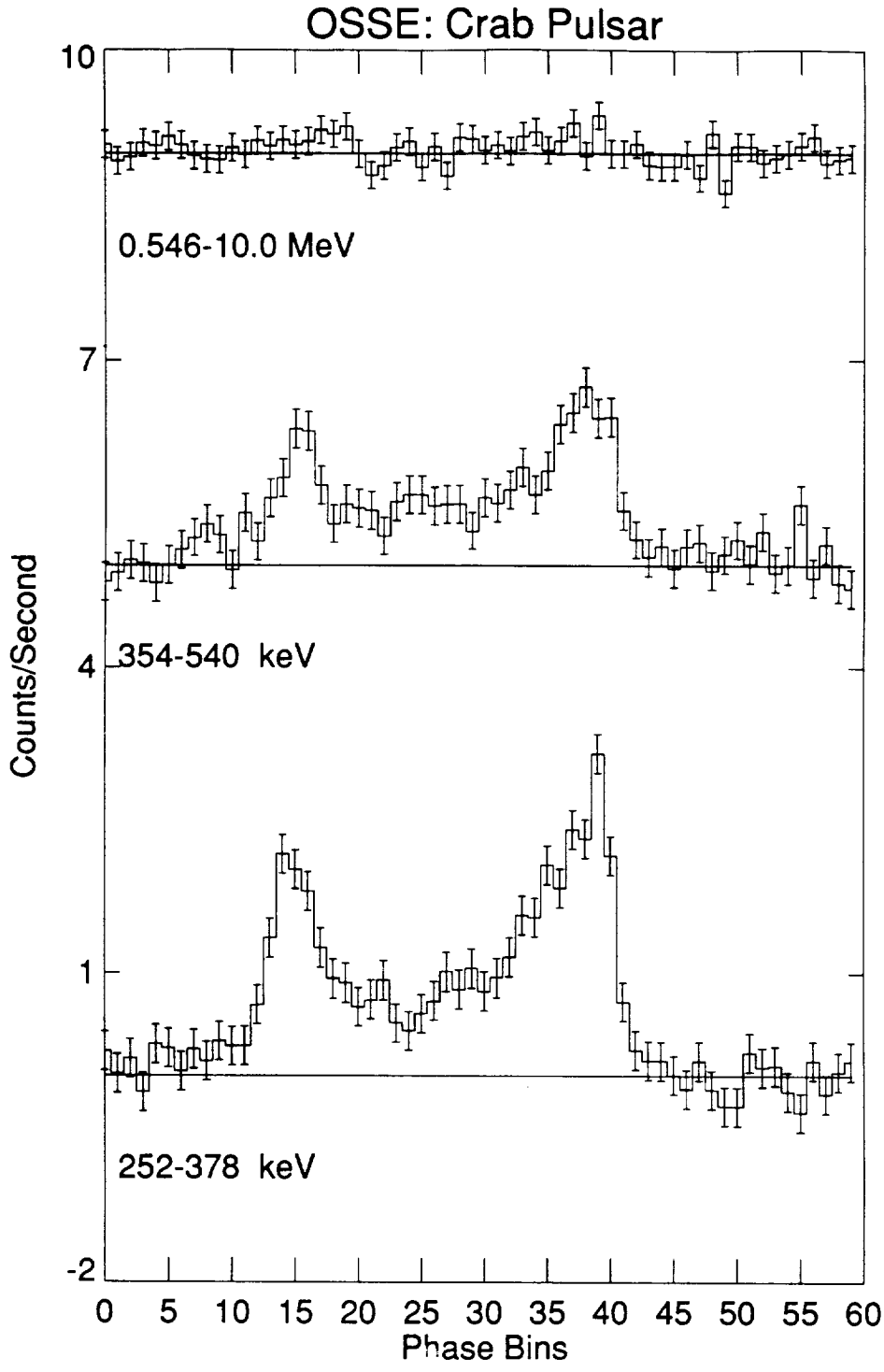

Figure 2: The Crab pulsar light curve in different energy ranges.

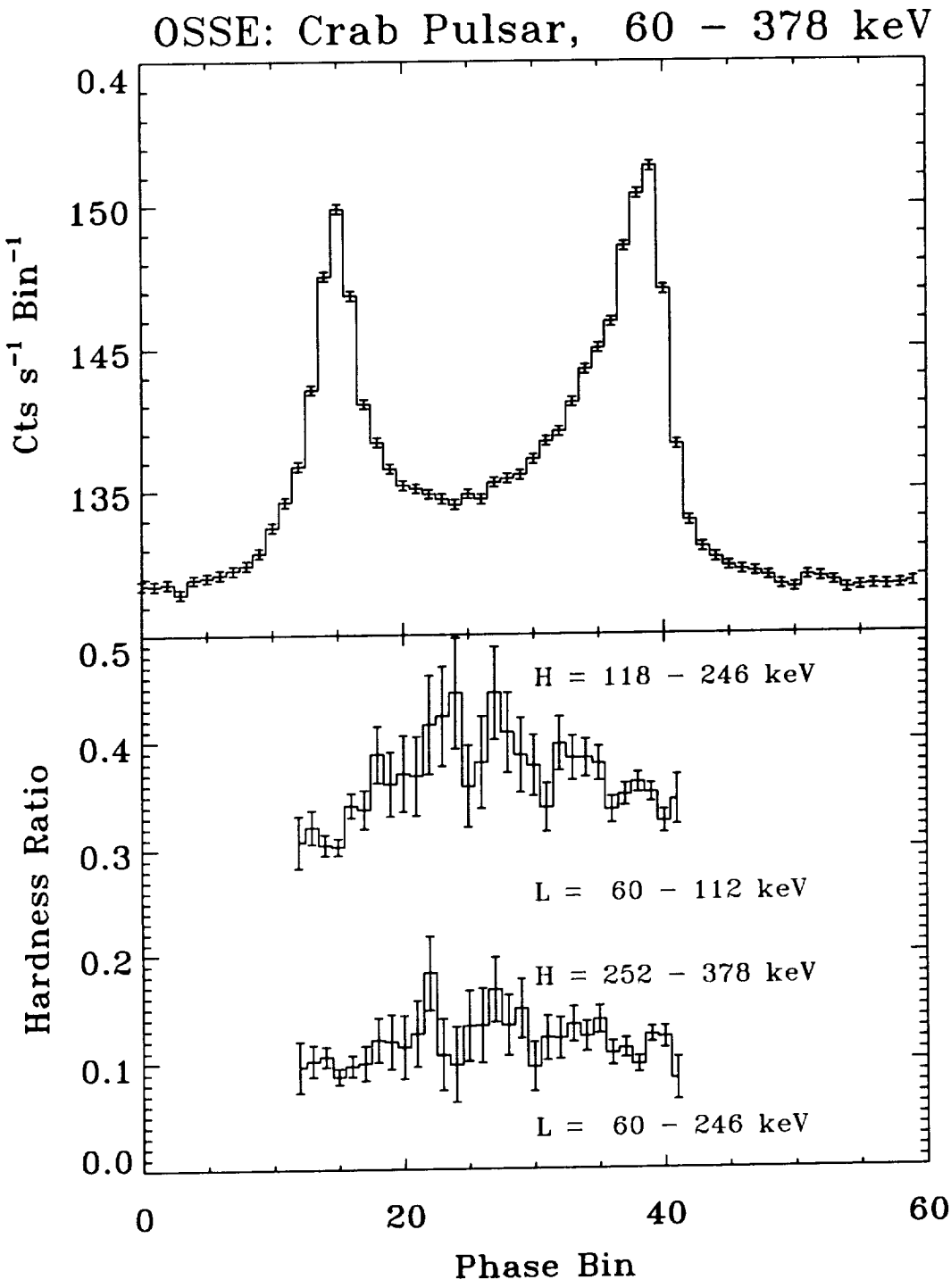

Figure 3: The Crab pulsar light curve compared with the hardness ratio, plotted as the ratio of the higher energy channel counts over the lower energy channel.

The average spectrum is shown in Figure 4 where we see very good agreement with previous experiments. Note, this is only an *approximate* photon spectrum since we used a simplified instrument response model which ignored Compton scattering.

We cannot conclusively exclude the existence of the 440 keV line in the spectrum of the second peak reported by the FIGARO group (Agrinier *et al.* 1990, Massaro *et al.* 1991) of $0.86 \pm 0.33 \times 10^{-4}$ photons cm^{-2} s^{-1}. The FIGARO result is based on combining data from balloon flights made on 11 July 1986 and 9 July 1990. In our data, we find that no features are obvious at 440 keV or elsewhere. Our 2σ upper limit to a line that is intrinsically much narrower than OSSE's $\sim 8.5\%$ detector resolution at 440 keV is $\sim 0.8 \times 10^{-4}$ photons cm^{-2} s^{-1}. On average, between 200 and 500 keV, our 2σ sensitivity to a narrow line for this observation is $\sim 10^{-4}$ photons cm^{-2} s^{-1}.

CONCLUSIONS

The OSSE pulsar mode is performing as designed. For the Crab pulsar, we find general agreement with previous experiments in terms of average spectra and pulse shape. We do not yet have any evidence for line features in the spectra, but further analysis must be done. The difference in spectral shape between the interpulse region and the peaks exhibited in our data is consistent with that reported by Knight (1982). This spectral difference suggests that the interpulse emission is coming from a different site than the peak emission. Comparison with concurrent radio observations made by Phase I Guest Investigators from Cornell University may help elucidate the nature of the emission sites (Lundgren and Cordes 1991).

REFERENCES

Agrinier, B., *et al.*, 1990, *Ap. J. Letters*, **355**, 645.

Johnson, W.N., *et al.*, 1989, *Proc. of the GRO Science Workshop*, ed. W.N. Johnson, pp. 2–22.

Knight, F.K., 1982, *Ap. J.*, **260**, 578.

Lundgren, S., and Cordes, J.M., 1991, this proceeding.

Mahoney, W.A., Ling, J.C., and Jacobson, A.S., 1984, *Ap. J.*, **278**, 784.

Massaro, E., *et al.*, 1991, *Ap. J. Letters*, in press.

Taylor, J.H., and Weisberg, J.M., 1989, *Ap. J.*, **345**, 434.

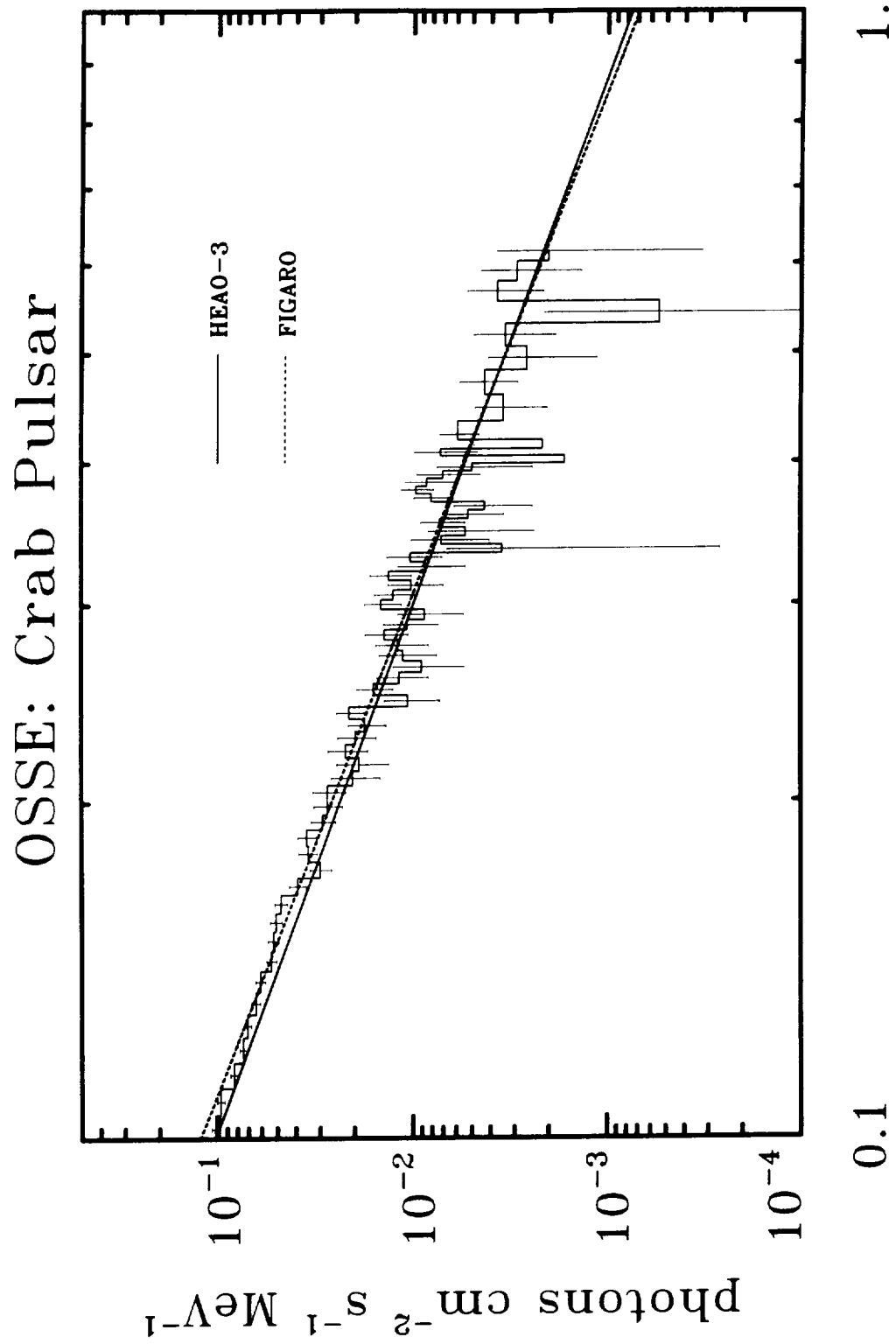

Figure 4: The average OSSE Crab pulsar spectrum, unfolded using only the instrument photopeak response, compared with the spectra measured by HEAO-3 (Mahoney *et al.* 1984) and FIGARO (Agrinier *et al.* 1990).

Crab Pulsar Giant Pulses: Simultaneous Radio and GRO Observations

Scott C. Lundgren and James M. Cordes (Cornell University)
Roger Foster (NRL)
Tim Hankins (NMMT and NRAO,VLA)
Mel Ulmer (Northwestern University)
Chris Garasi (Case Western Reserve University)

Abstract

We report observations of the Crab pulsar made at radio frequencies concurrent with OSSE observations from 15 to 27 May 1991. Using the 43 m telescope at Green Bank at 0.8 and 1.4 GHz, we sampled continuously for 10 hours per day at intervals of 100 to 300 microseconds. Our analysis of the radio data includes calculation of histograms of pulse intensities, absolute timing to about 20 microsecond precision, and characterization of intensity variations on time scales from the 33 ms spin period to days. We present the most detailed analysis made of giant pulses. The ultimate goal is to bin the radio data into giant and non-giant pulses and to form average waveforms of OSSE data for the corresponding pulse periods. We will thereby test whether the violent radio fluctuations (which are not seen in other radio pulsars to the same degree) are correlated with low energy gamma-rays, yielding constraints on the radio coherence mechanism and the steadiness of the electron-positron outflow in the magnetosphere. Timing analysis of our radio data provides a well defined ephemeris over the specified range of epochs, including a contemporaneous measurement of the dispersion measure. We can predict the gamma-ray pulse phase with an error of less than 70μs.

Introduction

Giant radio pulses from the Crab pulsar have been observed almost since its discovery (Heiles, Campbell, Rankin 1970; Staelin and Sutten 1970). Both the main and interpulses exhibit this phenomenon, but not the precursor component (Gower and Argyle 1972; Argyle 1973). The long tail on the pulse energy histogram distinguishes the Crab fluctuations from all other pulsars. The modulation index (ratio of average fluctuations to average level) of unity measured for the Crab is comparable to many other pulsars (Bartel, Sieber, Wolszczan 1980). However, the Crab modulations span many orders of magnitude, while pulse energy histograms for other pulsars show a maximum energy of 10 times the average. Typical pulsars have Gaussian or exponential pulse energy histograms (Hesse and Wielebinski 1974). For observable individual pulses, the Crab pulse energy histogram obeys a power law.

A variety of mechanisms cause pulse energy modulations on time scales of a few to many pulse periods. Diffractive scintillations due to turbulence in the interstellar plasma cause fluctuations with a decorrelation bandwidth on the order of 100 kHz for the Crab at 800 MHz (Manchester and Taylor 1977). In our observations with a 20 MHz bandwidth, these modulations are quenched. Other mechanisms seem to be intrinsic modulations in the effectiveness of the emission mechanism. Many pulsars display pulse nulling in which the emission turns off entirely for many consecutive pulse periods (Ritchings 1976). Switching a coherence mechanism on and off may cause these nulls. Alternatively, an enhancement or suppression of pair creation may influence the radio emission. Other pulsars switch between two different emission modes (Backer 1970). In such cases, the average profile switches between two shapes depending on observation time. Since most Crab pulses are hidden by the brightness of the nebula background, it is not clear whether giant pulses are caused by a different mechanism from smaller pulses, or they are simply an extension of a continuous distribution of pulse energies.

Simultaneous observations of the Crab pulsar at gamma-ray and radio wavelengths will distinguish between enhanced pair cascade and radio coherence mechanisms for giant pulse emission. Changes in pair production efficiency would affect both radio and gamma-ray emission. On the other hand, improved radio coherence would have no effect on gamma-ray emission. The long term goal of this project is to compare gamma-ray emission of the Crab during giant pulses and lesser pulses, in the hope of constraining emission mechanism theories for young pulsars.

Observations

For our radio observations of the Crab pulsar, we used the spectral processor at the NRAO's Green Bank 43 m telescope at 1330 MHz for 2 days, at 800 MHz for 1 day and at 812.5 MHz for 10 days. We sampled every 200 μs or 300 μs in hour long scans 10 hours per day (May 15-27). This resulted in 24 Gbytes of data containing over 10^7 pulse periods and 3×10^4 giant pulses.

At radio frequencies, interstellar plasma dispersion delays lower frequency signals with respect to higher frequencies, thus smearing a pulsed signal. To remove this effect, the spectral processor divides the 20 MHz bandwidth into 256 channels and compensates for the relative delays between channels to dedisperse the signal using the known dispersion measure of the Crab pulsar. This reduces the dispersion smearing from 18 ms across 20 MHz at 800 MHz to 70 μs across each 78 kHz channel. The spectral processor provides intensity outputs in individual polarizations and in two contiguous bandpasses of 10 MHz each. Pulsar pulses could be discriminated from interference by requiring that the correct dispersion delay appear in spikes that occur in the two 10 MHz bandpasses.

Data Analysis and Results

We developed analysis software to produce average pulse profiles and to extract giant pulses from the fast sampled data. Due to Earth rotation, orbital motion, and pulsar spindown, the pulsar period changes significantly over an hour long observation. The program TEMPO (from J.H. Taylor) calculates the topocentric period behavior given input parameters for the pulsar period, period derivative, and sky position. Our program uses pulse phase prediction from TEMPO in creating average profiles.

To quantify giant pulse behavior, we calculated an average fluctuation profile in addition to the average profile (fig. 1a). With no variation in pulse intensity the fluctuation average would be zero. The modulation index (ratio of fluctuations to the average) is determined by the intensity distribution of giant pulses. Typically for the Crab pulsar, the ratio of the fluctuation waveform to the mean waveform is near 1, indicating that the intensity is 100% modulated. Most of this modulation comes from giant pulses. In fact, in several of our hour averages, a single giant pulse more than 400 times the average increases the modulation index to more than 8. By contrast, optical measurements (Hegyi, Novick and Thaddeus 1971) place an upper bound of 1% on pulse to pulse fluctuations.

While most individual pulses are not observable (signal to noise ratio S/N=0.07), individual giant pulses may greatly exceed the noise (fig. 1b). This allows us to extract the area ('pulse energy'), arrival time and width for each giant pulse above the noise in our data. By designating giant pulses as only spikes with the correct dispersion offset between the lower 10 MHz band and the upper 10 MHz band, we lowered the giant pulse flux threshold to 3 sigma or 0.1 times the nebula without introducing spurious giant pulses.

By cross correlating each average profile with a high signal to noise template we calculated precise arrival times from each average profile. The program TEMPO references these topocentric arrival times to the Solar System barycenter. By fitting barycentric arrival times to a model, the program provides current values for the pulsar period and spindown. From the offset between 1330 MHz

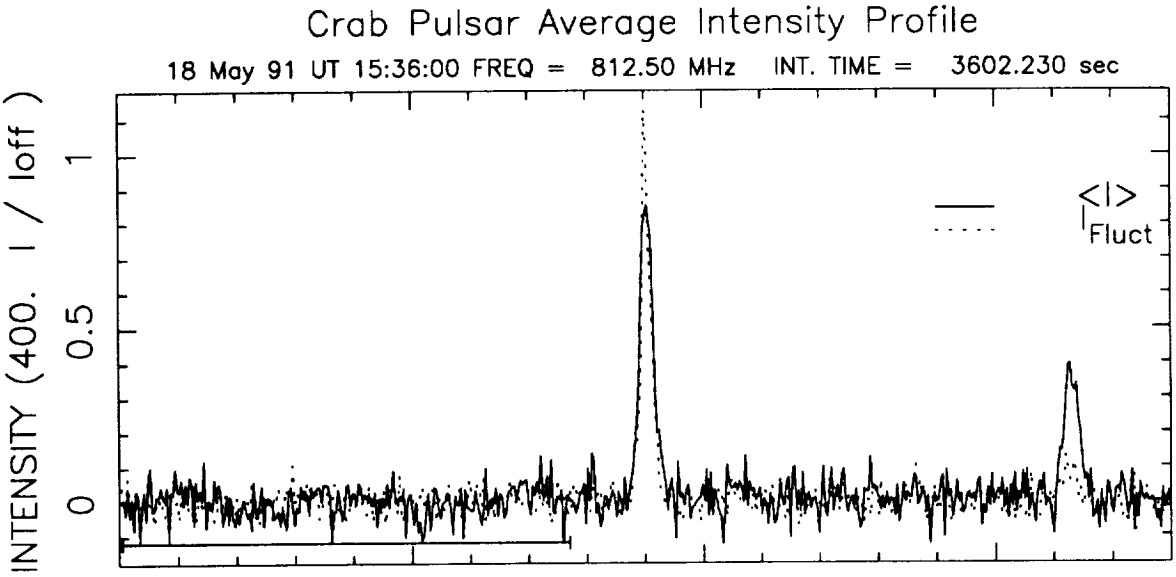

Figure 1a shows a typical average profile from one hour of data. The solid line average profile is centered on the main pulse. On this intensity scale 400 corresponds to the intensity of the Crab Nebula, the background from which dominates the system temperature. The dotted line fluctuation average ($(< I^2 > - < I >^2)^{0.5} - \sigma_{OffPulse}$) indicates the presence of giant pulses.

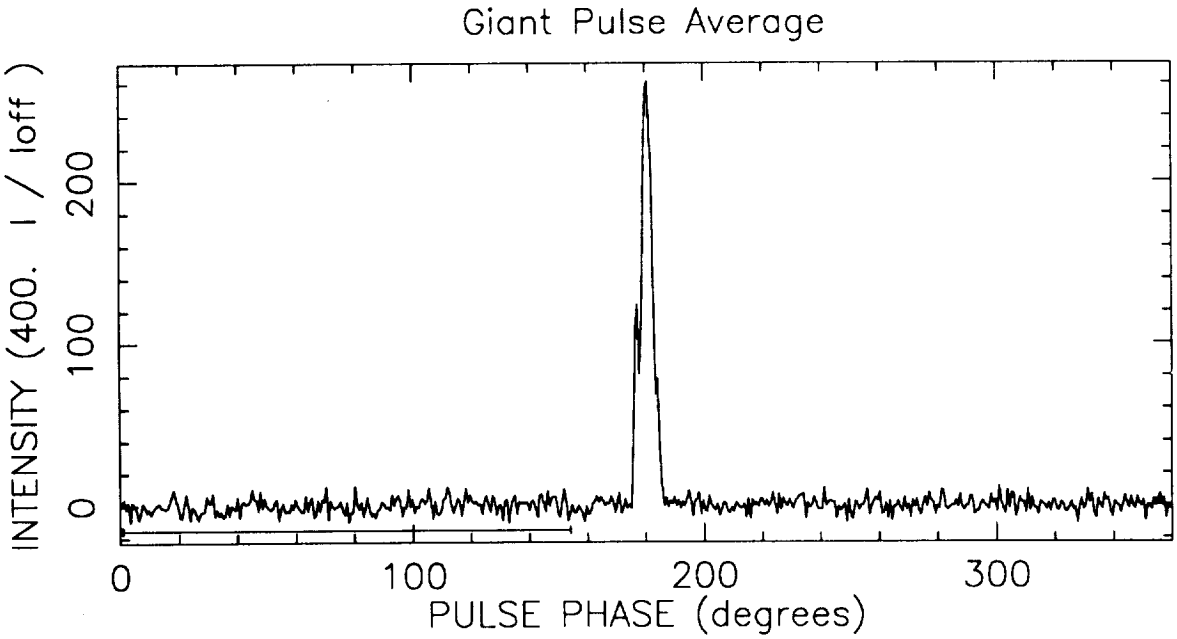

Figure 1b shows a sub-average which includes only giant main pulses above a threshold of 200 in our units. An average of 15 of these occur per hour.

and 812.5 MHz arrival times, we fit for dispersion measure (DM) as well. An accurate dispersion measure is necessary to compare radio pulse arrival times (delayed by the interstellar plasma) to gamma-ray arrival times (unaffected by dispersion).

We used the 10 days of 812.5 MHz data to fit for period and period derivative, holding period second derivative fixed to the known value. Then, while holding these fixed, we added the 1330 MHz data to fit for DM. This resulted in the following parameters:

P	=	33.3264436338 ms	or	ν =	29.9483705571866
$\dot{p}$	=	$419.4132 \times 10^{-15} ss^{-1}$		$\dot{\nu}$ =	-3.77628×10^{-10}
pepoch	=	46625.5 (jd)		epoch =	48403

DM=56.776 ± 0.005

Our DM accuracy allows conversion to infinite frequency arrival times to within 70 μs.

The rms residual for the average profiles is 20 μs (fig. 2a). Giant pulses, on the other hand, are spread over $\pm 300\mu$s. Since this spread is much larger than the 205 μs or 307.5 μs sample interval used, we attribute it to intrinsic jitter in arrival times. The offset between the average giant pulse residual and the average profile residual agrees with zero within the errors (6 μs ± 3 μs).

The number of giant pulses varies from day to day. During the first two days, we observed at 1330MHz. The pulsar signal is much weaker at this frequency, so we saw many fewer giant pulses above the noise threshold. However, even at a single frequency, the rate of giant pulses varies. For example, giant pulses were much less frequent on day 48400 than they were on day 48402.

To describe the time distribution of giant pulses (fig. 3), we postulated that the mechanism is a Poisson process. This requires that each giant pulse is statistically independent of every other giant pulse. Rotation of the pulsar beam through our line of sight samples the Poisson process at discrete intervals determined by the period. Sampling an exponential distribution of times at integer multiples of the period gives a histogram which agrees well with our observations. The small deviations observed will require more detailed future analysis to determine their significance. Overall, the giant pulses are randomly distributed in time.

We also examined the energy distribution of giant pulses at 812.5 MHz. The giant main pulse energy histogram in figure 4 displays a steep power law distribution (index=-3.46 ± 0.04). This is significantly steeper than the -2.5 power law found by Argyle at 146 MHz (Argyle and Gower 1974), suggesting that the giant pulse mechanism is less efficient at higher frequencies. The largest giant pulse measured in 2 weeks was 12.5 times the nebula flux or 5000 times the average main pulse flux! The roll off at low energies is most likely due to our noise thresholding. Hankins has made high time resolution observations at the Very Large Array (VLA). These observations resolve giant pulse fine structure into multiple 10 μs spikes. Earlier work determined an exponential decay time scale for spike energy of 90 μs at 430 MHz (Hankins and Rickett 1975) that is caused by interstellar scattering.

Future Work

For each giant pulse in our data we have the arrival time, the width and energies for that pulse, the interpulse, the next pulse and interpulse, and the previous pulse and interpulse. From correlations between arrival times, rates, widths and energies we hope to constrain theoretical models for giant pulse emission mechanisms. Additionally, we will cross-correlate our data with gamma-ray data from GRO. We will provide our giant pulse barycentric arrival times to the GRO community. These times can be converted to spacecraft arrival times. Averages of those gamma-ray pulses which correspond to giant radio pulses can then be formed and compared to non-giant

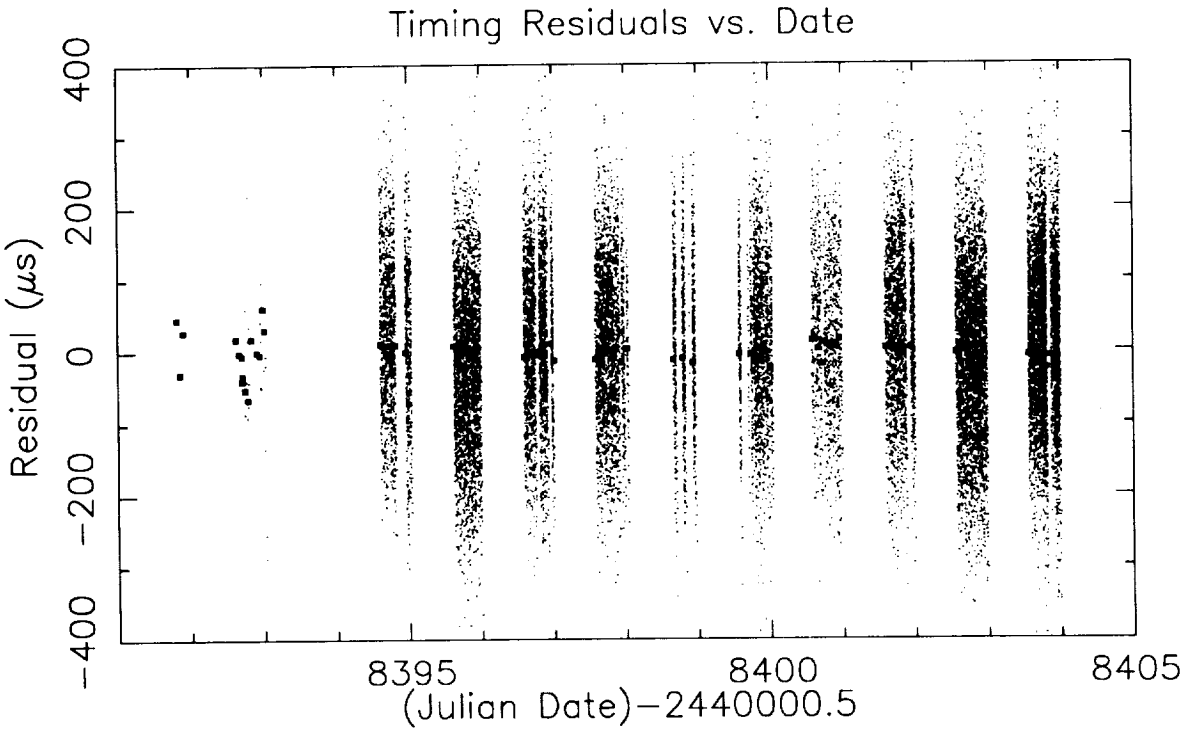

Figure 2a We have plotted the residuals from our timing fit. The large squares correspond to residuals for the average profiles. On the same plot we included residuals for the individual giant pulse arrival times, as small dots. Blank strips in the plot correspond to times when we were not observing.

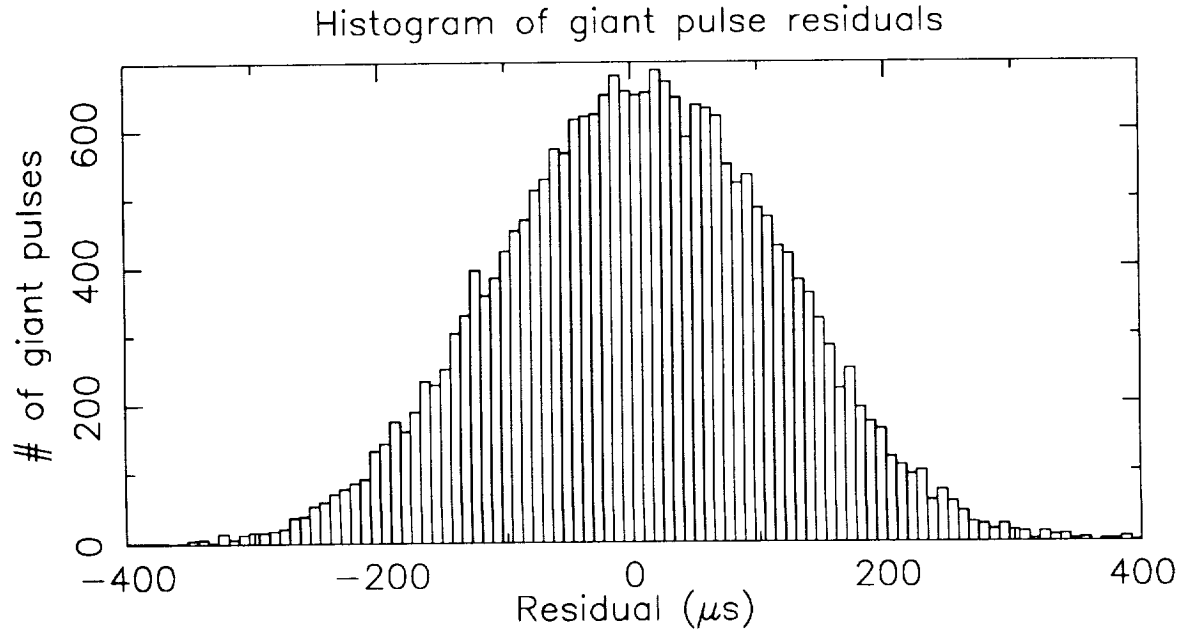

Figure 2b shows a histogram of giant pulse arrival time residuals.

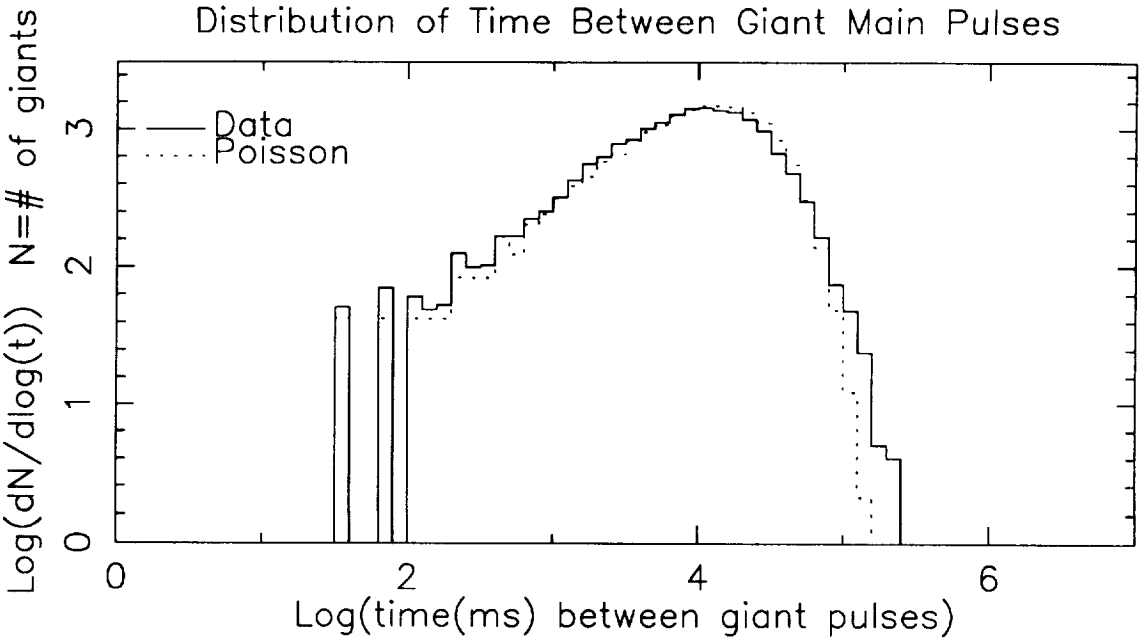

Figure 3 We plotted a histogram of the time between giant pulses at 812.5 MHz, using a logarithmic scale with logarithmic bins. The two spikes at 1.5 and 1.8 correspond to one period and two period separation respectively. The dotted curve is a theoretical prediction, $dN/dt = N/t_0 \times \exp(-t/t_0)$, where N=# of giant pulses and t_0 =average time between giant pulses. The exponential distribution has been binned in the same manner as the data.

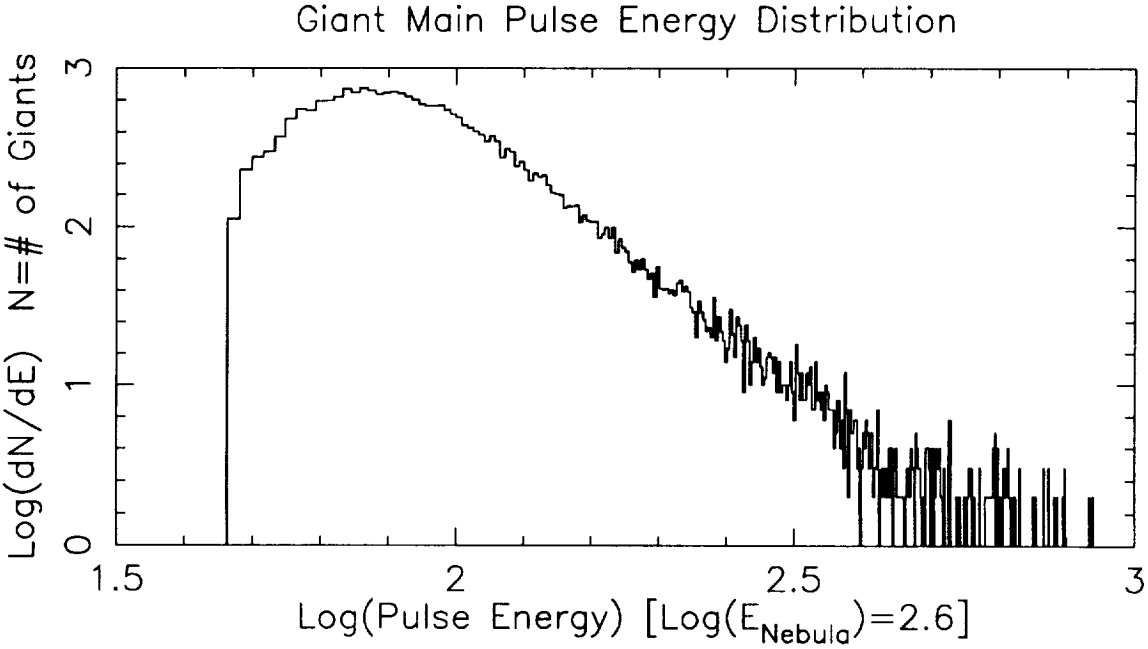

Figure 4: Histogram of giant pulse energies at 812.5 MHz plotted logarithmically.

pulse averages. Detection of correlations, anti-correlations, or uncorrelated results will constrain pulsar emission theories, distinguishing between fluctuations in the pair production cascades and changes in the effectiveness of radio coherence mechanisms.

For a giant pulse arrival time file contact us by email at lundgren@astrosun.tn.cornell.edu or contact Mel Ulmer at ULMER@ossenu.astro.nwu.edu.

This work was supported by NASA through a grant for GRO Phase I research and by the NSF through an REU grant. The National Radio Astronomy Observatory is operated by Associated Universities Inc., under cooperative agreement with the National Science Foundation.

References

Argyle, E. 1973, *Ap. J.*, **183**, 973-975.

Argyle, E. and Gower, J.F.R. 1974, *Ap. J.*, **175**, L89-L91.

Backer, D.C. 1970, *Nature*, **228**, 1297.

Bartel, Sieber and Wolszczan, A. 1980, *AA*, **90**, 58-64.

Gower, J.F.R. and Argyle, E. 1972, *Ap. J.*, **171**, L23-L26.

Hankins, T.H. and Rickett, B.J. 1975, *Methods in Computational Physics*, **14**, 55

Hegyi, D., Novick, R., and Thaddeus, P. 1971, *IAU Symp.*, **46**, "The Crab Nebula", p129-140.

Heiles, C., Campbell, D., and Rankin, J. 1970, *Nature*, **226**, 529-531.

Hesse, Wielebinski 1974, *AA*, **31**, 409-413.

Manchester, R.N. and Taylor, J.H. 1977, *Pulsars*, W.H. Freeman and Company, 137-146.

Ritchings, R.T., *MNRAS*, **176**, 249-263.

Staelin, D.H. and Sutton, J.M. 1970, *Nature*, **228**, 69.

Gamma Ray Pulsar Analysis from Photon Probability Maps

Lawrence E. Brown, Donald D. Clayton, and Dieter H. Hartmann
Department of Physics and Astronomy
Clemson University
Clemson, SC 29634-1911, U.S.A.

Abstract

We present a new method of analyzing skymap-type γ-ray data. Each photon event is replaced by a probability distribution on the sky corresponding to the observing instrument's point spread function. The skymap produced by this process may be useful for source detection or identification. Most important, the use of these photon weights for pulsar analysis promises significant improvement over traditional techniques.

1 The Method

We have used the derived point spread function for the COS-B experiment to develop data analysis tools with improved ratios of signal to background with applications to source identification and searches for faint γ-ray pulsars. We generate a weighted photon probability map to enhance any significant γ-ray signal present in the data and suppress undesirable background fluctuations. The basis for this method can be formulated in two equivalent ways:

a) By definition, the point spread function (PSF) of an imaging instrument describes the redistribution of photons from a particular direction on the sky into the observed distribution. Thus, each event may be represented as a continuous distribution of event weights on the sky (for COS-B, the PSF vanishes for $\theta > 20°$).

b) Correspondingly, any location on the sky receives some weight from each γ-ray seen during the experiment. In other words, each observed photon has a certain probability, given by the PSF, to have originated at that location.

Based on this concept, we smooth each photon arrival direction into an extended probability map. When investigating a particular source location, our analysis includes *all* γ-ray events through their weights at that position. To demonstrate the usefulness of this approach we apply it to the light curve of the Crab pulsar. The extraction of a source list from our COS-B probability map is in progress.

2 COS-B Probability Maps

The observed direction of each photon event does not correspond directly to its point of origin on the sky. Information on the detector angular resolution is contained in the PSF of the detector. To identify γ-ray sources, the intrinsic fuzziness of γ-ray detectors can be included in the analysis by creating a skymap of "probability flux" rather than "photon count flux".

The weight of a γ-ray event with observed direction α for a small solid angle $\Delta\theta$ centered on a point p is defined as

$$w(p;\alpha) = PSFSR(\theta(\alpha,p))\Delta\theta,$$

where PSFSR is the point spread function per steradian. We use the PSFSR derived by the COS-B team using the Vela pulsar (Mayer-Hasselwander 1985).

The celestial γ-ray intensity, I_c, at a point on the sky (in terms of weight) is

$$I_c(p) = \frac{\Sigma_{\gamma's} w(p) - \int_{sky} d\Omega w(\Delta N_b(p))}{\int_{sky} d\Omega w(\Pi(p))} - I_b,$$

where the summations are taken over all events seen by the experiment, the $w(p)$'s are the weights of the individual events, $w(\Delta N_b(p))$ is the weight, at p, of the instrumental background correction for all other points on the sky, and $w(\Pi(p))$ is the weight, at p, of the exposure (in $cm^2\ s$) for all other points on the sky. I_b is the "standard" background correction as given by the COS-B team. The units of I_c are $photons/cm^2\ s\ sr$.

This defines our weighted sky intensity probability distribution. We have sampled this continuous map at .5° intervals for the whole sky. The resultant maps in the energy ranges 50-150 MeV, 150-300 MeV, and 300-5,000 MeV are shown in figure 1.

This technique may not be ideal for some aspects of *source identification.* It results in a skymap which may be "too fuzzy" since the photons are effectively convolved twice through the PSF. That is, they are spread once in passing through the detector and again by our technique. However, it does not make any arbitrary smoothing assumptions. A comparison of our source list (in progress) with those resulting from other techniques (e. g.Simpson & Mayer-Hasselwander 1987; Bloemen 1989) will be useful. For instance, our technique finds a possible source of high intensity but low statistical weight at $l = 309.5, b = -30.5$ in the middle energy range (see figure) it should be instructive to see if the maximum likelihood methods of Grenier et al. confirm this source candidate.

3 Lightcurve of the Crab Pulsar

For analysis of periodic sources, we analyze weights vs. phase instead of counts vs. phase. Superimposed on a background that is $\sim$ uniform in space and time, the γ-ray pulsar adds a signal that is localized both in space and time. Standard analysis of γ-ray phases considers all photons within a given acceptance cone equally. Photon arrival directions

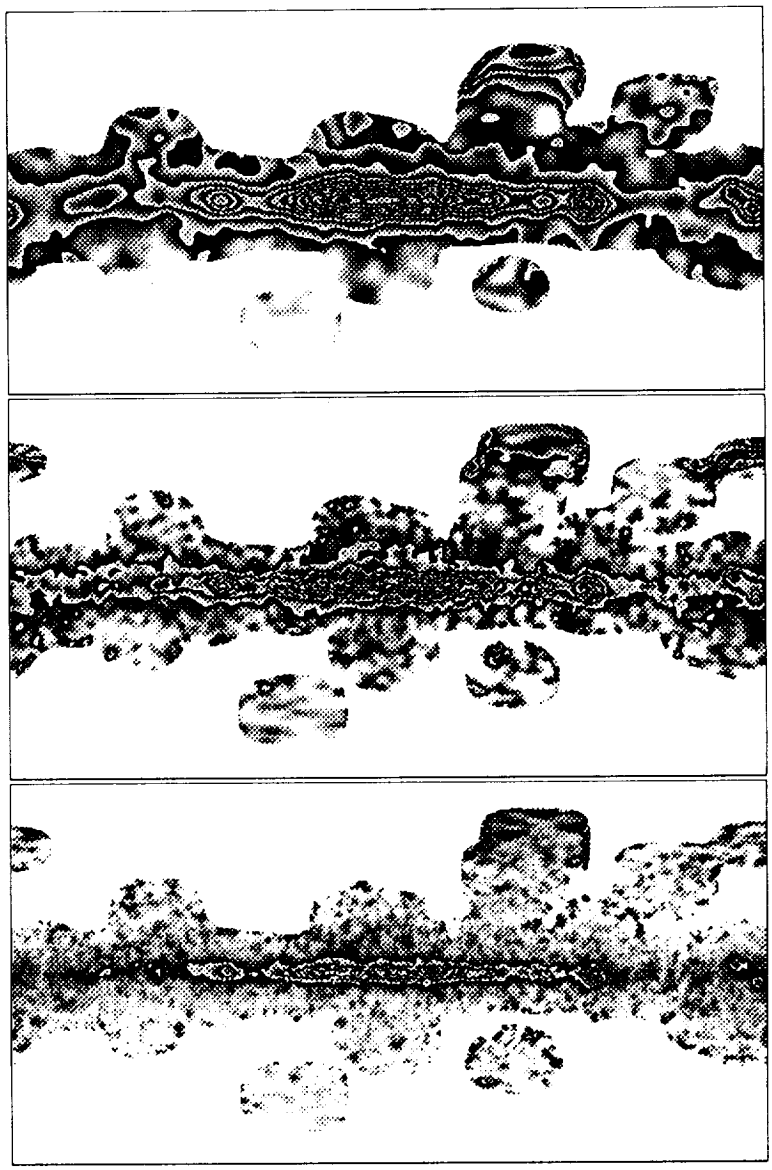

Figure 1: *Skymaps of photon weight of the COS-B observations for the energy ranges 50-150 MeV, 150-300 MeV, and 300-5,000 MeV. The photon weight distribution on the whole sky is sampled on a grid of .5 degree spacing. Since COS-B did not observe all areas of the sky, some regions of the map at high galactic latitudes are blank. The graymaps used here represent intensity of* photons/cm^2 s sr, *with intensity increasing from black to white. This graymap is wrapped around 10 times between the faintest and brightest spots for better monochrome resolution. It is, essentially a grayscale "contour map". The graymaps are assigned individually for each map (i. e. equal gray intensities on different maps do not represent equal photon fluxes).*

TABLE 1: Signal to background

Observation	Peak Signal (Std. Dev.)		Integrated Signal (Std. Dev.)	
	weights	counts	weights	counts
Crab Pulsar	43	18	176	101
1/2 Crab Pulsar	33	12	107	59

closer to the pulsar position have a higher probability of containing the sought after pulsed signal. Thus, by considering both space and time, we gain an added degree of freedom for extracting the signal from the background.

The standard binning technique folds solar barycentric arrival times with the measured period characteristics obtained from radio observations (Buccheri et al. 1983). Traditionally, one defines an acceptance cone around the source direction with opening angle

$$\theta_{max} = 12.5E(MeV)^{-.16}.$$

Inside this cone, all photons contribute equally to the light curve. In our approach, PSF weighting implicitly performs this task; thus, we can utilize the maximum aperture consistent with a non-zero PSF ($\theta_{max} = 20°$ for COS-B).

Then, instead of binning counts by phase to create a light curve histogram, we bin weights by phase. Results for the two methods for the Crab Pulsar are shown in our figure 2.

Figure 3 highlights the differences between the two approaches. Essentially, the traditional method uses a uniform probability function inside an acceptance cone that has an energy dependent width. We have used, instead, a probability function which extends over the full range of non-zero PSF, but binned into 3 energy ranges. This binning follows COS-B tradition, could easily be made finer.

To allow direct comparison of the two methods, we plot the standard deviation for each bin. To calculate the average background level, we have used the "flat" portion of the Crab pulsar's γ-ray light curve between the second peak and the end of the period. The resulting plot shows counts (weights) minus average background divided by standard deviation from background. We show results for all, and half of the Crab pulsar observations of COS-B to demonstrate the performance of this technique for reduced sampling times. The results in terms of maximum signal above background and total integrated signal are given in table 1. While the exact numbers are dependent on bin size, the improvement is dramatic in all cases.

This obvious increase in significance of detected pulses should also benefit the cluster analysis algorithm of Buccheri, et al. (1988). We are currently investigating this and other extensions to the general weighting technique.

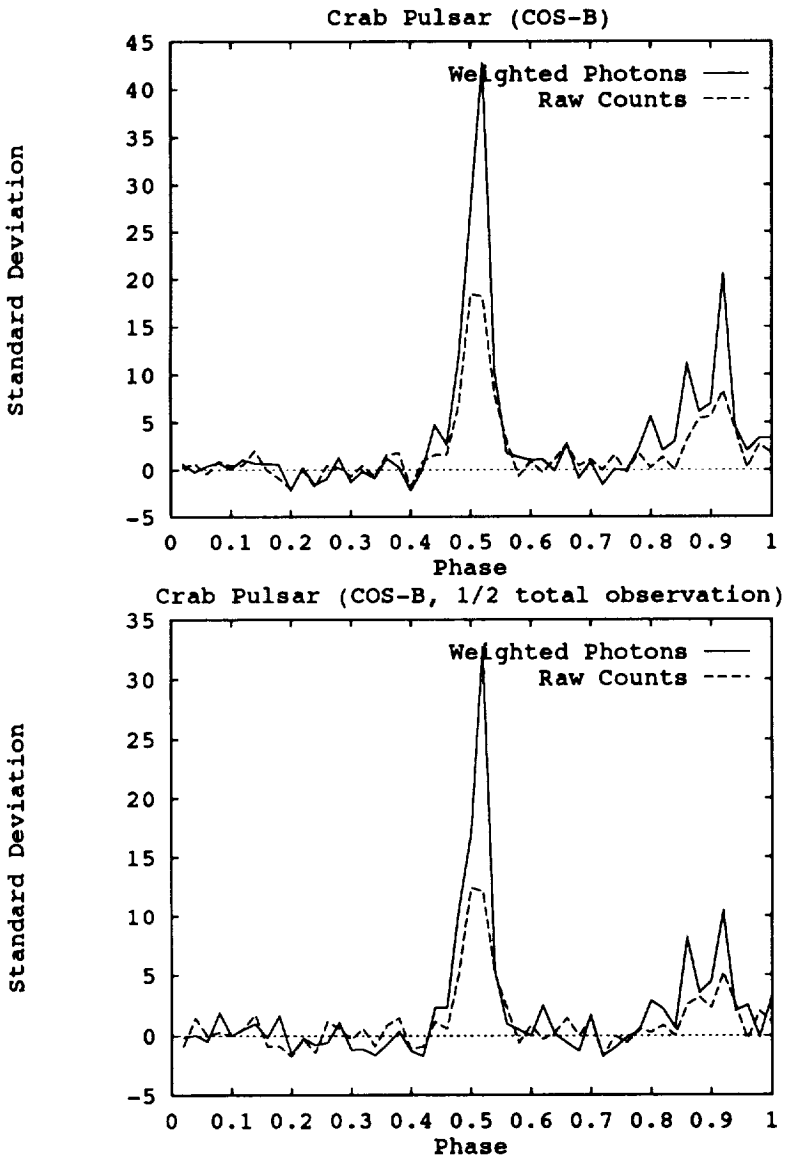

Figure 2: *Shown are the weighted photon method (solid) and the standard count method (dashed) of phase binning for the full COS-B data set for the Crab pulsar. Note the dramatically improved signal for the weighted photon method. (Number of bins = 50.)*

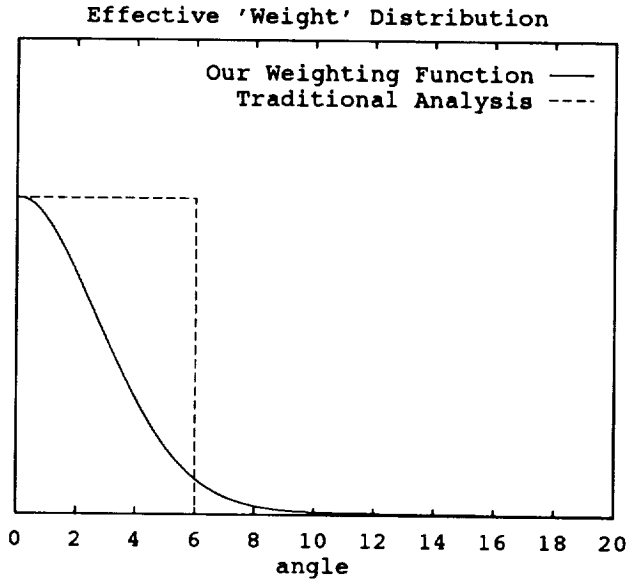

Figure 3: *Schematic drawing comparing the effective probability "weight" distribution for traditional pulsar analysis (dashed) and our weighting function (solid) for a given energy* ($\sim 100 MeV$).

Acknowledgements

This research was supported in part by NASA Grant NAG 5-1578. We thank Mark Leising and Lih-Sin The for many valuable discussions.

References

Bloemen, H. 1989, *Ann. Rev. Astron. Astrophys.*, **27**, 469

Buccheri, R., et al. 1983, *Astron. Astrophys.*, **128**,245

Buccheri, R., Di Gesu', V., Maccarone, M.C., and Sacco, B. 1988, *Astron. Astrophys.*, **201**,194

Grenier, I.A., Hermsen, W., and Pollock, A.M.T. 1991, in *AIP Conference Proceedings*, (New York), p. 3.

Mayer-Hasselwander, H. A. , ed. 1985, *Explanatory Supplement to the COS-B Final Database.*

Simpson, G., and Mayer-Hasselwander, H.A. 1987, *Proceedings of the 20th ICRC*, (Moscow), 1:89

4.
GAMMA-RAY BURSTS

ISSUES IN THE ANALYSIS AND INTERPRETATION OF CYCLOTRON LINES IN GAMMA-RAY BURSTS

D. Q. LAMB
Department of Astronomy and Astrophysics and Enrico Fermi Institute
University of Chicago, 5640 S. Ellis Avenue, Chicago, IL 60637

ABSTRACT

We discuss the Bayesian approach to establishing the existence of lines, the importance of observing multiple cyclotron harmonics in determining physical parameters from the lines, and evidence from cyclotron lines of neutron star rotation.

I. INTRODUCTION

Gamma-ray bursts continue to confound astrophysicists nearly a quarter of a century after their discovery. The challenge of deciphering their nature is exacerbated by the fact that one cannot predict when or from where the bursts will occur, and the fact that it has been impossible to date to find quiescent counterparts of the bursts at radio, infrared, optical, ultraviolet, X-ray, or γ-ray energies. The latter puts a premium on garnering knowledge from the bursts themselves.

The shape of the continuum spectrum can provide important constraints on theory, but inverting it uniquely to determine the radiation mechanism, let alone physical parameters like the density and temperature, is exceedingly difficult. In contrast, the power of lines is well known: Analyses of atomic lines transformed astronomy into astrophysics. Because atomic lines are unavailable above $\sim$ 7 keV, studies of γ-ray bursts must rely on cyclotron and, possibly, pair annihilation lines.

Gamma-ray bursts offer a particularly promising opportunity to study cyclotron lines because the bursts are bright and their X-ray continuum spectra are unusually hard. As a result, the locations, strengths, and widths of several harmonics may often be measured. This contrasts with, *e.g.*, accretion-powered pulsars, whose continuum spectra fall rapidly, even exponentially, above $\sim 20 - 30$ keV, making it difficult to detect, let alone measure the properties of, higher harmonics. Comparison of Figure 1, which shows the observed count rate and best-fit theoretical photon number spectra for the accretion-powered pulsar X0115+634, and Figure 2, which shows the same spectra for the γ-ray burst GB880205, illustrates this point.

Observations using the Los Alamos/ISAS burst detector on the *Ginga* satellite have demonstrated the existence of statistically significant harmonically spaced line features in three γ-ray bursts: GB870303 (Graziani *et al.* 1991), GB880205 (Fenimore *et al.* 1988), and GB890929 (Yoshida *et al.* 1992). Radiation transfer calculations have shown that cyclotron resonant scattering in a strong magnetic field can account quantitatively for the positions, strengths, and widths of these lines (Lamb *et al.* 1989; Wang *et al.* 1989). The success of this model convincingly demonstrates the existence of a strong magnetic field ($B \approx 2 \times 10^{12}$

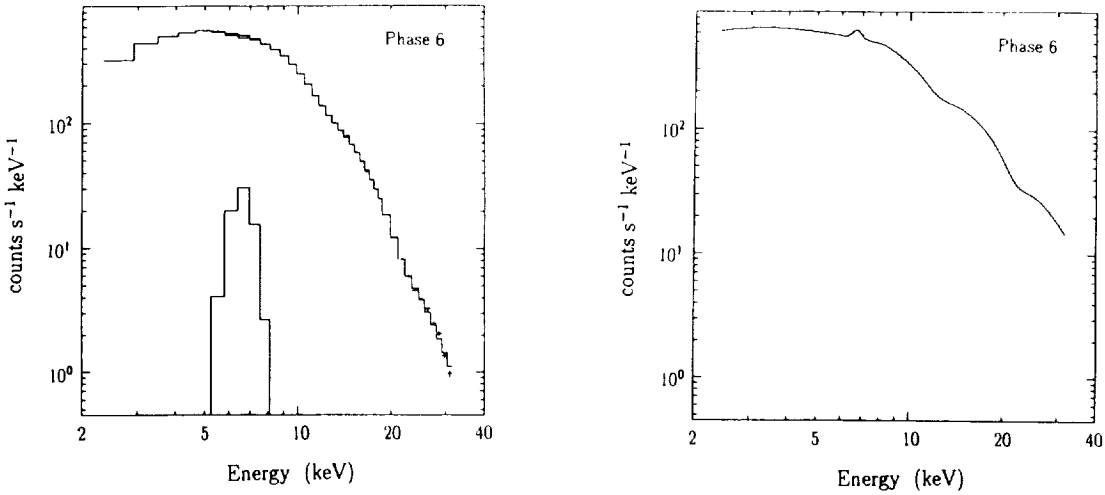

Fig. 1—*Ginga* Large Area Counter observation of the accretion-powered pulsar X0115+634 at phase 6 of the pulse. Left panel: Count rate spectrum (crosses), normalized to the width of the detector energy loss channels and best-fit theoretical count rate spectrum (histogram) and iron line contribution (narrow histogram). Right panel: Best-fit theoretical photon number spectrum. Note the cyclotron scattering lines at $\approx$ 12 and 24 keV. (After Nagase *et al.* 1991.)

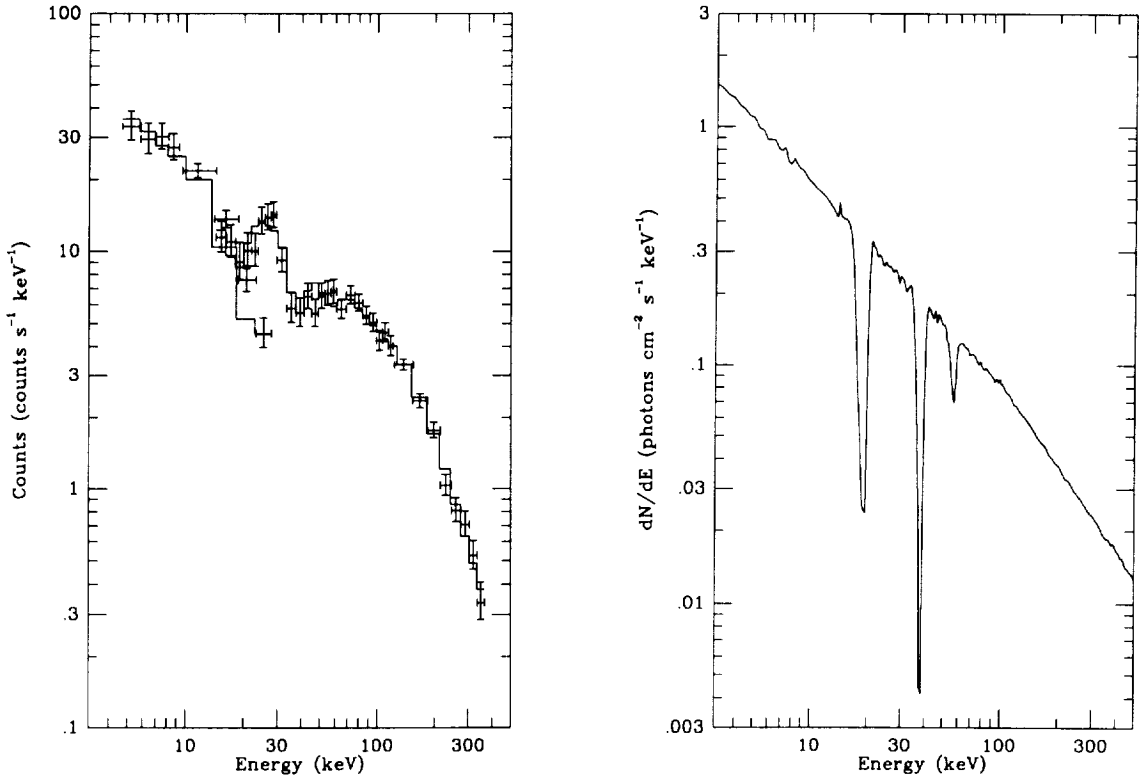

Fig. 2—*Ginga* Gamma-Ray Burst Detector spectrum of the γ-ray burst GB880205, during the 5 second interval labeled (b) in Figure 2 of Murakami *et al.* (1988). Left panel: Count rate spectra (crosses), normalized to the width of the detector energy loss channels and best-fit theoretical count rate spectra (histograms) for the PC and SC. Right panel: Best-fit theoretical photon number spectrum. Note the cyclotron scattering lines at $\approx$ 20 and 40 keV. (After Murakami *et al.* 1988 and Wang *et al.* 1989.)

G) in the sources of these γ-ray bursts. This result, taken together with the *Ginga* (Yoshida *et al.* 1991) and Konus (Mazets *et al.* 1981) data, which show low-energy lines in $\approx 15\%$ of all classical γ-ray bursts, provides compelling evidence that many γ-ray bursts come from strongly magnetic neutron stars in the Galaxy. These conclusions take on added significance with the discovery that even faint γ-ray bursts are distributed isotropically on the sky (Fishman *et al.* 1991), and the ensuing debate about whether some, or all, γ-ray bursts are cosmological in origin.

Here we explore issues in the analysis and interpretation of cyclotron lines in the spectra of γ-ray bursts; in particular, we discuss the Bayesian approach to establishing the existence of lines, the importance of observing multiple cyclotron harmonics in determining physical parameters from the lines, and evidence from cyclotron lines of neutron star rotation.

II. MODEL COMPARISON

One of the most important, yet nettlesome, issues in the analysis of cyclotron lines in γ-ray bursts is establishing the existence of the lines themselves. Here we describe a rigorous method derived from Bayesian inference; our presentation closely follows Loredo (1992; for discussions of the conceptual and methodological advantages of the Bayesian approach, see Loredo 1990).

In Bayesian inference, the probability for a model as a whole is the product of a prior probability and a global likelihood. In the absence of any information suggesting otherwise, we take the prior probabilities of competing models to be equal. Then the odds ratio in favor of one model over another is given by the ratio of their global likelihoods. Suppose that model 1 has M_1 parameters, denoted A_α, and has a minimum χ^2 equal to $\chi^2_{1,\min}$. Suppose model 2 has M_2 parameters, denoted A'_α, and has a minimum χ^2 equal to $\chi^2_{2,\min}$. Assuming Gaussian errors, the odds ratio in favor of model 2 over model 1 is,

$$O_{21} = e^{\Delta\chi^2/2}(2\pi)^{(M_2-M_1)/2}\sqrt{\frac{detV_2}{detV_1}}\frac{\prod_{\alpha=1}^{M_1}\Delta A_\alpha}{\prod_{\alpha=1}^{M_1}\Delta A'_\alpha}\,, \tag{1}$$

where $\Delta\chi^2 = \chi^2_{1,\min} - \chi^2_{2,\min}$, V_1 and V_2 are the covariance matrices for the estimated parameters, and ΔA_α and $\Delta A'_\alpha$ are the prior uncertainties for the parameters A_α and A'_α. An interesting special case of model comparison is the case of *nested models*, where one model is a special case of a more complicated model when the additional parameters in the more complicated model take on some default value (often zero). Line detection is an example of this kind of comparison: we want to compare a model consisting only of a continuum spectrum to a model with an additional feature in it. Figure 3 illustrates the simple case of a Gaussian line, where the extra parameters are the centroid energy E, the strength A, and the width ΔE of the line.

Suppose that there are C continuum parameters common to both models, and that model 2 is the larger model with L extra parameters. If the common parameters are measured with about the same precision by both models and the extra parameters are only weakly correlated with the common parameters, $\det V_2 \approx \det V_C \det V_L \approx \det V_1 \det V_L$, where V_C is the covariance matrix of the parameters common to models 1 and 2, and V_L is

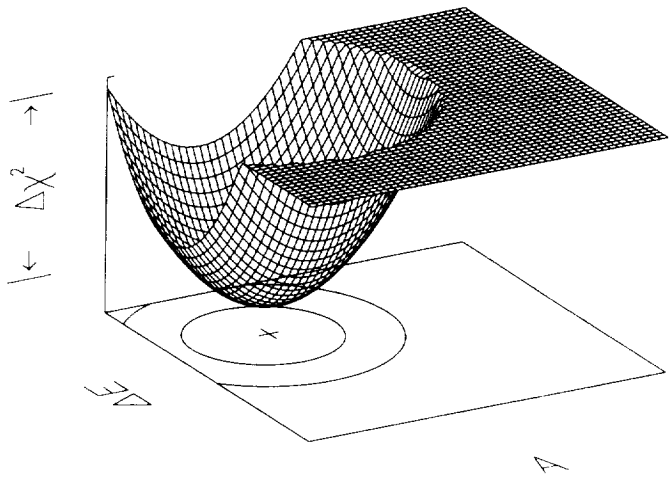

Fig. 3—χ^2 surface for two of the three additional parameters (line centroid energy E, strength A, and width ΔE) required to describe a line feature in the spectrum. The cross and the two contours in the (A,ΔE)-plane show the best-fit values of A and ΔE, and the boundaries of the 68% and 95% confidence regions for the model with a line. The vertical axis corresponds to a model with no line. $\Delta\chi^2$ is the difference in χ^2 between the best-fit theoretical models without and with a line.

the covariance matrix of the extra parameters in model 2. Further, if the covariance matrix V_L is diagonal its eigenvalues are σ_L^2, the variances for the extra parameters A'_L of model 2. Substituting these results in equation (1) gives,

$$O_{21} \approx e^{\Delta\chi^2/2} \prod_{\alpha=C+1}^{C+L} (2\pi)^{1/2}(\sigma_\alpha/\Delta A'_\alpha) \; . \tag{2}$$

Equation (2) reveals the odds ratio to be the product of the maximum likelihood ratio and a factor which includes the ratio of the posterior uncertainty of the extra parameters to their prior uncertainty. The maximum likelihood ratio will always favor the more complex model, since χ^2 of the more complex model can never be larger than that of the simpler model and therefore $\Delta\chi^2 \geq 0$. But the second factor penalizes the larger model, since the posterior uncertainty for the extra parameters will generally be smaller than their prior uncertainty. Thus an "Ockham's Razor" automatically appears in Bayesian model comparison (the dependence of this factor on the prior range superficially resembles correcting a frequentist statistic for the number of parameter values examined, but the horrendous problems associated with choosing the number and location of the examined values are absent in the Bayesian approach). Thus $\Delta\chi^2$ must exceed some critical value before the more complex model is favored.

Equation (2) also suggests an appealing intuitive connection between model comparison and parameter estimation. The quantity $\chi^2_{1,\rm min}$ corresponds to χ^2_2 minimized with respect to the common parameters, with the extra parameters fixed at their default values (*i.e.*, E arbitrary and $A = \Delta E = 0$ in the case of a simple Gaussian line; see Figure 3). But the boundary of a credible region for a subset of L parameters of a model is given by a surface of constant $\chi^2 = \chi^2_{\rm min} + \Delta\chi^2$, with $\Delta\chi^2$ chosen from the χ^2 distribution with L degrees of freedom. Thus $\Delta\chi^2 = \chi^2_{1,\rm min} - \chi^2_{2,\rm min}$ defines the boundary of a credible region for model 2 that just includes model 1 on its boundary. We can thus interpret equation (2) as stating that the data favor the more complex model (the odds ratio exceeds unity) only when the credible region that just includes the simpler model is larger than some critical size. This

critical value is

$$\Delta\chi^2 = 2\log \prod_{\alpha=C+1}^{C+L} \frac{\Delta A'_\alpha}{(2\pi)^{1/2}\sigma_\alpha} . \tag{3}$$

These results can be extended in a straightforward way to include the case of time-dependent lines. As do all Bayesian model comparisons, this case requires the explicit specification of two or more alternative models. To the extent that these models involve timescale parameters, Ockham factors will arise which penalize complicated models.

Thus Bayesian inference offers a rigorous method of establishing the existence of spectral lines which holds great promise for the analysis of γ-ray bursts.

III. PHYSICS OF CYCLOTRON SCATTERING

Cyclotron *resonant scattering*, in which electrons undergo radiative $0 \rightarrow 1 \rightarrow 0$ Landau transitions, produces a dip at the first harmonic frequency $\omega \approx \omega_B$. No simple description can be used to explain the first harmonic line, whose appearance depends critically on the outcome of the multiple resonant scatters required in order for individual photons to escape (Wang, Wasserman, and Salpeter 1988), as well as on the introduction of new photons at energies near that of the first harmonic which are "spawned" by Raman scattering at the higher harmonics, as described below.

Resonant Raman scattering, in which electrons undergo $0 \rightarrow n \rightarrow n-1 \rightarrow ... \rightarrow 1 \rightarrow 0$ radiative transitions, produces dips at the second and higher harmonics ($\omega \approx N\omega_B$). Resonant scattering of second and higher harmonic photons, in which electrons undergo radiative Landau transitions in which $\Delta n > 1$ (*i.e.*, $0 \rightarrow 2 \rightarrow 0$) are rare because $B/B_c \ll 1$. Because most of the photons which undergo scattering at the second and higher harmonics are destroyed, the resulting line feature is approximately that for absorption.

Figure 4 shows theoretical photon number spectra for two different viewing angles θ relative to the magnetic field. The bottom and middle lines show the line profiles that would result, were they due to absorption, and resonant and Raman scattering without photon spawning, respectively. The (heavy) top line gives the actual line profiles, which are due to resonant scattering and Raman scattering with photon spawning. Figure 4 shows that the strengths of the first and second harmonic lines are comparable. Figure 4 also shows that the profiles of the second and third harmonics closely resemble those for absorption and are asymmetric due to relativistic kinematics in one dimension.

The resonant scattering cross section at the $N^{\rm th}$ harmonic is $\propto (1+\cos^2\theta)\sin^{2N-2}\theta$. Thus scattering of photons at the first harmonic is moderately peaked along the magnetic field, while scattering at higher harmonics is strongly peaked away from the magnetic field. Therefore Raman scattering primarily removes photons traveling perpendicular to the magnetic field. However, the photons spawned at the first harmonic by resonant Raman scattering at higher harmonics are created with the angular distribution characteristic of the first harmonic, and therefore have an angular distribution moderately peaked along the magnetic field. In scattering, a photon undergoes on average a relative shift in frequency $\approx (v_{th}/c)\cos\theta$ due to the thermal motion of the electrons along the magnetic field. Therefore the Doppler width of the cyclotron lines is large looking along the magnetic field

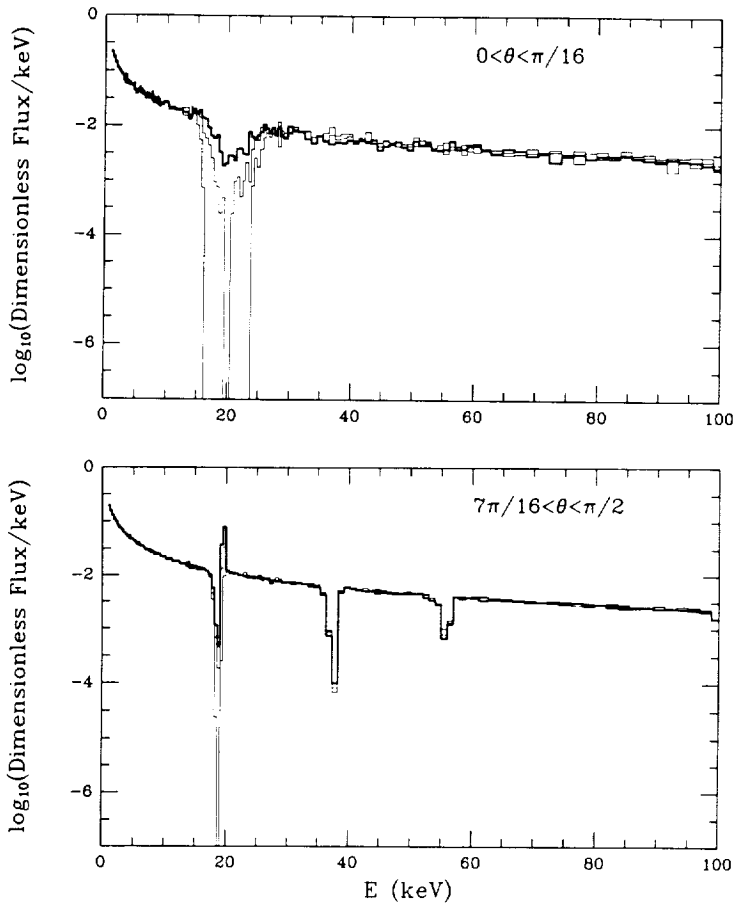

Fig. 4—Theoretical photon number spectra for $B = 1.71 \times 10^{12}$ G, $N_e = 1.2 \times 10^{21}$ electrons cm^{-2}, $T = 5.3$ keV, and two different viewing angles θ relative to the magnetic field. The bottom and middle lines show the line profiles that would result from absorption, and resonant and Raman scattering without photon spawning. The (heavy) top line gives the actual profiles, which are due to resonant scattering, and Raman scattering with photon spawning. (From Lamb, Wang, and Wasserman 1991.)

and decreases as one looks away from it. Figure 4 shows that these two effects produce pronounced variations in the strengths and widths of the various harmonics as a function of viewing angle θ.

IV. PARAMETER ESTIMATION

Observations using the Los Alamos/ISAS burst detector on *Ginga* have demonstrated the existence of statistically significant harmonically spaced cyclotron lines in three γ-ray bursts. Analysis of these observations using radiation transfer calculations have shown that cyclotron resonant scattering in a strong magnetic field can account quantitatively for the positions, strengths, and widths of these lines. Here we emphasize that the power of this analysis depends crucially on the observation of *multiple* lines.

As described in the previous section, the relative strengths of the first and higher harmonics show a pronounced variation with viewing angle θ: at small θ only the first harmonic is visible, while at large θ the second harmonic is dominant (see Figure 4). This is particularly the case for current detectors, which effectively integrate over the scattering dip and the spawned photon peak at the first harmonic because of modest spectral resolution. As a result, if we observe one line only, we have no way of knowing whether this line corresponds to the first or second harmonic. Obviously, the value of the magnetic field will be uncertain by a factor of two (as in, *e.g.*, the Konus bursts).

TABLE 1
BEST-FIT MODEL PARAMETERS

Line Parameters	Absorption Model	Scattering Model
B (10^{12} G)	1.69 ± 0.04	1.71 ± 0.07
N_e (10^{21} cm^{-2})	—	1.2 ± 0.6
$\mu(=\cos\theta)$	—	0.31 ± 0.05
$kT_{\parallel}\cos^2\theta$ (keV)	6.6 ± 2.4	—
$N_{e,1}^{los}(1+\cos^2\theta)$ (10^{21} cm^{-2})	≈ 0.23	—
$N_{e,2}^{los}(1-\cos^4\theta)$ (10^{21} cm^{-2})	≈ 2.4	—

Worse, however, is the fact that analysis of the line cannot determine the physical parameters of the line-forming region, *i.e.*, its optical depth (or column density), temperature (or velocity), and the geometry (or viewing angle). This is because the physics of the line formation is very different for the first and second harmonics; without knowing which harmonic we are observing, we do not know which physics to apply. Even if we somehow knew which harmonic we are observing, analysis of a single cyclotron line cannot determine the physical parameters of the line-forming region. This is because the line is a function of four parameters (the magnetic field strength B, the temperature T and column depth N_e of the line-forming region, and the viewing angle θ), but current detectors are sensitive only to two (*e.g.*, the centroid energy E and the equivalent width EW) because of modest spectral resolution. As a result, a single line can be fit by an infinite family of solutions in which N_e decreases and T increases as θ increases.

This situation is illustrated by the cyclotron absorption model, which has been used by many authors. The choice of this model is motivated by the facts that the model is analytic and that approximating cyclotron Raman scattering by cyclotron absorption is valid at higher harmonics. However, such an approximation is not valid at the first harmonic, and therefore *different temperatures and column densities must be allowed at the first and second harmonics.* The situation then becomes equivalent to fitting a single line, even if the first and second harmonic are both strongly present.

The free parameters of the cyclotron absorption model are then the line centroid energies $E_1 = E_2$, the line widths $\Delta E_N = E_N(2kT_{\parallel}\cos^2\theta/mc^2)$, where θ is the viewing angle relative to the magnetic field, and the line strengths $A_N = N_{e,N}^{los}\alpha_N$, where $N_{e,N}^{los}$ and α_N are the column density along the line of sight and the absorption coefficient of the N^{th} harmonic. The physical parameters that may be deduced from the fit are $N_{e,1}^{los}(1+\cos^2\theta)$ and $N_{e,2}^{los}(1-\cos^4\theta)$, and $kT_{\parallel,1}\cos^2\theta/mc^2$ and $kT_{\parallel,2}\cos^2\theta/mc^2$. However, $N_{e,1}^{los}$ and $kT_{\parallel,1}\cos^2\theta/mc^2$ have no straightforward physical meaning because the cyclotron absorption model is not valid at the first harmonic, respectively. Table 1 gives the best-fit parameters of the model for GB880205 (Fenimore *et al.* 1988); as expected, B is well-determined but θ is undetermined and T and $N_e^{\rm los}$ are therefore poorly constrained.

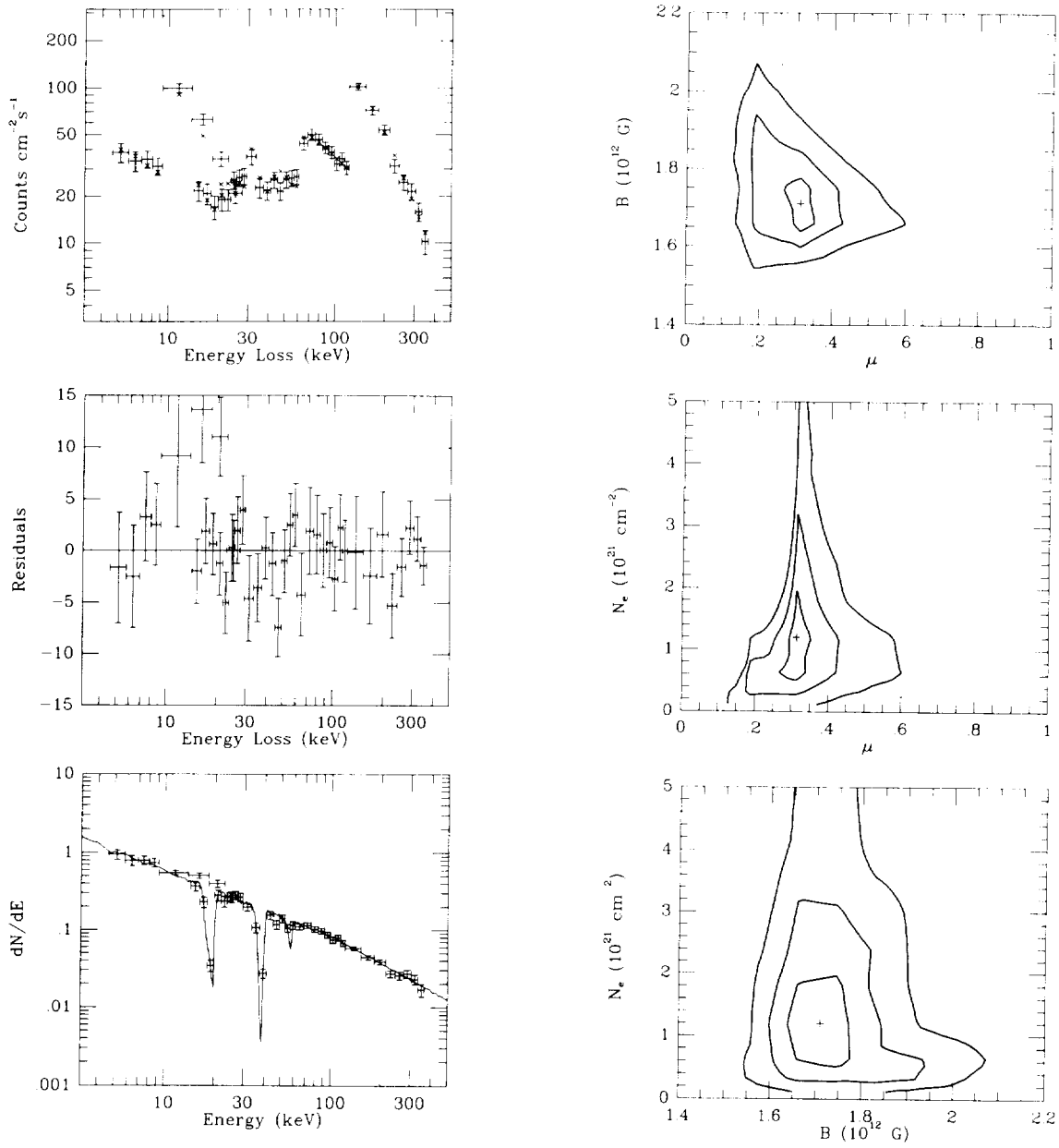

Fig. 5—(top) Observed (crosses) and best-fit theoretical (x's) count rate spectrum of the proportional counter (PC) and scintillation counter (SC) on *Ginga* for GB880205. (middle) Residuals for the PC and SC counters. (bottom) Best-fit theoretical photon number spectrum (solid curve) and *Ginga* PC and SC data (crosses). (From Wang *et al.* 1989.)

Fig. 6—The 68.3%, 95.4%, and 99.7% confidence regions in (B, N_e, μ)-space, as determined by χ^2 fits of theoretical photon number spectra to the *Ginga* data for GB880205: (top) projected in the (μ, B)-plane; (middle) projected in the (μ, N_e)-plane; (bottom) projected in the (B, N_e)-plane. (From Wang *et al.* 1989.)

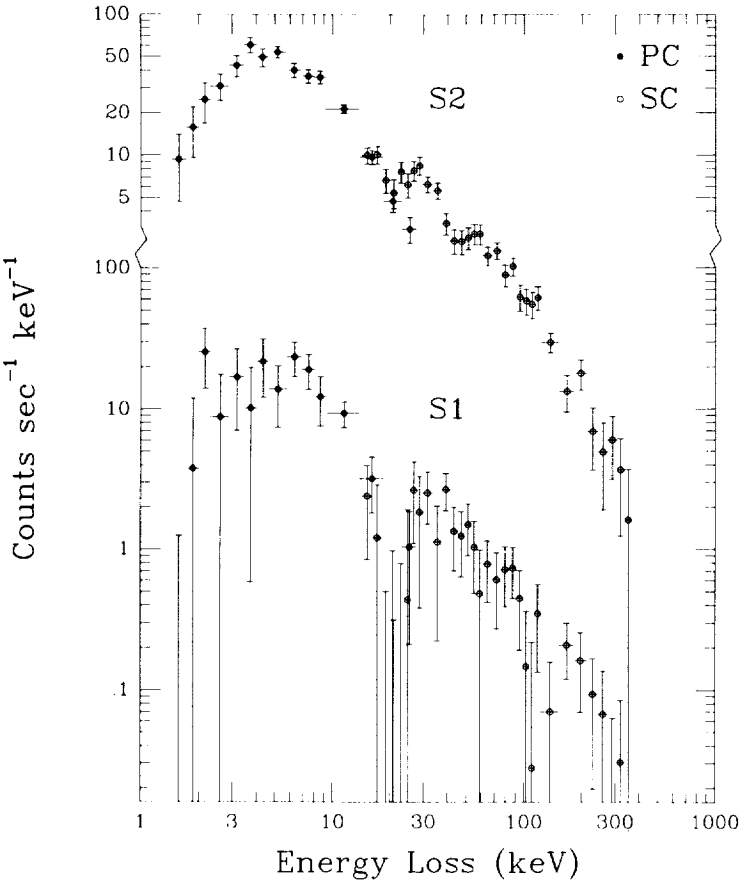

Fig. 7—Count rate spectra for intervals S1 and S2 of GB870303, normalized by energy bin width, for the proportional counter (PC) and scintillation counter (SC) on *Ginga*. Note the strong dip at $\approx$ 20 keV in S1 and the dips at $\approx$ 20 and 40 keV in S2. (From Graziani *et al.* 1991.)

In contrast, if *multiple lines* are strongly present, the physical parameters B, N_e, kT, and θ can be determined.

If only the first and second harmonics are present, theoretical radiation transfer calculations are required. This approach is illustrated by the fits to the spectrum of GB880205 carried out by Wang *et al.* (1989). Folding Monte Carlo spectra through the *Ginga* detector response functions, they fit the observed photon count rate spectrum. Figure 5 shows the predicted and observed photon count-rate spectra, the residuals, and the incident photon-number spectrum for the best-fit parameters. Figure 6 shows the 68.3%-, 95.4%-, and 99.7%-confidence regions in (B, N_e, μ)-space. Table 1 gives the best-fit parameters of the model. The resonant cyclotron Compton temperature is not a free parameter, but is fixed by their model to be $T_C = 5.3^{+0.3}_{-0.2}$ keV.

If multiple higher harmonic lines are strongly present, one has three observed quantities ($E_1 = 2E_2$, EW_1, and EW_2) and some information about two others (ΔE_1 and ΔE_2) to determine the four physical parameters (B, T, N_e or $N_e^{\rm los}$, and θ). The physical parameters can then be determined using either the absorption model or theoretical radiation transfer calculations. However, multiple higher harmonic lines will be strongly present only if the column density of the line-forming region is large. To date, such column depths have not been seen in γ- ray bursts.

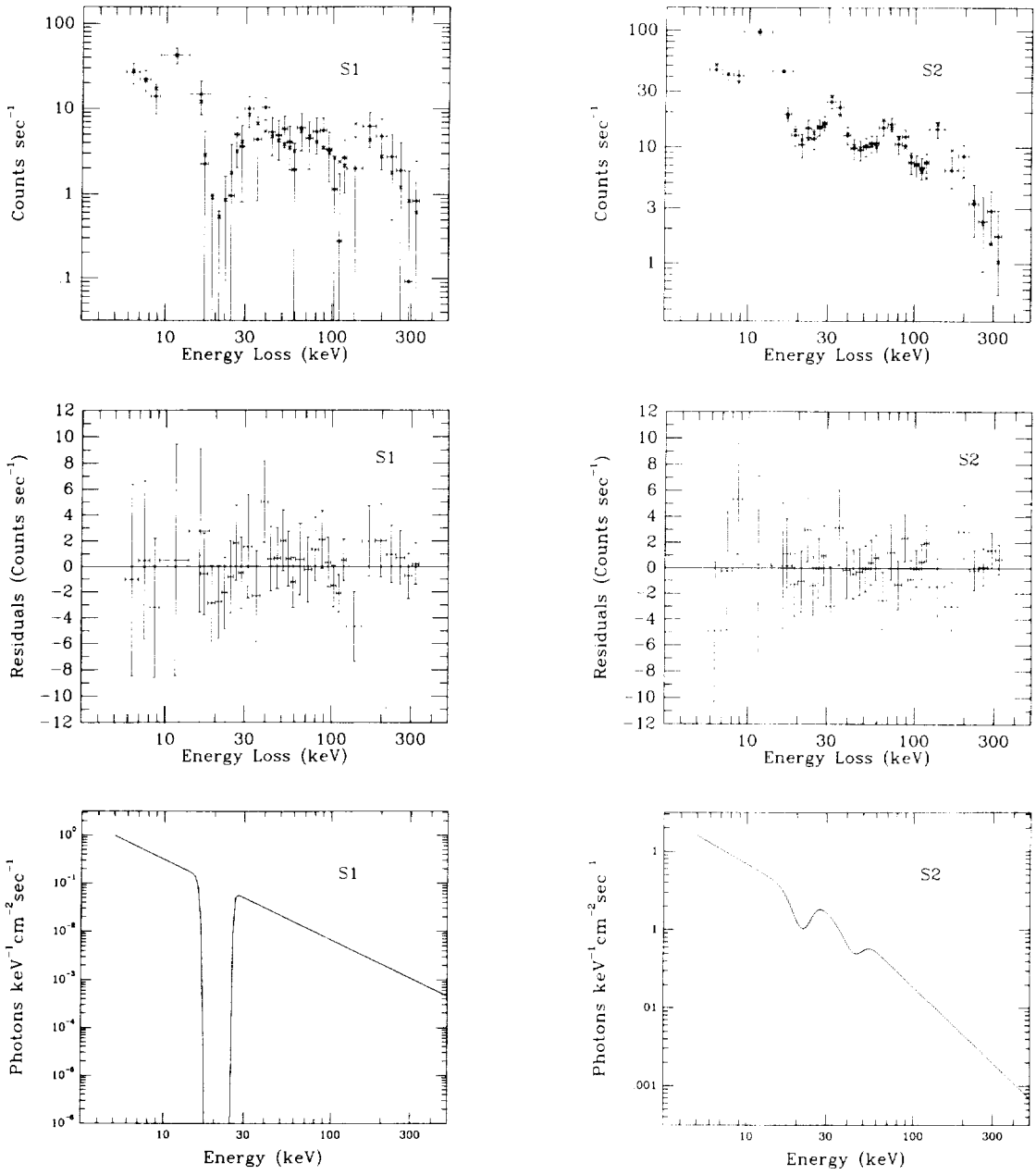

Figure 8—(top) Observed count-rate spectra (+'s) and best-fit absorption model count-rate spectra (x's) for intervals S1 and S2 of GB870303 for the PC and SC data on *Ginga*. (middle) Residuals. (bottom) Best-fit absorption model photon-number spectra. (From Graziani *et al.* 1991.)

V. NEUTRON STAR ROTATION

The pronounced variations in the strengths and widths of the cyclotron lines as a function of θ provide *a distinct signature of neutron star rotation.* As a simple example, consider cyclotron lines formed in a small region near one magnetic pole of an orthogonally rotating neutron star with the observer located in the plane perpendicular to the rotation axis. Then the rotation angle $\phi = \theta$. As the neutron star rotates, θ varies, producing

TABLE 2
BEST-FIT ABSORPTION MODEL PARAMETERS

Line Parameters	S1	S2
E_1 (keV)	$21.1^{+1.1}_{-1.0}$	21.4 ± 0.7
$kT_1 \| \cos^2\theta$ (keV)	< 15	$8.18^{+7.15}_{-4.29}$
$N^{los}_{e,1}(1+\cos^2\theta)$ (cm^{-2})	$> 3.14 \times 10^{20}$	$(1.19^{+0.23}_{-0.20}) \times 10^{20}$
$kT_2 \| \cos^2\theta$ (keV)	—	$10.5^{+10.5}_{-5.77}$
$N^{los}_{e,2}(1-\cos^4\theta)$ (cm^{-2})	—	$(2.33^{+0.48}_{-0.45}) \times 10^{21}$
EW_1 (keV)	10.5 ± 2.1	$4.81^{+0.90}_{-0.82}$
EW_2 (keV)	—	$8.45^{+0.26}_{-0.21}$

pronounced variations in the strengths and widths of the cyclotron lines. Looking down the magnetic field ($\theta = 0$), the first harmonic is strong and wide, due to Doppler broadening, but no higher harmonics are visible. As the viewing angle θ increases, the strength of the first harmonic decreases while the strengths of the higher harmonics, particularly the second, increase. At the same time, the Doppler widths of all the lines decrease. Figure 4 illustrates this behavior.

While such a combination of variations in line strengths and widths may not be unique, simple changes in the temperature or column depth of the line-forming region do not suffice to produce it. A decrease in the temperature produces narrower lines, but does not change the strength of the first harmonic relative to the higher harmonics. A decrease in the column depth of the line-forming region produces a weaker first harmonic, but also produces weaker, not stronger, higher harmonics.

Graziani *et al.* (1991) find that the burst GB870303 exhibits two broad peaks and lasts approximately 45 sec. An exhaustive search of the data revealed two time intervals (hereafter S1 and S2) in which statistically significant spectral lines are seen. S1 is a previously unreported 4 sec interval; S2 is the 9 second interval reported in Murakami *et al.* (1988). The midpoints of S1 and S2 are separated by 22.5 sec. Figure 7 shows the count rate spectra for S1 and S2, normalized to the width of the energy loss channels; the spectrum for S2 is identical to that reported in Murakami *et al.* (1988). Note the line at $\approx$ 20 keV in the S1 spectrum, and the two lines at $\approx$ 20 and 40 keV in the S2 spectrum.

Graziani *et al.* (1991) carried out a one-line (3-parameter) fit to S1 and a separate two-line (5-parameter) fit to S2, using the cyclotron absorption model. Figure 8 shows the observed count-rate spectra (+'s) and best-fit absorption model count-rate spectra (x's) for S1 and S2. Also shown are the residuals and the best-fit absorption model photon-number spectra. Table 2 gives the best-fit parameters and 1σ errors for the absorption model fits to S1 and S2. The values of $kT_\parallel \cos^2\theta/mc^2$ and $(\rho h)_1(1+\cos^2\theta)$ for S1 are only upper and lower 95% confidence limits, respectively, because the line feature is so deep that, after background subtraction, the net counts in some channels are negative,

although the error bars extend to positive values. Thus the fit can always be made slightly better by increasing β_1 and compensating by decreasing ΔE_1. Table 2 implies very similar magnetic field strengths for S1 and S2: $B = (1.82^{+0.095}_{-0.086}) \times 10^{12}$ G and $(1.86 \pm 0.06) \times 10^{12}$ G, respectively. Table 2 also shows that the Doppler widths of the first and second harmonics are similar for S1 and S2, within statistical uncertainties; in contrast, the strengths (and EW) of the first and second harmonics differ greatly for the two intervals.

Comparison of Figures 4 and 8 shows that the change in the line spectrum between S1 and S2 is qualitatively similar to that produced by a change in the viewing angle θ. We conjecture that this change is due to rotation of the neutron star. We suggest that during S1 our line of sight is nearly parallel to the field, so that only the first harmonic is visible, while during S2 our line of sight is nearly perpendicular to the field, so that both first harmonic and second harmonics are visible, with comparable strengths (see Figure 4). The time Δt between the centers of S1 and S2 is 22.5 sec. Within the framework of the rotation picture, we may associate Δt with either a minimum change in rotational phase $\Delta\phi \approx \pi/4$ or a maximum change $\Delta\phi \approx \pi$. These values constrain the rotation period P of the neutron star to lie in the range 2×22.5 sec ≈ 45 sec $\lesssim P \lesssim 8 \times 22.5$ sec ≈ 180 sec.

This result, if confirmed, has profound implications for the location, extent, and stability of the γ-ray burst line-forming region, and for the origin and evolution of the magnetic neutron stars which are the sources of many γ-ray bursts.

We gratefully acknowledge the contributions of our collaborators, particularly Ed Fenimore, Tom Loredo, Toshio Murakami, John Wang, Ira Wasserman, and Atsumasa Yoshida, to the work described here. This work was supported in part by NASA grants NAGW-830 and NAGW-1284.

REFERENCES

Fenimore, E. E. *et al.* 1988, *Ap. J. Lett.*, **335**, L71.

Fishman, G. J., *et al.* 1991, these proceedings.

Graziani, C., *et al.* 1991, in *Proceedings of the Taos Workshop on Gamma-Ray Bursts*, ed. C. Ho, R. I. Epstein, and E. E. Fenimore (Cambridge U. Press: Cambridge), p. 407.

Lamb, D. Q., *et al.* 1989, *Ann. NY Acad. Sci.*, **571**, 460.

Lamb, D. Q., Wang, J. C. L., and Wasserman, I. 1990, in *Proceedings of the Taos Workshop on Gamma-Ray Bursts*, ed. C. Ho, R. I. Epstein, and E. E. Fenimore (Cambridge U. Press: Cambridge), p. 415.

Loredo, T. J. 1990, in *Maximum Entropy and Bayesian Methods*, ed. P. F. Fougère (Dordrecht: Kluwer Academic Publishers), p. 81.

Loredo, T. J. 1992, in preparation.

Mazets, E. P., *et al.* 1981, *Nature*, **290**, 378.

Murakami, T. *et al.* 1988, *Nature*, **335**, 234.

Nagase, F., *et al.* 1991, ISAS Report No. 476.

Wang, J. C. L. *et al.* 1989, *Phys. Rev. Lett.*, **63**, 1550.

Wang, J. C. L., Wasserman, I., and Salpeter, E. E. 1988, *Ap. J. Suppl.*, **68**, 735.

Yoshida, A., *et al.* 1991, *Pub. Astron. Soc. Japan*, in press.

ON THE GALACTIC ORIGIN OF GAMMA-RAY BURSTS

Bohdan Paczynski

Princeton University Observatory, Princeton, NJ 08544-1001

ABSTRACT

If gamma-ray bursters are in the galactic disk, then the average value of the V/Vmax parameter cannot be lower than 0.4, no matter what is the source luminosity function or what is the disk thickness. The value of 0.4 is reached only asymptotically when the range of observations is much larger than the disk scale height, and almost all sources are within a very thin galactic equatorial belt. This distribution is in a direct conflict with the BATSE results as presented at this workshop.

If the bursters have a galactic halo distribution similar to that of any other known class of objects, then a strong dipole moment in their angular distribution should be seen, *i.e.*, a strong concentration towards the galactic center. To make the dipole moment unmeasurable, the hypothetical burster's halo must have a core radius of at least 14 kpc (a 3 sigma limit) to be consistent with the BATSE results as presented at this workshop.

Full account of this work is given by Paczynski (1991) for standard candle sources, and by Mao and Paczynski (1991) for sources with very diverse luminosity functions.

Paczynski, B. 1991, Acta Astronomica, **41**, 157.
Mao, S., and Paczynski, B. 1991, submitted to *Ap. J. (Letters)*.

Ulysses/BATSE Observations of Cosmic Gamma-Ray Bursts

K. Hurley
University of California
Space Sciences Laboratory
Berkeley, CA 94720

M. Boer, M. Sommer
Max-Planck Institut fur Physik und Astrophysik
D-8046 Garching-bei-Munchen, Germany

G. Fishman, C. Meegan, W. Paciesas, R. Wilson, C. Kouveliotou
Marshall Space Flight Center ES 62
Huntsville, AL 35812

T. Cline
Goddard Space Flight Center Code 661
Greenbelt, MD 20771

ABSTRACT

The gamma-ray burst detector aboard the ESA-NASA Ulysses spacecraft, in operation since November 1990, has detected numerous gamma-bursts in conjunction with the BATSE experiment aboard the Compton Observatory. We present initial results on burst locations for three events (April 21, May 2, and May 3 1991) obtained by arrival time analysis, and compare them with the BATSE locations. The arrival time analysis annuli have typical widths of 5'. Our preliminary analysis indicates that both experiments are likely to have unresolved systematic errors, but that further work will improve the location accuracy substantially.

INTRODUCTION

The Ulysses gamma-burst experiment is the farthest point from Earth in the 3rd Interplanetary Network (presently consisting of a cluster of near-earth spacecraft including the Compton Observatory, with Pioneer Venus Orbiter and Ulysses as interplanetary spacecraft). A full description of the Ulysses mission and its investigations is currently in press (see, e.g., Hurley et al., 1991). Briefly, the burst detectors are two NaI(Tl) hemispherical crystals, 3 mm thick by 51 mm in diameter, coupled to two photomultiplier tubes. They cover the energy range from about 20 to 150 keV, using fast memories to record gamma-bursts with up to 8 ms resolution. They achieve a sensitivity of around 10^{-6} ergs/cm^{2}s, view 4π sr., and have a duty cycle exceeding 90%. Because the Ulysses mission passes by Jupiter and out of the plane of the ecliptic, the Earth-Ulysses baseline is the longest that has ever been achieved for gamma-ray burst studies, and the resulting localization accuracy is of the order of arcminutes or less. Here we discuss the intial results obtained for the localization of 3 events which occurred shortly after the launch of the Compton Observatory.

OBSERVATIONS

The three events we present here are among the very first dozen or so found in an initial search of the Compton and Ulysses data; they occurred on April 21, 1991 around 09:14 UT, on May 2, 1991 around 22:37 UT, and on May 3, 1991 around 07:04 UT (Earth-crossing times). Pioneer

Venus Orbiter may have recorded a rate increase at the time of the first event, but was off during the second and third bursts (J. Laros, private communication). However, the May 3 burst was also observed by the COMPTEL (Schonfelder, 1991) and EGRET (Schneid, 1991) experiments. The Compton Observatory/Ulysses distances ranged from about 1380 to 1520 light-seconds for these observations.

In each case, we have used the BATSE and Ulysses time histories to construct an annulus of arrival directions. The assumed timing uncertainties used were ±300 ms, with an approximately equivalent amount of uncertainty assumed for the Ulysses spacecraft location, taken from predict orbit tapes. Both of these uncertainties can be considerably reduced: the final timing to perhaps ±50 - 100 ms., and the spacecraft position to a completely negligible amount. Thus the widths of the annuli will eventually shrink by a factor of up to 6, to the <1' range.

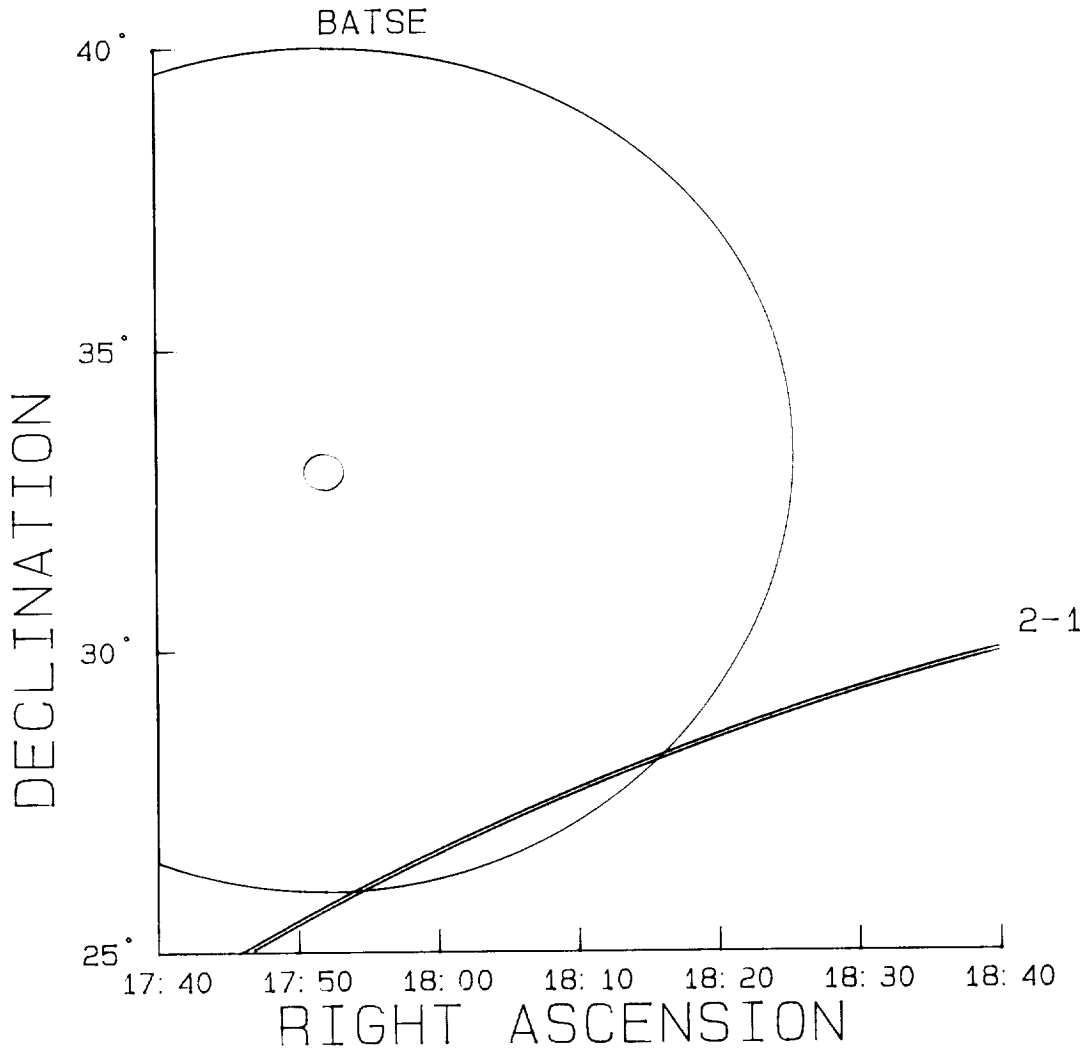

Figure 1. Sky map for the April 21, 1991 burst. "2-1" is the Ulysses-BATSE annulus. Two BATSE error circles are also indicated; the inner circle takes only the formal statistical errors into account, while the outer circle is for estimated systematic errors.

Figures 1 and 2 show the regions around the BATSE locations of the April 21 and May 2 events, and Figure 3, for the May 3 event, includes the COMPTEL error box (Schonfelder, 1991). In all cases, two BATSE error boxes are shown, one taking only the formal statistical errors into account, and the other, estimated systematic errors. The Ulysses-BATSE annuli include the uncertainties mentioned above; the resulting annulus widths are around 4', 3', and 6' in these figures, respectively.

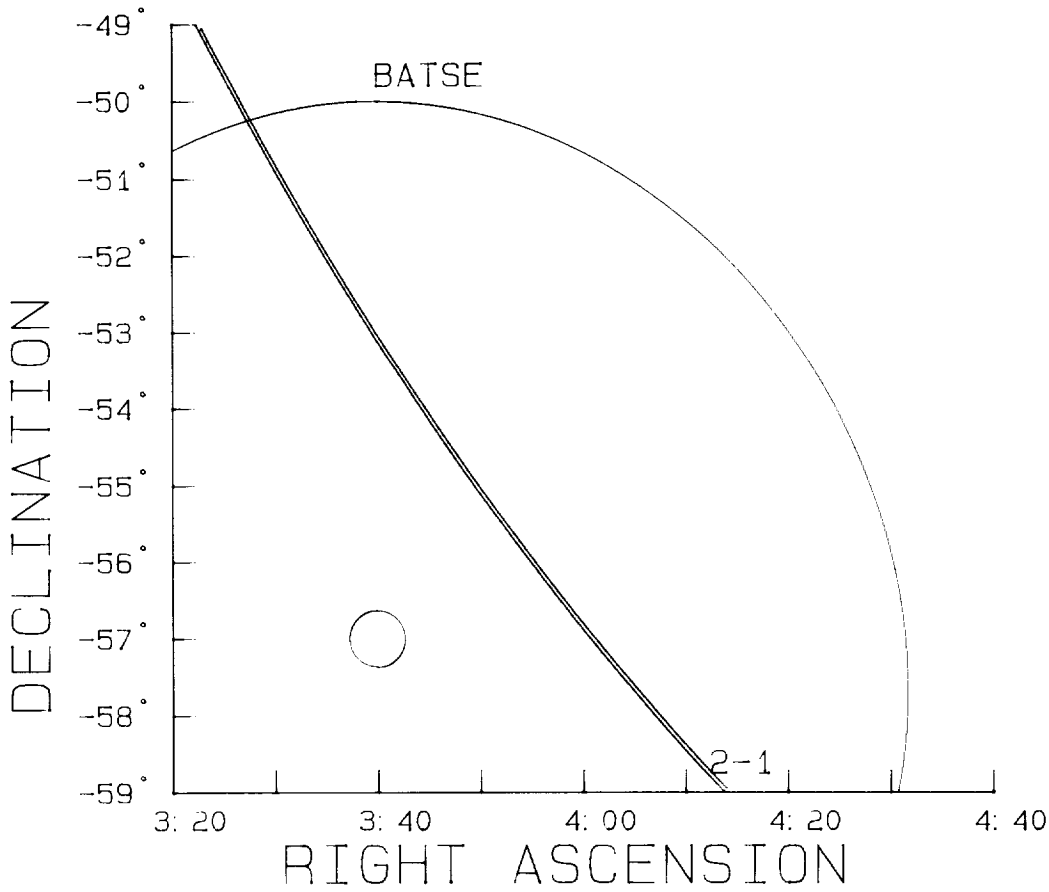

Figure 2. Sky map for the May 2, 1991 event. "2-1" is the Ulysses-BATSE annulus. Two BATSE error circles are also shown; the inner circle includes only statistical errors, while the outer circle is for estimated systematic errors.

DISCUSSION AND CONCLUSION

The initial results presented here indicate that the centers of the error boxes obtained by the BATSE experiment alone are up to several degrees from the Ulysses/BATSE arrival time annuli. We attribute these differences to unresolved systematic errors. In the case of BATSE, these include the effects of atmospheric and spacecraft scattering, which can be corrected by semi-empirical modeling. In the case of Ulysses, they include spacecraft location uncertainties and systematic timing errors. Both of these can be reduced considerably: the spacecraft range is now known to an accuracy of several kilometers, and the right ascension and declination to about 500 nanoradians. The timing is currently verified to an accuracy of around 100 ms, and

ultimately can be demonstrated to be accurate to about 1/10th this amount. An annulus-only location does not determine a unique position for the BATSE error box, but rather, only a minimum error. We are currently localizing a number of PVO/BATSE/Ulysses bursts to resolve this uncertainty.

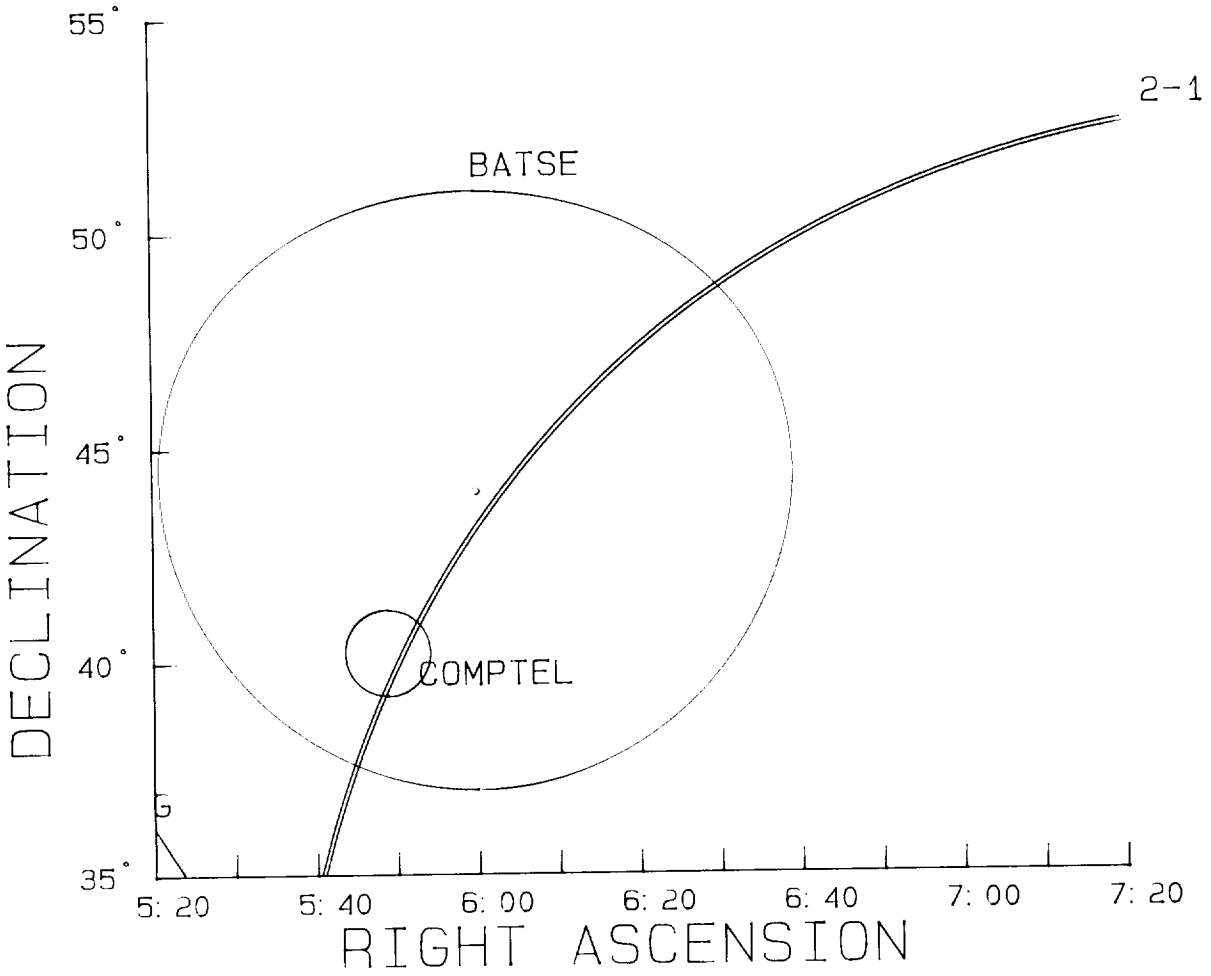

Figure 3. Sky map for the May 3, 1991 burst. "2-1" indicates the Ulysses/BATSE arrival time annulus. Two BATSE and one COMPTEL (Schonfelder, 1991) error boxes are indicated. The inner BATSE error circle takes only formal statistical errors into account; the outer circle is for estimated systematic errors. "G" is the galactic plane.

ACKNOWLEDGMENTS

The Ulysses localization work was supported by JPL Contract 958056 and by NASA Grant NAG5-1560.

REFERENCES

Hurley, K. et al., Astron. Astrophys. Suppl., in press, 1991

Schneid, E. et al., presented at the Huntsville Gamma-Ray Burst Workshop, Huntsville, Alabama, October 1991

Schonfelder, V., IAUC 5368, October 16, 1991

MAGNETIC PHOTON SPLITTING AND GAMMA-RAY BURST SPECTRA

MATTHEW G. BARING
Department of Physics
North Carolina State University

ABSTRACT

The splitting of photons into two photons becomes both possible and significant in magnetic fields in excess of 10^{12} Gauss. Below the threshold energy $2m_e c^2$ for single-photon pair production, splitting can be an astrophysically-observable phenomenon evident in gamma-ray burst spectra. In such circumstances, it has been found that magnetic photon splitting reprocesses the gamma-ray burst continuum by degrading the photon energy, with a net effect that is quite similar to pair cascade reprocessing of the spectrum. Results are presented for the spectral modifications due to splitting, taking into account the different probabilities for splitting for different polarization modes. Unpolarized and polarized pair cascade photon spectra form the input spectra for the model, which calculates the resulting splitting-reprocessed spectra numerically by solving the photon kinetic equations for each polarization mode. This inclusion of photon polarizations is found to not alter previous predictions that splitting produce a significant flattening of the hard X-ray continuum and a bump at MeV energies below a pair production turnover. The spectrum near the bump is always strongly polarized. The spectra of bursts detected by GRO may provide observational confirmation of magnetic photon splitting.

INTRODUCTION

Magnetic photon splitting $\gamma \rightarrow \gamma\gamma$ is an exotic and comparatively recent prediction of quantum electrodynamics in strong magnetic fields: the first correct calculations of the reaction rate were performed by Bialynicka-Birula and Bialynicki-Birula (1970), Adler *et al.* (1970) and Adler (1971). When $B = 0$, splitting is kinematically possible but is forbidden by a charge conjugation symmetry of QED known as Furry's theorem (e.g. see Jauch and Rohrlich, 1980). The theorem states that ring diagrams that have only external lines corresponding to photons, and that have an odd number of vertices, contribute zero to the interaction matrix elements. This symmetry is broken by the presence of an external field. The splitting of photons is therefore a purely quantum effect, and has appreciable reaction rates only when the magnetic field is at least a significant fraction of the quantum critical field $B_c = m_e^2 c^3/(e\hbar) = 4.413 \times 10^{13}$ Gauss. Neutron stars, and especially gamma-ray bursts (GRB) associated with neutron stars, with their high γ-ray luminosities, therefore provide good environments for testing for the existence of splitting.

The potential importance of magnetic photon splitting, suggested by Baring (1988) and Mitrofanov *et al.* (1986), has been explored in detail by Baring (1991) in the context of spectral implications for gamma-ray bursts. Splitting was found to degrade the photon

continuum in a manner similar to the reprocessing effect of a pair cascade. In magnetized neutron star environments, where $B \gtrsim 10^{12}$ Gauss, $\gamma \rightarrow \gamma\gamma$ produces a flattening of the hard X-ray continuum and a broad bump at energies around 1 MeV (Baring, 1991). This feature is potentially observable, and if detected, would be a significant verification of QED in strong magnetic fields. In particular, the instruments aboard the GRO mission have the capability to make such a detection. In the model of Baring (1991), the source of continuum photons was generated by a synchrotron radiation pair cascade initiated by some quasi-isotropic injection of non-thermal electrons.

Here the basic nature of the splitting process is reviewed, and the spectral modifications to the GRB continuum reconsidered: the new development in this work is the inclusion of an exact treatment of the individual polarization states of the photons participating in the splitting process. This extension of the work in Baring (1991) is an important step, particularly since it has long been recognized that splitting may be an important polarizing mechanism in neutron star sources such as pulsars (Adler *et al.*, 1970; Usov and Shabad, 1983). It is found here that consideration of the photon polarization states does not qualitatively change the spectral reprocessing nature of $\gamma \rightarrow \gamma\gamma$, and that the MeV bump still appears. However, the resultant spectra are strongly polarized by the splitting process, and any detailed GRB spectral model should include the photon polarizations in order to make quantitative predictions even for observational detections without polarimetric capability.

In this paper, it is convenient to use a simple dimensionless notation for various quantities in relativistic, magnetized environments. Therefore all magnetic fields will be expressed hereafter in units of the critical field B_c, and all photon and particle energies will be scaled by $m_e c^2$.

MAGNETIC PHOTON SPLITTING

Photon splitting is a third-order QED process that must have a reaction rate that is strongly dependent on the magnetic field strength. The calculation of its rate by standard QED techniques is both difficult and laborious, because of the complications introduced by the presence of the field. The most formidable difficulty is the complicated form for the electron propagator in the external field, which renders the evaluation of the general expression for the splitting rate analytically intractable. The earliest research on this process therefore specialized to the low photon energy $\varepsilon \ll 1$ (in units of $m_e c^2$), low field ($B \ll 1$) limit where dramatic simplifications can be made. This limit corresponds to the case of small dispersion. Since the presence of a magnetic field polarizes the vacuum, dispersive effects naturally occur. However when the field is low ($B \lesssim 0.1$) and the energy of photons that are splitting is moderate ($\varepsilon \lesssim 1$) these dispersive effects are small: this corresponds to the situation in gamma-ray bursts (Baring, 1991). The most general calculation of splitting valid for any values of ε and B was performed by Stoneham (1979).

The calculations of Bialynicka-Birula and Bialynicki-Birula (1970), Adler *et al.* (1970) and Adler (1971) were all in this limit of low dispersion. An expression for the

splitting rate for this case, averaged over all photon polarizations, was obtained by Papanyan and Ritus (1972). For the splitting of photons of energy $\varepsilon m_e c^2$ with $\varepsilon \ll 1$ into photons of energies $\omega m_e c^2$ and $(\varepsilon - \omega) m_e c^2$, their result can be expressed as an optical depth for an emission region of size R (see Baring, 1991):

$$\tau_{sp}(\varepsilon,\omega) \approx \frac{3\alpha_f^3}{\pi^2}\left(\frac{19}{315}\right)^2 \frac{R}{\lambda_c} B^6 \sin^6\theta\, \omega^2(\varepsilon-\omega)^2 \quad . \tag{1}$$

Here $\alpha_f \approx 1/137$ is the fine structure constant, $\lambda_c = \hbar/(m_e c)$ is the Compton wavelength, and θ is the angle of propagation of the photon that splits with respect to the field lines. This is also the propagation angle for both of the produced photons: by energy and momentum conservation the splitting process is collinear in the absence of dispersive effects. The total rate for photon splitting is obtained by integrating eq. (1) over ω, yielding

$$\tau_{sp}(\varepsilon) \approx \frac{\alpha_f^3}{10\pi^2}\left(\frac{19}{315}\right)^2 \frac{R}{\lambda_c} B^6 \varepsilon^5 \sin^6\theta \quad . \tag{2}$$

For neutron star atmospheres, $\tau_{sp}(\varepsilon)$ can be greater than unity if θ is not too small.

Adler (1971) observed that in the low-energy limit, the splitting rate had the same field dependence but a different magnitude for different combinations of the initial and final photon polarizations. Therefore, photon splitting must be a powerful polarizing mechanism. The polarization-dependent rates can be taken from eq. (23) of Adler (1971), which can be related to eq. (1), using the optical depth notation preferred here, via

$$\tau_{\perp\to\parallel\parallel} = \frac{1}{2}\tau_{\parallel\to\perp\parallel} = \left(\frac{13}{24}\right)^2 \tau_{\perp\to\perp\perp} = \frac{1}{6}\left(\frac{26}{19}\right)^2 \tau_{sp}(\varepsilon,\omega) \quad , \tag{3}$$

The photon polarization labelling convention of Stoneham (1979) is adopted here (this standard form was not used by Adler, 1971): the label $\parallel$ refers to the state with the photon's *electric* field vector parallel to the plane containing the magnetic field and the photon's momentum vector, while $\perp$ denotes the photon's electric field vector being normal to this plane. The splitting modes $\perp\to\perp\parallel$, $\parallel\to\perp\perp$ and $\parallel\to\parallel\parallel$ are forbidden in the low energy, low dispersion limit.

In order for photon splitting to have observable effects in gamma-ray burst spectra, not only must its optical depth in the GRB emission region exceed unity, but it must not also be dominated by any other photon absorption process. Its main rival as a mechanism for gamma-ray attenuation is single-photon pair production $\gamma \to e^+e^-$, which has a kinematic threshold at $\varepsilon \sin\theta = 2$. Above this threshold, which is strongly dependent on θ, the reaction rate for $\gamma \to e^+e^-$ is so great that it totally dominates photon splitting and renders the GRB emission region opaque to gamma rays (e.g. Baring, 1989). Therefore, as was deduced by Baring (1991), there is a small but significant energy range below the pair production threshold for which photon splitting can act effectively to modify the gamma-ray spectra, provided that θ is not small. This is sufficient for photon splitting to create observable effects in the MeV continuum of burst sources.

SPLITTING EFFECTS IN GAMMA-RAY BURST SPECTRA

The principal effect of photon splitting on a gamma-ray spectrum is to reprocess the spectrum by degrading the energies of the photons. A pile-up of photons might therefore be expected at energies near where the splitting optical depth in eq. (2) drops below unity, which is about 0.5 MeV when $\theta \approx \pi/2$ and $B \approx 0.1$. To determine the modifications that photon splitting makes to the gamma-ray burst continuum, it is appropriate to numerically solve the time-independent kinetic equations for the two photon polarization states. The solution then has two equilibrium populations, $n_\perp(\varepsilon)$ and $n_\parallel(\varepsilon)$, for the different polarizations. In the simplest model, photons can be injected into the neutron star magnetosphere with some energy distribution $q(\varepsilon)$ for a specific emission angle θ and then be allowed to split or escape from the emission region (the effect of pair production can be included in $q(\varepsilon)$). Since photon splitting is a collinear process, the kinetic equation can be solved separately for each θ, and then integrated over emission angles.

The kinetic equations can be written down quickly: the injection rates (possibly polarized) are $q_{\perp,\parallel}(\varepsilon)/t_{\rm esc}$ and the photon escape rates are $n_{\perp,\parallel}(\varepsilon)/t_{\rm esc}$, where $t_{\rm esc} = R/c$ is the photon escape time for the emission region. Note that here spatial and angular diffusion of the photons due to splitting is negligible because $\gamma \rightarrow \gamma\gamma$ is an angle-preserving process. Since photon splitting absorbs photons and also creates them at lower energies, it provides both source and loss terms to the kinetic equations. If σ denotes the polarization modes $\perp$ and $\parallel$, the loss terms are the absorption rates $\tau_\sigma(\varepsilon) n_\sigma(\varepsilon)/t_{\rm esc}$ ($\tau_\sigma(\varepsilon)$ is defined in eq. (4b)), while the source terms are proportional to the integral of the spectral rates in eq. (3) when weighted by the photon populations $n_\sigma(\varepsilon)$. The kinetic equations are therefore integral equations. Scaling by $t_{\rm esc}$, these equations assume the form

$$n_\sigma(\varepsilon)\{1+\tau_\sigma(\varepsilon)\} = q_\sigma(\varepsilon) + 2\int_\varepsilon^\infty d\omega \sum_{\sigma',\sigma''} \tau_{\sigma'\rightarrow\sigma\sigma''}(\omega,\varepsilon)\, n_{\sigma'}(\omega) \quad , \qquad (4a)$$

for $\sigma = \perp, \parallel$, where

$$\tau_\sigma(\varepsilon) = \sum_{\sigma',\sigma''} \int_0^\varepsilon \tau_{\sigma\rightarrow\sigma'\sigma''}(\varepsilon,\omega)\, d\omega \qquad (4b)$$

is the absorption optical depth for polarizations $\sigma = \perp, \parallel$, obtained using eq. (3). Note that the term with the integral includes an extra factor of two to account for the duplicity of photons created in the splitting process. If the photon polarizations are unobservable, these two integro-differential equations reduce to one.

The injection spectrum $q(\varepsilon)$ is chosen to be a typical output of the synchrotron pair cascade model of Baring (1989). The continuum spectrum is therefore formed by synchrotron radiation, though it could also be produced by other mechanisms such as inverse Compton scattering and curvature radiation. For synchrotron photons supplied by non-thermal electrons, generally a power-law continuum results, though this is truncated due to the strong absorption of gamma-rays by pair production $\gamma \rightarrow e^+e^-$ (Baring, 1989). A canonical spectrum representing the injection expected from a synchrotron pair cascade

is then

$$q_\sigma \;=\; \frac{Q_\sigma \varepsilon^{-(1+\alpha)}}{1+\tau_{pp}(\varepsilon)} \quad , \qquad \sigma = \perp , \parallel \; , \tag{5}$$

where the optical depth of the emission region (of size R) to single-photon pair production can be obtained from Baring (1991):

$$\tau_{pp}(\varepsilon) \;\approx\; \alpha_{\rm f} \frac{R}{\lambda_c} B \sin\theta \, \frac{3\varepsilon_\perp^2 - 4}{2\varepsilon_\perp^2(\varepsilon_\perp + 2)^2} \sqrt{\frac{\varepsilon_\perp^2 - 4}{\phi(\varepsilon_\perp)\mathcal{L}(\varepsilon_\perp)}} \, \exp\left\{ -\frac{\phi(\varepsilon_\perp)}{4B} \right\} \quad . \tag{6a}$$

Here $\varepsilon_\perp = \varepsilon \sin\theta$ and

$$\phi(\varepsilon_\perp) \;=\; 4\varepsilon_\perp - (\varepsilon_\perp^2 - 4)\mathcal{L}(\varepsilon_\perp) \qquad , \qquad \mathcal{L}(\varepsilon_\perp) \;=\; \log_e\left(\frac{\varepsilon_\perp + 2}{\varepsilon_\perp - 2} \right) \quad . \tag{6b}$$

This approximation is valid for $2 < \varepsilon_\perp \ll 1/B$, i.e. near the threshold for pair production. The spectral index α of the injection in eq. (5) is independent of the polarization state since synchrotron radiation and most other radiation mechanisms do not produce polarization-dependent indices from non-thermal electrons. Validity of an injection such as in eq. (5) requires that the pair cascade spectrum is generated much faster than the photons can split. This injection is therefore physically reasonable because synchrotron radiation and pair production generally have much shorter timescales than does photon splitting.

The solutions of eq. (4) for an unpolarized injection of photons from a pair cascade are displayed in Fig. 1. The reprocessing effect of magnetic photon splitting generates an absorption of photons just below the pair production threshold and an overproduction of photons at lower energies. The net effect is a flattening of the hard X-ray continuum and a broad spectral bump around 0.5 MeV when the photon emission angle is $\theta = \pi/2$. This bump appears in both polarization states and is qualitatively similar to the prediction made in the work of Baring (1991), where consideration of the photon polarizations was neglected. It is clearly an observable feature, and is moved to higher energies and becomes less prominent as θ decreases. The pair production truncations to the hard gamma-ray spectrum are evident in Fig. 1 and generally occur at energies $\varepsilon \sim 2/\sin\theta$ for $B = 0.1$. The polarization $\mathcal{P}(\varepsilon)$ of the photons at energy ε is given by

$$\mathcal{P}(\varepsilon) = \left| \frac{n_\perp(\varepsilon) - n_\parallel(\varepsilon)}{n_\perp(\varepsilon) + n_\parallel(\varepsilon)} \right| \quad , \tag{7}$$

and is clearly quite large in Fig. 1. In fact, in the idealized situation that the emission region has an enormous optical depth to $\gamma \rightarrow \gamma\gamma$, repeated splitting of photons generates a strongly-polarized photon population, 5/7 of which is in the $\perp$ state: this result can be obtained from a close consideration of eqs. (3) and (4). This preferential polarization of the continuum, corresponding to $\mathcal{P} = 3/7$, is realized near the $\gamma \rightarrow e^+e^-$ cutoff for the $\sin\theta = 1.0$ case in Fig. 1.

The photon injection from a synchrotron pair cascade will not be unpolarized, as assumed in Fig. 1, so a more realistic injection is needed. Standard synchrotron radiation

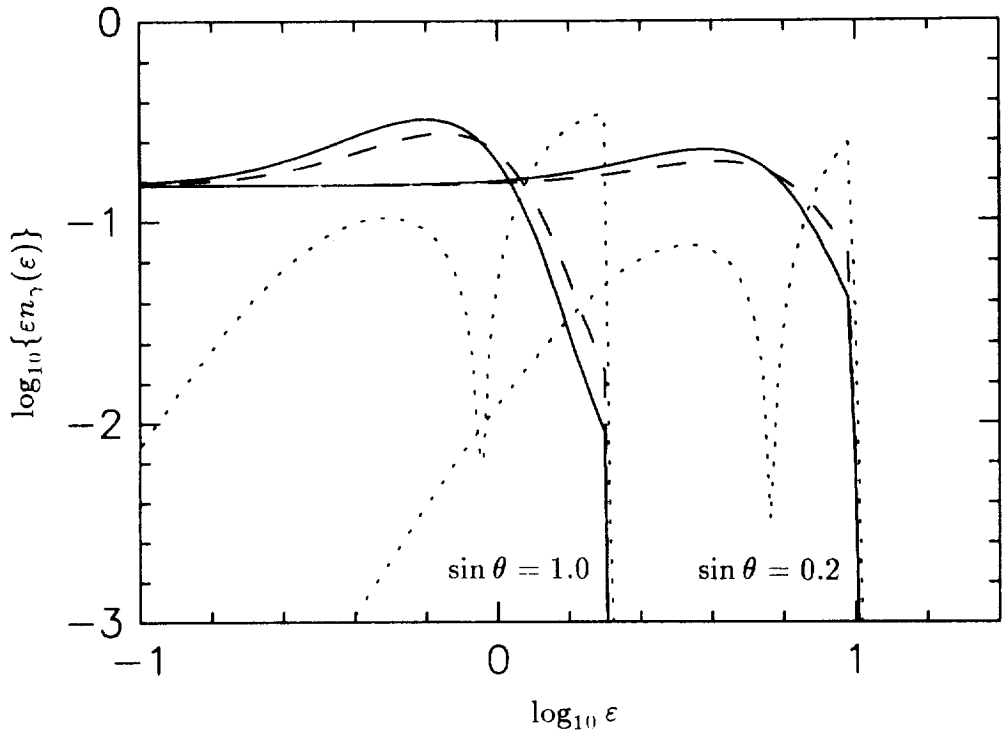

Fig. 1: The solutions of the photon kinetic equations in eq. (4), illustrating the reprocessing effects of splitting for different emission angles θ. The polarization components $n_\perp(\varepsilon)$ (solid curves) and $n_\parallel(\varepsilon)$ (dashed curves) of the photon spectrum are shown. The injected photon spectrum is a truncated power-law as in eq. (5) with $\alpha = 0$, and is unpolarized ($Q_\perp = Q_\parallel$). The field is $B = 0.1$. The dotted curves depict the polarization $\mathcal{P} = |(n_\perp - n_\parallel)/(n_\perp + n_\parallel)|$. Reducing θ clearly diminishes the reprocessing and polarization effects of splitting.

theory for power-law electrons predicts that a synchrotron spectrum of index α will have a corresponding polarization $\mathcal{P} = (\alpha + 1)/(\alpha + 5/3)$ (e.g. see Bekefi, 1966), independent of the photon energy. This corresponds to $n_\perp(\varepsilon)/n_\parallel(\varepsilon) = 3\alpha + 4$, which for $\alpha = 0$ is 4. The pair production process only generates non-thermal pairs and so does not influence the synchrotron polarization. Fig. 2 shows the photon splitting-reprocessed spectrum for the case of a synchrotron injection spectrum that is polarized according to the above prescription (i.e. $Q_\perp/Q_\parallel = 3\alpha + 4$). Clearly the synchrotron polarization tends to dominate the emergent photon polarization, without affecting the prominence of the splitting bump. However, in contrast to Fig. 1, near the pair production cutoff, where photon splitting is most effective, $\gamma \rightarrow \gamma\gamma$ actually acts to *depolarize* the synchrotron radiation towards the value of $\mathcal{P} = 3/7$ that is "preferred" by magnetic splitting.

Modelling gamma-ray burst spectra could plausibly include an integration over emission angles θ: indeed observations are unlikely to sample just a single value of θ. This can be represented by an enveloping of spectra like those in Fig. 1, resulting in Fig. 3 when summed over polarizations. The angular distribution of radiation is chosen for

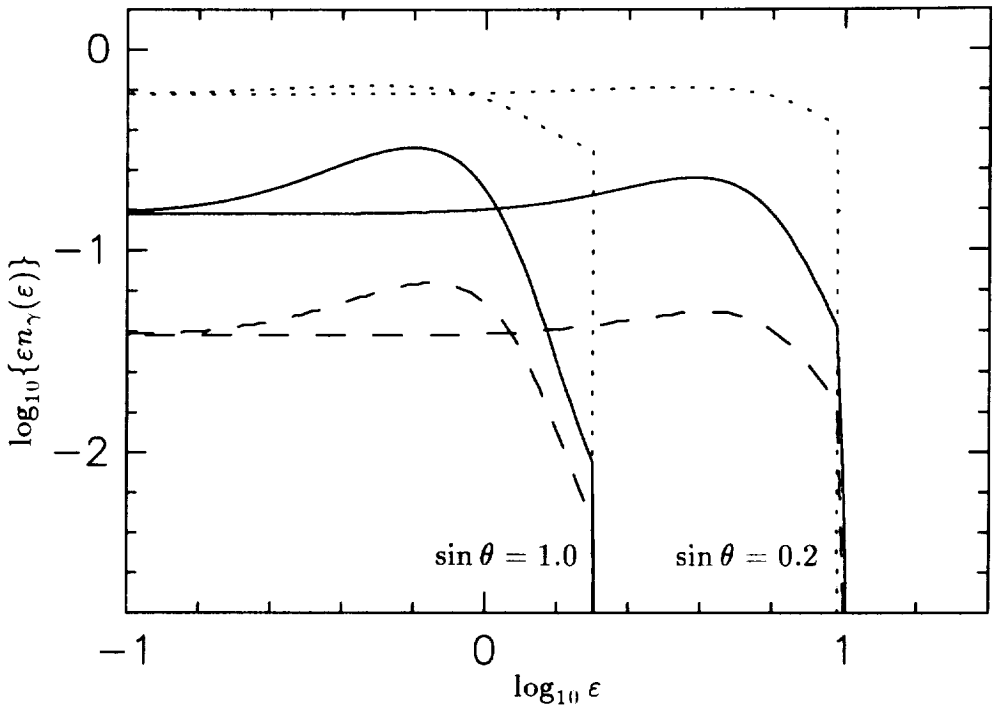

Fig. 2: The solutions of the photon kinetic equations in eq. (4), for a case almost identical to that depicted in Fig. 1: here the photon injection is again a truncated power-law with $\alpha = 0$, but this time it is polarized as would be expected from synchrotron radiation (i.e. $Q_\perp/Q_\parallel = 3\alpha + 4 = 4$). The reprocessing due to splitting is again evident, however now the polarization is mostly determined by the synchrotron process.

convenience (see Baring, 1991) to be $\phi(\sin\theta) = \sin^\kappa\theta$, and negative values of κ occur in models where the emitting electrons cool in energy and decrease their pitch angle during their synchrotron emission lifetime (this amounts to a pile-up of electrons with small pitch angles). The high-energy spectral break is by an index (see Baring, 1991) of $(1+\alpha+\kappa)$, which becomes zero when $\kappa = -(1+\alpha)$. It is due to the enveloping of the pair production cutoffs for different θ. The photon splitting bump in the continuum around 1 MeV, which is still polarized, remains very prominent. The bump appears near 1 MeV because the dominant contribution to the splitting reprocessing comes from $\theta \approx \pi/2$: it is unlikely to be confused with a two-photon pair annihilation line because it is so broad (Baring, 1991).

In conclusion, magnetic photon splitting can produce a significant bump in the gamma-ray spectrum of GRBs, a prediction that is not altered by the accurate treatment of the photon polarization states that is presented here. The instruments aboard the GRO mission have the capability to detect this feature in burst sources, which would then be an important verification of the theory of quantum electrodynamics in strong magnetic fields.

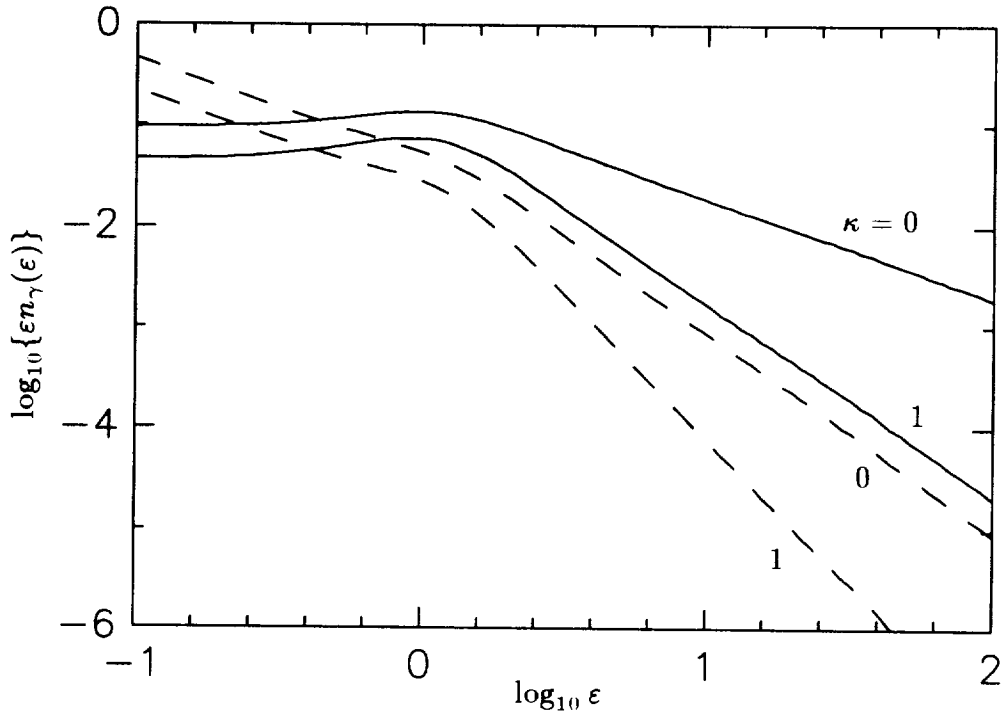

Fig. 3: Photon spectra resulting from an integration over emission angles and a sum over photon polarizations of spectra like those in Fig. 1, for $B = 0.1$. The sum is weighted by the angular distribution $\phi(\sin\theta) \propto \sin^\kappa\theta$, with κ as labelled. The photon injections are unpolarized ($Q_\perp = Q_\parallel$), truncated power-laws as in eq. (5), with $\alpha = 0$ (solid lines) and $\alpha = 1$ (dashed lines). The splitting bump is more pronounced for flatter spectra, and the overall spectral break is $(1 + \alpha + \kappa)$.

REFERENCES

Adler, S. L.: 1971 *Ann. Phys.* **67**, 599

Adler, S. L., Bahcall, J. N., Callan, C. G., and Rosenbluth, M. N.: 1970 *Phys. Rev. Lett.* **25**, 1061

Baring, M. G.: 1988 *Mon. Not. R. astr. Soc.* **235**, 79

Baring, M. G.: 1989 *Astron. Astrophys.* **225**, 260

Baring, M. G.: 1991 *Astron. Astrophys.* in press.

Bekefi, G.: 1966 *Radiation Processes in Plasmas*, (Wiley and Sons, New York)

Bialynicka-Birula, Z., and Bialynicki-Birula, I.: 1970 *Phys. Rev. D* **2**, 2341

Jauch, M. M., and Rohrlich, F.: 1980 *The Theory of Photons and Electrons* (2nd edn. Springer, Berlin)

Mitrofanov, I. G., *et al.*: 1986 *Sov. Astron.* **30**, 659

Papanyan, V. O., and Ritus, V. I.: 1972 *Sov. Phys. JETP* **34**, 1195

Stoneham, R. J.: 1979 *J. Phys. A* **12**, 2187

Usov, V. V., and Shabad, A. E.: 1983 *Sov. Astron. Letters* **9**, 212

GAMMA-RAY BURST ASTROMETRY II: NUMERICAL TESTS

L. G. TAFF and S. T. HOLFELTZ
SPACE TELESCOPE SCIENCE INSTITUTE
3700 San Martin Drive
Baltimore, MD 21218

Since the announcement of the discovery of sources of bursts of gamma-ray radiation in 1973, many more reports of such bursts have been published. Numerous artificial satellites have been equipped with gamma-ray detectors including GRO. Unfortunately, we have made almost no progress in identifying the sources of this high energy radiation. Only one visible counterpart is known. We suspect that this is a consequence of the methods currently used to define gamma-ray burst source 'error boxes'. An alternative procedure was proposed in 1988 by Taff. In the current paper we report on Monte Carlo simulations of the efficacy of this technique using realistic burst timing uncertainties and satellite location errors as well as a variety of satellite constellations. Since these are controlled numerical experiments, we can examine the dependence of the statistics of the errors in the deduced burst wavefront normal as a function of the timing inconsistencies, detector location standard deviations, and especially the number and distribution of the detectors. The results clearly show that an arc minute prediction of a unique burst location is routinely obtainable once there are at least two interplanetary detectors.

I. INTRODUCTION

An alternative to the customary "time difference of arrival" method of gamma-ray burst source location was presented by Taff in 1988. This technique predicts a unique location for the source of the burst independent of the number of different gamma-ray detectors registering the burst. All the detector locations and times of observation are folded into a single, simple computation. In contrast, the standard method only defines a (circular) locus of points on the celestial sphere on which the burst source location should reside. When there are multiple detections of the same burst, a finite area on the celestial sphere is, in practice, delineated via a pair-wise analysis of the location and timing data. With real data—and with a very difficult problem of time registration of bursts observed with detectors of different responsivities and sensitivities, spacecraft clock errors, timing errors arising from binning the recorded photons, differing thresholds before recording is initiated, and so forth—the geometrically pure problem is degraded into one whose best possible outcome is that all the intersection points lie near each other. This small area is used to define an 'error-box' in which the burst source is thought to lie (see Fig. 1).

The location deduced in this fashion will, in general, not be the statistically most likely position for the source of the burst. The hope that the circle drawn for each pair of detecting sensors is centered in a region of high source location probability will not be consistently realized in practice; indeed, the circle must lie completely outside the one-sigma error region fairly often. Furthermore, the supposition of a probabilistically uniform region surrounding

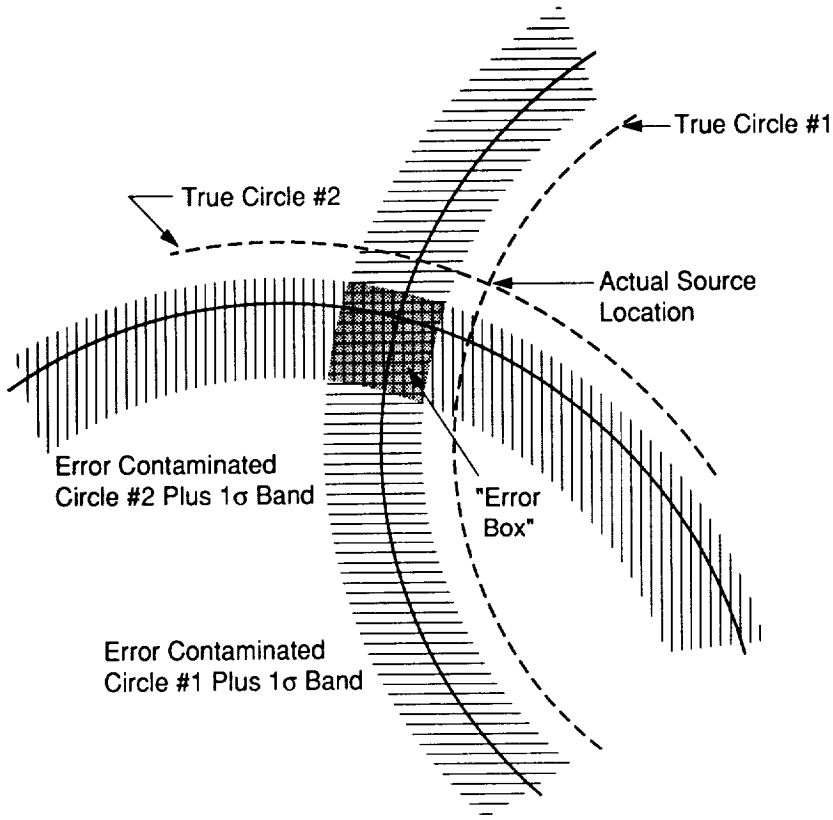

Fig. 1. General intersection area for "time difference of arrival" gamma-ray burst source location determination. Note error bands need not be symmetrically placed relative to circular locus nor include the true circle.

the most probable source location circle may be too simplistic—it is not clear that the underlying probability function is that well-behaved.

Finally, *random* errors in detector location became *systematic* errors in the "time difference of arrival" method circle (see Fig. 2; timing errors change the radius of the circle). In Fig. 2 the random error in the location of the spacecraft at P causes us to place it at P' instead. This alters the axis of the cone from OP to OP' thereby systematically shifting the locus of possible source locations. Similarly, a random error in the relative timing between the two spacecraft will cause θ to be over-estimated or under-estimated thereby systematically enlarging or decreasing the locus of possible source locations. One could compute the one-sigma regions in an attempt to produce reliable error estimates. However, none have been published and the amount of computation necessary for the customary method must exceed that necessary to similarly characterize the results of Taff's method by the ratio of (number of points in a circle):one since this is the ratio of their prediction volumes. Hence, such a calculation would be unwieldy and extremely expensive computationally. A more complete comparison between the different aspects of the two methods is given in Table 1.

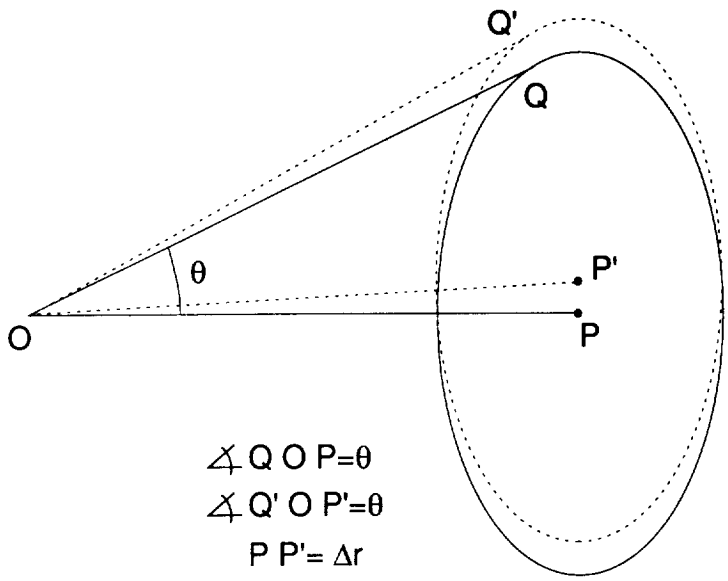

Fig. 2. Locus of potential burst source locations systematically shifted by the random spacecraft positional error PP'.

TABLE 1. COMPARISON OF THE TWO METHODS

ASPECT	TAFF'S METHOD	CUSTOMARY METHOD
PREDICTS A UNIQUE LOCATION	YES	NO
SIMULTANEOUSLY USES ALL THE OBSERVATIONAL DATA	YES	NO
SUBSUMES THE OTHER METHOD AS A SPECIAL CASE	YES	NO
IS EASILY AMENABLE TO MONTE CARLO SIMULATION	YES	NO
CAN EASILY ASSESS THE QUALITY OF THE PREDICTION	YES	NO

The technique developed in Taff (1988) is easily amenable to numerical simulation. This paper reports on extensive Monte Carlo computations of its predictions for the location of gamma-ray bursts. These calculations explore ranges of numbers of potential spacecraft-carrying burst detectors, in cislunar (2, 3, or 4) and interplanetary (1, 2, 3, or 4) space, and all 4π steradians of potential burst source locations. In addition, because these are controlled numerical experiments, we can statistically characterize both the accuracy and the precision of the results. In sum, they conclusively show that a minute of arc is routinely available once there are two interplanetary spacecraft in the burst detection network.

In the next section we briefly review the fundamental ideas behind this method. The third section of the paper describes the Monte Carlo simulations we have performed. Comments on our oral presentation have defined additional areas of research; these are outlined in the fourth section. Because of the closeness of the Huntsville meeting, we shall report there on these additional topics. These will include more realistic simulations and analytical progress on solving our form of the problem. Using our software, within a year an entirely new catalog of burst source locations, for every gamma-ray burst multiply detected, could be computed. Moreover, each new source location would be described by a reliable error estimate (once access to the data is obtained).

II. CONCEPT

The essential concept behind the technique is to use the one piece of information about the gamma-ray burst that we indisputedly know; to wit, that the phase of the burst (whether planar or spherical) is an invariant for all the detectors. Could the detectors on the interplanetary burst network measure the phase ϕ of the burst wavefront, they would all obtain the same value (absent observational errors of course), namely

$$\phi = \mathbf{k} \cdot \mathbf{r} - \omega t \tag{1}$$

where $\mathbf{r}$ is the solar system barycentric location of the spacecraft, t is the time of arrival of the burst at that spacecraft (t is assumed to be a shared inertial timescale), $\mathbf{k}$ is the wave vector of the burst wavefront, and ω is the angular frequency of the burst ($= 2\pi\nu$ where ν is the frequency of the photon; $\nu = c/\lambda$ where c is the speed of light in vacuo and λ is the wavelength of the burst). Rewriting $\mathbf{k}$ as $k\mathbf{u}$, where $\mathbf{u}$ is the wavefront normal, the pseudo-invariant Φ can be defined, viz.

$$\Phi = \mathbf{u} \cdot \mathbf{r} - ct. \tag{2}$$

Although neither ϕ nor Φ can be directly measured, they do include all the observational data at our disposal and the quantity we want to determine — $\mathbf{u}$. Taff's (1988) concept was, that especially in the presence of unknown systematics and the very difficult time registration problem we have, enforcing the constraint that each sensor's (albeit unknown and unmeasurable) value of Φ be the same would lead to a mathematically well-posed problem for the computation of $\mathbf{u}$. The explicit method Taff (1988) proposed for doing so was to minimize the quantity

$$T = \frac{1}{2} \sum_{n,m=1}^{N} (\Phi_n - \Phi_m)^2 \tag{3}$$

subject to the constraint that $\mathbf{u} \cdot \mathbf{u} = 1$. Taff suggested that the constraint be incorporated via a Lagrange multiplier.

By explicit computation, Taff (1988) further showed that the customary time of arrival analysis was contained in this principle as a special case of minimizing Eq. (3) (*i.e.*, they are represented by the cases of $N = 2$ and $N = 3$). Taff also explicitly computed the coplanar solution for $\mathbf{u}$ when N was equal to 4.

III. MONTE CARLO SIMULATIONS

The only drawback of the first paper was that it did not contain any numerical testing of this novel form of statistical estimation. This defect will be repaired immediately.

Since many of the gamma-ray bursts detected in the past have involved at least two near-Earth (*i.e.*, within cislunar space) detectors and at least one interplanetary detector, this formed the minimum configuration for our simulations. All configurations of $N_{close} = 2$, 3, or 4 and $N_{far} = 1$, 2, 3, or 4 have been considered. Not surprisingly, the algorithm works much better once N_{far} is at least two.

In addition to considering two groups of spacecraft, we considered a bifurcated distribution of spacecraft location uncertainties. For those in near-Earth orbit location uncertainties of 100 or 200 km were allowed (that is to the actual location of the spacecraft we added a vector for which each component was normally distributed about zero with a standard deviation of 100 or 200 km in length). For those spacecraft in interplanetary space we used the larger values of 1000 and 2000 km to span likely uncertainties. Finally, we also had to assign timing errors. These represent a convolution of spacecraft clock errors, detection timing (*e.g.*, binning), sensor-to-sensor correlation, and so on. We used standard deviations of 25 and 50 milli-seconds coupled with the zero mean normal distribution to represent these errors. Note that 25 milli-seconds represents 7500 km at the speed of light. Hence, since spacecraft locations are bound to improve, timing errors will continue to dominate the problem.

The spacecraft were always coplanar, in the plane of the ecliptic. This is a very good (numerical) approximation to the real case and significantly simplifies the (analytic aspects of the) computations. Spacecraft in cislunar space where deposited uniformly in azimuth relative to the Earth-Sun line and uniformly in distance between geosynchronous distance (42,000 km) and the mean lunar distance (400,000 km). Similarly, the interplanetary spacecraft were uniformly distributed in azimuth relative to the Earth-Sun line and uniformly in heliocentric distance between 0.5 and 4 A. U.

Once the standard deviations of the locations and timing were set, and the numbers of spacecraft fixed, the spacecraft were strewn across the solar system. For this constellation of spacecraft we then chose 100 different unit wavefront normal vectors to represent the gamma-ray burst ($\mathbf{n}$). These were uniformly distributed over the celestial sphere. We next computed the relative timings, corrupted the spacecraft locations and timings as described above, and solved for $\mathbf{u}$. The angle θ, given by the scalar product between $\mathbf{n}$ and $\mathbf{u}$,

$$\cos\theta = \mathbf{n} \cdot \mathbf{u} \tag{4}$$

tells us the angular mis-distance between the actual direction of gamma-ray burst source and the calculated one (note that the direction of the gamma-ray burst source is $-\mathbf{n}$ and the computed direction is $-\mathbf{u}$). Another way to think of θ is that it is the 3σ radius of our error

TABLE 2. RESULTS OF MONTE CARLO SIMULATIONS

N_{close}	N_{far}	$\sigma_{r_{close}}$ (km)	$\sigma_{r_{far}}$ (km)	σ_t (msec)	$\langle\theta\rangle$ (′)	σ_θ (′)	$\sigma_{r_{close}}$ (km)	$\sigma_{r_{far}}$ (km)	$\langle\theta\rangle$ (′)	σ_θ (′)
2	1	10	100	25	452.60	380.60	100	1000	359.20	333.80
2	2	10	100	25	1.26	2.45	100	1000	2.50	4.20
2	3	10	100	25	0.88	1.51	100	1000	0.87	1.50
2	4	10	100	25	0.84	1.34	100	1000	0.81	1.32
3	1	10	100	25	107.60	123.30	100	1000	112.10	130.20
3	2	10	100	25	1.60	2.88	100	1000	4.14	6.31
3	3	10	100	25	0.81	1.31	100	1000	0.80	1.33
3	4	10	100	25	0.79	1.20	100	1000	0.78	1.16
4	1	10	100	25	81.12	100.10	100	1000	75.77	91.00
4	2	10	100	25	1.87	3.29	100	1000	4.63	7.10
4	3	10	100	25	0.83	1.39	100	1000	0.68	1.10
4	4	10	100	25	0.73	1.16	100	1000	0.77	1.19
2	1	20	100	25	542.30	460.40	200	1000	467.80	427.80
2	2	20	100	25	1.66	2.59	200	1000	11.70	22.05
2	3	20	100	25	0.90	1.53	200	1000	0.83	1.44
2	4	20	100	25	0.76	1.15	200	1000	0.70	1.13
3	1	20	100	25	119.60	138.40	200	1000	121.20	137.60
3	2	20	100	25	2.36	4.03	200	1000	2.06	3.94
3	3	20	100	25	0.77	1.33	200	1000	0.80	1.39
3	4	20	100	25	0.73	1.16	200	1000	0.73	1.16
4	1	20	100	25	72.86	90.62	200	1000	71.43	93.99
4	2	20	100	25	1.30	2.48	200	1000	1.25	2.25
4	3	20	100	25	0.76	1.24	200	1000	0.75	1.32
4	4	20	100	25	0.76	1.23	200	1000	0.72	1.15
2	1	10	200	25	370.20	324.70	100	2000	397.40	370.80
2	2	10	200	25	2.37	4.07	100	2000	1.45	2.66
2	3	10	200	25	0.75	1.24	100	2000	0.84	1.49
2	4	10	200	25	0.73	1.13	100	2000	0.74	1.22
3	1	10	200	25	123.80	141.10	100	2000	115.70	133.10
3	2	10	200	25	2.72	5.21	100	2000	1.15	2.12
3	3	10	200	25	0.81	1.39	100	2000	0.80	1.27
3	4	10	200	25	0.75	1.22	100	2000	0.76	1.29
4	1	10	200	25	72.13	93.13	100	2000	82.14	105.50
4	2	10	200	25	1.85	3.41	100	2000	1.64	2.95
4	3	10	200	25	0.79	1.32	100	2000	0.76	1.37
4	4	10	200	25	0.71	1.16	100	2000	0.77	1.17
2	1	20	200	25	491.50	423.50	200	2000	442.70	401.00
2	2	20	200	25	2.98	4.31	200	2000	3.29	4.67
2	3	20	200	25	0.77	1.29	200	2000	0.81	1.34
2	4	20	200	25	0.77	1.19	200	2000	0.72	1.16
3	1	20	200	25	116.60	126.70	200	2000	124.30	143.50

Table 2. *Continued.*

N_{close}	N_{far}	$\sigma_{r_{close}}$ (km)	$\sigma_{r_{far}}$ (km)	σ_t (msec)	$\langle\theta\rangle$ ($'$)	σ_θ ($'$)	$\sigma_{r_{close}}$ (km)	$\sigma_{r_{far}}$ (km)	$\langle\theta\rangle$ ($'$)	σ_θ ($'$)
3	2	20	200	25	2.68	4.20	200	2000	2.07	4.15
3	3	20	200	25	0.75	1.22	200	2000	0.87	1.42
3	4	20	200	25	0.72	1.14	200	2000	0.84	1.30
4	1	20	200	25	72.60	92.00	200	2000	76.02	92.77
4	2	20	200	25	1.66	2.99	200	2000	1.34	2.77
4	3	20	200	25	0.80	1.32	200	2000	0.81	1.35
4	4	20	200	25	0.83	1.30	200	2000	0.78	1.21
2	1	10	100	50	685.60	575.30	100	1000	718.70	615.70
2	2	10	100	50	2.27	4.89	100	1000	6.35	9.42
2	3	10	100	50	1.01	1.76	100	1000	1.14	1.99
2	4	10	100	50	0.86	1.38	100	1000	0.92	1.49
3	1	10	100	50	227.80	219.50	100	1000	197.90	195.20
3	2	10	100	50	2.84	4.77	100	1000	3.02	4.81
3	3	10	100	50	1.07	1.86	100	1000	1.02	1.78
3	4	10	100	50	0.89	1.39	100	1000	0.78	1.27
4	1	10	100	50	137.20	147.90	100	1000	128.90	138.20
4	2	10	100	50	2.10	3.95	100	1000	2.44	4.03
4	3	10	100	50	1.00	1.61	100	1000	0.97	1.78
4	4	10	100	50	0.84	1.30	100	1000	0.80	1.37
2	1	20	100	50	729.50	605.20	200	1000	616.50	536.50
2	2	20	100	50	1.93	3.67	200	1000	3.89	5.74
2	3	20	100	50	0.99	1.55	200	1000	1.10	1.93
2	4	20	100	50	0.97	1.50	200	1000	0.88	1.37
3	1	20	100	50	208.10	197.20	200	1000	206.10	199.50
3	2	20	100	50	1.95	3.39	200	1000	2.43	4.67
3	3	20	100	50	0.96	1.62	200	1000	0.95	1.67
3	4	20	100	50	0.93	1.43	200	1000	0.80	1.23
4	1	20	100	50	152.10	157.70	200	1000	148.10	154.90
4	2	20	100	50	3.50	5.09	200	1000	2.15	3.81
4	3	20	100	50	0.93	1.61	200	1000	1.00	1.63
4	4	20	100	50	0.94	1.44	200	1000	0.82	1.31
2	1	10	200	50	662.60	560.00	100	2000	617.80	534.40
2	2	10	200	50	3.73	5.66	100	2000	2.31	4.11
2	3	10	200	50	0.99	1.70	100	2000	1.06	1.76
2	4	10	200	50	0.98	1.57	100	2000	0.91	1.41
3	1	10	200	50	235.40	224.40	100	2000	194.50	192.70
3	2	10	200	50	2.66	4.03	100	2000	2.47	4.40
3	3	10	200	50	1.05	1.75	100	2000	0.94	1.52
3	4	10	200	50	0.90	1.53	100	2000	0.82	1.26
4	1	10	200	50	116.00	125.50	100	2000	164.40	173.10
4	2	10	200	50	3.32	5.96	100	2000	3.30	4.93

Table 2. *Continued.*

N_{close}	N_{far}	$\sigma_{r_{close}}$ (km)	$\sigma_{r_{far}}$ (km)	σ_t (msec)	$\langle\theta\rangle$ (′)	σ_θ (′)	$\sigma_{r_{close}}$ (km)	$\sigma_{r_{far}}$ (km)	$\langle\theta\rangle$ (′)	σ_θ (′)
4	3	10	200	50	0.91	1.64	100	2000	0.97	1.62
4	4	10	200	50	0.87	1.50	100	2000	0.85	1.44
2	1	20	200	50	653.10	550.60	200	2000	530.40	472.00
2	2	20	200	50	12.94	13.02	200	2000	2.44	4.55
2	3	20	200	50	1.10	1.86	200	2000	1.13	2.05
2	4	20	200	50	0.87	1.35	200	2000	0.90	1.46
3	1	20	200	50	220.30	209.80	200	2000	215.00	216.00
3	2	20	200	50	4.96	6.59	200	2000	2.92	5.19
3	3	20	200	50	1.03	1.90	200	2000	0.96	1.76
3	4	20	200	50	0.89	1.46	200	2000	0.80	1.25
4	1	20	200	50	144.50	150.40	200	2000	138.30	151.40
4	2	20	200	50	1.96	3.45	200	2000	1.71	3.03
4	3	20	200	50	0.92	1.55	200	2000	1.06	1.90
4	4	20	200	50	0.82	1.34	200	2000	0.81	1.36

circle. By averaging over the 100 randomly chosen wavefront normals, and then again over 100 different constellations of the same set of sensors, we can unambiguously demonstrate the power of the technique. These results are given in the right-hand portion of Table 2 for the larger location uncertainties.

Table 2's mid-section has the identical format to its right-hand portion except that all the location uncertainties have been reduced by an order of magnitude (*i.e.,* 10 and 20 km for spacecraft in cislunar space and 100 and 200 km for those in interplanetary space). Clearly, once there are at least two detectors located in interplanetary space an arc minute is the routine performance of the technique. Finally, since we do know the true location of the burst source, we can also compute the standard deviation about the mean [which is necessarily non-zero owing to the form in Eq. (4)]. These values are also in Table 2 (*i.e.,* σ_θ).

IV. ADDITIONAL AREAS OF RESEARCH

One consequence of the oral presentation of these results were the following suggestions for future work: (1) Simulations tailored to the Ulysses, Pioneer-Venus Orbiter, GRO, and GRANAT configuration; (2) More analytical work in describing the error distribution of this method, and (3) Simulations of the BATSE instrument alone as a gamma-ray burst source location detector. These additional computations will be reported on in paper III to be given at the Huntsville Gamma-Ray Burst Workshop.

Reference

Taff, L. G., 1988, Ap J 326, 1032

N92-21914

UNTHERMALIZED POSITRONS IN GAMMA-RAY BURST SOURCES

W. Tkaczyk, S. Karakuła

Institute of Physics, University of Łódź
ul. Pomorska 149/153, 90-236 Łódź, Poland

Abstract. The spectra of the broadening 0.511-MeV annihilation line produced by high temperatures was calculated in the case of unthermalized plasma; i.e., $T_{e^+} \neq T_{e^-}$. The flattening in the spectrum of the annihilation lines for large differences of electron and positron temperatures is a strong indication that the observed features of the hard-tailed spectrum of the gamma bursts can be well described by annihilation of unthermalized positrons.

We propose the charge separation occurring in Eddington limited accretion onto a neutron star or the one-photon pair production in strong magnetic fields as a mechanism for the production of unthermalized positrons in the sources of gamma bursts.

From the best fit of experimental spectra by our model, the parameters of sources for which the regions with different plasma temperatures can exist is evaluated.

1. Introduction. The gamma-ray bursts are short flashes of hard photons with an energy of 1 keV a to few tens of MeV. The gamma-ray bursts are bright, energetic, short-lived phenomena that are characterized by extremely hard spectra. The spectroscopic study of gamma-ray burst spectra on the Solar Maximum Mission (SMM) satellite [1,2] have provided a rich materials avenue towards the understanding the origin of these events. For detailed discussions of the experimental data of gamma-ray bursts, see review articles [2,3,4,5].

The major characteristic of gamma-ray bursts are as follows [3]:

1. The bursts are divided by their duration into two classes: short (< 1 s) and long (1 s to a few minutes).
2. The continuum spectra of bursts evolve rapidly with time.
3. The absorption features in the energy range of 30-100 keV are, in most cases, the strongest in the initial phase of the burst.
4. The broad annihilation lines of 350-450 keV are also the strongest at the beginning of the burst or at intense peaks of the time profile.
5. The total energy release in a gamma-ray burst is not constant; it increases approximately in proportion to the time duration of the event.
6. Gamma-ray bursts may be accompanied by intense X-ray emission and optical flashes.

The localization of gamma burst sources are not clear yet, but the log n (number of events) versus log N_{max} (maximum count rate in the time profile) plots are in full agreement with an isotropic distribution of the sources over the celestial sphere. The above argument prefers a Galactic origin of gamma bursts. Neutron stars are proposed as a candidate for that source distribution. The lines in the 30-100 keV region have been interpreted as broad cyclotron scattering in a strong magnetic field. Emission features in the 350-450 keV range have been interpreted as gravitationally redshifted annihilation e^+e^- lines produced near the surface of neutron stars. Hard power-law tails observed in the spectra of gamma bursts

continue in some cases to at least ≈10 MeV. The existence of such high-energy photons and cyclotron absorption-line spectra have caused difficulty in the construction of self-consistent models of gamma burst sources. The high-energy emission region should be nearer to the neutron surface than the cyclotron absorption region in the case of interpreting observations of annihilation lines as gravitational redshifts. Moreover, the detailed analysis of relations between redshifted annihilation lines and their widths in observed gamma burst spectra shows significant disagreements when thermal pair dominant plasma annihilation has been assumed [6].

In this paper, we propose annihilation of unthermalized plasma ($T_e+ \neq T_e-$) as the mechanism of producing gamma-ray burst spectra with line e^+e^- and hard-tail features. In that case, the redshifts of line e^+e^- are mainly due to kinematics of the annihilation process, so the relativistic emission region can be located on larger distances than absorption from the surface of a neutron star. The spectra with hard tails measured by KONUS, SMM and HEAO A-4 experiments have been fitted by thermal bremsstrahlung in soft-energy regions, and in annihilation lines of unthermalized plasma in hard-energy regions. From the best fit, we have evaluated the temperature of electrons T_e-, positrons T_e+ and the clumpiness parameter of gamma-ray burst sources.

2. The spectra from annihilation. The broadening of the annihilation line 0.511 MeV can be produced by high temperatures, a strong magnetic field and Doppler shift due to bulk

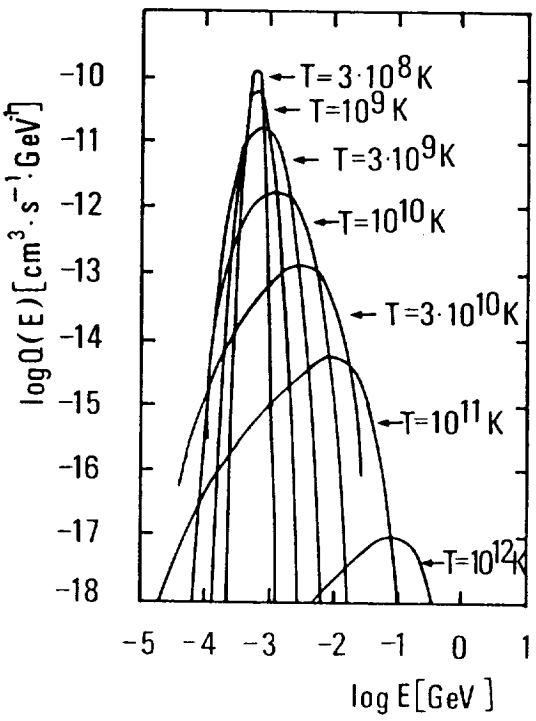

Fig. 1.

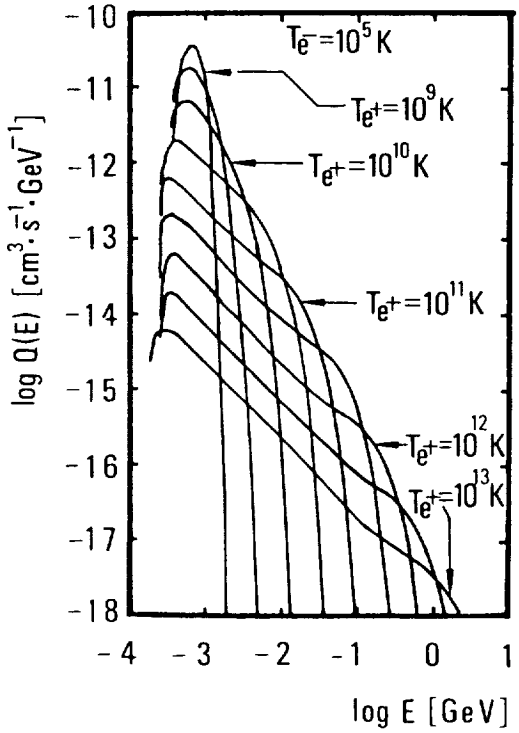

Fig. 2.

motion and the gravitational field. Recently we have calculated the spectra of annihilation lines for two cases: thermalized $T_e- = T_e+$ [7] and unthermalized $T_e+ \neq T_e-$ [7]. Figure 1 shows spectra for a thermalized plasma. Figure 2 shows spectra for an unthermalized

plasma with electron temperatures of 10^5 K and selected temperatures of positrons. The peak energies and widths of annihilation spectra are different in the case of unthermalized plasma in comparison with annihilation spectra for equal temperatures of electrons and positrons [8,9].

We should note that the peak energy in the spectra is not blueshifted when the temperature positron increases, but in fact, it even decreases below 0.511 MeV. For large differences between component temperatures, the peak energy approaches the value $m_e/2$.

Moreover, the spectra from unthermalized plasma at that point are harder and approach the power-law type with a power index ≈ 1. The spectra indicate similar features as observed in gamma-ray burst spectra with hard tails.

3. Models of gamma burst source. Recently the states of plasma in gamma burst sources have been investigated in many papers. The main question is, when can the line be seen? As was shown by Svensson [10] and Zdziarski [11], the annihilation line is not expected from plasma in the pair equilibrium; i.e., the pair annihilation rate balances the pair production rate. Moreover, the gamma-ray burst spectra cannot be explained by an optically thick thermal model with plasma in a weak magnetic field; i.e., $B << B_{cr}$ (magnetic field B is much lower than critical $B_{cr}=4.413\times10^{12}$ Gs). For plasma in a magnetic field $B \geq B_{cr}$, one-photon pair e^+e^- production and annihilation rates should be included. Harding [12] shows that a thermal model of gamma bursts with pair production and annihilation in a strong magnetic field requires a maximum source size which is much smaller than a neutron star radius. Moreover, the time scale of synchrotron emission in the gamma-ray burst sources in a magnetic field above 10^{12} Gs is on the order of less than 10^{-16} s. In that case, the synchrotron emission dominates the annihilation line. The above results show that in both cases, a low and strong magnetic-field thermal, optically thick model with plasma in equilibrium is not convenient for explaining all features in gamma-ray burst spectra. We propose a thermal bremsstrahlung, optically thin model of gamma bursts with unthermalized plasma $T_e+ \neq T_e-$. The continuum component of the spectrum is due to bremsstrahlung of a hotter source region but the relativistic component is due to annihilation of a hotter plasma of positrons with a cooler plasma of electrons. The region of continuum emission and the relativistic component are separated. The annihilation region can be placed far from the neutron star surface. This supports the fact that the burst spectra do not cut-off above a few MeV and indicates that few high-energy gamma rays are eliminated by photon-photon or one-photon pair production in the magnetic field. The photon beaming along magnetic field lines avoids these difficulties. In our proposition, the annihilation line is redshifted due to kinematics. The unthermalized plasma can exist in the case of turbulent motion or additional heating of positrons or electrons. Figure 3 shows the annihilation time of unthermalized plasma (full lines) and relaxation time (broken line) for plasma with a concentration of $n_e+=n_e-=10^{20}$ as a function of temperature. From comparison of those times, we can conclude that annihilation time is shorter than the relaxation time if the temperature of the electrons is less than 10^8K and the temperature of the positrons is greater than 10^{10}K. For both types of models of gamma bursts: i) accretion matter on neutron star [13], and ii) thermonuclear explosion [14], a hot plasma with a temperature $> 10^9$K is predicted.

In the accretion model recently proposed by Colgate and Petschek [13], details of producing unthermalized plasma were discussed in our paper [7,15]. We have proposed that the charge separation in the matter of Eddington limited accretion onto a neutron star can

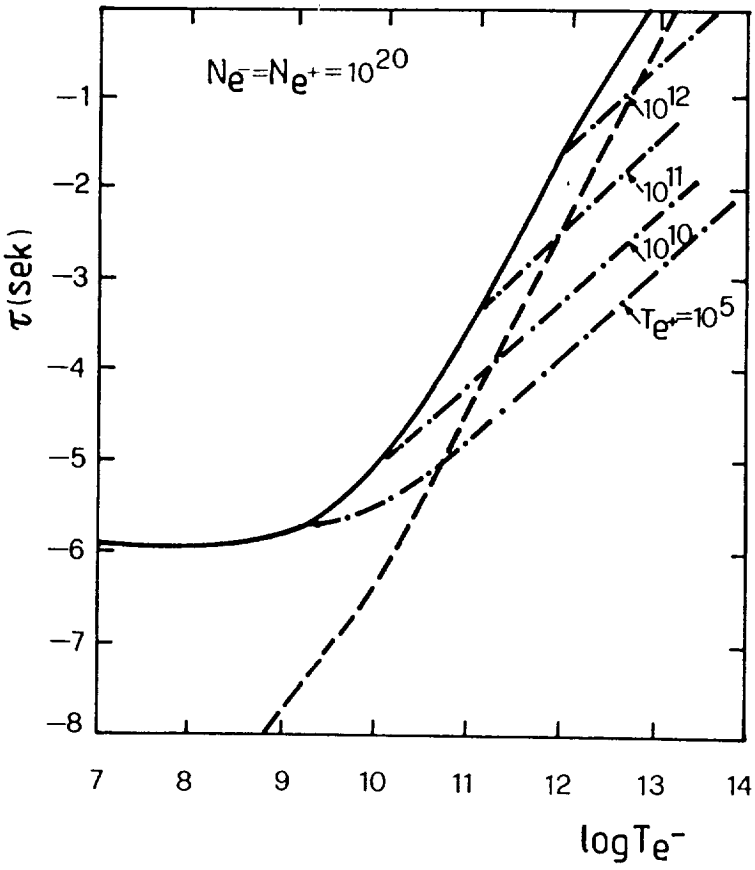

Fig. 3

produce unthermalized positrons. The scenario can be briefly described as follows: a layer of the thickness $\tau \simeq 1$ falls onto the neutron star. The electrons will be pushed away from the star by the photon flux outgoing from the surface. This produces a charge separation and consequently, an electric field. The electrons are heated by interaction with the photons. Photons are produced by annihilation of positrons and by the compression caused by the matter falling onto the star surface. The pair production processes caused by photons or other particles are the source of the positrons which are accelerated not only by photon interactions, as are the electrons, but also by the electric field.

In a thermonuclear explosion model, the strong electric field generated by the motion of matter in a magnetic field, accelerated electrons up to relativistic energies.

In a strong magnetic field, the electron energy is converted to the hot pair dominated plasma. The plasma is considered to occupy a region of size R[cm], which is in a constant homogeneous magnetic field of strength $B'=B/B_{cr}$, ($B_{cr}=m^2\cdot c^3/e\hbar=4.414\times10^{13}$Gs). The pair plasma's equilibrium state is determined by its temperature, $T_-^* = kT/mc^2$ (mc^2 is the electron rest energy) and the values of B′ and R. In order to calculate the positron concentration n, we made the following assumptions: i) the plasma is confined, so that positrons do not escape before annihilation; ii) the pair annihilation occurs by the two-photon process in unthermalized plasma; iii) one-photon pair production by synchrotron photons dominates over photon-photon and photon-particle processes (for some parameters of plasma it is a good approximation [16]; and iv) the electrons with temperature T_-^* have an isotropic Maxwellian energy distribution.

a) Photons. The source of photons is the synchrotron emission of thermal electrons ($T_-^* < 1$). The photon production spectrum was obtained from the emissivity of the synchrotron radiation [17], and is done by formula:

$$n_\gamma(E,\Omega)= n_- \cdot \frac{2^{3/2}\cdot\pi\cdot r_e}{3\cdot c}\cdot\left(\frac{m\cdot c^2}{h}\right)^2\cdot A(T_-^*)\cdot T_-^*\cdot\exp\left\{-\left(\frac{4.5}{\sin\theta}\cdot\frac{1}{T_-^{*2}}\cdot\frac{E}{B'}\right)^{1/3}\right\},$$

where: θ is the angle between the emitted photon momentum and magnetic field line, c - velocity of light, n- concentration of electrons, $A(T_-^*)$ - normalization constant, $E=E_\gamma/mc^2$ is the photon energy in mc^2 units, and $r_e=e^2/mc^2$ is the classical electron radius.

We have evaluated the photon density by solving simple diffusion equations, taking into account photon escaping time and one-photon pair creating rate.

b) Positrons. The synchrotron photon spectrum was taken to determine the rate of pair production by the one-photon process:

$$R_{1\gamma}=\int d\Omega\cdot\int_{E_{min}} n_\gamma(E,\Omega)\cdot r_{1\gamma}(B',E,\Omega)\cdot dE,$$

where: $n_\gamma(E,\Omega)$ - the photon spectrum, $r_{1\gamma}(B',E,\Omega)$ - the rate of pair production per photon of energy E.

The spectra of positrons was calculated using the formula:

$$\frac{dR_{1\gamma}}{dE_+}=\frac{1}{2}\int d\Omega\cdot\int_{E_{min}}^{\infty} n_\gamma(E,\Omega)\cdot\frac{r_{\gamma_B}(\varepsilon)}{d\varepsilon}\cdot\frac{d\varepsilon}{dE_+}\cdot dE\ ,$$

where: $\varepsilon=E_+/E$ is the fractional energy of one particle in the pair, $E_{min}=E_+ +1/\sin(\theta)$, $r_{\gamma_B}(\varepsilon)$ is the pairs production rate for an individual photon.

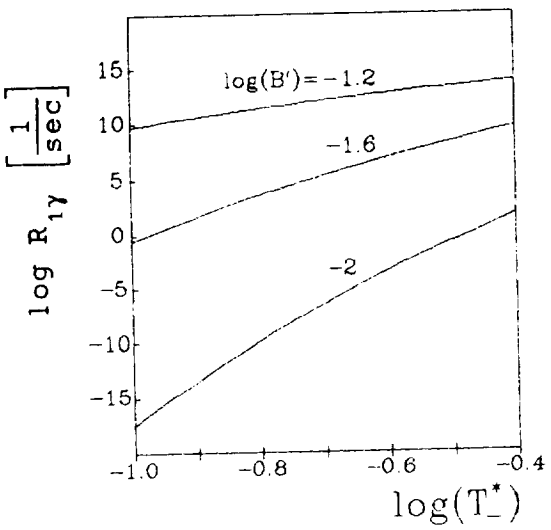

Fig. 4. The rate of one-photon pair production by electrons synchrotron emission as function of temperature T_-^* for the different values of magnetic field strength and R=1cm.

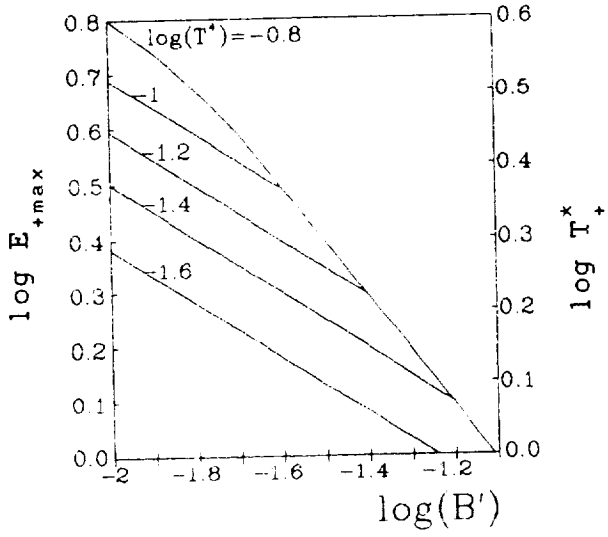

Fig. 5. The peak energy of positrons in units $E_+^*=E_+/mc^2$ (left hand scale) and temperature of positrons (right hand scale) as a function of magnetic field.

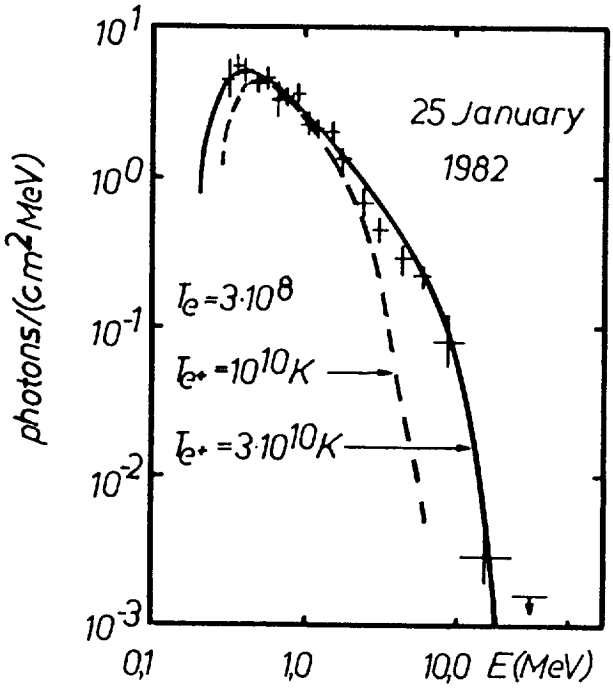

Fig. 6

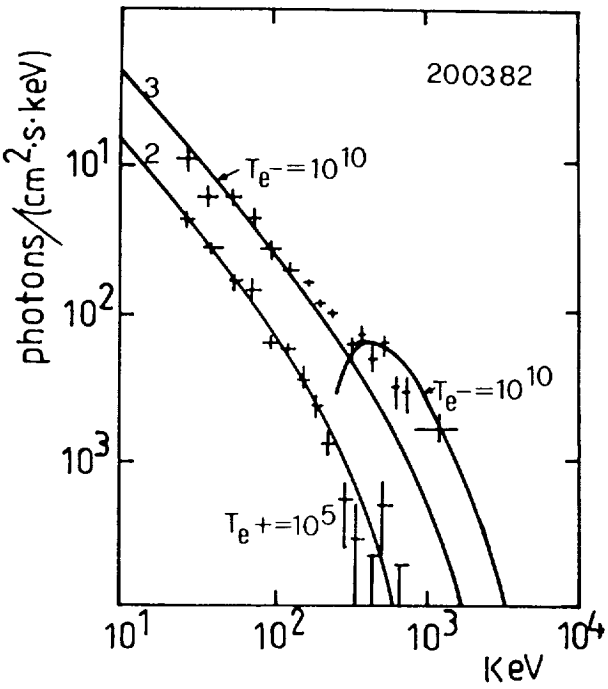

Fig. 7

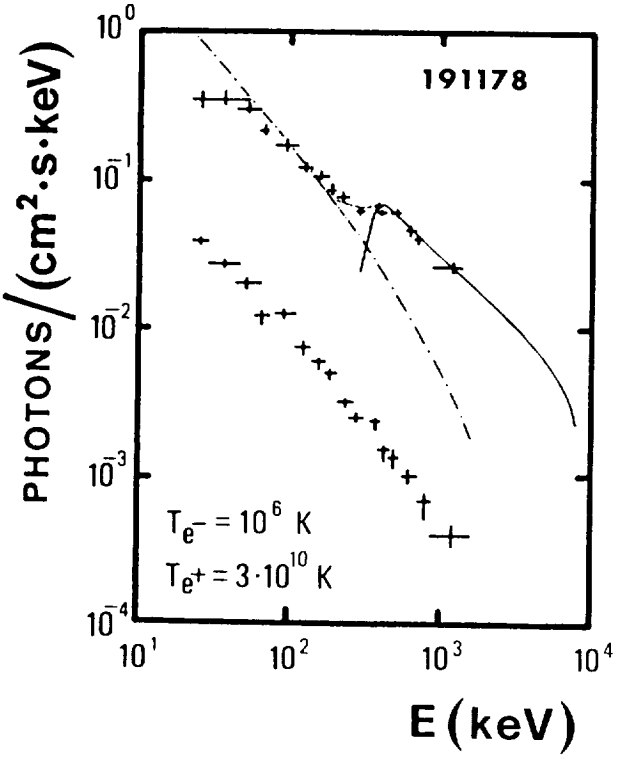

Fig. 8

Because of the threshold of the one-photon pair production process, the positron spectra has a peak at some energy. From this peak energy, we have evaluated the temperatures in units $T\ddagger=kT_+/mc^2$. The positron temperature is greater than (30-60) times the temperature of parental electrons. The generated pairs rapidly lose their transfer energy by synchrotron emission. Before annihilation they move along magnetic field lines at a large distance from a neutron star surface where the magnetic field is weaker and the plasma is cooler. Hot positrons annihilate with cold electrons. The photons can escape from the magnetosphere without appreciable attenuation.

4. The results. Figures 6, 7 and 8 show the spectra of two gamma-ray bursts described by our model. The temperatures of the hot and cold components are indicated on the graphs. The efficiency of bremsstrahlung emission is dependent on the concentration squared (n^2 hot component), but annihilation is proportional to the product of (n_e-n_e+). Thus from the best fit of experimental data, it is possible to evaluate the clumpiness parameter defined as:

$$f \equiv \frac{4 \cdot \langle n_e^+ \cdot n_e^- \rangle}{\langle n \rangle^2},$$

where $n = n_e^+ + n_e^-$.

In Table 1 we have collected parameters of 9 gamma-ray burst sources evaluated from the best fit of experimental data by our model.

Table 1.

	GRB	T_e^+	T_e^-	f
1	19.04.80	10^{10}-$3 \cdot 10^{10}$	$3 \cdot 10^9$	$6.3 \cdot 10^{-3}$
2	19.11.80	10^{10}-$3 \cdot 10^{10}$	$3 \cdot 10^9$	0.10
3	06.04.79	$<10^8$	10^{10}	0.41
4	31.12.81	$<10^8$	$3 \cdot 10^9$	0.02
5	25.03.78	$<10^8$	10^{10}	0.41
6	20.03.82	$<10^8$	10^{10}	0.37
7	13.01.79	$<10^8$	10^9	$1.3 \cdot 10^{-3}$
8	08.09.82	$<10^8$	$3 \cdot 10^9$-10^{10}	0.33
9	19.11.78	$3 \cdot 10^{10}$	$<10^8$	0.88

5. Conclusions. The detailed analysis shows that in short time scales, the unthermalized-pair-dominant plasma can exist. The annihilation time scale is shorter than the bremsstrahlung time scale, when temperatures of components are as follows:

$T_e^- < 10^8$K and $T_e^+ > 10^{10}$K or $T_e^+ < 10^8$K and $T_e^- > 10^{10}$K.

The spectra of gamma bursts with a hard tail are very well described by a thermal bremsstrahlung (continuum component) and the annihilation line of an unthermalized plasma. From a best fit of our spectra to experimental data, it is possible to evaluate the temperatures of electrons and positrons and the ratio of concentration (Table 1). The temperatures of electrons and positrons evaluated from the best fit satisfy the condition of unthermalized plasma.

The Gamma Ray Burst spectra from BATSE on the GRO can support or reject our model.

6. Acknowledgements. This work was sponsored by Polish Ministry of Education.

References

[1] Nolan, P.L. et al., 1983, AIP Conf. Proc. No 101 (ed. Burns et al.).
[2] Nolan, P.L. et al., 1984, AIP Conf. Proc. No 115 (ed. Woosley, S.E.), (AIP New York), 399.
[3] Mazets, E.P. and Golenetskii, S.V.:1988, Sov. Sci. Rev. E. Astrophys. Space Phys., vol. 6, 281.
[4] Teegarden, B.J.: 1984 in: High Energy Transients in Astrophysics, ed. Woosley, S.E., AIP Conf. Proc. No 115, 45.
[5] Harding, A.K.
[6] Kluźniak, W.: 1989, Astrophys. J., 336, 387.
[7] Karakuła, S., Tkaczyk, W.: 1985 in: Multifrequency Behaviour of Galactic Accreting Sources, ed. F. Giovannelli, 243.
[8] Svensson, R.: 1982, Astrophys. J., 258, 321.
[9] Ramaty, R. and Meszaros, P.: 1981, Astrophys. J., 250, 384.
[10] Svensson, R.: 1984, M. N. R. A. S., 209, 175.
[11] Zdziarski, A.A.: 1984, Astrophys. J., 283, 842.
[12] Harding, A.K.: 1984, Proc. of Varena Workshop on Plasma Astrophysics (ESA SP-207), 205.
[13] Colgate, S., Petschek, A.: 1983, AIP Conf. Proc. No 101 (ed. Burns et al.), 94-97 (AIP, New York).
[14] Woosley, S.E. and Wallance, R.K.: 1982, Astrophys. J., 258, 716.
[15] Tkaczyk, W., Karakuła, S.: 1987 in: Multifrequency Behaviour of Galactic Accreting Sources, ed. F. Giovannelli, 254.
[16] Burns, M.L., Harding, A.K.: 1984, Astrophys. J., 285, 747.
[17] Petrosian, V.: 1981, Astrophys. J., 251, 757.

Ultrasoft X-ray Bursts: A clue to the Origin of Gamma-ray Bursts?

D.J. Helfand, E. Gotthelf, and T.T. Hamilton

Columbia Astrophysics Laboratory, Columbia University
538 West 120th Street, New York, NY 10027

ABSTRACT

We have conducted a search for short timescale ($\lesssim 10$ s) faint X-ray bursts in the complete 201,000,000 photon *Einstein Observatory* imaging proportional counter (IPC) database. Excluding 'bad' observing time intervals, we extracted 73,000,000 events distributed among 11,230 observing intervals with an average observing time of $\sim$ 1400 seconds. To exclude all sources, particularly the bright sources so often found in the center of the field of view, we searched only those spatial pixels with a count rate less than 6×10^{-4} counts/sec arcmin^2. The mean count rate was substantially less. All files with less than 400 seconds of observing time were excluded. We then binned the data into overlapping cells 4.'3 by 4.'3 by 10 seconds in volume, and searched all the space-time cells in the database to locate cells with more than 5 counts in a 10 second interval; i.e., a minimum flux enhancement of 50 over the mean rate for that point in space. We found 52 such events. Formally, we would expect less than three events of such intensity as a result of Poisson noise. We then inspected an annulus around the event to see if it coincided with a general rise in the counter's event rate. Ten events did coincide with counter phenomena; these events were associated with sunrise, sunset, or the approach of the South Atlantic Anomaly and were of course excluded. We then examined the remaining 42 isolated events in detail in an attempt to associate them with instrumental or environmental artifacts. The event occurrence times are uniformly distributed over the course of the mission and show no correlation with local solar time; their positions are randomly distributed in geographic, Galactic, and celestial coordinates. Their summed radial distribution is consistent with the point-response function of the IPC for a soft source, indicating that the events are focused by the Observatory's mirror system. The integrated spectrum is, indeed, quite soft and is very similar to that of the cataclysmic variable star U Gem in outburst. Most of the events have risetimes of $\lesssim 1$ sec and decay times ranging from 1 – 20 sec. Their positions are not associated with any class of catalogued objects. We discuss several possible origins for the events; if we associate them with gamma-ray bursters, they provide interesting constraints on the space density and repetition rate of the underlying source population.

This work was supported under NASA grant NAG8-183.

5.
ACTIVE GALAXIES

GAMMA-RAY MONITORING OF A.G.N. AND GALACTIC BLACK HOLE CANDIDATES BY THE COMPTON GAMMA-RAY OBSERVATORY

R. T. Skelton, James C. Ling, Wm. A. Wheaton,
Jet Propulsion Laboratory, California Institute of Technology

Alan Harmon, G. J. Fishman, C. A. Meegan, William S. Paciesas[1],
Brad Rubin[2], R. B. Wilson,
Marshall Space Flight Center, NASA

Duane E. Gruber,
Center for Astrophysics and Space Science, UCSD

ABSTRACT

The Compton Gamma-Ray Observatory's Burst and Transient Source Experiment (BATSE) has a powerful capability to provide nearly uninterrupted monitoring in the 25 keV–10 MeV range of both A.G.N. and galactic black hole candidates such as Cygnus X-1, using the occultation of cosmic sources by the Earth. Since the Crab is detected by the BATSE Large Area Detectors with roughly 25σ significance in the 15–125 keV range in a single rise or set, a variation by a factor of two of a source having one-tenth the strength of Cygnus X-1 should be detectable within a day. Methods of modeling the background are discussed which will increase the accuracy, sensitivity, and reliability of the results beyond those obtainable from a linear background fit with a single rise or set discontinuity.

[1]University of Alabama at Huntsville
[2]USRA

The Burst and Transient Source Experiment (BATSE) aboard the Compton Gamma Ray Observatory (CGRO) offers a capability to provide almost uninterrupted monitoring of gamma-ray sources by Earth occultation. "Almost" means that one gets a measure of a source whenever it rises or sets in the 96-minute CGRO orbit. Those sources continuously above the horizon cannot be monitored, but the orbit precesses so that a source can spend only about two weeks continuously up before setting and again being subject to Earth occultation. BATSE consists of eight modules which are located octahedrally at the corners of the CGRO. Each module consists of a Large Area Detector (LAD), which is a NaI scintillator 50 cm in diameter and 1.25 cm thick, and a Spectroscopy Detector (SD), which is a 12.5 cm by 7.5 cm NaI scintillator. Data are accumulated in 2.048-second bins for each of 16 energy bands for the LADs; more sophisticated modes exist but have not been used to date in this investigation. BATSE is described in detail by Fishman *et al.* (1989).

The need for continuous monitoring of gamma-ray sources is illustrated by the fragmentary record of the premiere galactic candidate, Cygnus X-1, compiled by Ling *et al.* (1987a). It was noted to exhibit a two-week period of low flux below about 140 keV with a simultaneous high flux in the ≈ 1 MeV region in the form of a broad emission hump (Ling *et al.* 1983; Ling *et al.* 1987b). The hump can be interpreted as a Doppler-broadened and blue-shifted signature of electron-positron annihilation in an electron-positron plasma theoretically expected to result from photon-photon interactions near a luminous compact gamma-ray emitter (Liang 1979; Zdziarski 1980). Evidence, albeit at a $1.9\,\sigma$ level, has recently been noted (Ling and Wheaton 1989) of a narrow 511-keV line, present only during the time of the MeV hump, which could result from positrons being blown away by radiation pressure and annihilating in the primary star or its wind (Liang and Dermer 1988; Dermer and Liang 1988). For a positron-electron plasma, radiation pressure exceeds gravity by a factor of 20 in Cygnus X-1 (Kovner 1984). The Cygnus X-1 spectrum is similar to that observed for the galactic center (Lingenfelter and Ramaty 1983; Lingenfelter and Ramaty 1989; Riegler *et al.* 1981; Riegler *et al.* 1985). Variable MeV emission has been reported for NGC 4151, Cen A, and MCG 8-11-11 (Bazzano *et al.* 1989; Bassani and Dean 1983). Confirming the tentative results and establishing that the observed time variability and correlated spectral shifts constitute a pattern would allow better insight into the physics of compact objects.

The power of BATSE/Earth occultation is illustrated by Figure 1, which shows raw count rates for two orbits from the LAD most closely facing the Crab; the Crab becomes occulted at 1.9 hr and 3.4 hr and rises 0.5 hr later in each case, producing the prominent steps. A model consisting of a linear background (*vs* time) with a step discontinuity at the rise or set yields a statistical significance (combining all energy channels and LADs) of around $25\,\sigma$ for a single rise or set of the Crab with a fit window of ± 262 sec. BATSE Mission Operations uses this simple model (which was quite effective at detecting the flaring of GX339−4 in June-July 1991, reported by Fishman *et al.* 1991) with a suitably selected time window to monitor the gamma-ray sky. The purpose of this paper is to report progress for an improved analysis which will allow monitoring to greater precision. Cutting measurement errors by, say, a factor of two would be of some value for a strong source like the Crab, but the greater motivation is to improve accuracy and sensitivity for weaker sources.

The linear-plus-step model is limited by the time window in which the background flux can be treated as linear. We have considered improvements along the lines of more polynomial terms, but the risk of introducing systematic errors outweighs the additional formal precision. A further fundamental problem is that polynomials are complete, and that the signal, a step function, can be represented by a sum of polynomials. Any complete mathematical model (Fourier series, etc.) shares the same shortcoming. Our approach will therefore be to model the sources of background with parameters that have a physical basis. In this manner we expect to increase the fit window substantially without introducing comparable systematic errors.

To illustrate the elements that must go into this model, we consider the general characteristics of the raw data. Figure 2 shows the first 12 hours of 17 April 1991 in the 1100–1800 keV band for each of the eight LADs. The count rates oscillate twice per orbit, and all LADs oscillate in phase. The dominant source of counts is cosmic-ray secondaries; the oscillations result from variations in the geomagnetic latitude. Variations from one LAD to another result primarily from Earth angles; at this relatively high energy, the Earth is bright from cosmic-ray secondaries compared to the diffuse cosmic background. Figure 3 shows the same time frame in the 24–32 keV band. The count rates oscillate once per orbit, with a narrow minimum compared to the broad maximum; oscillation amplitudes and phases differ. The dominant cause of variation is Earth blockage of the diffuse cosmic background. The narrow minimum corresponds to detector nadir. Two LADs whose numbers sum to seven face in opposite directions, and it is clear that count rates are 180° out of phase for such pairs.

Not shown are data from orbits wherein the CGRO passes through the South Atlantic Anomaly (SAA); the high voltage is switched off during actual passage, and activation decays are an obvious additional feature once HV is turned back on.

In light of this discussion, the dominant background contributors which must be modeled are diffuse cosmic gamma rays, cosmic-ray secondaries produced at the CGRO, cosmic-ray secondaries produced in the atmosphere, and activation. An enhanced model also needs to take account of the source confusion problem; combining set and rise data from the source into a single fit should alleviate this problem, because sources which are widely separated on the sky but which happen, for example, to set together will usually rise well separated.

Diffuse cosmic gamma rays refers to the aggregate output of sources too weak to catalogue individually, as well as truly diffuse sources. Since this contribution is approximately isotropic (with a nonisotropic galactic component), the primary modeling involved will be to define its spectral parameters and to account for blockage of it by the Earth.

Background due to prompt effects of cosmic rays is expected to be proportional to the SD upper level discriminators, based on experience with HEAO-3 (Mahoney *et al.* 1984). Work is in progress to extend the simple HEAO-3 model to make use of the 8 BATSE Spectroscopy Detector ULD rates to characterize the cosmic-ray environment and also the spectral dependence of the response.

In principle, background due to cosmic-ray secondaries produced from interactions with the Earth atmosphere presents the most formidable challenge. To be very precise, one must model the atmospheric response as a function of energies, each depending on the zenith angle and on the angle from the detector normal; the total LAD response would then obtained by integrating over the Earth disk. Again, experience with HEAO-3 leads us to believe that this extremely computationally intensive approach can be circumvented by suitably parametrizing the problem.

Activation occurs throughout the orbit, but is most significant during SAA passages. In principle, one simply integrates the activation rate *vs* time, weighting with the appropriate exponential for each radioactive species, and sums such exponential terms. In practice, there is difficulty in determining activation rates, which will differ among detectors, and the sum-of-exponentials problem has a notorious tendency to be ill-conditioned. Experience with HEAO-1 (Gruber *et al.* 1989) has shown how these problems can be overcome.

There exists a considerable body of experience in dealing with these matters, both by the authors and by others in the community, on spacecraft such as HEAO-1, HEAO-3, and the Solar Maximum Mission Gamma Ray Spectrometer. We believe that the challenges of increasing the fit window to improve the data analysis can be met and that considerable scientific value will result from the unprecedented continuous monitoring capability afforded by the CGRO and BATSE.

REFERENCES

Bassini, L. and Dean, A. J. 1983, **Space Sci. Rev.**, **35**, 367.

Bazzano, A. *et al.* 1989, in **Proceedings of the GRO Science Workshop**, ed. W. N. Johnson, p. 4-22.

Dermer, C. D. and Liang, E. P. 1988, in **Nuclear Spectroscopy of Astrophysical Sources**, AIP Conference **Proceedings #170, ed. N. Gehrels and G. H. Share, (New York: AIP), p. 326.**

Fishman, G. J. *et al.* 1989, in **Proceedings of the GRO Science Workshop**, ed. W. N. Johnson, p. 2-39.

Fishman, G., Wilson, R., Meegan, C., Harmon, A., and Brock, M. 1991 Aug 19, IAUC Telegram #5327, "GX339−4."

Gruber, D. E., Jung, G. V., and Matteson, J. L. 1989, in **High Energy Background in Space**, AIP Conf. Proceedings #186, ed. A. C. Rester and J. I. Trombka (New York: AIP) p. 232.

Kovner, I. 1984, **Astr. Ap.**, **141**, 341.

Liang, E. P. 1979, **Ap. J.**, **234**, 1105.

Liang, E. P. and Dermer, C. D. 1988, **Ap. J. (Lett.)**, **325**, L39.

Ling, J. C., Mahoney, W. A., Wheaton, W. A., Jacobson, A. S., and Kaluzienski, L. 1983, **Ap. J.**, **275**, 307.

Ling, J. C. *et al.* 1987a, in **Proceedings of the 20th International Cosmic Ray Conference**, Moscow, paper OG 2.1-2, 1, 54.

Ling, J. C., Mahoney, W. A., Wheaton, W. A., and Jacobson, A. S. 1987b, **Ap. J. (Lett.)**, **321**, L117.

Ling, J. C. and Wheaton, W. A. 1989, **Ap. J. (Lett.)**, **343**, L57.

Lingenfelter, R. E. and Ramaty, R. 1983, in **Positron-Electron Pairs in Astrophysics**, AIP Conference Proceedings #101, ed. M. Burns, A. Harding, and R. Ramaty (New York: AIP), p. 267.

Lingenfelter, R. E. and Ramaty, R. 1989, in **Proceedings of the GRO Science Workshop**, ed. W. N. Johnson, p. 4-245.

Mahoney, W. A., Ling, J. C., Wheaton, W. A., and Jacobson, A. S. 1984, **Ap. J.**, **286**, 578.

Riegler, G. R., Ling, J. C., Mahoney, W. A., Wheaton, W. A., Willett, W. A., Jacobson, A. S., and Prince, T. A. 1981, **Ap. J. (Lett.)**, **248**, L13.

Riegler, G. R., Ling, J. C., Mahoney, W. A., Wheaton, W. A., and Jacobson, A. S. 1985, **Ap. J. (Lett.)**, **294**, L13.

Zdziarski, A. A. 1980, **Acta Astr.**, **30**, 371.

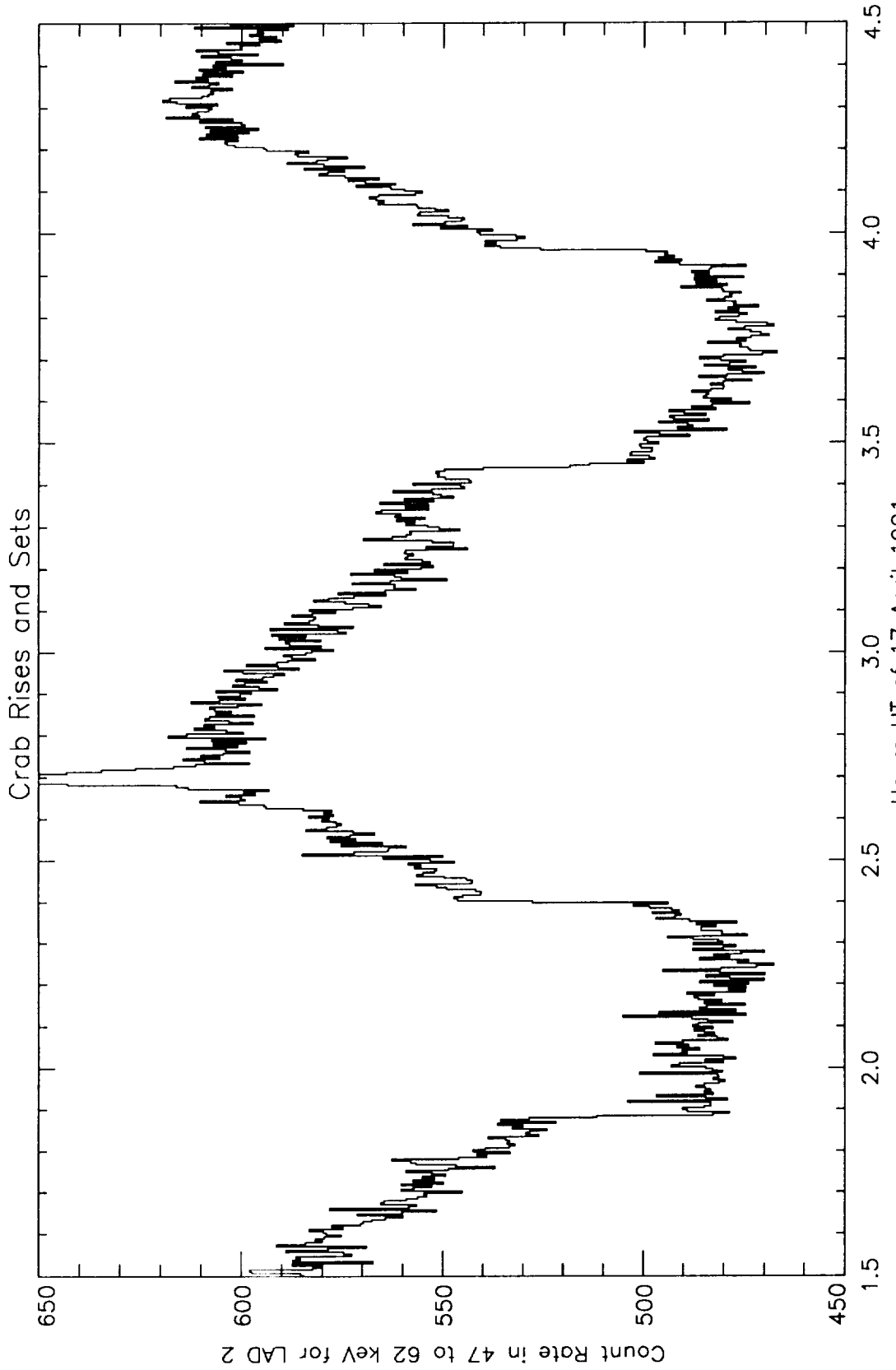

Figure 1. Raw data at 16.384-second time resolution showing step discontinuities at Crab sets (1.9 hr and 3.4 hr) and rises (2.4 hr and 3.9 hr)

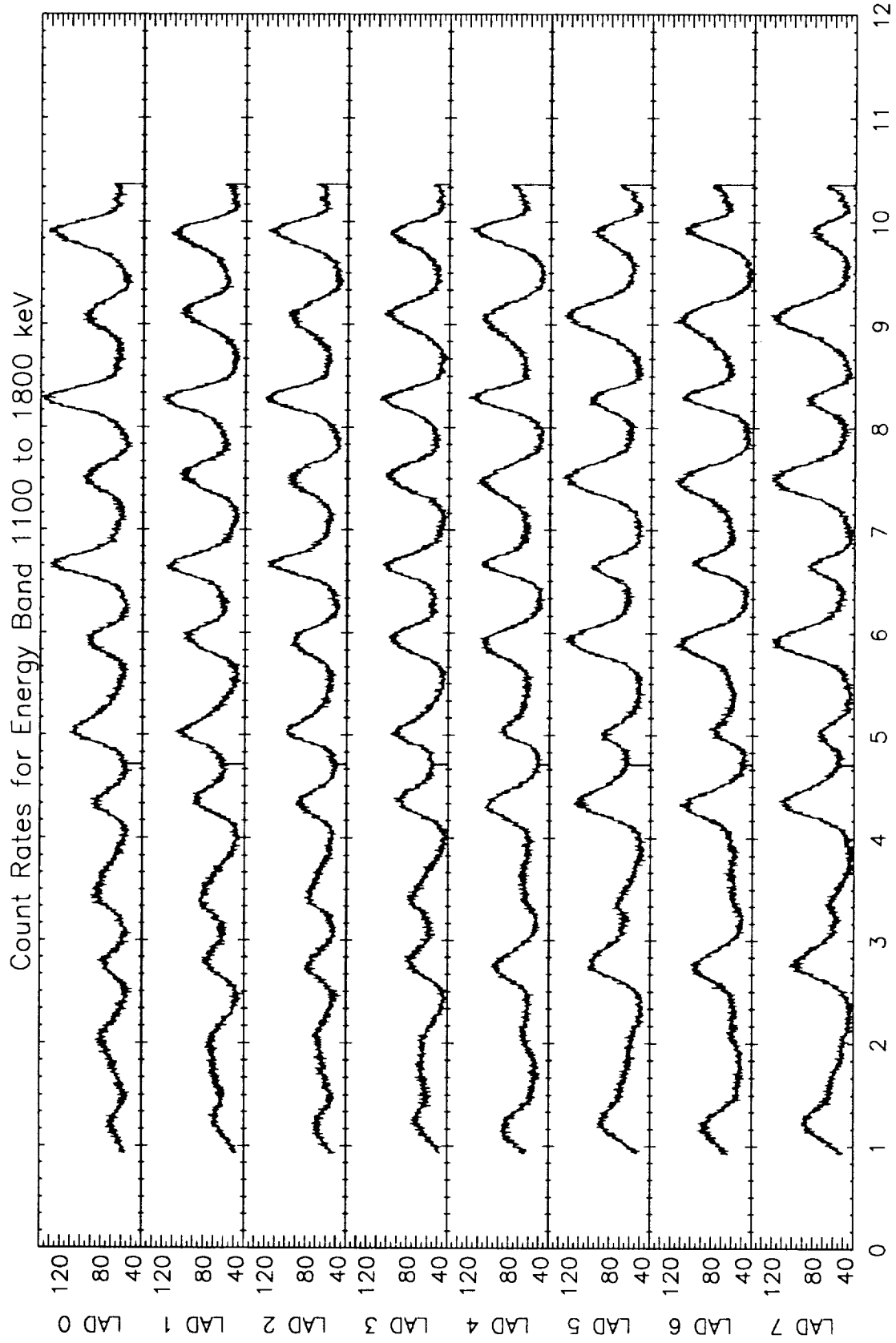

Figure 2. Sample high-energy raw data from the 8 BATSE Large Area Detectors (LADs)

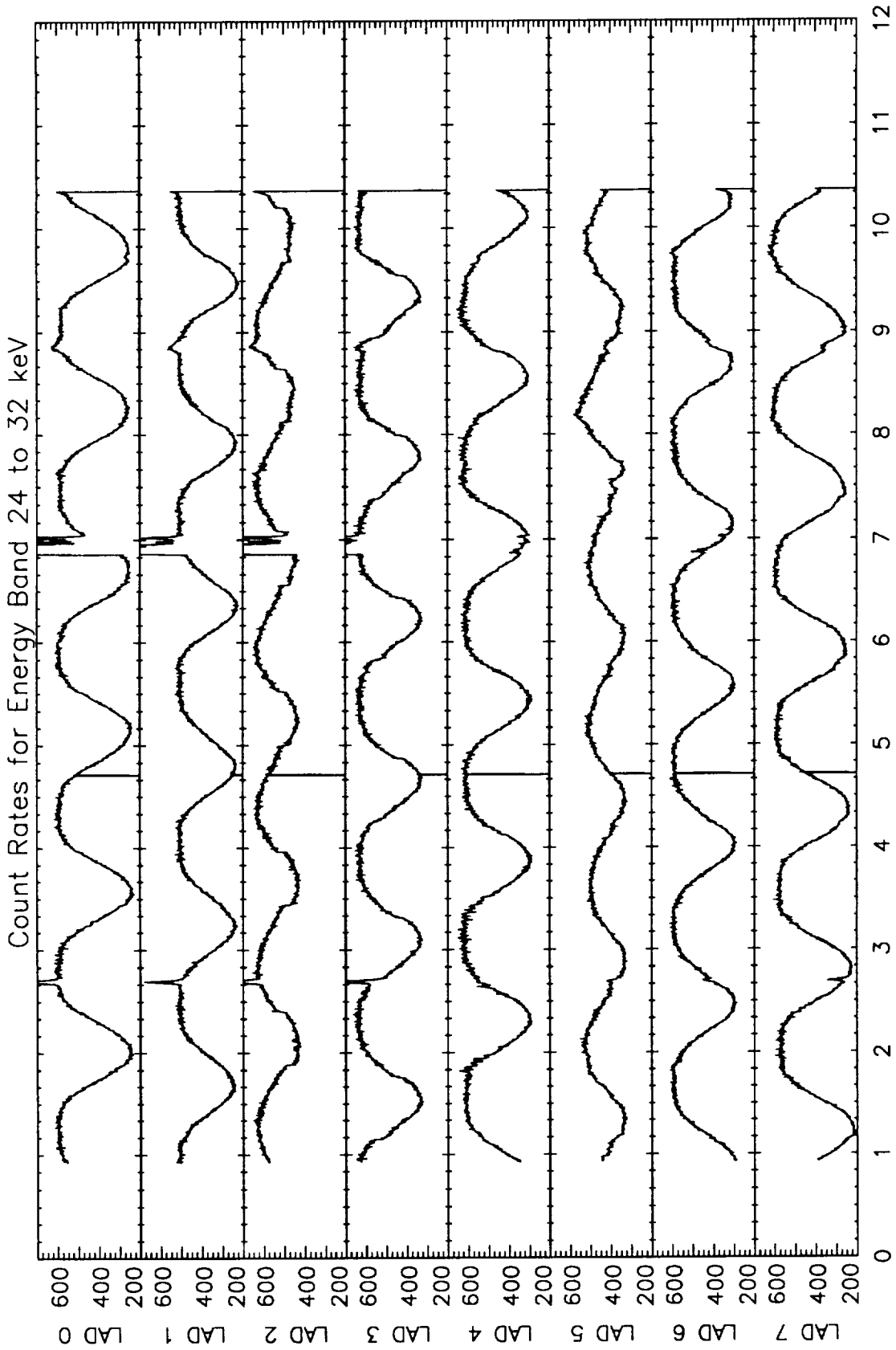

Figure 3. Sample low-energy raw data from the 8 BATSE Large Area Detectors (LADs)

GAMMA RAYS FROM EXTRAGALACTIC RADIO SOURCES

Charles D. Dermer
Department of Space Physics and Astronomy, Rice University, Houston, TX 77251, USA

Reinhard Schlickeiser
Max-Planck-Institut für Radioastronomie, Auf dem Hügel 69, D-5300 Bonn 1, Germany

Apostolos Mastichiadis
Max-Planck-Institut für Kernphysik, Postfach 10 39 80, Heidelberg, Germany

ABSTRACT

We propose that the important connection between 3C 273 and 3C 279, the first two extragalactic sources detected at > 100 MeV energies, is their superluminal nature. In support of this conjecture, we propose a radiation mechanism that focuses gamma rays in the superluminal direction, due to Compton scattering of accretion-disk photons by relativistic nonthermal electrons in the jet.

INTRODUCTION

A black-hole accretion disk with a collimated perpendicular jet currently represents the baseline model for explaining the origin of the luminous, broadband radiation emitted from the central engines of active galactic nuclei (AGN). In the unified scenario[1,2], line-of-sight determines family character: thus, Seyfert 2 galaxies are accretion disks seen through obscuring equatorial clouds; Sy 1s are the disks seen directly; and superluminal (SL) radio sources are seen when looking at small angles to the jet (polar) axis. > 100 MeV γ rays have now been detected from two extragalactic radio sources– 3C 273[3] and 3C 279[4]– both of which display strong SL behavior. We show that strong enhancements of gamma-ray emission near the SL direction occur when relativistic electrons in the outflowing radio-emitting blobs Comptonize UV and X-ray photons emitted by the accretion disk. An important consequence of this model is that BL Lac Objects should be rather feeble sources of high-energy radiation, because here we are looking nearly straight down the jet axis. Correlated radio and γ-ray observations will provide a strong test of this model and the AGN unification scenario.

MODEL

Radio observations of AGN are reviewed in Refs. 5 and 6, and theory in Ref. 7. In the relativistic jet model of Blandford & Rees[8], blobs of magnetized plasma with bulk velocity $\beta_\Gamma c$ and Lorentz factor $\Gamma = (1 - \beta_\Gamma^2)^{-1/2}$ erupt from the central nucleus at nearly right angles to the plane of the accretion disk. Relativistic electrons with a quasi-isotropic distribution *in the rest frame of the blob* (*BF*) produce incoherent synchrotron radiation which, because of the blob's motion, is focused into a cone with half-angle $\approx \Gamma^{-1}$ about the jet axis *in the observer's frame* (*OF*). The maximum apparent transverse velocity $\beta_{app}^{max} c = \beta_\Gamma \Gamma c$ is observed when the angle θ_s^* between the blob's velocity vector and the direction to the observer is given by $\theta_s^* \equiv \cos^{-1} \mu_s^* = \cos^{-1} \beta_\Gamma$ (see Fig. 1). The possible existence of sources showing apparent transverse velocities exceeding c was predicted by Rees[9]. The first-discovered and brightest known SLs, 3C 279 and 3C 273, respectively, each have exhibited SL components with $\beta_{app} > 8$ (Ref. 10).

In the standard model for jets from AGN, sketched in Figure 1, a plasma blob moves outward from the central nucleus with speed $\beta_\Gamma c$. We depart from this model[11] only by assuming that the relativistic radio-emitting electrons are homogeneously distributed throughout the blob, and that the randomly-oriented magnetic field has uniform strength everywhere in the blob. This simplification does not affect the central result, and can be relaxed in more detailed treatments. We also assume that (1) the energetic electrons have an isotropic energy distribution in the BF; (2) the accretion-disk source emits photons isotropically with spectrum $\dot{N}_{ph}(\epsilon^*)$ [photons s^{-1} ϵ^{*-1}] in the OF, where $\epsilon^* \equiv h\nu^*/m_e c^2$ is the dimensionless photon energy (asterisks refer to quantities measured in the OF); and (3) photons passing through the blob follow trajectories parallel to the jet axis. This last is true if the blob is sufficiently far from the central source. We also require that the blob be optically thin to Thomson scattering along the jet axis, which is necessary to produce highly polarized radio emission[8].

Neglecting redshift corrections, the flux from the central source seen by the observer is given by

$$\Phi(\epsilon^*) \cong \frac{\dot{N}_{ph}(\epsilon^*)}{4\pi d^2}, \tag{1}$$

where d is the distance between the observer and the AGN. In the BF, photons have energy $\epsilon = \Gamma(1 - \beta_\Gamma)\epsilon^* < \epsilon^*$, due to the Doppler effect. From the invariance[12] of $n_{ph}(\epsilon, \Omega)/\epsilon^2$, we find that the differential photon density in the BF is given by

$$n_{ph}(\epsilon, \Omega) = \frac{d^2}{2\pi r^2 c} \Phi[(1 + \beta_\Gamma)\Gamma\epsilon] \, \delta(\mu - 1), \tag{2}$$

where r is the distance of the blob from the central source and μ is the direction cosine

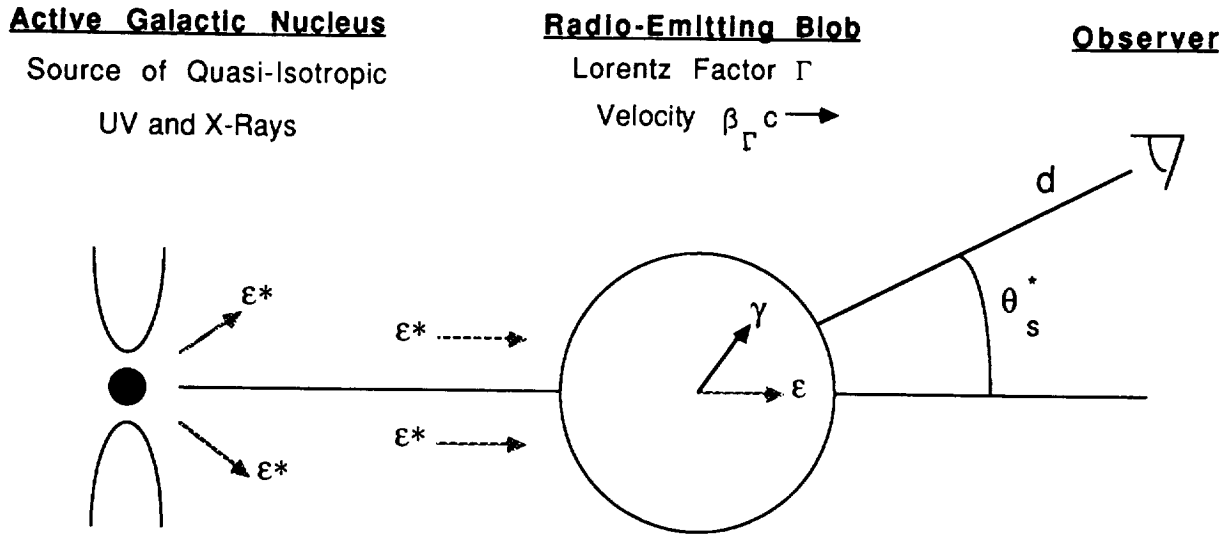

Fig. 1–Cartoon illustrating the proposed model for high-energy radiation from extragalactic radio sources. A plasma blob moving with speed $\beta_\Gamma c$ focuses its radio emission into a forward cone in the observer's frame. Relativistic electrons in the blob also scatter radiation from the central source. The most energetic of these *jai alai* photons (see final paragraph) are scattered preferentially in the direction $\cos\theta_s^* = 2 - \beta_\Gamma^{-1} \approx \beta_\Gamma$.

of the photons in the BF. We describe the electron distribution in the BF by the function $n_e(\gamma, \Omega)$ [electrons cm^{-3} γ^{-1} sr^{-1}], where γ is the electron Lorentz factor. For the isotropic case, $n_e(\gamma, \Omega) = n_e(\gamma)/4\pi$. The angle-dependent scattered photon spectrum in the BF is given by[13,14]

$$\dot{n}_{ph}(\epsilon_s, \Omega_s) = c \int_0^\infty d\epsilon \oint d\Omega \int_1^\infty d\gamma \oint d\Omega_e \, (1 - \beta \cos\psi) \, n_{ph}(\epsilon, \Omega) \, n_e(\gamma, \Omega_e) \, \frac{d^2\sigma}{d\epsilon_s d\Omega_s}, \quad (3)$$

where the subscript s refers to scattered quantities, $\cos\psi \rightarrow \mu_e$ when $\mu = 1$, and $d^2\sigma/d\epsilon_s d\Omega_s$ is the differential scattering cross section.

The electrons that produce the nonthermal radio emission are highly relativistic, so that $\gamma \gg 1$. If the accretion-disk photons are in the UV to X-ray range, $\epsilon^* \sim 10^{-4} - 10^{-1}$, and thus $\epsilon \ll 1$. We treat the Thomson limit of Compton scattering, where $\gamma\epsilon(1 - \beta\mu_e) \ll 1$. The average energy ϵ_s of scattered photons in the BF is $\approx \gamma^2\epsilon(1 - \beta\mu_e)$, and these photons are beamed into a cone with half-angle angle $\theta_s \approx \gamma^{-1} \ll 1$ about the original direction of the electron's motion. We therefore approximate the differential Compton cross section by

$$\frac{d^2\sigma}{d\epsilon_s d\Omega_s} \cong \frac{\sigma_T}{2\pi} \, \delta[\epsilon_s - \gamma^2\epsilon(1 - \beta\mu_e)] \, \delta(\mu_s - \mu_e). \quad (4)$$

Substituting equations (4) and (2) into equation (3), and transforming back to the OF using the invariance[12] of $\dot{n}_{ph}(\epsilon_s, \mu_s)/\epsilon_s$, we find that

$$\dot{n}_{ph}(\epsilon_s^*, \mu_s^*) = \frac{\sigma_T \, d^2}{2\Gamma(1-\beta_\Gamma \mu_s^*) \, r^2} \int_1^\infty d\gamma \, \gamma^{-2} \, n_e(\gamma) \, \Phi\{\frac{(1+\beta_\Gamma)\Gamma^2 \epsilon_s^*(1-\beta_\Gamma \mu_s^*)^2}{\gamma^2[1+\beta\beta_\Gamma - \mu_s^*(\beta+\beta_\Gamma)]}\}, \quad (5)$$

giving the photon emissivity per unit emission time. To determine the observed flux Φ_s^{rec} per unit reception time[15], note that the two time intervals are related through $t_{rec} = t_{em}(1-\beta_\Gamma \mu_s^*)$. For a blob with volume $V_b^* = V_b/\Gamma$, $\Phi_s^{rec}(\epsilon_s^*, \mu_s^*) = V_b \dot{n}_{ph}(\epsilon_s^*, \mu_s^*)/2\pi d^2 \Gamma(1-\beta_\Gamma \mu_s^*)$. Thus the scattered photon flux, in terms of the flux observed directly from the central source, is given by

$$\Phi_s^{rec}(\epsilon_s^*, \mu_s^*) = \frac{V_b \, \sigma_T}{4\pi r^2 \, \Gamma^2(1-\beta_\Gamma \mu_s^*)^2} \int_1^\infty d\gamma \, \gamma^{-2} \, n_e(\gamma) \, \Phi\{\frac{(1+\beta_\Gamma)\Gamma^2 \epsilon_s^*(1-\beta_\Gamma \mu_s^*)^2}{\gamma^2[1+\beta\beta_\Gamma - \mu_s^*(\beta+\beta_\Gamma)]}\}. \quad (6)$$

We now consider the δ-function properties of equation (6). Let $n_e(\gamma) = n_e^o \delta(\gamma - \bar{\gamma})$ and $\Phi(\epsilon^*) = \Phi_o \delta(\epsilon^* - \bar{\epsilon}^*)$. The energy of a scattered photon emitted into a given direction is related to the original photon energy $\bar{\epsilon}^*$ through the expression

$$\frac{\epsilon_s^*}{\bar{\epsilon}^*} = \frac{\gamma^2[1+\beta\beta_\Gamma - \mu_s^*(\beta+\beta_\Gamma)]}{(1+\beta_\Gamma)\Gamma^2(1-\beta_\Gamma \mu_s^*)^2}. \quad (7)$$

Equation (7) can also be obtained by making a series of transformations of a photon's energy and angle from the OF to the BF and then to the electron rest frame, and then retracing the steps after scattering. Figure 2 shows values of the ratio (7) for a blob moving with $\Gamma = 5$, and for isotropically-distributed electrons with $\gamma = 100$ in the BF. As can be seen, the scattered photon energy is increased relative to the original photon energy at all angles except in the extreme forward direction, where $\mu_s^* \cong 1$ and $\epsilon_s^*/\bar{\epsilon}^* \cong 1/2$. The weak forward scattering is a consequence of the factor $(1-\beta\mu_e)$, which reduces both the scattering rate (eq. 3) and the photon energy (eq. 4) in the electron's rest frame. The energy increase is greatest at shallow angles with respect to the forward direction. The angle $\mu_{s,max}^*$ of the peak scattered energy is determined by letting $\partial(\epsilon_s^*/\bar{\epsilon}^*)/\partial\mu_s^* = 0$, giving

$$\mu_{s,max}^* = \frac{\beta_\Gamma + 2\beta\beta_\Gamma^2 - \beta}{\beta_\Gamma(\beta+\beta_\Gamma)}. \quad (8)$$

If $\gamma \gg \Gamma$, then $\beta \approx 1$ and $\mu_{s,max}^* \to 2 - \beta_\Gamma^{-1}$. If the blob is also moving at relativistic speeds such that $\Gamma \gg 1$, which indeed is required for SL effects, then $\beta_\Gamma \approx 1 - (2\Gamma^2)^{-1}$, and $\mu_{s,max}^* \approx \beta_\Gamma$. *This is equal to the observer's direction at which the apparent SL velocity is greatest.* The maximum value of the scattered photon energy is given, from equations (7)

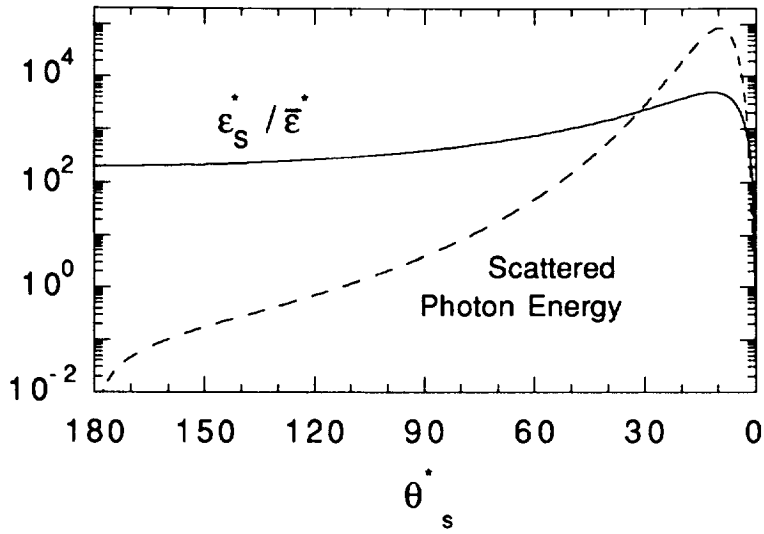

Fig. 2–Angle-dependences of the ratio of the photon energy before and after scattering as measured by an observer (solid curve), and of the relative amount of energy in scattered photons per unit reception time (dashed curve). In this calculation, the blob's Lorentz factor $\Gamma = 5$ and the electrons' Lorentz factor $\gamma = 100$. The most energetic photons are scattered in the direction $\theta^*_s \cong \cos^{-1}(2 - \beta_\Gamma^{-1}) \approx 11.7^o$, and the largest fraction of photon energy is scattered in the direction $\theta^*_s \cong \cos^{-1}[(3\beta_\Gamma - 1)/2\beta_\Gamma] \approx 8.2^o$. The maximum apparent superluminal velocity is observed at the angle $\cos^{-1}\beta_\Gamma \approx 11.6^o$. If $\Gamma = 10$, the most energetic photons are scattered at the superluminal angle 5.7^o, with the bulk of the energy scattered in the direction $\theta^*_s \approx 4.1^o$.

and (8), by $(\epsilon^*_s/\bar{\epsilon}^*)_{max} = \gamma^2(\beta + \beta_\Gamma)^2/4\beta\beta_\Gamma(1 + \beta_\Gamma) \rightarrow \gamma^2/2$, where the limiting expression holds when $\gamma \gg \Gamma \gg 1$.

We can also determine the directional dependence of the total energy in scattered photons by evaluating the quantity $\int_0^\infty d\epsilon^*_s \epsilon^*_s \Phi^{rec}_s(\epsilon^*_s, \mu^*_s)$. The principal angular dependence of this quantity is $\propto [1 + \beta\beta_\Gamma - \mu^*_s(\beta + \beta_\Gamma)]^2/(1 - \beta_\Gamma\mu^*_s)^6$, and is also plotted in Fig. 2. In the limit $\gamma \gg \Gamma$, the greatest amount of energy in scattered photons per interval of μ^*_s is produced in the direction $\mu^*_s \cong (3\beta_\Gamma - 1)/2\beta_\Gamma$. This is close to the direction into which the highest energy photons are scattered.

Recall that the maximum SL velocity occurs when $\mu^*_s = \beta_\Gamma$. Our results show that SL radio sources should scatter the most energetic photons in this direction, with the largest fraction of scattered photon energy scattered at a slightly shallower angle. However, the amount and energy of photon emission scattered directly forward is weak. Thus SL radio sources should be strong γ-ray emitters, but if observations are made directly down the symmetry axis of the jet, we should see very little X-ray and γ-ray emission. According to

the unified AGN scenario, BL Lac objects are sources where we happen to be looking very nearly directly down the jet axis. Thus we conclude that SL radio sources should be strong γ-ray sources, and BL Lac objects should be weak γ-ray sources.

Attempts to observe γ-ray emission from BL Lac objects have so far been unsuccessful[16], and the X-ray emission that has been observed is soft, with energy spectral index $\approx$1.6 in the 1-3 keV range[17]. The X-rays are probably the result of Comptonization of the synchrotron radiation emitted in the outflowing blob[18]. According to our model, the intensity of gamma-ray emission should be positively correlated with the appearance and apparent transverse velocity of SL components. By contrast, BL Lac objects that display no SL character should not be γ-ray sources. We strongly encourage correlated VLBI radio observations and GRO EGRET observations to test these predictions. Superluminal sources such as 3C 120 or 3C 345[5,10] are obvious candidate sources of extragalactic gamma radiation. Comparatively weak X-ray and γ-ray emission is expected from subluminal BL Lac objects such as 1803+78[19,5].

SUMMARY

We have proposed a model in which the relativistic electrons in an outflowing blob Comptonize photons from a central source. This process has much in common with the game jai alai, where the combined motions of the player and his basket shoot the ball forward with a much greater energy than would be possible were either the player stationary or his basket immobile. This model avoids γ-γ pair attenuation of $>$ 100 MeV photons[20] from a compact highly variable source such as 3C 273 by upscattering UV and X-ray photons far from the compact nucleus. Correlated multiwavelength variability could be associated with either the central photon source or the outflowing blob: each implies different relationships. The speed of the blobs may be explained by a Compton-rocket effect[21] produced by the Compton-scattering impulse. Such an interpretation avoids the difficulties in Rees' suggestion[22] that Compton drag of a parallel ultrarelativistic jet by disk photons regulates the jet's speed (for example, such jets should be highly unstable[23]). As discussed earlier, our model is in accord with the AGN unification scenario, and it could be argued that evidence in favour of it strengthens the unifying scheme. Spectral implications, which imply additional predictions that can be used to test this model, will be reported elsewhere.

Acknowledgements. C. D. acknowledges the kind hospitality of the Max Planck Institutes in Bonn and Heidelberg, discussions with Steven J. Sturner, and the support of the Gamma-Ray Observatory Guest Investigator Program through NASA grant NAG5-1547.

REFERENCES

1. Scheuer, P. A. G. & Readhead, A. C. S. *Nature* **277**, 182-185 (1979).
2. Barthel, P. D. *Astrophys. J.* **336**, 606-611 (1989).
3. Swanenburg, B. N. *et al. Nature* **275**, 298 (1978).
4. GRO-EGRET Team, Bertsch, D. L. *et al.*, IAU Circular 5311, 22 July 1991.
5. Zensus, J. A., in *BL Lac Objects* (eds. Maraschi, L., Maccacaro, T., & Ulrich, M.-H.) 3-12 (Springer, Berlin, 1989).
6. Bregman, J. N. *Astron. Astrophys. Rev.* **2**, 125-165 (1990).
7. Begelman, M. C., Blandford, R. D., & Rees, M. J. *Rev. Mod. Phys.* **56**, 255-351 (1984).
8. Blandford, R. D. & Rees, M. J., in *Pittsburgh Conference on BL Lac Objects* (ed. A. M. Wolfe), 328-347 (Pittsburgh, Pittsburgh Univ. Press, 1978).
9. Rees, M. J. *Nature* **211**, 468-470 (1966).
10. Porcas, R. W., in *Superluminal Radio Sources* (eds. Zensus, J. A. & Pearson, T. J.) 12-25 (Cambridge, Cambridge Univ. Press, 1987).
11. Marscher, A. P. *Astrophys. J.* **235**, 386-391 (1980).
12. Rybicki, G. B. & Lightman, A. P. *Radiative Processes in Astrophysics* (New York, Wiley, 1979).
13. Reynolds, S. P. *Astrophys. J.* **256**, 38-53 (1982).
14. Dermer, C. D. *Astrophys. J.* **360**, 197-214 (1990).
15. Zdziarski, A. A., Svensson, R. & Paczyński, B. *Astrophys. J.* **366**, 343-352 (1991).
16. Bignami, G. F., Fichtel, C. E., Hartman, R. C. & Thompson, D. J. *Astrophys. J.* **232**, 649-658 (1979).
17. Madejski, G. M. & Schwarz, D. A., in *BL Lac Objects* (eds. Maraschi, L., Maccacaro, T., & Ulrich, M.-H.) 267-280 (Springer, Berlin, 1989).
18. Königl, A. *Astrophys. J.* **243**, 700-709 (1981).
19. Witzel, A., Schalinski, C. J., Johnston, K. J., Biermann, P. L., Krichbaum, T. P., Hummel, C. A. & Eckart, A. *Astron. Astrophys.* **206**, 245-252 (1988).
20. Bassani, L. & Dean, A. J. *Nature* **294**, 332-333 (1981).
21. Cheng, A. Y. S. & O'Dell, S. L. *Astrophys. J.* **251**, L49-L54 (1981).
22. Abramowicz, M. A., Ellis, G. F. R. & Lanza, A., in *BL Lac Objects* (eds. Maraschi, L., Maccacaro, T., & Ulrich, M.-H.) 358-371 (Springer, Berlin, 1989).
23. Achatz, U., Lesch, H. & Schlickeiser, R. *Astron. Astrophys.* **233**, 391-409 (1990).

Universal Energy Spectrum from Point Sources

YUKIO TOMOZAWA

RANDALL LABORATORY OF PHYSICS
UNIVERSITY OF MICHIGAN
ANN ARBOR, MI 48109-1120

ABSTRACT

The suggestion is made that the energy spectrum from point sources such as galactic black hole candidates (GBHC) and active galactic nuclei (AGN) is universal on the average, irrespective of the species of the emitted particles, photons, nucleons or others. The similarity between the observed energy spectra of cosmic rays, γ-rays and X-rays is discussed. In other words, the existing data for gamma-rays and X-rays seem to support the prediction. The expected data from GRO (Gamma Ray Observatory) will provide a further test.

The fundamental hypothesis for cosmic ray acceleration has been the Fermi mechanism by magnetic fields and its variations including shock wave acceleration in supernovae.[1-3] Although the latter constitutes the most frequently discussed source, it has been pointed out that supernova acceleration fails[4] to accelerate protons beyond 10^{13} eV. Then, one has to propose some other mechanism[5] to produce the high energy component of cosmic rays beyond the knee energy (10^{15-16} eV). The difficulty of having two independent mechanisms for cosmic rays below and above the knee energy is that one has to rely on an accidental coincidence that the respective mechanisms fall down at the same energy (the knee energy) and attain equal intensity at the knee energy. This is too much to ask for in explaining the observed data. [This would not be a problem if the slope index, λ of the energy spectrum $\sim E^{-\lambda}$, were smaller on the high energy side than on the low energy side. The observed spectrum is, in fact, just the opposite; $\lambda = \sim 2.6$ and 3 below and above the knee energy.] In other words, a unified mechanism for the entire energy region is required for cosmic ray acceleration. Jokipii and Morfill proposed that shock wave acceleration in supernovae continues by the galactic wind.[6] So far the evidence for the existence of galactic wind which would enable the necessary accelerations of charged particles up to $\sim 10^{20}$ eV with the required intensity is yet to be found.

As a consequence, one may ask whether there exist some other sources or mechanisms for cosmic ray acceleration. Possible candidates are obviously quasars and active galactic nuclei (AGN). The observed luminosity ($\lesssim 10^{46}$ erg/sec) is galactic ($\lesssim 10^{13}\, L_\odot$) and relatively short variability ($\lesssim 10^5$ sec) indicates that massive black holes might be the source of energy. The observation of jets from some of the AGN also enforces such an assumption. Although the mechanism of the energy output from AGN are not known (the central engine problem), it appears that gravitational forces are the main cause of energy outflow. This paradoxical characteristic of black holes requires an unusual scenario for energy outflow from black holes. It may be due to the Penrose mechanism for the Kerr metric or something else. [The present author proposed a mechanism.[8]] Whatever the details of the acceleration mechanism, one may discuss the outcome of the assumption,

"Cosmic rays are accelerated by gravitational forces".

One possible outcome of the assumption is that the gravitational acceleration does not discriminate particles by charge. Therefore, such acceleration produces essentially the same result for any particles, charged or not.

This argument motivates us to suggest the following:
"All particles emitted by point sources such as quasars, AGN and galactic black hole candidates (GBHC) have a universal energy spectrum. The shape of the universal spectrum should be identical to that of cosmic rays, except for some corrections due to the difference between the trajectories of neutral and charged particles."

The energy spectrum for γ-rays from quasar 3C273 was obtained by the CosB satellite and was reported to be[9]

$$\sim E^{-(2.5\pm0.6)} \tag{1}$$

around $100 \sim 400$ MeV. At this energy cosmic rays suffer solar modulation[3] but it is generally assumed that the original spectrum is an extension of the spectrum at higher energy (≥ 1 GeV), $\sim E^{-2.6}$. Therefore, the spectrum in Eq. (1) is remarkably close to that of cosmic rays, although an improvement of the accuracy in the measurement is needed. The expected data from GRO (Gamma Ray Observatory) will provide a further test of the prediction.

The X-ray data from point sources do not show the energy spectrum of Eq. (1). Analysis of the X-ray data by the Ginga group suggests that there are two components[10] in X-rays from point sources, GBHC: One from black body radiation at a temperature T and the other constituting a power law energy spectrum, which photon index $\lambda_0 = 1.5 \sim 2.0$ with an average of 1.7. The former component would come from black body radiation from a disk surrounding the hole, while the latter would originate from

somewhere else and is Compton-scattered by the disk. The energy spectrum of the original X-rays before being Compton-scattered can be computed by[11]

$$\lambda = 2(\lambda_0 - 1) + 1. \tag{2}$$

It follows from Eq. (2) that the photon index of the original X-rays is

$$\lambda = 2.0 \sim 3.0 \tag{3}$$

with the average

$$\lambda_{\rm av} = 2.4. \tag{4}$$

For the case of AGN, the observed photon index is[11] $(\lambda_0)_{\rm AGN} = 1.3 \sim 2.3$ with the average 1.7. This corresponds to the photon index of the original X-rays to be

$$\lambda_{\rm AGN} = 1.6 \sim 3.6 \tag{5}$$

with the average

$$(\lambda_{\rm av})_{\rm AGN} = 2.4 \tag{6}$$

Again, the value in Eq. (4) and Eq. (6) is close to that for the power spectrum of cosmic rays ($2.5 \sim 2.6$). An improvement in statistics as well as data from many more sources is required from the future X-ray satellites.

Finally, some comments are in order concerning the knee energy in the cosmic ray energy spectrum. The reason for the existence of the knee energy is not known. It could be due to either

[A] galactic magnetic fields ($\sim 3\mu G$).

or

[B] some unknown but intrinsic reason for gravitational acceleration.

Case [A] implies that the galactic magnetic fields in the Milky Way provide the depletion of high energy cosmic rays exiting from the galaxy and/or of low energy cosmic rays entering into the galaxy [assuming a single power energy spectrum]. Case [B] suggests that the existence of the knee energy has something to do with the gravitational acceleration mechanism with an intrinsic energy scale (of a few hundred TeV). [The example in ref. 8 is of this kind.] Again, without going into a discussion of the details of the acceleration mechanism, these two cases can be decided indirectly by observing the energy spectrum of γ-rays from point sources at higher energies. If the γ-ray energy spectrum from point sources exhibits the knee energy spectrum (not necessarily at the same energy since the gravitational redshift and the Doppler blueshift might be relevant to the final outcome) one may conclude that Case [B] is true. The γ-ray data from point sources at higher energies (by the Fly's Eye, the Whipple Observatory and other high energy γ-ray observatories) can decide which of Case [A] or [B] is the correct answer.

ACKNOWLEDGEMENTS

It is a great pleasure to thank Hajime Inoue, Yasuro Tanaka, R. Akhoury, Martinus Veltman, David Williams, and Ed Y.-P. Yao for useful suggestions. Thanks are also due to David Williams for reading the manuscript. This work is supported in part by the U.S. Department of Energy.

REFERENCES

1. e.g., A.M. Hillas, Ann Rev. Astron. Astrophys. 22 , 425 (1984).
2. A.R. Bell, M.N.R.S. 182 , 147, 443 (1978); R.D. Blandford and J. P. Ostriker, Ap. J. 221 , L29 (1978).
3. e.g., M.S. Longair, *High Energy Astrophysics*, (Cambridge University Press, 1981); S. Hayakawa, *Cosmic Ray Physics*, (Wiley-Interscience, NY, 1969).
4. P.O. Lagage and C.J. Cesarsky, Astron. Astrophys.118 , 223; 125 , 249 (1983).
5. e.g., J.E. Gunn and J.P. Ostriker, Phys. Rev. Lett. 22 , 728 (1969).
6. J.P. Jokipii and G.E. Morfill, Ap. J. 290 , L1 (1985).
7. M.J. Rees, Ann. Rev. Astron. Astrophys. 22 , 471 (1984).
8. Y. Tomozawa, Lectures in the Proc. of the 2nd Workshop on Fundamental Physics (ed. E. Esteban, 1986), p. 144; in *Quantum Field Theory* (ed. F. Mancini, 1985), p. 241; in *Active Galactic Nuclei* (ed. R. Miller and P. Wiita, Springer Verlag, 1988), p. 236; in *Symmetry in Nature* (Scuola Normale Superiore, 1989), p. 779; Quasars, Galaxy Distribution and Cosmic Background Radiation, UM-TH-91-15, 1991.
9. G.F. Bignami et al., Astr. Ap. 93 , 71 (1981).
10. H. Inoue, X-Rays from Galactic Black Hole Candidates and Active Galactic Nuclei, an invited talk presented at the Texas/CERN Symposium, Dec. 17-21, 1990, Brighton, United Kingdom.
11. G.B. Rybicki and A.P. Lightman, *Radiative Processes in Astrophysics*, (Wiley-Interscience Pub.), 1979.

EXPECTED LEVEL OF SELF-COMPTON SCATTERING IN RADIO LOUD QUASARS

Steven D. Bloom and Alan P. Marscher

Department of Astronomy, Boston University

Abstract

Radio-loud quasars usually contain parsec-scale nonthermal jets. The most compact emission region ("the core"), and perhaps some of the moving "knots," are expected to be efficient producers of inverse Compton scattered X-rays and γ-rays since many of the synchrotron photons will upscatter before escaping. Through multifrequency flux density observations and VLBI measurements of angular sizes, one can predict the flux density of this self-Compton high-energy emission. It is not always the case that the brightest synchrotron sources are also the brightest X-ray and γ-ray sources. Perhaps a better predictor of high-energy brightness is the ratio of hard X-ray to high-frequency radio emission.

Using the synchrotron self-Compton relations, we predict the γ-ray fluxes of several sources we expect to be detected by EGRET. More accurate predictions will be made when we complete a program of contemporaneous radio-submillimeter and X-ray observations during the course of the EGRET all-sky survey.

1. INTRODUCTION

VLBI observations of the parsec-scale structure of quasars show that the radio jets are extremely luminous, suggesting high energy densities of soft photons. It is expected that the synchrotron photons will scatter off the relativistic electrons that produced them to create X-rays and possibly soft γ-rays. Second order scattering should produce hard γ-rays. The synchrotron self-Compton (SSC) process has been discussed in the context of quasars by several authors (e.g., Jones, O'Dell and Stein , 1974; Ghisselini, Maraschi, and Treves, 1985; Band and Grindlay, 1986; Marscher 1987). The large X-ray data base provided by the *Einstein Observatory* has made it feasible to test the relationship between radio and high-energy emission, at least in a statistical sense. Several authors show that a strong correlation exists between X-ray and radio emission (Owen, Helfand, and Spangler 1981; Worrall *et al.* 1987; Kembhavi, Feigelson, and Singh 1986; Browne and Murphy 1987). Also, 3C273 and 3C279, both strong radio sources, have been detected in γ-rays . These results would suggest a one-to-one correspondence between the high-energy flux and radio flux. However, a more detailed look at self-Compton theory shows that the X-ray flux density $F_{\nu x}$ will have, in addition to a dependence on the radio flux density, a strong dependence on several other parameters (e.g., angular size). Similar calculations can be extended to the second order Compton flux densities. The dependence on several parameters is even more extreme in this case. Modest uncertainties in these parameters are typical; thus, predictions for the γ-ray flux density made in this manner are quite rough. There is then sufficient reason to seek an alternative method of predicting the γ-ray flux density. We show that if

the X-ray flux density is measured, then the *ratio* $F_{\nu x}/F_{\nu r}$ can be used to predict $F_{\nu\gamma}/F_{\nu x}$. This method was discussed by Jones (1979); we present more precise formulae. Flux densities at energies within the EGRET band can then be predicted.

2. FIRST AND SECOND ORDER SCATTERING RELATIONSHIPS

For homogeneous sources with simple geometries (e.g., a sphere), the predicted X-ray flux density can be calculated using the standard expressions for first order scattering emissivities in the Thomson limit (Blumenthal and Gould 1970; Gould 1979; Rybicki and Lightman 1979; Hughes and Miller 1991). The first order flux density then has the following dependence on the physical parameters of the source:

$$F_\nu{}^{1C} \propto N_0 R F_\nu{}^S ln(\nu_u/\nu_m) \propto N_0{}^2 B^{\frac{(1+p)}{2}} R^4 D^{-2} ln(\nu_u/\nu_m). \quad (1)$$

Here, R is the radius of the source, and D is the distance. Using expressions for the synchrotron flux density and optical depth at spectral turnover for a self-absorbed synchrotron source, one can solve for B, the magnetic field stength, and the parameter N_0, where the number density of relativistic electrons of a given energy follows the relationship $N(E) \propto N_0 E^{-p}$, in terms of *observable* radio source properties. These expressions for the physical parameters are then substituted back into the derived equation for X-ray flux density (see Marscher 1987 for details). The major result is that the first order flux density at photon energy E_{keV} keV is highly dependent on these parameters:

$$F_\nu{}^{1C} \propto \theta^{-2(p+2)} F_m{}^{p+3} \nu_m{}^{-(3p+7)/2} E_{keV}{}^{(1-p)/2} ln(\nu_u/\nu_m) \left(\frac{1+z}{\delta}\right)^{p+3}. \quad (2)$$

Here, F_m and ν_m are the flux density and frequency at spectral turnover, z is the redshift, δ is the Doppler beaming factor (a correction for bulk relativistic motion within the source), and the optically thin $\log F_\nu{}^S$ vs. $\log \nu$ spectrum is assumed to be a power law of slope $(1-p)/2$ between frequencies ν_m and ν_u. In the remaining proportionalities, we will ignore the slowly varying logarithmic term.

The second order flux density is then even more strongly dependent on the observable parameters (due to an extra factor of $N_0 R$):

$$F_\nu{}^{2C} \propto N_0 R F_\nu{}^{1C} \propto (N_0 R)^2 F_\nu{}^S \propto \theta^{-4(p+2)} \nu_m{}^{-(7p+13)/2} F_m{}^{2p+5} \left(\frac{1+z}{\delta}\right)^{2(p+3)}. \quad (3)$$

Usually, real sources cannot be well modeled as a single homogeneous sphere; however, the VLBI components collectively can be approximated as a composite of homogeneous spheres (Marscher 1987). The predicted flux densities for each component are then added together and compared to the measured flux density. Such calculations are usually assumed to be in the Thomson limit ($h\nu_{initial} << mc^2/\gamma$) or in the extreme Klein-Nishina limit ($h\nu_{initial} \gtrsim mc^2/\gamma$) because the full expression for the electron differential cross section that goes into calculating the emissivities is greatly simplified in these two limits. However, to

a first approximation, the basic proportionalities of the first and second order flux densities on these radio source parameters are independent of these assumptions. More precise expressions, which explicitly use the full Klein-Nishina cross section, are discussed below.

Ideally, we would like to obtain an expression for predicting the γ-ray flux density that is not so highly dependent on parameters that are poorly known. We can see from expressions (1) and (3) that the ratio of second order (γ-ray) to first order (X-ray) self-Compton flux densities equals the ratio of the first order self-Compton to synchrotron flux density. Therefore, if the ratio $F_{\nu x}/F_{\nu r}$ is *measured* and assumed to be determined by the SSC process, $F_{\nu\gamma}/F_{\nu x}$ can be predicted without knowledge of the radio source parameters. For the first order Compton emissivity, it is safe to assume that the Thomson limit applies. However, for the second order emissivity the Thomson limit will only apply over a fraction of the spectrum. Thus we need to integrate numerically the full expression of Blumenthal and Gould (their eq. 2.75). Performing this calculation, we obtain:

$$F_\nu{}^{2C} = 3^{\frac{(3-p)}{2}} 2^{2p-3} \sigma_T{}^2 (mc^2)^{2(1-p)} F_1(p) N_0^2 R^2 F_\nu{}^S S(\frac{\nu_S}{\nu_2})^{\frac{p-1}{2}} \ln(\frac{\nu_u}{\nu_m}). \quad (4)$$

Here, ν_1 is the first order photon frequency, ν_2 is the second order photon frequency, and $F_1(p)$ is that of Hughes and Miller (1991). The parameter S represents the integral:

$$S(\nu_1, \nu_2, q) = \frac{\int d\nu_1 I_\nu(\nu_1) \nu_1{}^{\frac{(p-3)}{2}} \int_0{}^1 dq\, f(q, \nu_1, \nu_2)}{K_{1C}}. \quad (5)$$

Here, $I_\nu(\nu_1)$ is the first order self-Compton intensity, $K_{1C} \equiv I_\nu(\nu_1)\nu_1{}^{\frac{(p-1)}{2}}$ is the first order intensity without the frequency dependence, f is the complicated function in equation (2.75) of Blumenthal and Gould, and $q \equiv \frac{\nu_2}{4\gamma\nu_1(1-h\nu_1/mc^2)}$. The integral S is only weakly dependent on the upper and lower limits of the first order Compton spectrum and spectral index, and is of order unity. We can now solve for $F_{\nu\gamma}/F_{\nu x}$ in terms of $F_{\nu x}/F_{\nu r}$:

$$\frac{F_{\nu\gamma}}{F_{\nu x}} = \frac{3^{\frac{(p+1)}{2}}}{2} \left(\frac{F_{\nu x}}{F_{\nu r}}\right) \frac{S(\nu_2, \nu_1, q)}{F_1(p) ln(\nu_u/\nu_m)} \left(\frac{\nu_2 \nu_r}{\nu_1{}^2}\right)^{\frac{(1-p)}{2}}. \quad (6)$$

We must emphasize that using this equation does not eliminate all of the uncertainty of expression (3). For instance, a rigorous analysis would require calculating this ratio for each separate component of the radio source, which is not possible due to the comparatively low resolution of current X-ray and γ-ray instrumentation. Possible source variability in either the radio or X-rays will lead to inaccurate estimates of $F_{\nu x}/F_{\nu r}$ unless the measurements are nearly simultaneous. In addition, the Thomson limit is not valid over much of the γ-ray range. In this case, numerical calculations are required (see Marscher and Bloom, these proceedings).

We present the results of a numerical computation of the self-Compton spectrum of a model uniform source in Figure 1. Note that there is substantial curvature to the spectrum of the self-Compton emission, contrary to the popular myth that it is a power law over most X-ray and γ-ray energies.

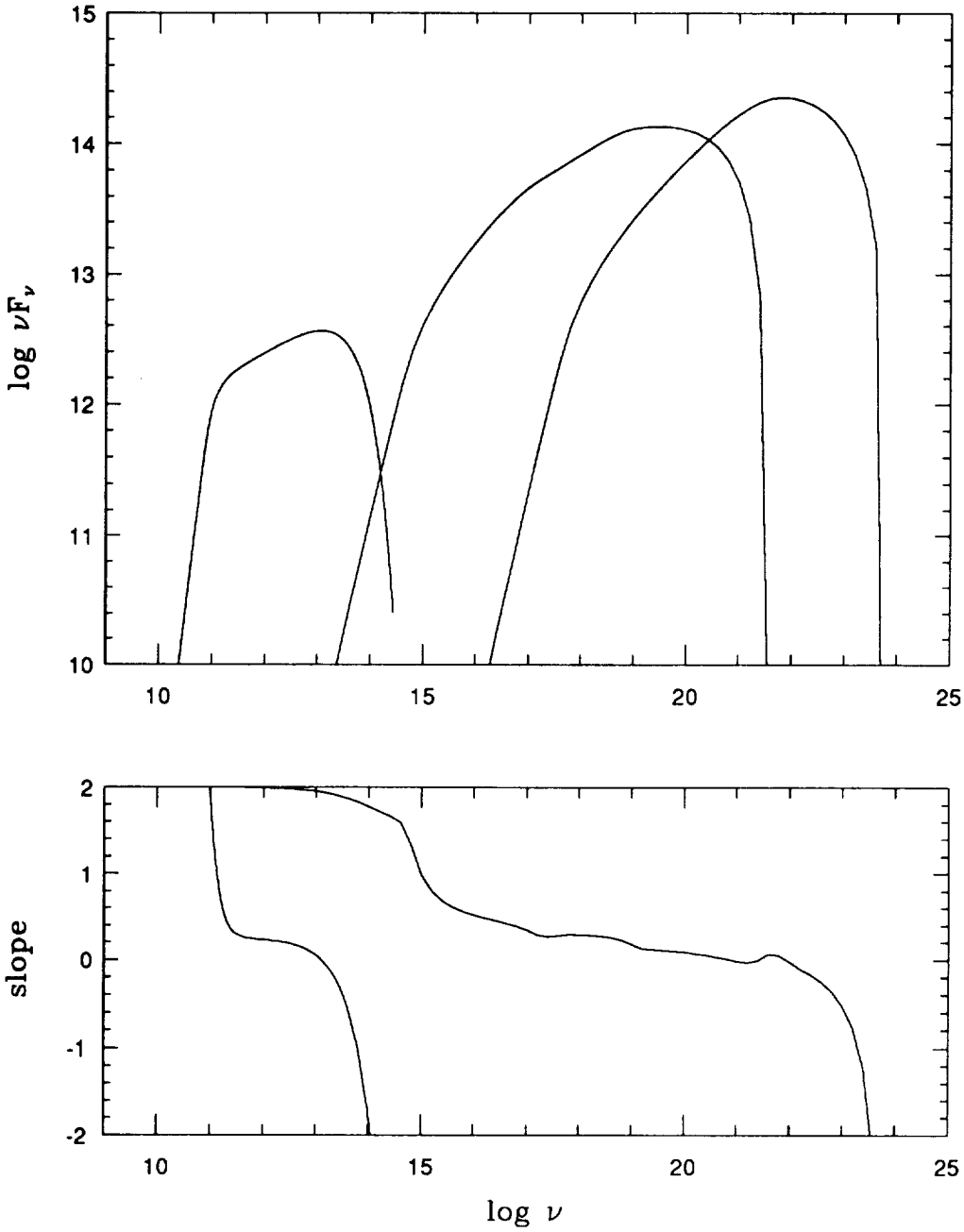

Figure 1 νF_ν spectrum of the synchrotron (left-most curve), first order self-Compton (middle curve), and second order self-Compton (right-most curve) emission from a model spherical, uniform, nonthermal source. The lower panel gives the slope of the νF_ν synchrotron (left-hand) and first + second order self-Compton (right-hand) spectrum as a function of frequency.

Equation (6) is still practical, especially if the detailed observations required for analysis of expression (3) are uncertain or non-existent. The best procedure would be to use both methods whenever the observations allow.

3. PREDICTIONS

Using equation (6) and taking the accompanying caveats to heart, we can predict which sources are likely to be detected by EGRET. We would like to find a sample of sources with recent simultaneous radio core and X-ray flux density measurements. Such a sample does not yet exist; however, Bloom and Marscher (1991) have compiled the X-ray data for all quasars and active galactic nuclei observed with both *Einstein Observatory* and with VLBI. We use these data as a rough guideline to predict $F_{\nu\gamma}$, although these calcuations are only valid for the epoch of the X-ray and radio observations, 1979-1981. Table 1 shows sources with highest values of predicted γ-ray flux that are above 5×10^{-8} photons cm^{-2} s^{-1}, the flux limit of EGRET (Kanbach 1989). The second column gives the X-ray flux density at 2 keV as measured by *Einstein*; the third column gives the measured ratio of X-ray flux density at 2 keV to the core radio flux density at 10.7 GHz in 1980; the fourth column gives the predicted ratio of γ-ray flux density at 100 MeV to X-ray flux density; and the last column gives the predicted photon flux in the EGRET band, integrated numerically between 100 MeV and 30 GeV . We have included effects due to the Klein-Nishina electron cross-section, which is significant at this energy range. We notice that some of the sources with high predicted γ-ray fluxes have rather modest X-ray and radio flux densities, implying again that it is not sufficient to use radio or X-ray flux alone as an indicator of which sources will be brightest in γ-rays. We see from equation (4) that the main requirement is that the source be compact. Alternatively, from expressions (1) and (3) we see that the γ-ray flux is proportional to $N_0{}^3$ and is therefore strongly dependent on the relativistic electron density within the source.

Table 1. Predicted γ-ray Fluxes, Epoch 1980

Source	$F_{\nu x}$ (μJy)	$\frac{F_{\nu x}}{F_{\nu r}}$ (10^{-6})	$\frac{F_{\nu\gamma}}{F_{\nu x}}$ (10^{-4})	F_γ (10^{-7}phot cm^{-2} s^{-1})
NRAO 140	1.65	2.8	3.6	0.9
3C 111	1.87	1.7	2.2	0.6
3C 120	5.2	5.8	7.7	6.0
3C 249.1	0.47	13.4	17.7	1.3
ON 231	0.31	0.4	0.5	0.02
3C 273	7.9	0.8	1.04	1.3
3C 279	0.40	0.1	0.1	0.01
3C 334	0.15	2.8	3.7	0.08
Mkn 501	7.4	11.2	14.8	17
1721+343	1.4	14.0	18.5	3.1
3C 390.3	1.0	2.4	3.2	0.5
BL Lac	1.87	1.9	2.5	0.7
3C 446	0.48	0.2	0.3	0.02

We note that the predicted γ-ray fluxes of several of the sources in Table 1 (especially Mkn 501) were above the detection level of COS-B. This result would imply that some of these sources (such as the BL Lac objects) are probably creating X-rays through some process other than the SSC mechanism. The predicted flux for 3C273, on the other hand, is approximately the same as that measured by COS-B (Swanenburg *et al.* 1978; see also Jones 1979). The predicted flux for 3C 279 is well below that recently measured by EGRET. This low prediction, which is based on X-ray and radio flux densities from 1980, is consistent with the non-detection of 3C 279 by COS-B. In addition, the radio flux at centimeter and millimeter wavelengths was considerably lower at the time of COS-B observations. For instance, the total flux density at 90 GHz went from 7-8 Jy in 1976-1978 (Landau *et al.* 1980) to approximately 14 Jy in July 1991 (extrapolated from the 150 GHz flux density; Robson 1991).

During 1991, 3C 279 has been flaring at millimeter and infrared wavelengths (Robson 1991). The self-Compton process acts as an amplifier of the synchrotron flare, leading to a very high γ-ray flux, as observed. Other quasars currently undergoing synchrotron flares are the bright radio quasar 4C 39.25 and the high $F_{\nu x}/F_{\nu r}$ quasar NRAO 140. We predict that these sources will also be detected by EGRET.

4. CONCLUSIONS

Compton theory for homogeneous sources shows that the second order flux density can be predicted if the ratio $F_{\nu x}/F_{\nu r}$ is measured. Equation (6) can then be used to estimate the γ-ray flux. However, it is clear from the predictions in section 4 that a more accurate analysis, looking at each component of the radio source and applying the first and second order scattering relationships, is necessary to test the dominance of the SSC process. Future work that will include multiwavelength VLBI radio and submillimeter radio observations at times close to ROSAT observations will allow for more reliable measurements of $F_{\nu x}/F_{\nu r}$, and a detailed component-by-component analysis for a number of quasars. Accurate fluxes can then be predicted and compared with EGRET observations.

REFERENCES

Band, D. L. , and Grindlay, J. E. 1986, *Ap. J.*, **308**, 576.

Bloom, S. D. , and Marscher, A. P. 1991, *Ap. J.*,**366**,16.

Blumenthal, G. R. and Gould, R. J. 1970, *Rev. Mod. Phys.*, **42**, 1970.

Browne, I. W. A., and Murphy, D. W. 1987, *M.N.R.A.S.*, **226**, 601.

Ghisselini, G. , Maraschi, L. , and Treves, A. 1985 , *Astr. Ap.*, **146**, 204.

Gould, R. J. 1979, *Astr. Ap.*, **76**, 306.

Hughes, P. A. , and Miller L. 1991, in *Beams and Jets in Astrophysics*, ed. P. A. Hughes (Cambridge: Cambridge University Press), p. 1.

Jones, T. W. 1979, *Ap. J.*, **233**, 796.

Jones, T. W. , O'Dell, S .L. , Stein, W. A. 1974, *Ap. J.*, **188**, 353.

Kanbach, G. *et al.* 1989 in *Proceedings of the Gamma Ray Observatory Workshop*, ed. W. N. Johnson (NASA: Washington, D.C.), p. 2-7.

Kembhavi, A. , Feigelson, E. D. , and Singh, K. P. 1986, *M.N.R.A.S.*, **220**, 51.

Landau, R. *et al.* 1980, *A.J.*, **85**, 363.

Marscher, A. P. 1987, in *Superluminal Radio Sources*, ed. J. A. Zensus, and T. J. Pearson (Cambridge: Cambridge University Press), p. 280.

Owen, F. N., Helfand, D. J., and Spangler, S. R. 1981, *Ap. J. (Letters)*, **250**, L55.

Robson, E. I. 1991, private communication.

Rybicki, G. B. , and Lightman, A. P. 1979, *Radiative Processes in Astrophysics* (New York: Wiley).

Swanenburg, B. N., *et al.* 1978, *Nature*, **275**, 298.

Worrall, D. M. , Giommi, P. , Tananbaum, H. , and Zamorani, G. 1987, *Ap. J.*, **313**, 596.

HARD GAMMA-RAY EMISSION FROM BLAZARS

Alan P. Marscher and Steven D. Bloom

Department of Astronomy, Boston University

Abstract

The γ-ray emission expected from compact extragalactic sources of nonthermal radiation is examined. The highly variable objects in this class should produce copious amounts of self-Compton γ-rays in the compact relativistic jet. This is shown to be a likely interpretation of the hard γ-ray emission recently detected from the quasar 3C 279 during a period of strong nonthermal flaring at lower frequencies. Ways of discriminating between the self-Compton model and other possible γ-ray emission mechanisms are discussed.

1. INTRODUCTION

The high flux of γ-rays recently observed toward the quasar 3C 279 (Hartman *et al.*, these proceedings) came as no surprise to astrophysicists who study nonthermal radiation from compact extragalactic radio sources. Highly variable nonthermal extragalactic sources (blazars) should, at least in theory, be strong hard γ-ray emitters.

At radio to infrared, and often optical, frequencies, the emission from blazars is almost surely incoherent synchrotron radiation. The evidence for this lies in the characteristic polarization properties – modest linear polarization and very small circular polarization – as well as the measured brightness temperatures, which lie in the few$\times 10^{11}$ K range expected for incoherent synchrotron emitters (see, e.g., Jones, O'Dell, & Stein 1974). In the most compact regions of the source, the synchrotron photon density is quite high, and therefore inverse Compton scattering of the synchrotron photons off the relativistic electrons – "self-Compton" emission – is expected to be important. In fact, if upper limits to the size of the source are derived from timescales of brightness variability, the photon densities would be so high that most of the luminosity should emerge in the X-ray and γ-ray regions of the spectrum (e.g., Burbidge, Jones, & O'Dell 1974; Marscher *et al.* 1979). In a few well observed cases, this over-prediction of high-energy emission is substantiated by actual measurements of the photon density (e.g., Marscher & Broderick 1985; Unwin *et al.* 1985). The most likely resolution of this discrepancy is that the emission regions in such sources are moving at relativistic speeds almost directly toward us, which also provides an explanation for the faster-than-light ("superluminal") apparent motions found in the compact jets of such sources (see Marscher 1987 for a review).

For a well-observed source, the major uncertainty in the self-Compton calculation is the precise value of relativistic beaming (Doppler) factor $\delta \equiv [\Gamma(1 - \beta\cos\phi)]^{-1}$, where the bulk velocity of the emitting plasma is βc directed at an angle ϕ to the line of sight, and $\Gamma \equiv (1 - \beta^2)^{-1/2}$ is the bulk Lorentz factor. The higher the beaming factor is, the lower is the photon density needed to account for a given observed nonthermal flux from the source. The superluminal apparent speed is given by $\beta_{\rm app} = \frac{\beta\sin\phi}{1-\beta\cos\phi}$, which is a maximum

of $\beta_{\rm app} = \Gamma$ at $\phi = \sin^{-1}(1/\Gamma)$. Observation of the apparent superluminal motion therefore constrains both Γ and ϕ, but does not uniquely determine them. The Doppler factor also causes a time contraction in the observer's frame relative to the rest frame of the emitting plasma. A source that varies by a large factor on a timescale $t_{\rm var}$ therefore can be as large as $\sim ct_{\rm var}\delta/(1+z)$, where z is the redshift of the entire object.

The fact that COS B did not detect lots of blazars indicates that the Doppler factors are in general high enough so as to allow the photon density in the rest frame of the emitting plasma to be sufficiently low for the self-Compton process to be only a modest source of high-energy photons most of the time. Whether the EGRET and COMPTEL detectors will be sensitive enough to detect this "quiescent" γ-ray emission from any blazars remains to be seen. However, during the major synchrotron flares that are observed in most blazars from radio to infrared (and often visual) frequencies, the synchrotron photon density should increase to a level sufficient to cause a major flare in self-Compton X-rays and γ-rays.

In what follows, we discuss the expected spectrum and other observational signatures of a self-Compton flare, with application to the EGRET detection of 3C 279 in June 1991. We then review briefly various other models that could possibly produce hard γ-ray emission from blazars, and show how future observations are potentially capable of discriminating among these possibilities.

2. SELF-COMPTON EMISSION FROM BLAZARS

Bloom and Marscher (these proceedings) give the formulae for first and second order self-Compton emission from a compact nonthermal source. In Figure 1 we display the numerically calculated synchrotron and self-Compton spectrum of a model compact nonthermal source that is meant to approximate very roughly the observed characteristics of 3C 279 in summer 1991, which was a time of flaring at submillimeter wavelengths (Robson 1991) similar to that which occurred during the pronounced X-ray flare of 1988 (Makino *et al.* 1989). The slope of the νF_ν vs. ν spectrum is given as a function of frequency in the bottom panel of Figure 1. For the particular model spectrum shown, first order scattering dominates over second order, which is suppressed owing to the Klein-Nishina limit. Although we have not exhausted all parameter space, it appears difficult to reproduce the γ-ray emission of 3C 279 in June 1991 by second order scattering using a simple self-Compton model because of the Klein-Nishina suppression.

The general characteristics of the synchrotron spectrum are: a low-frequency ($\nu < \nu_{\rm m}$) drop-off owing to synchrotron self-absorption; a high-frequency ($\nu \gtrsim \nu_{\rm u}^{\rm S}$) cut-off corresponding to the synchrotron critical frequency of the highest energy electrons; and a power-law of slope $-\alpha = -(p-1)/2$ at intermediate frequencies, where p is the slope of the presumed power-law energy distribution of the relativistic electrons. The first-order self-Compton spectrum, for which the scattering is almost surely completely within the Thomson limit, is a spread-out version of the synchrotron spectrum, with low-frequency fall-off below $\nu_\ell^{\rm IC} \sim \gamma_\ell^2 \nu_{\rm m}$ and high-frequency drop-off above $\nu_{\rm u}^{\rm IC} \sim \gamma_{\rm u}^2 \nu_{\rm u}^{\rm S}$. Here, γ_ℓ and $\gamma_{\rm u}$ are the lower and upper Lorentz factor limits of the relativistic electron energy distribution. In between $\nu_\ell^{\rm IC}$ and $\nu_{\rm u}^{\rm IC}$, the spectrum is roughly a power law with the same slope as for the synchrotron spectrum. Note, however, that there is significant curvature to the

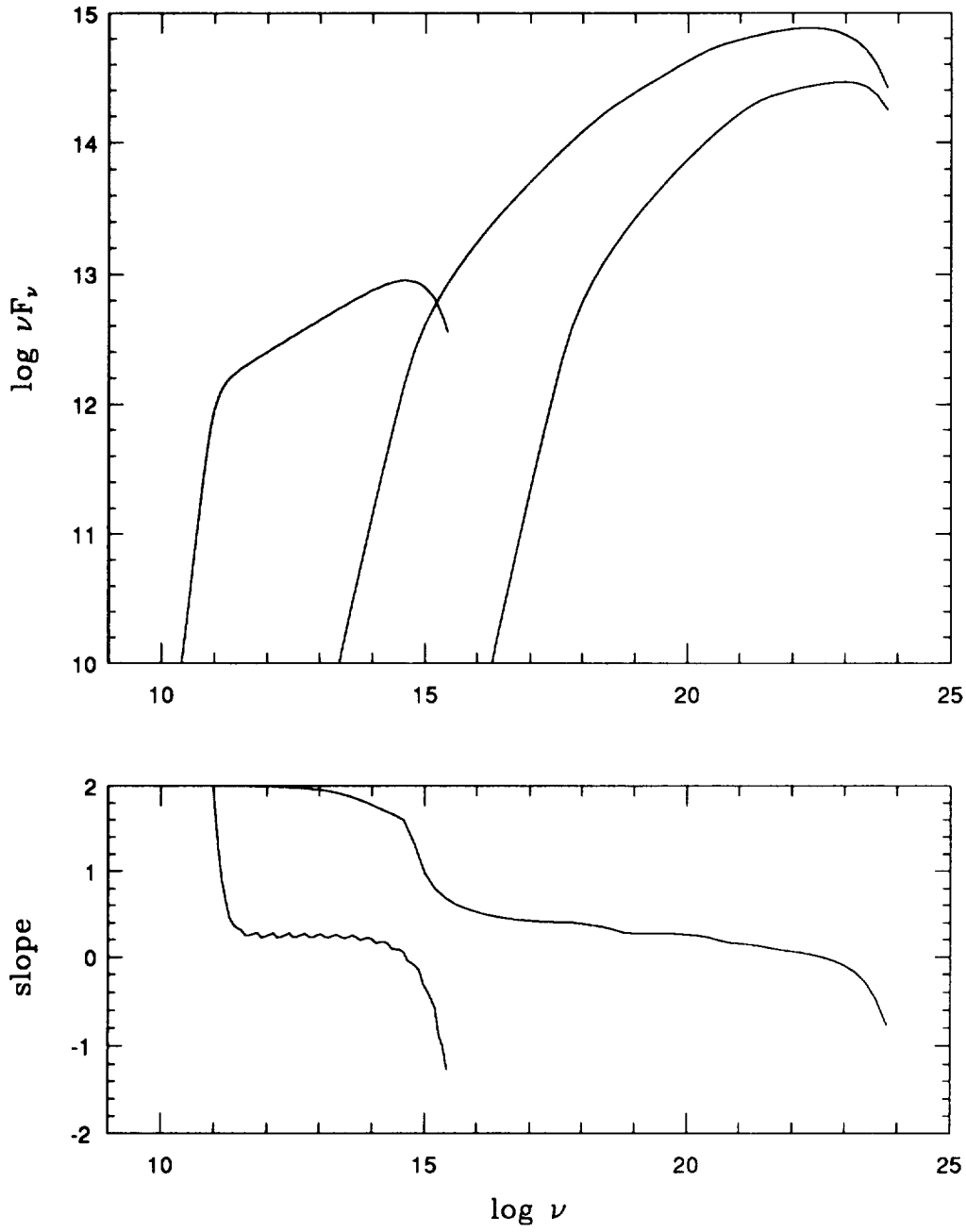

Figure 1 νF_ν spectrum of the synchrotron (left-most curve), first order self-Compton (middle curve), and second order self-Compton (right-most curve) emission from a spherical, uniform, nonthermal source whose overall spectrum is similar to that of 3C 279 in June 1991. The lower panel gives the slope of the νF_ν synchrotron (left-hand) and first + second order self-Compton (right-hand) spectrum as a function of frequency.

self-Compton spectrum unless there are several decades between both the upper and lower synchrotron spectral cut-offs and the upper and lower electron energy cut-offs. In addition,

the self-Compton high and low frequency cut-offs are not as sharp as is the case for the synchrotron spectrum.

The character of the second order self-Compton spectrum depends on the values of γ_ℓ, γ_u, ν_m, and ν_u^S. Since the scattered photon (with initial photon energy less than $m_e c^2$) cannot have greater energy than that of the incoming electron, the upper frequency cut-off is $\nu_u^{2C} \sim \gamma_u m_e c^2/h$, where h is Planck's constant. As is seen in Figure 1, this Klein-Nishina cut-off significantly suppresses the second order self-Compton γ-ray luminosity.

The self-Compton X-ray and γ-ray luminosity can be considerably higher than that of the synchrotron emission. [As has been pointed out by R. Blandford (1991), above some high luminosity ratio one must consider quantum effects leading to induced Compton scattering.] The conditions under which this occurs correspond precisely to those that would cause a substantial synchrotron flare, since the ratio of first order self-Compton to synchrotron flux increases as the synchrotron brightness temperature raised to the $(3+2\alpha)$ power (Marscher 1987). (The brightness temperature is proportional to the flux density divided by the square of the angular size.) The self-Compton process therefore acts as an amplifier of the synchrotron fluctuations.

The synchrotron spectrum of 3C 279 is described by a power law of spectral index $\alpha \approx 0.6$ between about 10^{11} Hz and 10^{14} Hz, above which it steepens (Robson 1991). Without contemporaneous VLBI observations at 90 GHz, we cannot determine the angular size of the variable component, and therefore cannot derive the magnetic field strength. If we assume that the magnetic field in the core is of order 0.1 gauss, which is near the value derived for 3C 273 (Marscher & Gear 1985), then the upper electron Lorentz factor cut-off is $\gamma_u \sim 10^4$. The high-frequency drop-off of the first order self-Compton emission then occurs at $\nu \gtrsim \nu_u^{1C} \sim \gamma_u^2 \nu_u^S \sim 10^{22}$ Hz, or about 40 MeV. The spectrum of γ-rays detected by EGRET should then be somewhat steeper than the expected X-ray value of about -0.6. (Note: this is the so-called "energy index" as opposed to the "photon index.") If the hard γ-rays from 3C 279 are from second order self-Compton, the spectrum gradually steepens with frequency (see Fig. 1).

Discerning between a first and second order origin for the hard γ-rays only requires contemporaneous submillimeter or infrared, X-ray, and γ-ray observations. For second order self-Compton, the ratio of hard γ-ray to X-ray flux density $(F_{\nu,\gamma}/F_{\nu,X})(\nu_\gamma/\nu_X)^\alpha$ (corrected for Klein-Nishina suppression) should equal the ratio of X-ray to synchrotron luminosity $(F_{\nu,X}/F_{\nu,IR})(\nu_X/\nu_{IR})^\alpha$ (Jones 1979; Bloom and Marscher, these proceedings).

A more detailed analysis of the γ-ray emission from 3C 279 must include the as yet unpublished contemporaneous radio VLBI, submillimeter–infrared, and (if any) X-ray observations.

3. OTHER γ-RAY EMISSION MECHANISMS

Although one can imagine (and a number of authors have) that copious γ-ray production might occur close to the central engine of an active nucleus, any hard γ-rays thus produced will almost surely be destroyed by pair production off the observed strong X-ray radiation field (McBreen 1979). Since the only two confirmed identification of quasars with hard γ-ray sources are the superluminal sources 3C 273 (Swanenburg *et al.* 1978) and

3C 279 (Hartman *et al.*, these proceedings), it is reasonable to assume for the time being that the γ-ray production arises from the relativistic jets in these objects. A self-Compton origin of the γ-rays from 3C 273 is possible despite the steep slope measured by COS B (Bignami *et al.* 1981), since steep spectra are in fact produced at the high frequency end of the scattered spectrum (see Fig. 1). As is discussed in Marscher and Gear (1985) and Marscher, Gear, & Travis (1992), the observed rapid variability in the X-ray flux of 3C 273 does not necessarily imply that the X-rays are produced close to the central engine: fluctuations in the relativistic jet are capable of producing surprisingly short timescales of variability, especially at high frequencies.

Other processes besides self-Compton emission have been proposed for producing hard γ-rays from blazars. Begelman and Sikora (1987) and Melia and Königl (1989) show that, if the jet originates closer to the central engine than the smallest observed radio component ($\sim$ 1 pc), Compton scattering ("reflection") of the X-rays emitted from an assumed accretion disk will generate a high flux of X-rays and γ-rays. Dermer, Schlickeiser, and Mastichiadis (these proceedings) propose that this process will occur even at the distance of the radio jet. Eichler and Wiita (1978), Giovanoni and Kazanas (1990), and Mastichiadis and Protheroe (1990) have proposed that much of the energy from the central engine is released in the form of high-energy neutrons generated in collisions of relativistic protons. Neutrons with Lorentz factors $\gtrsim 10^5$ would decay about 1 pc from the central engine, thereby injecting relativistic electrons into the radio jet at this distance. γ-rays from the proton-proton collisions could be beamed from the vicinity of the central engine, possibly avoiding complete depletion from pair production. The secondary electrons are also free to engage in self-Compton emission in the radio jet. For the 3C 273 jet, it has been proposed (Bignami *et al.* 1981; Morrison, Roberts, & Sadun 1984) that the γ-rays could be produced through inverse Compton scattering in the extended jet.

In principle, multifrequency observations of variability of the emission from a blazar can discriminate among these disparate models. In the case of self-Compton models, the high-energy emission should amplify the variations of the underlying synchrotron source. The high-energy variations should therefore be simultaneous with the synchrotron variations. It is important to note that this is only true for the *optically thin* synchrotron variations, i.e., those occurring at frequencies higher than the self-absorption turnover frequency $\nu_{\rm m}$. Since $\nu_{\rm m}$ typically lies above $\sim 10^{11}$ Hz, the high-energy fluctuations must be compared with those observed in the submillimeter-wave to infrared part of the spectrum. The radio variations are often time delayed until the variable component expands sufficiently to lower the optical depth to a value $\lesssim 1$. Also, since the high-energy emission is subject to rapid fluctuations on top of major flares (Marscher *et al.* 1992), one should not make too much of short timescale high-energy variations with amplitudes of a few tens of percent that are not coincident with similar infrared fluctuations.

Inverse Compton reflection of uv or X-ray photons from an accretion disk (or other region close to the central engine) off the electrons in a relativistic beam (precursor of the observed radio jet) could have two different signatures. If the incident photon flux varies, one should observe an X-ray or uv flare followed by a time-delayed γ-ray flare, although the time delay would probably be quite short ($\sim$ days). If the flare is caused by an increase in the number of relativistic electrons injected into the beam, the source could be steady in the

soft X-ray and uv while a γ-ray flare is observed, followed by a submillimeter-infrared flare that could be time-delayed by weeks or months.

If the γ-rays are produced in proton-proton collisions near the central engine, one would expect the γ-ray flares to precede synchrotron flares, again by weeks or months unless the jet points directly at us. Also, the luminosity in γ-rays should be roughly proportional to the synchrotron luminosity in radio-loud active galaxies (cf. Giovanoni & Kazanas 1990).

Finally, if the γ-rays result from inverse Compton scattering in the extended radio jet, no variability should be seen on timescales of years.

4. WHAT WE CAN LEARN FROM SELF-COMPTON γ-RAYS

If, as seems likely, the hard γ-rays from 3C 279 are of self-Compton origin, contemporaneous radio, submillimeter, infrared, optical, X-ray, and γ-ray observations can nail down many of the physical parameters of the source. As is discussed by Bloom and Marscher (these proceedings), the first and second order self-Compton fluxes depend on the Doppler beaming factor δ and the observed parameters (flux density, angular size, self-absorption turnover frequency) raised to very high powers. This works against obtaining a precise prediction of the high-energy self-Compton flux through observations of the synchrotron source. However, once the self-Compton X-ray and γ-ray fluxes are observed, the parameters of the source are extremely well determined since they depend on the high-energy fluxes raised to very low powers. For a source with $\alpha = 0.6$, one obtains (cf. the relations given by Bloom and Marscher)

$$\delta \propto (F_\nu^{1C})^{-0.19} F_m \nu_m^{-1.3} \theta^{-1.6}. \quad (1)$$

Here, F_m is the synchrotron flux density at the self-absorption turnover frequency ν_m, and θ is the angular size of the emitting region. The angular size is not easy to measure, since the most compact radio components are unresolved, even with VLBI, in the majority of sources. The other parameters can, however, be measured rather accurately. Using the second order self-Compton flux, we can derive a second relation:

$$\delta \propto (F_\nu^{2C})^{-0.10} F_m^{0.90} \nu_m^{-1.4} \theta^{-1.6}. \quad (2)$$

Unfortunately, the Doppler beaming factor depends on angular size in precisely the same way in the two expressions (which is why the γ-ray flux can be predicted from the ratio of X-ray to infrared flux densities). The two expressions at least provide a consistency check on the assumption that the self-Compton process is the mechanism that generates the γ-rays.

Expressions (1) and (2) can therefore be used to determine the value of the Doppler beaming factor δ to within the accuracy of measuring the angular size θ. Notice that, since at least an upper limit to θ can be measured, at least a lower limit to δ can be calculated. Also notice that this procedure is completely independent of the distance scale. However, the apparent superluminal motion of a source is dependent on the distance scale: $\beta_{app} \propto \mu d$, where μ is the proper motion of the superluminal component and d is the distance, which depends on both Hubble's constant H_0 and the deceleration parameter q_0. Once VLBI at millimeter wavelengths becomes commonplace (it can now be done on a limited basis), the

values of (rather than upper limits to) θ will be able to be measured for many sources. This, plus observations of the superluminal motion and adoption of particular values of q_0 (necessary for higher redshift objects only) and H_0, will be sufficient to determine both the Lorentz factor and Doppler beaming factor of the variable emission regions in the jet. Given a sufficient number of sources for which this procedure can be carried out, it could even be possible to determine the values of q_0 and H_0 themselves from the expected statistical distribution of orientation angle ϕ (see Marscher and Broderick 1982).

If the hard γ-rays from 3C 279 arise from the self-Compton process within the relativistic jet, the actual luminosity is $L_\gamma \approx 10^{48}\delta^{-4}$ erg s^{-1}. Two factors of δ correspond to beaming within an aberrated angle of δ^{-1}, another factor comes from time contraction (blueshift) for a variable component, and the last factor is the frequency boost (the photons are δ times more energetic in the observer's frame than in the source's rest frame). The apparent superluminal speed, for $q_0 = 0.5$ and $H_0 = 100h$ km s^{-1} Mpc^{-1}, is $\beta_{\rm app} = 2.2h^{-1}$ as determined over the period 1981–1986 by Unwin *et al.* (1989), and about 4 times this value between 1970 and 1972 as determined by Cotton *et al.* (1979). The earlier value results from very limited data by current standards and is based on very simple source models, while the later observations show the source structure to be fairly complex much of the time. On the other hand, the model fitting of Hughes, Aller, and Aller (1991) to the radio flux density and polarization variations implies that the time sampling of the Unwin *et al.* observations is too sparse to identify individual components accurately as they change position on the multi-epoch images. These authors suggest a value of $\beta_{\rm app}$ at least twice that of Unwin *et al.*, but not as high as that of Cotton *et al.* The more frequent monitoring that will be available with the VLBA (to be completed in early 1993) should resolve the issue. Note that δ can be considerably greater than $\beta_{\rm app}$ if the beaming angle $\phi < \sin^{-1}\phi$. From the above considerations, the actual γ-ray luminosity of 3C 279 is likely to be $\lesssim 10^{46}$ erg s^{-1}.

5. CONCLUSIONS

It appears highly likely that the hard γ-rays detected by EGRET toward the blazar 3C 279 in June 1991 were generated by the self-Compton process within the compact relativistic jet apparent on radio VLBI images. Multifrequency monitoring (at least once every few months) of 3C 279 and other similar sources will provide excellent tests of the self-Compton and other emission processes. It is especially important that the observations of the synchrotron emission include both multifrequency radio VLBI and total flux density observations at radio, submillimeter, and infrared wavelengths.

At least one other source, the quasar 4C 39.25, is undergoing a prolonged synchrotron flare of roughly equal amplitude to that of 3C 279 (Marscher *et al* 1991). In addition, the quasar NRAO 140, with high X-ray to radio flux ratio, is also flaring in the radio (Aller and Aller 1991). Both these objects are excellent candidates for detection by EGRET and possibly COMPTEL. We are currently engaged in a project to measure the multifrequency properties of a sample of 31 radio-loud quasars (including the two mentioned above) under the CGRO Guest Investigator Program using the COMPTEL and EGRET sky surveys. We will propose to make repeated pointed observations of those sources from our sample that are detected by CGRO. The scientific return from such studies should be very high.

The work discussed in this paper has been supported in part through the GRO Guest Investigator Program, NASA grant NAG5-1566.

REFERENCES

Aller, H.D., and Aller, M.F. 1991, private communication

Begelman, M.C., and Sikora, M. 1987, ApJ, 322, 650

Bignami, G.F., *et al.* 1981, A&A, 93, 71

Blandford, R.D. 1991, private communication

Burbidge, G.R., Jones, T.W., and O'Dell, S.L. 1974, ApJ, 193, 43

Cotton, W.D., *et al.* 1979, ApJ, 229, L115

Eichler, D., and Wiita, P.J. 1978, Nature, 274, 38

Giovanoni, P.M., and Kazanas, D. 1990, Nature, 345, 319

Hughes, P.A., Aller, H.D., and Aller, M.F. 1991, ApJ, 374, 57

Jones, T.W. 1979, ApJ, 233, 796

Jones, T.W., O'Dell, S.L., and Stein, W.A. 1974, ApJ, 298, 301

Makino, F., *et al.* 1989, ApJ, 347, L9

Marscher, A.P. 1987, in *Superluminal Radio Sources*, ed. J.A. Zensus and T.J. Pearson (Cambridge University Press), p. 280

Marscher, A.P., and Broderick, J.J. 1982, in IAU Symposium 97, *Extragalactic Radio Sources*, ed. D.S. Heeschen and C.M. Wade (D. Reidel), p. 359

Marscher, A.P., and Broderick, J.J. 1985, ApJ, 290, 735

Marscher, A.P., and Gear, W.K. 1985, ApJ, 298, 114

Marscher, A.P., Gear, W.K., and Travis, J.P. 1992, in *Variability of Blazars*, ed. E. Valtaoja (Cambridge University Press), in press

Marscher, A.P., Marshall, F.E., Mushotzky, R.F., Dent, W.A., Balonek, T.J., and Hartman, R.F. 1979, ApJ, 233, 498

Marscher, A.P., Zhang, Y.F., Shaffer, D.B., Aller, H.D., and Aller, M.F. 1991, ApJ, 371, 491

Mastichiadis, A., and Protheroe, R.J. 1990, MNRAS, 246, 279

McBreen, B. 1979, A&A, 71, L19

Melia, F., and Königl, A. 1989, ApJ, 340, 162

Morrison, P., Roberts, D., and Sadun, A. 1984, ApJ, 280, 483

Robson, E.I. 1991, private communication

Swanenburg, B.N., *et al.* 1978, Nature, 275, 298

Unwin, S.C., Cohen, M.H., Biretta, J.A., Hodges, M.W., and Zensus, J.A. 1989, ApJ, 340, 117

Unwin, S.C., *et al.* 1985, ApJ, 289, 109

CONSTRAINTS ON REFLECTION IN AGN

M. Maisack[1,2], T. Yaqoob[3], R. Staubert[1], E. Kendziorra[1]

[1] Astronomisches Institut Tuebingen, FRG
[2] George Mason University, Fairfax, VA, USA
[3] Institute of Space and Astronautical Science, Kanagawa, Japan

ABSTRACT

Models including photon-photon pair production (e.g. Ref.1) and reprocessing by cold material (e.g. Ref.2) have recently received wide attention, especially since Ginga spectra of Seyfert galaxies have shown a hard X-ray tail as expected from the latter process.

Zdziarski et al. Ref.3) have proposed a model for the canonical energy index alpha ~ 0.7 (e.g. Ref.4) that includes both effects. According to this model, the canonical index is the result of the superposition of a steeper (alpha ~ 0.9), pair-dominated spectrum of a source with high compactness and a reprocessed component.

High energy X-ray data (20-120 keV) have been taken with the HEXE instrument on the Mir space station (Ref. Reppin) of three AGN (3C 273, NGC 4151 and Cen A).

We have examined these data in the light of the reflection model.

References

1 Lightman, A.P. & Zdziarski, A.A. 1987, Ap.J. 319, 643
2 Lightman, A.P. & White, T.R. 1988, Ap.J. 335, 57
3 Zdziarski, A.A. et al 1990, Ap.J. 363, L1
4 Rothschild, R.E. et al 1983, Ap.J. 269, 423

GAMMA-RAYS FROM CLUSTERS OF GALAXIES

W. Thomas Vestrand
Space Science Center
University of New Hampshire
Durham, NH 03824, U.S.A.

Abstract

We examine the possibility that Coma-type radio halos are powered by secondary electrons produced during the decay of energetic charged pions. These pions are generated by the collision of cosmic ray protons with thermal ions in the intracluster medium. A calculation of both the cosmic ray concentration and the spectrum needed to power the halo in the Coma cluster is presented. The gamma-ray flux is predicted and it is shown that this model can be tested with GRO EGRET.

GAMMA-RAY FLARES IN AGN

M. Kafatos, Institute for Computational Sciences and Informatics
and Department of Physics,
George Mason University, Fairfax VA 22030

I. INTRODUCTION

Active galactic nuclei have long been suspected as being sources of gamma-rays. For example, 3C 273 was observed by *COS B* (Swanenburg *et al.* 1978) to be a strong source of gamma-rays in the range 50-500 MeV. The small number of gamma-rays involved even in the strongest extragalactic gamma-ray sources prevented astronomers from determining if gamma-rays were highly variable.

The inner regions of accretion disks onto supermassive black holes can become unstable when the existing temperatures are sufficiently high (Shapiro, Lightman, and Eardley 1976; Eilek and Kafatos 1983). This naturally occurs for two-temperature disks in the case of rapidly spinning (Kerr) black holes. Physical effects in the hot, inner regions are such that non-steady flows can result. We here focus on three such effects which would be relevant in producing variability in intense gamma-ray sources (MeV to GeV range), such as the recent discovery of strong gamma-ray emission in 3C 279 discovered by the EGRET instrument on board the *Compton Telescope* (Hartman *et al.* 1991).

II. VARIABILITY IN THE INNER ACCRETION DISK

Theoretically predicted effects may have relevant observational consequences. The first effect relates to the production of the most energetic (GeV) e^+e^- pairs in a hot disk scenario via Penrose pair production (Kafatos and Leiter, 1979; Kafatos 1980). Such a production is intrinsically a gravitational effect. Order of magnitude estimates are easy to obtain because the natural timescales associated with it would be the light travel time in the ergosphere, 8000 M_8 sec where M_8 is the central mass in 10^8 solar masses. Penrose pair production (PPP) would yield pairs up to $\sim 4\ m_p c^2$ or ~ 4 GeV with an approximately exponential distribution that over a limited energy range would fit a power law. The pairs would be emitted in bursts as long as a source of copious gamma-ray emission existed close to the horizon. An ion-dominated inner accretion disk could be the source of seed gamma-rays needed to produce the pairs via scattering with the protons.

The second relates to the existence of an intrinsic dynamical effect that operates even when the disk is assumed to, initially, be steady-state. Instabilities of standard disks, two temperature disks and ion-supported tori have been extensively discussed in the literature (e.g. Lightman and Eardley 1974; Shapiro, Lightman and and Eardley 1976). Eilek and Kafatos (1983) assumed that a steady flow occurs. It is likely, however, that the dynamic (Coulomb) viscosity is very large when the temperatures are sufficiently high. Both the two-temperature model with $T_i \sim 10^{12}$ - 10^{13} °K (Eilek and Kafatos 1983) and the hot corona model with $T \sim 10^{11}$ °K (Liang and Thompson 1980) would be subject to large viscosities,

$\alpha \sim 37\ (\dot{M}_\bullet/M_8)^{3/7}\ r_\bullet^{-9/28}\ y^{-3/7}$ and

$\alpha \sim 1.2 \times 10^4\ (\dot{M}_\bullet/M_8)^{12/7}\ r_\bullet^{-18/7}\ b^{6/7}$,

respectively, when the accretion rate is sufficiently close to the Eddington limit, $0.01 \lesssim \dot{M}_\bullet/M_8 \lesssim 1$. Here $\dot{M}_\bullet$ is the accretion rate in $M_\odot\ yr^{-1}$, y is the Comptonization parameter and $r_\bullet$ is the radial distance in units of gravitational radii.

When the viscosity parameter α exceeds unity, the disk will collapse over dynamical timescales (Shakura and Sunyaev 1973). Such a collapse would trigger a flare in an AGN. The gas would then return to a quasi-steady accretion until the temperature in the inner disk or hot corona builds up again. It is clear that these provide for time-dependent conditions where Comptonization is an important process in the accreting/collapsing gas. Since high viscosities imply copious production of gamma-rays (MeV - several 100 MeV) and energetic (70 MeV) pairs, this mechanism would be relevant to AGNs observed both by OSSE and EGRET.

These ideas provide the possibility of, at least, a variable accretion flow.

On the topic of steady-flows, the requirement of steady accretion flow in real astrophysical sources is probably an oversimplification. Accretion into black holes may actually not follow the usual steady inflow process assumed in standard disks. Accretion onto black holes may always be a transonic phenomenon with the transonic radius close to the black hole if the accretion occurs in a thin disk configuration (Liang and Thompson 1980).

At George Mason University, we have have developed the relativistically correct continuity and Euler's equations in the Kerr metric ignoring viscosity terms. We have numerically solved the resulting inflow assuming a polytropic equation relating the pressure to the density for the special case of Schwarzschild metric. For a variety of initial conditions in the

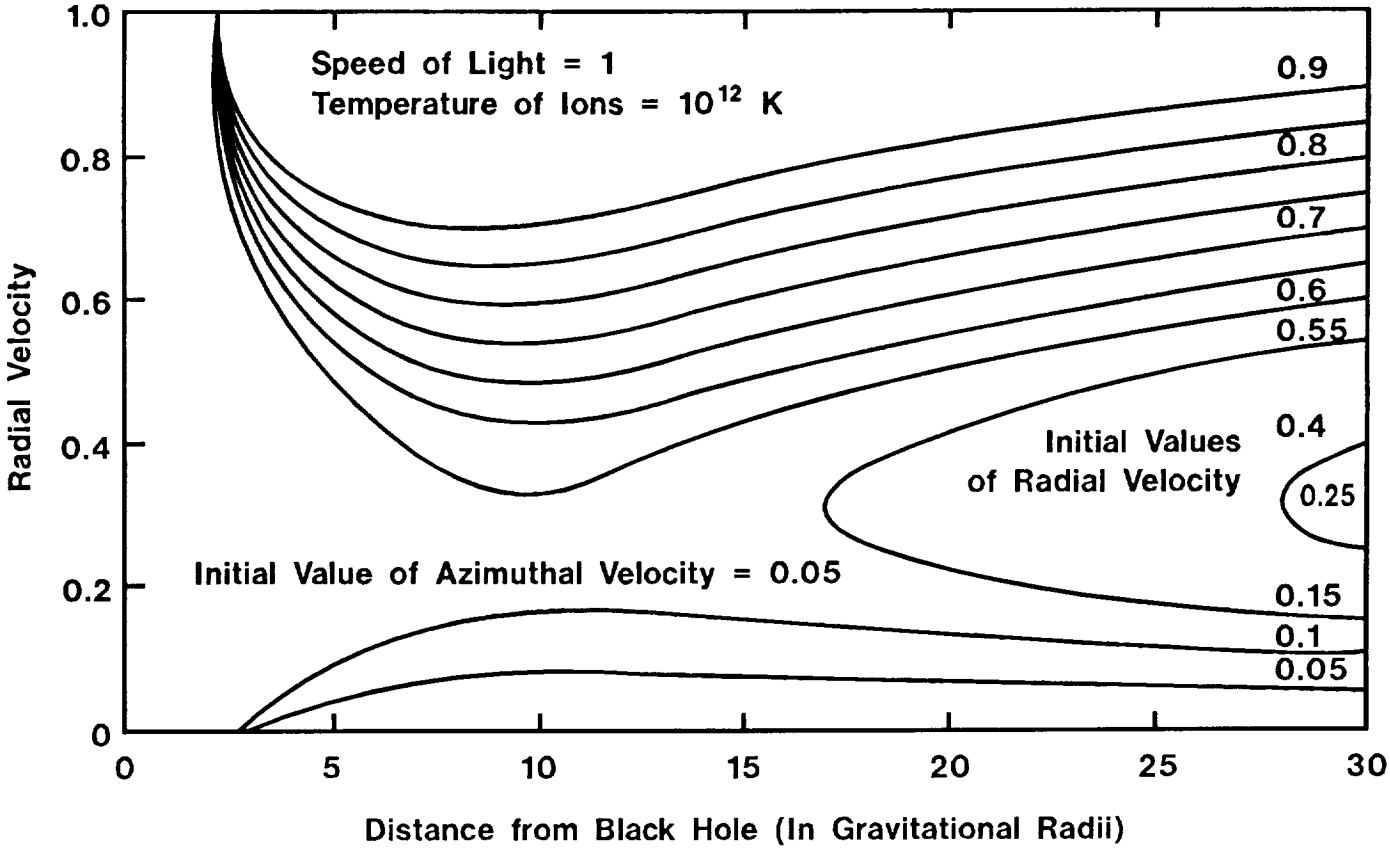

Figure 1: Steady transonic flow in the Schwarzschild metric (in units of c = 1)

isothermal case, we find that the velocity of the flow becomes supersonic and rapidly approaches the speed of light for radii closer than about 30 r_g (see Figure 1). We are presently in the process of examining the case of isentropic flow in the Schwarzschild metric.

We emphasize that that the inclusion of viscosity would enhance the effect of transonic solutions since angular momentum would be lost and the inflow would be even more rapid. The existence of these effects will result in the collapse of the inner disk whenever the ion temperatures become sufficiently high and would, therefore, also be relevant to strong gamma-ray AGN sources, and specifically 3C 279. It follows that considerations of whether accretion disks in the centers of AGNs exist or not cannot ignore the flow of the gas close to the horizon and the associated instabilities. The *Compton Telescope* could provide important insights in our understanding of inner accretion disk flows.

REFERENCES

Eilek, J.A., and Kafatos, M. 1983. *Ap. J.*, **271**, 804.
Hartman, R.C., *et al.* 1991, *Ap. J. (Lett.)*, in press.
Kafatos, M. 1980, *Ap. J.*, **236**, 99.
Kafatos, M., and Leiter, D. 1979, *Ap. J.*, **229**, 46.
Liang, E.P.T., and Thompson, K.A. 1980, *Ap. J.*, **240**, 271.
Lightman, A.P., andEardley, D.M. 1974, *Ap. J. (Lett.)* **187**, L1.
Shakura, N.I., and Sunyaev, R.A. 1973, *Astr. Ap.*, **24**, 337.
Shapiro, S.L., Lightman, A.P., and Eardley, D.M. 1976, *Ap. J.*, **204**, 187.
Swanenburg, B.N., *et al.* 1978, *Nature*, **275**, 298.

SPECTRAL-LUMINOSITY EVOLUTION OF ACTIVE GALACTIC NUCLEI AND THE COSMIC X- AND GAMMA RAY BACKGROUND

Darryl Leiter, FSTC, Charlottesville, VA 22901
Elihu Boldt, NASA/GSFC, Greenbelt, MD 20771

ABSTRACT

Coherent electromagnetic dynamo acceleration processes, which act on charged particles within the context of black hole accretion disk scenarios, are generally regarded as the underlying central power source for active galactic nuclei (AGN) (Rees 1984). If the precursor active galaxies (PAG) for such AGN are formed at high redshift and contain initial seed black holes with mass $\sim 10^4$ solar masses, then the Eddington limited X-ray radiation emitted during their lifetime will undergo the phenomenon of "spectral-luminosity evolution". When accretion disks are first formed at the onset of galaxy formation the accretion rate occurs at very high values of luminosity/size compactness parameter $L/R > 10^{30}$ erg/cm-sec. In the absence of extended structure, such high values of L/R generate dynamic constraints (Cavaliere & Morrison, 1980; Guilbert, Fabian, & Rees, 1983) which suppress coherent, black-hole/accretion disk dynamo particle acceleration processes. This inhibits nonthermal radiation processes and causes the spectrum of X-radiation emitted by PAG to be predominantly thermal. A superposition of PAG sources at $z \gtrsim 6$ can account for the residual cosmic X-ray background obtained from the total cosmic X-ray background (CXB) after subtraction of foreground AGN sources associated with present epoch Seyfert galaxies (Leiter & Boldt 1982 ,1990); (Boldt & Leiter 1984, 1986, 1987); (Zdziarski 1988). At the end of the PAG lifetime the compactness parameter of the black hole-accretion disk dynamo system falls below $\sim 10^{30}$ erg/cm-sec and coherent dynamo acceleration processes for charged particles become dominant. Under these conditions the black-hole/accretion disk dynamo system can create localized clouds of nonthermal electron-positron pairs above the accretion disk via the photon-photon --> electron-positron process. Because these clouds of electron-positron pairs gain their energy from an incoherent acceleration process above cool regions of the accretion disk, the cloud compactness can exceed $\sim 10^{30}$ erg/cm-sec while still generating a broad band of nonthermal radiation, including X-rays and gamma rays. In this manner the PAG undergo spectral-luminosity evolution into Seyfert galaxies whose spectral structure includes Compton reflection processes from regions of cool matter. (Zdziarksi et.al, 1990, 1991).

I. PRECURSOR ACTIVE GALAXIES (PAG) AND THE CXB

PAG initially undergo Eddington limited accretion. Since the hard X-radiation from thermal processes in the PAG accretion disk comes from a region on the order of 10 gravitational radii, L/R can be written in terms of L/L_{Edd} as

$$L/R = (L/L_{Edd})\ 10^{32} \quad erg/cm\text{-}sec \tag{1}$$

where

$$L_{Edd} = 4\pi GMm_p c/\sigma_T \tag{2}$$

is the Eddington luminosity, σ_T is the Thomson scattering cross section, m_p is the proton mass, M is the mass of the central black hole, G is the gravitational constant and c is the speed of light.

Since $L/R > 10^{30}$ erg/sec the PAG emit a flat comptonized spectrum with exponential roll-off energy and spectral index on the order of $E \cong 160$ KeV and $\alpha \cong 0$ respectively (Zdziarski 1988). In this context the observed redshifted PAG exponential roll-off energy and roll-off spectral index are consistent with the observational constraints associated with the residual CXB (Leiter & Boldt 1982) given by

$$23\ KeV \leq E/(1+z) \leq 35\ KeV, \qquad 0 \leq \alpha \leq 0.2 \tag{3}$$

For Eddington limited accretion the initial PAG black hole mass M_i increases exponentially to M_{PAG}. This is given by

$$M_{PAG} = M_i \exp(A_{PAG}\ \Delta t_{PAG}) \tag{4}$$

$$A_{PAG} = 30\ (\ (1 - \epsilon)/\epsilon\ )\ . \tag{5}$$

In the above Δt_{PAG} is the Eddington limited lifetime of the PAG phase in units of $(2/3H_o) = 1.3 \cdot 10^{10}$ years, corresponding to H_o=50 km/(sec-Mpc), and $\epsilon \lesssim 0.3$ is the accretion disk mass-energy conversion efficiency (Thorne 1974).

If z_{MAX} is the maximum redshift associated with the onset of the PAG and z_{MIN} is the minimum redshift for this population, corresponding to the associated onset of daughter AGN such as Seyfert galaxies, then the relationship between light-travel lookback times $t_{MAX,MIN}$ in $(2/3H_o)$ units and redshifts $z_{MAX,\ MIN}$ is given by

$$t_{MAX\ ,\ MIN} = [\ 1 - (1+z_{MAX\ ,\ MIN})^{-3/2}\ ]\ . \tag{6}$$

In this context the total PAG lifetime is given by the relation

$$\Delta t_{PAG} = (\ t_{MAX} - t_{MIN}\ )\ . \tag{7}$$

For $z_{MIN} < z < z_{MAX}$, the surface density of PAG sources

is given by

$$\sigma_{PAG} = [\ \sigma(t_{MAX}) - \sigma(t_{MIN})\ ] \text{ sources/deg}^2 \quad (8)$$

$$\sigma(t) = (1.75\ 10^4 \cdot (N_o(PAG)/10^{-4}\ Mpc^{-3}))\ [\ t+3(1-t)^{2/3}-3(1-t)^{1/3}\ ] \quad (9)$$

$N_o(PAG)$ Mpc^{-3} is the constant co-moving density of PAG, and observational constraints on the flucuations in the CXB (Hamilton, Helfand 1987) require the surface density of PAG sources in equation (8) to be greater than 5000 sources/deg.

The ensemble averaged proper bolometric PAG luminosity, emitted in the form of an X-ray spectrum during the Eddington limited PAG lifetime, is

$$L_{PAG}(t) = 13 \cdot 10^{45}\ (M_i/10^8\ M_o)\ \exp(\ A_{PAG}(t_{MAX}-t)\ ) \quad \text{erg/sec.} \quad (10)$$

where M_i is in units of solar mass (M_o).

Using $\Omega = 1$ and $h_{50} = 1$, and equation (6) and (10) to obtain the PAG luminosity evolution function $L_{PAG}(z)$, the total PAG energy flux, in erg/cm^2 -sec-sr, contributed to the RCXB is

$$I_{PAG} = (3t_oc/8\pi)\ N_o(PAG) \cdot \int_{z_{MIN}}^{z_{MAX}} dz(\ L_{PAG}(z)/(1+z)^{-3.5}\ ) \quad (11)$$

where $t_o = 2/3H_o$.

The differential PAG energy flux in units of erg/cm^2 -sec-sr-erg, whose integral yields equation (11) is given by

$$I_{PAG}(E) = (3t_oc/8\pi)\ N_o(PAG) \cdot \int_{z_{MIN}}^{z_{MAX}} dz(\ L_{PAG}(z) \cdot S_{PAG}(E(1+z),\ \alpha)\ /(1+z)^{-2.5}\ ) \quad (12)$$

In (11) and (12) the Eddington limited PAG luminosity evolution function $L_{PAG}(z)$ is obtained from (6) and (10), and the Eddington limited PAG X-ray source spectral function $S(E,\alpha)$ is given by (Zdziarski 1988) as

$$S_{PAG}(E,\ \alpha) = [W_o^{\alpha-1}/\Gamma(1-\alpha)] \cdot E^{-\alpha}\exp(-E/W_o) \quad (13)$$

153 KeV $\leq W_o \leq$ 165 KeV, $0.07 \leq \alpha \leq 0.17$. Note that on the basis of HEAO-1 observations equation (11) obeys the constraint $I_{PAG} \lesssim 2.2\ 10^{-7}$ erg/cm^2-sec-sr.

II. SPECTRAL-LUMINOSITY EVOLUTION OF PAG INTO SEYFERT GALAXIES

At the end of the PAG lifetime the overall compactness parameter L/R of the black-hole/accretion disk dynamo system falls below 10^{30} erg/cm-sec and globally coherent dynamo

acceleration processes for charged particles become dominant. Under these conditions the coherent accretion disk dynamo system can create localized regions of nonthermal electron-positron pairs above the accretion disk, which generate a broad band of nonthermal radiation including X-rays and gamma rays, and the PAG undergo spectral-luminosity evolution into Seyfert galaxies (Zdziarksi et al, 1990, 1991). To see this more specifically we convert the Compactness Parameter L/R (erg/cm-sec) into a dimensionless compactness quantity

$$l = (L/R) \cdot (\sigma_T/mc^3) , \qquad (14)$$

When the appropriate fundamental constants are inserted

$$l = 2.3 \cdot 10^3 \cdot (L/LEdd) \; / \; (R_*/10) \qquad (14\text{-a})$$

where $R_* = R/r_G$, and $r_G = GM/c^2$ is the gravitational radius. Solving (14) for L/R we have

$$L/R = (3.8 \cdot 10^{28}) \cdot l \quad \text{erg/cm-sec.} \qquad (14\text{-b})$$

Equations (14-a,b) are used in the analysis which follows.

A. PAG State

In the case of an Eddington limited PAG there is no extended structure above the black-hole/ accretion disk dynamo and most of the hard radiation is emitted from a hot inner region of the disk of size on the order of 10 gravitational radii. Hence for a PAG it follows that $R_* \cong 10$, $L/LEdd \cong 1$. From (14-a,b) we see that this implies that the PAG dimensionless compactness is ~ 2300 which is equivalent to $L/R \cong 8.8 \cdot 10^{31}$ erg/cm-sec. Hence coherent nonthermal dynamo particle acceleration processes are inhibited (Cavaliere & Morrison 1980) and the Eddington limited PAG emits thermalized X-radiation (Zdziarski 1988) similar to that of the CXB as described in section I.

B. Seyfert AGN State

At the end of the PAG lifetime the Eddington ratio falls to $L/LEdd \lesssim 0.1$ and at the same time the black-hole/accretion disk develops extended structure above the accretion disk such that $R_*(\text{dynamo}) \cong 10^3$. The dimensionless compactness of the dynamo falls to values $\lesssim 23$ and $L/R \lesssim 10^{30}$ erg/cm-sec allows coherent dynamo particle acceleration processes to become dominant. The coherent, nonthermal particle acceleration processes in the black-hole\accretion disk dynamo running at such a low dimensionless compactness produce clouds of nonthermal electron-positron pairs above the cool regions of the accretion disk. Black-hole/accretion disk dynamo processes lead to hard photons that produce such clouds via pair cascades resulting from their interaction with soft photons radiated by the accretion

disk (Begelman, Blanford, Phinney 1982).

$$\gamma_{hard} + \gamma_{soft} \text{ -----> } e^+ + e^- \ .$$

Because of the incoherent nature of the photon-photon pair production process as a charged particle acceleration mechanism, these highly compact (i.e. size $R_* \hat{=} 10$, dimensionless compactness $\lesssim 230$, $L/R \gtrsim 10^{31}$ erg/cm-sec) clouds of electron-positron pairs above the black-hole/accretion disk dynamo are not constrained by the coherent acceleration limitations associated with the $\sim 10^{30}$ erg/cm-sec criteria discussed in section I. Hence they can generate via Comptonization and Compton reflection the nonthermal X-ray and gamma ray emission spectra similar to that of Seyfert AGN (Zdziarski 1990, Zdziarski et al. 1991). In addition the Seyfert galaxies which emerge may emit Penrose Compton Scattering (PCS) gamma ray transients (Leiter 1980, Leiter & Boldt 1990) with time variabilty on the order of hours, which have a kinematic cutoff in the spectrum $\lesssim$ 3 MeV. In this context the OSSE/COMPTEL instruments on the Gamma Ray Observatory (GRO) are appropriate instruments to carry out further tests of this model.

III. THE PAG-SEYFERT SPECTRAL EVOLUTION MODEL FOR THE CXB

If the PAG-Seyfert spectral evolution occurs in a supply limited regime similar to that described by low luminosity galaxy evolution models (Murphy, Cohn, and Durisen 1991), the supply limited luminosity evolution of Seyfert galaxies is given over the redshift region $0 \lesssim z \lesssim z_{MIN}$ by

$$L_{SEY}(z) = L_{SEY} \cdot f(z) \qquad (15\text{-a})$$

$$L_{SEY} = 13 \cdot 10^{45} \, (M_{PAG}/10^8) \, \lambda_{SEY} \quad \text{erg/sec.} \qquad (15\text{-b})$$

$$f(z) = [\ \{(1+z_{MIN})^{\beta} \cdot \phi(z_{MIN}-z) \cdot \phi(z-z_{ZMIN}+\Delta z)\} + \{(1+z)^{\beta} \cdot \phi(z_{MIN}-\Delta z-z) \cdot \phi(z)\}\ ] \qquad (15\text{-c})$$

in (15), M_{PAG} is in solar masses, $\phi(z)$ is the step function and the $\beta \hat{=} 2$ and $\Delta z \hat{=} 3.7$ for the case of a supply limited accretion regime which is dominated by stellar mass loss mechanisms. Figure 1-a shows the total luminosity evolution function $L(z)$, $(0 \lesssim z \lesssim z_{MAX})$ where $L(z) = L_{PAG}(z) + L_{SEY}(z)$.

We assume that the Seyfert source spectral function $S(E,\alpha)$ has the observed Seyfert -0.7 power law structure given by

$$S_{SEY}(E,\alpha) = (0.083)/(1.6 \cdot 10^{-3}) \cdot (E/3)^{-0.7} \qquad (15\text{-d})$$

Then in a manner similar to the case of the PAG in (12) and (13), we calculate the differential energy flux from a superposition of Seyferts which have evolved from PAG at $z = z_{MIN}$ to the present epoch as given by

$$I_{SEY}(E) = (3t_0c/8\pi)\, N_0(SEY) \cdot \int_0^{z_{MIN}} dz\; L_{SEY}(z) \cdot S_{SEY}(E(1+z), \alpha)\; /(1+z)^{-2.5} \qquad (15\text{-e})$$

Padovani, Burg & Edelson (1990) suggest that the low value observed for the average Seyfert central black hole mass $\sim 2 \cdot 10^7$ Mo favors scenarios in which AGN activity occurs in recurrent bursts over time intervals $\sim 10^8$ years. We adopt this point of view and assume that supply-limited Seyfert AGN activity cycles "on-off" in a quasi-periodic manner related to internal galactic accretion instabilities (Shlosman, Begelman & Frank 1990). If the number of "on-off" cycles of the Seyfert galaxy from light travel look-back time t_{MIN} to the present epoch is given by "n", and the "on time" and "off-time" per Seyfert cycle are given respectively by Δt_{SEY-ON}, $\Delta t_{SEY-OFF}$ then

$$t_{MIN} = n \cdot (\Delta t_{SEY-ON} + \Delta t_{SEY-OFF}) \quad . \qquad (16)$$

Because Seyfert activity cycles on and off stochastically, the observed co-moving density of Seyfert galaxies in the "on" state is equal to the product of the co-moving density of PAG times the probability of a Seyfert being "on" during t_{MIN}, viz:

$$N_0(SEY) = N_0(PAG) \cdot ((n\, \Delta t_{SEY-ON}) / t_{MIN}). \qquad (17)$$

Note that (17) implies that $N_0(PAG) > N_0(SEY)$. In this context the mass of the Seyfert central black hole in the present epoch is given by

$$M_{SEY} = M_{PAG} (1 + A_{SEY} \cdot n \cdot \Delta t_{SEY-ON}) \qquad (18)$$

$$A_{SEY} = (30\, L(SEY)/LEdd) \cdot ((1 - \epsilon) / \epsilon) \quad . \qquad (19)$$

IV. TECHNIQUES FOR SOLVING THE PAG-SEYFERT MODEL EQUATIONS

(a) We assume a $\gtrsim$ 10% foreground contribution to the CXB from Seyfert galaxies with no luminosity evolution (i.e. $f(z) = 1$ in equation (15-c), and the inputs:

$$N_0(SEY) \gtrsim 2\ 10^{-4}\ Mpc^{-3}, \quad M_{SEY} \cong 2 \cdot 10^7\ M_0,$$

$$L(SEY)/LEdd \gtrsim 10^{-2}, \quad \Delta t_{SEY-ON,OFF} \lesssim 10^8 \text{ years} .$$

Then we use the Newton-Raphson variation method to solve equations (1)-(19) to determine an initial range of acceptable output parameters, assuming no Seyfert evolution (i.e. f(z) = 1) in (15-c). With the above inputs we calculate the outputs:

$z_{max} \gtrsim 6, \quad z_{min} \gtrsim 4, \quad No(PAG) \gtrsim 10^{-3},$

$M_i \cong 10^4 M_o, \quad \Delta t_{PAG} \cong 5\ 10^8$ years, $\quad \langle L_{PAG} \rangle \cong 10^{45}$ erg/sec

(b) Using the parameters determined above, and now taking into account the full Seyfert galaxy luminosity evolution f(z) given in equation (15-c), we calculate the foreground Seyfert differential energy flux $I_{SEY}(E)$ given by (15-e). Then the total differential energy flux is

$$I_{CXB}(E) = I_{PAG}(E) + I_{SEYFERT}(E) \qquad (20)$$

Using (20), and varying the parameters about values determined in (a), an excellent fit of the PAG-SEYFERT spectral evolution model to the observed CXB differential energy flux (erg/erg-cm^2 -sec-sr)

$$I_{CXB}(E) = 5.7 \cdot (E/3KeV)^{-0.25} \cdot \exp(-E/40Kev) \qquad (21)$$

over (3 KeV $\lesssim$ E $\lesssim$ 50 KeV) can be obtained as shown in figure 1-b.

REFERENCES

Begelman, M.C., Blandford, R.D., & Phinney, E.S., 1982, NATURE, 295, 17.295, 17.

Boldt, E., 1987, "Cosmic X-ray Background", Physics Reports, 146,215

Boldt, E., Leiter, D, 1987, Ap. J., 322, 689; 1986, Struc. & Evol. of AGN (Reidel 1986), 383; 1984, Ap. J., 276, 427.

Cavaliere, A., Morrison, P., 1980, Ap. J., 238, L63.

Guilbert, P.W., Fabian, A.C., Rees, M.J., 1983, M.N.R.A.S., 205, 593.

Hamilton, T., Helfand, D., 1987, Ap. J. 318, 93.

Leiter, D., Boldt, E., 1990, "After the First Three Minutes" PROC. AIP ,222, 339; 1982, Ap. J., 260, 1; 1989, "Proc. GRO Science Workshop, 4-14"; 1990,"GRO-Egret Science Symposium", NASA Conf. Pub. 3071, 277.

Leiter, D., 1980, Astr. Ap., 89, 370.

Murphy, B.W., Cohn, N.H., & Durisen, H.D., 1991, Ap. J., 379, 60.

Padovani, P., Burg, R., Edelson, R.A. 1990, Ap. J., 353, 438.

Rees, M.J., 1984, Ann. Rev. Astr. & Ap., 22, 471; Rees, M.J., Shlosman, I., Begelman, M.C., Frank, J., 1990, NATURE, 345, 679.

Thorne, K, 1974, Ap. J., 191,507.

Zdziarski, A.A., 1988, M.N.R.A.S., 233, 739; 1990.

Zdziarski, A.A. Ghisellini, G., George, I.M., Svensson, R, Fabian, A.C., & Done, C., 1990, Ap.J., 363. L1.

Zdziarski, A.A., Coppi, S., 1991, Ap. J., 376,480.

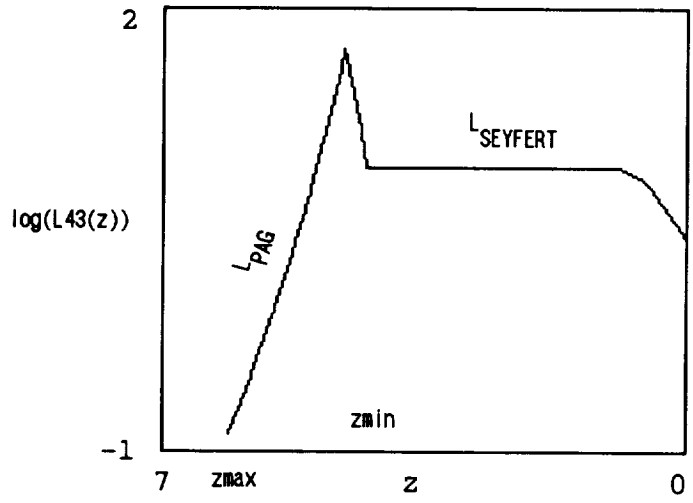

Figure 1-a. Logarithmic Plot of the Luminosity Function L43(z) (Associated With Eddington Limited PAG -- Supply Limited Seyfert Spectral Evolution) Is Similar to That of Low Luminosity Galaxy Evolution Models of Murphy, Cohn, & Durisen (1991)

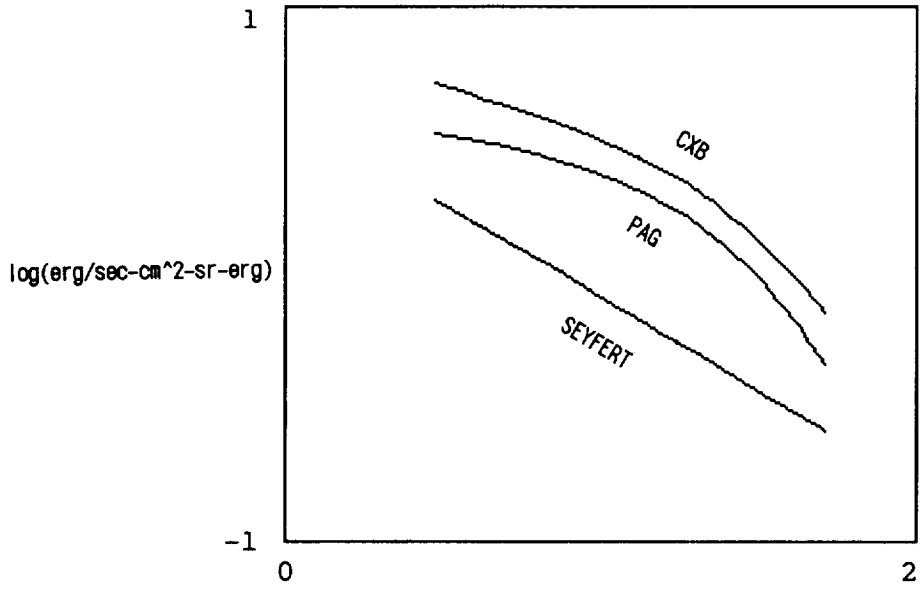

Figure 1-b. Model Fit of PAG + SEYFERT = CXB Spectra Within 2% Error Associated With: Luminosity Evolution Function L43(z) In Figure 1-a. And a 36% Seyfert X-ray Foreground At 3 KeV, zmax = 6.12, zmin = 4.46, $M8_i$ = 0.0001, ϵ = 0.1 W_0 = 153 KeV, α = 0.07, No(SEY) = 0.0004 1/Mpc^3, $M8_{Sey}$ = 0.23

6.
NOVA AND SUPERNOVA

X-RAY AND GAMMA-RAY EMISSION FROM CLASSICAL NOVA OUTBURSTS

James W. Truran
Department of Astronomy and Astrophysics
Enrico Fermi Institute
University of Chicago

Sumner Starrfield
Department of Physics and Astronomy
Arizona State University

and

Warren M. Sparks
Los Alamos National Laboratory

ABSTRACT

The outbursts of classical novae are now recognized to be consequences of thermonuclear runaways proceeding in accreted hydrogen-rich shells on white dwarfs in close binary systems. For the conditions that are known to obtain in these environments, it is expected that soft x-rays can be emitted, and indeed x-rays have been detected from a number of novae. We will describe the circumstances for which we expect novae to produce significant x-ray fluxes and provide estimates of the luminosities and effective temperatures. We now also know that, at the high temperatures that are known to be achieved in this explosive hydrogen-burning environment, significant production of both ^{22}Na and ^{26}Al will occur. In this context, we identify the conditions for which gamma-ray emission may be expected to result from nova outbursts.

I. INTRODUCTION

It is now well established that the outbursts of the classical novae result from thermonuclear runaways in accreted hydrogen shells on white dwarfs in close binary systems (see, e.g. the reviews by Truran 1982; Starrfield 1989; Shara 1989). The temperatures that are typically achieved at the peak of the outburst, 200-300 million degrees Kelvin, drive explosive (hydrogen) burning of the available nuclear fuel and allow the formation of significant abundances of the interesting radioactive nuclei ^{22}Na ($\tau_{1/2}$ = 2.6 years) and ^{26}Al($\tau_{1/2}$ = 7.2 x 10^5 years). It follows that novae in outburst might yield detectible flux levels of decay gamma rays from ^{22}Na and that they may also contribute to the observed level of ^{26}Al decay gamma rays in the Galaxy. During the later stages of the outbursts, the effective temperatures characteristic of the hydrogen burning white dwarf remnants will evolve to values in excess of 200 thousand degrees

Kelvin, as the surface radius retreats with progressive depletion of the residual hydrogen fuel. Photospheric temperatures in this range, together with the fact that nuclear burning on white dwarfs proceeds at luminosities near Eddington, would allow an understanding of the levels of x-ray emission observed by EXOSAT for several novae.

The aim of this paper is to identify and to discuss the characteristics of the outbursts of the classical novae that dictate the expected levels and timescales of x-ray and gamma-ray emission. A brief review of the salient features of the thermonuclear runaway model for classical nova explosions is presented in the next section. The observational situation regarding x-rays and gamma rays from novae is reviewed in section III. Theoretical expectations for x-ray and gamma-ray emission and the possible interpretation of the observed soft x-ray output of classical novae are presented in section IV. Theoretical expectations concerning the detection of ^{22}Na and ^{26}Al gamma ray lines from novae are then discussed in section V. A brief summary and conclusions follow.

II. THE THERMONUCLEAR RUNAWAY MODEL

The outbursts of classical novae are a consequence of thermonuclear runaways occurring in accreted hydrogen shells on white dwarfs. The runaway is generally initiated at or near the base of the accreted envelope, when a critical pressure is achieved. The high temperatures typically achieved in the burning regions, ~ 1.5-3 x 10^8 K, drive convection, which is efficient in transporting the released nuclear energy to the surface. During the earliest stages of the runaway, the convective burning shell extends outward to encompass the entire envelope. The convective timescale characteristic of nova envelopes is well less than a day. This ensures the realization of a luminosity approaching or exceeding the Eddington limit, ~ 2-4 x 10^4 $L_\odot$, on a rapid timescale with respect to the timescale of envelope expansion, and therefore of a high effective temperature, ~ 5 x 10^5 K. During this early (pre-maximum) phase, novae are therefore expected to be soft x-ray sources and UV sources.

Convection at this stage also acts to mix the products of thermonuclear burning, in the shell source to the surface. In this instance, substantial quantities of the short-lived positron-unstable products of explosive hydrogen burning, ^{13}N, ^{14}O, ^{15}O, ^{17}F, and ^{18}F, can be transported to the surface. Decay of these radioactive isotopes in the surface regions, occurring in novae prior to the realization of visual maximum, can possibly produce a strong gamma-ray flux (Leising and Clayton 1987). We should also note that these same explosive hydrogen burning conditions can result in the production of significant concentrations of the longer lived radioactivities ^{22}Na and ^{26}Al, as will be discussed further in a later section.

Hydrodynamic studies of nova eruptions predict that, following runaway, and a relatively brief phase of evolution at luminosities that can exceed Eddington (Truran 1982), shell hydrogen burning of the residual matter defines a phase of evolution characterized by a constant bolometric luminosity. During this phase, there occurs a gradual hardening of the spectrum with time, as the photospheric

radius decreases slowly with the depletion of the envelope mass. Classical novae will then become, progressively, first strong ultraviolet sources and then soft x-ray sources. Both the timescale for the realization of the stage of soft x-ray emission, and the timescale for the duration of this stage, are dependent upon the mass of the underlying white dwarf and the efficiency of mass loss mechanisms in depleting the hydrogen envelope mass (MacDonald, Fujimoto, and Truran 1985). It is this stage of soft x-ray emission that, presumably, was detected and identified with EXOSAT for several recent novae (Ögelman, Krautter, and Beuermann 1987). Following the depletion of the envelope fuel and the termination of shell hydrogen burning, the nova white dwarf remnant evolves rapidly to minimum along a path consistent with evolution to lower luminosity at constant radius.

III. OBSERVATIONS OF X-RAYS AND GAMMA RAYS

Observations of classical novae at x-ray wavelengths have been performed to date both with Einstein and with EXOSAT. Einstein detections include V841 Oph 1848, V1059 Sgr 1898, GK Per 1901, V603 Aql 1918, RR Pic 1925, CP Pup 1942, RR Tel 1946, and V1500 Cyg 1975 (Becker 1989; Ögelman 1990). These include novae ranging in speed class from slow to very fast, with no apparent correlation. Of these, only RR Tel 1946 and V1500 Cyg 1975 can be said in any sense to have been observed in outburst; RR Tel is an extremely slow nova, often referred to as a symbiotic nova, which still exhibits a rich ultraviolet spectrum, while V1500 Cyg was observed approximately 1000 days into its outburst.

The EXOSAT detections of x-rays from the three classical novae GQ Mus 1983, PW Vul 1984, and QU Vul 1984 (Ögelman, Krautter, and Beuermann 1987) comprise the most comprehensive study of novae and provide extremely interesting and important constraints on the late evolution of classical novae in outburst. The data for PW Vul and QU Vul both indicate a rise in the x-ray flux occurring on a timescale of less than approximately one year, while the emission from GQ Mus is seen to remain roughly constant over the second year of it's outburst, following which it falls on approximately the same timescale. The fact that the rise in the x-ray luminosity occurs so early in the outburst, and ultimately disappears on a timescale of several years, confirms a rapid evolution of novae in outburst consistent with the fact that the mean mass of classical novae observed in outburst is rather high, of order 1.2 solar masses (Truran and Livio 1986, 1989; Ritter et al. 1991). The level of x-ray emission detected is also consistent with the fact that a significant fraction of the nova luminosity appears in the soft x-ray regime (Ögelman, Krautter, and Beuermann 1987).

The observational situation with regard to gamma rays from classical novae may be summarized very rapidly. ^{22}Na decay gamma rays have not yet been detected from any nova in outburst, although we now expect that such detection may be possible with GRO. Alternatively, gamma rays from ^{26}Al decay have been detected (Mahoney et al. 1982, 1984), but the nucleosynthesis site for ^{26}Al production has not been clearly identified. These issues will be discussed further in section V.

IV. THEORETICAL EXPECTATIONS FOR X-RAYS AND GAMMA RAYS

X-rays

The evolution of a nova through its outburst that we have outlined above reveals that novae may be expected to be sources of soft x-ray (and EUV) emission in two distinct phases. Soft x-ray emission arises here when photospheric effective temperatures typically exceeding approximately 200,000 K are achieved in hydrogen shell burning at near Eddington luminosities. A brief early phase (occurring prior to maximum) and an extended late phase of such x-ray emission are expected.

The early phase of emission is associated with the early dynamic phase prior to the achievement of visual maximum. When the convective region driven by the thermonuclear runaway in the shell source first reaches the surface, the high luminosity (near to or even exceeding the Eddington limit) and small radius (of order 10^9 cm) imply a photospheric temperature of some hundreds of thousands of degrees. Indeed, for a white dwarf of mass approaching the Chandrasekhar limit, a photospheric temperature exceeding a million degrees is expected.

Unfortunately, this phase of evolution is found to be of extremely short duration. The large energy deposition into the nova envelope by convection triggers a rapid expansion of the envelope, an increase in the radius of the photosphere, and a concomitant decrease in T_{eff}. A typical expansion velocity of $10^7 - 10^8$ cm s^{-1}, for example, would yield a radius in excess of 10^{11} cm on a timescale of less than a day; at this radius, T_{eff} has fallen below 100,000Kand significant soft x-ray emission does not occur. Such an event, if detectable by a sensitive all sky survey, would appear as a very soft x-ray transient.

The second and more extended period of soft x-ray and EUV emission occurs subsequent to visual maximum, when all novae are found to experience a phase of evolution at constant bolometric luminosity associated with hydrogen shell burning at near Eddington luminosities. The timescale of this phase is a function of the timescale for the depletion of the residual envelope hydrogen by some yet undetermined combination of nuclear burning, wind-driven mass loss, and common-envelope driven mass loss (see, e.g. the discussion by MacDonald, Fujimoto, and Truran (1985)). As the envelope mass is depleted, the photospheric radius decreases and consequently the photospheric temperature rises; this ultimately gives rise to a hardening of the radiation to UV, EUV, and soft x-ray wavelengths. Theoretical estimates of the time required to reach temperatures consistent with x-ray emission are very uncertain. It is therefore necessary to rely on observations to determine this timescale and thereby impose critical constraints on theoretical models. The x-ray observations of several recent novae with EXOSAT (Ögelman, Krautter, and Beuermann 1987), now seem to have identified this second phase of soft x-ray emission from classical novae.

Gamma rays

Considerations of gamma-ray emission from classical novae are primarily concerned with gamma-ray line emission from the radioactive nuclei ^{22}Na (2.6

years) and ^{26}Al (7.2×10^5 years), which are known to be formed under the high temperature hydrogen burning conditions associated particularly with the peak of the thermonuclear runaway. Clayton and Hoyle (1974) first noted that individual novae might produce detectible flux levels of ^{22}Na decay gamma rays, and recent calculations (Weiss and Truran 1990; Politano, Starrfield, Truran, Sparks, and Weiss 1991) provide estimates of ^{22}Na production at levels sufficient to allow the detection of gamma rays from nearby novae. Significant ^{26}Al production can also be expected to occur, but it currently appears unlikely that ^{26}Al produced in novae can have contributed significantly to the flux of ^{26}Al decay gamma rays detected by Mahoney et al. (1982,1984). These issues will be discussed at greater length in section V.

We also note, again, that there exists the possibility of an early phase of gamma-ray emission from novae in outburst, driven by the decay of the short lived radioactivities ^{13}N, ^{14}O, ^{15}O, ^{17}F, and ^{18}F in the outermost regions of the nova envelope (Leising and Clayton 1987). A further investigation of this problem is now in progress, based upon an improved treatment of the thermonuclear reaction sequences leading to the production of these isotopes.

V. ^{22}Na and ^{26}Al DECAY GAMMA RAY LINES

Several recent papers have addressed the question of ^{22}Na and ^{26}Al production in classical nova explosions. Weiss and Truran (1990) and Nofar, Shaviv, and Starrfield (1991) have calculated nucleosynthesis accompanying nova explosions for representative temperature histories extracted from hydrodynamic models. These studies confirmed the findings of earlier work (Hillebrandt and Thielemann 1982; Wiescher et al. 1986) that only relatively low levels of ^{22}Na and ^{26}Al are formed in nova envelopes of initial solar composition and revealed, alternatively, that significantly increased ^{22}Na and ^{26}Al production can occur in envelope matter characterized by large initial concentrations of elements in the range from neon to aluminum.

The significance of this latter finding arises from the fact that the ejecta of a significant fraction of well studied novae are found to be enriched in nuclei in the Ne-Al region (see e.g. the review by Truran 1990). Since the source of these large abundance enrichments is assumed to be matter dredged up from the underlying white dwarf, this is taken to reflect the fact that such systems involve massive oxygen-neon-magnesium (ONeMg) white dwarfs, rather than CO white dwarfs. It is understood that the relatively large observed number of such massive systems is a natural consequence of selection effects (Truran and Livio 1986): more massive white dwarfs require less accreted matter (hence shorter accretion phase timescales) to achieve runaway conditions. Indeed, a more careful analysis by Ritter et al. (1991) now indicates that a fraction 0.32-0.65 of all systems observed in outburst may be expected to involve ONeMg white dwarfs.

Specific estimates of ^{22}Na and ^{26}Al synthesis are provided by the calculations of Weiss and Truran (1990). They obtain ^{22}Na mass fractions as high as 10^{-4}, for an assumed ONeMg enrichment at a level 0.25 by mass of the ejecta, and values

exceeding 10^{-3} when the ONeMg mass fraction is taken to be 0.75. The corresponding concentrations achieved for ^{26}Al for the same two levels of ONeMg enrichment are 10^{-3} and 10^{-4}, respectively. These high levels of production of ^{22}Na and ^{26}Al associated with the ONeMg enrichment of nova envelopes have now been confirmed by detailed studies of nova nucleosynthesis performed with large nuclear reaction networks coupled directly to the hydrodynamics (Politano et al. 1991). We now briefly consider the implications of these findings for observational studies with the Compton Gamma Ray Observatory.

The principal question of interest regarding ^{26}Al is whether novae can have contributed significantly to the production of the 3 $M_\odot$ of ^{26}Al in the Galaxy that is required to explain the 1.809 MeV gamma ray line emissions reported by Mahoney et al. (1982, 1984). The mass of ^{26}Al in the Galaxy that is attributable to nova explosions can be estimated from the following expression (Weiss and Truran 1990):

$$M_{26} = 0.4\ M_\odot \left(\frac{R_{nova}}{40\ yr^{-1}}\right) \left(\frac{f_{26}}{0.25}\right) \left(\frac{M_{ej}}{2 \times 10^{-5}\ M_\odot}\right) \left(\frac{X_{26}}{2 \times 10^{-3}}\right)$$

Here, we have assumed a rate of occurrence of nova events of 40 yr^{-1}, a fraction 0.25 of all nova events that produce ^{26}Al, an ejected mass of 2×10^{-5} $M_\odot$ per event, for these more massive systems, and a ^{26}Al mass fraction in the ejecta of 2×10^{-3}. This result clearly falls short of the approximately 3 $M_\odot$ required to account for the gamma ray observations. It would thus appear that some other source, e.g. supernovae or, more likely, red giant stars, must be the dominant source. Information concerning specifically the distribution of ^{26}Al in the Galaxy may ultimately be able to distinguish between these possible sources.

The high levels of ^{22}Na that our calculations indicate may characterize the ejecta of ONeMg enriched novae, allowing the exciting possibility that such novae can produce detectable flux levels of 1.275 MeV gamma rays from ^{22}Na decay. The predicted flux is given by

$$F_{1.275} = 1.6 \times 10^{-4}\ cm^{-2}\ sec^{-1} \left(\frac{e^{-t/3.75}}{(D/500pc)^2}\right) \left(\frac{M_{ej}}{10^{-4}\ M_\odot}\right) \left(\frac{X_{22}}{10^{-4}}\right)$$

where M_{ej} is the total mass of nova ejecta and X_{22} is the mass fraction of ^{22}Na in the ejecta. The specific choices of $X_{22} = 2 \times 10^{-4}$ and $M_{ej} = 2 \times 10^{-5}$ correspond to reasonable (but not extreme) estimates, for the ONeMg enriched novae in which the ^{22}Na is most likely to be synthesized in significant quantities.

The strategy with regard to searches for 1.275 MeV ^{22}Na decay gamma rays from novae thus seems clear. If one knows from early observations both that a nova is at a distance less than approximately one kiloparsec and that its

envelope is significantly enriched in neon and magnesium, it follows that it constitutes a more promising target. We also call attention to the fact that the radioactive decay of ^{22}Na may play an interesting role in the production of hard x-rays, particularly in novae enriched in oxygen, neon, and magnesium (Livio et al. 1991).

VI. CONCLUSIONS

Conclusions to be drawn from these considerations of classical nova outbursts include the following.

1) Significant x-ray and gamma-ray emission is expected to accompany the outbursts of classical novae. X-rays have been observed, while gamma rays have not been detected to date.

2) Soft x-ray emission is expected to be associated with nova outbursts, as effective photospheric temperatures exceeding 300,000 K will be achieved in the presence of shell hydrogen burning at luminosities approaching Eddington on the white dwarf. A brief period of x-ray emission may occur early, prior to optical maximum. A more extended phase of x-ray emission is expected to occur in the late stages of evolution at constant bolometric luminosity, as the white dwarf surface retreats with the exhaustion of the envelope matter.

3) The observed features of this late phase of x-ray emission – an increase on a timescale of 300–500 days, to a plateau which lasts approximately 300–500 days, followed by a decay (Ögelman et al. 1987) – have been interpreted by Truran and Livio (1991) as due to an early epoch of rapid (common envelope driven) mass loss followed by a phase of nuclear burning through fuel exhaustion.

4) The hot hydrogen burning conditions achieved at the peak of the thermonuclear flashes in novae are consistent with the synthesis of concentrations of both ^{22}Na and ^{26}Al. The levels of production of these isotopes are sensitive functions of both the peak temperature achieved and the level of enrichment of heavy elements in oxygen, neon, and magnesium.

5) The observed level of ^{26}Al in the Galaxy is unlikely to have arisen from classical novae. We estimate that only perhaps 10 percent of the observed ^{26}Al can have been synthesized in this environment.

6) Our estimates of ^{22}Na and ^{26}Al emission are strongly dependent upon the strength and extent of convective mixing during the course of the nova outburst. The detection of ^{22}Na gamma rays from novae could therefore provide interesting constraints on the convective history of the nova envelope and on our theoretical modeling of convective mixing.

ACKNOWLEDGEMENTS

This work was supported in part by NSF and NASA grants to the University of Illinois and Arizona State University and by the DOE.

REFERENCES

Becker, R.H. 1989, in Classical Novae, ed. M.F. Bode and A. Evans (New York: Wiley), 215

Hillebrandt, W. and Thielemann, F.-K. 1982, Ap.J., *255*, 617

Leising, M.D. and Clayton, D.D. 1987, Ap.J., *323*, 159

Livio, M., Mastichiadis, A., Ögelman, H., and Truran, J.W. 1991, Ap.J., in press

MacDonald, J., Fujimoto, M.Y., and Truran, J.W. 1985, Ap.J., *294*, 263

Mahoney, W.A., Ling, J.C., Jacobson, A.S., and Lingenfelter, R.E. 1982, Ap.J., *262*, 742

Mahoney, W.A., Ling, J.C., Wheaton, W.A., and Jacobson, A.S. 1984, Ap.J., *286*, 578

Nofar, I., Shaviv, G., and Starrfield, S. 1991, Ap.J., *369*, 440

Ögelman, H. 1990, in The Physics of Classical Novae, ed. A. Cassatella and R. Viotti (Heidelberg: Springer-Verlag), p. 148

Ögelman, H., Krautter, J., and Beuermann, K. 1987, Astr. Ap., *177*, 110

Politano, M., Starrfield, S., Truran, J.W., Sparks, W.M., and Weiss, A. 1991, in preparation

Ritter, H., Politano, M., Livio, M., and Webbink, R.F. 1991, Ap.J., *376*, 177

Starrfield, S. 1989, in Classical Novae, ed. M.F. Bode and A. Evans (New York: Wiley), p. 39

Truran, J.W. 1982, in Essays in Nuclear Astrophysics, ed. C.A. Barnes, D.D. Clayton, and D.N. Schramm (Cambridge: Cambridge University Press), p. 467

Truran, J.W. 1990, in The Physics of Classical Novae, ed. A. Cassatella and R. Viotti (Heidelberg: Springer-Verlag), p. 373

Truran, J.W. and Livio, M. 1986, Ap.J., *308*, 721

Truran, J.W. and Livio, M. 1989, in White Dwarfs, ed. G. Wegner (Berlin: Springer-Verlag), p. 498

Truran, J.W. and Livio, M. 1991, in preparation

Weiss, A. and Truran, J.W. 1990, Astr. Ap., *238*, 178

Wiescher, M., Gorres, J., Thielemann, F.-K., and Ritter, H. 1986, Astr. Ap., *160*, 56

A BURST FROM A THERMONUCLEAR RUNAWAY ON AN ONeMg WHITE DWARF

S. Starrfield[1,3] M. Politano[1,2], J. W. Truran[4], and W. M. Sparks[2]

[1]Department of Physics and Astronomy, Arizona State University, Tempe, AZ
[2]Applied Theoretical Physics Division, Los Alamos National Laboratory, Los Alamos, NM
[3]Theoretical Division, Los Alamos National Laboratory, Los Alamos, New Mexico
[4]Department of Astronomy and Astrophysics, Enrico Fermi Institute, University of Chicago, Chicago, IL

ABSTRACT

We have performed studies which examine the consequences of accretion, at rates of $10^{-9}M_{\odot}yr^{-1}$ and $10^{-10}M_{\odot}yr^{-1}$, onto an ONeMg white dwarf with a mass of $1.35M_{\odot}$. In these studies, we used our Lagrangian, hydrodynamic, one-dimensional computer code that now includes a network with 89 nuclei up to ^{40}Ca, elemental diffusion, new opacities, and new equations of state. Our initial abundance distribution corresponded to a mixture that was enriched to either 25%, 50%, or 75% in products of carbon burning (Arnett and Truran 1969). The remaining material in each case is assumed to have a solar composition. The evolution of the thermonuclear runaway on the $1.35M_{\odot}$ white dwarf, with $M = 10^{-9}M_{\odot}$, produced peak temperatures in the shell source exceeding 300 million degrees. The sequence produced significant amounts of ^{22}Na from proton captures onto ^{20}Ne and significant amounts of ^{26}Al from proton captures on ^{24}Mg. This sequence ejected $5.2 \times 10^{-6}M_{\odot}$ moving with speeds from ~ 100km/s to ~ 2300km/s. When the mass accretion rate was decreased to $10^{-10}M_{\odot}$, the resulting thermonuclear runaway produced a shock that moved through the outer envelope of the white dwarf and raised the surface luminosity to $L > 10^{7}L_{\odot}$ and the effective temperature to values exceeding $10^{7}K$. The interaction of the material expanding from off of the white dwarf with the accretion disk should produce a burst of γ-rays.

I. Introduction

A classical nova outburst occurs on the white dwarf component of a close binary system which is a member of the general class of Cataclysmic Variables (hereafter, CV). In a CV, the secondary is commonly assumed to be filling its Roche Lobe and losing hydrogen-rich material through the inner Lagrangian point onto an accretion disk that surrounds the white dwarf primary. The physical process, which drives the secondary into filling its Roche Lobe, is still to be determined as is the physical process which removes angular momentum from the gas in the accretion disk and allows it to spiral onto the white dwarf. Other members of the class are dwarf novae, AM Her variables, intermediate polars, recurrent novae, and some of the symbiotic variables. Those systems in which the compact object is either a neutron star or a black hole are called low mass x-ray binaries (LMXRB's) and some of them may be the evolutionary consequences of the secular evolution of some classes of nova systems.

II. The Outburst and β^+-unstable Nuclei

In this paper, we concentrate on those explosions in which the compact object is a white dwarf. Theoretical studies have shown that a gradually accumulating shell of hydrogen-rich material on a massive white dwarf is unstable to a thermonuclear runaway (hereafter, TNR). The simulations of this evolution reproduce most of the observed features of the nova outburst. The calculations further imply that the energetics of the outburst, and thus the nova speed class, is sensitive to the abundances of the CNONeMg nuclei and also depends on the mass of the accreted shell, the white dwarf mass, and the accretion rate. The hydrodynamic calculations of the evolution of the TNR show that the early evolution is very slow and that the time scale is determined by the rate of accretion of material from the secondary onto the white dwarf. Once the temperature in the nuclear burning region reaches about 30 million degrees, a convective region forms above the region of peak temperature and slowly grows toward the surface. The rest of the evolution involves the interaction between the rapidly growing temperature in the nuclear burning region and convection, which continually mixes material in the nuclear burning region with the layers closer to the surface.

One of the most important results arising from the hydrodynamic simulations has been the identification of the role played by the four β^+-unstable nuclei: ^{13}N, ^{14}O, ^{15}O, and ^{17}F. As soon as the temperature in the shell source exceeds 10^8K, the abundances of these nuclei increase to where their presence severely impacts the nuclear energy generation in the envelope since every proton capture must now be followed by a waiting period before the β^+ decay occurs and another proton can be captured on the daughter nucleus. In addition, because of the existence of a convective region, which ultimately encompasses the entire accreted envelope, the most abundant of the CNO nuclei in the envelope at the peak of the outburst will be the β^+-unstable nuclei.

This has important and exciting consequences for the subsequent evolution. (1) Since

the energy production in the CNO cycle comes from proton captures followed by a β^+-decay, the rate at which energy is produced, at temperatures exceeding 10^8K, depends only on the half-lives of the β^+-unstable nuclei and the numbers of CNO nuclei initially present in the envelope. This is because the CNO reactions do not create new nuclei, but only redistribute them among the various CNO isotopes (Starrfield, Truran, Sparks, and Kutter 1972; Truran 1982). (2) Since the convective turn-over time scale is usually about 10^2 sec near the peak of the TNR, a significant fraction of the β^+-unstable nuclei can reach the surface without decaying and the rate of energy generation at the surface will exceed 10^{12} to 10^{13} erg gm^{-1} s^{-1} (Starrfield 1989). This will produce a burst of γ-rays prior to optical maximum light. (3) Since convection operates over the entire accreted envelope, it brings unburned CNO nuclei into the shell source, when the temperature is rising very rapidly, and keeps the CNO nuclear reactions operating far from equilibrium.

Once peak temperature is reached and the envelope begins to expand, the simulations of the outburst, which include a detailed calculation of the abundance changes with time, show that the rate of energy generation declines only as the abundances of the β^+-unstable nuclei decline since their decay is neither temperature nor density dependent (see Starrfield 1989 for a detailed review). The numerical calculations performed with the CNO nuclei enhanced show that more than 10^{47} erg are released into the envelope after its expansion has begun and it will reach radii of more than 10^{10}cm before all of the ^{13}N has disappeared (Starrfield, Truran, and Sparks 1978; Starrfield and Sparks 1987). Finally, since these nuclei decay when the temperatures in the envelope have declined to values that are too low for any further proton captures to occur, the final isotopic ratios in the ejected material will not agree with those ratios predicted from studies of equilibrium CNO burning.

We predict that the large abundance of β^+-unstable nuclei at the surface, early in the outburst, will produce γ-ray emission. As mentioned above, the peak rate of energy generation in the surface layers can reach (or even exceed under some circumstances) $\sim 10^{13}$erg gm^{-1}s^{-1} from the decays of the β^+-unstable nuclei. This amount of energy is released in the outer layers which have a mass of $\sim 10^{22}$gm. Therefore, we estimate that the peak luminosity from the decays, which will appear primarily as 0.5Mev photons, could exceed 10^{35}erg s^{-1}. Of course, we realize that only those photons emitted within a layer that is less than ~ 1 γ-ray optical depth from the surface will actually appear as photons with these energies. The remaining photons will only be emitted after they have experienced a few scatterings. This means that we need to perform a Monte-Carlo simulation of this phase of the outburst in order to make useful predictions of the γ-ray and hard x-ray emission at this time. Nevertheless, an observation of γ-ray emission from a nova early in the outburst would strongly constrain, in our simulations, the extent of the convective region during the early phases of the explosion.

We emphasize that the results described in the last paragraph are based entirely on the hypothesis that, in order for an outburst to occur, the shell source must be sufficiently degenerate for the peak temperature to exceed 10^8K. If this is the case, and if convection is as efficient as predicted by normal stellar evolution modeling, then the effects of the β^+-unstable nuclei are inevitable. In addition, it is an observational fact that the abundances

of the CNONeMg nuclei are enhanced in the ejecta of some novae (Truran 1990), and consequently they must also be enhanced in the nuclear burning region. Our simulations have shown that the presence of enhanced CNO nuclei in the envelope is required in order to produce a fast nova outburst. No calculation involving only a solar mixture has been successful in reproducing a realistic fast nova outburst and none of the observational studies of the elemental abundances in the ejecta reports that the material is of solar composition; the ejecta are always enriched in nitrogen and a number of other elements.

Theoretical calculations show that the evolution described above will release enough energy to eject material with expansion velocities that agree with observed values and that the predicted light curves produced by the expanding material can agree quite closely with the observations (see Starrfield 1989, 1990; Shara 1989; Truran, Starrfield, and Sparks 1992).

III. Oxygen-Neon-Magnesium Novae

In a companion paper in these proceedings, we discuss the observational and theoretical situation concerning γ-ray emission from the decay of ^{26}Al in the interstellar medium (Truran, Starrfield, and Sparks 1992). However, it is important to point out that the recent theoretical predictions of ^{26}Al production in nova outbursts (Nofar, Shaviv, and Starrfield 1991; Weiss and Truran 1990) critically depend on the existence of oxygen-neon-magnesium (hereafter, ONeMg) white dwarfs in nova systems. Therefore, in this section we review the observational evidence for such occurrences. ONeMg novae are one of the more important discoveries made with the **IUE** satellite, which has provided temporal coverage from **Einstein** to **GRO**. It has been discovered that there are two distinct composition classes of novae, those that occur on carbon-oxygen (CO) white dwarfs and those that occur on ONeMg white dwarfs.

If a CO nova is caught early enough in the outburst, an **IUE** spectrogram will show a continuum rising to the red, broken by what appear to be emission and absorption lines (see, for example, Starrfield 1990). However, the application of modern techniques in NLTE, spherical, expanding, stellar atmospheres, to these spectra of novae (Hauschildt et al. 1992), have shown that the spectral features are all caused by overlapping absorption lines of Fe II. The "emission" lines are, in reality, regions of transparency in these overlapping lines.

In contrast, fast ONeMg novae show a very hot continuum at maximum plus emission lines, which can be identified as characteristic of a low density gas. The speed of decline of such a nova also implies that fast ONeMg nova outbursts occur on very massive white dwarfs with small envelope masses. However, early spectra of QU Vul 1984, the only slow ONeMg nova studied in outburst with the **IUE** satellite, show features similar to those of CO novae (Stryker et al. 1988; Hauschildt et al. 1992).

A recent ONeMg nova occurred in the LMC in 1990 and exhibited outburst behavior very similar to that of the galactic ONeMg nova V693 CrA 1981 (Williams et al. 1985; Sonneborn, Shore, and Starrfield 1990). The initial **IUE** spectra, shown in Figure 1, were obtained over a period of a few days. The date of observation is given on each panel. One

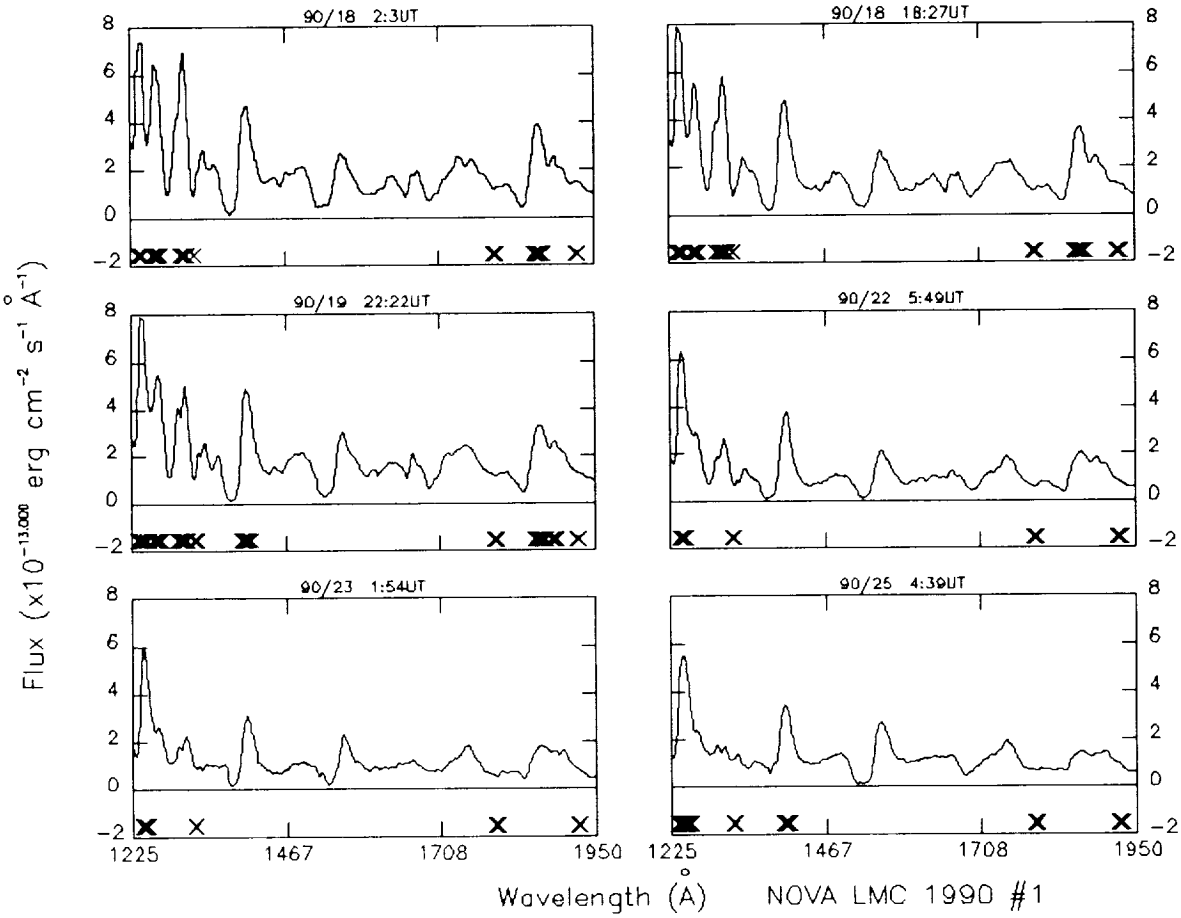

Figure 1. A montage of early spectra of Nova LMC 1990 #1 obtained with the **IUE** satellite early in the outburst. The date and time that each spectrum was obtained are listed on top of each spectrum.

can identify a hot continuum and emission lines from N V, Si IV, C IV, and Al III. All of the strong lines exhibited P-Cygni profiles, with flat-bottomed absorption troughs extending to more than -6000 km s^{-1}. There is no resemblance to early spectra of slow CO novae (Stryker et al. 1988; Hauschildt et al 1992). Analysis of these spectra indicate that fast ONeMg novae do not eject much material and that the expanding shell has become optically thin in the lines at maximum light (Sonneborn, Shore, and Starrfield 1990).

The optical spectra obtained by Dopita and Rawlings (1990; IAUC 4964) provided additional evidence that LMC 1990 #1 was an extragalactic analog of V693 CrA and, thereby, an ONeMg nova. They reported that [Ne III] 3868Å appeared on 22 January, and [Ne V] 3426Å on 29 January. By 13 February 1990, [Ne V] was the strongest emission feature in the optical spectrum. The ultraviolet forbidden neon lines seen at late stages in other ONeMg novae ([Ne IV] 1602Å and 2420Å) were not detected in the **IUE** spectra. This is not surprising, since they did not appear in either V693 CrA or QU Vul until well into the nebular stage, when the densities in the ejecta had dropped by a large factor from the values

determined at maximum light. Finally, the ultraviolet light curve suggests that the luminosity in the wavelength region from 1200Å to 3300Å reached a value of 3 x 10^{38} erg s^{-1} at maximum brightness. This value assumes a distance to the LMC of 55 kpc and shows that the luminosity in this nova exceeded the Eddington luminosity for a $1.0M_{\odot}$ white dwarf.

IV. A Burst From Accretion onto an ONeMg White Dwarf

Given both the existence of ONeMg white dwarfs and the success of the one-zone nucleosynthesis calculations (Weiss and Truran 1990; Nofar, Shaviv, and Starrfield 1991), it becomes appropriate to examine the consequences of accretion of hydrogen rich material onto such a white dwarf. We have done this, using our one dimensional hydrodynamic computer code which incorporates a large nuclear reaction network to follow the changes in abundance of 89 nuclei (Kutter and Sparks 1972; Weiss and Truran 1990; Nofar, Shaviv, and Starrfield 1991; Politano et al. 1991a). A detailed description of the current version of this code will appear elsewhere (Politano et al. 1991a). Here, we briefly discuss one set of calculations.

In our most recent studies of the accretion of hydrogen-rich material onto white dwarfs, we have varied both the white dwarf mass (Politano et al. 1991a) and the amount of enriched material (Politano et al. 1991b). Table 1 presents the results for accretion onto $1.35M_{\odot}$ white dwarfs for the 4 evolutionary sequences discussed in Politano et al (1991b), where we have both varied the amount of ONeMg material assumed to have been mixed up into the accreted layers (Sequences 1, 2, and 3) and, in addition, decreased the rate of mass accretion from 1.6 x $10^{-9}M_{\odot}$ (Sequences 1, 2, and 3) to 1.6 x $10^{-10}M_{\odot}$ (Sequence 4). Here we concentrate on Sequence 4 which produced a burst of γ-rays.

This sequence accretes at a rate of 1.6 x $10^{-10}M_{\odot}$ for 3 x 10^{5}yr until it has accumulated an accreted envelope with a mass of nearly 5 x $10^{-5}M_{\odot}$. At this time, the temperature at the interface between the accreted and core layers (hereafter, CEI) exceeds 80 million degrees and we end the accretion phase of the evolution. The temperature continues to rise, but slowly, initially, since a significant fraction of the hydrogen at these depths has been burned. However, a convective region has formed above the CEI and is slowly moving into layers closer to the surface, where there is still a significant abundance of hydrogen. As soon as the convective region reaches this hydrogen, it is mixed down to the CEI, where the temperature has grown to $\sim$200 million degrees. The addition of fresh fuel to the shell source causes the temperatures and rates of energy production to increase precipitously. Over the next .01 s, the rate of energy generation flashes to 1.36 x 10^{20}erg gm^{-1} s^{-1} and the temperature reaches 623 million degrees.

This high a temperature causes a significant overpressure in these layers and a pressure wave begins to move both inward and outward. As this wave moves outward, it produces a deflagration which causes a marked increase in the rate of energy generation and temperature in each zone. For example, the CEI is at zone 60 and, by the time the deflagration has reached to zone 70, the temperature exceeds 762 million degrees and ϵ_{nuc} $\sim$ 7.1 x 10^{20} erg gm^{-1} s^{-1}. Even at zone 80, the temperature still exceeds 640 million degrees

and ϵ_{nuc} exceeds 5.5 x 10^{20} erg gm^{-1} s^{-1}. The deflagration continues to move outward and we show, in Figures 2 through 5 the observable effects of this phenomenon on the surface layers. Figure 2 is the light curve, which shows that the luminosity rapidly grows to 2 x $10^7 L_\odot$ as the effective temperature climbs to 6.5 x 10^6K (Figure 4). As the deflagration passes through the surface layers, it causes ϵ_{nuc} near the surface to increase to values exceeding 4 x 10^{17} erg gm^{-1} s^{-1}. However, unlike our earlier discussion about other evolutionary sequences, the energy is not being produced by β^+ decays but rather by (p,γ) reactions on the abundant nuclei. We are now trying to determine the time scale of this burst, and will model the emission in the outer layers with a Monte-Carlo investigation of the γ-ray photon transport.

Once this deflagration has passed through the outer layers, the intense heating causes the velocities to increase to values exceeding 19,000 km s^{-1}. The accelerations are very large and the rise to this velocity takes only a small fraction of a second. The layers begin to

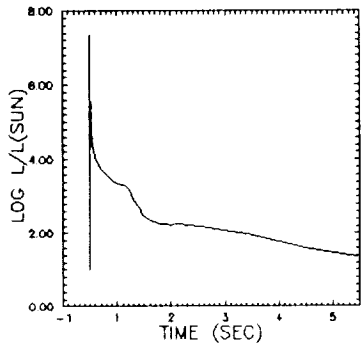

Figure 2. The luminosity as a function of time at shock break out.

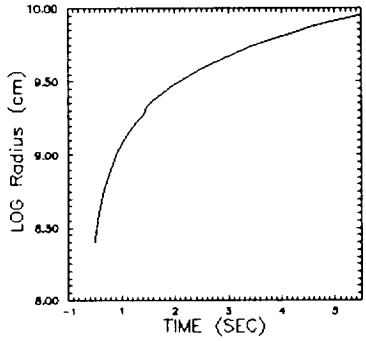

Figure 3. The radius as a function of time at shock break out.

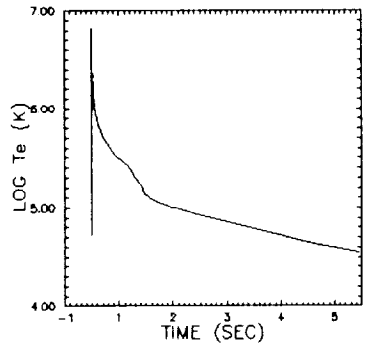

Figure 4. The effective temperature as a function of time.

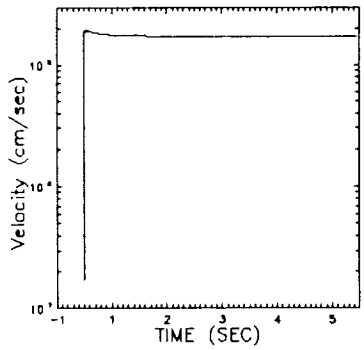

Figure 5. The velocity as a function of time at shock break out.

expand and reach radii of 10^{10}cm within a few seconds (Figure 3). By this time, 5 x $10^{-7} M_\odot$ have been ejected in a shell with most of the material moving at speeds exceeding ~ 10^4 km s^{-1}. We continued this evolution and will report on the final results elsewhere.

TABLE 1
EVOLUTIONARY RESULTS

Sequence	1	2	3	4
MASS ($M_\odot$)	1.35	1.35	1.35	1.35
ONeMg (% mf)	25	50	75	75
$L/L_\odot$ (10^{-3})	9.60	9.60	9.60	9.60
T_{eff} (K)	30,300	30,300	30,300	30,300
Radius(km)	2488.	2488.	2488	2488.
M ($10^{-9}M_\odot yr^{-1}$)	1.6	1.6	1.6	0.16
τ_{TNR} (10^3 yr)	3.3	4.6	11.3	304.7
M_{acc} ($10^{-5}M_\odot$)	.53	.73	1.8	4.8
$\epsilon_{nuc\text{-}MAX}$ (10^{17})	.19	1.1	3.9	7080.
T_{PEAK} (10^6K)	257	302	390	762
$T_{eff\text{-}MAX}$ (10^5K)	3.40	6.42	9.02	65.4
M_{ej} ($10^{-6}M_\odot$)	0.0	.36	15.0	.5
V_{max}(km s^{-1})	110	240.	3360	19,400.

Although this has been the most intense burst that we have produced to date in our evolutionary studies of accretion onto white dwarfs, it does not qualify as a γ-ray burst since the peak conditions are really in the hard x-ray regime. However, we must emphasize that our treatment of the surface boundary is characteristic of a normal stellar evolution code and assumes equilibrium conditions. Any non-equilibrium effects will probably act to increase the temperatures and luminosities that are produced in this event. In addition, it is also appropriate to consider the systems in which we have assumed this evolution was occurring. Since this is a white dwarf in a CV system, it should be surrounded by an accretion disk. It then becomes necessary to ask what the consequences will be of the collision of the expanding material with the accretion disk. We also note that the material within the accretion disk is moving at supersonic speeds and the interaction will produce a strong oblique shock. It appears to us that we will have to do some fairly sophisticated modeling to follow the passage of the expanding layers of the white dwarf through the accretion disk;

here, we note only a few important considerations.

First, the time scale of the burst will be broadened by the time it takes the expanding layers to pass through the accretion disk. At the speeds predicted by the simulation, 19,000 km s^{-1}, it should lengthen the time scale of the burst to a few seconds, instead of the fractions of a second seen in Figure 2. Second, the post shock temperature of an ideal gas moving with speeds of 19,000 km s^{-1} exceeds 4 x 10^9K or ~300keV (Kaplan 1966) while, if we use the development of Brecher, Ingham, and Morrison (1977) for a shock passing through a low density envelope, we arrive at a value of ~850keV. In either case, such a strong shock moving through the low density accretion disk will produce and radiate very high energy photons. This certainly does represent a burst of γ-rays, although it is not a γ-ray burst.

V. Summary and Discussion

In this paper, we have first described the evidence for the existence of nova outbursts occurring on ONeMg white dwarfs and then presented the results of hydrodynamic simulations of the consequences of accretion of hydrogen-rich material onto such white dwarfs. These studies involved accretion onto 1.35$M_\odot$ ONeMg white dwarfs at either ~$10^{-9}M_\odot yr^{-1}$ or ~$10^{-10}M_\odot yr^{-1}$. Either value is in reasonable agreement with the observations. We found that as we increased the heavy element abundance, and thereby reduced the hydrogen abundance, both the accretion time scale and the accreted mass increased. Our sequence with a lower rate of accretion accreted a factor of three more material than the equivalent sequence done with the larger mass accretion rate. This is because the envelope temperatures grew more slowly since there was a smaller amount of accretion heating and more time for the compressional energy to be radiated.

One sequence was so degenerate, at the time of the thermonuclear runaway, that a shock was initiated at the core-envelope interface; when this shock reached the surface of the white dwarf it produced a burst of high energy photons. It also accelerated the surface layers to speeds of ~19,000 km s^{-1}. The peak luminosity exceeded $10^7L_\odot$ and, simultaneously, the peak T_{eff} exceeded 6 million degrees. Although these conditions alone are not necessarily appropriate for the production of a strong γ-ray burst, we note that in fact, we can expect the expanding layers to collide both with the accretion disk and with the secondary star, which has been supplying the hydrogen rich fuel for the outburst. Simple estimates of the peak temperature that should obtain in this interaction suggests that it could exceed 500 keV. This would produce a very luminous burst of γ-ray photons over a time scale of a few seconds. The fact that such a burst was, apparently, not observed by **GRO** during the July outburst of Nova Sgr 1991 implies either that such an event cannot accompany all ONeMg nova outbursts or that the nova was behind the earth at the appropriate time (Shrader 1991, private communication).

We are grateful to a number of our colleagues for valuable discussions and assistance. We would especially like to thank S. Shore and G. Sonneborn for allowing us to display spectra of LMC 1990 #1 prior to publication and providing us with the IDL programs that

prepared the montage of spectra. We would also like to thank P. Hauschildt, J. Krautter, I. Nofar, G. Shaviv, C. Shrader, and R. Wehrse for their help. This work was supported in part by NSF and NASA grants to the University of Illinois and Arizona State University and by the DOE.

REFERENCES

Arnett, W. D., and Truran, J. W. 1969, *Ap.J.*, **157**, 339.

Hauschildt, P. H., Wehrse, R., Starrfield, S., and Shaviv, G. 1992, *Ap.J.*, in press.

Kaplan, S. A. 1966, *Interstellar Gas Dynamics* (Oxford: Pergamon).

Kutter, G. S., and Sparks, W. M. 1972, *Ap. J.*, **175**, 407.

Nofar, I., Shaviv, G., and Starrfield, S. 1991, *Ap.J.*, **369**, 440.

Politano, M., Starrfield, S., Truran, J. W., Sparks, W. M., and Weiss, A. 1991a, in preparation.

Politano, M., Starrfield, S., Truran, J. W., Sparks, W. M. 1991b, in preparation.

Shara, M. M. 1989, *Pub. Ast. Soc. Pac*, **101**, 5.

Sonneborn, G., Shore, S. N., and Starrfield, S. 1990, in *Evolution in Astrophysics: IUE Astronomy in the Era of New Space Missions*, ed. E. Rolfe (ESA SP-310; Noordwijk), p. 439.

Starrfield, S. 1989, in *Classical Novae*, ed. N. Evans and M. Bode (New York: Wiley), p. 123.

Starrfield, S. 1990, in *Evolution in Astrophysics: IUE Astronomy in the Era of New Space Missions*, ed. E. Rolfe (ESA SP-310; Noordwijk), p. 101.

Starrfield, S., Truran, J. W., and Sparks, W. M., 1978, *Ap. J.*, **226**, 186.

Starrfield, S., Truran, J.W., Sparks, W.M. and Kutter, G. S. 1972, *Ap. J.*, **176**, 169.

Starrfield, S., and Sparks, W. M. 1987, in *Cataclysmic Variables. Recent Multifrequency Observations and Theoretical Developments*, ed. H. Drechsel, Y. Kondo, and J. Rahe, (Dordrecht: Reidel), p. 379.

Stryker, L. L, Hestand, J., Starrfield, S., Wehrse, R., and Shaviv, G. 1988, in, *A Decade of UV Astronomy with the IUE Satellite*, ed E. Rolfe (Noordwijk: Estec Publications: SP-263), p. 149.

Truran, J. W. 1982, in *Essays in Nuclear Physics*, eds. C. A. Barnes, D. D. Clayton and D. N. Schramm (Cambridge: Cambridge U. Press), p. 467.

Truran, J. W. 1990, in *The Physics of Classical Novae*, ed. A. Cassatella and R. Viotti, (Heidelberg: Springer-Verlag), p. 373.

Truran, J. W., Starrfield, S., and Sparks W. M. 1992, these proceedings.

Weiss, A. and Truran J. W. 1990, *A&A*, **238**, 178.

Williams, R.E., Ney, E.P., Sparks, W.M., Starrfield, S., Truran, J.W. 1985, *M.N.R.A.S.*, **212**, 753.

SUPERNOVAE AS SOURCES OF GAMMA-RAYS

Adam Burrows
University of Arizona

ABSTRACT

Most supernovae are profoundly radioactive and GRO is an ideal instrument for detecting their unique gamma-ray line and x-ray signatures. How the observation of these hard photons can be used to do supernova science will be addressed, with particular emphasis being placed on Type Ia explosions and nearby events.

Gamma-Ray Constraints on the Galactic Supernova Rate

D. Hartmann, L.-S. The, D. D. Clayton, M. Leising,
Department of Physics and Astronomy
Clemson University, Clemson, SC 29634
and
G. Mathews
Department of Physics
Lawrence Livermore National Laboratory
Livermore, CA 94551
and
S. E. Woosley
Board of Studies in Astronomy and Astrophysics
UCO/Lick Observatory, University of California
UCSC, Santa Cruz, CA 95064

Abstract

Most Galactic supernovae are hidden from our view due to severe extinction in the Galactic plane. In the γ-ray band the Galaxy is almost transparent so that we could detect supernovae that are obscured. ^{44}Ti is among the potentially detectable isotopes in supernova ejecta. Surveys carried out with the HEAO 3 experiment and γ-ray detectors aboard the Solar Maximum Mission (SMM) have not detected γ-ray lines expected from the decay chain $^{44}\mathrm{Ti} \rightarrow {}^{44}\mathrm{Sc} \rightarrow {}^{44}\mathrm{Ca}$. These observations thus constrain the rates and nucleosynthesis of supernovae. We perform Monte Carlo simulations of the expected γ-ray signatures of Galactic supernovae of all types to estimate the significance of the lack of a γ-ray signal due to supernovae occuring during the last millenium. Using recent estimates of the nuclear yields we determine mean Galactic supernova rates consistent with the historic supernova record and the γ-ray limits. Another objective of these calculations of Galactic supernova histories is their application to surveys of diffuse Galactic γ-ray line emission.

1 Introduction

Detection of γ-ray line emission from ongoing Galactic nucleosynthesis is one of the major observational goals of γ-ray astronomy. We consider the signal from the decay $^{44}\mathrm{Ti} \rightarrow {}^{44}\mathrm{Sc} \rightarrow {}^{44}\mathrm{Ca}$. Measurements of the ^{44}Ti half-life prior to 1965 implied $t_{1/2} \leq 50$ years, but recent Brookhaven measurements suggest a much longer half-life of 66.6 years (Adelberger & Harbottle 1990). Here we adopt the intermediate half-life of 54.2 years (Frekers *et al.* 1983), corresponding to $\tau = 78.2$ years, which was also employed by Mahoney *et al.* (1991). Pinning down the correct value remains an important objective in nuclear astrophysics. Because of this short life-time, detection of a γ-ray signal from ^{44}Ti involves either very recent or very near supernovae.

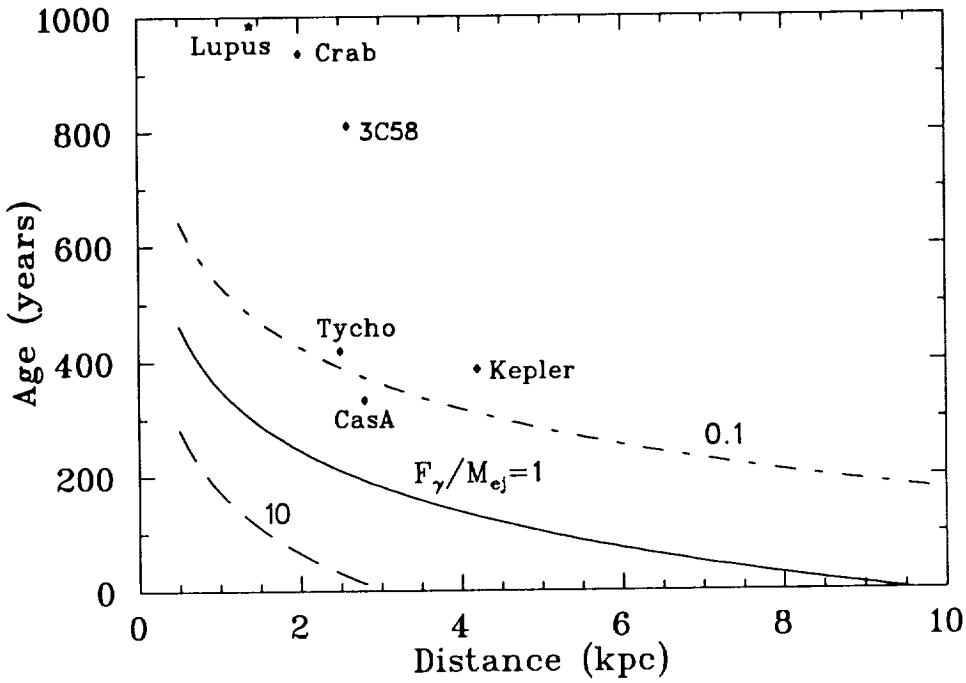

Figure 1: *Age distance relationship for γ-ray line emission from ^{44}Ti. Source detectability depends on the ratio of flux limit to ejected mass, F_γ/M_{ej}. Six historic supernovae are shown.*

The decay of ^{44}Ti generates three γ-ray photons with energies of 78.4 keV, 67.9 keV, and 1.157 MeV. The resulting line flux at earth is

$$F_\gamma \sim 1 \times 10^{-2}\ M_{-4}\ \exp(-t/78.2\ \mathrm{yrs})\ D^{-2}(kpc)\ \ \mathrm{photons\ cm^{-2}s^{-1}}\ ,$$

where M_{-4} is the ejected ^{44}Ti mass in units of 10^{-4} $M_\odot$ The detectability of such emission from recent supernovae in our Galaxy and perhaps from a few older but nearby remnants make this nucleus a prime γ-ray target (Figure 1). It is clear, however, that the search for ^{44}Ti line emission from previously undetected Galactic supernovae deals with the few events of the past couple of centuries, so that the interpretation of line detection, or lack thereof, is statistical in nature. This is similar to the situation of ^{22}Na, and our Monte Carlo analysis is conducted in the spirit of Higdon and Fowler's (1987) analysis of ^{22}Na detectability from novae.

Searches for ^{44}Ti line emission have been carried out using the high-resolution γ-ray spectroscopy experiment on HEAO 3 (Mahoney *et al.* 1991) and the γ-ray spectrometer aboard the SMM satellite (Leising & Share 1991). No signal was detected with either instrument. Mahoney *et al.* (1991) used the HEAO 3 limit to constrain the combination of supernova rate and mass of ^{44}Ti ejected per event, but considered the relevant supernovae to be of Type Ia and ignored constraints from the optical signature of these events. Current nucleosynthesis estimates for ^{44}Ti suggest that in fact supernovae involving massive stars (Type Ib and II) may dominate the production of this isotope. We take a somewhat different approach and utilize current yield estimates (and their uncertainties) to constrain exclusively the mean Galactic supernova rate.

2 Yields and Sites

To achieve full solar production of ^{57}Fe and ^{44}Ca their γ-ray emitting progenitors ^{57}Ni and ^{44}Ti must be produced in environments that guarantee a significant contribution from the so called "alpha-rich freeze-out" (Woosley, Arnett, & Clayton 1973). This component can be expected when low density matter falls out of nuclear statistical equilibrium (NSE) while being cooled so rapidly that free alpha particles have insufficient time to reassemble back into more massive nuclei. In contrast to normal freezeout from NSE at high densities, the large mass fraction of surviving alpha particles drastically alters the resulting nucleosynthesis. It is generally believed that alpha-rich freeze-out must be invoked to explain solar abundances of several isotopes, including ^{57}Fe, ^{59}Co, ^{58,60,61,62}Ni, and ^{64}Zn (Woosley 1986). We utilize the fact that the synthesis of ^{44}Ti and ^{57}Ni occurs in similar, if not the same, astrophysical sites, and take advantage of observations of SN 1987A to estimate ^{44}Ti yields. Mahoney *et al.* (1991) treated the titanium yield as a free parameter and assumed it to be the same for all events.

The bolometric luminosity of SN 1987A at late times is dominated by the radioactivity of ^{44}Ti (e.g., Woosley, Pinto, & Hartmann 1989). The abundance of ^{44}Ti is sensitive to pre-explosive details of stellar evolution as well as the explosion mechanism. For SN 1987A Kumagai *et al.* (1989) and Woosley & Pinto (1988) estimate Ti production near 10^{-4} $M_\odot$. This result is uncertain by at least a factor of two. Parametrized nucleosynthesis studies (Woosley & Hoffman 1991: WH) can also be used to constrain production of ^{44}Ti. Assuming that ^{56}Ni is the dominant constituent of iron group elements ejected in SNII and using a conservative lower limit on the neutron enrichment parameter $\eta \lesssim 10^{-3}$, the parametrized synthesis calculations constrain the ratio $r_{57} = X(^{57}Ni)/X(^{56}Ni)$. To avoid overproduction of ^{58}Ni by a factor of 5 or more, WH finds $r_{57} \lesssim 2r_{57\odot}$. The lower limit on η corresponds to a lower limit $r_{57} \gtrsim 0.3$ $r_{57\odot}$ in the case that an α-rich freeze-out does not occur. For the most realistic η values and a modest α-rich freeze-out WH find $r_{57} \gtrsim 0.7$ $r_{57\odot}$.

Production of ^{44}Ti and ^{57}Co is dominated by stellar zones that have experienced some alpha-rich freeze-out. Thus, the limits on ^{57}Co also provide a constraint on the ^{44}Ti yields. WH find that a Ti production ratio $P_{44} = {}^{44}Ti/{}^{56}Fe$ close to solar ($P_{44\odot} \sim 1.2\times10^{-3}$) occurs for a variety of conditions and that the upper limit on r_{57} restricts P_{44} to less than twice solar. Recent observations of the bolometric light curve of SN 1987A suggest $r_{57} \sim 5$ (Suntzeff *et al.* 1991), which implies copious co-production of ^{44}Ti ($P_{44} \sim 2P_{44\odot}$) in Type II supernovae, but the uncertainties in modeling the bolometric lightcurve are still very large. Dynamic simulations of explosive nucleosynthesis (Hashimoto *et al.* 1989; Kumagai *et al.* 1989; Woosley, Pinto, & Weaver 1988; Woosley 1991) estimate $P_{44} \sim 1.5$–2.5 $P_{44\odot}$, so that a typical Type II supernova might eject $10^{-4}M_\odot$. However, these simulations are not yet realistic, because they assume either a piston or instantaneous energy deposition. We randomly select the ejected ^{44}Ti mass in SNII from $M_{ej} \sim \zeta\ P_{44\odot}\ M_{56}$, where ζ is randomly chosen between 0.5 and 2.0, and the ejected mass of ^{56}Fe varies between $2\times10^{-3}M_\odot$ and 0.3 $M_\odot$ for stars with initial mass between 10 $M_\odot$ and 35 $M_\odot$. The initial mass was selected from a Salpeter IMF by another random number. The same prescription is used for SNIb, but the amount of ejected ^{56}Fe is kept fixed at 0.3 $M_\odot$, because not enough SNIb have been observed to estimate their intrinsic spread in iron production. For SNIa we randomly draw an ejected iron mass between 0.25 $M_\odot$ and 0.75 $M_\odot$, and select ζ between 0.03 and 0.08. The titanium synthesis in these exploding carbon-oxygen white dwarfs is not very well known, but recent models of delayed detonations (DD) support

the ζ range employed here. In DD models of Type Ia supernovae substantial production of intermediate mass isotopes (O, Mg, Si, Ca..) occurs because the detonation wave propagates through low density matter in the pre-expanded white dwarf envelope. Estimates of the yields of isotopes in this mass range are sensitive to the uncertain transition density where the initial deflagration turns into a detonation.

The rate of SNIa is about a factor 10 smaller than that of supernovae involving massive stars (Ib & II). Thus, the Galactic nucleosynthesis of ^{44}Ti could be dominated by SNII and SNIb, but from the point of view of γ-ray searches for individual Galactic events only the product $\zeta P_{44\odot}\ M_{56}$ matters. Although uncertain, the values discussed above clearly indicate that one must include all supernova classes in the analysis.

3 Event Distribution

3.1 Spatial Distributions

The standard scenarios for Type Ia supernovae involve accreting white dwarfs, which motivates the use of distribution models derived for novae (Higdon & Fowler 1987; Mahoney *et al.* 1991). The Galactic nova distribution is not well known because of severe extinction corrections. To alleviate this problem one relies on nova surveys of M31 where sample completeness is much higher (e.g., Ciardullo *et al.* 1987). From these observations one expects contributions from two distinct populations: disk and spheroid. We follow Higdon & Fowler (1987) who generate Monte Carlo representations of these populations from integral probability distributions for an axisymmetric disk and a spherically symmetric bulge component. The observations of M31 seem to suggest that the nova rate traces the blue light distribution. Using the Bahcall-Soneira Galaxy model Mahoney *et al.* (1991) argue that the fraction of SNIa occuring in the spheroid is about 1/6. The remaining two classes of events are thought to be associated with massive stars and thus follow a Pop I spatial distribution. We assume that birth places are exponentially distributed in height above the plane with a scale length of 100 pc. Ignoring spiral structure we assume smooth radial birth functions that are either constant within some radius σ_r, fall off exponentially with distance from the Galactic center (with scale length σ_r), or are ring-like $\rho(r) \propto \exp\left((r - r_0)^2/\sigma_r^2\right)$, where H_2 observations suggest that $r_0 \sim 5$ kpc.

3.2 Supernova Rates

Instead of treating the total Galactic rate of each supernova class as a free parameter, we fix the relative rates based on observations of external galaxies and vary the total rate. Relative supernova rates are sensitive to the type of the host galaxy (e.g., Tammann 1991). The Hubble type of the Milky Way is not accurately known, but is most likely between Sbc and Sd, so that the observations suggest the following breakdown (Ia:Ib:II) = (1:1.6:8) (Tammann 1991). We thus assume that a fraction $F_{Ia} \sim 0.09$ of all events is of type Ia. Similarly, the fraction of type Ib events among supernovae involving massive stars is $F_{Ib} \sim 0.16$. These values are used to randomly assign an event class.

4 Optical Constraints

4.1 The Historic Record

Supernovae are rare events in our Galaxy, only six are known to have occured during the last millenium. Without doubt, additional supernovae occured during that period but were not observed because of obscuration by interstellar matter. Still, we can use these historic events to constrain the range of acceptable mean Galactic supernova rates. Classification and peak magnitudes of historic events are uncertain, but we follow van den Bergh (1990) for the breakdown (Ia:Ib:II) $\sim$ (1:2:3). All of these events were brighter than $m_V = 0$. We assume that the historic record is complete above this level. On the other hand, the record of historic nova discoveries above the same limit suggests a rather strong time dependence, suggesting that the historic supernova record could be very incomplete as well (van den Bergh & Tammann 1991; van den Bergh 1991b; Tammann 1991). We allow for a factor 2 in all of the above numbers, so that there could have been a total of 12 detectable events.

Within about 4 kpc of the sun there were between 3 and 4 core collapse supernovae. From a comparison of the total Galactic Pop I content to that within a cylinder of that radius Ratnatunga and van den Bergh (1989) infer that the total Galactic core collapse rate is of order 6-8 events per century. This value is well above theoretical estimates based on integrating a reasonable IMF (van den Bergh 1991a) or values derived from extragalactic evidence (Evans, van den Bergh & McClure 1989) that give $\sim 2.2 \pm 2$ and 2.6 ± 0.7, respectively. This problem of an unexpectedly high apparent frequency of nearby supernovae has been discussed in detail by van den Bergh (1990). A supernova rate as high as 1/10 yrs requires a star formation rate that exhausts the available gas supply in the Galactic annulus of the solar neighborhood in less than $\sim 10^9$ yrs (van den Bergh 1991b). This is inconsistent with age estimates of the Galactic disk ($T_d \sim 10^{10}$ yrs) derived from white dwarf luminosity functions. We consider the possibility that the actual mean supernova rate is in fact as low as indicated by extragalactic observations and that the observed large number of local supernovae during the past millenium is just a statistical fluctuation.

4.2 Peak Magnitudes

Observations suggest that the absolute magnitude in the B-band for Type Ia supernovae is so well defined that we can use SNIa as standard candles (e.g., Leibundgut 1991; Branch & Tammann 1991). We follow Leibundgut and Tammann (1990) by employing $M_B(max) = -18.3 + 5\ log(h)$, where h is the Hubble constant normalized to 100 km/s/Mpc. Furthermore, the observations suggest that B-V $\sim$ 0 at maximum light. Throughout this paper we assume h=1. Supernovae of Type Ib are fainter than SNIa (e.g., Porter and Filipenko 1987). Because of its recent establishment as an independent class, too few events have been studied well enough to determine accurately their peak magnitude and intrinsic spread. We therefore assume a single value (Evans, van den Bergh, & McClure 1989) $M_B(max) = -16.7 + 5\ log(h)$. Still fainter at peak than SNIb's are Type II supernovae. We follow Tammann & Schröder (1990) and use $M_B(max) = -15.7 + 5\ log(h)$. To include the possibility of underluminous SNII, such as 1987A, we add uniform random fluctuations with amplitude $\delta M_B = 1.2$ mag. Tammann & Schröder (1990) use a Gaussian distribution that rarely gives such underluminous events, although these events could be common (e.g., Branch 1990; Schmitz & Gaskell 1988).

4.3 Extinction

Galaxy counts and photometric studies of stellar reddening at high Galactic latitudes imply a polar photographic extinction A_{ph} of about 0.25 mag or less than 0.1 mag, respectively (Heiles 1976; Burstein & McDonald 1975). However, a careful re-analysis of galaxy counts (Burstein & Heiles 1978) has shown that these data are too noisy to distinguish between zero extinction and a csc(b) law with an amplitude of 0.25 mag. The study by Burstein and Heiles also showed that a smooth csc(b) law does not give a good representation of extinction because of the patchiness in the interstellar dust component.

From the more reliable photometric studies of stars and globular clusters it appears that the extinction toward the galactic poles is of order of 0.2 mag or less. An extinction of 1 mag corresponds roughly to a hydrogen column density along the line of sight of $N(HI) = 10^{21}$ cm^{-2} (Burstein and Heiles 1978). Extinction and optical depth, τ, at some wavelength are related by $A_\lambda = 1.086\ \tau_\lambda$. Although there still is considerable debate about the correct value of the polar extinction, the average optical depth of the half disk in spiral galaxies is commonly assumed to be of order $\tau_p = 0.2$ (e.g., Sandage and Tammann 1981). However, the question whether galaxy disks are optically thin or opaque is still debated (e.g., Disney, Davies, and Phillips 1989; Valentijn 1990). Because the radial scale length of the Galaxy is so much larger than the vertical scale height of the dust layer (which produces the bulk of the extinction) a total optical depth to the Galactic center may be as high as $\tau_c \sim 40$. In the solar neighborhood the average extinction per unit length is of order $\tau_a = 1$ kpc^{-1} (Mihalas and Binney 1981).

We employ simple extinction models that assume either constant, exponentially decaying, or ring-like density distributions with respect to galactocentric radius and that are either constant, exponentially decaying, or Gaussian with respect to the height above the Galactic plane. We normalize the resulting density distribution such that the polar optical depth is exactly equal to $\tau_p = 0.2$. To determine the extinction correction for a particular event in the Galaxy we first integrate along the line of sight and then add a maximally 50% correction, reflecting the patchiness of the ISM, by $\tau_{eff} = \tau(D)\ (1 - (r - 1/2)\exp(-\tau(D))$, where r is a uniform random variable between 0 and 1. The exponential factor reduces the fluctuations for observations of objects with large intervening column depths. After applying extinction corrections we consider a supernova optically detected when its apparent magnitude is brighter than m_v=0.

4.4 Results and Conclusions

Because of the short life time of ^{44}Ti the γ-ray glow of our Galaxy is expected to be dominated by perhaps a few recent events. However, as Figure 1 shows, none of the known historic supernovae is either close or young (or both) enough to be detectable in the "titanium window" (assuming standard yields). Thus one searches for emission from recent supernovae that remained unrecognized due to either Galactic absorption or gaps in sky coverage during the past millenium.

Mahoney *et al.* (1991) searched through the scan-by-scan data of the HEAO 3 γ-ray experiment. Of the three γ-ray lines associated with the decay of ^{44}Ti emission at 68.9 keV and 78.4 keV is most easily detectable by the HEAO 3 spectrometer. Mahoney *et al.* (1991) searched for flux enhancements in 16 channels covering the energy range 58–90 keV. The high-resolution spectrometer aboard HEAO 3 scanned the sky with a field of view of $\sim 30°$ and a period of about 20 minutes. Mahoney *et al.* (1991) analyzed the scans, searching for a point source at a

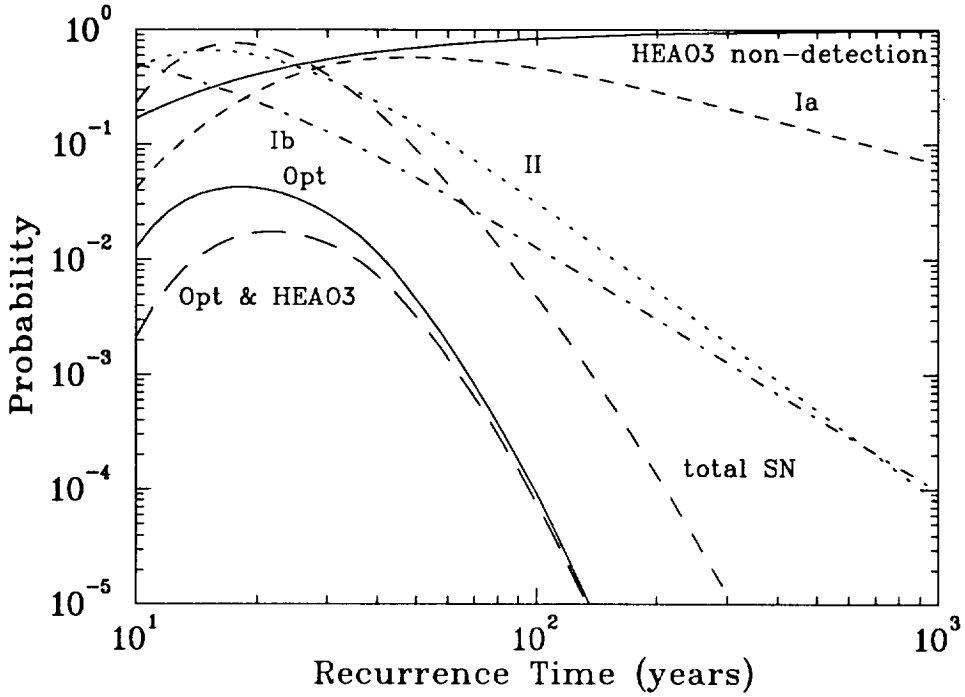

Figure 2: *Optical and γ-ray probabilities using the HEAO 3 flux limit.*

given location on the sky whose flux is modulated by the time dependent instrument response. Hypothetical point sources were assumed to be spaced 10° apart in Galactic longitude to assure maximum instrumental sensitivity. None of the resulting 36 bins along the Galactic plane showed any significant flux enhancement. HEAO 3 would have detected a source line flux of $\sim 2\times10^{-4}$ photons / cm^2 s about 99% of the time. This limit is used in this study.

Leising and Share (1991) have searched nearly ten years of data from NASA's Solar Maximum Mission (SMM) Gamma-Ray Spectrometer for evidence of γ-ray line emission from the decay of ^{44}Ti. They modeled the expected signals resulting from the annual scan of the ecliptic by SMM, considering point sources of various individual undiscovered events which might eject ^{44}Ti. They find no evidence of Galactic emission from ^{44}Ti, and find 99% confidence limits of 10^{-4} photons cm^{-2} s^{-1} for the 1.16 MeV line from ^{44}Sc from arbitrary points near the Galactic center. The limits on 1.16 MeV flux from longitudes near $\pm$ 90° rise to 2×10^{-4} cm^{-2} s^{-1} due to the reduced sensitivity in those directions.

Using the previously described procedures for randomly generating Galactic supernova events of all types, we perform a sufficient number of Monte Carlo simulations to determine the probabilities for detection of these events in the γ-ray band and the optical band. For a given average supernova rate in the Galaxy one can then analytically calculate the total probabilities for such histories to be consistent with the observed historic supernova record and the lack of γ-ray detections. Figure 2 shows a typical Monte Carlo result for a specific model of yields, extinction, relative SN frequencies, etc. The full curve "Opt" gives the probability that a history satisfies simultaneously the historic limits of each supernova type (i.e., 1-2 Ia; 2-4 Ib; 3-6 II). Individual probabilities are also shown. The dashed curve "total SN" gives the

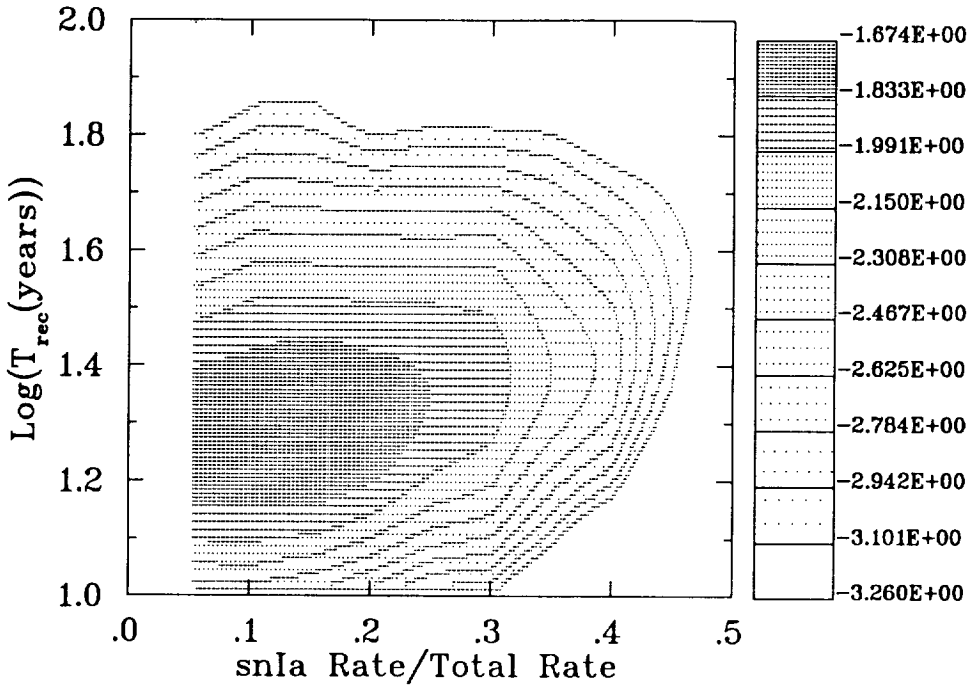

Figure 3: *Contours of combined optical and γ-ray probabilities as a function of total supernova rate and ratio Ia/(Ia+Ib+II). The labels give the logarithm of the joint probability for model histories to match the supernova record and to avoid HEAO 3 γ-ray detection.*

probability for the total number of SNe to be within the historic range (6-12), independent of type. The upper solid curve gives the probability for non-detection of γ-rays using the HEAO-3 limit. The lower dashed curve ("Opt&HEAO3") is the total combined probability for a model to satisfy both optical and γ-ray constraints. Based on optical data alone, the particular model shown in Figure 2 has a most likely supernova recurrence time of $\sim$ 18 years and the observed Galactic historic record is reproduced in about 4% of all Monte Carlo histories (this is still an acceptable model for Galactic supernova histories). Recurrence rates as short as 10 years yield only a 7% probability for non-detection of ^{44}Ti γ-ray lines. The combined optical/γ-ray model is thus severely constrained on the high frequency side, resulting in a most likely recurrence time of $\sim$ 23 years with peak probability to match both data sets of 1%. This model is thus still acceptable. Varying the total supernova rate and the ratio Ia/(Ia+Ib+II), we perform Monte Carlo simulations to determine the extent of the acceptable parameter space in which the combined probabilities exceed, say, 1%. The results (Figure 3) are fully consistent with those derived from extragalactic supernova searches, but we emphasize that γ-ray constraints on the recurrence times clearly rule out supernova frequencies as high as 1/10 years.

A detailed paper on these simulations is in preparation. This research was supported in part by NASA grants NAG 5-1578 and NAGW-2525, NSF grants 8813649 and 9115367, and grants SF-ENG-48 and W-7405-ENG-48.

REFERENCES

Adelberger, D. C. & Harbottle, G. 1990, Phys. Rev. C, 41, 2320

Branch, D. 1990, in *Supernovae*, ed. S. Bludman, R. Mochkovitch & J. Zinn-Justin, in press

Branch, D. & Tammann, G. A. 1991, ARA&A, in press

Burstein, D., & Heiles, C. 1978, ApJ, 225, 40

Burstein, D., & McDonald L. H. 1975, AJ, 80, 17

Ciardullo, R., Ford, H. C., Neill, J. D., Jacoby, G. H., & Shafter, A. W. 1987, ApJ, 318, 520

Disney, M., Davies, J., and Phillips, S. 1989, MNRAS, 239, 939

Evans, R., van den Bergh, S., & McClure, R. D. 1989, ApJ, 345, 752

Frekers, D., *et al.* 1983, Phys. Rev. C, 28, 1756

Hashimoto, M., Nomoto, K., & Shigeyama, T. 1989, A&A, 210, L5

Heiles, C. 1976, ApJ, 204, 379

Higdon, J. C., & Fowler, W. A. 1987, ApJ, 317, 710

Kumagai, S., *et al.* 1989, ApJ, 345, 412

Leibundgut, B. 1991, in *Supernovae*, ed. S. E. Woosley, (Springer: Heidelberg), 751

Leibundgut, B. & Tammann, G. A. 1990, A&A, 230, 81

Leising, M. & Share, G. 1991, ApJ, in preparation

Mahoney, W. A., Ling, J. C., Wheaton, W. A., & Higdon, J. C. 1991, in *Gamma-Ray Line Astrophysics*, ed. P. Durouchoux & N. Prantzos, (AIP: New York), 291

Mihalas, D. & Binney, J. 1981, *Galactic Astronomy*, (Freeman: San Fransisco).

Porter, A. C. & Filipenko, A. V. 1987, AJ, 93, 1372

Ratnatunga, K. U. & van den Bergh, S. 1989, ApJ, 343, 713

Sandage, A., & Tammann, G. 1981, *Revised Shapley Ames Catalog of Bright Galaxies*, Carnagie Institute, Washington

Schmitz, M. R. & Gaskell, C. M. 1988, in *Supernova 1987A in the Large Magellanic Cloud*, ed. M. Kafatos & A. G. Michalitsianos, (Cambridge Univ. Press: Cambridge), 112

Suntzeff, N. B., Phillips, M. M., Depoy, D. L., Elias, J. H., & Walker, A. R. 1991, AJ, 102, 1118

Tammann, G. & Schröder, A. 1990, A&A, 236, 149

Tammann, G. A. 1991, in *Supernovae*, ed. S. Bludman, R. Mochkovitch, and J. Zinn-Justin, (Elsevier Sci. Publ.), in press

Valentijn, E. A. 1991, Nature, 346, 153

van den Bergh, S. 1990, AJ, 99, 843

van den Bergh, S. 1991a, in *Supernovae*, ed. S. E. Woosley, (Springer: Heidelberg), 711

van den Bergh, S. 1991b, *Phys. Rep.*, in press

van den Bergh, S. & Tammann, G. A. 1991, ARA&A, 29, 363

Woosley, S. E., Arnett, W. D., & Clayton, D. D. 1973, ApJS, 175, 731

Woosley, S. E. 1986, in *Nucleosynthesis and Chemical Evolution*, 16th Adv. Course of the Swiss Soc. of A&A, ed. B. Hauck, A. Maeder, and G. Meynet, (Geneva Obs.: Geneva), 1

Woosley, S. E. 1991, in *Gamma-Ray Line Astrophysics*, ed. P. Durouchoux & N. Prantzos, (AIP: New York), 270

Woosley, S. E & Pinto, P. 1988, in *Nuclear Spectroscopy of Astrophysical Sources*, ed. N. Gehrels & G. Share, (AIP: Washington DC), AIP 170, 98

Woosley, S. E., & Hoffman, R. D. 1991, ApJL, 368, L31 (WH)

Woosley, S. E., Pinto, P., & Weaver, T. A. 1988, *Proc. Astr. Soc. Australia*, 7, No. 4, 355

Woosley, S. E., Pinto, P., & Hartmann, D. 1989, ApJ, 346, 395

7.
VHE GAMMA-RAY OBSERVATIONS

Locating very high energy γ-ray sources with arc minute accuracy

C. W. Akerlof,[1] M. F. Cawley,[2] M. Chantell,[3] D. J. Fegan,[4] K. Harris,[3] A. M. Hillas,[5] D. G. Jennings,[6] R. C. Lamb,[6] M. A. Lawrence,[3] M. J. Lang,[4] D. A. Lewis,[6] D. I. Meyer,[1] G. Mohanty,[6] K. S. O'Flaherty,[4] M. Punch,[4] P. T. Reynolds,[6] M. S. Schubnell,[1] T. C. Weekes,[3] and T. Whitaker[3]

Abstract

The angular accuracy of γ-ray detectors is intrinsically limited by the physical processes involved in photon detection. Although a number of point-like sources were detected by the COS-B satellite, only two have been unambiguously identified by time signature with counterparts at longer wavelengths. By taking advantage of the extended longitudinal structure of VHE γ-ray showers, measurements in the TeV energy range can pinpoint source coordinates to arc minute accuracy. This has now been demonstrated with new data analysis procedures applied to observations of the Crab Nebula using Čerenkov air shower imaging techniques. With two telescopes in coincidence, the individual event circular probable error will be 0.13°. The half-cone angle of the field of view is effectively 1°.

Detecting the incident direction of energetic photons is a technically difficult problem. For quanta which cannot be focussed by coherent optical techniques, there are no elegant methods for accurately determining the source location in the sky. In the energy range from 100 KeV to 40 MeV, the two most common detection methods are scintillators shadowed by coded aperture masks and Compton scattering telescopes. Both require extensive deconvolution of the data to obtain a sky image. Above the electron pair production threshold, the obtainable accuracy improves with energy but practical limitations of size and weight limited the angular precision to the order of 25 arc minutes for satellite-borne instruments such as SAS-2 and COS-B. The consequence is that even though 12 γ-ray sources are listed in the most recent COS-B catalog (Grenier, Hermsen, & Pollock 1991), only two can be unambiguously identified by their characteristic time signatures with objects observed at longer wavelengths. This obviously poses severe problems for understanding their physical characteristics. The angular resolution of the EGRET instrument on the Gamma Ray Observatory is expected to be better, in the range of 5 to 10 arc minutes (Kanbach *et al.* 1989).

Recently, ground-based experiments have demonstrated the ability to unambiguously detect TeV γ-rays from the Crab Nebula (Weekes *et al.* 1989, Akerlof *et al.* 1989a). The Čerenkov air shower technique, using a tenuous radiator (air), detects an electromagnetic shower cascade several kilometers long and a few tens of meters wide. The characteristic narrow transverse dimensions of these showers permits rejection of the far greater

[1] Randall Laboratory of Physics, University of Michigan, Ann Arbor, Michigan 48109-1120
[2] Physics Department, St. Patrick's College, Maynooth, County Kildare, Ireland
[3] Fred Lawrence Whipple Observatory, Harvard-Smithsonian Center for Astrophysics, Amado, Arizona 85645-0097
[4] Physics Department, University College, Belfield, Dublin 4, Ireland
[5] Department of Physics, University of Leeds, Leeds, LS2 9JT, England, United Kingdom
[6] Department of Physics and Astronomy, Iowa State University, Ames, Iowa 50011-3160

background flux of hadronically initiated events. By selecting air showers based on the predicted characteristics of Čerenkov light images, a 20 σ detection of the Crab at γ-ray energies above 400 GeV has proven the efficacy of this technique. This method has been described extensively in previous papers (Weekes *et al.* 1989, Vacanti *et al.* 1991).

The image selection reduces the hadronic background for two independent reasons. First of all, the hadronic showers are broader in width because the typical interaction imparts a transverse momentum of the order of a pion mass to the secondary particles. The comparative transverse momentum for electromagnetic showers is set by the electron mass which is 270 times smaller. Secondly, hadronic shower directions are isotropic since the trajectory of the parent charged particle is thoroughly randomized by the intervening galactic magnetic fields. Thus, a selection based on the apparent arrival direction of the shower considerably favors γ-rays from a compact source relative to the hadronic background.

Roughly speaking, Čerenkov light images of electromagnetic showers can be characterized as elongated ellipses with the major axis representing the projection of the shower trajectory on the image plane. The location of the source must lie along this axis near the tip of the light distribution corresponding to the initial interaction of the shower cascade. With a single imaging telescope, one shower image alone cannot pinpoint the source direction but many events can be combined to restrict the common phase space to a relatively small area of the sky. The characteristic ratio of shower width to length implies that the shower direction can be measured to the precision of the order of 0.2°. By averaging over N events, the source location error can be reduced by $1/\sqrt{N}$, at least until systematic errors begin to dominate. We have carried through this type of analysis for two sets of observations of the Crab Nebula, one with the telescope pointing directly at the known sky position and the other with the telescope tracking a fixed point shifted in declination by 0.4° above the Crab. The number of events associated with the Crab signal was significantly larger than 100 for both measurements so that systematic tracking errors are more significant than the statistical errors. In each case, we find that the source location reconstructed from the shower images agrees with the tracking location to approximately 2 arc minutes. At this level, the dominant error can be attributed to the telescope angle encoders and the drive system which have 5 arc minute tolerances. This performance was predicted by Hillas several years ago on the basis of Monte Carlo simulations of air shower imaging (Hillas 1989).

Two different methods have been developed to recover the spatial origin of γ-rays from the Crab Nebula. The first technique can best be understood in terms of the schematic diagram of the Whipple 10-meter telescope high resolution camera shown in figure 1 (a detailed description of this apparatus can be found in Cawley *et al.* 1990). Three different geometric structures are depicted in overlapping layers. The 109-tube photomultiplier array of the high resolution camera is shown at the lowest level. The camera consists of an inner cluster of 91 29 mm diameter tubes surrounded by an outer ring of 18 51 mm diameter tubes.

The second overlapping structure is a Cartesian grid system covering an interval of $\pm 1.0°$ in both right ascension and declination directions. Each mesh point will be treated as a possible γ-ray source direction in the sky. Finally, a hatched ellipsoid depicts the outline of a typical shower image and three associated image parameters. Note that the image WIDTH and LENGTH are independent of the source position but the so-called AZWIDTH parameter depends sensitively on this assumed location. In figure 1, the indicated AZWIDTH value corresponds to a source direction at the center of the Cartesian grid. In general, each of the 441 mesh points will be associated with a different value. The procedure is to consider every mesh point as a possible source location. For each event, the image parameters are checked for compatibility with the γ-ray selection criteria previously developed (Weekes *et al.* 1989).

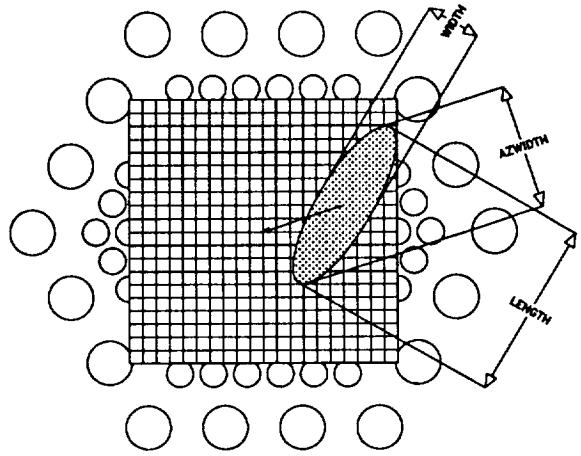

Figure 1. A schematic diagram of the analysis to evaluate the correlation of shower direction with right ascension and declination. A Cartesian grid consisting of 21 × 21 points spanning $\pm 1.0°$ in right ascension and declination is shown superimposed on the 109-tube Whipple high resolution PMT camera. A typical γ-ray shower image is depicted by the shaded elliptical figure. The indicated AZWIDTH parameter is associated with the center point of the Cartesian grid.

Those mesh points far from the true source direction will tend to have large values of AZWIDTH and so few events will be consistent with γ-rays emanating from a point source from these parts of the sky. Conversely, for mesh points near the source direction, most true γ-ray events will be accepted. By carrying out this process for every shower in the data sample, a three dimensional histogram can be constructed of events versus right ascension and declination within a field of view of $\pm 1.0°$. The results are shown in figure 2 for data taken on the Crab Nebula during 1988-1989. The total exposure was approximately 60 hours, divided equally between on-source and off-source observations. In figure 2a, the number of showers is plotted for data accumulated with the telescope pointed directly at the Crab Nebula and figure 2b shows data taken off-source with the telescope pointed several degrees away. Clearly, the on-source data is qualitatively different in shape. The broad central maximum apparent in the off-source data is an artifact of the event selection criteria. This effect can be reliably modeled by Monte Carlo techniques. Figure 2c shows a plot of the difference signal. The statistical significance of the signal is greater than 20 σ. As can be seen from the figure, the signal is an approximately Gaussian function of right ascension and declination with a circular probable error of $0.21°$ (13 arc minutes). The center of the distribution can be determined to a small fraction of this value.

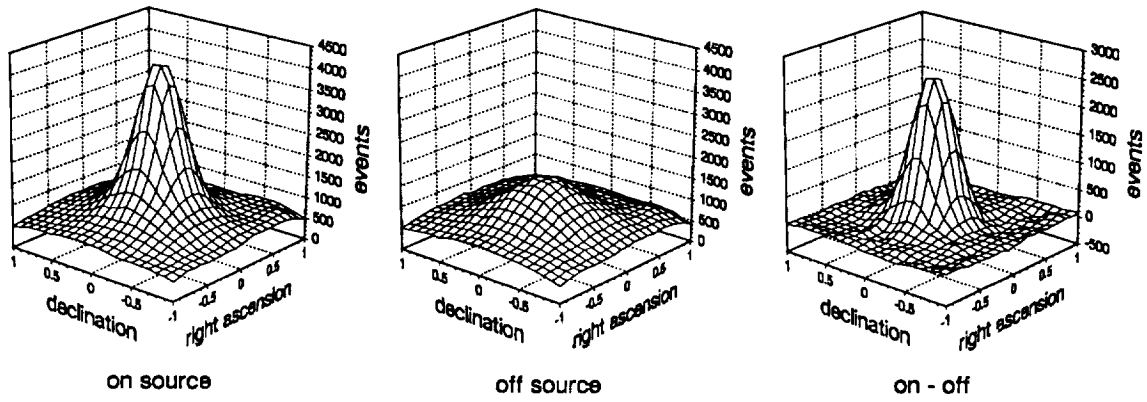

Figure 2. Histograms of data from the Crab Nebula: (a) on-source events plotted against right ascension and declination; (b) off-source events plotted against right ascension and declination; (c) on-source minus off-source events.

To prove this last point, a much shorter data exposure (4 hours on-source, 4 hours off-source) was taken with the γ-ray telescope tracking a celestial coordinate deliberately offset by a fixed angle from the Crab Nebula (0.4° in declination). The results are shown in figure 3. A contour plot of the on-source minus off-source distribution shows an 8 σ peak displaced from the origin. The center of the peak was determined by interpolation and compared with the known tracking offset. The values agreed to an accuracy of 0.036° or 2 arc minutes. The point spread function was the same as for the on-axis data discussed earlier. At this level of precision, the telescope tracking error will predominate so for future data taking, a CCD camera has been coaxially mounted to record the true sky position by simultaneous direct optical measurement of several nearby field stars. The Crab Nebula was also observed for a total of 11 hours on-source, 11 hours off-source with a 1.0° offset to the tracking

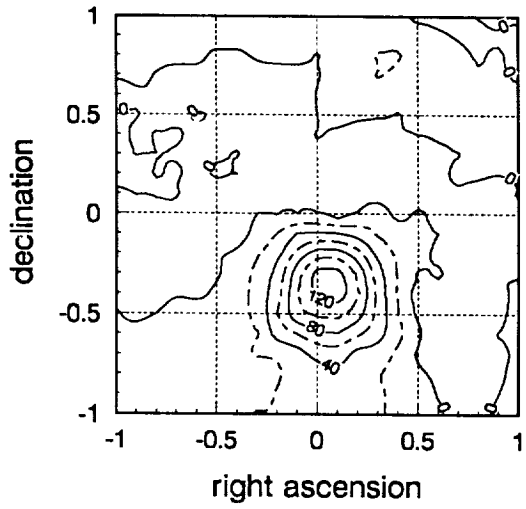

Figure 3. Contour plot of events from the 0.4° off-axis observations of the Crab Nebula plotted as a function of right ascension and declination.

direction. At this limit of the telescope field of view, the efficiency for detecting γ-rays was noticeably diminished ($\sim$ 50%). Nevertheless, a 6 σ signal was detected at the expected location.

A second analysis method has also been developed which similarly demonstrates the angular accuracy of the air shower imaging technique. The basic idea is depicted in figure 4. If the data sample is completely free of background hadronic events, the apparent source location can be obtained by finding the common intersection of the major axes of the images from two different showers. The method was applied to showers with shapes consistent with a γ-ray origin but whose orientation was completely unspecified. The analysis computed the intersection points for all possible pairs of such events, weighting each set of coordinates by the factor, sin^2(intersection angle) to compensate for the greater geometrical errors when the shower axes are almost parallel. Intersections are ignored if the distance from the intersection to the center of either shower is inconsistent with the shower's width-to-length ratio. Even with the admixture of some background, a distinctive sharp peak emerges for the Crab '88-'89 data plotted in figure 5. For a single telescope, the combinatorial background becomes relatively severe as the signal-to-noise ratio decreases. Coincident stereo shower imaging is not constrained by this problem so that figure 5 gives a good estimate of the expected performance of the Whipple twin γ-ray telescope system which is scheduled for completion in September 1991 (Akerlof *et al.* 1989b). From the on-source distribution (figure 5a), the circular probable error for a single pair of shower images was estimated to be 0.13°, (8 arc minutes). After averaging over a number of events, source coordinates should be obtainable with arc minute accuracy.

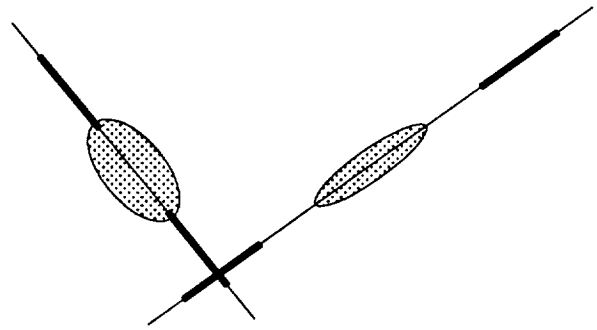

Figure 4. A schematic diagram of the shower axis intersection method for determining the γ-ray source direction. The light distribution for the two shower images is indicated by the shaded ellipses. The intersection of each possible shower pair is binned in right ascension and declination to find the most probable source location. The darkened portion of each shower axis corresponds to the expected arrival direction ±0.3°, based on the image width-to-length ratio. Only intersections of darkened lines are counted.

These analyses show that Čerenkov air shower imaging techniques are sensitive over a moderately large field of view with spatial accuracies considerably better than any other available γ-ray detector at any energy. For comparison, the COS-B collaboration quoted a circular probable error of 0.4° (24 arc minutes) for the location of Geminga. Figure 6 shows a map of radio and X-ray sources that lie within this boundary. The expected error circles for EGRET and the Whipple twin γ-ray telescope system are also plotted. The arc minute resolution of ground-based observations would almost certainly provide a

unique identification of Geminga with the radio and X-ray counterparts. The single event circular probable error is still too large to distinguish if γ-ray emission from the Crab Nebula extends over the optically luminous region which covers roughly 4 by 6 arc minutes (Baade 1942) or is confined more closely to the vicinity of the pulsar.

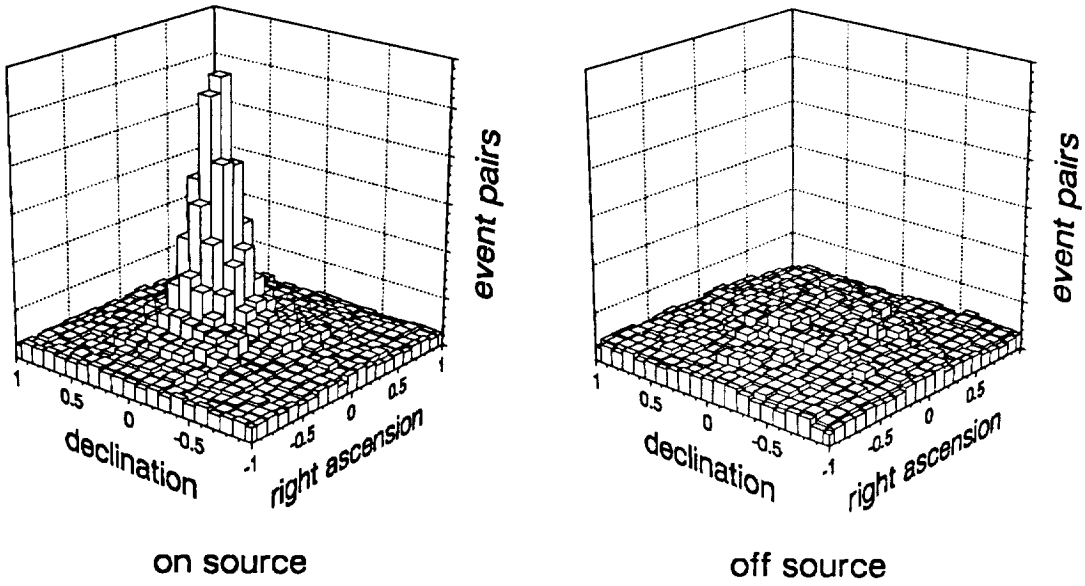

Figure 5. Histograms of shower pair intersection data from the Crab Nebula. Each event is weighted according to the prescription given in the text. (a) on-source data plotted against right ascension and declination; (b) off-source data plotted against right ascension and declination.

We can now take advantage of the image localization to double the available exposure time for data taking. In the past, equal periods were spent recording events from on-source and off-source directions. The off-source direction was typically $\pm 7.5°$ in right ascension from the expected source coordinates. The data shown in figures 2 and 3 prove that on-source and off-source data can be recorded in overlapping fields. For example, we have recently operated in a mode where the telescope alternately tracked a sky coordinate displaced $\pm 0.5°$ in right ascension on either side of the source of interest. The benefit is a factor of two greater exposure time with a negligible loss of apparent signal strength due to the on-off subtraction. A side benefit is an additional reduction in systematic errors since the on and off data more closely measure the same regions of sky. If the sensitivity of this new generation of VHE detectors can reach the flux levels required, ground-based experiments may provide considerable help in identifying the specific sources responsible for energetic γ-ray emission.

Acknowledgments

This work was supported, in part, by the U. S. Department of Energy contracts DEAC02-76ER01112, DE-AC02-80ER10774, and DE-AC02-826ER40063, the Smithsonian Scholarly Studies Fund, and Eolas, the Irish Scientific Funding Agency. Support by NASA grants NAG 5-1381 and NAG 5-1591 is also acknowledged.

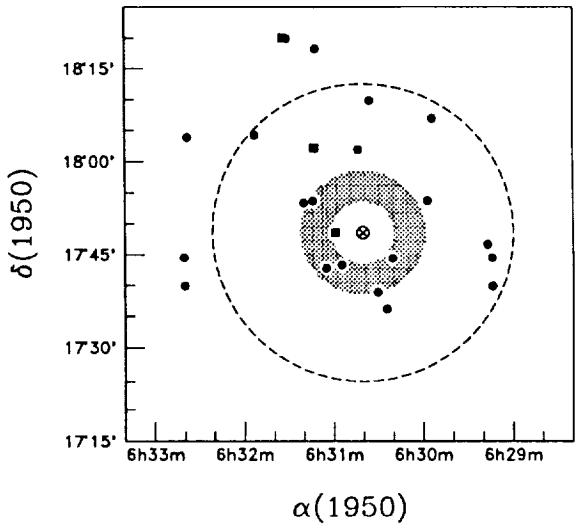

Figure 6. A plot of X-ray and radio sources near Geminga (taken from Spelstra and Hermsen 1984). The three solid squares are Einstein X-ray sources; the solid circles are radio sources measured at Westerbork. The large dotted circle shows the circular probable error for the location of Geminga. The shaded annulus is the 5-10 arc minute resolution predicted for EGRET. The inner radius of this ring corresponds to the measured resolution of the 10-meter Whipple telescope which is currently limited by the drive shaft angle encoder accuracy. The small circle near the center represents the one arc minute error obtainable with the Whipple twin Čerenkov air shower telescopes.

References

Akerlof, C. W., *et al.* 1989a, in *Proceedings of the Gamma Ray Observatory Workshop*, pp. 4.49-4.56, NASA/Goddard SFC, Greenbelt, MD (April 10-12, 1989).

Akerlof, C. W., *et al.* 1989b, in *Proceedings of the SPIE 33rd Annual International Symposium, EUV, X-Ray, and Gamma-Ray Instrumentation for Astronomy and Atomic Physics*, vol. 1159, pp. 270-279, San Diego, CA (August 7-11, 1989).

Baade, W. 1942, Ap.J. **96,** p. 188.

Cawley, M. F., *et al.* 1990, *Experimental Astronomy* **1**, p. 173.

Grenier, I. A., Hermsen W., and Pollock, A. M. T. 1991, in *High Energy Gamma-Ray Astronomy,* AIP Conference Proceedings 220, ed. J. Matthews, Ann Arbor, Michigan, pp. 3-12.

Hillas, A. M. 1989, in *Proceedings of the International Workshop on Very High Energy Gamma Ray Astronomy,* ed. A. A. Stepanian, D. J. Fegan, and M. F. Cawley, Crimea, USSR, pp. 134-137.

Kanbach, G., *et al.* 1989, in *Proceedings of the Gamma Ray Observatory Workshop*, pp. 2.1-2.10, NASA/Goddard SFC, Greenbelt, MD (April 10-12, 1989).

Spelstra, T. A. Th., and Hermsen, W. 1984, Astr.Ap. **135,** p. 135.

Vacanti, G. *et al.* 1991, Ap.J. **377,** p. 467.

Weekes, T. C. *et al.* 1989, Ap.J. **342**, p. 379.

Status of the Whipple Observatory Cerenkov Air Shower Imaging Telescope Array

C.W.Akerlof(1), M.F.Cawley(2), D.J.Fegan(4), S.Fennell(4), S.Freeman(1), D.Frishman(1), K.Harris(3), A.M.Hillas(5), D.Jennings(6), R.C.Lamb(6), M.A.Lawrence(3), D.A.Lewis(6), D.I.Meyer(1), M.Punch(4), P.T.Reynolds(6), M.S.Schubnell(1), T.C.Weekes(3)

(1) University of Michigan
(2) St. Patrick's College, Maynooth
(3) Harvard-Smithsonian Center for Astrophysics
(4) University College, Dublin
(5) University of Leeds
(6) Iowa State University

Introduction

Recently the power of the Cerenkov imaging technique in VHE gamma-ray astronomy has been demonstrated by the detection of the Crab nebula at high statistical significance by the Whipple collaboration [1]. This was independently confirmed using a similar method by the University of Michigan group [2]. In order to further develop this technique to allow the detection of weaker or more distant sources a second 10 m class reflector has been constructed about 120 m from the original instrument. Figure 1 shows the location of the two reflectors on the 2300 m ridge of Mount Hopkins, Arizona. The addition of the second reflector will allow both a reduction in the energy threshold and an improvement in the rejection of the hadronic background. The design and construction of the second reflector, GRANITE (Gamma Ray Astrophysics New Imaging TElescope) [3] is described below.

Mount and Optical Support Structure

The mount was manufactured by McDonnell Douglas to be used as a solar concentrator for electrical power generation. It consists of a pedestal with an elevation over azimuth drive system and a parabolic dish framework of 7.62 m focal length. The dish was modified to accommodate our mirror mounting system by welding brackets to the frame to hold the **aluminum** bars to which the mirror mounting plates are bolted. The pedestal and drive were installed in October 1990 and the dish elements were attached in March 1991. Two views of the reflector are shown in Figure 2. The elevation and azimuth are driven by identical 1/2 hp 480 V motors

running at 1760 rpm through helical gear systems. Motion of the dish is governed by a microprocessor controller located in the pedestal which reads the mount sensors and switches power to the motors accordingly. This in turn is controlled through a serial line by either a hand-held remote control or a DEC PDP-11/23 computer. The computer software is a version of the solar tracking program modified to track sidereally and to communicate with the GRANITE data acquisition computer.

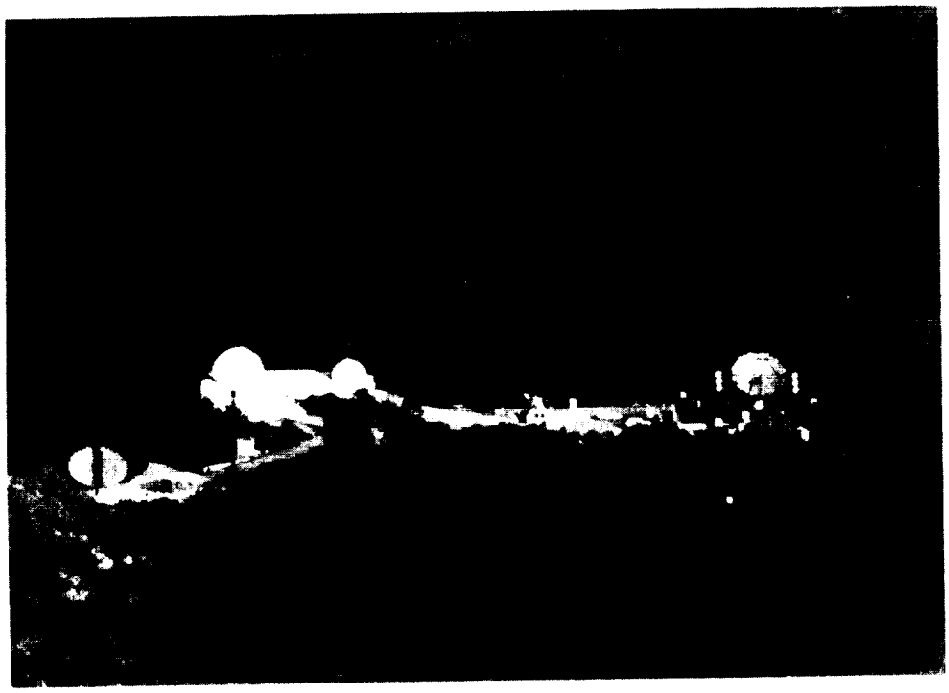

Figure 1: The Whipple Observatory Cerenkov imaging reflectors. The original 10 m reflector is on the right. The central building houses 1.5 m and 1.2 m optical telescopes.

Mirrors

The mirrors are hexagonal elements measuring 46 cm across the flats. They were designed to be robust and to withstand many years of use in an exposed position without significant degradation of the optical quality. The mirrors were fabricated by cutting 5 cm thick foam glass to the required hexagonal shape and then grinding the desired figure into the material using abrasive paper glued to an aluminium form with the appropriate curvature. Then epoxy was applied to both the foam glass and a hexagon of 0.7 mm thick back-aluminized glass and the two pieces pressed together with a weighted form identical to that used in the grinding process. Only a few pounds of weight were required to deform the thin glass to the desired shape; no heating is used. Finally the outer edge was beaded with polyurethane caulk and the foam glass painted with

mastic and latex paint to enhance durability. This construction technique using second surface reflection and durable materials produces mirrors which can be washed if necessary and will not require recoating. Resistance to hail damage was tested by dropping ice cubes onto the mirrors from 15 m. Should the glass be shattered at a point the adhesive tends to limit the propagation of the cracks. A test mirror has been mounted on the 10 m reflector for over a year with no sign of deterioration. Four different focal lengths were fabricated to approximate the parabola defined by the structure of the reflector. The rms error in all the mirror surfaces was measured to be less than 0.3 mr [4].

The mirrors have a 15 cm square plate epoxied to the back to facilitate mounting. They are mounted by a three point system with two threaded adjusters to allow for alignment. The three mounting rods are attached to an aluminium plate which is bolted to the mirror bars on the dish. A total of 366 mirrors are currently mounted on the reflector giving a reflective surface of 66.3 m^2. The total mass of mirrors and mounting system is approximately 1550 kg.

The alignment of the mirrors was performed using a retro-reflection technique. The alignment device consists of a 10 mW He-Ne laser mounted on an optical bench aligned with the optic axis of the dish. The optic axis is defined by a similar laser mounted on the reflector. The alignment beam, expanded to cover the area of a single mirror, is reflected from each of the mirrors in turn and the mirror orientation adjusted to reflect the light back along the outgoing path to a screen placed around the laser exit aperture.

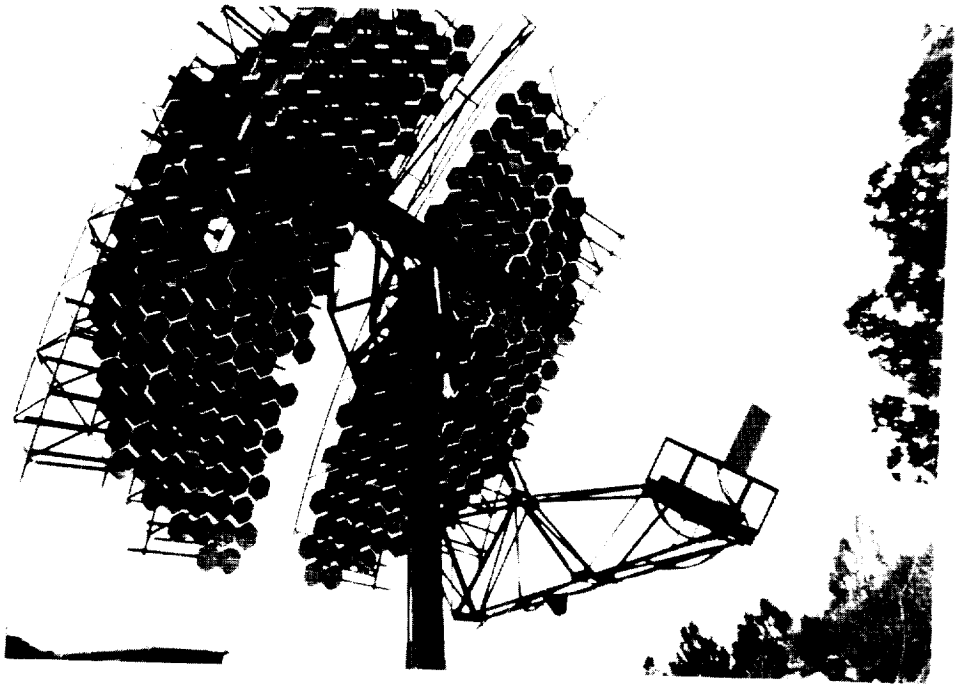

Figure 2a: The 11m reflector in a stow position, facing north and about 30 degrees below the horizontal.

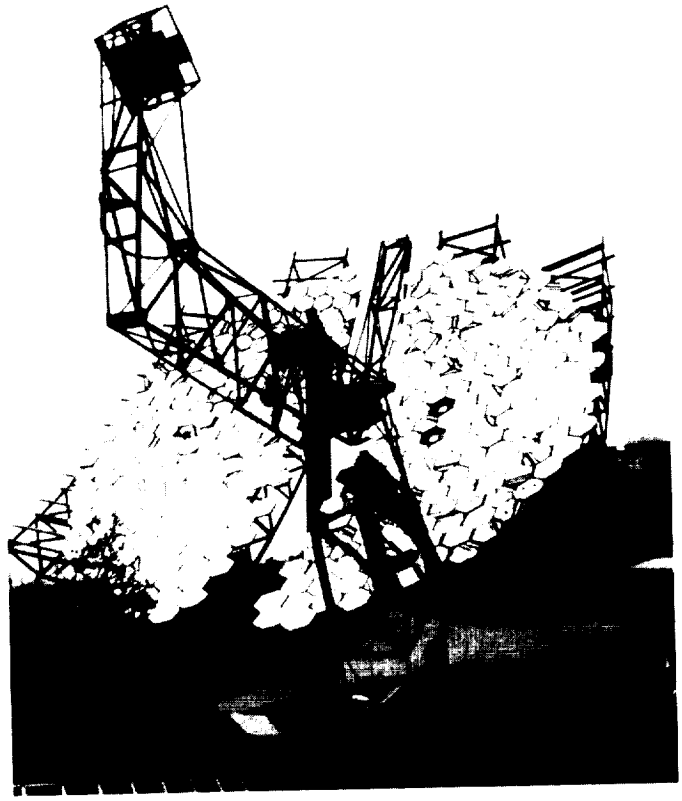

Figure 2b: The 11m reflector at about 45 degrees elevation.

Camera and Electronics

The camera currently at the focus of the reflector consists of 37 photomultipliers of 5 cm diameter (Amperex XP2230) each with a 0.5 degree field of view. This camera design is essentially identical to that used previously in the Whipple Observatory 10 m reflector [5]. The focus box includes a motorized shutter system to protect the photomultipliers during daylight. The camera will be upgraded to 109 photomultipliers to match the current configuration of the 10 m reflector as funds allow.

The data acquisition system has been designed to extract as much information as possible from each event. For every

photomultiplier pulse the integrated charge, arrival time and pulse width will be measured. The recording system is able to operate both independently and in coincidence with the 10 m reflector and with event burst rates of up to 1 kHz. Two levels of trigger are implemented: a low-level trigger accepted in coincidence with a signal from the remote dish or a higher level trigger recorded independently of the status of the remote instrument. The front-end electronics are an in-house design incorporating two discriminators and a wide band amplifier for each channel [6]. The majority of the remainder of the electronics are commercial CAMAC modules, controlled by an in-crate LSI-11 microcomputer. The LSI-11 writes the data in a memory buffer which is read out by the VAXstation 3200 which controls the overall data acquisition system and also the photomultiplier high voltage supply. The UTC time of each event will be established by a GPS clock to an absolute accuracy of 750 ns. In addition events at both reflectors will be tagged by a counter module clocked at 20 MHz to facilitate offline matching of coincident events. This will also allow the Cerenkov light signals in the two telescopes to be correlated to an accuracy of better than 1 ns.

Anticipated Performance

It is estimated that the combined effect of stereoscopic imaging and a lowered energy threshold will permit roughly an order of magnitude increase in flux sensitivity for showers imaged in both telescopes. The angular resolution for these events will be approximately one arc-minute [7], and the energy threshold is expected to be 100 GeV, with a trigger rate of approximately 50 Hz. The angular resolution exceeds that of any gamma ray detector, whilst the energy threshold approaches the upper energy limit of the EGRET instrument on GRO. The stereoscopic imaging will allow the arrival direction and ground impact point of showers to be determined unambiguously. This will enable accurate measurement of the sensitive area of the telescope, resulting in better measurements of energy spectra and absolute flux levels.

The GRANITE twin telescope system will serve as a prototype for a much larger array of imaging detectors, CASITA (**Cerenkov** Air Shower Imaging Telescope Array). In an array the Cerenkov light pool would be sampled by a number of imaging detectors simultaneously, giving further improvements in rejection of the hadronic background. A high altitude site combined with a large Cerenkov light collecting area will lower the energy threshold, and triggering on coincidences between the detectors will enable the array to operate at very low light levels. Improved optics and higher resolution cameras will enhance the hadron rejection obtained by imaging. Operation of GRANITE will assist in the determination of the optimum design parameters for a future imaging telescope array both directly and by providing a check on simulations performed for this purpose.

References

[1] Vacanti G. et al. Ap. J. 377, 467 (1991)
[2] Akerlof C.W et al. Proceedings of the Gamma-Ray Observatory Workshop, G.S.F.C., Ed. W.N Johnson, **4-49**, (1989)
[3] Akerlof C.W et al. Nucl. Phys. B., 14A, 237 (1990)
[4] Weaverdyck C et al. 1991, submitted to N.I.M
[5] Weekes T.C et al. Ap. J. 342, 379, (1989)
[6] Levy H. et al. N.I.M. A292 715, (1990)
[7] Akerlof C.W et al. Ap. J. Lett. 377, L97 (1991)

Underground Muons from the Direction of Cygnus X-3

Soudan 2 Collaboration

Argonne National Laboratory, University of Minnesota, University of Oxford, Rutherford Appleton Laboratory and Tufts University

(Paper presented by M. L. Marshak, University of Minnesota)

We have measured the flux of underground muons from the direction of the binary Cygnus X-3 using the Soudan 2 proton decay detector. This time-projection calorimeter is located at a depth of 2200 m water equivalent in northern Minnesota at latitude 48° N, longitude 92° W. We then performed an analysis comparing both the total observed flux and the observed flux per transit with the number of events expected in the absence of a source. This expected number of events was determined by combining the detector acceptance as a function of time with the detector acceptance as a function of the local spatial coordinates. These functions were evaluated by use of off-source events. The direction of Cygnus X-3 was defined as a 2° half-angle cone, centered on the nominal source coordinates. This definition is consistent with the expected appearance of a point source in the Soudan 2 detector after consideration of track reconstruction errors, multiple scattering in the rock and possible systematic effects. Details of this analysis and the results are described in Ref. 1.

The integrated muon flux from January 1989 through February 1991 is consistent with the expected background, suggesting that Cygnus X-3 is not a steady-state source of particles which produce muons at a level observable by the Soudan 2 detector. The background calculation for the integrated flux was checked by comparing off-source observations with the background expectation. A folding of the total event sample using the Cygnus X-3 orbital ephemeris also indicated good consistency with background.

The validity of the daily background flux calculations is shown in Fig. 1, which plots the distribution of observed minus expected events for 41355 sources x days for fake sources located at the same declination as Cygnus X-3 but at differing right ascensions. The line is the expectation of a Poisson probability distribution. Fig. 2 shows events observed vs. events expected for 696 days of data for the Cygnus X-3 direction. The lines indicate Poisson probabilities of 10^{-3}. Two days are distinguished—20 and 23 January 1991. Both these days correspond to the major radio flux peak of one of 5 large radio flares of Cygnus X-3 which occurred between January 1989 and February 1991. Muon fluxes during the other radio flares showed no significant excess, although the Soudan 2 detector was smaller and had less sensitivity in 1989 and 1990. A subsequent analysis also indicated no significant deviation from background for the muon flux during the July 1991 Cygnus X-3 radio flare. Event arrival times within the days of 20 and 23 January 1991 are not significantly modulated either by time of arrival or by Cygnus X-3 orbital phase. The estimated muon flux for these two days is $\approx 7.5 \times 10^{-10}$ cm^{-2} s^{-1}. The estimated chance probability of this result is 5.5×10^{-4}.

This work is supported by the U.S. Department of Energy and the U.K. Science and Engineering Research Council. We acknowledge the cooperation of the State of Minnesota, Department of Natural Resources.

[1] M. A. Thomson *et al.*, Phys. Lett. **B269**, 220 (1991)

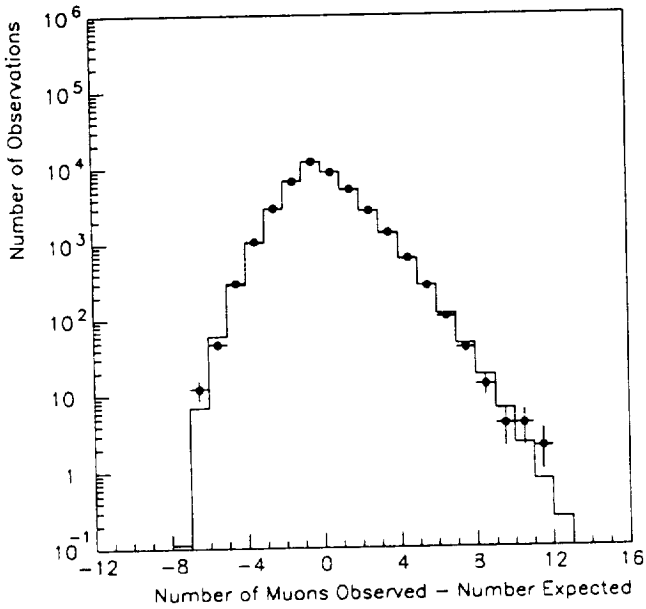

Fig. 1—The points are a histogram of the number of observed minus number of expected events for each live day for each of sixty 2.0° half-angle cones at the declination of Cygnus X-3. The solid curve is the prediction of Poisson statistics. A total of 41355 sources x days have been considered.

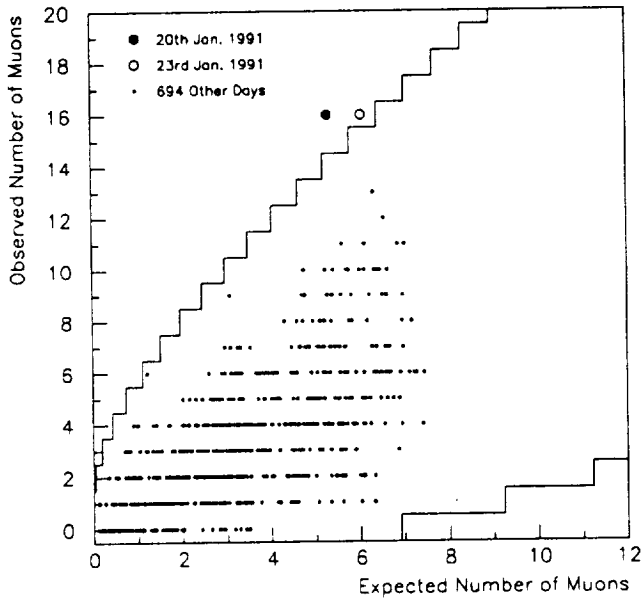

Fig. 2—A scatter plot of the number of muons observed from the direction of Cygnus X-3 on a given day vs. the number expected on that day for a total of 696 days. The lines show the 10^{-3} probability boundaries.

8.
STELLAR SOURCES

A NEW CLASS OF GALACTIC DISCRETE γ-RAY SOURCES: CHAOTIC WINDS OF MASSIVE STARS

Wan Chen[1,2] and Richard L. White[1]

[1] Space Telescope Science Institute
3700 San Martin Drive, Baltimore, MD 21218

[2] Department of Physics and Astronomy
The Johns Hopkins University, Baltimore, MD 21218

ABSTRACT

We propose a new class of galactic discrete γ-ray sources, the chaotic, high mass-loss-rate winds from luminous early-type stars. Early-type stellar winds are highly unstable due to intrinsic line-driven instabilities, and so are permeated by numerous strong shocks. These shocks can accelerate a small fraction of thermal electrons and ions to relativistic energies via the first-order Fermi mechanism. A power-law-like photon spectrum extending from keV to above 10 MeV energies is produced by inverse Compton scattering of the extremely abundant stellar UV photons by the relativistic electrons. In addition, a typical π^0-decay γ-ray spectrum is generated by proton-ion interactions in the densest part of the winds.

1. INTRODUCTION

Until recently the theoretical and observational studies of discrete cosmic γ-ray sources were focused on those where a large fraction of their total energy output is believed to be in γ-rays (*e.g.*, neutron stars, supernovae, or candidates for black holes), because in general they are also the brightest. The capability of the *Compton Gamma Ray Observatory (CGRO)* to detect much fainter sources than before marks the beginning of a new era. We can now not only study the luminous γ-ray sources at larger distances, but we can also explore the intrinsically weak sources whose γ-ray radiation may represent only a small fraction of their total energy output. As we have shown in recent papers (Chen & White 1991c; Chen & White 1992a), the chaotic winds of massive stars may well possibly be such a new class of Galactic discrete γ-ray sources.

Many authors have pointed out (White 1985; Pollock 1987a; Montmerle 1990) that γ-rays may be produced in the entire circumstellar atmosphere of the hot stars by relativistic particles (electrons and ions), which are accelerated from the thermal population via the first-order Fermi mechanism by shocks embedded in the winds. Since these stellar winds generally have simple spherical geometries and well measured stellar/wind parameters, they provide a particularly clean astrophysical laboratory to study shocks, Fermi particle acceleration and other high energy physical processes which are in general confused by complex geometries, unknown physical parameters and/or other complications in neutron stars, accreting binaries or AGNs.

In this paper, we draw an overall picture of the γ-ray production by chaotic stellar winds. Its specific application to Cyg OB2 stellar association is addressed elsewhere (Chen & White, this volume).

2. CHAOTIC WINDS

Early-type stars (O, early B and Wolf-Rayet stars) occupy the upper-left corner of the Hertzsprung-Russell diagram. They are all very hot ($T_{eff} > 20,000$ K), massive ($M > 20\,M_\odot$, progenitor mass for WR stars) and luminous ($L_{bol} > 10^5 - 10^6\,L_\odot$). While the enormous radiation of a massive star provides abundant ionizing UV photons for the surrounding HII region, its extremely large radiation pressure drives the outer atmosphere outwards to form a strong stellar wind. The typical mass-loss rate of a massive star ranges from $10^{-6} - 10^{-4}\,M_\odot\,\mathrm{yr}^{-1}$, and the typical wind terminal velocity is usually greater than $10^3\,\mathrm{km\,s}^{-1}$ (Cassinelli 1979). Such strong stellar winds ($L_w \geq 10^{37}\,\mathrm{ergs\,s}^{-1}$) are one of the major sources of mass and energy input into the interstellar medium (Abbott 1982).

The radiation force in the early-type stellar winds accelerates the mass outflow through scattering and absorption by thousands of spectral lines of the heavy elements rather than just electron scattering (Castor, Abbott & Klein 1975; Pauldrach, Puls & Kudritzki 1986). The progressive Doppler shifting of the line opacity into the unattenuated photospheric radiation field can result in a very rapid acceleration to the terminal wind velocity, $V(r) = V_\infty(1 - R_*/r)^\beta$ where $\beta \sim 1$.

Since the line-driven force depends strongly on the velocity gradient, however, it also introduces severe intrinsic instabilities to the wind flow (Owocki & Rybicki 1984). If a gas parcel in a line center moves a little faster than the surrounding gas, it moves to the blue wing where it sees a less attenuated radiation field. It consequently is subjected to greater radiative acceleration and moves even faster. Recent numerical simulations (Owocki, Castor & Rybicki 1988) show that such an instability can grow exponentially into a nonlinear phase with strong multiple shocks in the winds; the resulting wind velocity structure agrees well with Lucy's (1982) speculations. However, Lucy's theory predicts about a few percent or so of the wind kinetic power will go into shocks, $L_s \geq 10^{35}\,\mathrm{ergs\,s}^{-1}$, but Owocki *et al.*'s simulations generate considerably less power in shocks.

Due to the large column density of the winds, the post-shock gas cools very quickly. The thickness of the post-shock cooling region is only a tiny fraction of the typical length scale in the winds, so the shocks are usually isothermal (Lucy 1982; Krolik & Raymond 1985; Owocki, Castor & Rybicki 1988; Chen & White 1991a).

The existence of strong shocks permeating in winds has long been used to explain the soft X-ray emission from early-type stars (Lucy & White 1980; Lucy 1982) observed by the *Einstein Observatory* in early 1980's (*e.g.*, Rosner, Golub & Vaiana 1985). The small amount of absorption observed at the low energy band of the IPC favors the shock interpretation over other alternatives like the corona model (Cassinelli & Olson 1979) in which soft X-rays from a hot corona of a few million degrees located deep at the base of the winds would have suffered severe photoelectric attenuation. The once-in-a-lifetime observation of Orion OB supergiants by the SSS on *Einstein* (Cassinelli & Swank 1983) reveals

a hard X-ray component above 2 keV which places a more severe constraint on the corona model: to explain this one needs an even-hotter corona of a few 10^7 K superimposed on the cooler one. It seems not conceivable to build such a two-component corona above the fully radiative upper photosphere of early-type stars.

On the other hand, if we adopt the shock model, the hard X-ray excess can be naturally explained by the inverse-Compton scattering of the stellar UV photons by relativistic electrons accelerated by the shocks in the winds (Chen & White 1991a). The existence of relativistic electrons in the hot stellar winds gains its primary support from radio observations: a synchrotron radiation model (White 1985) can account for the nonthermal radio emission observed from about 25% of early-type stars (Abbott *et al.* 1986; Bieging, Abbott & Churchwell 1989). These successes have prompted many authors to speculate that the relativistic particles accelerated by shocks in the winds may provide a natural platform for a unified theory of non-thermal emissions from hot stars (White 1985; Pollock 1987a; Montmerle 1990; Chen & White 1991b).

3. PARTICLE ACCELERATION

Particle acceleration at astrophysical shock fronts via the first-order Fermi mechanism is believed to be responsible for the production of relativistic particles (cosmic rays) in a variety of astrophysical circumstances (see recent reviews by Blandford & Eichler 1987 and Jones & Ellison 1991). For strong steady-state shocks, results from a simple test particle method (Bell 1987) agree well with that from other more advanced (but more complicated) approaches (Blandford & Eichler 1987; Jones & Ellison 1991).

The accelerated particle spectral index α depends only on the shock velocity jump χ, $\alpha = (\chi+2)/(\chi-1)$. An isothermal shock with large velocity jump produces a much flatter particle spectrum than an adiabatic shock. However, if the diffusion length of particles is a function of energy, less energetic particles may travel only across the adiabatic sub-shock front. In this case the particle spectrum is concave: it is steep at low energies and flattens towards higher energies (Chen & White 1991a).

In stellar winds, the electron spectrum is further modified (Chen & White 1991a) by the severe inverse Compton losses even at fairly large radii (Pollock 1987a; Chen & White 1991a). While the competition between the acceleration and radiative cooling completely determines the electron high energy cutoff, it also tends to encourage electrons to pile up just below the cutoff. The electron spectrum near the shock front in winds exhibits a high energy hump (Webb, Drury & Biermann 1984; Fritz 1989) that develops into a sharp spike farther away from the shock (Fritz 1989; Chen & White 1991a).

We do not know yet how the post-shock pressure is distributed between the thermal and nonthermal components (Blandford & Eichler 1987; Jones & Ellison 1991). A simple phenomenological approach to this problem is to assign a fixed post-shock pressure ratio of the nonthermal particles to the thermal gas and then compare the model results with observations. Comparison of the thermal X-ray spectra of Orion stars observed by SSS (Cassinelli & Swank 1983) with the predictions from Lucy's model reveals this ratio to be $\sim$ 20% (Chen & White 1991a), a value that agrees well with direct measurements at the

Earth's bow shock (Ellison, Möbius & Paschmann 1990).

The electrons are harder to accelerate (Blandford & Eichler 1987; Jones & Ellison 1991) and in general have softer spectra (Chen & White 1991a). Fitting the hard X-ray component with our inverse Compton model suggests a self-consistent post-shock electron pressure ratio of about 5% (Chen & White 1991a; Chen & White 1991c). These values are used for our calculations for all stars and the expected uncertainty is less than a factor of a few.

The multiple shock structure in the massive stellar winds raises another interesting theoretical challenge: to find an effective method to deal with multiple acceleration of particles by shocks. We have developed a powerful analytical formula for this problem (Chen & White 1992b) based on a revised version of Bell's (1978) single particle method which includes the inverse Compton cooling effects (Chen & White 1991a). Our results generally agree well with White's (1985) simpler analysis: multiple acceleration flattens the electron spectrum.

4. γ-RAY PRODUCTION

Both relativistic ions and electrons may potentially produce γ-ray radiation in winds, though through different emission mechanisms and in different energy ranges. Pollock (1987a) suggests that γ-rays up to GeV energies from massive stellar winds may come from bremsstrahlung radiation of the relativistic electrons. But our study shows that for electrons inverse Compton cooling is the most important energy loss mechanism (Chen & White 1991a) and so almost all the energies pumped into suprathermal electrons is radiated away via inverse Compton scattering. The up-scattered photon spectrum is a quasi-power-law from keV to ≥ 10 MeV energies (Chen & White 1991c).

The relativistic ions in winds produce γ-rays through decays of neutral pions which are generated by the ion-ion collisions with thermal ions in the winds (White 1985). A power-law spectrum of nonthermal ions produces a typical π^0-decay γ-ray hump peaking at ~ 67 MeV (*e.g.*, Trombka & Fichtel 1983).

The γ-ray luminosity of the inverse-Compton and π^0-decay components can be roughly estimated from the wind energy budget argument (Chen & White 1991c). The total energy going into nonthermal ions is $\geq 10\%$ of the shock's kinetic power, *i.e.*, $L_i \geq 10^{34}\,\mathrm{ergs\,s^{-1}}$, and the energy going into nonthermal electrons is about an order of magnitude less, $L_e \geq 10^{33}\,\mathrm{ergs\,s^{-1}}$. The electron-generated inverse Compton γ-ray luminosity is roughly of the same order of the total electron power, $L_{\gamma,e} \sim 10^{33}\,\mathrm{ergs\,s^{-1}}$; but the ion-generated π^0-decay γ-ray luminosity is $< 10\%$ of the total ion power, *i.e.*, $L_{\gamma,i} \sim 10^{33}\,\mathrm{ergs\,s^{-1}}$, since the ion-ion interaction optical depth in the winds is usually < 0.1.

The π^0-decay γ-ray luminosity is expected to be much larger from high mass-loss-rate winds, including many Wolf-Rayet stars and some of the early O stars, since it depends on the densities of both thermal and nonthermal ions (which scale roughly the same way), $L_{\gamma,i} \propto \dot{M}^2/(R_* V_\infty{}^2)$. The driving mechanism of Wolf-Rayet winds, however, is still a subject of debate which introduces large uncertainties in their expected γ-ray fluxes (Chen & White 1992a). On the other hand, the inverse-Compton γ-ray luminosity depends also on the stellar photospheric luminosity, $L_{\gamma,e} \propto \dot{M}\, L_{bol}/(R_* V_\infty)$. So in general high luminosity

stars may have higher flux at sub-MeV energies and high mass-loss-rate winds will be brighter in GeV energies.

The stellar magnetic fields have a profound effects on both the inverse-Compton and π^0-decay γ-ray fluxes. This is simply because the local field strength defines the particle diffusion length scale near the shock front (White 1985). A larger field means a smaller mean free path for both ions and electrons, which then gives a greater high energy cutoff for the particle spectra. Since we have fixed the total energy share of the nonthermal particles in the post-shock region, a larger energy span leads to a lower number density of the particles. This in turn produces a more energetic photon spectrum but less flux at peak energies. In our models we choose low field strength for O stars ($\sim$ 1 Gauss) and higher values ($\geq$ 100 Gauss) for Wolf-Rayet stars based on earlier estimates from radio and X-ray observations (White 1985; Abbott *et al.* 1986; Pollock 1987a; Bieging, Abbott & Churchwell 1989; Chen & White 1991a; Chen & White 1992a).

The detectability of γ-ray emission from early-type stellar winds by various *CGRO* instruments depends sensitively on the spectral shape and relative intensity of the two components of ions and electrons for a given star. Our calculations show that γ-ray flux from some nearby ($\leq$ 2 kpc) massive stars are marginally detectable by both OSSE and EGRET (Chen & White 1991c; Chen & White 1992a). Given the moderate spatial resolution of *CGRO*, the combined γ-ray flux from a dense stellar association can have a much better chance of being detected. We will address this in more detail in a companion paper (Chen & White, this volume).

5. OUTLOOK

Though the idea of potential γ-ray emission from early-type stellar winds is not new (White 1985; Pollock 1987a; Montmerle 1990), our recent studies have put these ideas on a firm physical foundation, and we have constructed a quantitative model that can be compared directly with observations. Exploration by *CGRO* will not only reveal/confirm the violent nature of these otherwise "normal" stars but also will help improve our understanding of Fermi acceleration of particles by shocks. The knowledge we gain here can be applied to a variety of astrophysical circumstances.

Our study of stellar wind γ-ray emission is an important part of our much larger effort to draw a unified picture of nonthermal emissions from chaotic massive stellar winds (Pollock 1987a; Montmerle 1990; Chen & White 1991b). Figure 1 shows such a broadband spectrum we envision for a luminous massive star and its circumstellar wind. Notice that the dashed lines represents the flux predicted from our theoretical calculations. Observations in all the wavelengths will help to solidify this picture, and we expect pioneering observations by *CGRO* to play a very important role.

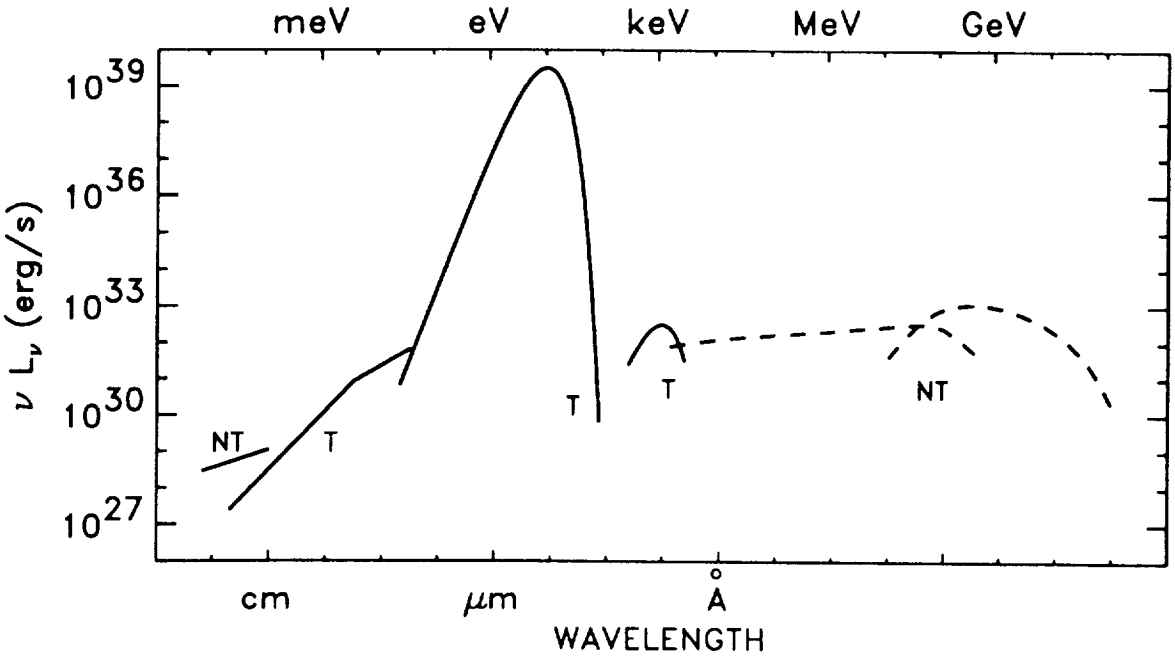

Figure 1. The broad band spectrum from radio to γ-ray for a typical early-type massive star. Spectra marked NT are the nonthermal components, marked T are the thermal components. Thermal radio-IR is the free-free radiation of the hot wind. Thermal X-ray emission is from the shocks in the wind. All the nonthermal radio, X-ray and γ-ray emission are produced by relativistic particles accelerated by the shocks. We see that γ-rays dominate the nonthermal emission.

REFERENCES

Abbott, D.C. 1982, ApJ, 263, 723

Abbott, D.C., Bieging, J.H., Churchwell, E., & Torres, A.V. 1986, ApJ, 303, 239

Bell, A.R. 1987, MNRAS, 182, 147

Bieging, J.H., Abbott, D.C., & Churchwell, E. 1989, ApJ., 340, 518

Blandford, R.D., & Eichler, D. 1987, Phys. Rep., 154, 1

Cassinelli, J.P. 1979, Ann.Rev.A.Ap., 17. 275

Cassinelli, J.P., & Olson, G.L. 1979, ApJ, 229, 304

Cassinelli, J.P., & Swank, J.H. 1983, ApJ, 271, 681

Castor, J.I., Abbott, D.C., & Klein, R.I. 1975, ApJ, 195, 157

Chen, W., & White, R.L. 1991a, ApJ, 366, 512

Chen, W., & White, R.L. 1991b, BAAS, 22, 1201

Chen, W., & White, R.L. 1991c, ApJ, 381, L63

Chen, W., & White, R.L. 1992a, ApJ, submitted

Chen, W., & White, R.L. 1992b, in preparation

Ellison, D.C., Möbius, E., & Paschmann, G. 1990, ApJ, 352, 376

Fritz, K.D. 1989, A&A, 214, 14

Jones, F. C., & Ellison, D. C. 1991, Spa. Sci. Rev., in press

Krolik, J.H., & Raymond, J.C. 1985, ApJ, 298, 660

Lucy, L.B. 1982, ApJ, 255, 286

Lucy, L.B., & White, R.L. 1980, ApJ, 241, 300

Montmerle, T. 1981, Phil.Trans.R.Soc.Lond., A 301, 489

Montmerle, T. 1990, in IAU Symp. 143, eds. K.A. van der Hucht & B. Hidayat (Kluwer:Dordrecht), 397

Owocki, S.P., & Rybicki, G.B. 1984, ApJ, 284, 337

Owocki, S.P., Castor, J.I., & Rybicki, G.B. 1988, ApJ, 335, 914
Pauldrach, A., Puls, J., & Kudritzki, R.P. 1986, A&A, 164, 86
Pollock, A.M.T. 1987a, A&A, 171, 135
Pollock, A.M.T. 1987b, ApJ, 320, 283
Rosner, R., Golub, L., & Vaiana, G.S. 1985, Ann.Rev.A.Ap., 23, 413
Trombka, J. I., & Fichtel, C. E. 1983, Phys. Rep., 97, 173
Webb, G.M., Drury, L.O'C., & Biermann, P. 1984, A&A, 137, 185
White, R.L. 1985, ApJ, 289, 698

LOW ENERGY γ-RAY EMISSION FROM THE CYGNUS OB2 ASSOCIATION

Wan Chen[1,2] and Richard L. White[1]
[1]Space Telescope Science Institute
3700 San Martin Drive, Baltimore, MD 21218
[2]Department of Physics and Astronomy
The Johns Hopkins University, Baltimore, MD 21218

ABSTRACT

According to our newly developed model of γ-ray emission from chaotic early-type stellar winds, we predict the combined γ-ray flux from the circumstellar winds of many very luminous early-type stars in the Cyg OB2 association can be detectable by EGRET (and maybe also by OSSE) on *CGRO*. Due to different radiation mechanisms, the γ-ray spectrum from stellar winds can be quite different from that of Cyg X-3; this spectral difference and the time-variation of Cyg X-3 flux will help to distinguish the γ-ray components from different sources in this small region, which is spatially unresolvable by *CGRO*.

1. OVERVIEW

The region of the Cyg OB2 association is of interest to γ-ray astronomy because it contains one of the most important and mysterious Galactic γ-ray sources, Cyg X-3, which has been detected in keV, TeV and even PeV energies (see Bonnet-Bidaud & Chardin (1988) for a critical review of Cyg X-3 observations and theories). Surprisingly enough, however, Cyg X-3 was not detected in $0.7-5$ GeV range by *COS B*, in conflict with earlier *SAS II* results. It has long been expected that observations by EGRET onboard *CGRO* will help to clarify this situation.

We suggest here that there may be some new confusion. As we discussed earlier (Chen & White, this volume), γ-rays can be produced by the circumstellar winds of early-type stars. The dense Cyg OB2 association, harboring the hottest and most luminous massive stars known in the Galaxy, may be a particularly interesting γ-ray source competing with Cyg X-3 at EGRET energies. Another complication is that the diffuse γ-ray background in the Cygnus region is among the highest on the Galactic plane (Mayer-Hasselwander *et al.* 1987). It may severely reduce the sensitivity of detecting weak point sources for γ-ray telescopes with moderate spatial resolution like EGRET.

2. WHAT'S KNOWN?

Cyg X-3 has been well measured at hard X-ray energies. It has a steep photon spectrum from 20 keV to 140 keV (Hermsen *et al.* 1987),

$$\frac{dN}{dE} = (40.3^{+17.6}_{-10.1})\, E_{keV}^{-(3.19^{+0.11}_{-0.07})} \text{ photon cm}^{-2}\,\text{s}^{-1}\,\text{keV}^{-1}. \quad (1)$$

C-6

Above 140 keV, the situation is not clear (Bonnet-Bidaud & Chardin 1988). At very high energies (VHE) and ultra-high energies (UHE), Cyg X-3 has been a popular target in the last twenty years and many detections have been reported (Chardin & Gerbier 1989), though the statistics for the detections are usually rather poor. The reported photon spectrum from 10^{11} eV to 10^{17} eV can be best represented by a pure power-law (Rana *et al.* 1984),

$$\frac{dN}{dE} = 2.7 \times 10^{-4}\, E_{keV}^{-1.78}\, \text{photon cm}^{-2}\,\text{s}^{-1}\,\text{keV}^{-1}. \qquad (2)$$

The γ-ray flux of Cyg X-3 at GeV energies is quite controversial (Bonnet-Bidaud & Chardin 1988). The *SAS II* observations reported detection of Cyg X-3 with a flux of $\sim 1.1 \times 10^{-5}$ photon cm^{-2} s^{-1} above 35 MeV (Lamb *et al.* 1977). Subsequent observations by *COS B* for a total of $\sim$ 300 days, however, did not detect Cyg X-3. The *COS B* upper limit is about an order of magnitude below the *SAS II* flux but it is consistent with the extrapolation of the UHE power-law spectrum (equation 2) down to GeV energies (Hermsen *et al.* 1987).

The distribution of the diffuse γ-ray background on the Galactic plane is very lumpy (Mayer-Hasselwander *et al.* 1987). The Galactic center region has the strongest diffuse emission. There is also a peak in the background in the Cygnus region, with an average flux about a factor of two below the Galactic center value. The diffuse γ-ray emission in the Cygnus region has extensive structure which does not always follow the gas distribution derived from H I and CO observations of the region (Hermsen *et al.* 1987). Cyg X-3 is located just outside the local maximum in the background and is also a few degrees away from three unidentified point sources detected by *COS B*.

Table 1. Massive stars in Cyg OB2 (1.7 kpc) near Cyg X-3 (8.4 kpc)

Name	Sp	l^{II}	b^{II}	$\delta\theta_{X-3}$[a]	$L_{bol,40}$[b]	$\dot{M}_{-5}$[c]	$V_{\infty,3}$[d]	R_*[e]
Cyg X-3	79.90	0.70						
Cyg OB2								
No. 22	O4 IIIf	80.14	0.75	14′.7				
No. 9	O5 If	80.17	0.76	16′.6	1.57	1.9	2.6	34
No. 5	O6 If†	80.10	0.90	17′.0	1.04	2.5	2.2	34
No. 18	B1 Ib	80.21	0.71	18′.6				
No. 8A	O6 Ibf	80.22	0.79	20′.0	0.77	3.2	3.2	30
No. 8B	O6.5 IIIf	80.22	0.79	20′.0				
No. 8C	O5 IIIf	80.23	0.78	20′.4				
No. 7	O3 If	80.24	0.80	21′.3	0.97	1.9	2.7	20
No. 19	O9.5 III	80.28	0.73	22′.9				
No. 16	O7.5 V	80.24	0.94	25′.0				
No. 15	O8 V	80.24	0.98	26′.4				
No. 4	O5 IIIf	80.22	1.02	27′.2				

† Binary, only parameters for the primary are listed; [a] Angular distance from Cyg X-3; [b] Stellar bolometric luminosity in 10^{40} ergs s^{-1}; [c] Stellar mass loss rate in $10^{-5}\,M_\odot$ yr^{-1}; [d] Wind terminal velocity in 10^3 km s^{-1}; [e] Stellar radius in $R_\odot$; Ref. Massey & Thompson (1991) and Bieging, Abbott & Churchwell (1989).

Less than 1° northeast of Cyg X-3, there is the classical "cluster of blue giants", the Cyg OB2 association, which contains a large number of massive OB stars (Massey & Thompson 1991). In fact, a dozen of the brightest and most massive stars known in the region are located within 30′ of Cyg X-3 (Table 1). (This is also roughly the angular size of the point-spread-function (PSF) of EGRET at $E > 0.5$ GeV.) Though it is believed that there is large amount of interstellar gas in the Cyg OB2 region, there is no significant diffuse γ-ray enhancement seen in the *COS B* contour map (Hermsen *et al.* 1987).

3. WHAT'S EXPECTED?

We expect that substantial γ-ray radiation can be produced in the massive circumstellar winds of early-type stars (see Chen & White, this volume and references therein). The stellar wind γ-rays have two origins: the electron-generated inverse Compton quasi-power-law component extending from keV to > 10 MeV energies, and the ion-produced π^0-decay γ-ray hump peaking at $\sim$ 67 MeV. The most luminous stars should have large inverse Compton luminosities, and the most massive winds may produce large π^0-decay γ-ray luminosities. Usually the most luminous stars also have the most massive winds because the winds of O stars are believed to be radiatively driven (Castor, Abbott & Klein 1975). Since we do not have the stellar and wind parameters for all the stars in Table 1, we calculated the expected γ-ray fluxes from only 4 stars, Cyg OB2 No. 5, No. 7, No. 8A and No. 9, for which we have good data (Table 1).

Figure 1 shows our prediction of the γ-ray emission from the Cyg X-3/Cyg OB2 region in the *CGRO* energy range. The dot-dashed lines marked OB2 are the accumulated γ-ray fluxes from the four stars in Cyg OB2 association. We expect the real total flux, including all the stars in the association, will be less than a factor of 2 greater than the flux shown here since the included stars are also the brightest and have the most massive winds in the group.

Also shown in Figure 1 with the dotted lines are the 3σ point source continuum sensitivities[1] for OSSE, COMPTEL and EGRET during a normal two-week on-axis observations.

The solid line marked X3 is the observed hard X-ray spectrum of Cyg X-3 (Hermsen *et al.* 1987), and the dashed line is a power-law extrapolation. Also marked X3 and shown with a dashed line in the EGRET range is the power-law extrapolation of the Cyg X-3 spectrum at VHE and UHE (equation 2; Rana *et al.* 1984).

The solid line marked GB is the diffuse γ-ray background spectrum of the Galactic center region (Fichtel & Kniffen 1984), divided by a factor of 2 and convolved with the energy dependent PSF[1] of EGRET and COMPTEL. It increases sharply at low energies because of the decreasing spatial resolution of both EGRET and COMTEL at low energies.

[1]From Appendix G of NRA 91-OSSA-22: The Gamma Ray Observatory as a Guest Investigator Facility, (NASA/GSFC:Greenbelt)

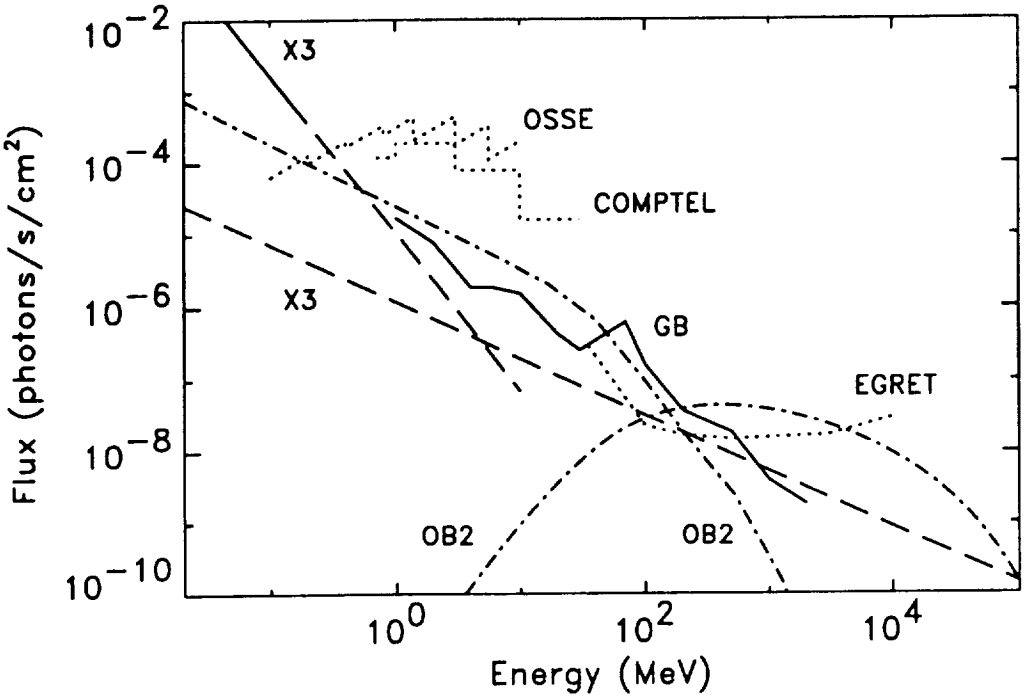

Figure 1. γ-ray spectra in the Cyg X-3/Cyg OB2 region. The solid lines are observed spectra, the dashed and dot-dashed lines are predicted spectra, and the dotted lines are instrument sensitivity curves. As marked X3 stands for Cyg X-3; OB2 for Cyg OB2; GB for the Galactic diffuse background.

3. WHAT CAN BE DONE?

We see that the chances of detecting Cyg X-3 with OSSE are very good, since we can reasonably expect the hard X-ray spectrum of Cyg X-3 will extend to at least a few hundred keV. The Cyg OB2 flux in the OSSE range is confined to the low-energy end, where it is completely dominated by the flux from Cyg X-3 with a much steeper spectrum. At COMPTEL energies neither Cyg X-3 nor Cyg OB2 can be detected.

The Cyg OB2 flux becomes dominant at the high energy end of EGRET where the fluxes of both Cyg X-3 and the diffuse background are low. However, from a recently developed theory on high energy emission from accreting X-ray pulsars (Cheng *et al.* 1991), the potential γ-ray flux from Cyg X-3 at EGRET energies could be about an order of magnitude higher than we have shown here. If this is the case, Cyg X-3 could have a similar flux to Cyg OB2.

At the lower energy range of EGRET, the competition is between Cyg OB2 and the diffuse background. We see that both sources have similar spectra in this energy range, so it will be fairly difficult to distinguish them.

If Cyg X-3 has a much greater flux (Cheng *et al.* 1991), it may become a major competitor over the whole energy range of EGRET; this could probably be recognized through

its characteristic 4.8 hr time modulation (Bonnet-Bidaud & Chardin 1988). This time variation is observed in almost all the energy bands where Cyg X-3 has been detected (Bonnet-Bidaud & Chardin 1988). We may expect the emission at EGRET energies also to be modulated.

We conclude from the above analysis that observations of the Cyg X-3/Cyg OB2 region can be very fruitful. The diffuse γ-ray background in the region makes it much more difficult to detect and distinguish Cyg X-3 and Cyg OB2 at the spatial resolution of the present instrument. The most promising energy band for detection of the Cyg OB2 association is at the high energy end of the EGRET range. If Cyg X-3 has much larger flux than we have shown here, the 4.8 hr time variation will be the most likely criterion to reveal the true identity of the γ-ray source.

REFERENCES

Bieging, J.H., Abbott, D.C., & Churchwell, E.B. 1989, ApJ, 340, 518

Bonnet-Bidaud, J.-M., & Chardin, G. 1988, Phys.Rep., 170, 161

Castor, J.I., Abbott, D.C., & Klein, R.I. 1975, ApJ, 195, 157

Chardin, G., & Gerbier, G. 1989, A&A, 210, 52

Chen, W., & White, R.L. 1991, ApJ, 381, L63

Chen, W., & White, R.L. 1992, ApJ, submitted

Cheng, K.S., Yu, K.N., Cheung, T., & Lau, M.M. 1991, ApJ, 379, 290

Fichtel, C.E., & Kniffen, D.A. 1984, A&A, 134, 13

Hermsen, W., Bennett, K., Bloemen, J.B. G.M., Buccheri, R., Jansen, F.A., Mastichiadis, A., Mayer-Hasselwander, H.A., Özel, M.E., Pollock, A.M.T., & Strong, A.W. 1987, A&A, 175, 141

Lamb, R.C., Fichtel, C.E., Hartman, R.C., Kniffen, D.A., & Thomson, D.J. 1977, ApJ, 212, L63

Massey, P., & Thompson, A.B. 1991, AJ, 101, 1408

Mayer-Hasselwander, H.A., Bernnett, K., Bignami, G.F., Buccheri, R., Caraveo, P.A., Hermsen, W., Kanbach, G., Lebrun, F., Lichti, G.G., Masnou, J.L., Paul, J.A., Pinkau, K., Sacco, B., Scarsi, L., Swanenburg, B.N., & Wills, R.D. 1987, A&A, 105, 164

Rana, N.C., Sadzinska, M., Wdowczyk, J., & Wolfendale, A.W. 1984, A&A, 141, 394

9.
GALACTIC CENTER

OSSE Observations of Galactic 511 keV Annihilation Radiation

W. R. Purcell*, D. A. Grabelsky*, W. N. Johnson†, G. V. Jung‡,
R. L. Kinzer†, J. D. Kurfess†, M. S. Strickman†, M. P. Ulmer*

ABSTRACT

The Oriented Scintillation Spectrometer Experiment (OSSE) on the *Compton Gamma-Ray Observatory* has performed several observations of the Galactic plane and Galactic center region to measure the distribution of Galactic 511 keV positron annihilation radiation. Preliminary analysis of data collected during the observation of the Galactic center region over the period July 13–24, 1991, indicates the presence of a 511 keV line and positronium continuum superimposed on a power-law continuum. The line flux was found to be $(2.7 \pm 0.5) \times 10^{-4}$ γ cm^{-2} s^{-1}, with a positronium fraction of (0.9 ± 0.2). The 3σ upper limit to daily variations in the 511 keV line flux from the mean during the observation interval is 3×10^{-4} γ cm^{-2} s^{-1}. If all of the observed annihilation radiation is assumed to originate from the X-ray source 1E 1740.7–2942, the corresponding 511 keV line flux would be $(3.0 \pm 0.6) \times 10^{-4}$ γ cm^{-2} s^{-1}. The 3σ upper limit for 511 keV line emission from the X-ray binary GX1+4 is 6×10^{-4} γ cm^{-2} s^{-1}. Results from the Galactic plane observations at Galactic longitudes of 25° (August 16–21, 1991) and 339° (September 6–11, 1991) suggest that the emission is concentrated near the Galactic center. The observations and the preliminary results are described.

INTRODUCTION

While positron annihilation radiation has been observed from the Galactic center region by numerous balloon and satellite-borne experiments since the 1970s, the location and distribution of the emission has not yet been identified (see Lingenfelter and Ramaty 1989 for a recent review). The situation is further complicated by the possibility that the 511 keV annihilation line may vary in intensity by as much as $\sim 10^{-3}$ γ cm^{-2} sec^{-1}, leading to the suggestion that the observed emission is composed of two separate sources: a steady state diffuse Galactic component and a time variable point source near the Galactic center (Lingenfelter and Ramaty 1989). The source of the diffuse Galactic component is thought

*Northwestern University, Evanston, IL
†Naval Research Laboratory, Washington DC
‡Universities Space Research Association, Washington DC

Table 1: OSSE Galactic Center / Galactic Plane Observations

Galactic Longitude	Position Angle	Background Offset Angle	Observation Interval	On-Source Time (sec)
0°	90°	±10°	13–24 July	10^5 / 10^5
25°	90°	±10°	16–21 Aug	5×10^4
339°	90°	+4.3/−8.5	6–11 Sept	5×10^4

to be the β^+-decay products from radioactive nuclides produced by supernovae, novae or Wolf-Rayet stars (Clayton 1973), while γ-γ interactions in the vicinity of an accreting black hole has been suggested as a possible source of time variable annihilation emission (Lingenfelter and Ramaty 1982). At this time, however, few details about of the source(s) of the positrons is known. One of the scientific goals of the OSSE team is to map the distribution of positron annihilation radiation and to search for time variability from the Galactic center region.

The OSSE instrument consists of four separate, nearly identical detectors. The primary detecting element of each detector is a large area NaI(Tl)-CsI(Na) phoswich crystal, providing an effective area of 450 cm^2 at 0.5 MeV. The phoswich is actively shielded and passively collimated. Tungsten collimators provide a field-of-view which is 3.8° × 11.4° (FWHM), with the long direction of the collimators oriented parallel to the spacecraft Y-axis. Each detector has a separate elevation control system which provides independent positioning of the detectors about an axis parallel to the spacecraft Y-axis. During source observations, periodic background measurements are performed by offset-pointing the detectors from the target. A detailed description of the OSSE instrument and its operation can be found in Johnson *et al.* (1989).

ANALYSIS METHOD

Table 1 provides a description of the OSSE observations of the Galactic center and Galactic plane used to generate the preliminary results reported here. The position angle represents the angle between the long direction of the OSSE field-of-view and Galactic North. For the observations described here, the long direction of the OSSE collimator was oriented parallel to the Galactic plane to maximize the response to a diffuse Galactic distribution. The background offset angle represents the Galactic latitude at which the background observations were performed. The Galactic center observation included additional source pointings at Galactic latitudes of $b = \pm 1.5°$ and $\pm 3.0°$. The on-source time for the Galactic center observation indicates the total on-source time for both the $b = 0°$ and the $b = \pm 1.5°$, $\pm 3.0°$ observations. The Galactic plane observation at $l = 339°$ included an

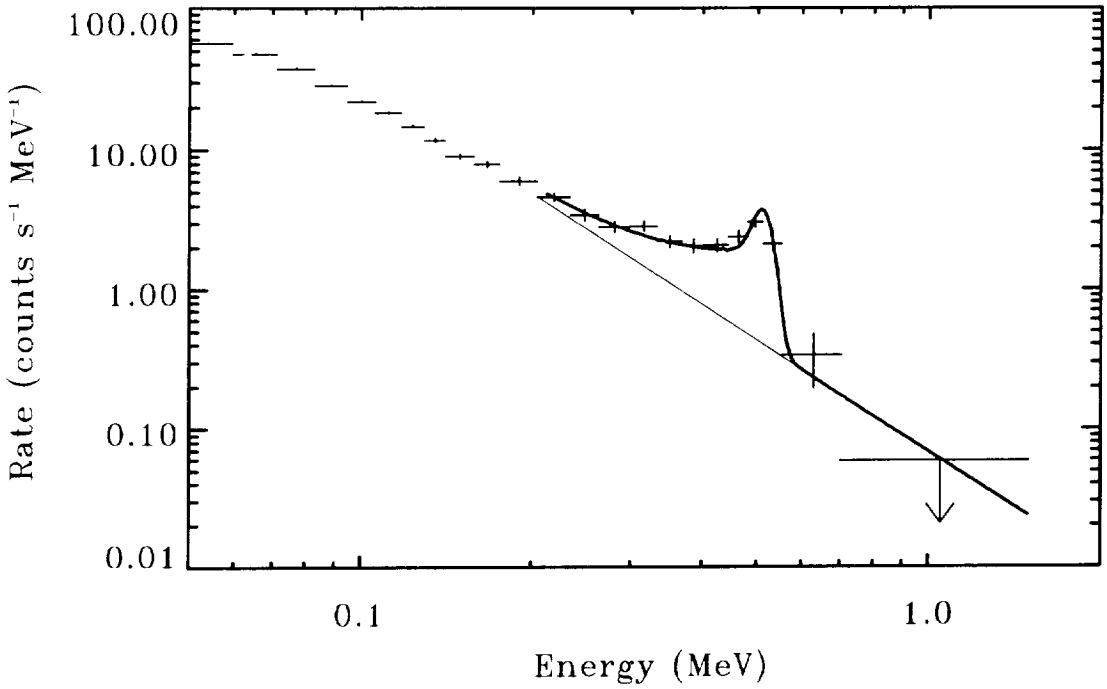

Figure 1: The OSSE Galactic center ($b = 0°$) spectrum summed from all four detectors over the period 13–24 July, 1991. The fitted function consists of a power law, a photopeak line and a term approximating the positronium continuum. See text for details.

additional source pointing at the target GX339–4.

The instrumental background is measured by offset-pointing the OSSE detectors from the source position. Source and background measurements are typically alternated at two minute intervals, with backgrounds being sampled on each side of the source position along the instrument scan plane. The background offset angles for the Galactic center and Galactic plane observations were selected to minimize possible residual response to a diffuse latitude distribution. For the analysis described here, data having low live-times, telemetry errors or in which the detector zenith angle was greater than 100° were excluded. Background estimation and subtraction was performed for each detector separately. In order for a source observation to have been included in the analysis two background measurements were required, one before and one after the source observation. For these source observations, the background spectrum was estimated by linearly interpolating in time, channel-by-channel, between the two background spectra. The individual background-subtracted spectra were then summed by detector and by day to perform the spectral analysis.

The summed background-subtracted spectra for the Galactic center $b = 0°$ observation is shown in Figure 1. This spectrum shows strong evidence for a 511 keV line and positron-

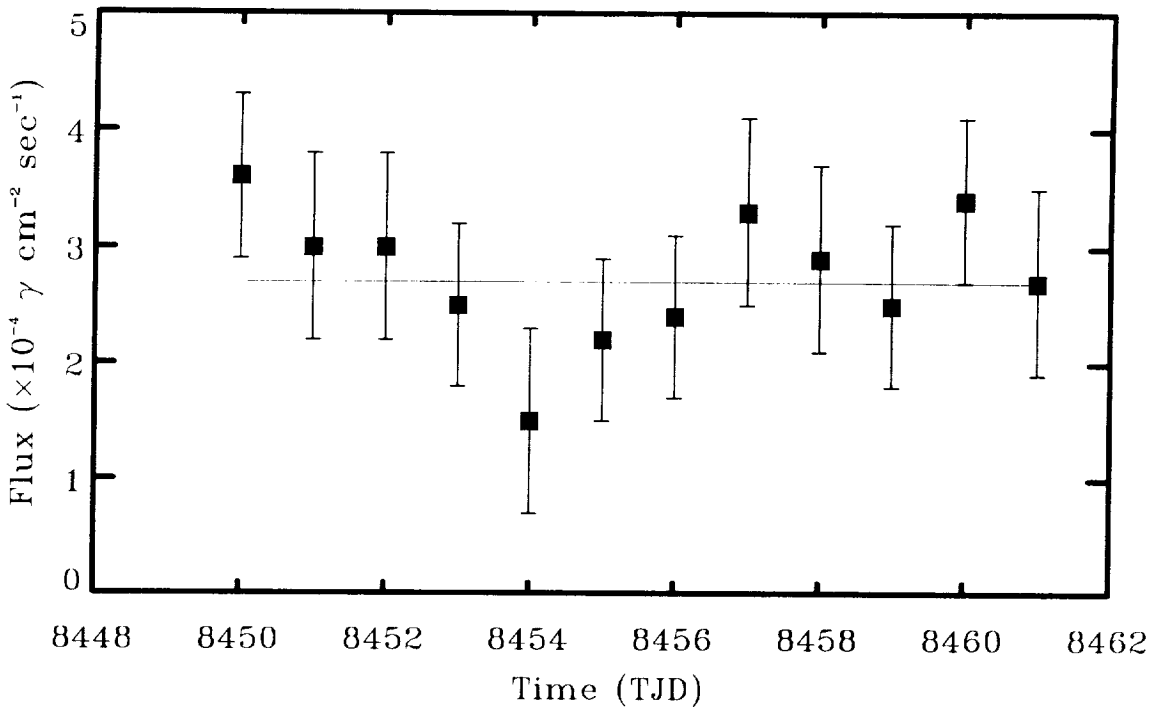

Figure 2: The fitted daily 511 keV line flux for the Galactic center $b = 0°$ observations.

ium continuum. The position of the line is consistent with an energy of 511 keV, and the line width is consistent with the instrumental resolution. For the spectral studies reported here, the spectral fits were performed in count space over the energy range 0.2 – 1.5 MeV. The fitting model consisted of a power law, a photopeak line fixed in energy at 511 keV and in width at the instrumental resolution, and a term approximating the positronium continuum. The positronium continuum component consisted of a triangle having a maximum at 511 keV and decreasing linearly with energy and which was smoothed by the instrumental resolution. The intensity of the positronium continuum component was a free parameter in the spectral fits. The spectral fits were performed in count space and did *not* include folding the model through the instrument response.

PRELIMINARY RESULTS

Using the fitting model described above, the summed background-subtracted spectra for the Galactic center $b = 0°$ observation results in a fitted 511 keV line flux of $(2.7 \pm 0.5) \times 10^{-4}$ γ cm^{-2} s^{-1} and a positronium fraction of (0.9 ± 0.2). The spectral fit is shown in Figure 1. Time variability of the 511 keV line flux was investigated by summing the background-subtracted spectra for each day of the observation interval separately. The resulting line fluxes are shown in Figure 2. No significant time variability of the line flux is observed. The 3σ upper limit to daily variations from the mean is 3×10^{-4} γ cm^{-2} s^{-1}.

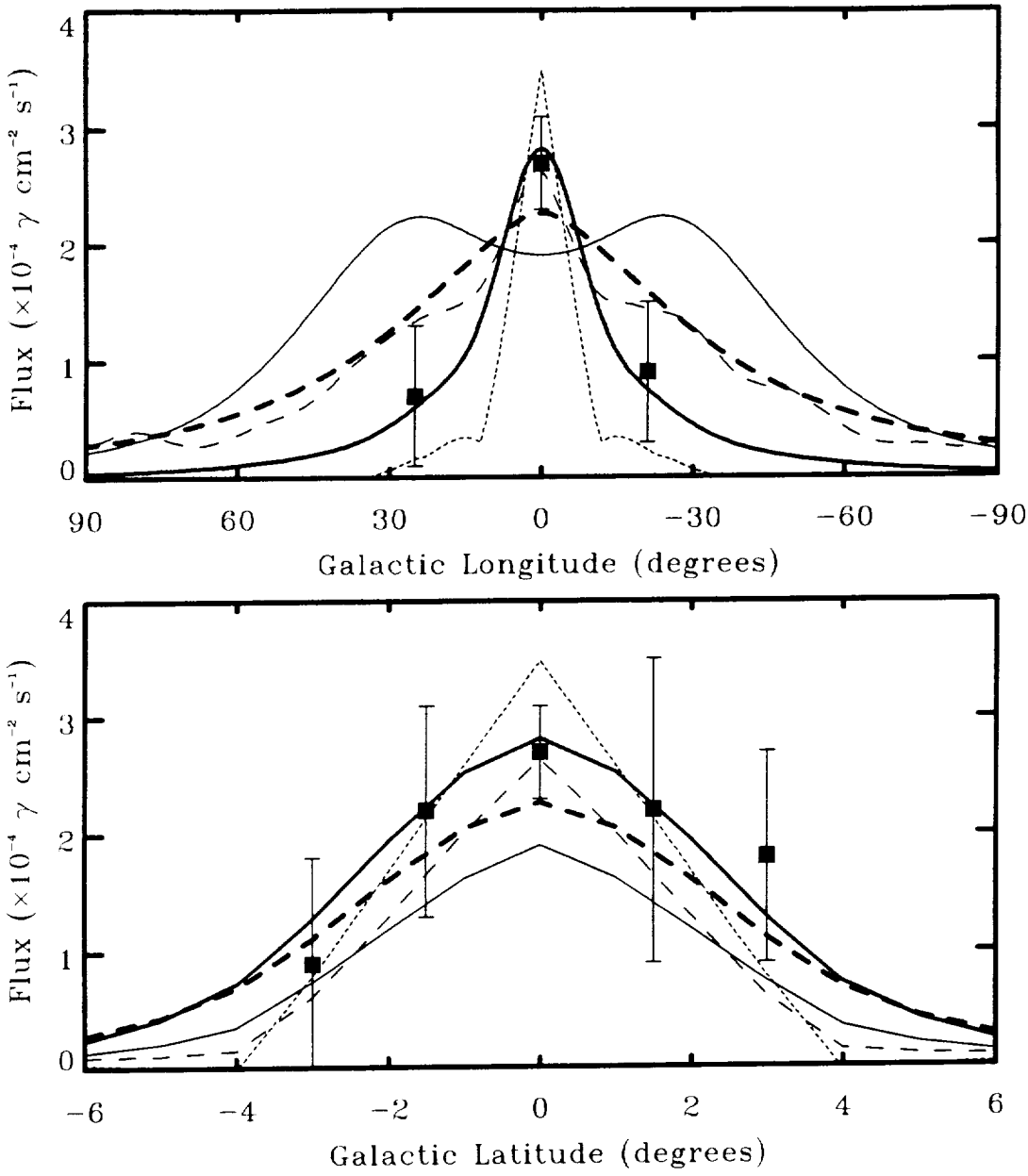

Figure 3: The fitted 511 keV line flux for the Galactic plane (top) and Galactic center latitude scan (bottom) observations. The curves represent the expected OSSE responses for several Galactic distribution models, fitted simultaneously to the observed longitude and latitude data shown. The thin solid line represents the CO model of Leising and Clayton (1985), the thick solid line represents the Nova model of Leising and Clayton (1985), the thin dashed line represents the observed CO distribution (Dame *et al.* 1987), the thick dashed line represents a model following the Galactic visual luminosity (Bahcall and Soneira 1980), and the dotted line represents the response for a point-source located at $l = 0°$, $b = 0°$.

The results of fitting the summed background-subtracted spectra for the Galactic plane ($l = 0°, 25°$ and $339°$) and the Galactic center latitude scan ($b = 0°, \pm 1.5°$ and $\pm 3.0°$) are shown in Figure 3. Also shown in this figure is the expected OSSE responses for several Galactic distribution models, fitted simultaneously to the observed latitude and longitude data. As can be seen, the data are sharply peaked in longitude near the Galactic center, consistent with the reported GRIS observations (Gehrels *et al.* 1991). The Galactic center latitude scan suggests that the emission is centered near the plane and may be slightly broadened compared with the expected point source response.

From the Galactic center latitude scan shown in Figure 3, it can be seen that the bulk of the emission can not be from the X-ray binary GX1+4. If the $\sim 1\sigma$ excess observed for the $b = +3°$ observation is assumed to be due to emission from GX1+4, the 3σ upper limit to the 511 keV flux is 6×10^{-4} γ cm^{-2} s^{-1}. If the observed Galactic center flux of $(2.7 \pm 0.5) \times 10^{-4}$ γ cm^{-2} s^{-1} is assumed to originate entirely from the X-ray source 1E 1740.7–2942, the corresponding 511 keV line flux would be $(3.0 \pm 0.6) \times 10^{-4}$ γ cm^{-2} s^{-1}. If a point source of annihilation radiation with a 511 keV line flux of 2×10^{-3} γ cm^{-2} s^{-1} was active during the Galactic center observation interval, its position (1σ) must be outside of the region bounded by $l = \pm 8°$, $b = \pm 4°$.

If all of the observed emission is assumed to originate from a diffuse Galactic source, the OSSE data are inconsistent ($> 2.5\sigma$) with a distribution following the CO model of Leising and Clayton (1985). Further, the fitted OSSE intensities for the models following the observed CO distribution (Dame *et al.* 1987) and the Novae model of Leising and Clayton (1985) are only $\sim 50\%$ of the 511 keV intensity reported by SMM (Share *et al.* 1990), suggesting either that the distribution does not follow these models, or that the SMM observations included a time-variable component which was not active during the OSSE observations. The latter is not yet required, however; the fitted OSSE intensity for a model following the Galactic visual luminosity is consistent with the reported SMM flux.

CONCLUSION

The preliminary results described here are based on four weeks of OSSE observations of the inner Galactic plane. The observation of the Galactic center region over the period July 13–24, 1991, indicates the presence of a 511 keV line and positronium continuum superimposed on a power-law continuum, with a line flux of $(2.7 \pm 0.5) \times 10^{-4}$ γ cm^{-2} s^{-1} and a positronium fraction of (0.9 ± 0.2). No evidence for daily variations in the line flux was observed during this period, with a 3σ upper limit to daily variations from the mean of 3×10^{-4} γ cm^{-2} s^{-1}. The Galactic longitude observations at $l = 25°$ and $339°$ suggest that the 511 keV line emission is concentrated near the Galactic center.

Five further OSSE observations of the Galactic center with various collimator position angles are scheduled for the remainder of the GRO Phase 1 viewing plan which will

provide an additional 10 weeks of data. These observations will allow OSSE to monitor the Galactic center for variability of the annihilation radiation and to measure the distribution of the emission within $\sim 5° - 10°$ of the Galactic center. Simultaneous observations of the Galactic center region with SIGMA are scheduled which will aid in separating point source contributions from the diffuse component. Ten additional weeks of Galactic plane observations are also scheduled which will further aid in measuring the diffuse distribution.

REFERENCES

Bahcall, J. N., and Soneira, R. M., 1980, *Ap. J. Suppl.*, **44**, 73.

Clayton, D. D., 1973, *Nature Phys. Sci.*, **244**, 137.

Dame, T. M., *et al.*, 1987, *Ap. J.*, **322**, 706.

Gehrels, N., *et al.*, 1991, *Ap. J. (Letters)*, **375**, L13.

Johnson, W. N., *et al.*, 1989, in *Proc. of the GRO Science Workshop*, ed. W. N. Johnson, p. 2–22.

Leising, M. D., and Clayton, D. D., 1985, *Ap. J.*, **294**, 591.

Lingenfelter, R. E., and Ramaty, R., 1989, *Ap. J.*, **343**, 686.

Lingenfelter, R. E., and Ramaty, R., 1982, in *The Galactic Center*, ed. G. R. Riegler and R. D. Blandford (New York:AIP), p. 148.

Share, G. H., *et al.*, 1990, *Ap. J. (Letters)*, **358**, L45.

GRIS Observations of the Galactic Center and the Gamma-Ray Galactic Diffuse Continuum

J. Tueller, S. Barthelmy, N. Gehrels, and B. J. Teegarden
Laboratory for High Energy Astrophysics
NASA/Goddard Space Flight Center
Code 661, Greenbelt, MD 20771

M. Leventhal
Physical Research Laboratory
AT&T Bell Laboratories
Murray Hill, NJ 07974

C. J. MacCallum
Dept. of Physics and Astronomy
University of New Mexico
800 Yale Blvd., Albuquerque, NM 87131

ABSTRACT

On two flights in 1988, the Gamma-Ray Imaging Spectrometer (GRIS) discovered the Galactic Center in a high state (>1 x 10^{-3} ph cm^{-2} s^{-1}) of positron annihilation line emission (511 keV) after nearly a decade of failed attempts to confirm the exciting early results of balloon and satellite instruments. These two flights represented the first flights of a new generation of high resolution germanium spectrometers designed to achieve significantly greater sensitivity for astrophysical observations. During the fall flight, an observation of the galactic plane at 335° longitude was also performed. This observation showed a very low level of 511 keV emission (2±1 x 10^{-4} ph cm^{-2} s^{-1}), confirming the Galactic Center origin of the line, and a high level of hard x-ray and gamma-ray continuum emission (1 x 10^{-4} ph cm^{-2} s^{-1} keV^{-1} at 100 keV), which we attribute to galactic diffuse emission. Improved fits to the spectrum of the Galactic Center are presented with the proposed diffuse component subtracted. We conclude that our Galactic Center continuum spectrum is consistent with the sum of the 1E1740.7-2942 spectrum observed by SIGMA/GRANAT and our l=335° galactic plane spectrum. The predicted diffuse flux should be easily measurable by the OSSE experiment on GRO.

INTRODUCTION

The Galactic Center region has been known to be a source of 511 keV gamma rays from positron annihilation since the 1970's, but the nature of this source was poorly understood. The line was first observed in 1970 by a balloon instrument (Johnson, Harnden & Haymes 1972), but was not convincingly identified as positron annihilation radiation until the high resolution germanium detector measurements of Leventhal, MacCallum & Stang (1978) in 1977, also a balloon instrument. The germanium spectrometer on HEAO-3 observed the source twice (Riegler *et al.* 1981), once in 1979 and again in 1980, and detected a significant decrease in the source

intensity, which was subsequently confirmed by balloon measurements (Leventhal *et al.* 1982, 1986; Paciesas *et al.* 1982). At the same time, measurements by a very broad field-of-view (~130°) moderate resolution instrument on SMM showed a strong line with little variability (Share *et al.* 1990). To explain this discrepancy, Lingenfelter & Ramaty (1989) proposed a two component model with a variable point source near the Center and a diffuse line source to explain the excess observed by SMM.

In 1988, as part of a major campaign to observe Supernova 1987A (Tueller *et al.* 1990), the first two flights of the new GRIS instrument also observed the Galactic Center, which is conveniently separated by ~12 hours in Right Ascension from SN1987A. GRIS discovered that the annihilation line from the Galactic Center had returned to the high state observed by instruments in the 1970's. The difference in line flux between the Spring and Fall measurements indicated a statistically significant variability. In the Fall 1988 measurement, the line was observed to be significantly broadened, providing the first unambiguous evidence that the line is not narrow. We were very fortunate to get a long flight (>40 hours) in the Fall, that allowed a second pass on the galactic plane. We used this opportunity to make an observation of the plane at a galactic longitude l=335° and observed a very low 511 keV flux, confirming that the source was strongly concentrated toward the Galactic Center and placing significant new constraints on diffuse 511 keV line emission. These Galactic Center results from the GRIS balloon flights are published (Leventhal *et al.* 1989 and Gehrels *et al.* 1991), but in this paper we are presenting a more complete analysis of the continuum, including all the data from 25 keV to 8 MeV and with slightly improved data analysis procedures. These results are generally consistent with our previous publications.

In the Spring of 1990, an instrument similar to GRIS (HEXAGONE) observed the Galactic Center 511 keV line confirming the return of this source to a high state and providing more evidence for variability (Chapuis *et al.* 1991). Since the GRIS observations, the SIGMA experiment on GRANAT (a coded aperture imaging instrument) has provided exciting new information, including a possible identification of the variable point source of positrons. The strongest hard x-ray source in the Galactic Center region is usually 1E1740.7-2942. Because of the remarkable similarity of the spectrum of the Einstein source and CYG X-1, it has been suggested that the Einstein source is a black hole (Skinner *et al.* 1987; Cook *et al.* 1991). SIGMA observed a broad transient feature near 511 keV (~200 keV FWHM; <1 day; ~400 keV peak energy) from this source which may be associated with the production of positrons (Paul *et al.* 1991). Very recently, this source has also been observed by SIGMA in a low state where it is much weaker than the other Galactic Center hard x-ray sources (Sunyaev *et al.* 1991). The imaging observations raise an important question about the interpretation of the spectra from the earlier observations: how many and which sources are contributing to the observed spectra? In particular, the sum of the sources observed in the imaging instruments falls below the GRIS total spectrum by about a factor of two (Gehrels *et al.* 1991).

OBSERVATIONS AND DATA ANALYSIS

The GRIS instrument is a balloon-borne high resolution gamma-ray spectrometer which operates in the energy range 20 keV to 8 MeV (Tueller *et al.* 1988). It is one of a new generation of instruments that use arrays of cooled germanium detectors and heavy active shielding to achieve high sensitivity ($<2 \times 10^{-4}$ ph cm^{-2} s^{-1} 3σ narrow line upper limits for E>100 keV) and fine energy resolution (~2keV at 1 MeV). The field-of-view of the active collimator is ~17° at relevant energies. The Galactic Center was observed twice for ~12 hours in both the Spring (May 1) and Fall (Oct. 29) of 1988. A similar observation of the galactic plane at a longitude of l=335° was made in the Fall a day later. Alternate 20 minute pointings, on-source and off-source (background), were accumulated and the difference (source-background) was used to calculate

the source flux. For more information on the observing program see Gehrels *et al.* 1991 and for the data analysis procedures see Tueller *et al.* 1990 and Barthelmy *et al.* 1991.

The data analysis procedures used here have minor improvements over those used in our previous publication (Gehrels *et al.* 1991). The procedures have been altered to perform the sum over energy for large continuum energy bins before calculating source minus background in each interval. This allows us to use directly determined statistical weights in calculating the average over observing intervals, even at the highest energies where the statistics are poor. Using this technique, we have extended our analysis to 8 MeV. Data in the energy range 25 to 35 keV, which was excluded from the previous analysis, has been included here. Finer energy bins are used for the continuum fit to provide for a better comparison of different models. Forward folding least-squares fits using the full detector response matrix including atmospheric corrections have been performed on a variety of models. The results of these fits, for the same models used in Gehrels *et al.* 1991, are essentially identical to the previous publication.

RESULTS

In our original analysis of the GRIS galactic plane observation, we were struck by the unexpectedly high level of hard x-ray continuum observed (roughly half the level observed from the Galactic Center). We had also noted a significant discrepancy between the sum of the hard x-ray point source spectra from imaging instruments (GRIP and SIGMA) and our Galactic Center continuum (also roughly a factor of two). Since the coded aperture imaging instruments are relatively insensitive to diffuse emission, this suggested a possible model to explain both results. Perhaps our galactic plane spectrum is truly diffuse emission from the plane, which extended to the Galactic Center and explains the discrepancy with the imaging instruments. Another anomaly in our fits to the galactic plane spectrum was the high level of the positronium tail observed on the positron annihilation line. (The best fit was an unphysical 121±8 %.) We have performed fits to some more complex models to help quantify and clarify these issues.

Table 1 and figure 3 show the results of a fit to the galactic plane spectrum with a broken power law plus a 511 keV line with positronium tail. The line is of 2σ significance only and does not appear at the correct energy, but there is a slightly higher minimum in χ^2 at 511 keV. The best fit to a broken power law includes no positronium continuum, but the data are consistent at the 1σ level with 100 % positronium. The introduction of a break is statistically significant, reducing χ^2_{min} from 39 for 38 degrees of freedom to 32 for 36 d.o.f. With the introduction of a break in the continuum spectrum the evidence for a 511 keV line in our galactic plane data is not compelling and should be interpreted as an upper limit.

Assuming this spectrum reflects diffuse emission from the plane, we have used a Comptonized disk model with 511 keV line and tail plus a fixed galactic plane model to perform fits to our Galactic Center spectra from the Spring and Fall of 1988. The results of these fits are given in table 1 and figures 2 and 4. The galactic plane 511 line (using the higher minimum at 511 keV) was included in the model and this explains the differences in the line parameters derived here from those in our previous publication. These differences should be considered as reflecting the possible systematic error in our Galactic Center 511 keV line measurement due to the uncertain level of contribution from a diffuse 511 keV line, but if we choose to fit the narrow line component as a free parameter, the resulting best fit is nearly identical to table 1 for Fall 1988. The 511 keV line profile shown in figure 1 is essentially the same as in our previous publication. Using a larger set of models, it was possible to find fits to our Galactic Center continuum spectra consistent at the 2σ level with no positronium tail on the 511 keV line. This is a minor discrepancy with our previously reported results and illustrates the sensitivity of positronium fraction determination to the underlying continuum model. In both cases a good fit to the

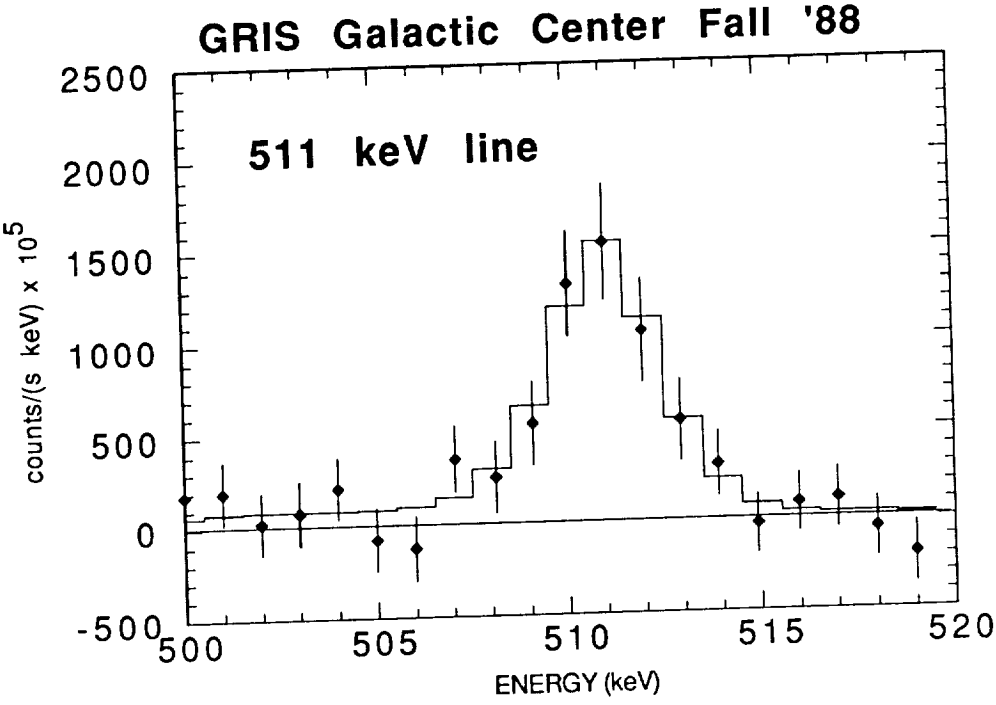

Figure 1 Galactic Center positron annihilation line and binned model (solid line).

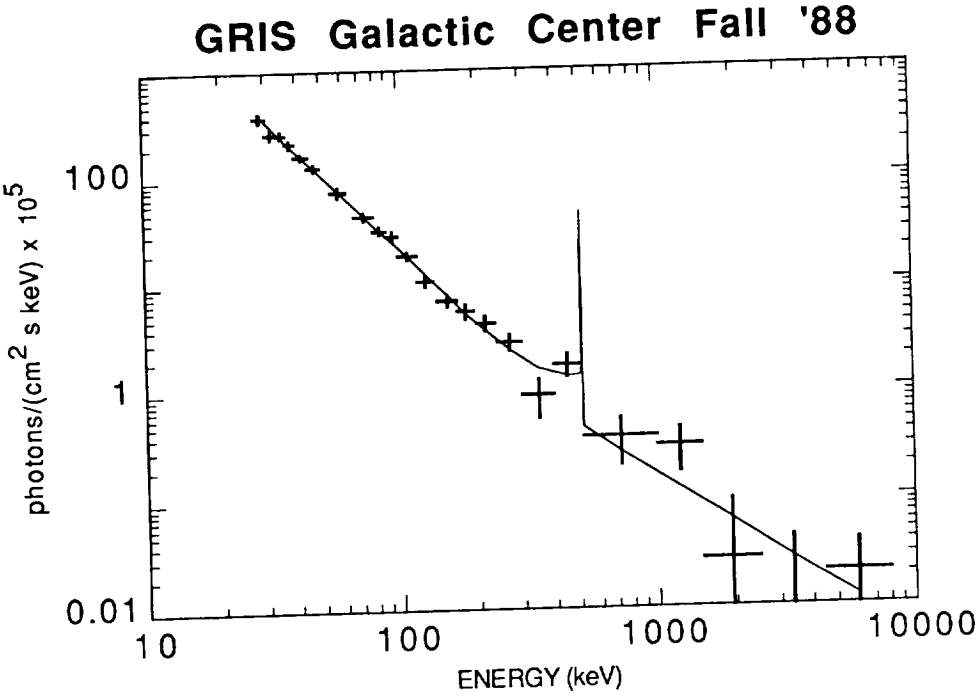

Figure 2 Galactic Center continuum data and fit (solid line).

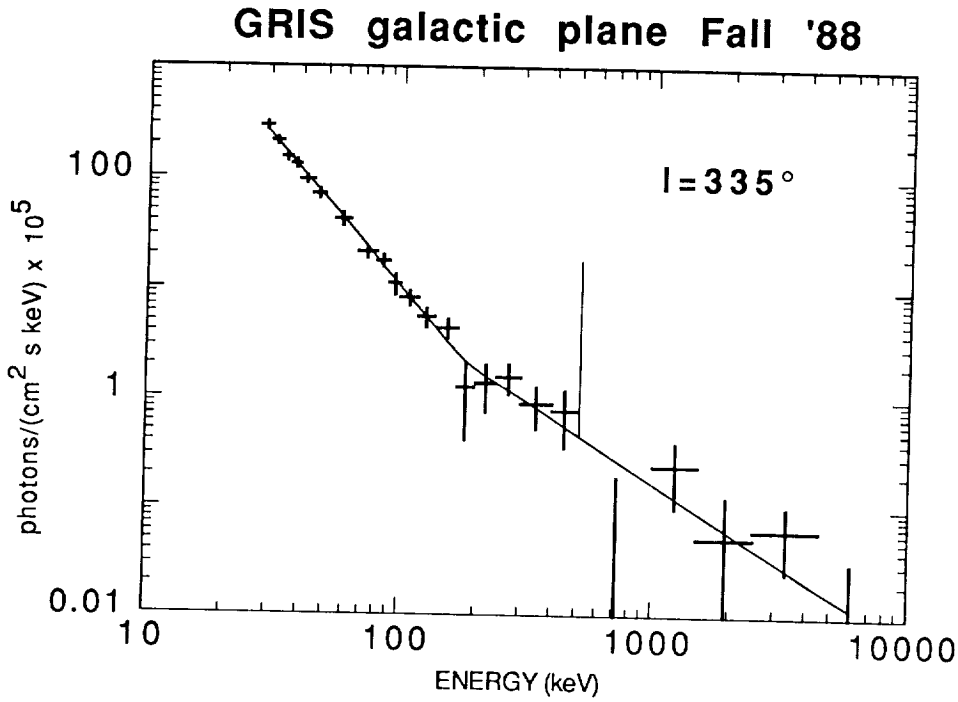

Figure 3 Galactic plane continuum data and fit (solid line).

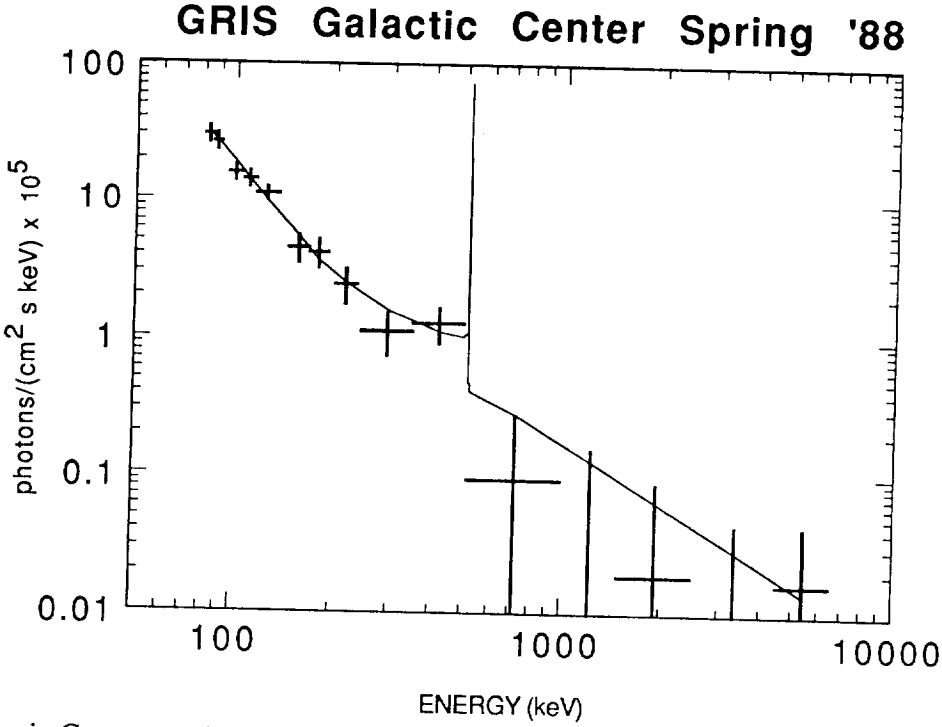

Figure 4 Galactic Center continuum data and fit (solid line).

TABLE 1 FIT RESULTS

galactic plane l=335°	Fall '88		Galactic Center - galactic plane model	Spring '88		Fall '88	
χ^2 minimum	31.9	36 d.o.f.	χ^2 minimum	36.9	30 d.o.f.	30.2	36 d.o.f.
flux at 100 keV (ph/(cm^2 s keV) x 10^5)	10.0	±0.5	flux at 100 keV (ph/(cm^2 s keV) x 10^5)	7.8	±0.9	11.3	±0.7
slope γ E < break	2.64	±0.06	electron temp KT (keV)	35	+13 -10	52	+25 -11
break energy (keV)	182	+34 -43	optical depth τ	2.7	+∞ -2.2	2.3	±0.6
slope γ E > break	1.47	+0.24 -0.17					
line flux (ph/(cm^2 s) x 10^5)	18	±8	line flux (ph/(cm^2 s) x 10^5)	54	±15	98	±15
peak energy (keV)	509	±0.4	peak energy (keV)	511.1	±0.7	511.0	±0.3
line FWHM (keV)	0	< 6	line FWHM (keV)	0	< 4	3.4	±0.8
positronium flux (ph/(cm^2 s) x 10^5)	0 to	80	positronium flux (ph/(cm^2 s) x 10^5)	157	±79	225	+84 -109
positronium fraction (%)	0 to	100	positronium fraction (%)	88	+19 -31	81	+14 -26

Galactic Center spectrum minus the galactic plane broken power law model can be achieved with a Comptonized disk model similar to that used by the SIGMA and GRIP teams to fit 1E1740.7-2942 (Sunyaev *et al.* 1991; Cook *et al.* 1991). Note that the flux above the line is almost entirely due to the proposed diffuse component and does not show an MeV hump that was reported by HEAO 3 (Riegler *et al.* 1981).

DISCUSSION

We predict, by scaling our 2σ upper limit to the OSSE FOV (11°), that OSSE will see less than 2 x 10^{-4} ph cm^{-2} s^{-1} of diffuse 511 keV emission from the galactic plane at 25° from the Center (see OSSE results in these proceedings). Taking all previous measurements into account, we predict that OSSE will observe variable levels of 511 keV line emission from the Galactic Center. We propose, as a model, that the GRIS galactic plane spectrum at l=335° is dominated by diffuse emission from our Galaxy which extends at least to the Galactic Center region. The GRIS Galactic Center continuum measurements are consistent with a model where the spectrum is dominated by this diffuse emission and a Comptonized disk spectrum from the 1E1740.7-2942 source (each roughly contributing equally). This model would also explain the discrepancy between the sum of the point source spectra observed by imaging instruments and the GRIS spectrum for the Galactic Center region. It is, of course, also possible to explain these results by invoking variable sources, such as the known hard x-ray transient source GX339-4, to explain our galactic plane spectrum. Similarly, there are many known transient sources in the Galactic Center region at could be used to explain any discrepancies between imaging and non-imaging spectra that were not measured simultaneously. A detailed comparison of other measurements of the Galactic Center spectrum and this model is presented in an accompanying paper in these proceedings (Gehrels and Tueller 1991). This paper shows that the measured Galactic Center spectrum has never been less than our proposed diffuse spectrum, but it has been identical to our spectrum in a few instances, presumably when all the point sources were turned off. This diffuse continuum emission would be easily detected by OSSE observations of the galactic plane as shown in figure 5 (60σ at 100 keV) and OSSE will provide a definitive test for our proposal.

REFERENCES

Barthelmy, S. D., et al. 1991, in Proc. of the Symposium on Gamma-Ray Line Astrophysics, ed. Ph. Durouchoux and N. Prantzos (New York: AIP) 205.

Cook, W. R., Grunsfeld, J. M., Heindl, W. A., Palmer, D. M., Prince, T. A., Schindler, S. M., and Stone, E. C. 1991, ApJ,372,75

Chapuis, C. G. L., et al. 1991, in Proc. of the Symposium on Gamma-Ray Line Astrophysics, ed. Ph. Durouchoux and N. Prantzos (New York: AIP) 52.

Gehrels, N., Barthelmy, S. D., Teegarden, B. J., Tueller, J., Leventhal, M., and MacCallum, C. J. 1991, ApJ (Letters), 375, L13.

Gehrels, N., and Tueller, J. 1991, Proc. of the 2nd GRO Science Workshop in Annapolis, MD, September 23-25, in press.

Johnson, W. N., Harnden, F. R., and Haymes, R. C. 1972, ApJ (Letters), 172, L1

Leventhal, M., MacCallum, C. J., and Stang, P. D. 1978, ApJ (Letters), 225, L11

Leventhal, M., MacCallum, C. J., Huters, A. F., and Stang, P. D. 1982, ApJ (Letters), 260, L1

Leventhal, M., MacCallum, C. J., Huters, A.F. and Stang, P.D. 1986, ApJ, 302, 459

Leventhal, M., MacCallum, C. J., Barthelmy, S. D., Gehrels, N., Teegarden, B. J., and Tueller, J. 1989, Nature, 339, 36

Lingenfelter, R. E., and Ramaty, R. 1989, ApJ, 343, 686

Paciesas, W. S., Cline, T. L., Teegarden, B. J., Tueller, J., Durouchoux, Ph., and Hameury, J. M. 1982 ApJ (Letters), 260, L7

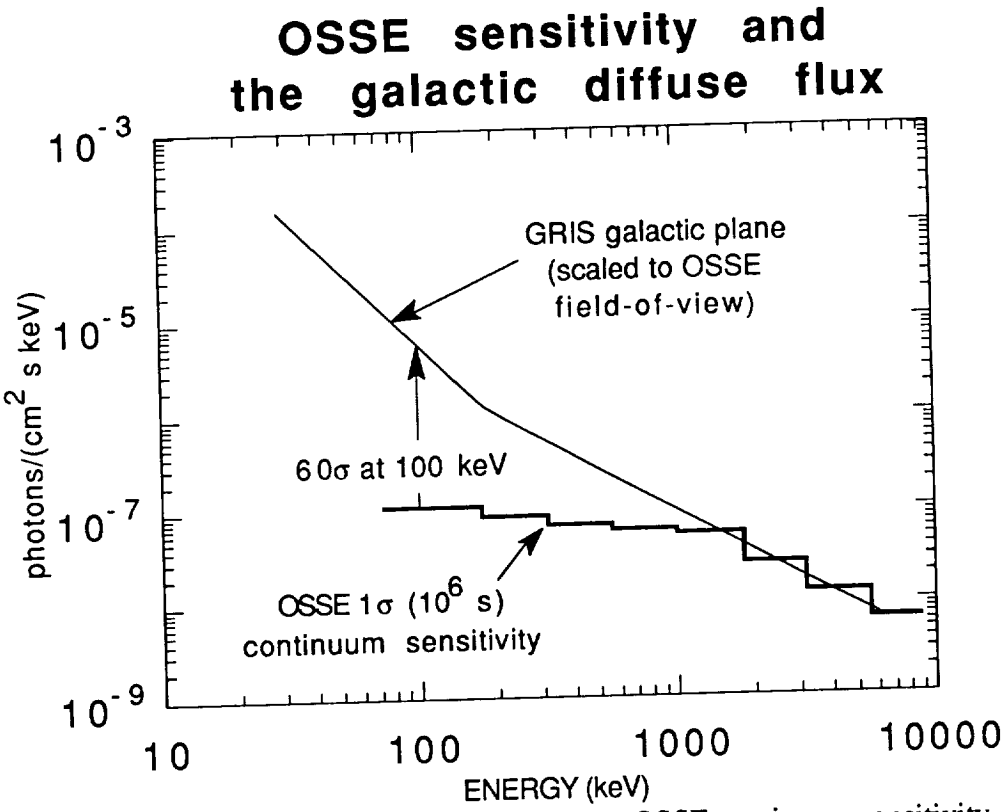

Figure 5 Proposed galactic diffuse component and the OSSE continuum sensitivity.

Paul, J., et al. 1991, in Proc. of the Symposium on Gamma-Ray Line Astrophysics, ed. Ph. Durouchoux and N. Prantzos (New York: AIP) 17
Riegler, G. R., et al. 1981, ApJ (Letters), 248, L13
Share, G. H., Leising, M. D., Messina, D. C., and Purcell, W. R. 1990, ApJ (Letters), 358, L45
Skinner, G. K., et al. 1987, Nature, 330, 544
Sunyaev, R. et al. 1991, "Three Spectral States of 1E1740.7-2942: . . .", submitted to ApJ (letters).
Tueller, J., et al. 1988, in Nuclear Spectroscopy of Astrophysical Sources, ed. N. Gehrels and G. H. Share (New York: AIP), p. 439
Tueller, J., et al. 1990, ApJ (Letters), 351, L41

The Gamma-Ray Continuum Spectrum from the Galactic Center Disk and Point Sources

Neil Gehrels and Jack Tueller
Laboratory for High Energy Astrophysics
NASA / Goddard Space Flight Center
Greenbelt, MD 20771 USA

ABSTRACT

A light curve of gamma-ray continuum emission from point sources in the galactic center region is generated from balloon and satellite observations made over the past 25 years. The emphasis is on the wide field-of-view instruments which measure the combined flux from all sources within ~20° of the center. These data have not been previously used for point-source analyses because of the unknown contribution from diffuse disk emission. In this study, the galactic disk component is estimated from observations made by the GRIS instrument in October 1988. Surprisingly, there are several times during the past 25 years when all gamma-ray sources (at 100 keV) within about 20° of the galactic center are turned off or are in low emission states. This implies that the sources are all variable and few in number. The continuum gamma-ray emission below ~150 keV from the black hole candidate 1E1740.7-2942 is seen to turn off in May 1989 on a time scale of less than two weeks, significantly shorter than ever seen before. With the continuum below 150 keV turned off, the spectral shape derived from the HEXAGONE observation on 22 May 1989 is very peculiar with a peak near 200 keV. This source was probably in its normal state for more than half of all observations since the mid 1960's. There are only two observations (in 1977 and 1979) for which the sum flux from the point sources in the region significantly exceeds that from 1E1740.7-2942 in its normal state.

INTRODUCTION

Recent monitoring of the galactic center region by the GRANAT hard X-ray and gamma-ray imaging instruments has shown that almost all gamma-ray sources within a few degrees of the center are variable[1-3]. These include 1E1740.7-2942, GRS1758-258, and GX1+4. Other observations by imaging and scanning instruments over the past 25 years[4-17] give occasional snap shots of the point sources in the region. There are additionally more than a dozen observations of the galactic center since 1968 by wide (>10° FWHM) field-of-view instruments. These wide-field measurements can, in principle, be used to determine the sum of the gamma-ray emission from point sources in the region. Efforts to do this in the past[10] were inhibited by an uncertain knowledge of the diffuse continuum gamma-ray emission from the galactic disk. In this paper, we use a recent observation[18,19] by the balloon-borne Gamma-Ray Imaging Spectrometer (GRIS) to estimate the diffuse continuum component. We then subtract this component from the historical wide-field measurements to obtain the first estimate of the long-term light curve of point-source flux from the galactic center region.

DIFFUSE DISK SPECTRUM

An estimate of the diffuse disk component of the gamma-ray continuum radiation near the galactic center is derived in the paper by Tueller *et al.* [18] in this volume. We summarize the key points and results here. The derivation is based on observations of the galactic center by the GRIS instrument. GRIS is a high resolution spectrometer[20] with an array of germanium detectors (1530 cm^3 active volume) surrounded by a 15-cm-thick active sodium-iodide shield. The field-of-view is 17° FWHM below 100 keV increasing to ~ 23° FWHM in the MeV range.

Observations[20] were made by GRIS on 28 - 29 October 1988 of the galactic center and of a point in the galactic plane 25° west of the center ($l = 335°$, $b = 0°$). The point in the plane was chosen to just exclude the center from the field-of-view. The spectrum at $l = 335°$ is well fit by a broken power law with $F = 9.99 \times 10^{-5}$ (E/100 keV)$^{-2.64}$ photons cm^{-2} s^{-1} keV^{-1} below 182 keV and $F = 4.96 \times 10^{-5}$ (E/100 keV)$^{-1.47}$ photons cm^{-2} s^{-1} keV^{-1} above 182 keV (see Figure 3 of Tueller *et al.*[18]).

We make two key assumptions in this study: *1)* GRIS was predominantly measuring the diffuse disk gamma-ray emission in this observation, and *2)* this emission has an approximately flat distribution in galactic longitude over the central radian of the disk. With these assumptions the $l = 335°$ GRIS measurement can be used as an estimate of the diffuse disk spectrum at the galactic center. Assumption *(1)* would be false if point sources near $l = 335°$, $b = 0°$ contribute significantly to the measurement. The only source in the region with a known hard spectrum is GX339-4 in its low X-ray, high gamma-ray state. However, GX339-4 was observed[21] by Ginga to be in the opposite high X-ray, low gamma-ray state 1.5 months before the GRIS observation. Assumption *(1)* is therefore probably accurate, although there is some possibility of contamination from GX339-4 (it is a variable source) or other point sources. Assumption *(2)* would be false if the longitude distribution of the diffuse continuum emission were strongly peaked toward the galactic center. However, the diffuse emission in the 20 keV to 10 MeV energy range is thought to be due to bremmstrahlung of cosmic ray electrons[22] and should have a fairly flat distribution over the central radian.

Figure 1 shows the GRIS $l = 335°$ spectrum plotted per radian of the galactic plane and compared with previous observations near the galactic center. If anything, the GRIS spectrum is lower than the others. However, as will be seen in the next sections, there are at least two observations of the galactic center by wide-field instruments that see exactly this same spectrum. The implication is that at these times (23 April 1968 and 22 May 1989) all point sources in the region were in very low-emission states and that the diffuse spectrum estimated from GRIS data is approximately correct for the galactic center region.

ANALYSIS METHOD

The 12 galactic-center observations by wide field-of-view instruments used in this analysis are listed in Table 1. Observations by instruments with fields-of-view greater than 35° were not included due to uncertainties in the disk spectrum beyond the central radian. A few observations by Bell/Sandia and HEAO-1 were not included in this initial study due to the unavailability of detailed spectral data.

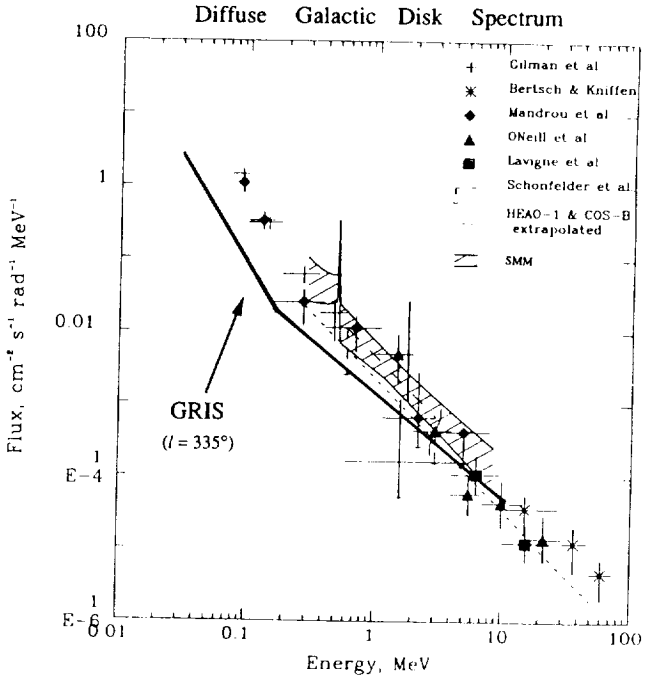

Figure 1 – GRIS spectrum at $l = 335°$ divided by the ~0.3 radian GRIS field-of-view, compared with previous measurements of the diffuse gamma-ray emission from the galactic disk near the galactic center. Adapted from Harris *et al.*[23]

The procedure used in our analysis was to digitize the published energy spectrum from each observation, subtract off the diffuse component and fit the residual. Examples are shown in Figure 2 for the HEAO-3 observations in 1979 and 1980, where the original and residual spectra are both plotted. The diffuse component was calculated by multiplying the GRIS $l = 335°$ spectrum (per radian of the galactic plane) shown in Figure 1 by the FWHM fields-of-view of the instruments (Table 1). The residuals are estimates of the sum of the spectra of point sources within the fields-of-view. We fit the residual spectra up to ~150 keV with a power-law of the form A (E/100 keV)$^{-\alpha}$. Our emphasis in this initial study is on the hard X-ray spectrum up to 100 keV, so we did not include any data above 200 keV. In this way we also largely avoided contamination from any positronium continuum emission.

RESULTS

Some surprising results are obtained in this analysis. For several of the observations (1968.31, 1974.25, 1980.2, 1989.39) the diffuse component was found to dominate the continuum spectrum. With the diffuse component subtracted off , the residual point-source component is small, and in two cases (1968.31, 1989.39) actually consistent with zero. For example, the HEAO-3 March/April 1980 residual spectrum in Figure 2(b) is seen to be less than one part in ten of the measured spectrum in the hard X-ray band.

The results of the fits (flux at 100 keV, A, and spectral slope, α) to the residual spectra are listed in Table 1 with the flux at 100 keV plotted in Figure 3. Also shown in the figure for comparison is the flux at 100 keV for the source 1E1740.7-2942 in its "normal" state observed by GRIP in 1988[13] and 1989[14], Mir/HEXE[16] in 1989, and GRANAT/Sigma[1-3] in 1990.

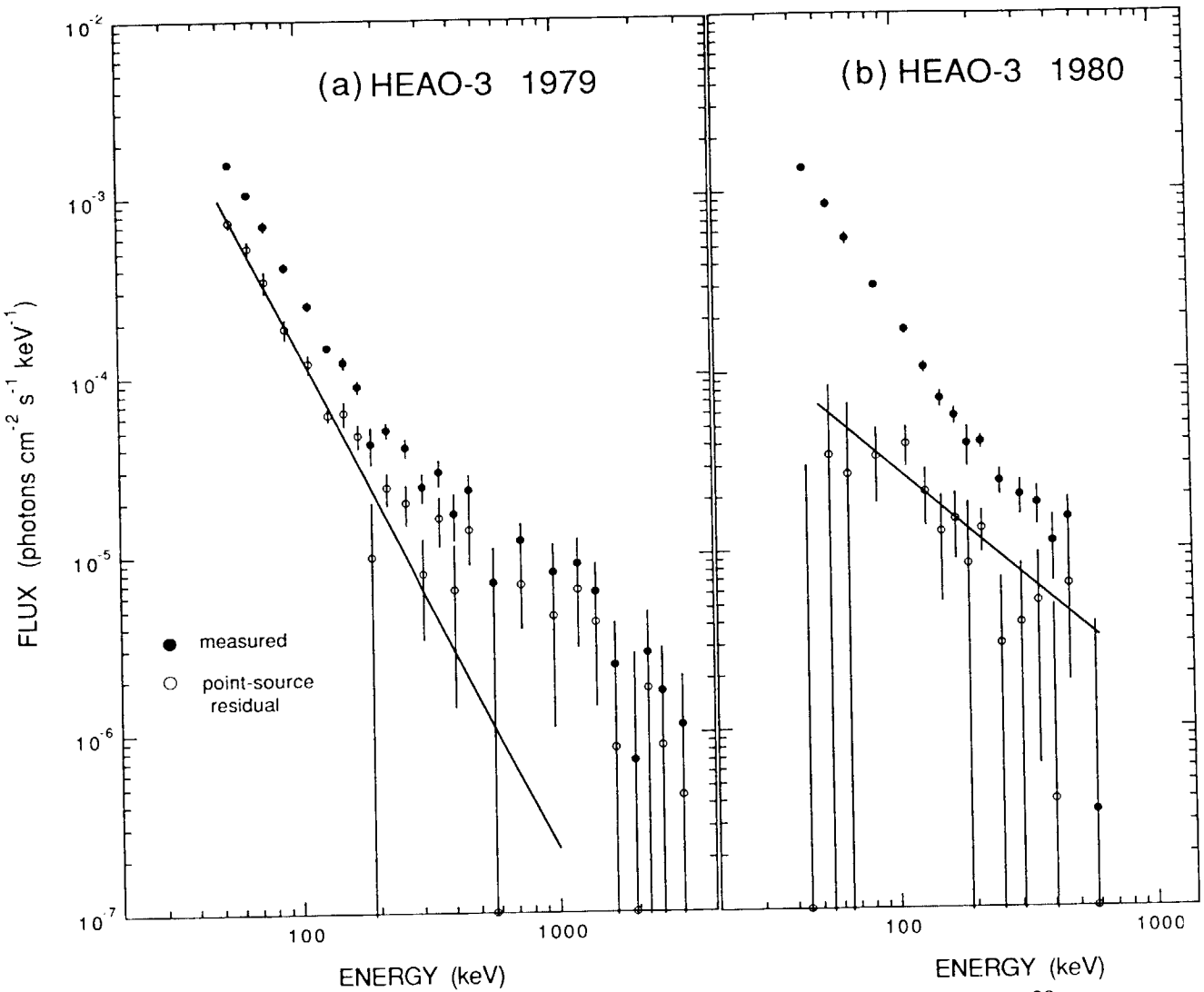

Figure 2 – HEAO-3 galactic center spectrum in (a) September/October 1979 and (b) March/April 1980 as measured[30] (filled circles) and with the diffuse disk component subtracted (open circles). The residual spectrum is an estimate of the sum of the point sources in the 30° field-of-view. The best-fit power-law to the residual spectra (lines in figure) in the 50 - 200 keV range is $(1.41\pm0.06)\times10^{-4}$ (E/100 keV)$^{-(2.8\pm0.1)}$ for (a) and $(2.8\pm0.6)\times10^{-5}$ (E/100 keV)$^{-(1.2\pm0.5)}$ for (b).

TABLE 1

Wide-Field Observations of the Galactic Center

Date	Date	Instrument	Field-of-View[a] (FWHM)	Flux at 100 keV, A[b] (10^{-5} photons cm^{-2} s^{-1} keV^{-1})	Power-Law α[b]	Reference
23 Apr 1968	1968.31	Rice Univ.	24°	-2.2 ± 2.4	2.6 ± 3.2	24
25 Nov 1970	1970.90	Rice Univ.	24°	7.1 ± 1.1	2.7 ± 0.4	25
20 Nov 1971	1971.89	Rice Univ.	24°	8.5 ± 1.4	3.5 ± 0.3	26
1-2 Apr 1974	1974.25	Rice Univ.	13°	3.1 ± 0.3	3.0 ± 0.2	27
11-12 Nov 1977	1977.86	Bell/Sandia	15°	18. ± 1.2	2.5 ± 0.3	28
15 Apr 1979	1979.29	Bell/Sandia	15°	9.4 ± 1.9	2.1 ± 0.8	29
Sept/Oct 1979	1979.8	HEAO-3	~30°	14. ± 0.6	2.8 ± 0.1	30
Mar/Apr 1980	1980.2	HEAO-3	~30°	2.8 ± 0.6	1.2 ± 0.5	30
20 Nov 1981	1981.89	Goddard	15°	10. ± 3.3	2.7 ± 1.0	31
1 May 1988	1988.33	GRIS	17°	7.8 ± 1.0	2.8 ± 0.6	18, 19
29 Oct 1988	1988.83	GRIS	17°	11. ± 0.7	2.0 ± 0.1	18, 19
22 May 1989	1989.39	HEXAGONE	19°	0.6 ± 1.0	2.0 ± 2.2	32

a) At 100 keV.

b) Fit to residual point-source flux after diffuse flux is subtracted. Flux = A $(E/100\ keV)^{-\alpha}$.

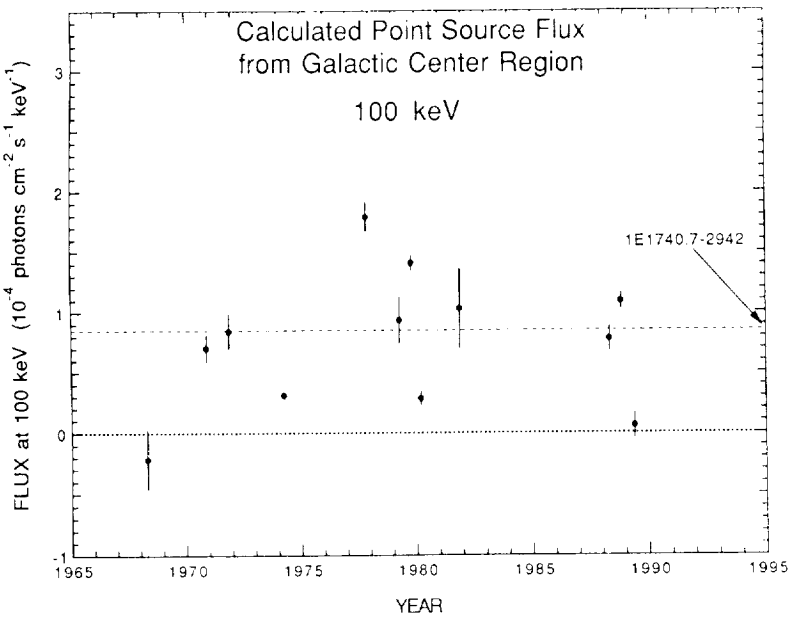

Figure 3 – Residual total point-source flux at 100 keV calculated from wide field-of-view measurements. Fluxes are from Table 1. The 100 keV flux level for 1E1740.7-2942 in March/April 1990[1-3] is shown by the dashed line.

DISCUSSION

In terms of point-source emission, the 12 wide-field observations in Figure 3 can be grouped as follows:

1) 2 observations (1968.31, 1989.39) are consistent with no point-source emission.

2) 2 observations (1974.25, 1980.2) have low point-source emission of $\sim 3 \times 10^{-5}$ photons cm^{-2} s^{-1} keV^{-1}. Many sources are candidates for this emission. The flux level is about right for GRS1758-258 as observed[3] in March/April 1990, 1E1740.7-2942 in its low state as observed[1] in February 1991 or GX1+4 as observed[33] in the 1970's.

3) 6 observations (1970.90, 1971.89, 1979.29, 1981.89, 1988.33, 1988.83) have 100 keV flux levels consistent with that of 1E1740.7-2942 in its normal state, although significant contributions from other sources such as GX1+4 and GRS1758-258 can not be ruled out. The 1988.33 observation by GRIS was just 18 days after an observation by GRIP in which 1E1740.7-2942 was indeed found to be in its normal state and the only strong 100 keV source in the region.

4) 2 observations (1977.86, 1979.8) have flux levels significantly exceeding that of 1E1740.7-2942 in its normal state. The 1977.86 observation by Bell/Sandia was just 12 days before an observation[34] by the NRL high-energy X-ray balloon instrument, which scanned the galactic center region. The scans revealed comparable 100 keV fluxes from 1742-294, which is very likely the same source as 1E1740.7-2942, and from 1743-322.

We thus conclude that there are few strong point sources of 100 keV emission within ~20° of the galactic center and that all of them are variable. The black hole candidate 1E1740.7-2942 is probably a dominant contributor to the high energy flux for more than half of the observations.

1E1740.7-2942 Turn-Off

There are 5 observations of 1E1740.7-2942 within a period of two months in March-May 1989. Two are with imaging instruments (GRIP[14], EXITE[17]), two with narrow (< 2°) field-of-view instruments (Mir/HEXE[16], POKER[15]) and one with the wide-field HEXAGONE[32] (Table 1). A plot of the 1E1740.7-2942 60 keV flux as a function of time from these observations is shown in Figure 4. The HEXAGONE data point is the residual after the diffuse disk flux was subtracted and represents an upper limit for any point source in the field-of-view. The source turned off in gamma-ray continuum emission in 13 days. This is the fastest variability ever seen in 1E1740.7-2942 and implies a compact emission region of size less than 13 light days.

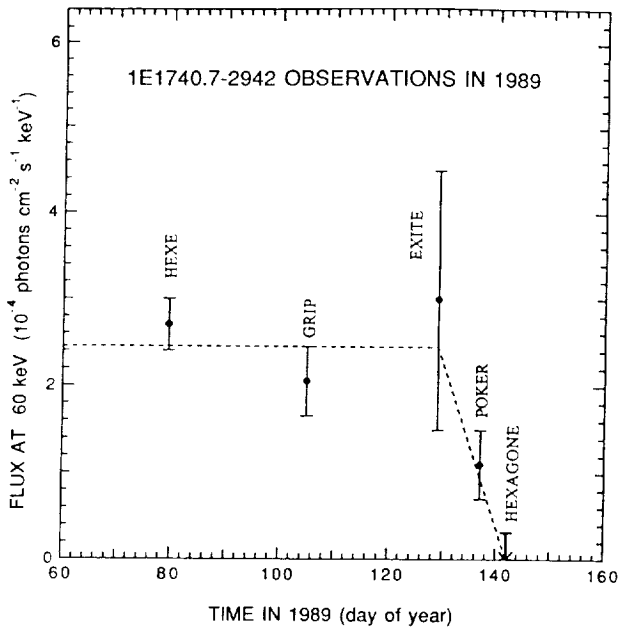

Figure 4 – The flux at 60 keV from 1E1740.7-2942 vs. time for observations between 20 March and 22 May 1989 by Mir/HEXE[16], GRIP[14], EXITE[17], POKER[15] and HEXAGONE[32]. The HEXAGONE point is a 1σ upper limit for all sources in the ~19° field-of-view. The source turn-off occurs in 13 days. Note that in order to have best statistics for all measurements, this plot is at 60 keV instead of the 100 keV used elsewhere.

170 keV Feature

The 130-180 keV feature observed[32] in the 22 May 1989 HEXAGONE spectrum of the galactic center becomes more prominent when the diffuse disk emission is subtracted, as shown in Figure 5. The point-source spectrum actually has a maximum at ~170 keV. This feature has been interpreted[35] as a Compton backscatter peak from an accretion disk or cloud surrounding a source of 511 keV positron annihilation photons. Figure 5 shows that on 22 May 1989, the only significant gamma-ray emission from the galactic center region was in two lines (170 and 511 keV) both probably associated with positron annihilation.

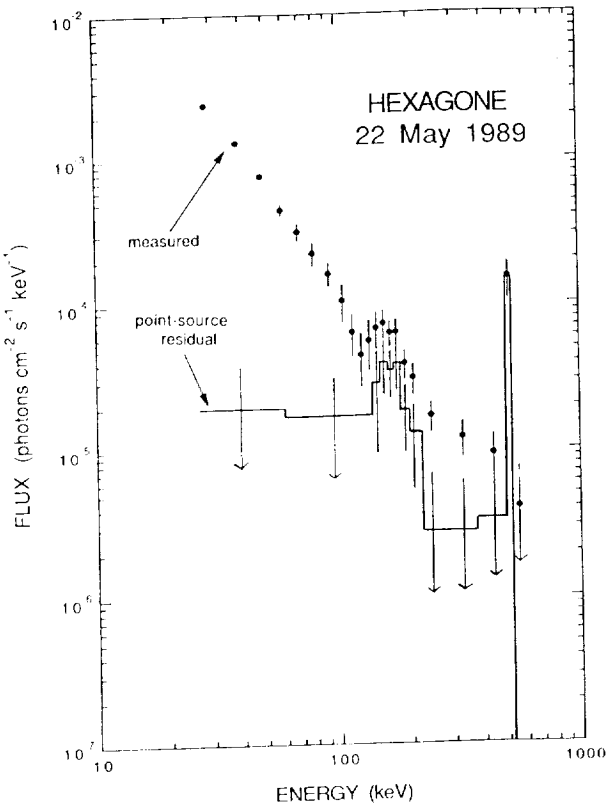

Figure 5 – HEXAGONE galactic center spectrum on 22 May 1989 as measured[32] (filled circles) and with the diffuse disk component subtracted (histogram). The data points below 130 keV for the residual spectrum have been averaged to improve statistics.

ACKNOWLEDGEMENTS

We greatly appreciate discussions with J. Grindlay, T. Prince, G. Ricker and P. Ubertini concerning *1)* the series of balloon measurements just preceeding the HEXAGONE observation in May 1989, *2)* the possible contamination to our diffuse spectrum from GX339-4, and *3)* the 1970's balloon observations of GX1+4. We thank K. Pollock for assistance in the data analysis and in preparing this paper.

REFERENCES

1. R. Sunyaev, *et al.*, 1991, Ap. J. Lett., submitted.
2. L. Bouchet, *et al.*, 1991, Ap. J. Lett., accepted.
3. R. Sunyaev, *et al.*, 1991, Astron. & Astrophys. Lett., 247, L29.
4. G. Riegler, E. Boldt, and P. Serlemitsos, 1968, Ap. J. Lett., 153, L95.
5. W. H. G. Lewin, G. Clark, and W. B. Smith, 1968, Ap. J. Lett., 152, L49.
6. G. Buselli, *et al.*, 1968, Nature, 219, 1124.
7. W. H. G. Lewin, G. R. Ricker, and J. E. McClintock, 1971, Ap. J. Lett., 169, L17.
8. G. R. Ricker, *et al.*, 1973, Ap. J., 184, 237.
9. G. R. Ricker, *et al.*, 1976, Ap. J., 207, 333.
10. J. L. Matteson, 1982, in The Galactic Center, ed. F. R. Riegler and R. D. Blandford (AIP: New York), p. 109.

11. F. K. Knight, *et al.*, 1985, Ap. J., 290, 557.
12. G. K. Skinner, *et al.*, 1987, Nature, 330, 544.
13. W. R. Cook, *et al.*, 1991, Ap. J. Lett., 372, L75.
14. J. Grunsfeld, *et al.*, 1991, in 28th Yamada Conf. on Frontiers of X-ray Astronomy, Nagaoya, Japan.
15. A. Bazzano, *et al.*, 1991, in Gamma Ray Line Astrophysics, ed Ph. Durouchoux and N. Prantzos (AIP: New York), p. 61.
16. G. K. Skinner, *et al.*, 1991, Astron. & Astrophys., submitted.
17. C. E. Covault, R. P. Manandhar, and J. E. Grindlay, 1991, Proc. 22nd Int. Cosmic Ray Conf. (Dublin), OG 1.6.
18. J. Tueller, *et al.*, 1991, this volume.
19. N. Gehrels, et al., 1991, Ap. J. Lett., 375, L13.
20. J. Tueller, *et al.*, 1988, in Nuclear Spectroscopy of Astrophysical Sources, ed. N. Gehrels and G. H. Share (AIP: New York), p. 439.
21. K. Ebisawa, 1991, Thesis, Astronomy, University of Tokyo, p. 105.
22. W. Sacher and V. Schönfelder, 1984, Ap. J., 279, 817.
23. M. Harris, *et al.*, 1990, Ap. J., 362, 135.
24. R. C. Haymes, *et al.*, 1969, Ap. J., 157, 1455.
25. W. N. Johnson, F. R. Harnden, and R. C. Haymes, 1972, Ap. J. Lett., 172, L1.
26. W. N. Johnson and R. C. Haymes, 1973, Ap. J., 184, 103.
27. R. C. Haymes, *et al.*, 1975, Ap. J., 201, 593.
28. M. Leventhal, C. J. MacCallum, and P. P. Stang, 1978, Ap. J. Lett., 225, L11.
29. M. Leventhal, *et al.*, 1980, Ap. J., 240, 338.
30. G. R. Riegler, *et al.*, 1985, Ap. J. Lett., 294, L13.
31. W. S. Paciesas, *et al.*, 1982, Ap. J. Lett., 260, L7.
32. S. Slassi, *et al.*, 1991, Proc. 22nd Int. Cosmic Ray Conf. (Dublin), OG 3.2.8.
33. G. R. Ricker, *et al.*, 1973, Ap. J., 184, 237.
34. F. K. Knight, *et. al.*, 1985, Ap. J., 290, 557.
35. R. E. Lingenfelter and X.-M. Huo, 1991, Ap. J., 381, 426.

10.
SOLAR

BATSE FLARE OBSERVATIONS IN SOLAR CYCLE 22

R.A. Schwartz[1,2], B.R. Dennis[1], G.J. Fishman[3], C.A. Meegan[3], R.B. Wilson[3], and W.S. Paciesas[3,4]

[1]Laboratory for Astronomy and Space Physics, NASA Goddard Space Flight Center, Greenbelt, MD 20771
[2]Hughes STX, Lanham, MD
[3]Space Science Laboratory, NASA Marshall Space Flight Center, Huntsville, AL, 35812
[4]Dept. of Physics, University of Alabama in Huntsille, AL, 35899

1. INTRODUCTION

As much as 10^{32} ergs can be released during a solar flare in times as short as 100 to 1000 s, with intense emission detected over most of the electromagnetic spectrum. It is believed that this energy comes from the dissipation of the non-potential components of strong magnetic fields in the solar atmosphere, possibly through magnetic reconnection. Much of the energy appears in the form of high-energy particles and hot plasma, with accelerated electrons with energies of tens of keV probably containing a major fraction. The most direct diagnostic of these energetic electrons is the hard x-ray and gamma-ray bremsstrahlung that they emit as they move from the acceleration site through the solar atmosphere. This bremsstrahlung is emitted before the electrons are thermalized in the ambient atmosphere and, thus, retains unique information about the energy release, energy transport, and particle acceleration processes of the flare that are not available in the radiation signatures of the thermal plasma.

The Hard X-ray Burst Spectrometer (HXRBS) group at Goddard Space Flight Center has developed and is maintaining a quick-look analysis system for solar flare hard x-ray data from the Burst And Transient Source Experiment (BATSE) on the recently launched Compton Gamma-Ray Observatory (GRO) (Fishman et al. 1989). The instrument consists, in part, of 8 large planar detectors, each 2025 cm^2, placed on the corners of the GRO spacecraft with the orientation of the faces being those of a regular octahedron. Although optimized for the detection of gamma-ray bursts, these detectors are far more sensitive than any previous spacecraft-borne hard x-ray flare instrumentation both for the detection of small microflares and the resolution of fine temporal structures. The data in this BATSE solar database are from the DISCLA (Discriminator Large Area) rates. From each of eight detectors there are hard x-ray data in 4 energy channels, 25-50, 50-100, 100-300, and >300 keV with a time resolution of 1.024 seconds. These data are suitable for temporal correlation with data at other wavelengths and they provide a first look into the BATSE and other GRO instrument flare data sets. The BATSE and other GRO principal investigator groups should be contacted for the availability of data sets at higher time or spectral resolution or at higher energies.

2. BATSE DATABASE

Since the beginning of BATSE science operations on 19 April through 19 September 1991, 1262 solar flares had been detected in hard X-rays above 25 keV with the Large Area Detectors (LAD). Their distribution vs. time is shown in Figure 1 together with that for flares observed with the Solar Maximum Mission Hard X-ray Burst Spectrometer (SMM/HXRBS) from February 1980 through November 1989. These rates have not been scaled for the instrument duty cycle which varied some due mainly to the phasing of orbital parameters. Solar flares were reliably detected in the HXRBS data down to a count rate of 30 counts s^{-1} above background for the 70 cm^2 detector area and 400 counts s^{-1} in the BATSE LAD data where this rate is scaled to that of a single LAD of 2000 cm^2 pointing directly at the Sun. The BATSE instrument has a sensitivity which is roughly three times that of HXRBS due to its larger area, despite a higher background per unit area and a thick aluminum window which significantly attenuates the solar spectrum at oblique angles. The strong activity in June 1991 during the passage of Active Region 6659 across the solar disk produced the peak during the time of the BATSE measurements although it was well below the frenetic level of activity seen during the passage of Active Region 5395 in March of 1989. Starting from the commencement of BATSE observations, the level of activity appears more uniform than during the earlier time period of

HXRBS measurements in Cycle 22. This greater uniformity may be because BATSE has been able to detect flares down to an intrinsically smaller flux than possible with the HXRBS detector. Flares in both data sets were found by visually inspecting the count rate for transient events which satisfied the directional, spectral, and temporal characteristics of a solar flare and which were sometimes corroborated with lists of optical, radio, and soft x-ray flares provided through the Space Environment Laboratory.

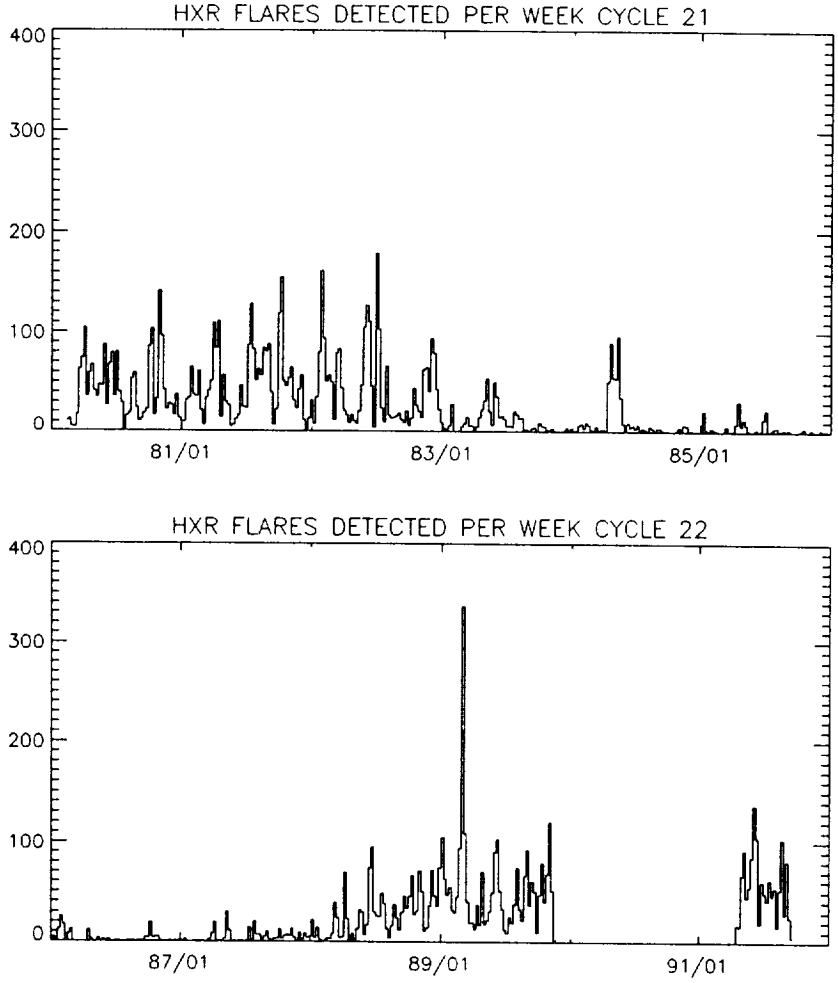

Fig. 1. The distribution of hard x-ray flares vs. time during solar Cycles 21 and 22 measured with HXRBS from February 1980 through November 1989 and measured with BATSE from April 1991 through September 1991. The rates are computed by taking the number of flares detected and dividing by the total time interval without any corrections for the detector duty cycle which typically ranged from 40-60%.

Figure 2 presents the distribution of peak hard x-ray count rates for four time periods including Cycle 21 measured with HXRBS from 80/02/14 - 86/12/31, the full SMM mission from 80/02/14 - 89/11/15, Cycle 22 measured with HXRBS from 87/01/01 - 89/11/15, and Cycle 22 measured with BATSE from 91/04/19 - 91/09/20. The fluxes are background subtracted and the BATSE data have been corrected for solar aspect and normalized to the smaller area of the HXRBS detector. The characteristic slope of these distributions is obtained by fitting a power law over three decades in peak rate from just above the knee caused by the roll-off at the detector sensitivity threshold to a HXRBS flux of ~50,000 s^{-1}. The indices corresponding to the time periods above are respectively -1.75±0.01, -1.73±0.01, -1.66±0.02, and -1.61±0.03. The fact that these distributions are well fit by featureless power laws has been taken as evidence that

solar flares are avalanches of many small reconnection events (Lu & Hamilton 1991). While all of these indices are close to -1.7 there is a statistically significant difference between those from Cycle 21 and Cycle 22. However, the Cycle 22 measurements were made with HXRBS near the end of the mission when the detector's low energy sensitivity had been degraded and with the BATSE LAD's which have the aforementioned aluminum windows which reduces their low energy response. This fact could have resulted in flatter number-size distributions since the smaller flares tend to have softer photon energy spectra which would reduce their peak rates relative to the larger flares with harder spectra. If these differences in the logarithmic slope prove to be true characteristics of the two solar cycles then this would suggest some intrinsic difference in the flare process from cycle to cycle.

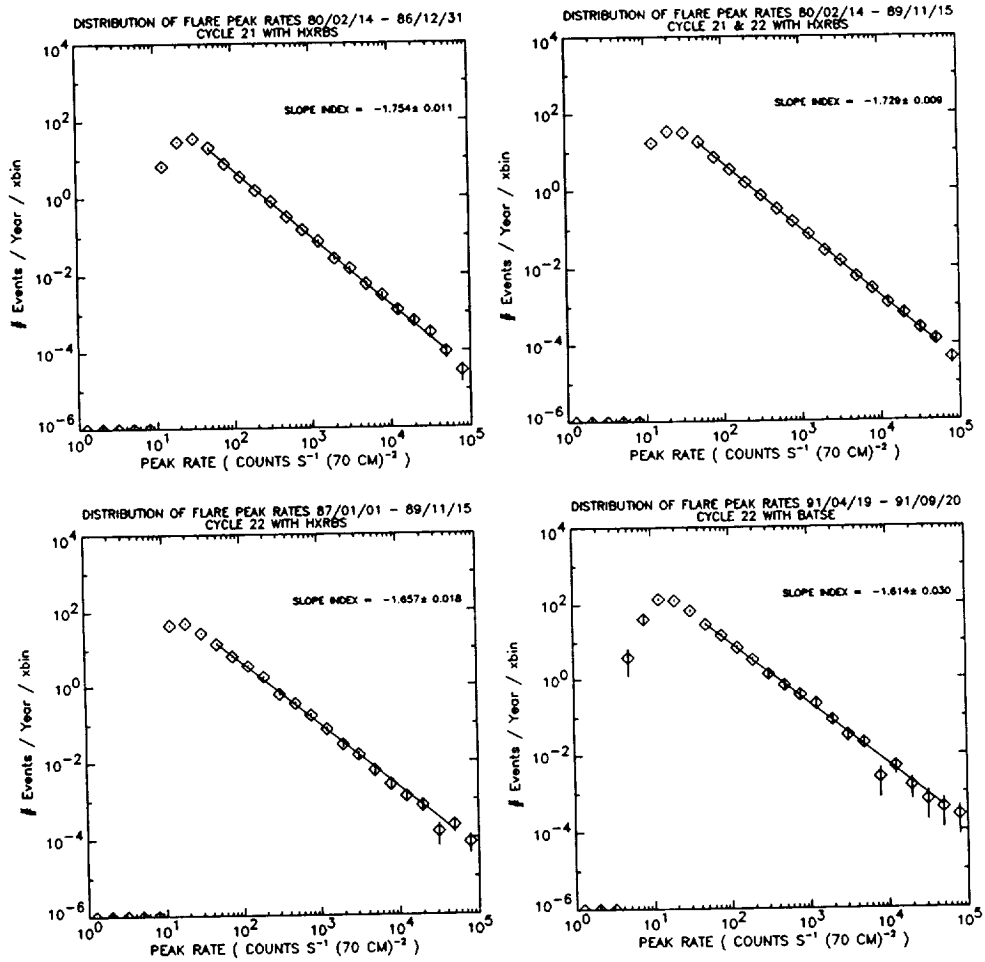

Fig. 2. The number of flares vs. peak flux for four time periods measured with HXRBS and BATSE. The event rates are not corrected for the detector duty cycles. The BATSE flux has been normalized to that expected from a HXRBS detector pointed directly at the Sun.

3. FAST RISING HARD X-RAY SPIKES

Hundreds of fast hard x-ray spikes were observed with HXRBS having durations of less than 1 s, some with rise and decay times of some tens of milliseconds (Kiplinger et al., 1983). The existence of such variations in hard X-rays offers the opportunity to correlate variations at differing energies on timescales that are considerably less than one second. For non-thermal models, the observed hard x-ray time profile is the convolution of the temporal evolution of the electron acceleration process with propagation effects associated with the beam of electrons interacting in the target (Emslie, 1983). For typical flare loop dimensions of 1-5 $\times$ 10^4 km, 50 keV electrons will traverse the loop in 0.1-0.5 s or longer depending upon their pitch angle with respect to the loop's magnetic field. Hence, spectral observations on these timescales can resolve electron time-of-flight effects and constitute a critical test of the thick-target model.

The flare on 17 June 1991 at 1:11:30 UT is just such a fast rising flare which offers the opportunity to test this model. In Figure 3 the time history of this flare is presented for the 50-100 keV and 100-300 keV energy channels at time resolutions of 1.024 s and 0.064 s. The flare is a GOES class C5.9 with no known optical counterpart despite good seeing from Big Bear Solar Observatory (private communication). The hard x-ray burst is moderately hard with a spectral index of about 4 as determined from the ratios of the DISCLA channels. The second row of frames shows the time structures around 1:11:30 UT at the higher resolution. The burst rises from near background levels to maximum in about 400 ms and falls in a comparable time. The time histories in the third row are simulations of what HXRBS data would have been for an identical flare. While the peaks are visible in the simulated HXRBS data, the statistics would have been too poor to enable any meaningful time-resolved spectral analysis for time-of-flight effects. In the HXRBS data, it seemed that fast time structures were a more common feature at fluxes which were too low for quantitative analysis. However, this event shows that data from such flares obtained with the BATSE LADs are ideal for this kind of study.

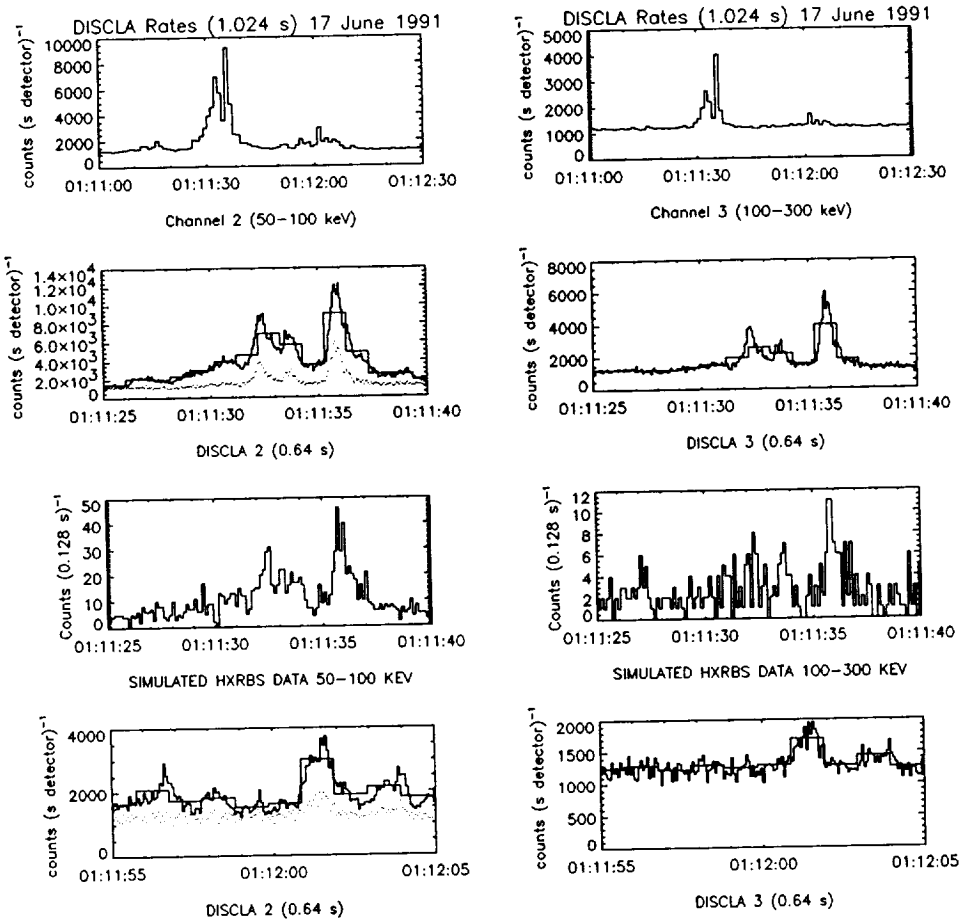

Fig. 3. The time history of a fast rising spike flare on 17 June 1991 observed with the BATSE LADs. The top row of panels shows the BATSE DISCLA rate from the two most sunward pointing detectors at a time resolution of 1.024 s in channel 2 (on the left) and channel 3. Below each panel the geometric area of the included BATSE detectors are given in terms of the cosine of senith angle of the Sun so negative values indicate detectors facing away from the Sun. The DISCLA energy channels are also indicated although channel 6 refers to the charged-particle detector rate. The two frames below are from the same detectors in the same energy ranges at a time resolution of 0.64 s for the time structures around 1:11:30 UT. The dots in the left hand frame shows the time history of DISCLA channel 3 and the histogram shows channel 2. The overlay shows the 1.024 s resolution data from the frame above. The plots in the third row are of a simulation of the count rate which would have been seen by HXRBS for an identical flare at the time resolution of HXRBS, 0.128 s. The bottom frames are similar to the second row except that it expands the structures near 1:12:00 UT.

4. GIANT FLARES OF JUNE 1991

During June of 1991 there were six large flares with a soft x-ray size of GOES class X10 or higher, four of which were well observed with BATSE on 4, 6, 9 and 11 June. Of these, the most intense in hard X-rays was the flare of 4 June 1991 from region 6659 at N30E65 which started at 3:37 UT, continued through the end of the orbit at 4:10 UT and well into the

daytime portion of the next orbit. The time history of the flare is shown in three energy-loss bands in Figure 4 although the rate shown in the top frame from 3:39-3:42 UT is severely distorted due to an extremely high detector count rate in excess of 10^6 counts s^{-1}. The large area of the BATSE detectors makes them sensitive to small flares, but it also makes them prone to saturation, i.e. severe deadtime and pulse pile-up problems, during the largest solar flares. However, the BATSE instrument is comprised of 16 independent x-ray detectors some of which are always masked from the direct solar flux. Thus, during large flares, the backside detectors give the most accurate indication of the hard x-ray flux when the frontside detectors are saturated. However, it is more difficult to deconvolve the counting rates in the different energy-loss channels into a photon spectrum because the photon path to the detector involves either a Compton scattering or transmission through considerable passive material. The bottom frame of Figure 4 is from channel 6 which is the event rate in the plastic scintillator normally used to reject energetic particle events in the LADs. This detector is also sensitive to energy-loss events from photons with energies in excess of 1 MeV without any of the pileup effects in the LADs because of the high threshold and an interaction cross-section of about 5%. The peak at 3:41 UT corresponds to a rate of photons above an MeV of ~300 cm^{-2} s^{-1} which is larger than for any flare observed with SMM. Also, it is possible to estimate the peak hard x-ray flux from the backside detector rates and by extrapolating the high energy flux to lower energies. While the maximum flare rate seen with HXRBS was slightly over 200,000 s^{-1} during 9.75 years of operation, our estimate for the flux for the 4 June 1991 flare is 2-4 times as great with an uncertainty of at least 50%.

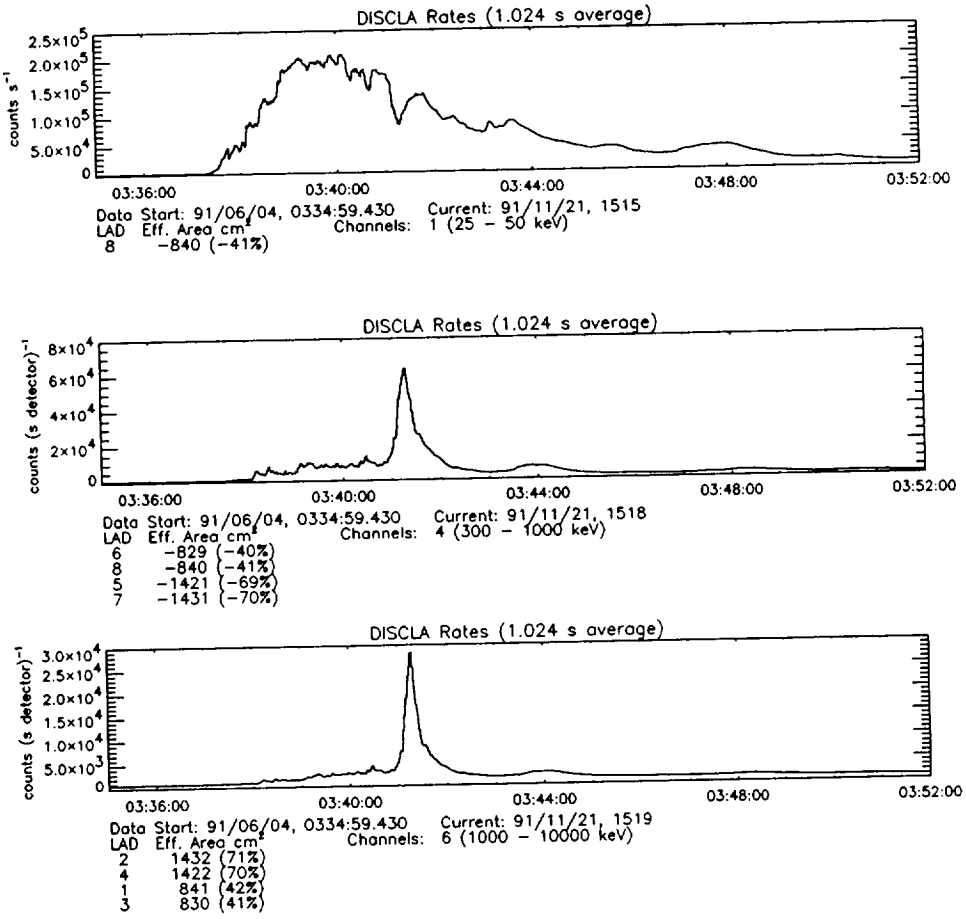

Fig. 4. Hard x-ray count rate history of the giant flare of 4 June 1991. The top two frames are the energy-loss rates in the backside detectors in two energy channels, 25-50 keV and 300-1000 keV. Although these detectors are shielded from the direct flare flux, the count rates were still too high to accurately measure the peak at 3:41 UT. The bottom rate was obtained from the sum of all of the frontside charged-particle detectors which are sensitive to photons of energies greater than 1 MeV and therefore did not become saturated by the lower energy photons. The peak corresponds to a photon rate of more than 300 cm^{-2} s^{-1} above an MeV.

Although the extremely high hard x-ray flux makes much of the BATSE LAD data unsuitable for detailed quantitative analysis near the flare peak, the high sensitivity of BATSE can be put to good use at the start and during the decay phase of the flare. In Figure 5 the flare start is shown in three energy channels using the two most sunward detectors. The hard X-rays are detectable just at 3:37:00 UT in channel 1 (25-50 keV) and the rate climbs quickly within a few seconds without any evidence of pre-flare activity. The 50-100 keV rate does not increase until 3:37:07 UT and only rises steeply after 3:37:15 UT. The 100-300 keV rate starts to rise at 3:37:20 some 20 seconds after the flare start at lower energy. In fact, the photon spectrum must be steeper than a power-law index of -6 during the initial stages of the flare even though

it probably hardens to a value between -2 and -3 near the peak. As soft as the flare spectrum is at the start, it is interesting that there is a persistent high energy component more than 25 minutes after the peak at 3:41 UT. In Figure 6 the count rates are shown from the lowest to the highest energies near the end of the daytime portion of the spacecraft orbit. Just after 4:08 UT the Sun passes behind the GRO horizon and the extinction of the flux is clear at all energies, even above 1 MeV. The extinction takes longer at high energy because the attenuation cross-section of the atmosphere decreases with energy.

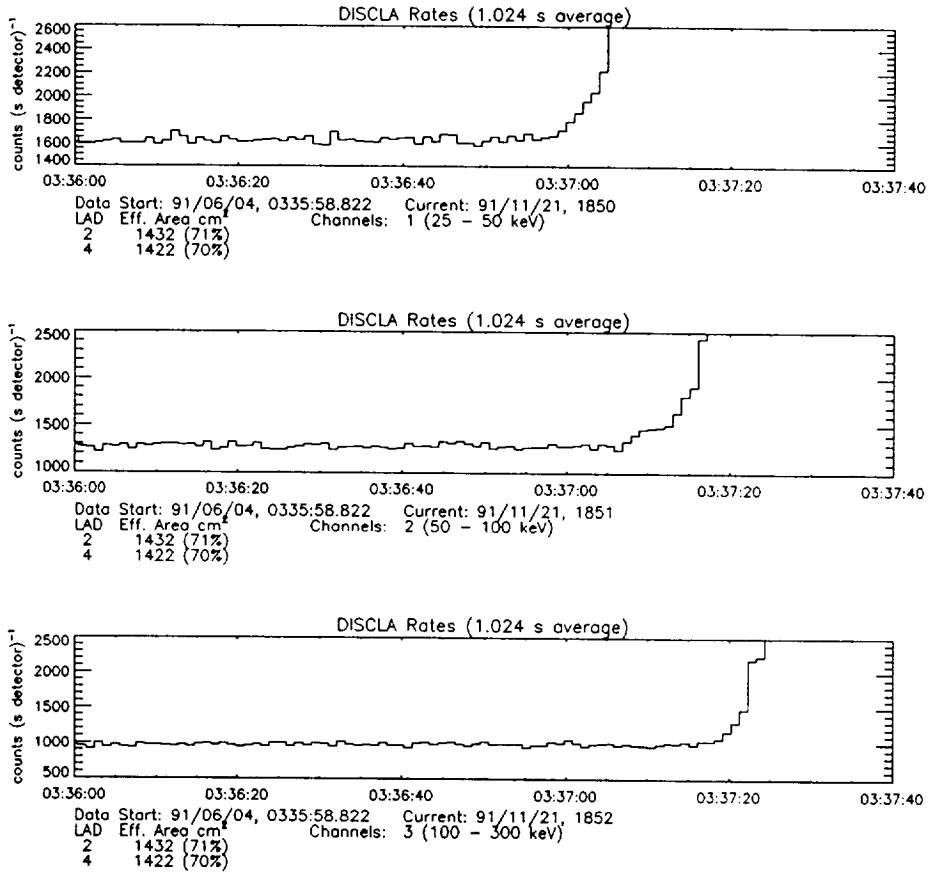

Fig. 5. Start of the 4 June 1991 flare at three energies, 25-50, 50-100, and 100-300 keV. The detectors did not begin to suffer extreme pile-up problems until after the end of these plots at 3:37:40 UT.

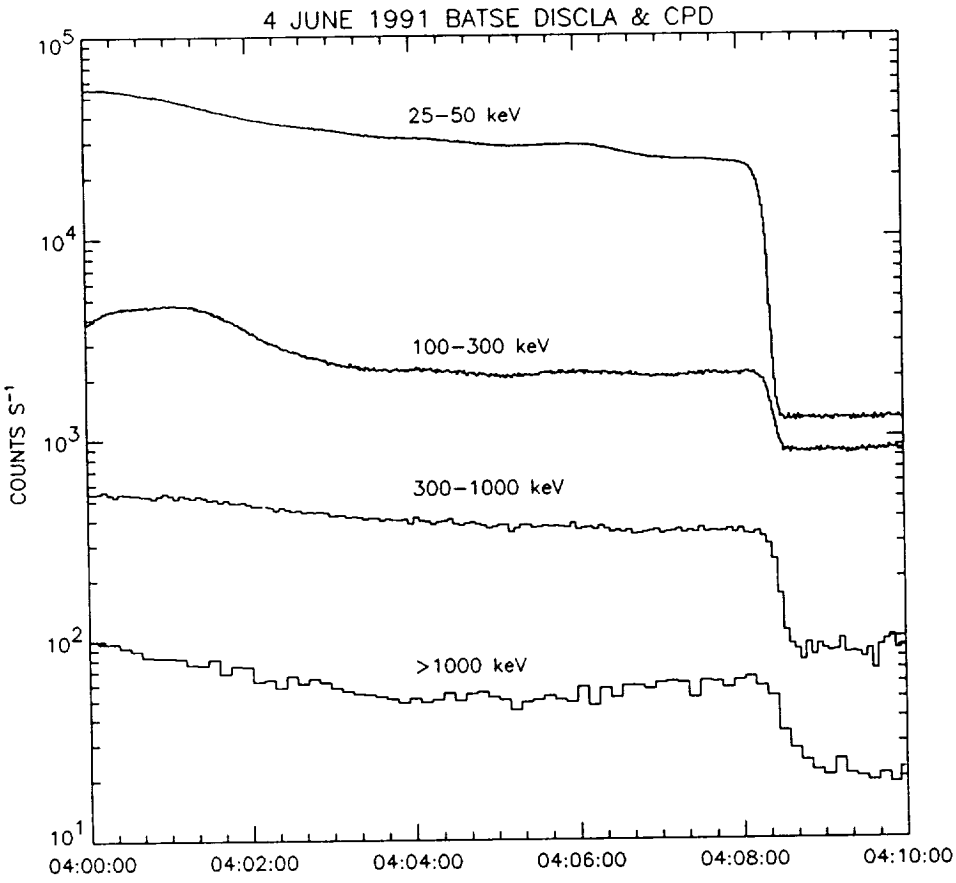

Fig. 6. Decay of the 4 June 1991 flare. These top three rates are from the sunward facing LADs and the bottom rate (>1000 keV) is from the sum of all eight charged-particle detectors. Just at 4:08:20 UT the GRO spacecraft enters night and the extinction of the solar flux is clearly seen.

GRO observed three more X10+ flares throughout their impulsive phases. They are all shown in Figure 7 at the highest energies observable with the BATSE LADs and charge-particle detectors starting at 1:04 UT on 6 June, at 1:36 UT on 9 June, and at 1:59 UT on 11 June at 1:59 UT. While none were as large as the 4 June flare all of the frontside detectors suffered saturation near the peak of the events.

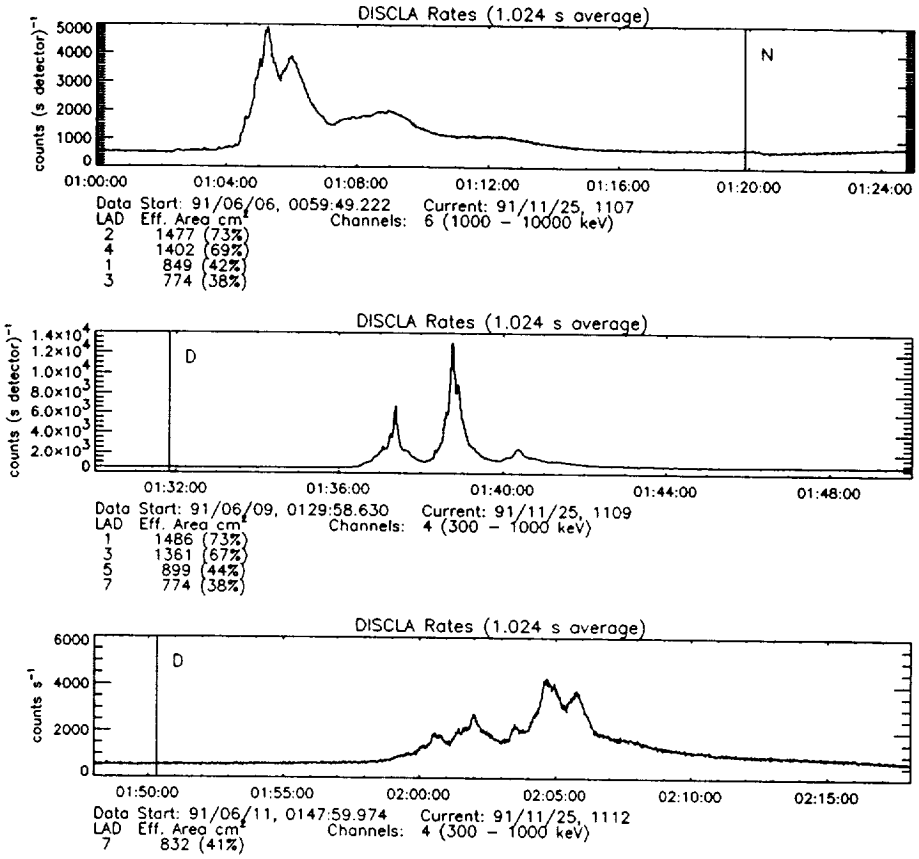

Fig. 7. High energy time histories of three gamma-ray flares observed with BATSE on 6 June, 9 June, and 11 June 1991.

5. HARD SPIKE EVENT OF 30 JUNE 1991

The high sensitivity obtained from the raw stopping power of these large detectors opens a new high time resolution window in the several hundred keV range. An example of the new phenomena available for study is provided by the flare on 30 June 1991 at 2:56 UT which occurs just before the spacecraft enters night. The four DISCLA energy bands are displayed in Figure 8. There was no reported optical counterpart for this GOES M5.0 event. There were strong microwave emission and Type III bursts. The flare profile is fairly smooth in the 25-50 and 50-100 keV bands with the peak at 2:56:31 UT. However, not the strong peak in the 300-1000 keV band at 2:56:28 UT which is not detectable in the lowest energy band. Presumably this peak must be masked by the intense flux at lower energy, but this also implies that the spectrum from this peak is extraordinarily flat, flatter than the power-law index of -3 to -4 which would characterize the spectrum below 100 keV based on the ratio of the two low energy channels. This flat impulsive spectrum is characteristic of the events reported above 10

MeV by Reiger and Marschhauser which they have designated as electron dominated flares. It should be possible to study the several hundred keV component of these flares using data from the BATSE LADs and Spectroscopy detectors.

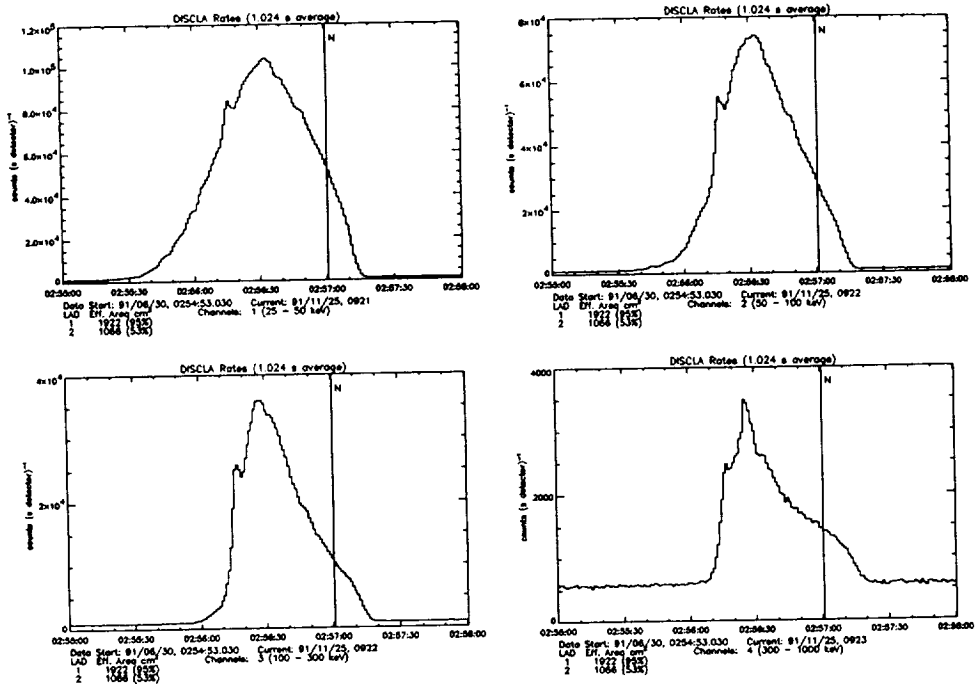

Fig. 8. High energy spike flare observed with BATSE at 2:56 UT on 30 June 1991. The four panels show the time history in the four DISCLA channels running from left to right and top to bottom in the energy ranges 25-50, 50-100, 100-300, and 300-1000 keV. Note that the impulsive spike visible at the highest energy at 2:56:28 UT is completely masked by the low energy time history

References

Dennis, B.R. 1988, Solar Phys., **118**, 49.
Dennis, B.R. and Schwartz, R.A. 1989, Solar Phys., **121**, 75.
Emslie, A. G. 1983, Ap.J., **271**, 367.
Fishman, G. J., et al. 1989,"Proceedings of the First GRO Science Workshop," (W. N. Johnson, ed.), 2-39.
Kiplinger, A. L., Dennis, B. R., Emslie, A. G., Frost, K. J., and Orwig, L. E. 1983, Ap.J. Letters, **265**, L99.
Lu, E.T. and Hamilton, R.J. 1991, Ap. J., **380**, L89..
Rieger, E. and Marschhauser, H. 1990, "Proceedings of the Third Max'91 Workshop," (R. M. Winglee and A. L. Kiplinger, ed.), 68.

GRO SOLAR FLARE OBSERVATIONS

R. J. Murphy
Naval Research Laboratory
Washington, DC 10375

ABSTRACT

Although the GRO instruments are not dedicated to solar observing, their capabilities are such that they can extend and expand the solar hard X-ray and gamma-ray observations accomplished by instruments such as those of SMM and Hinotori. These capabilities are discussed, with emphasis on the use of the instruments by guest investigators. Instrumental problems associated with observations of large flares are also discussed. The various issues will be illustrated with data obtained during the recent period of extraordinary activity on the Sun.

N92-21938

COMPTEL Solar Flare Observations

J.M. Ryan[3], H. Aarts[2], K. Bennett[4], H. Debrunner[5], C. de Vries[2], J.W. den Herder[2], G. Eymann[4], D.J. Forrest[3], R. Diehl[1], W. Hermsen[2], R. Kippen[3], L. Kuiper[2], J. Lockwood[3], M. Loomis[3], G. Lichti[1], J. Macri[3], M. McConnell[3], D. Morris[3], V. Schönfelder[1], G. Simpson[3], M. Snelling[4], H. Steinle[1], A. Strong[1], B.N. Swanenburg[2], W.R. Webber[3], and C. Winkler[4]

[1]Max-Planck Institut für Extraterrestrische Physik, Garching, Germany

[2]Laboratory for Space Research Leiden, PB 9504, 2300 RA Leiden, The Netherlands

[3]Space Science Center,Institute for the Study of Earth, Oceans and Space University of New Hampshire Durham, NH

[4]Space Science Division of ESA, ESTEC, Noordwijk, The Netherlands

[5]University of Bern, Bern, Switzerland

COMPTEL as part of a solar Target of Opportunity campaign observed the sun during the period of high solar activity from 7 June to 15 June 1991. Major flares were observed on June 9 and 11. Although, both flares were large GOES events ($\geq$ X10), they were not extraordinary in terms of γ-ray emission. Only the decay phase of the June 15 flare was observed by COMPTEL. We report the preliminary analysis of data from these flares, including the first spectroscopic measurement of solar flare neutrons. The deuterium formation line at 2.223 MeV was present in both events, and for at least the June 9 event, was comparable to the flux in the nuclear line region of 4 - 8 MeV, consistent with SMM observations. A clear neutron signal was present in the flare of 9 June with the spectrum extending up to 80 MeV and consistent in time with the emission of γ-rays, confirming the utility of COMPTEL in measuring the solar neutron flux at low energies. The neutron flux below 100 MeV appears to be lower than that of the 1982 June 3 flare by more than an order of magnitude. The neutron signal of the 11 June event is under study. Severe dead time effects resulting from the intense thermal X-rays require significant corrections to the measured flux which increase the magnitude of the associated systematic uncertainties.

1. Introduction

As a secondary scientific objective of the COMPTEL γ-ray telescope on the Arthur Holly Compton Gamma Ray Observatory, observing and measuring solar flares assumed an unexpected importance due to the unusually high level of solar activity early in the mission. During the two week period of 1991 June 1 to June 15 region 6659 (Boulder reference number) transited the disk producing an unprecedented number of large flares. After the first week of this activity, the prospect of more flares was such that the sun was declared a Target of Opportunity and on June 7 the observation of the Cygnus region was suspended and the Compton Observatory was reoriented so as to place the sun near the spacecraft z axis. Since the spacecraft z axis coincides with the axis of the COMPTEL field-of-view, this enabled COMPTEL to utilize its full capabilities in measuring the gamma ray and neutron fluxes from the flares which occurred the following week. Major flares were recorded on June 9, 11 and 15 after which the Compton Observatory re-assumed its original objective of the all-sky survey.

2. COMPTEL γ-Ray and Neutron Response

COMPTEL is a two element γ-ray detector in which the Compton scattering process is used to measure the photon's energy and incident direction. Similarly, it can also detect and measure neutrons. However, rather than using Compton scattering, neutron detection relies upon neutron-proton scattering. Both forms of neutral radiation are important in studying high energy solar flare processes. A description of the instrument and its in-flight performance is given by den Herder *et al.* (1991).

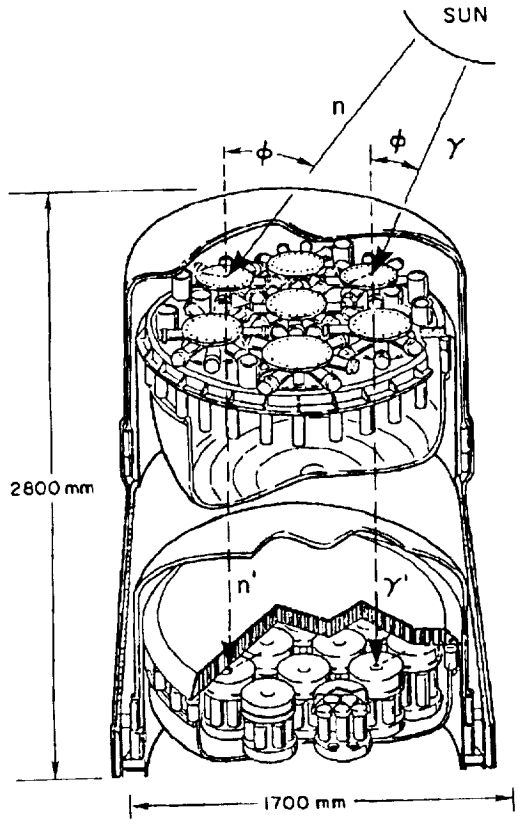

Figure 1. Schematic of COMPTEL showing the interactions of γ-rays and neutrons. The scatter angle ϕ for γ-rays is given by $\phi = \cos^{-1}(1 - \varepsilon/E_2 + \varepsilon/(E_1 + E_2))$; where ε = 511 keV. The non-relativistic hard sphere, neutron-proton scattering formula is $\tan^2 \phi = E_1/E_s$.

The basic scattering process for photons (and neutrons) is illustrated in Fig. 1. The quantities that COMPTEL measures are the location of the scatter in the seven element forward detector D1, the energy E_1 of the scattered electron (proton), the location of the scatter in the fourteen element rearward detector D2 and the energy deposit E_2 in that detector. One computes

from these interaction locations the direction of the scattered photon's (neutron's) velocity vector. For γ-rays, one computes the scatter angle ϕ and the total γ-ray energy $(E_1 + E_2)$, where

$$\phi = \cos^{-1}(1 - \varepsilon/E_2 + \varepsilon/(E_1 + E_2)).$$

Here, ε is the electron rest mass energy and ϕ is the Compton scatter angle provided $E_1 + E_2$ is the full incident γ-ray energy. Without measuring the direction of the scattered electron in D1, only the polar angle and not the azimuth angle of the scatter is known. The time-of-flight (TOF) is also measured and used to help identify γ-ray scatters; whereas for neutron detection, it is used to measure the energy of the scattered neutron.

Much like a γ-ray event, the ideal type of neutron interaction in COMPTEL occurs when the incoming neutron elastically scatters off a hydrogen nucleus in the D1 detector. The scattered neutron then proceeds to the D2 detector where it interacts, depositing some of its energy to produce a trigger signal as indicated in Figure 1. The energy of the incident neutron is computed by summing the proton recoil energy E_1 in the D1 detector with the energy of the scattered neutron E_s deduced from the TOF from the D1 to the D2 detector. The scatter angle for non-relativistic neutrons (< 100 MeV) can be computed by the formula:

$$tan^2 \phi = E_1/E_s .$$

Relativistic corrections become important above 100 MeV, in which case the expression becomes

$$tan^2\phi = \frac{E_1/E_s}{1 + E_n/2m_n},$$

where $E_n = E_1 + E_s$ is the incident neutron kinetic energy.

The material in D1 is a liquid organic scintillator, NE213A, with the properties of low density and low Z (H/C ratio = 1.286). The material elastically scatters both γ-rays and neutrons off atomic electrons and hydrogen nuclei, respectively. The detector thickness has been chosen such that it is a fraction of a mean free path thick, meaning that the incident γ-ray (or neutron) can scatter in D1 and usually leave D1 without scattering again.

The liquid organic scintillator in D1 (NE213A) possesses pulse shape discrimination properties, in that energetic protons produce light pulses with longer rise times than those of electrons (and other minimum ionizing particles). This capability allows for efficient identification of recoil proton signals produced by fast neutrons elastically scattering off hydrogen in D1. Any reaction producing a recoil proton can be identified by these means, such as inelastic scattering of fast neutrons off carbon producing a γ-ray and either a knock-on proton or neutron (which can then elastically scatter off hydrogen). Pure γ-ray producing neutron-carbon reactions in D1 also occur and represent an intrinsic background in both γ-ray and neutron measurements.

Since only the scatter angle ϕ is measured, the incident particle direction is constrained to a cone mantle of half angle ϕ. For γ-rays, errors in the measured energy and placement of the cone mantle occur via uncertainties in the measured energies in D1 and D2 and uncertainties in the measured interaction positions. Partial energy absorption in D2 (from an escaping γ-ray) yields a low value for the total γ-ray energy and a large value for the scatter angle ϕ. Similar errors are inherent in the neutron measurement as well, except that the TOF resolution is the primary component in the scattered neutron energy uncertainty. The neutron energy resolution (σ) of about 6% results in an uncertainty in the production time of the neutron at the sun of ~ 1 minute for a 40 MeV neutron.

Since a full γ-ray energy deposit in D2 is necessary to obtain a correct measure of the scatter angle ϕ, we have a means for selecting only photopeak events in the data. For a solar flare γ-ray interacting in COMPTEL, the inferred scatter angle ϕ about the vector of the scattered γ-ray should be such that the photon is assigned a solar origin as indicated schematically in Figure 1. Hence, we know that the photon deposited its full energy in the detector. The response of the telescope to such events is simple. The energy or pulse height distribution is basically Gaussian in shape with a heavily suppressed Compton tail at low energies. Since the solar γ-ray spectra are rich in lines from C, N, O, Ne, Mg etc., a simple instrumental response function will facilitate correct de-convolution of the pulse height spectra. The response of a telescope prototype to monoenergetic 1.375 and 2.75 MeV photons from a ^{24}Na source is shown in Figure 2.

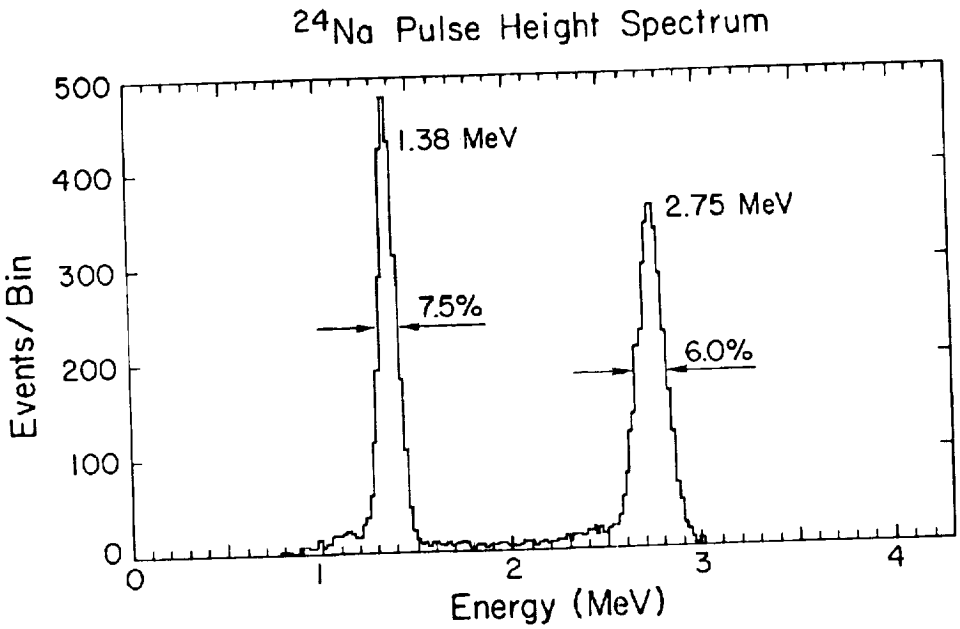

Figure 2.
The energy spectrum from a monoenergetic γ-ray source produced under the constraint that the γ-ray scatter angle ϕ be consistent with the source direction.

Similarly, in detecting and measuring neutrons from the sun the neutrons can be traced backwards from D2 to D1 through the angle ϕ onto a cone mantle restricting the incident direction so as to include the sun. This geometrical constraint is identical to that of the γ-ray measurements. For neutrons, energy is more often lost in D1 through inelastic scatters with carbon with consequent indeterminate scattering kinematics. Such reactions are suppressed by requiring a scatter angle ϕ which is consistent with the solar direction.

4. γ-ray Flare Overview

γ-ray emission was detected from at least three flares observed by COMPTEL in the June 1991 solar Target of Opportunity observation. Shown in Figure 3 is the time-intensity profile above 1 MeV and the count spectrum of the June 9 solar flare. This event, as well as the flare on June 11, lasted on the order of 10 minutes above 1 MeV and both show evidence of nuclear line emission, particularly at the deuterium formation line of 2.223 MeV. Images of the sun were produced with these data and were of sufficient angular resolution to show the

apparent motion of the sun over the course of two days. Figure 4 is the COMPTEL image of the sun on June 9 during the impulsive phase of the flare. The angular resolution of COMPTEL is on the order of one degree while the diameter of the sun is one half that, so the images do not reveal any information on the location of the γ-ray emission on the solar disk. The flare on June 15 was not observable until about 0900 UT, approximately 40 minutes after the X-ray maximum. Before this the spacecraft was in orbit night or in the South Atlantic Anomaly. However, an image of the sun could still be constructed, supporting the conclusion of Akimov *et al.* (1991) of prolonged (> 1 hour) γ-ray emission from this flare.

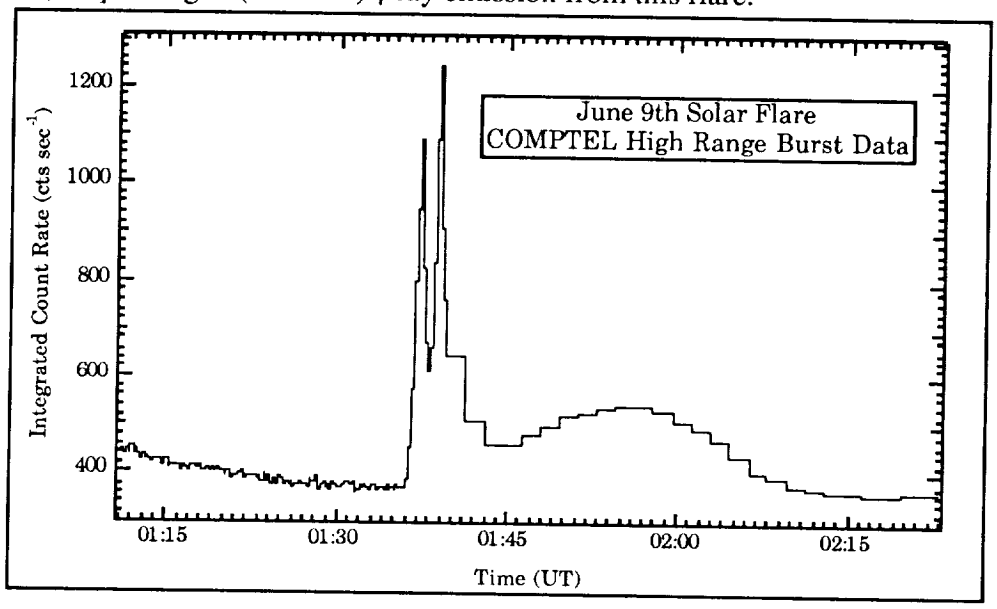

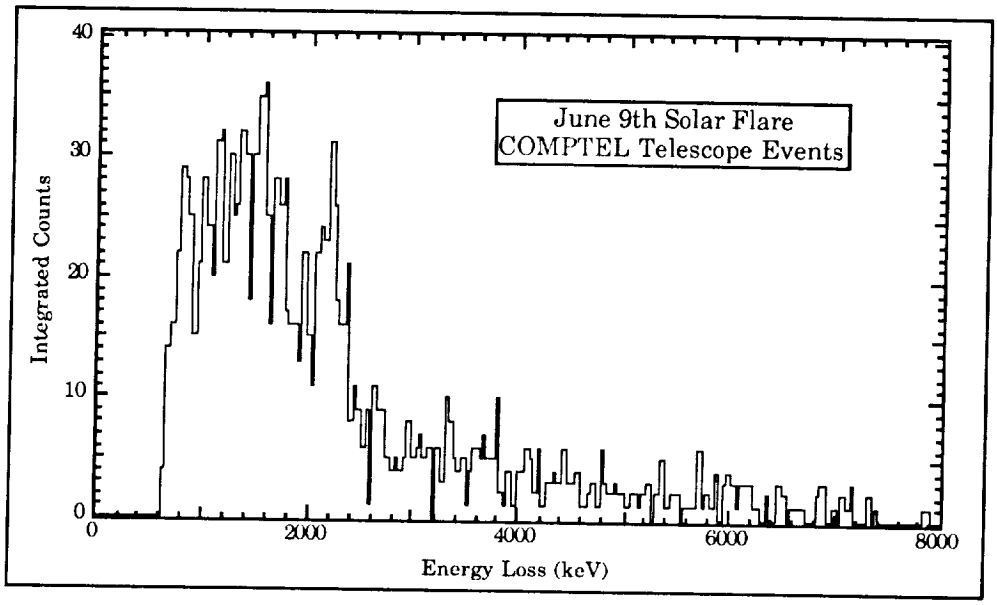

Figure 3. The intensity-time profile > 1 MeV and the time-integrated count spectrum from the solar flare of 1991 June 9.

The intense solar flare on June 4 was also measured by COMPTEL, although the sun was not in the field-of-view. The COMPTEL burst detector system measured the γ-ray spectrum above 1 MeV. The burst detector was occulted by other components of the spacecraft, so that the de-convolution of the count rate spectrum will be more complex than for the flares in the field-of-view. This flare emitted a flux of neutrons which was detectable at ground level at Mt. Norikura in Japan (Muraki *et al.* 1991).

5. Analysis of the 1991 June 9 Solar Flare

Only the June 9 flare which occurred during the Target of Opportunity period has been analyzed in any detail. The analysis includes both γ-rays and neutrons.

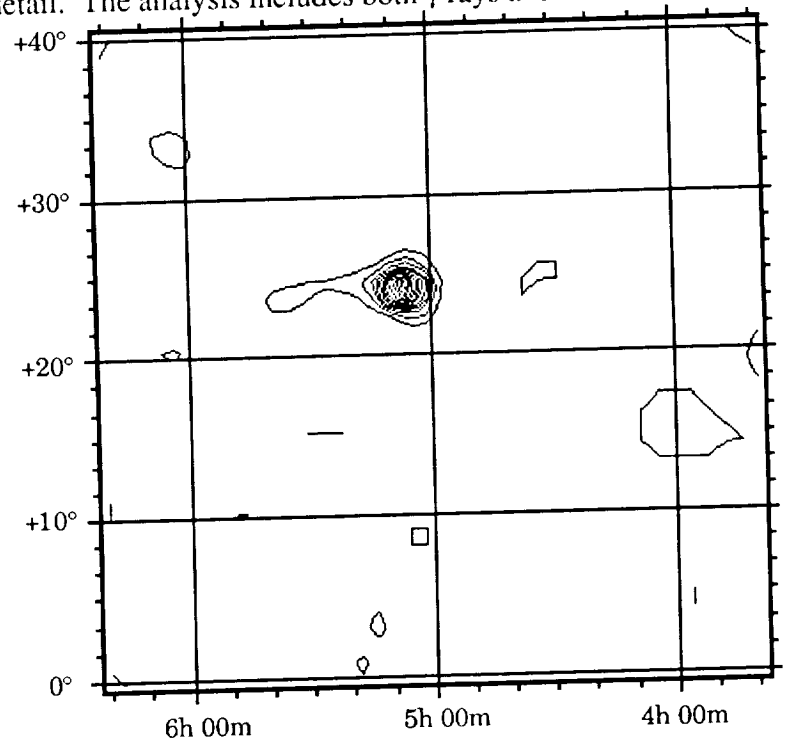

Figure 4. The COMPTEL image of the sun taken during the impulsive phase of the flare. The coordinates are declination as Right Ascension. The image is consistent with a point source response. The correct solar position is α = 5h 07m and δ = 22.9°.

5a. γ-Ray Analysis

The June 9 flare (3B, X10.0) occurred in active region 6659 at N34E04 with the X-ray start at 0134 UT and maximum at 0143 UT. From the COMPTEL data we define the impulsive phase to be from 0136 UT to 0146 UT. The γ-ray intensity-time profile is shown in Figure 3. These data were obtained from the COMPTEL high range burst detector which has a threshold of ~ 1 MeV. The broad maximum near 0158 UT is due only to the increased background count rate from the spacecraft excursion to higher latitudes in the course of its orbit. The telemetry of COMPTEL is basically divided into two separate channels, denoted γ1 and γ2 with γ1 being devoted to γ-rays of the highest quality (most amenable to analysis). The γ2 channel which is normally used for background studies is tailored to accept solar neutrons during flares. During

the impulsive phase the γ-ray count rate was high, filling up the γ1 telemetry channel and precluding the transmission of any γ2 events. During this same time interval the activity in the forward veto detector V1 was high as well. This was due to the intense thermal X-ray flux at a few keV piling up in V1, continuously triggering that detector and producing a large and variable dead time effect in COMPTEL. The thermal X-ray flux remained high, well beyond the impulsive phase. This required additional analysis to estimate the dead time for both the impulsive phase and the period of time afterward during which we expect the arrival of solar neutrons. The dead time correction was estimated by the throughput of LED calibration events in D1 during the impulsive phase and the period afterward. During the impulsive phase the average live time fraction was (28 ± 1)%, while from 0146 to 0205 UT the effect was (78 ± 4)%.

In the analysis of the γ-ray data it is important to estimate both the integrated flux of the 2.223 MeV emission from deuterium formation and the integrated flux in the nuclear line region of 4 - 8 MeV. The emission of the 2.2 MeV line depends upon the number of free, low energy neutrons within the photosphere, while emission in the broad nuclear line region depends upon the energy spectrum of protons above 30 MeV as they interact with the solar atmosphere. Since the production cross sections of neutrons and nuclear lines have very different energy dependences, the comparison of the γ-ray emission at 2.2 MeV and in the range of 4 - 8 MeV is a useful indicator of the parent proton spectral shape (Murphy and Ramaty 1984).

The broad band efficiency from 4 - 8 MeV was estimated by a Monte Carlo simulation calculation under the same restrictions as imposed on the real data. The instrument efficiency in the line at 2.2 MeV was obtained through interpolation of calibration simulations, again with restrictions similar to those applied to the real data. Using both the live time estimates and the estimates of the telescope efficiencies, we calculate from the time-integrated count rate spectrum (Fig. 3) the time-integrated fluxes to be 32 and 35 $\gamma\text{-cm}^{-2}$ for the the γ-ray emission in the range of 4 - 8 MeV and in the 2.223 MeV line, respectively. The uncertainties for these quantities are estimated to be 50 and 30%, respectively. The uncertainties are largely determined by the systematic errors in the estimated efficiencies rather than by dead time corrections or statistics. No other spectral analysis has been performed, although there is evidence for other identifiable lines in the spectrum.

5b. Neutron Analysis

Additional processing must take place in the neutron data analysis. All the quantities normally measured and telemetered are in terms of γ-ray interactions. Quantities appropriate to neutrons must be computed. These include (1) converting the electron-equivalent energy measured in D1, the upper liquid organic scintillator, into the proton-equivalent energy, (2) calculating the energy of the scattered neutron (from D1 to D2) from the time-of-flight, (3) computing the scatter angle ϕ from the n-p scattering kinematics, (4) discarding events which have electron-recoil pulse shape signatures in D1 and (5) discarding events which fall within the γ-ray time-of-flight window. The neutron differential flux can then be calculated based upon the data satisfying these criteria along with the live time and the neutron detection efficiency.

Presently, the best figures for the COMPTEL neutron detection efficiency are the extrapolations of the COMPTEL prototype neutron measurements to the full COMPTEL configuration. The calibrations were performed at only a few energies and incident angles (Ryan *et al.* 1987). The efficiencies needed for the flux calculations were interpolated between calibration points. The differential flux was calculated taking into account the limited number of operating detectors and the live time during the neutron measurements.

In principle the data restrictions listed above coupled with data restrictions that are usually used for γ-ray spectral studies should be all that is required to derive a solar neutron spectrum and intensity-time profile. The main selection criterion needed for spectral studies is that the scatter angle ϕ of an event be consistent with the position of the sun. This means that

the event circle whose center is defined by the velocity vector of the scattered neutron and whose diameter is defined by the scatter angle, comes within, in this case, 10° of the sun. This requirement implies that the measured energy is correct since in Compton telescopes the imaging and spectral analysis properties are intertwined. The amount of background which needs to be identified and adjusted for was unknown prior to the launch of the GRO.

We found that the usual data restrictions were inadequate to reject all background neutrons. One can propagate the potential solar neutrons backward, taking out neutron velocity dispersion effects, to calculate the production time at the sun in order to compare with the same quantity for γ-rays. By doing this, we found that many neutron events originated before the solar γ-rays and that neutron production extended beyond the end of the impulsive phase (once the time-of-flight of the γ-rays over 1 AU is taken into account). We found that we could eliminate these background neutrons by tightening the geometrical constraints on the data. Background neutrons can come directly from the earth's atmosphere, from the spacecraft or from the instrument itself via neutron initiated cascades in the upper D1 detector. Specifically, we require that a neutron event must have a measured ϕ less than 15° and also that the scattered neutron velocity vector be no closer to the earth's limb than 35°. These two restrictions reduce the effective field-of-view of the telescope and severely restrict the neutron events which could be attributable to the earth albedo. These selection criteria greatly reduce the number of analyzable neutron events. For the June 9 flare after making this data cut there were no longer any neutrons which originated before impulsive phase. A few events, though, had production times after the impulsive phase. These we take as background neutrons rather than as solar. Twenty one neutron events were contained in the impulsive phase time interval.

A complication occurs because the tighter selection criteria are not the same as those used to analyze the neutron calibration data on which we base the efficiencies. The calibration data were only constrained by the hardware; no additional geometrical constraints were imposed on the data. These additional constraints affect the net efficiency of the telescope. Consequently, the telescope efficiencies (Ryan *et al.* 1991) had to be adjusted to account for the reduced ϕ range.

The distribution of ϕ as measured by COMPTEL is limited at the low end by the energy threshold in the D1 detector, and limited at the high end by E_S, the energy of the scattered particle. In this case, the low-energy E_S threshold is determined simultaneously by the limit of the time-of-flight range and the neutron reaction threshold in NaI, both being approximately 10 MeV. The constraint of a maximum ϕ of 15° translates into a reduction in the solid angle of the scattering process in D1. We have corrected the efficiencies, therefore, with a simple solid angle factor. The correction is greatest for low neutron energies because the lower instrumental ϕ threshold is higher due to the scattering kinematics. The solid angle corrections corresponding to reducing ϕ from 35° to 15°, are 0.042, 0.11 and 0.15 for the calibration energies of 18.5, 35.7 and 77 MeV, respectively. The uncertainties in these numbers are considerable and could be as high as a factor of two. Better figures for these corrections, in addition to the total efficiencies, await Monte Carlo telescope simulations.

After correcting the efficiencies, the differential flux was calculated and then corrected for the loss of neutrons through β^- decay over the 1 AU flight path. The resulting differential flux was then integrated over energy yielding a time-integrated neutron flux of 2×10^{28} n-sr^{-1} over the energy range of 15 to 80 MeV. By far, the largest uncertainty in the integrated flux arises from the extrapolation of prototype COMPTEL efficiencies to those of the flight telescope and the subsequent analytical corrections to those efficiencies. Therefore, the flux value stated above is only good to about a factor of three. Some small number of background neutron events are present at times later than the impulsive phase, but this effect is small compared to the uncertainties in the net detection efficiencies. The integrated flux figure of 2×10^{28} n-sr^{-1} is more than an order of magnitude below the spectrum published by Evenson, Meyer, and Pyle (1983) for the 1982 June 3 solar flare. That spectrum from 20 to 100 MeV was constructed

from the measurement of neutron-decay protons in interplanetary space. Based upon the difference between our value and the spectrum of Evenson *et al.*, we can conclude that there should be no measurable signal in any ground level neutron monitor as there was for the 1982 June 3 flare, which was measurable at the few σ level.

6. Conclusions

(1) The sun was imaged in γ-rays for the first time.

(2) The first direct energy measurement of solar neutrons was performed.

(3) The γ-ray fluence in the nuclear line range of 4-8 MeV was approximately 30 γ-cm^{-2}. Within errors this equals the fluence in the 2.2 MeV line, making it consistent with many flares measured by SMM (Forrest, priv. comm.).

(4) The integrated neutron spectrum from 15 to 80 MeV is on the order of 2×10^{28} n-sr^{-1} at the sun.

(5) The neutron emission was consistent in time with the γ-ray emission, i.e. from 0136 - 0150 UT. There is strong evidence against precursor neutron emission. Prolonged emission after the impulsive phase appears to be consistent with background.

(6) The neutron background measured by COMPTEL was surprising large and required severe data cuts to eliminate, reducing the effective area accordingly. Consequently, we have revised our estimate of the neutron sensitivity to ~ 6 n-cm^{-2} for a 20 minute observation, or equivalently, 5×10^{-3} n-cm^{-2}-s^{-1} in the range of 15 to 80 MeV.

7. References

den Herder, J.W., H. Aarts, K. Bennett, H. de Boer, M. Busetta, W. Collmar, A. Connors, R. Diehl, W. Hermsen, J. Ryan, M. Kippen, L. Kuiper, G. Lichti, J. Lockwood, J. Macri, M. McConnell, D. Morris, R. Much, V. Schoenfelder, G. Stacy, H. Steinle, A. Strong, B. Swanenburg, B.G. Taylor, M. Varendorff, C. de Vries, and C. Winkler 1991, these proceedings.

Evenson, P., P. Meyer, and K.R. Pyle 1983, *Ap. J.*, **274** : 875.

Muraki, Y., K. Murakami, M. Miyazaki, K. Mitsui, S. Shibata, S. Sakakibara, T. Sakai, T. Takahashi, T. Yamada, and K. Yamaguchi 1991, submitted to *Ap. J. (Letters)*,

Murphy, R.J., and R. Ramaty 1984, *Adv. Space Res.*, **4** : 127.

Ryan, J.M., H. Aarts, K. Bennett, R. Byrd, C. de Vries, J.W. den Herder, A. Deerenberg, R. Diehl, G. Eymann, D.J. Forrest, C. Foster, W. Hermsen, J. Lockwood, G. Lichti, J. Macri, M. McConnell, D. Morris, V. Schönfelder, G. Simpson, M. Snelling, H. Steinle, A. Strong, B.N. Swanenburg, T. Taddeucci, W.R. Webber, and C. Winkler 1991, *Proc. Workshop on Gamma Ray Astron.*, Erice, Italy.

Ryan, J.M., V. Schönfelder, R. Diehl, G.G. Lichti, H. Steinle, B. Swanenburg, H. Aarts, A. Deerenberg, W. Hermsen, G. Kiers, J. Lockwood, J. Macri, D. Morris, G. Simpson, K. Bennett, G. Eymann, M. Snelling, C. Winkler, R. Byrd, C. Foster, and T. Taddeucci 1987, *Proc. 20th Intl. Cosmic Ray Conf. (Moscow)*, **4** : 425.

NEUTRON AND GAMMA RAY PRODUCTION IN THE 1991 JUNE X-CLASS FLARES

R. Ramaty
Laboratory for High Energy Astrophysics, GSFC, Greenbelt, MD 20771

X. M. Hua
ISTS, Concord, Ontario L4K 3C8 Canada

B. Kozlovsky
Department of Physics and Astronomy, Tel Aviv University, Israel

R. E. Lingenfelter
Center for Astrophysics and Space Science, UCSD, LaJolla, CA 92093

N. Mandzhavidze
Institute of Geophysics, Tbilisi 93, Georgia, USSR

ABSTRACT

We present new calculations of pion radiation and neutron emission from solar flares. We fit the recently reported high energy GAMMA-1 observations with pion radiation produced in a solar flare magnetic loop. We calculate the expected neutron emission in such a loop model and make predictions of the neutron fluences expected from the 1991 June X-class flares.

Neutrons and gamma rays are produced in solar flares by accelerated particles interacting with the ambient solar atmosphere (e.g. Ramaty & Murphy 1987, Hua & Lingenfelter 1987a). Gamma ray continuum, gamma ray lines, and neutrons ranging in energy from tens of MeV to several GeV have been observed (e.g. Chupp et al. 1987; Rieger 1989). A series of X-class flares, accompanied by a variety of gamma ray and neutron signatures, occurred during the first two weeks of June 1991. The gamma ray spectrum observed from one of these flares (June 15) extended to energies in excess of 1 GeV (Akhimov et al. 1991). The comparison of these observations with calculations of solar flare gamma ray emission resulting from pion decay (Mandzhavidze & Ramaty 1992) allows us to derive the number of protons accelerated to energies greater than several hundred MeV and the proton energy spectrum in this energy range. We use this information, as well as information from flares observed previously, to provide estimates of the neutron and 4 - 7 MeV nuclear gamma ray fluences expected from the June 1991 flares. Our neutron study is based on new calculations of anisotropic neutron production and transport in the solar atmosphere.

We perform our calculations in a solar flare magnetic loop model in which the bulk of the nuclear reactions occur in the sub-coronal portions of the loop where the magnetic field decreases with height from the photosphere to the corona (Zweibel & Haber 1983; Hua, Ramaty & Lingenfelter 1989; Gueglenko et al. 1990). We take into account the mirror force in the sub-coronal portions and pitch angle scattering due to plasma turbulence in the coronal portion. We calculate the neutron and gamma ray production by taking into account all the relevant production cross sections as well as the loss mechanisms affecting

the primary particles. We also evaluate the attenuation of the emergent radiations due to the interactions of the neutrons and gamma rays with the ambient atmosphere.

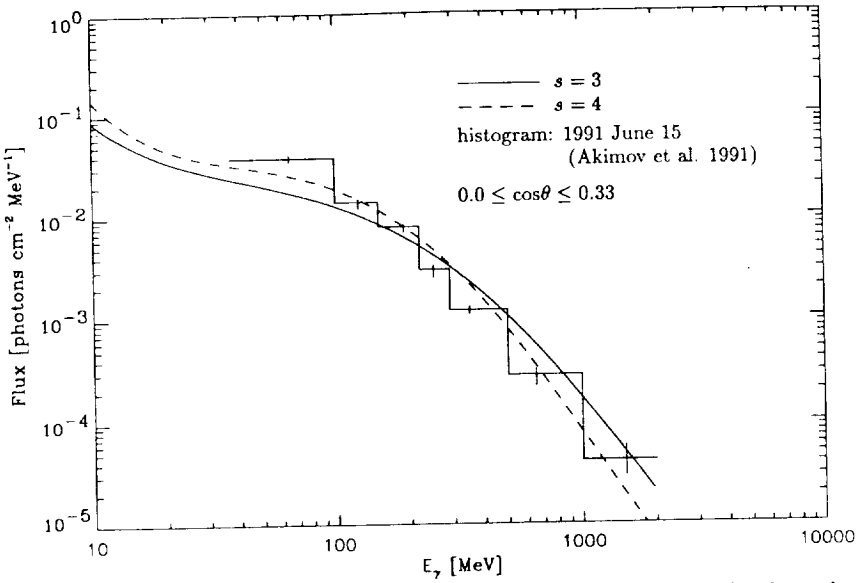

Fig. 1. Observed solar flare gamma ray spectrum fitted with time integrated, directional pion radiation averaged over the indicated range of heliocentric angles. The density in the sub-coronal portions of the loop is assumed to have a constant scale height of 200 km, the coronal portion of the loop has a radius of 10^9 cm, and pitch angle scattering in the corona is ignored. The primary particles have power law spectra with indexes s normalized to $N_p(> 30\text{MeV}) = 1.4 \times 10^{31}$ for $s = 3$ and $N_p(> 30\text{MeV}) = 4.5 \times 10^{32}$ for $s = 4$.

We first consider the high energy gamma ray emission resulting from pion decay. The neutral pions decay into gamma rays directly, while the charged pions decay (via muons) into positrons and electrons which produce gamma rays by bremsstrahlung and annihilation in flight (Murphy, Dermer & Ramaty 1987). Calculations of pion radiation in a magnetic loop model have recently been carried out by Mandzhavidze & Ramaty (1992). In Figure 1 we show their results, extended to 2 GeV and fitted to the high energy gamma ray spectrum observed (Akimov et al. 1991) from the 1991 June 15 flare (location: N33, W69; heliocentric angle cosine $\cos\theta = 0.30$). The calculated spectra, representing angle integrated averages over $0 < \cos\theta < 1/3$, are for power law proton and α particle spectra with spectral index s and no pitch angle scattering in the corona. The normalization to the data requires that the total number of protons above 300 MeV (the effective pion production threshold) be 1.4×10^{29} and 4.5×10^{29} for $s = 3$ and $s = 4$ respectively. As can be seen from Figure 1, the spectrum for $s = 4$ provides a somewhat better fit to the data than that for $s = 3$, although neither the $s = 4$ nor the $s = 3$ curves can account for the observed emission below 100 MeV. It is possible that some of this emission is bremsstrahlung from primary electrons. It is also possible that the spectrum of the interacting protons varies during the course of the flare, as was the case for the 1982 June 3 flare (see Mandzhavidze & Ramaty 1992).

To calculate the neutron and nuclear deexcitation line fluences it is necessary to extrapolate the proton and α particle spectra to lower energies. The above normalizations

for the 1991 June 15 flare yield $N_p(> 30\text{MeV}) = 1.4 \times 10^{31}$ for $s = 3$ and $N_p(> 30\text{MeV}) = 4.5 \times 10^{32}$ for $s = 4$. These values of $N_p(> 30\text{MeV})$ are very similar to those derived (Murphy & Ramaty 1984; Hua & Lingenfelter 1987a) from 4 - 7 MeV deexcitation line and neutron observations of a dozen previous flares seen with SMM and other experiments.

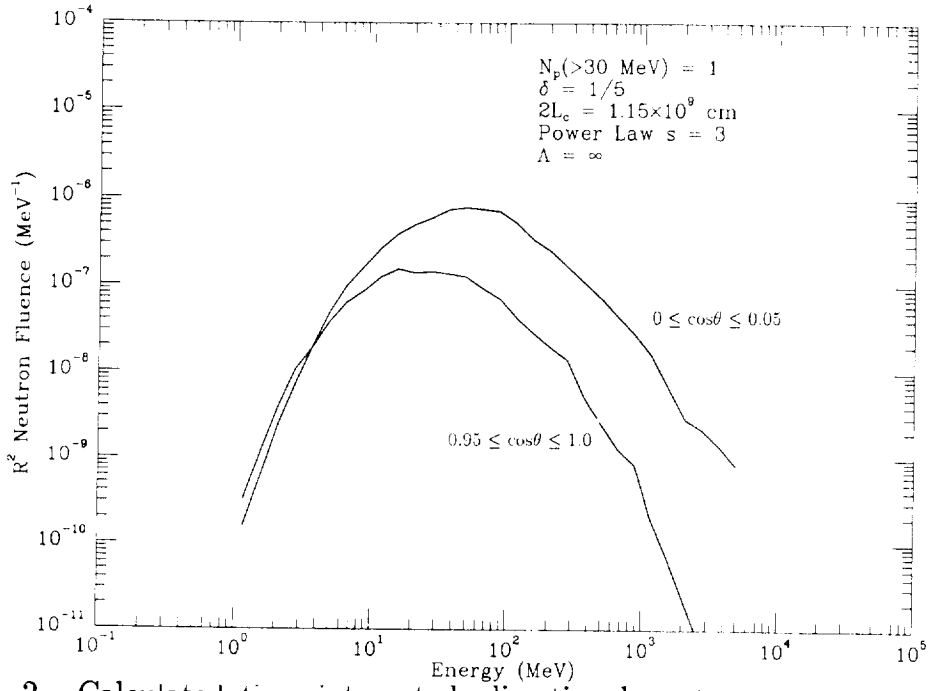

Fig. 2. Calculated time integrated, directional neutron spectra at Earth. The primary particles have power law spectra with indexes s; θ is the heliocentric angle at the flare site, δ is the convergence parameter of the sub-coronal magnetic field, $2L_c$ is the loop length, and Λ is the pitch angle scattering diffusion mean free path (see Hua et al. 1989 for details).

We turn now to the neutron calculations. Using the loop model described in detail by Hua et al. (1989) and updating the nuclear data given in Murphy et al. (1987) and Hua & Lingenfelter (1987a), we have carried out new calculations of neutron production. Then using the neutron transport code developed by Hua & Lingenfelter (1987b), we have calculated the time dependence, angular distribution and energy spectrum of the neutrons escaping from the Sun. In Figures 2, 3, 4 and 5 we show time integrated directional neutron energy spectra at Earth for power law proton and α particle spectra at the Sun ($s = 3$ and $s = 4$) normalized to $N_p(> 30\text{MeV}) = 1$. The parameter δ defines the convergence of the magnetic flux tube and $2L_c$ is the total length of the loop. For $\delta = 1/5$ the magnetic field increases by a factor of 10 from the corona to the photosphere. In Figures 2 and 4 there is no pitch angle scattering ($\Lambda = \infty$), whereas in Figures 3 and 5 the pitch angle scattering rate is close to saturation ($\Lambda = 4.6 \times 10^{10}$ cm). In this case the particles are isotropized in the corona on a time scale comparable to their transit time along the loop. The quantity Λ is the pitch angle scattering mean free path, which can be related to the energy density in the turbulent plasma waves (see Miller & Ramaty 1989). The net effect of saturated pitch angle scattering is to cause the particles to interact in the loss cone rather than near their mirror points. This moves the interaction region deeper into the atmosphere and causes the angular distribution of the interacting particles

to be more downward peaked than in the case of no pitch angle scattering when their distribution peaks at directions tangential to the photosphere (for a mean loop magnetic field which is radial in the photosphere). The two curves in each figure correspond to averages over the indicated ranges of heliocentric angle cosines.

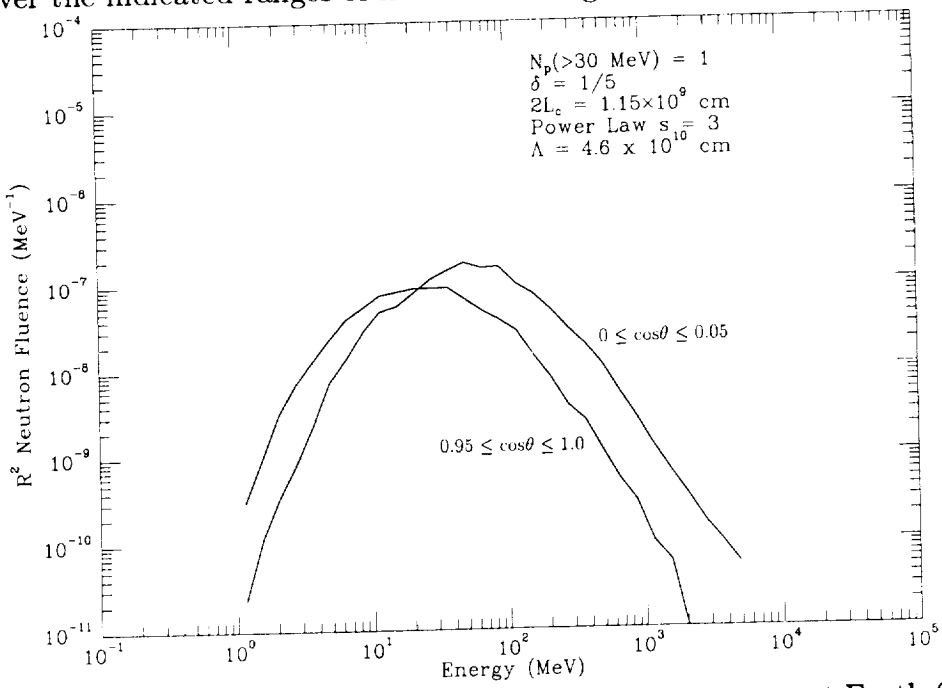

Fig. 3. Calculated time integrated, directional neutron spectra at Earth (see caption to Fig. 2)

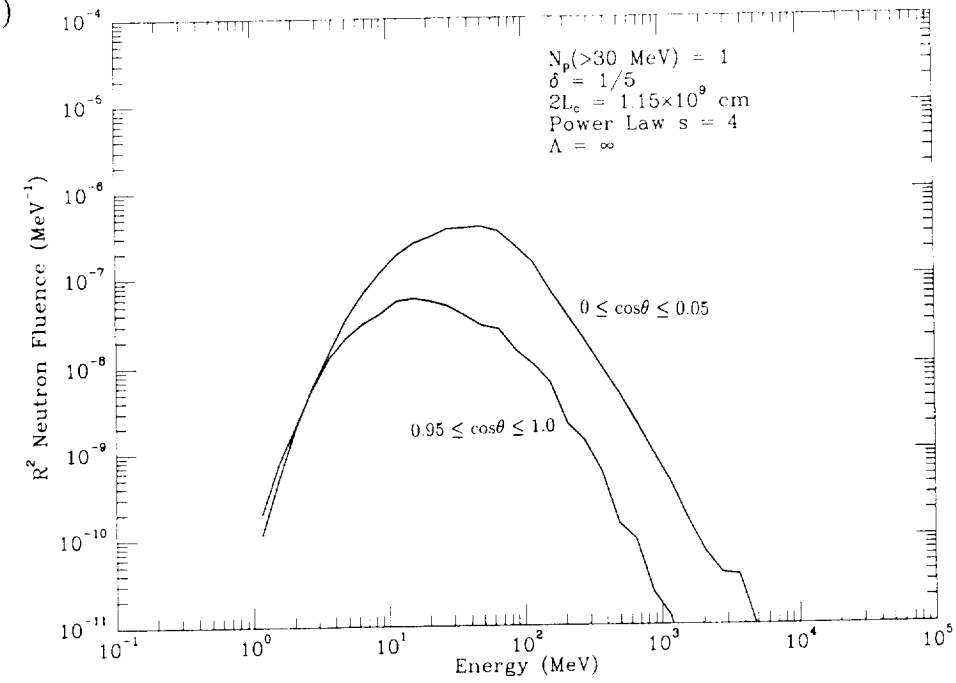

Fig. 4. Calculated time integrated, directional neutron spectra at Earth (see caption to Fig. 2).

We see that the differential neutron spectra at Earth reach their maxima in the energy range from about 10 to 100 MeV, owing to the combined effects of the decreasing neutron production spectra and increasing neutron survival probability with increasing energy. Neutron emission from solar flares is quite anisotropic, the anisotropy being most pronounced at high energies and when there is no pitch angle scattering. In general, the neutron emission from limb flares is larger than from flares at disk center, except at low energies where the neutron fluence from limb flares is attenuated during transit in the solar atmosphere. By causing the neutrons to be produced deeper in the atmosphere, pitch angle scattering increases the attenuation and hence decreases the anisotropy. In fact, as can be seen from Figures 3 and 5, the neutron emission is significantly limb darkened at low energies ($\lesssim$ 10 MeV).

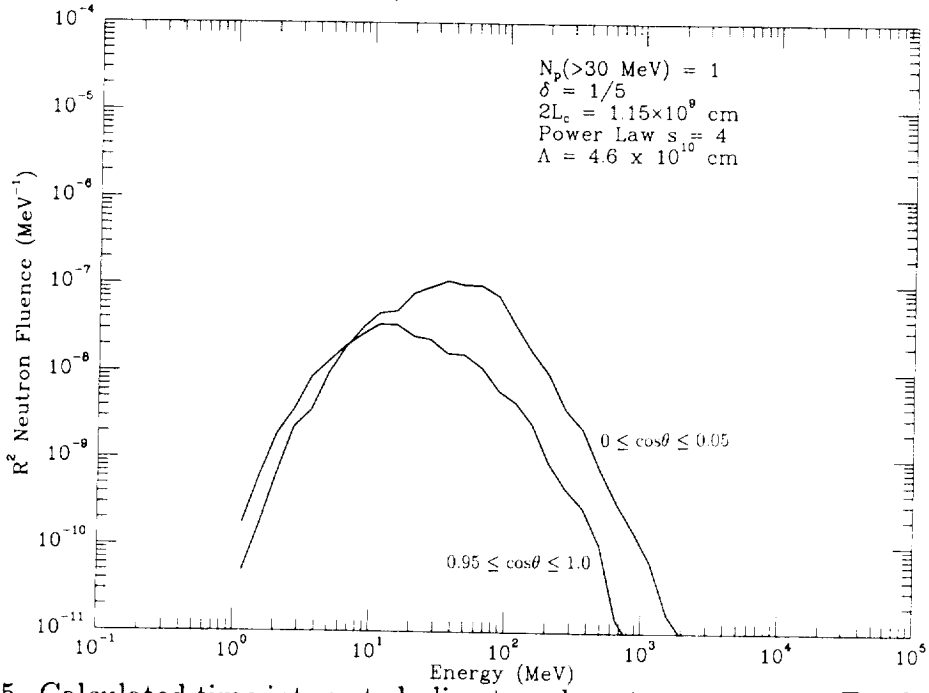

Fig. 5. Calculated time integrated, directional neutron spectra at Earth (see caption to Fig. 2).

To better assess the expected neutron fluxes from large (class X) flares, we show in Table 1 energy integrated neutron fluences in two energy bands for a fixed normalization ($N_p(> 30\text{MeV}) = 5 \times 10^{32}$), for limb and disk-center flares, and for the cases of no pitch angle scattering and saturated scattering. Also shown in Table 1 are nuclear deexcitation line fluences derived from the calculations of Murphy & Ramaty (1984). This line emission is essentially isotropic and unattenuated, even in the case of saturated pitch angle scattering (Hua et al. 1989). We see that the neutron fluences above 100 MeV are very strongly limb brightened, especially when there is no pitch angle scattering. With pitch angle scattering the limb brightening is less pronounced, although it is still quite strong above 100 MeV. There is also limb brightening below 100 MeV (we expect limb darkening only below about 10 MeV), although with saturated pitch angle scattering and the flatter primary particle spectrum ($s = 3$), the limb brightening amounts to only a factor of 2.

Given that the normalization assumed in Table 1 is typical of the X-class flares of June 1991, the neutron fluences shown in this Table should be representative of the

expected neutron fluxes. The detailed modeling of these flares, however, must await the release of all the available data, including deexcitation line emission, 2.223 and 0.511 MeV line emission, neutrons, and gamma ray emission from pion decay and primary electron bremsstrahlung.

Acknowledgements. We thank NASA for support under grant NAG 5-1324 (REL) and the Province of Ontario for support at ISTS (XMH).

TABLE 1

Nuclear deexcitation and neutron fluences at Earth for the case of no pitch angle scattering in the coronal portion of the loop (no pas) and saturated pitch angle scattering (pas). The normalization is $N_p(>30\text{MeV}) = 5 \times 10^{32}$.

	s = 3		s = 4	
Φ_{4-7} (ph/cm^2)	62		132	
	$\Phi_n(<100$ MeV) (n/cm^2)			
	no pas	pas	no pas	pas
Limb	138	28	63	18
Disk	22	13	6.7	3.3
	$\Phi_n(>100$ MeV) (n/cm^2)			
	no pas	pas	no pas	pas
Limb	250	41	33	7.1
Disk	14	6.5	2.2	0.9

REFERENCES

Akimov, V. V. et al. 1991, *22nd Internat. Cosmic Ray Conf. Papers*, in press.
Chupp, E. L. et al. 1987, ApJ, 318, 913.
Gueglenko, V. G., Kocharov, G. E., Kovaltsov, G. A., Kocharov, L. G., & Mandzhavidze, N. Z. 1990, Solar Phys., 125, 91.
Hua, X. M. & Lingenfelter, R. E. 1987a, Solar Phys., 107, 351.
Hua, X. M. & Lingenfelter, R. E. 1987b, ApJ, 323, 779.
Hua, X. M., Ramaty, R., & Lingenfelter, R. E. 1989, ApJ, 341, 516.
Mandzhavidze, N. & Ramaty, R. 1992, ApJ, in press.
Miller, J. A., & Ramaty, R. 1989, ApJ, 344, 973.
Murphy, R. J., & Ramaty, R. 1984, Adv. Space. Res., 4, No. 7, 127.
Murphy, R. J., Dermer, C. D., & Ramaty, R., 1987, ApJ Suppl., 63, 721.
Ramaty, R., & Murphy, R. J. 1987, Space Sci. Revs., 45, 213.
Rieger, E., 1989, Solar Phys., 121, 323.
Zweibel, E.G., & Haber, D. 1983, ApJ, 264, 648.

Stereoscopic Observations of Hard X-Ray Sources in Solar Flares Made with GRO and Other Spacecraft

S. R. Kane, K. Hurley and J. M. McTiernan
Space Sciences Laboratory, University of California, Berkeley

J. G. Laros
Los Alamos National Laboratory

ABSTRACT

Since the launch of the Gamma Ray Observatory (GRO) in April 1991, the BATSE instrument on GRO has recorded a large number of solar flares. Some of these flares have also been observed by the Gamma-Ray Burst Detector on the Pioneer Venus Orbiter (PVO) and/or by the Solar X-Ray/Cosmic Gamma-Ray Burst Experiment on the Ulysses spacecraft. A preliminary list of common flares observed during the period May-June 1991 is presented and the possible joint studies are indicated.

1. MOTIVATION

Energetic solar flares accelerate electrons and ions over a wide range of energies. The electrons carry a large part of the energy released during the impulsive phase of a flare. They also play an important role in the transport of energy from the acceleration region to various parts of the flare. Determination of the spectral and spatial distribution of the energetic electrons at the sun is, therfore, a very important part of the current solar flare research.

As the energetic electrons accelerated in a flare interact with the ambient ions, they produce hard X-rays through bremsstrahlung. Hence the characteristics of the energetic electron distribution can be deduced from suitable observations of the hard X-ray emission. If the electrons propagate in a relatively well collimated beam, as assumed in some models of the hard X-ray source (cf. discussion in McTiernan and Petrosian, 1990a,b), the X-ray emission is expected to be anisotropic, the degree of anisotropy increasing with photon energy. The anisotropy may also vary with time during a flare and from one flare to another. It is therefore important that the observations of the hard X-ray spectrum with instruments aboard a single spacecraft which provides one view angle with respect to the flare be supplemented, whenever possible, with similar instruments aboard another spacecraft which provides a different view angle. In case of flares where the view from one of the spacecraft is partially occulted by the photosphere, important information about the height structure of the hard X-ray source can be obtained. Such stereoscopic observations of hard X-ray sources in solar flare were suggested earlier (cf Kane, 1980; Hurley, 1986) and have been used in the past to study the directivity and height structure of hard X-ray sources in solar flares (cf Kane et al, 1982, 1988). Multi spacecraft observations have also been used for confirming rapid intensity variations during a flare (Hurley et al, 1983). The past stereoscopic observations of flares had a limited range of

view angles and only a few partially occulted flares were observed. Therefore, analysis of new stereoscopic observations is essential. It is expected to provide important information for verifying theoretical models of solar flares.

TABLE 1
PRELIMINARY LIST OF COMMON SOLAR FLARES
(Flares observed by BATSE and Ulysses and/or PVO)

Date	Hard X-Ray	Soft X-Ray		Hα-Flare	
(1991)	Max (UT)	Class (GOES)	Imp.	Region	Location
30 May	0938	M 8.2	1F	6654	N07 E30
1 June*	1503	X 12		6659	N25 E>90
4 June	0339	X 12	3B	6659	N30 E70
6 June	0107	X 12	4B	6659	N33 E44
26 June**	2014	C 2.9			
28 June**	1430				
30 June***	0257	M 5.0	1N	6693	S06 W19

* Flare located behind the East limb of the Sun
** Flare probably located behind the East limb of the Sun
*** Flare identification uncertain

2. AVAILABLE OBSERVATIONS

The high sensitivity and large dynamic range of the BATSE instrument on GRO make BATSE a very desirable near-Earth component of a multi-spacecraft network for stereoscopic observations of the hard X-ray sources in solar flares. At present, hard X-ray spectrometers aboard two interplanetary spacecraft, Ulysses and PVO, are providing relatively good data coverage for solar flares. These two instruments have been described in the literature (Hurley et al, 1991; Kane et al, 1982). The BATSE, PVO, and Ulysses instruments cover the photon energy ranges 30-1900 keV, 100-2000 keV, and 15-150 keV respectively. Although the three energy ranges are not identical, there is enough overlap between them to permit scientifically important correlated studies.

After the launch of GRO, the first two-month period in which the solar flare activity was high was May-June 1991. During that period both Ulysses and PVO were located behind the East limb of the Sun. At present the Ulysses and PVO data sets for this period are incomplete. Additional data may be available in the near future. We have examined the available data for flares observed by Ulysses and/or PVO. The list of these flares was then compared with the list of flares observed by BATSE (Dennis and Schwartz, 1991) and the flares common to BATSE and Ulysses and/or PVO were identified.

A preliminary list of the "common" flares is presented in Table 1. Relevant information regarding the associated Hα-flares and soft X-ray bursts (GOES) is also given. The list includes (1) flares in full view of two or more spacecraft and (2) flares for which the view of one or more spacecraft was partially occulted by the photosphere.

Further analysis of these common flares requires the following: (a) confirmation of the identification of the associated Hα-flare flares and determination of the view angle for each instrument, (b) verification of the response characteristics of the three instruments to solar flare X-ray spectra, especially for large solar flares, and (c) comparison of the photon energy spectra observed by each instrument. Work on these aspects of the data analysis is in progress. Some early results are expected during the next few months.

Acknowledgements: The authors wish to acknowledge the cooperation and support from G. Fishman, M. Finger, B. Dennis, and R. Schwartz. The research at the University of California, Berkeley was partially supported by NASA under the GRO Guest Investigator grant NAG5-1559 and under JPL contract 958056 for Ulysses (HUS) data analysis. Research at the Los Alamos National Laboratory was also partially supported by a similar NASA grant.

REFERENCES

Dennis, B. R., and Schwartz, R. A., 1991, List of Solar Flares Observed by BATSE, available by e-mail.

Hurley, K. C., 1986, in *The Sun and Heliosphere in Three Dimensions*, ed. R. G. Marsden, D. Reidel Publ. Co., Dordrecht, Holland, p. 73.

Hurley, K. C., Niel, M., Talon, R., Estulin, I. V., and Dolidze, V. Ch., 1983, Ap. J., **265**, 1976.

Kane, S. R., 1980, Astrophys. Space Sc., **75**, 163.

Kane, S. R., Fenimore, E. E., Klebesadel, R. W., and Laros, J. G., 1982, Ap. J. Letters, **254**, L53.

Kane, S. R., Fenimore, E. E., Klebesadel, R. W., and Laros, J. G., 1988, Ap. J., **326**, 1017.

McTiernan, J. M., and Petrosian, V., 1990a, Ap. J., **359**, 524.

McTiernan, J. M., and Petrosian, V., 1990b, Ap. J., **359**, 541.

Coordinated Solar Observations Obtained During the GRO/Max'91 Target-of-Opportunity Campaign of June 1991

Alan L. Kiplinger
A.P.A.S. Department
University of Colorado
Boulder, Colorado
and
NOAA Space Environment Laboratory
Boulder, Colorado

ABSTRACT

Max '91 is a program designed to facilitate coordinated observations of solar activity. The program provides an infrastructure for supporting coordinated observations during observing "campaigns" through various means of electronic communications combined with the ability to monitor real-time solar conditions at NOAA's Space Environment Laboratory. Prior to the extreme solar activity exhibited by active region 6659 in June of 1991, Max '91 solar flare observing campaigns were conducted on a prescheduled basis. The activity from 6659 combined with the repointing of the GRO satellite provided Max '91 with its first opportunity to call an unscheduled campaign and the world community responded with a surprising degree of observational support. This presentation describes some of the activity and some of the types of observations that were collected simultaneously with the GRO complement of instruments.

MAGNETIC FIELD CONFIGURATION ASSOCIATED WITH SOLAR GAMMA-RAY FLARES IN JUNE 1991

M. J. Hagyard,[1] E. A. West,[1] J. E. Smith,[1] F.-M. Trussart,[2] and E. G. Kenney,[3]

Abstract: In this paper we describe the vector magnetic field configuration of the solar active region AR 6659 that produced very high levels of flare activity in June 1991. The morphology and evolution of the photospheric fields are described for the period June 7 to June 10, and the flares taking place around these dates and their locations relative to the photospheric fields are indicated. By comparing the observed vector field with the potential field calculated from the observed line-of-sight flux, we identify the nonpotential characteristics of the fields along the magnetic neutral lines where the flares were observed. These results are compared with those from an earlier study of γ-ray flares.

1. Introduction

In early June of 1991, the Sun produced some of the most intense solar flares of the present cycle of activity. These events were particularly significant for several reasons. First, there were a number of very large flares, five of which produced x-ray fluxes that saturated the NOAA GOES detectors. Second, the Gamma Ray Observatory mission was in progress and the Principal Investigators made the decision to make the Sun a target of opportunity in anticipation of the high level of activity. And finally, a coordinated campaign of ground-based observations was organized to observe the activity in all possible wavelengths.

The Marshall Space Flight Center (MSFC) Solar Observatory took part in this campaign and observed the active region (NOAA AR 6659) responsible for the high level of activity from June 2 through June 10. The primary instrument of the observatory, the MSFC vector magnetograph (Hagyard et al., 1982, 1985), obtained measurements of the magnetic field of AR 6659 for 7 days, June 4-10. For several of these days, vector magnetograms were obtained over a 10-hour period so the temporal evolution of the magnetic fields was well documented.

While the correlation of this evolution with the flare activity was of interest, our main emphasis in the observational program was to document the nonpotential characteristics of the magnetic field and their relation to the occurrence of γ-ray flares. This latter theme is the

[1]Space Science Laboratory, NASA, Marshall Space Flight Center
[2]Ecole Normale Supérieure de Lyon
[3]Boeing Integrated Information Services

basis of the MSFC GRO Guest Investigation so the June active region served as an excellent subject for this study.

In this paper, we will describe our progress in this Guest Investigation, starting first with a description of the active region, the morphology and evolution of its magnetic fields, and the flares and their locations relative to the fields. We will then describe the nonpotential features of the field for the period June 7-10 and relate them to the flare locations. Finally, we will analyze these nonpotential characteristics in the context of previous studies of γ-ray flares.

2. Observations of the Active Region

The region was very large in area, visible to the naked eye, in fact. Mt. Wilson sunspot data (T. Shieber, private communication) indicated that two umbral areas in the active region had field strengths $\geq$ 3000 G. The region was located at a high solar latitude (31° N), a location that has produced several difficulties in interpreting the observed vector magnetic field.

Numerous flares were observed to occur in this region during its disk passage; a total of 26 M-class and 6 X-class flares made up the list of "energetic" events. In Table 1 the relevant data on the X-class flares are listed (SESC/NOAA Preliminary Report and Forecast of Solar Geophysical Data 822-824).

Table 1. Major Flares in AR 6659, June 1991

	Time (UT)						
Date	Begin	Max	End	X-Ray	Imp	Location	Radio
June 1	1456	1520	1726	X12	1F	N25E90	II/IV
June 4	0337	0352	0800	X12	3B	N30E70	II/IV
June 6	0058	0108	0431	X12	4B	N33E44	II/IV
June 9	0134	0143	0152	X10	3B	N34E04	II/IV
June 11	0156	0209	0220	X12	3B	N31W17	II/IV
June 15	0810	0821	1402	X12	3B	N33W69	II/IV

Except for the June 1 event which could not be observed since it was literally at the east limb, all these flares occurred during the night at MSFC. As a consequence we did not obtain any magnetic field observations just before, during, or after these flares and we have had to rely on H-α data from other observatories to locate the flares within the region. The flare of June 9 is shown in Figure 1; these images were provided by the Big Bear Solar Observatory. This figure shows that the main emission in the flare was located in the northeastern part of the active region. Images of the flare on June 6 show this was also the area of the main emission in H-α for that flare. However, a 3B/M4 flare on June 7 was observed in the western part of the region.

Fig. 1. The 3B/X10 γ-ray flare of June 9, 1991. Images courtesy of Big Bear Solar Observatory.

An analysis of the morphology and evolution of the magnetic field from magnetograph observations showed that changes were taking place at these flare locations in the northeastern and western areas. The line-of-sight (LOS) component of the field over the period June 7-10 is shown in Figure 2. The area of maximum negative (black) polarity was the location of the largest umbrae in the region; these umbrae typically had maximum field strengths of 2800-3000 G. The area of maximum positive (white) polarity was associated with a single umbra in the northeastern part of the region; it had a maximum field strength of ≈3000 G. Very steep gradients were observed along the eastern "neutral line" separating positive and negative fields.

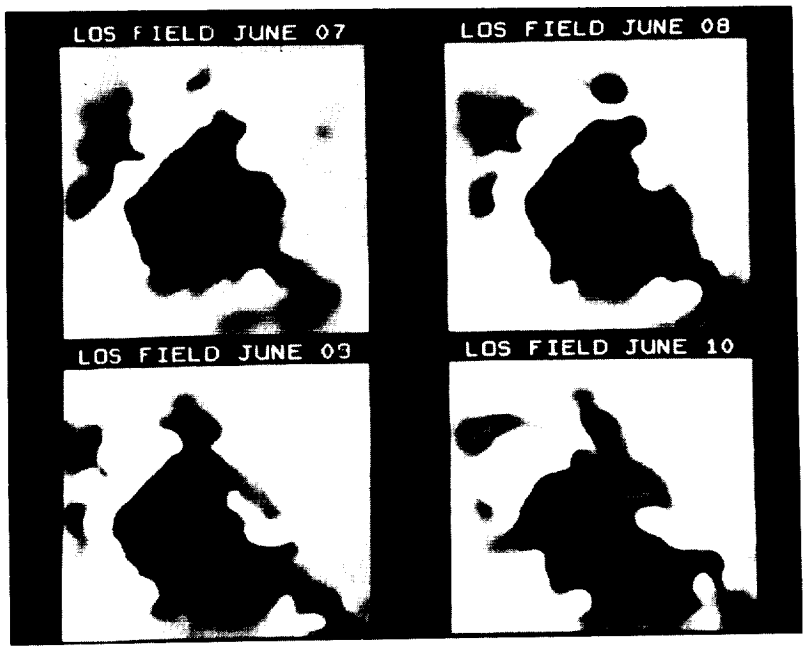

Fig. 2. Line-of-sight fields in AR 6659 for June 7-10. The grayscales run between ± 1500 G. North is up; west is to the right. The field of view is 2.8′ × 2.8′.

Several changes in the LOS field are seen over the time period June 7-10. The positive fields along the eastern neutral line are seen to change, notably from June 9 to June 10. Also, the area of negative polarity to the east of these positive fields that intrudes into the positive polarity is seen to disappear during this same interval. There is a notable development of the negative polarity in the northern part of the active region, particularly from June 7 to June 8. In the western part of the region one sees numerous changing patterns in both positive and negative polarities.

There is a caveat that must be kept in mind when looking at these changes: projection effects may be a source of some of them because of the high latitude of the region. However, these areas where the changes were occurring were also the locations of many of the flares

observed; this fact is a strong argument for believing that significant changes were taking place there.

The total vector field is represented in Figure 3 by superimposing the transverse field on the LOS fields of Figure 2. The strength of the transverse field is represented by the length of the line segments, and the direction (azimuth) of this field is indicated by the orientation of the segments.

The evolution of the transverse field is most notable in the same areas where the LOS field was changing. The positive fields in the southeastern area of the region weaken and change direction from June 9 to June 10, in step with the breaking up of the positive fields and the intrusion of negative polarity there. In the northern area where negative polarity develops from June 7 to June 8, the transverse field reconfigures with the azimuth of the field rotating almost 90°. In the western part of the region from June 9 to June 10 the field grows and rotates direction along the neutral line near the intrusion of positive polarity. Again, these changes are occurring in the areas where flares were observed.

3. Nonpotential Characteristics of the Magnetic Field

The strong magnetic field throughout a solar active region is believed to be the source of the energy released in a solar flare. If this is true, then the field must be in a configuration in which energy is stored in the field. If the field was a potential field, there would be no energy for release in a flare since the potential field represents the lowest energy state possible for a given distribution of flux over the surface. If the configuration of the potential field was known, then a comparison of it with the observed field would provide a measure of how "nonpotential" the real field is and thus an indication of stored energy.

This idea is the basis for our analyses of the nonpotential characteristics of the field of AR 6659. We use the distribution of the normal component of the field to calculate the potential field, using the method of Teuber et al. (1977) and compare its transverse component with that of the observed field. Such a comparison is shown in Figure 4 for the fields observed on June 9. The magnetic neutral lines are indicated by the dark lines; these mark the areas where flares generally occur. A comparison of the azimuths of the observed and potential fields show there are large discrepancies between them along the marked neutral lines. Indeed, the potential field is seen to cross the neutral line perpendicularly in these areas whereas the observed field lies almost parallel to the neutral lines. We refer to this difference between the potential and observed azimuths as angular "shear," $\Delta\phi$, and infer that the fields are highly stressed in these configurations. Thus, we believe this configuration of photospheric fields is an indication that magnetic energy is stored in these fields and can be released in the form of flares.

In previous studies of stressed fields in other active regions, we have developed quantitative measures of the angular shear (Hagyard et al., 1984; Hagyard and Rabin, 1986; Hagyard, 1990). Selecting those pixels that lie along the main magnetic neutral lines of an active region, we compute $\Delta\phi$ for those points that have field strengths B fitting the criteria 300 G $\leq$ B and B*/2 $\leq$ B, where B* is the maximum field strength along the selected neutral line.

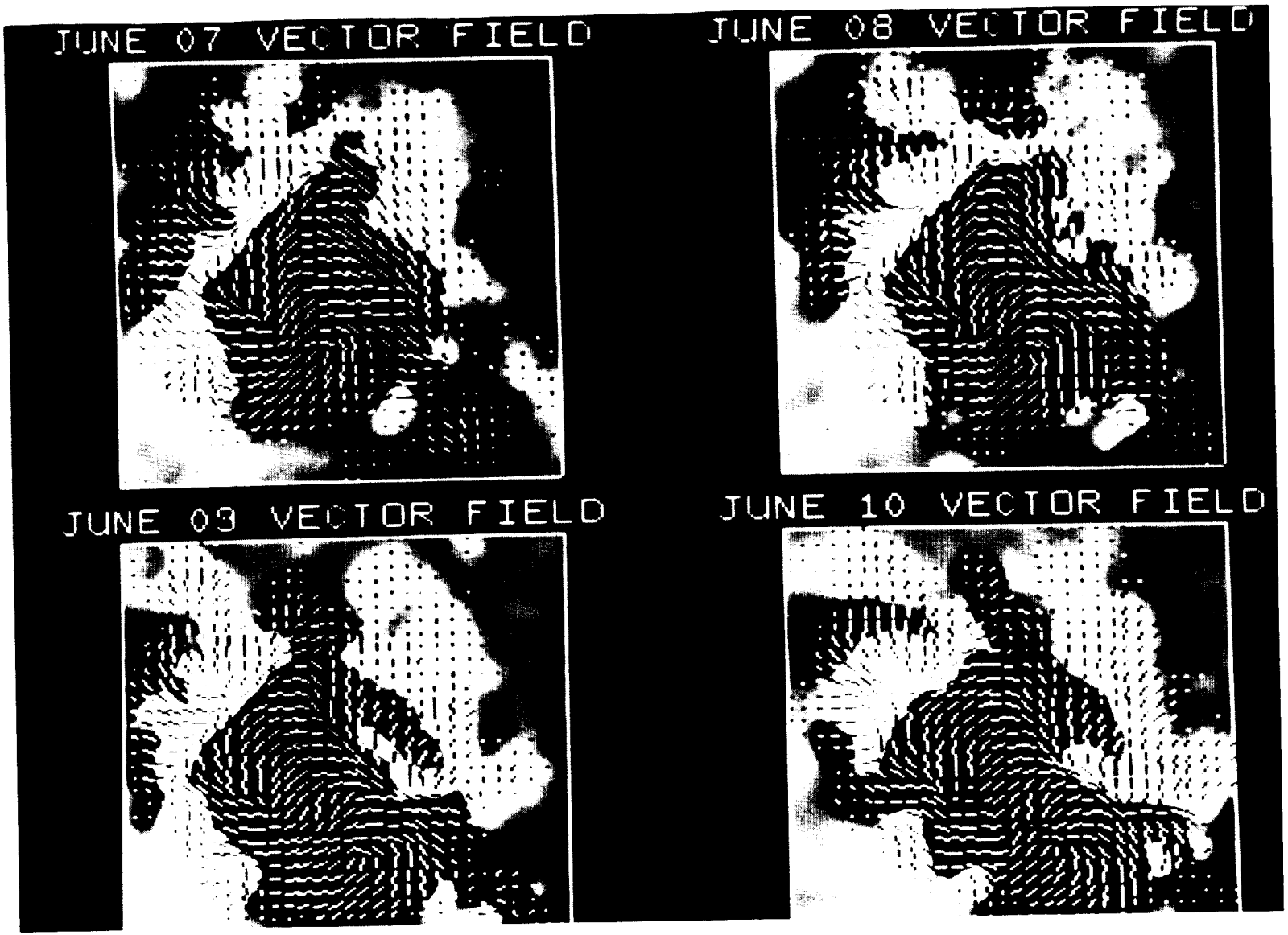

Fig. 3. Vector fields in AR 6659 for June 7-10. The grayscale represents the line-of-sight component of the field. The transverse component is represented by the line segments with scaling between 100 and 500 G.

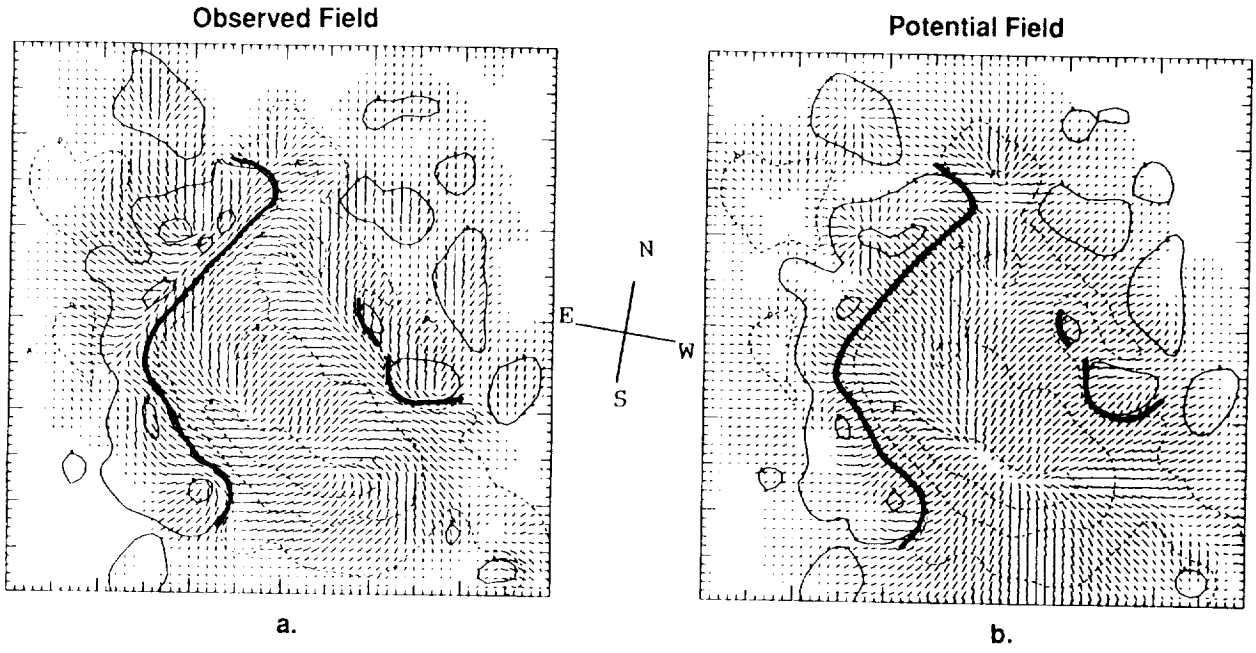

Fig. 4. The observed field and (computed) potential field in AR 6659 for June 9. Contours represent the line-of-sight field; line segments represent the transverse field. The main neutral lines are indicated by the dark contours.

Then we designate points to be moderately stressed if

$$70° \leq \Delta\phi < 80°$$

and highly stressed if

$$80° \leq \Delta\phi \leq 90°.$$

(In our definition of angular shear, 90° represents the maximum value attained by $\Delta\phi$.) Maps of these points of stress are made by using symbols for the two different ranges of $\Delta\phi$: + and * for the moderately and highly stressed points, respectively. Examples of "shear" maps for observations taken June 7-10 are shown in Figure 5. The shear map for June 9 (Figure 5c) illustrates quite graphically the differences seen in Figure 4 between the observed and potential fields. In particular, notice the line of seven contiguous points of high angular shear along the eastern neutral line and a longer one along the western neutral line for June 9. These extended lengths of shear indicate large areas of stressed fields at these locations and are signatures we have found in other active regions that produced big flares (Hagyard, 1990).

The analyses for nonpotential fields leading to the results shown in Figures 4 and 5 are not precisely correct since we did not take projection effects into account. An exact calculation of the potential field using the method of Teuber et al. (1977) requires the use of the true normal-to-the-surface component of the field rather than the line-of-sight one. With this region

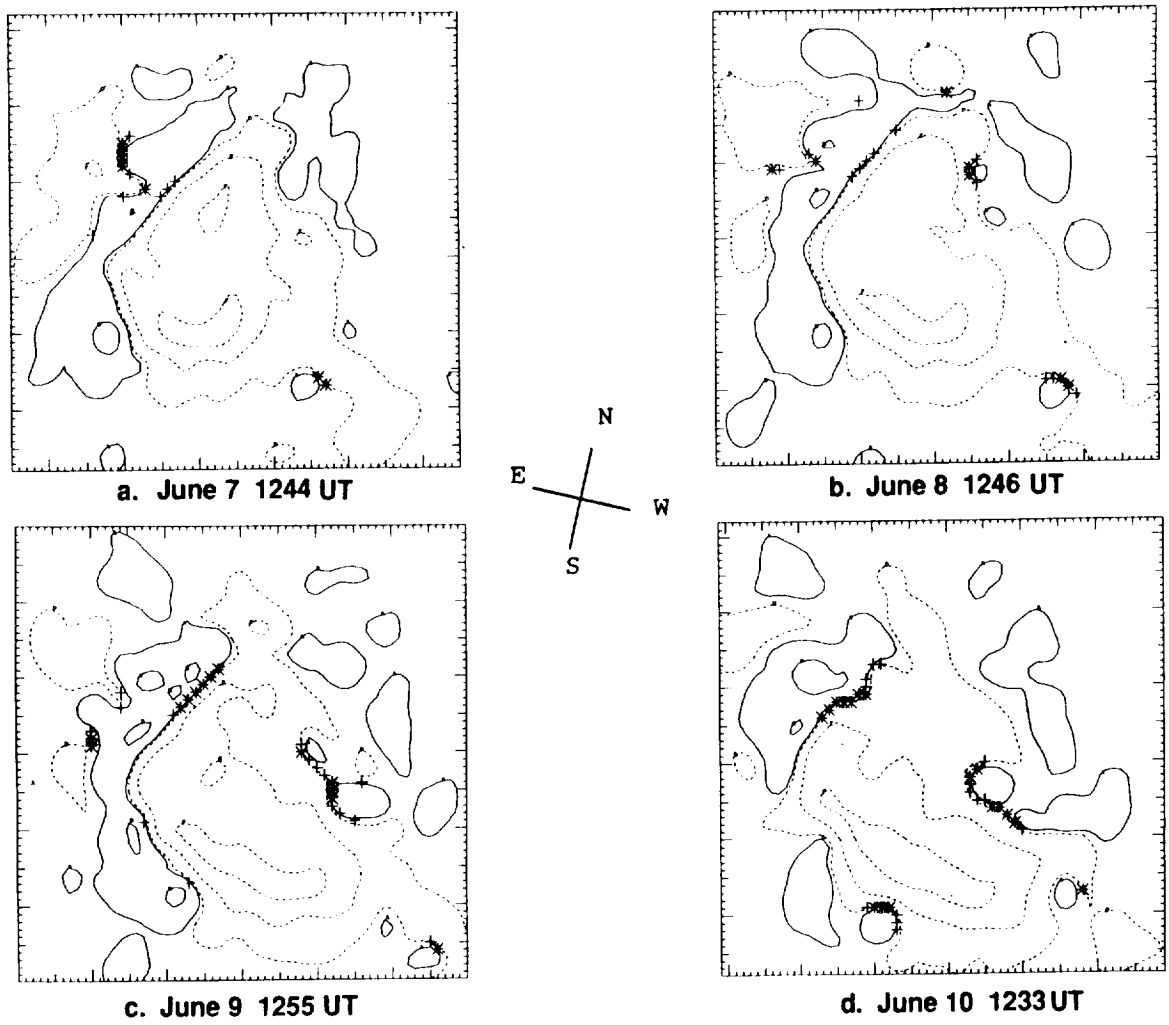

Fig. 5. Areas of strongly nonpotential fields along the neutral lines in AR 6659. Contours represent the line-of-sight component of the magnetic field. The symbols are defined in the text.

located at such a high latitude, the line-of-sight component is a poor approximation for the potential calculation. Projection effects will also change the neutral lines and thus the evaluation of shear along neutral lines (Gary and Hagyard, 1990).

To evaluate the nonpotential characteristics correctly, the measured field must be transformed into heliographic coordinates (Hagyard, 1987; Venkatakrishnan et al., 1988). However, to carry out this transformation, the ambiguity of 180° in the azimuth must be resolved. For complex active regions where the field is highly sheared, such as AR 6659, it is extremely difficult to determine the true direction of the transverse component. The methods we employ for this determination include comparisons with the direction of the potential field, comparisons with H-α structures, and connectivity between positive and negative fields *in heliographic coordinates.*

At this time we have performed this exercise to resolve the ambiguity in the azimuth for the observations of June 8 and 9 only. In Figure 6, the vector field for June 9 is shown in the image plane and heliographic coordinates. Note that the image plane field in this figure is identical with Figure 4a, except that now the line segments are given directions. Changes in the morphology of the magnetic field are evident as a result of the transformation. Such changes underscore the importance of the heliographic transformation in studying the evolution of the fields as a region transits the solar disk.

Heliographic shear maps for June 8 and 9 are shown in Figure 7. Several significant changes from the image-plane shear maps of Figure 5 are seen. For June 8, the major change is the increase in shear along the western neutral line; also, the magnitude of the angular shear has increased on the eastern neutral line at the same pixel locations. For June 9, the major change is the additional shear along the southern (lower) section of the eastern neutral line.

Looking at the magnitudes of field intensity (B) and angular shear ($\Delta\phi$) along the entire eastern neutral line, we find maximum field and shear of 1480 G and 89°, respectively, on June 8; for June 9, the maxima are found to be 1720 G and 87°. For the western neutral line, the maxima are 1765 G and 89° on June 8 and 1720 G and 89° on June 9. (The data for June 8 and 9 were calibrated for maximum fields of 2500 G. Subsequently, data from Mt. Wilson indicated maximum fields of $\approx$ 3000 G. Thus, the values given here are underestimates.)

The 3B/X10 flare shown in Figure 1 started about 13 hours after the observations that produced the shear map for June 8 and 11 hours before those for June 9. Within the accuracy of the observational data, there certainly does not seem to be any noticeable change in the degree of shear as a result of this flare. However, there can be no doubt that the magnetic field was highly sheared in the area where the flare erupted.

4. Discussion

In an earlier study, we analyzed the nonpotential characteristics for a small sample of flare-productive active regions observed by the Gamma Ray Spectrometer on the Solar Maximum Mission (Hagyard et al., 1990). Using the same quantitative analysis for angular shear, we compiled the data given in Table 2.

Table 2. Comparison of Nonpotential Parameters

Date of Flare	Max B (G)	Max $\Delta\phi$(°)	No. Points	Flare Class	γ Event
04/24/84	1700	90	15	3B/X13	yes
04/28/84	1920	90	8	2B/C6	no
02/04/86	1100	90	10	3B/X3	yes
11/05/80	1000	88	8	1B/M2	no
04/07/80	1000	85	8	1B/M4	no

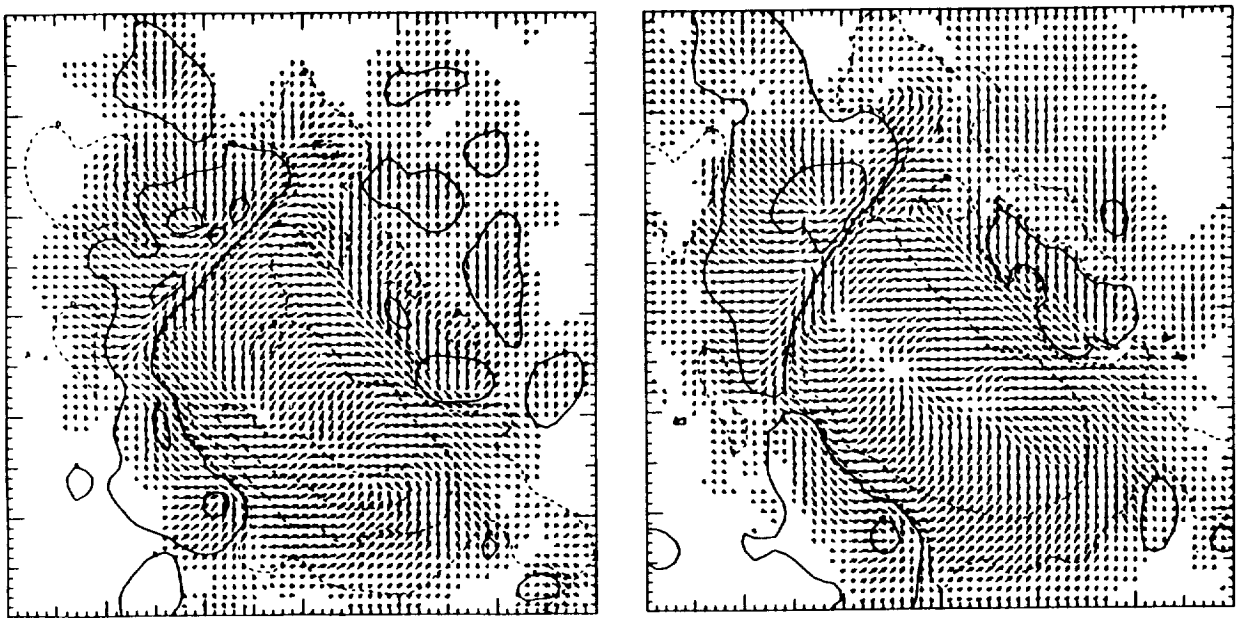

Fig. 6. June 9 vector field in image plane and heliographic coordinates.

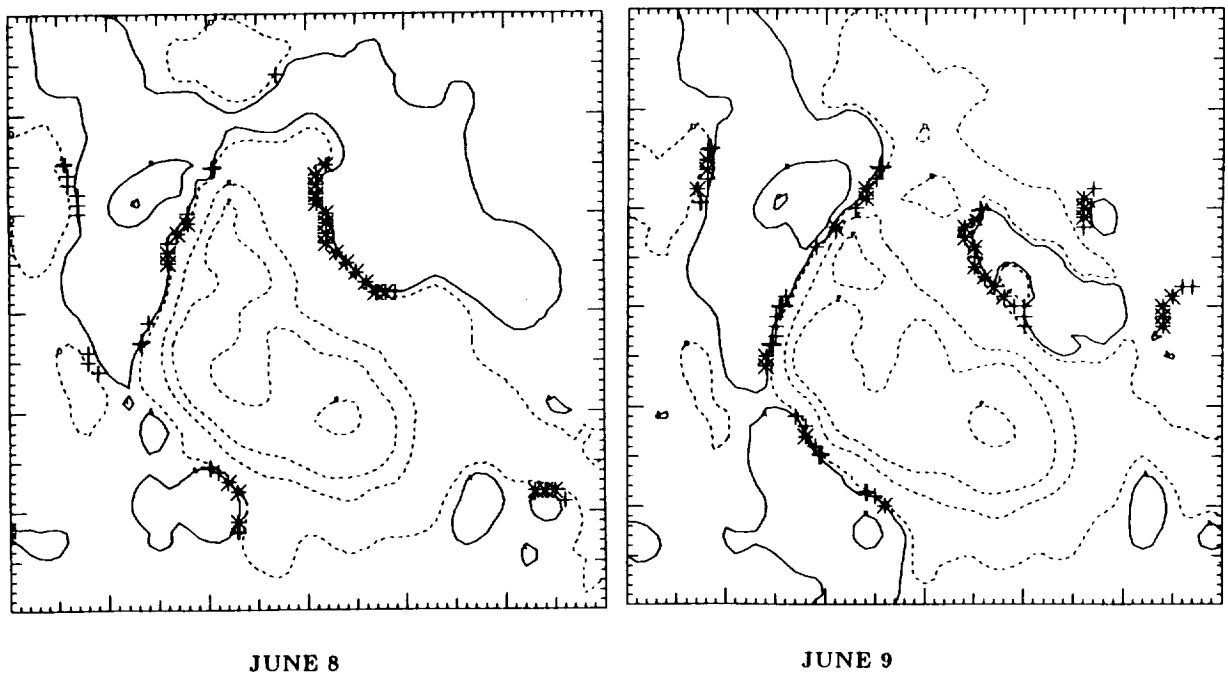

Fig. 7. Heliographic shear maps for June 8 and 9.

In this table, the numbers in the column "No. Points" indicate how many ≈ consecutive pixels along the neutral line are found in the area of maximum angular shear that satisfy $70° \leq \Delta\phi \leq 90°$ (i.e., ≈ consecutive pixels represented by + or *).

A similar table can be compiled for the data analyzed so far for AR 6659, although information about the flares occurring around the dates June 8 and 9 is limited to the one event along the eastern neutral line at 0134 UT on June 9. In this table, nonpotential parameters are given for the two separate neutral lines (NL in the table).

Table 3. Nonpotential Parameters for AR 6659

Date	NL	Max B (G)	Max $\Delta\phi$(°)	No. Points	Flare Class	γ Event
06/08/91	Northeast	1480	89	6	3B/X10	yes
	West	1765	89	16	??	??
06/09/91	Northeast	1720	87	7	3B/X10	yes
	Southeast	1335	84	8	same	yes
	West	1720	89	14	??	??

In the earlier study, the conclusion was made that the strength of the field along the neutral line and the corresponding degree of shear do not differ significantly between flares that produce γ-ray events and those that do not. However, it was also concluded that perhaps the extent of the nonpotential fields was a distinguishing factor, i.e., the number of consecutive pixels, since the two γ-ray events had somewhat larger numbers of consecutive pixels. Looking at the preliminary data in Table 3 for AR 6659, we see the same high field strengths and large angular shears that appear in Table 2. However, the number of consecutive points along the eastern neutral line is smaller than the numbers cited for the γ-ray flares in the earlier study. At first glance, the conclusion of that study needs to be re-examined based on the June 8 and 9 data. Perhaps when all the available magnetic observations for this active region have been analyzed, a clearer picture will emerge. Indeed, the goal of the MSFC Guest Investigation is to analyze observations for all active regions producing M-class or greater flares since the launch of GRO, classify these flares according to their productivity of γ-rays, and look for distinguishing characteristics in the nonpotential fields that correlate with these flares. At the end of this study, perhaps a more definitive set of criteria will emerge. Certainly, in June 1991, Mother Nature provided us with an excellent opportunity to begin this investigation.

5. References

Gary, G. Allen, and Hagyard, M. J.: 1990, *Solar Phys.* **126**, 21.

Hagyard, M. J.: 1987, *Solar Phys.* **107**, 239.

Hagyard, M. J.: 1990, *Mem. S. A. It.* **61**(2), 337.

Hagyard, M. J., and Rabin, D. M.: 1986, *Adv. Space Res.* **6**(6), 7.
Hagyard, M. J., Cumings, N. P., and West, E. A.: 1985, in *Proceedings of Kunming Workshop on Solar Physics and Interplanetary Travelling Phenomena*, C. De Jager and Chen Biao (eds.), Science Press, Beijing, China, p. 204.
Hagyard, M. J., Venkatakrishnan, P., and Smith, J. B., Jr.: 1990, *Astrophys. J. Suppl.* **73**, 159.
Hagyard, M. J., Cumings, N. P., West, E. A., and Smith, J. E.: 1982, *Solar Phys.* **80**, 33.
Hagyard, M. J., Smith, J. B., Jr., Teuber, D., and West, E. A.: 1984, *Solar Phys.* **91**, 115.
Teuber, D., Tandberg-Hanssen, E., and Hagyard, M. J.: 1977, *Solar Phys.* **53**, 97.
Venkatakrishnan, P., Hagyard, M. J., and Hathaway, D. H.: 1988, *Solar Phys.* **115**, 125.

Millimeter and Hard X-ray/γ-ray Observations of Solar Flares During the June 91 GRO Campaign

M. R. Kundu, S. M. White, N. Gopalswamy and J. Lim

Dept. of Astronomy, Univ. of Maryland, College Park MD 20742

Introduction

The millimeter region has perhaps been the most under-utilized observing wavelength range in solar physics, due to the lack of telescopes which can match the temporal and spatial resolution available at other wavelengths. The usefulness of millimeter-wave observations lies in the fact that they are sensitive to both the highest energy electrons in flares as well as to cool material in the chromosphere. Most millimeter-wave observations of solar flares have been hampered both by poor spatial resolution (because of the lack of synthesis interferometers) and by poor sensitivity (since the flux from the Sun's thermal emission is so high at millimeter wavelengths). The number of reported observations of bursts at millimeter wavelengths is relatively small, and there are none for which true high-spatial-resolution imaging data have been reported (see review by White and Kundu 1992).

The emission of solar flares at millimeter wavelengths is of great interest both in its own right and because it is generated by the very energetic electrons which also emit gamma rays. Since high-resolution imaging at gamma-ray energies is not presently possible, millimeter observations can act as a substitute. In addition, the millimetric emission is undoubtedly optically thin (except possibly for a small class of very large flares which have spectra rising beyond 100 GHz; Kaufmann *et al.* 1985), and thus is not subject to the same ambiguities of interpretation which are prevalent in the study of solar microwave bursts. It can be used as a powerful diagnostic of the energy distribution of electrons in solar flares and its evolution, and of the magnetic field.

We have carried out high-spatial-resolution millimeter observations of solar flares using the Berkeley-Illinois-Maryland Array (BIMA). At the present time BIMA consists of only three elements, which is not adequate for mapping highly variable solar phenomena, but is excellent for studies of the temporal structure of flares at millimeter wavelengths at several different spatial scales. The first dedicated observations of solar flares with a high-spatial-resolution millimeter-wavelength interferometer were made by us in March 1989 (Kundu *et al.* 1990) when a solar active region with the greatest X-ray flare production rate yet recorded appeared on the disk of the Sun. Our observations represented an improvement of an order of magnitude in both sensitivity and spatial resolution compared with previous solar observations at these wavelengths. We found that most of the flares occurring within the field of view during the March '89 observations were detected at millimeter wavelengths, including both very impulsive

and longer-duration events. Of 18 flares listed by SGD during our observations, BIMA detected 14, including all those with GOES X-ray classes of C or greater (3 X-class, 7 M-class and 2 C-class). The four flares which BIMA did not detect were all of optical class SF and undetected in X-rays. For 3 of the 4, no microwave emission was reported. Thus only in one flare was microwave emission reported without a detection at BIMA. On the other hand, there were 3 flares for which BIMA detected emission but no events were reported by microwave patrols.

Based on those early observations it appeared that millimeter burst sources were not much smaller than microwave sources; generally source sizes were in excess of 2″, but in some events sources may be $\sim$ 1″. Thermal gyrosynchrotron models for the radio emission in the impulsive phase could be ruled out because the flux at millimeter wavelengths was too high.

In this paper, we present BIMA observations made during the GRO/Solar Max '91 Campaign in June 1991 when solar activity was unusually high. Our observations covered the period June 8 – June 13, 1991; this period overlapped the period June 4–June 15 when the Compton Telescope made the Sun a target of opportunity because of the high level of solar activity.

Observations

During the period of June 8–13, 1991, BIMA was in its most compact configuration. The array presently has three antennas, providing three baselines. In effect each baseline provides a one–dimensional spatial Fourier transform of the brightness distribution on the sky. For a point source the phase gives us positional information, while the amplitude is the total flux of the source. For an extended source the response of the interferometer depends on the relationship of the source dimension to the fringe spacing of the Fourier transform: only if the source dimension is smaller than about one-third of the fringe spacing do we expect the amplitude variability to correspond to the total flux in the source. For the 1991 June observations the fringe spacing ranged from $\sim$ 30″ EW to $\sim$ 45″ NS; such large fringe spacings should guarantee that the correlated amplitude corresponds to the total flux of the source, at the expense of information about small spatial scales. To summarize the properties of millimeter-wavelength emission from solar flares, in Figure 1 we show the correlated amplitude on a single baseline (31) for the whole period of observation with the BIMA array in 1991 June. Most of the larger events can be seen (about 30 radio bursts in total were detected by BIMA and some of the smaller ones do not show up well on this plot). Two timescales of emission are readily seen in this figure: a rapid rise and fall component which appears as sharp spikes, and a much less rapidly varying component which often follows an impulsive spike. As we discuss further below, and as has long been expected, the impulsive component corresponds to nonthermal gyrosynchrotron emission from energetic electrons, while the long-duration events are produced by thermal bremsstrahlung in the hot dense plasma seen in the corona in the decay phase of solar flares. Two of the giant flares from the June period (early UT on June 9 and 11, here shown at the end of June 8 and 10) saturated the telescope receivers shortly after flare onset, and we will not discuss them here.

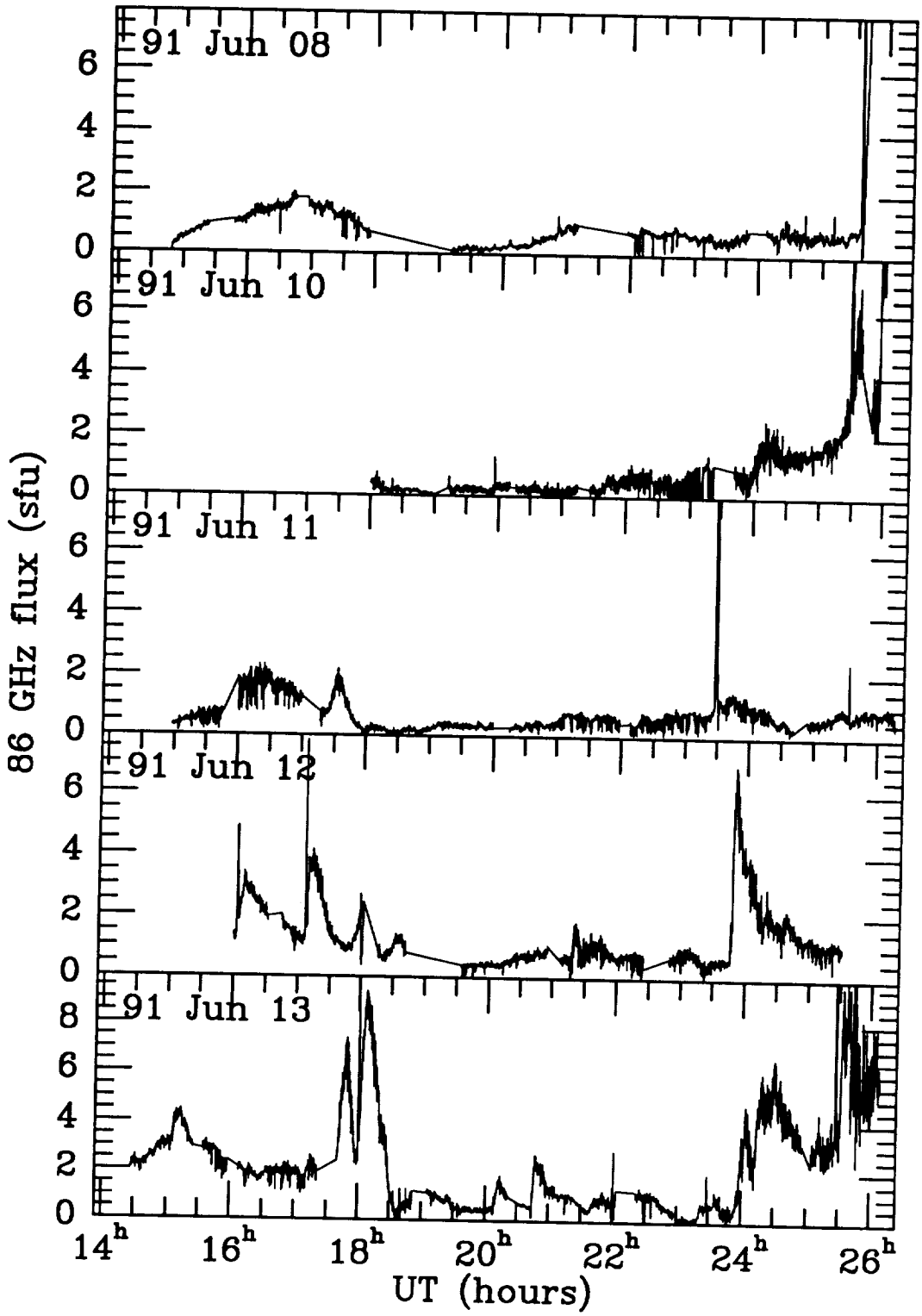

Figure 1 A plot of amplitude versus time (UT hours) summarizing the BIMA 86 GHz observations during the 1991 June GRO solar campaign.

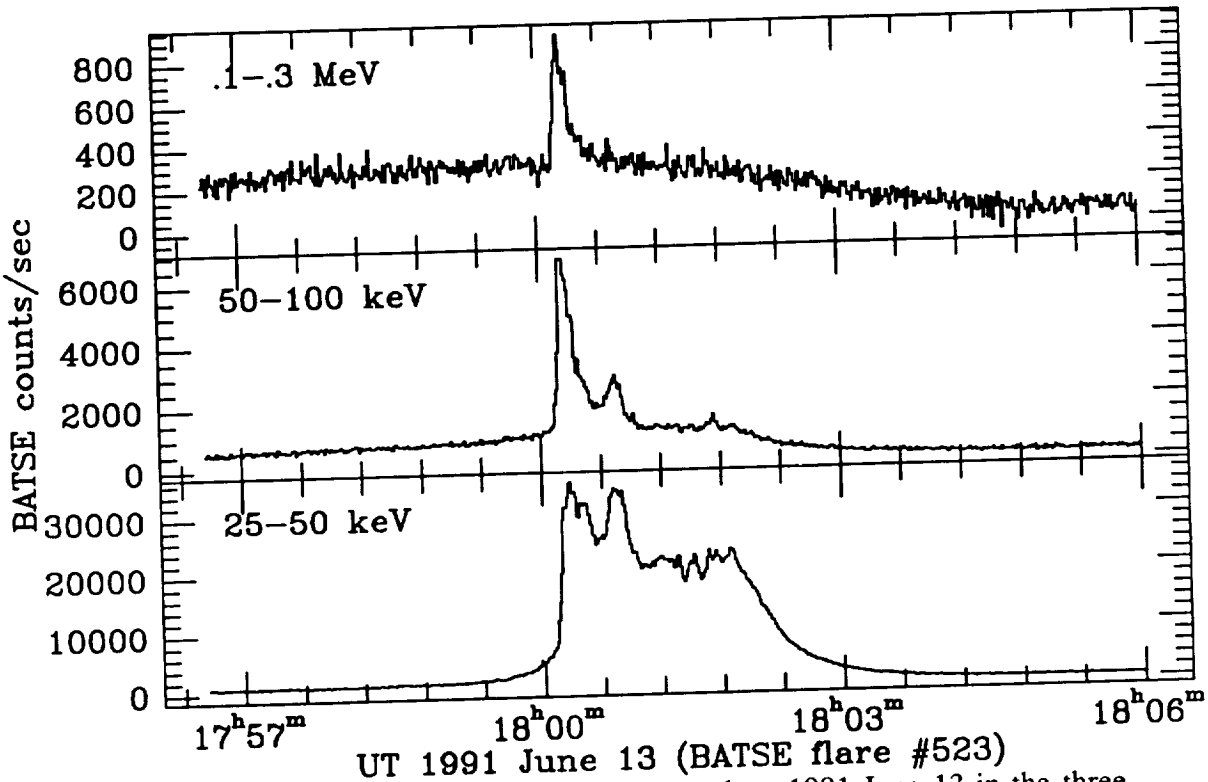

Figure 2 The time profile of a flare observed on 1991 June 13 in the three lowest energy ranges of the BATSE large-area detectors (as labelled). Note that the 25 – 50 keV emission continues much longer than do the higher-energy X-rays: the latter are confined to a hard spike at the onset of the flare. The time resolution of the BATSE data is 1.024 s.

Since we have not completed the analysis of these events along with other data obtained simultaneously, here we shall restrict ourselves to a morphological description of BIMA 86 GHz burst observations and comparison with GRO-BATSE gamma ray burst observations as well as GOES soft X-ray data. Where possible we will demonstrate the scientific results from this type of observation: these arise primarily from the fact that millimeter-wavelength emission is due to the same electrons which emit gamma rays, which we will demonstrate in the first event discussed.

Results

Figure 2 presents the BATSE data for a burst observed on June 13, 1991, ~ 17:57–18:06 UT. The flare evolution is shown for 3 different energy channels (25–50 keV, 50–100 keV, and 0.1–0.3 MeV; there were no significant counts above the background in the 0.3 – 1 MeV channel). The remarkable feature of this flare is that while the overall profile in the 25 – 50 keV range is relatively unremarkable, with a sharp rise to a plateau level containing a number of sub-peaks followed by a rapid decay, in the higher-energy channels we see a sharp spike right

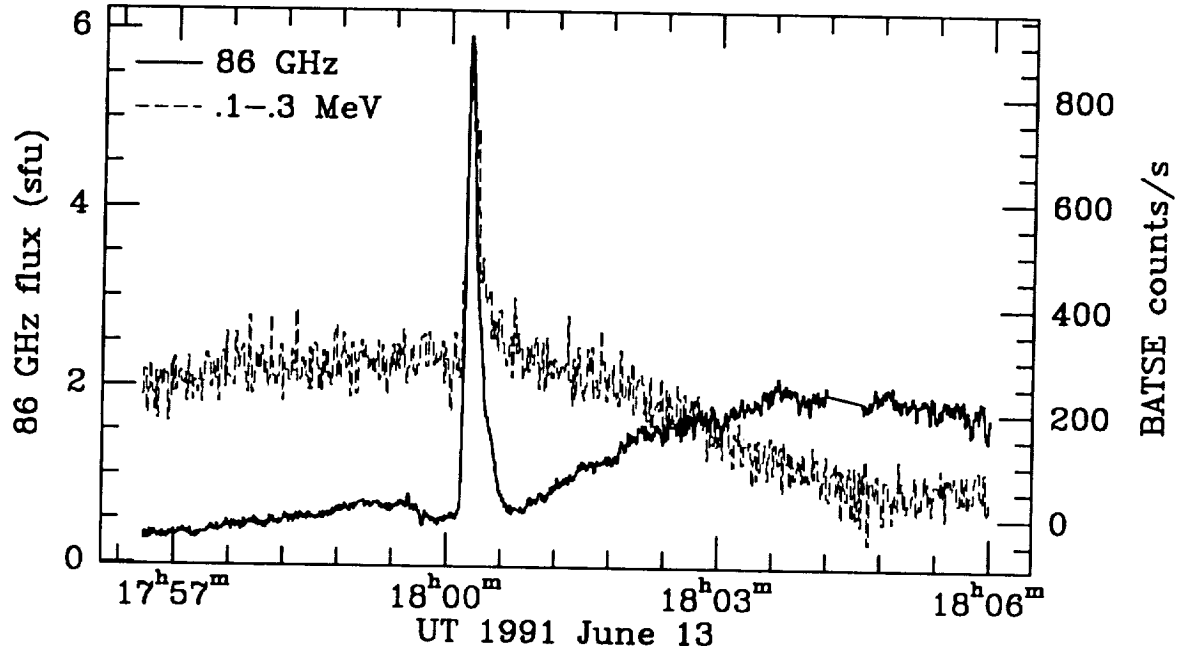

Figure 3 Comparison of the time profiles of the 1991 June 13 18 UT flare emission in the 100 – 300 keV hard X-rays seen by BATSE (broken line) and the 86 GHz emission recorded by BIMA (solid line).

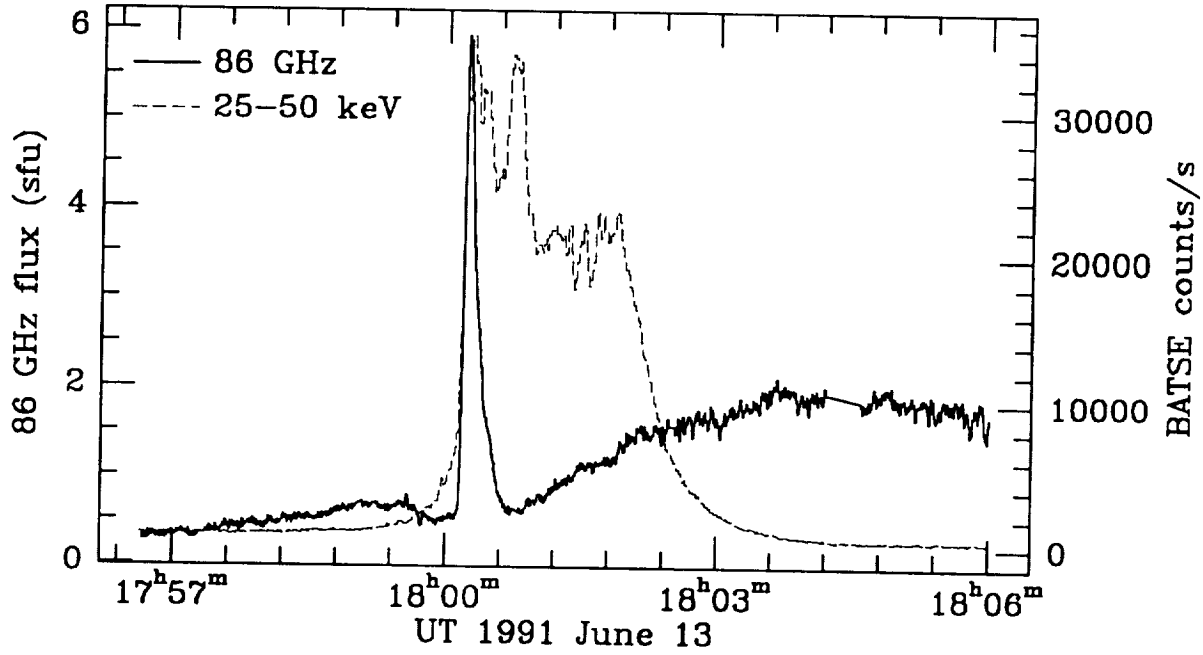

Figure 4 Comparison of the time profiles of the 1991 June 13 18 UT flare emission in 25 – 50 keV hard X-rays and the 86 GHz.

at the beginning of the flare. We and others have argued elsewhere (Ramaty 1969; Ramaty

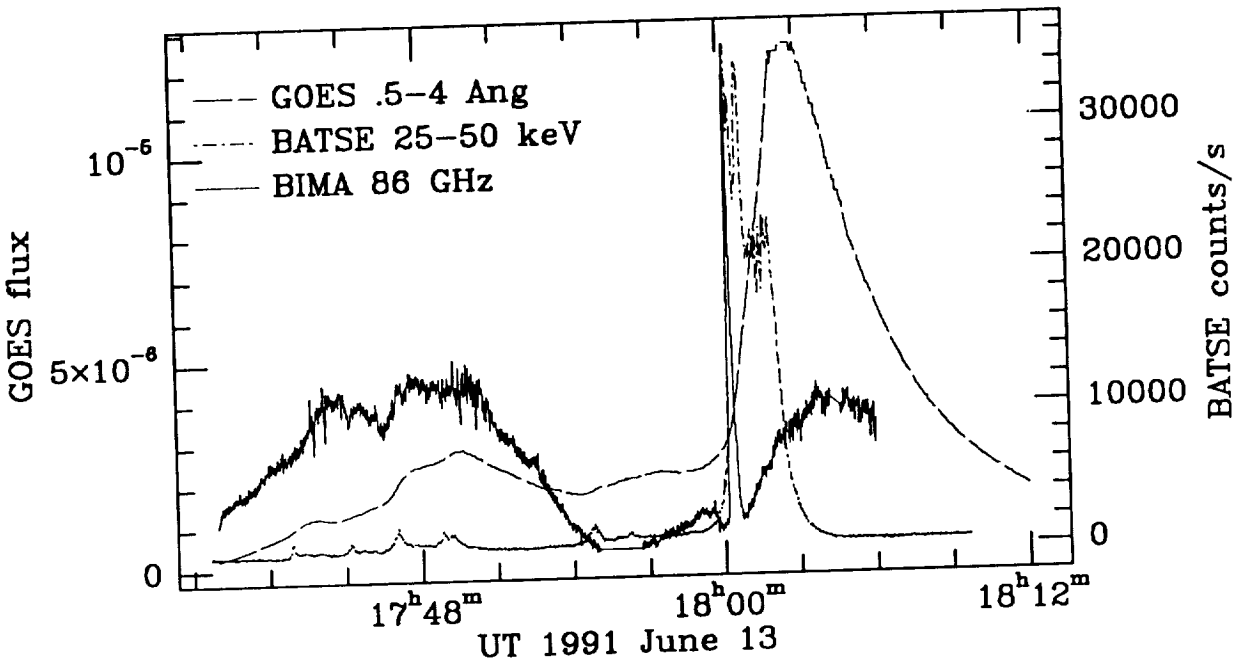

Figure 5 The evolution of emission around 18 UT on 1991 June 13 seen in soft X-rays recorded by the GOES satellite (3 – 25 keV; long-dashed line), in 25 – 50 keV X-rays detected by BATSE (short-dashed line), and at 86 GHz recorded by BIMA (solid line).

& Petrosian 1972; Kundu *et al.* 1990; White & Kundu 1992) that millimeter emission in the impulsive phase should be due to gyrosynchrotron emission from the most energetic electrons in a flare, and on this basis one would predict that the millimeter emission would also show a sharp spike in the onset phase. This is exactly what is seen. In Figure 3 we have plotted the BATSE 0.1–0.3 MeV time profile and the BIMA 86 GHz profile to the same scale. The BATSE data have a time resolution of 1.024 s, while the BIMA data have a time resolution of 0.4 s. The close similarity of the two profiles provides convincing evidence that the millimeter emission is indeed due to the most energetic electrons in a solar flare: the same energetic electrons that produce gamma ray continuum. The importance of this result is that we can obtain high-spatial-resolution information on source structures with millimeter-interferometer observations, which is not presently possible directly with gamma-ray observations.

To emphasize the point, in Figure 4 we compare the BIMA 86 GHz profile with the BATSE 25–50 keV time profile. We see that the sharp rise in the 25–50 keV range coincides exactly with the 86 GHz rise, although there is some emission in the 25 – 50 keV range just prior to the impulsive rise which has no signature at 86 GHz. However, unlike the 25 – 50 keV burst which has a plateau lasting $\sim$ 3 min and contains another major peak, the mm emission drops abruptly to almost its pre-burst emission. This figure also emphasizes that, in addition to the impulsive phase coinciding with the gamma ray emission, the millimeter emission shows an extended component which rises slowly and continues beyond 1806 UT. Thus in this event we clearly see two easily-distinguishable components in the millimeter

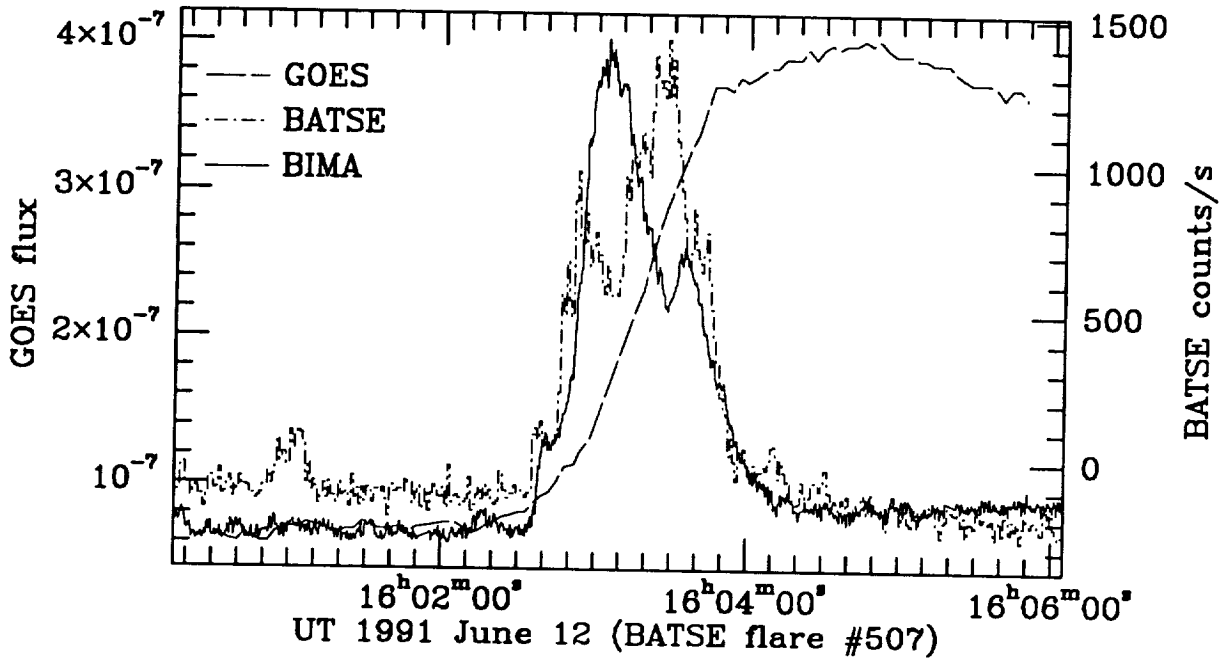

Figure 6 The soft X-ray, hard X-ray and 86 GHz time profiles of a flare at 16 UT on June 12.

emission: an impulsive component coinciding in time with the impulsive gamma ray emission, and a gradual extended component with no gamma ray counterpart. We also note the small dip in the 86 GHz emission immediately prior to the impulsive rise, which seems to be a common feature of pre-flare activity in millimeter-wave emission.

Figure 5 shows the complete June 13 event starting at $\sim$ 1736 UT as seen by the GOES satellite soft-X-ray detectors (0.5 - 4 Å, which corresponds to an energy range of 3 – 25 keV; 3 s time resolution), the GRO/BATSE 25–50 keV detectors and BIMA 86 GHz interferometer. This figure has a number of interesting features. The soft X-ray data characteristically show only very smooth variations in time, quite unlike the adjacent 25 – 50 keV time profile, and this is assumed to be because the GOES rates are dominated by low-energy (3 – 10 keV) soft X-rays which are produced by thermal plasma, as opposed to the nonthermal electrons which produce the 25 – 50 keV emission. Prior to the impulsive rise at 18 UT the 86 GHz emission shows a long-duration, slowly-varying emission at quite a high level; the GOES records also show emission at this time, and we attribute both to thermal plasma. In the BATSE profile we see a number of small impulsive peaks between 1736 and 1757 UT, which may be associated with the production of the thermal plasma. It is conceivable that both the BIMA 86 GHz emission and GOES soft X-ray emissions are manifestations of preflare activity. At 18 UT we see the impulsive phase of the main flare in the hard X-rays and at 86 GHz, as already discussed; the soft X-rays show the usual slow rise and fall, with a peak occurring well after the hard-X-ray peak. In the decay phase we also see that the thermal phase at 86 GHz matches the soft-X-ray profile quite well, confirming the interpretation that the long-duration millimeter emission in the decay phase is thermal and associated with the hot dense loops seen in soft X-rays.

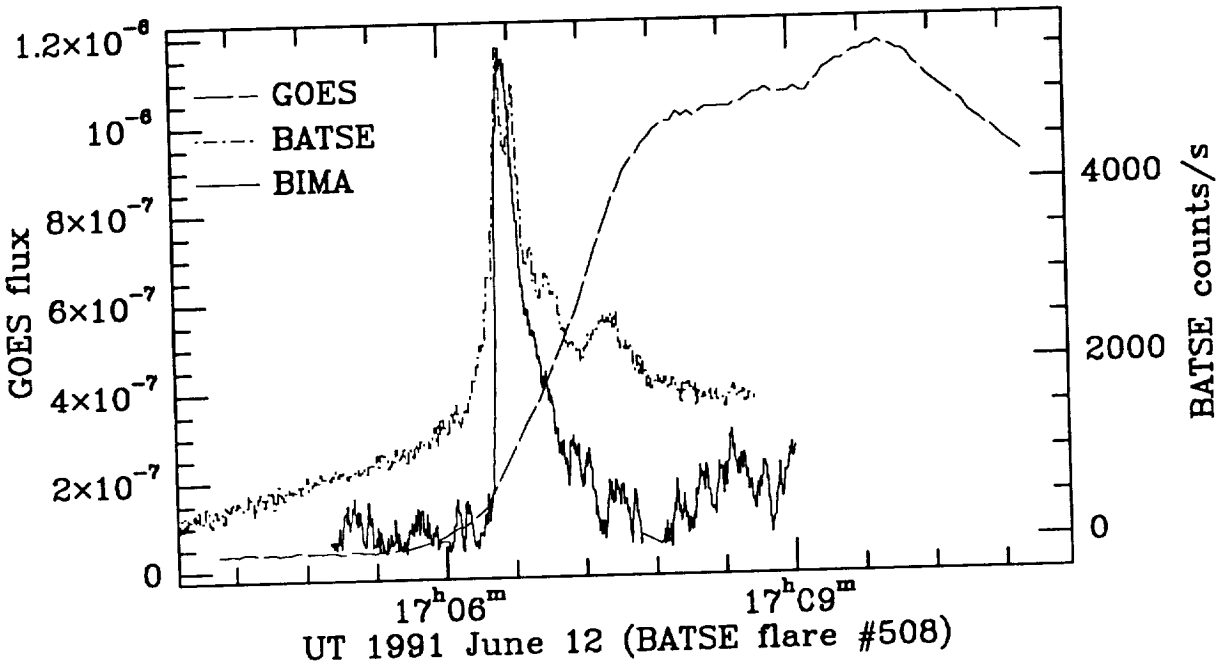

Figure 7 The soft X-ray, hard X-ray and 86 GHz time profiles of a flare at 17 UT on June 12.

Figures 6 and 7 show two examples of flares in which the 86 GHz emission and 25–50 keV hard X-ray emission in the impulsive phase match each other in general terms. We also show the GOES soft-X-ray profiles. Both flares occurred on 1991 June 12; note that the 17 UT flare (Fig. 7) occurred as GRO was emerging from spacecraft-night, which is why the flux is rising so sharply prior to the flare. In both cases the 86 GHz and hard X-ray emissions have impulsive peaks, and there seems to be a delay of the 86 GHz emission with respect to the hard X-ray peak by a few seconds; note, however, that not all hard X-ray peaks are observed in the mm data, as we also noted in the June 13 event discussed above. In these two events the GOES soft X-ray emission does not show any significant rise prior to the onset of 25 – 50 keV emission: it starts near the start of mm/hard X-ray emission, rises slowly and reaches a broad peak after 4-5 minutes and then decays even more slowly, as is normally the case.

Figures 8 and 9 show two cases of events in which impulsive 25 – 50 keV emission was seen, but there was little or no impulsive-phase emission at 86 GHz, even though the count rates at 25 – 50 keV were well above the levels of some small events which produced both 25 – 50 keV and 86 GHz impulsive-phase emission (e.g., Figure 10). The 86 GHz profile in each case shows gradual mm burst emission corresponding roughly with the GOES soft X-ray emission, although the BATSE data show sharp peaks. In one case (Fig. 9) the hard X-ray rise corresponds to the rise phase of both mm and soft X-ray emission; in the second case (Fig. 8), there are two hard X-ray peaks, one of which is located near the start of the GOES and 86 GHz profiles and the other near the peak of the mm emission and corresponding well with a "shoulder" in the GOES profile.

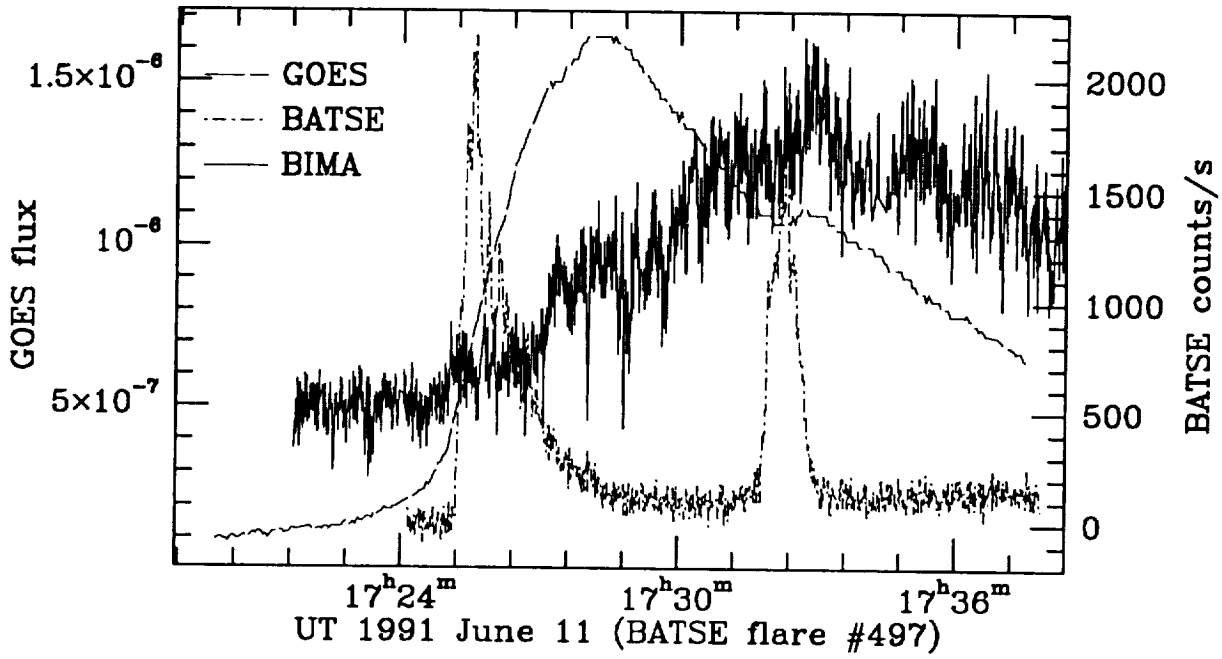

Figure 8 The soft X-ray, hard X-ray and 86 GHz time profiles of a flare at 17:24 UT on June 11. This flare shows impulsive hard X-ray behaviour but no corresponding 86 GHz impulsive phase; instead, an extended thermal phase is seen at 86 GHz.

The final example (Figure 10) is a small event which demonstrates that for simple impulsive events with a very sharp rise, like this one, we see a clear delay of several seconds between the 25 – 50 keV impulsive rise and the 86 GHz rise. In small events such as this there are no counts in the higher-energy BATSE detectors, so we cannot discuss the hard-X-ray spectrum. However, based on earlier discussion we can associate the 86 GHz emission with high-energy electrons (> 300 keV), and the implication is that there is a delay between the production of the 25 – 50 keV electrons and the > 300 keV electrons. Such delays can be attributed to the need to accelerate electrons from low to high energies, and can be used to constrain candidate emission mechanisms. Note also that in this event, unlike some others, the soft X-rays begin to rise well before the hard X-ray onset.

Discussion

Before we discuss our preliminary results, it is useful to consider a basic flare model. There are many flare models in the literature. For the present purpose it is enough to consider a model in which energy release takes place in the corona, resulting in the acceleration of nonthermal electrons. These propagate down magnetic field lines, strike the chromosphere, and produce hard X-rays by thick target bremsstrahlung. The nonthermal electrons deposit ther energy in the chromosphere as heat. The heated, dense chromospheric material produces the flare Hα

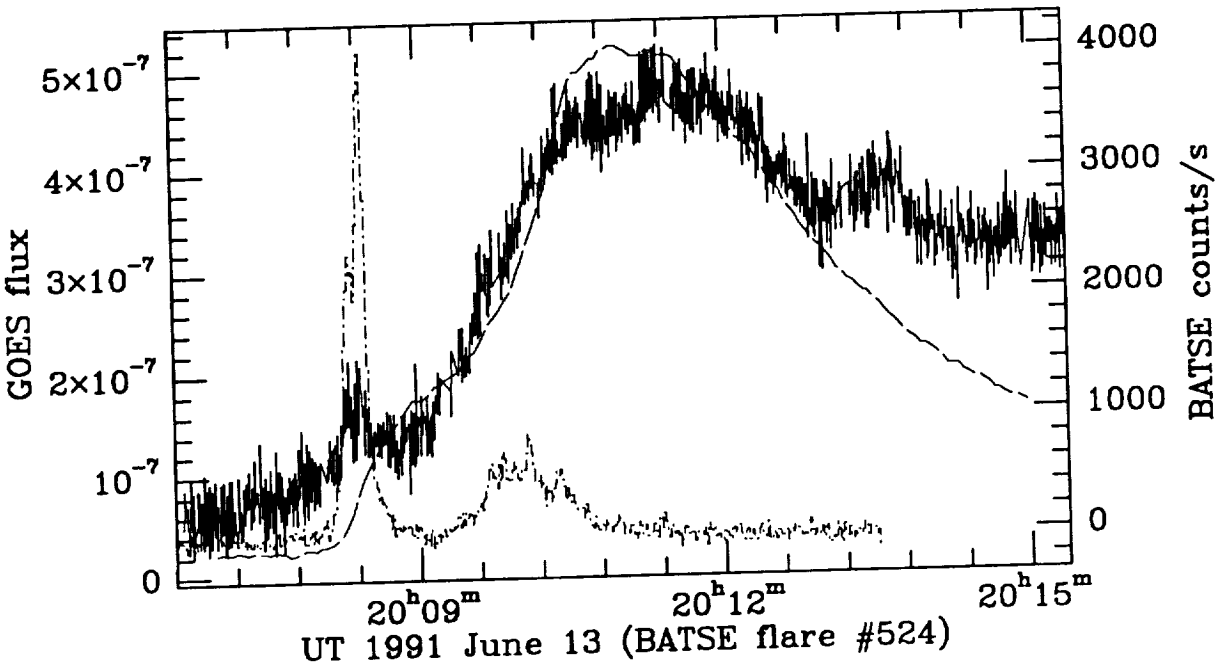

Figure 9 The soft X-ray, hard X-ray and 86 GHz time profiles of a flare at 20 UT on June 13. In this case the 86 GHz emission shows a faint enhancement at the time of the 25 – 50 keV impulsive phase, but is dominated by the thermal decay phase.

emission and rises up into the corona, filling magnetic loops, expanding and producing soft X-rays. Soft X-ray observations show large scale loops at temperatures of millions to several tens of millions of K, covering a much larger area than the original footpoints where nonthermal energy was deposited. There is also soft X-ray emission associated with the preflare phase which indicates the presence of preflare heating, and which often seems to merge smoothly in time with the decay-phase soft X-ray emission.

With these observations we have clearly demonstrated that the millimeter emission provides diagnostics of both the most energetic electrons in solar flares as well as of the thermal decay phase. It does not always bear a close relationship with the 10 – 100 keV electrons. We have shown that there are clear delays between those electrons and the production of the higher energy electrons which radiate at millimeter wavelengths in the impulsive phase.

Thus with the millimeter observations combined with GRO hard X-ray/γ–ray data we will be able to address many problems central to flare physics:

(i) acceleration: The mechanism by which MeV electrons are accelerated is not understood. For example, do the MeV electrons arise naturally as part of the production of 10 – 100 keV electrons, or are they a secondary effect? One type of evidence that GRO will provide will be spectral breaks in the hard X-ray observations, where a different acceleration mechanism takes over. The complementary information provided by BIMA is a more sensitive diagnostic of the numbers of MeV electrons present, and when they are present.

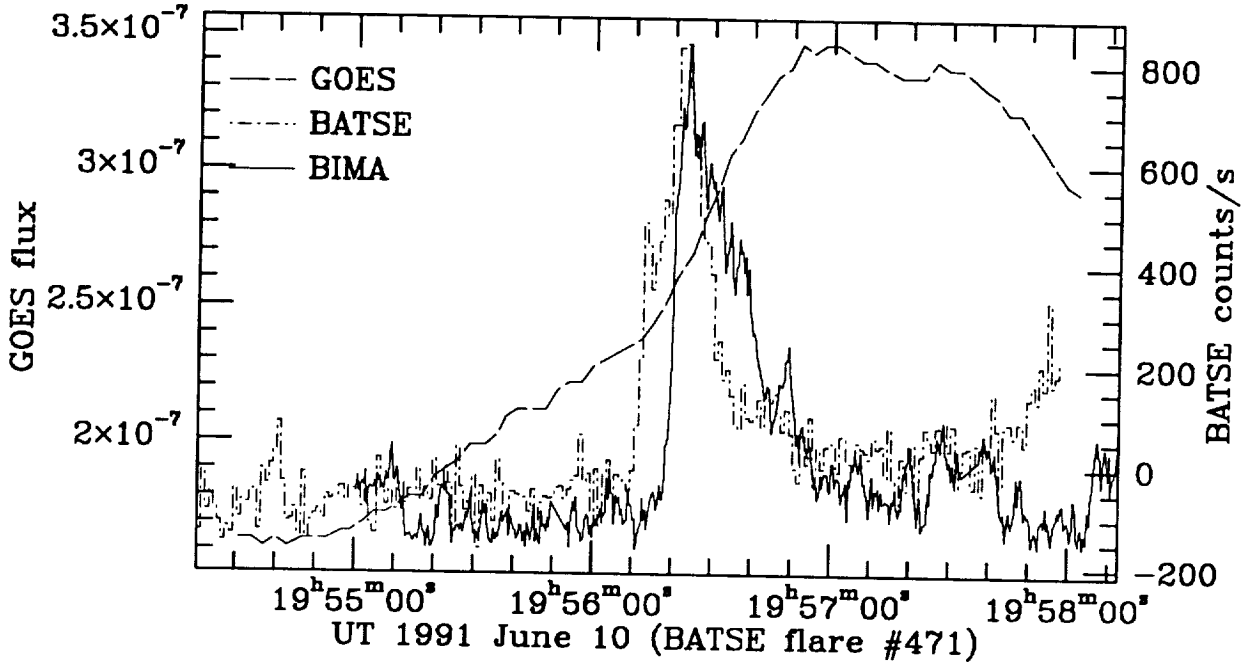

Figure 10 The soft X-ray, hard X-ray and 86 GHz time profiles of a flare at 20 UT on June 10. This small event was not given a GOES classification, and was barely noticeable in the usual log plots of soft-X-ray data. It shows a clear delay between the 86 GHz and hard X-ray profiles; the soft X-ray flux begins to rise well before the onset phase in hard X-rays.

The relationship of the MeV and keV electrons has been studied with SMM-GRS data, but we don't think the picture is at all clear. Millimeter observations give us a larger sample of flares to study than straight gamma-ray data; we can get a good estimate of the high-energy spectral index from radio data alone, and compare it with the lower-energy index derived from GRO data. This will allow us to study

(ii) delays, lifetimes: delays between BIMA (MeV electrons) and hard X-ray-emitting (25–50 keV) electrons will be important, since they can be interpreted as the time needed to accelerate electrons from 50 keV to 1 MeV, and thus can be compared with predictions of various models.

(iii) locations, source sizes: millimeter observations will provide images of the MeV electrons as long as they are in magnetic fields. The electrons might not strike the chromosphere at the footpoints of loops with strong fields because of magnetic mirroring. Do gamma ray-emitting electrons just occupy one loop or do they occupy several loops? Do γ-rays come from electrons precipitating in weak-field regions? This may require diffusion of electrons across field lines, usually a slow process. Are wave particle interactions needed to play a role?

Conclusions

Our 1991 June observations permit us to arrive at the following tentative conclusions.

1) There are two phases in millimeter burst emission: a nonthermal impulsive phase and a thermal gradual phase. Both phases are often observed in the same flare.
2) Impulsive-phase millimeter burst emission probes MeV electrons produced during flares. Some flares show no nonthermal impulsive phase at millimeter wavelengths, although they seem to show it at 25–50 keV electrons. These gradual phase flares correspond well to the GOES soft X-ray emission.
3) Even in flares which do show impulsive phase millimeter emission, correlation of the mm emission with electrons of 25 – 100 keV is often poor.
4) Millimeter emission usually occurs at the steep rise phase of the hard X-ray emitting electrons (25–100 keV). There appears to exist some delay between BIMA mm-emission onset and BATSE 25–100 keV X-ray data. Both results have implications in the particle acceleration process.

In 1992 the BIMA array will begin to operate with 6 dishes, providing 15 baselines. This will allow us to map the sources of 86 GHz emission in the impulsive phase of flares, and this should tell us a great deal about the spatial distribution and origin of the gamma-ray emitting electrons.

Acknowledgements

This work was made possible by NASA/GRO Phase I Guest Investigator grant NAG–5–1540. Partial support was also received from NASA grant NAG–W–1541 and NSF grant ATM 90–19893.

Bibliography

Kaufmann, P., Correia, E., Costa, J. E. R., Vaz, A. M. Z., & Dennis, B. R. 1985, *Nat*, **313**, 380.

Kundu, M. R., White, S. M., Gopalswamy, N., Bieging, J. H., & Hurford, G. J. 1990, *ApJL*, **358**, L69.

Ramaty, R. 1969, *ApJ*, **158**, 753.

Ramaty, R., & Petrosian, V. 1972, *ApJ*, **178**, 241.

White, S. M., & Kundu, M. R. 1992, *Solar Phys.*, in preparation.

Radio Synthesis Imaging During the GRO Solar Campaign

Dale E. Gary
Solar Astronomy 264-33, Caltech, Pasadena, CA 91125

ABSTRACT

The Owens Valley (OVRO) Solar Array has recently been expanded to 5 antennas. Using frequency synthesis, the 5-element OVRO Solar Array has up to 450 effective baselines, which can be employed as necessary to make maps at frequencies in the range 1 to 18 GHz. Fortuitously, the last of the 5 antennas was completed and brought into operation on 7 June, just in time for the GRO/Max '91 observing campaign.

Many events were observed jointly with OVRO and the BATSE experiment on GRO, including the six larger events shown in the accompanying table. Unfortunately, the X flares that occurred during the campaign all occurred outside the OVRO time range.

Table 1. BATSE Flares Observed With OVRO

BATSE Flare No.	Date (1991)	Time (UT)	GOES Class
433	06/09	2247	C4.4
464	06/10	1653	M3.2
499	06/11	2041	M5.3
508	06/12	1706	C7.7
544	06/14	1913	M1.6
599/600	06/16	2205	M1.1

The talk was accompanied by a 20 min video animation that introduced the ideas behind radio synthesis imaging. The technique of frequency synthesis is an extension of these ideas, and was also illustrated with the video. The *uv* coverage of the newly expanded Solar Array, combined with frequency synthesis, should give a more complete view of solar flares in the microwave range by providing simultaneous spatial and spectral resolution. A promising application of MEM (maximum entropy) is also being pursued that will use smoothness criteria in both the spatial and spectral domains to give brightness temperature maps at each observed frequency (up to 45 frequencies in every 10 s). Such maps can be compared directly with the theory of microwave emission to yield plasma parameters in the source—notably the number and energy distribution of electrons, for comparison with the X-ray and gamma-ray results from GRO.

VLA, PHOENIX and BATSE Observations of an X1 Flare

Robert F. Willson, Dept. of Physics and Astronomy, Tufts University, Medford, MA 02155
Markus J. Aschwanden, NASA/GSFC, Code 602.6, Greenbelt, MD 20771
Arnold O. Benz, Institute for Astronomy, ETH, CH-8082 Zürich, Switzerland

ABSTRACT: We present observations of an X1 flare (July 18, 1991) detected simultaneously with the Very Large Array (VLA), the PHOENIX Digital Radio Spectrometer and the Burst and Transient Source Experiment (BATSE) aboard the Gamma Ray Observatory (GRO). The VLA was used to produce snapshot maps of the impulsive burst emission on timescales of 1.7 sec at both 20 and 91 cm. Our results indicate electron acceleration in the higher corona (h$\approx$ 0.4 - 0.5$R_\odot$) several minutes before the onset of the hard X-ray burst detected by BATSE. Comparisons with high spectral ($\Delta\nu$= 3 MHz) and temporal (Δt = 40 ms) observations by PHOENIX reveal a variety of radio bursts at 20 cm, such as type III bursts, intermediate drift bursts, and quasi-periodic pulsations during differnt stages of the X1 flare. From the drift rates of these radio bursts we derive information on local density scale heights, the speed of radio exciters, and the local magnetic field. Radio emission at 90 cm shows a type IV burst moving outward with a constant velocity of 240 km/s.

The described X1 flare is unique in the sense that it appeared at the east limb (N06/E88), providing the most accurate information on the vertical structure of different flare tracers visible in radio wavelengths.

1. GOES and BATSE/GRO data

We present some preliminary data from the sofar largest flare simultaneously observed by VLA, PHOENIX and GRO, which occurred on July 18, 1991. A GOES X1-class soft X-ray event was reported near the east limb (North 06 , East 88) in NOAA/USAF active region 6734, starting at 1425 UT, with maximum at 1441 UT, and ending at 1519 UT. An Hα flare with importance 1N was detected during this time, associated with eruptive prominences and sprays.

BATSE recorded enhanced hard X-ray emission (> 25 keV) after 1425:34, which was interrupted by GRO spacecraft night from 1430:10 until 1503:00 UT, and lasted until 1510:10 UT. The BATSE hard X-ray time profile (Fig. 1) shows two peaks in the early rise of the impusive phase, and the end of the decay phase, while most of the main flare phase was missed during spacecraft night. The major HXR peak at 1429-1430 UT is correlated with a group of fast-drifting bursts at > 1.3 GHz.

2. VLA observations

The VLA observations were made at ν= 1441.6 MHz (20.8 cm) and 333 MHz (90 cm) with bandwidths of 3.25 MHz and a time resolution of 1.66 seconds. At the time of these observations, the VLA was in the A configuration which provided synthesized beamwidths of $\approx$ 1" at 20.8 cm and $\approx$5" at 90 cm.

Radio emission at 90 cm indicates impulsive and relatively low-intensity bursts (10-15 SFU) beginning at 14:19 UT, or about three minutes after the first enhancements of soft X-ray emission and about six minutes before the start of the BATSE hard X-ray burst. These metric bursts are located at different locations at heights of h = 0.4 - 0.5 $R_\odot$ above the limb (Fig. 2). They have angular sizes of $\approx$ 1.5' and peak brightness temperatures of T_b = 3.4 - 6.7 x 10^7 K.

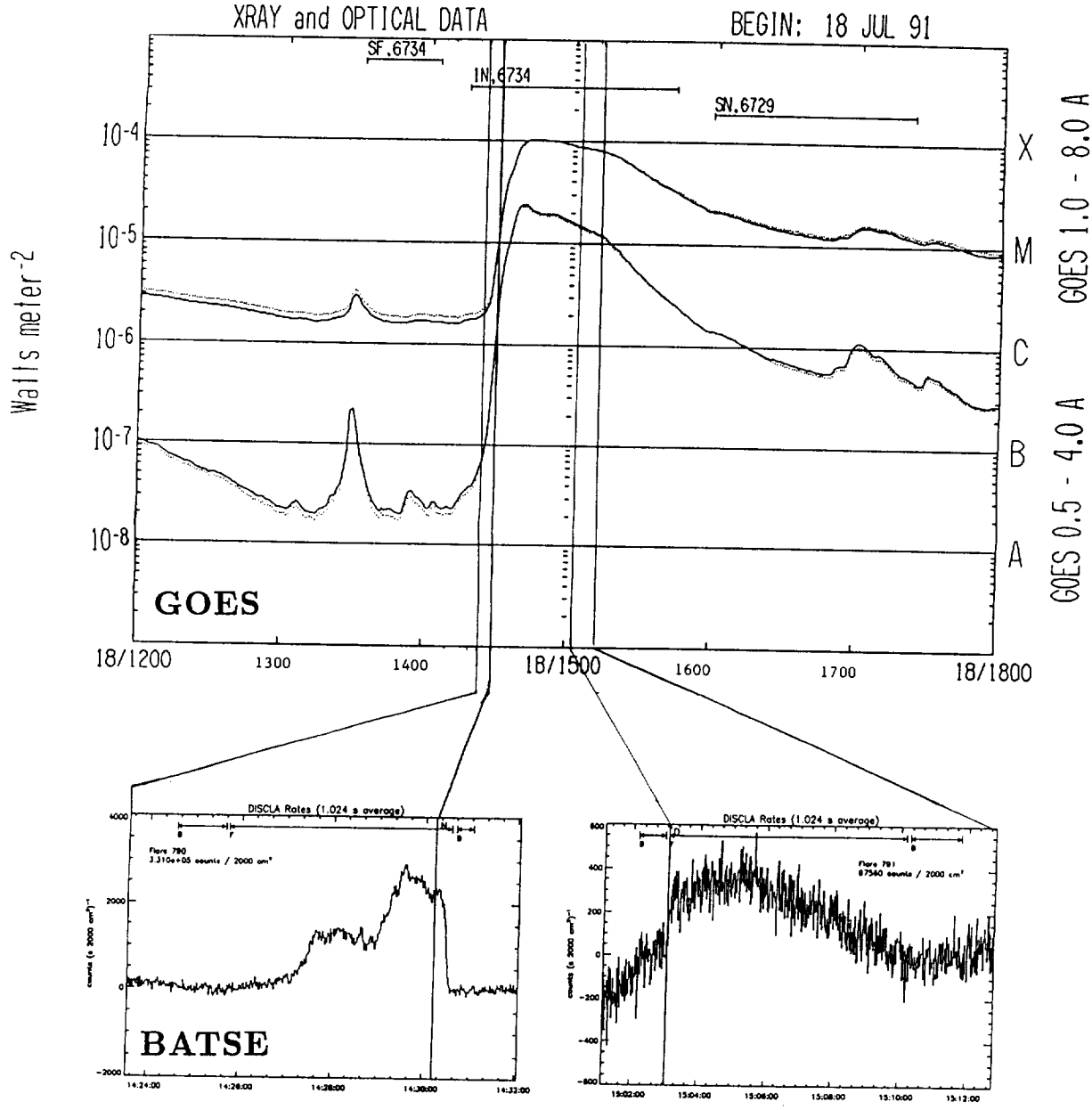

Fig. 1: *Time profile of the GOES soft X-ray data (0.5-4.0 and 1.0-8.0 Angstrom) and BATSE/GRO hard X-ray data (25-1000 keV) during the X1 class event on 1991 July 18, 1425-1510 UT. GRO observations are intermitted by spacecraft night from 1430 to 1503 UT.*

Between 14:40 - 14:50 UT, an intense 90 cm burst was observed to move systematically outward from the Sun with a velocity of $\approx$ 240 km s^{-1} (Fig. 3). This outward movement is characteristic for a moving Type IV burst. 90 cm sources associated with slowly-varying emission during the decay phase of the soft X-ray burst show no systematic movement, but again, are located at heights of h$\approx$ 0.4$R_\odot$ above the limb.

The time profile of 20 cm emission is depicted in Fig. 4 (top). Maps of the 20 cm emission during the times of maximum brightness (14:35:19 UT, 14:35:53 UT) show that the burst consists of at least two components (T_b = 2.8 x 10^7 K) which are located at heights of h $\approx$ 0.2$R_\odot$ (Fig. 2). The PHOENIX spectrometer data reveal a "broadband, quasi-periodic pulsation event" during this period of time.

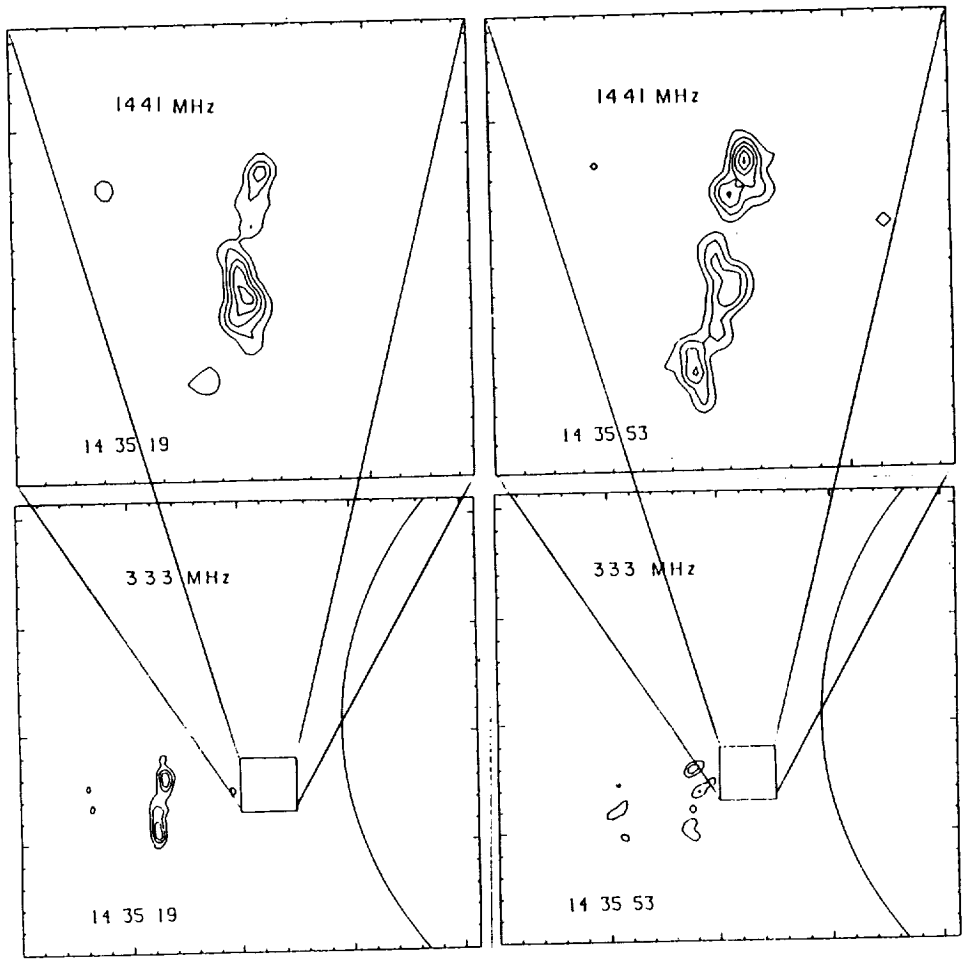

Fig. 2: *VLA snapshot maps with 3.3 s time resolution of total intensity at 1441 MHz (top) and 333 MHz (bottom) at the times indicated. The contours mark levels of equal brightness temperature, with an outermost contour and contour interval of T_b = 5.0 x 10^6 K at 1441 MHz and T_b = 8.4 x 10^6 K at 333 MHz. The fiducial marks are drawn at intervals of 10" for the 1441 MHz maps, and 60" for the 333 MHz maps. The boxes drawn on the 333 MHz maps denote the field of view of the 1441 MHz maps.*

3. PHOENIX observations

The frequency-agile PHOENIX broadband spectrometer of ETH Zurich (Switzerland) was operated in two frequency bands around the VLA frequencies 333 MHz and 1441 MHz: 20 frequencies with 3 MHz resolution in the 300-360 MHz range, and 60 frequencies with 10 MHz resolution in the 1150-1750 MHz band. The sweep spectrometer was operated with a time resolution of 40 ms. Both circular polarizations Stokes I and V are recorded, with a sensitivity of a few SFU at full time resolution. The PHOENIX spectrometer provides unique complementary information to VLA observations, such as high time resolution, broadband frequency spectra, and frequency-time drift rates.

The coregistered radio flux from VLA and PHOENIX is shown in Fig. 4 for the main flare phase, at the same frequency of 1441 MHz and with similar bandwidth ($\approx$10 MHz) in both instruments. The RCP correlated flux of the shortest VLA baseline is compared with Stokes I of the full sun disk observation of PHOENIX. The broadband PHOENIX data reveal a considerable variety of radio bursts: **type III bursts** in the metric 0.30-0.35 GHz band; **type IIIdm, quasi-periodic pulsations**, and **intermediate drift bursts** in the decimetric 1.2-1.7 GHz band. Enlarged dynamic spectra of two episodes are displayed in Fig. 5.

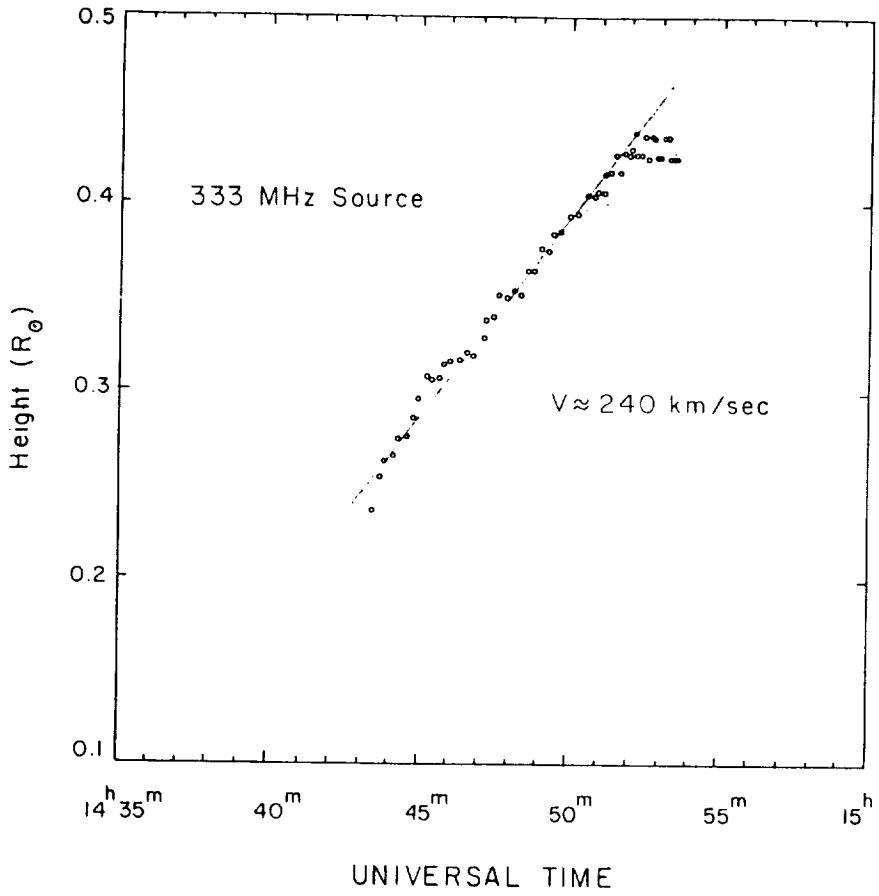

Fig. 3: *A plot of height versus time for the outwardly-moving 333 MHz source shown in Figure 2. The solid line represents a constant-speed fit to the data.*

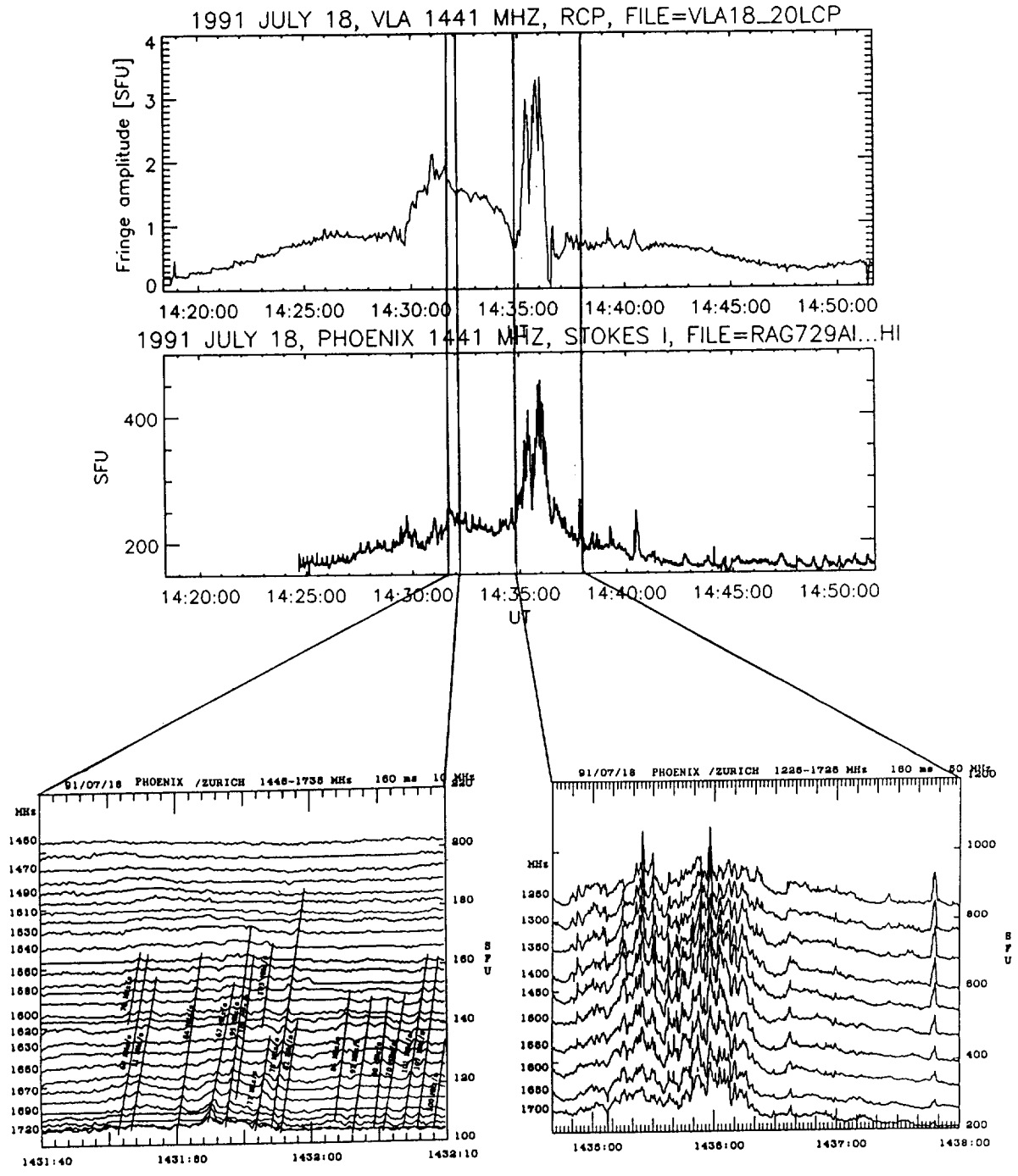

Fig. 4: *Comparison of VLA (top) and PHOENIX (middle) observations at 1441 MHz. The two enlargements (bottom) show broadband dynamic spectra of the "intermediate drift bursts" (bottom left) and of the "quasi-periodic pulsation" event (bottom right). The time resolution is 3.3 s (VLA, top), 0.04 s (PHOENIX, middle), and 0.16 s (PHOENIX, bottom). Note that the brightest radio emission during the flare is related to the quasi-periodic pulsation event.*

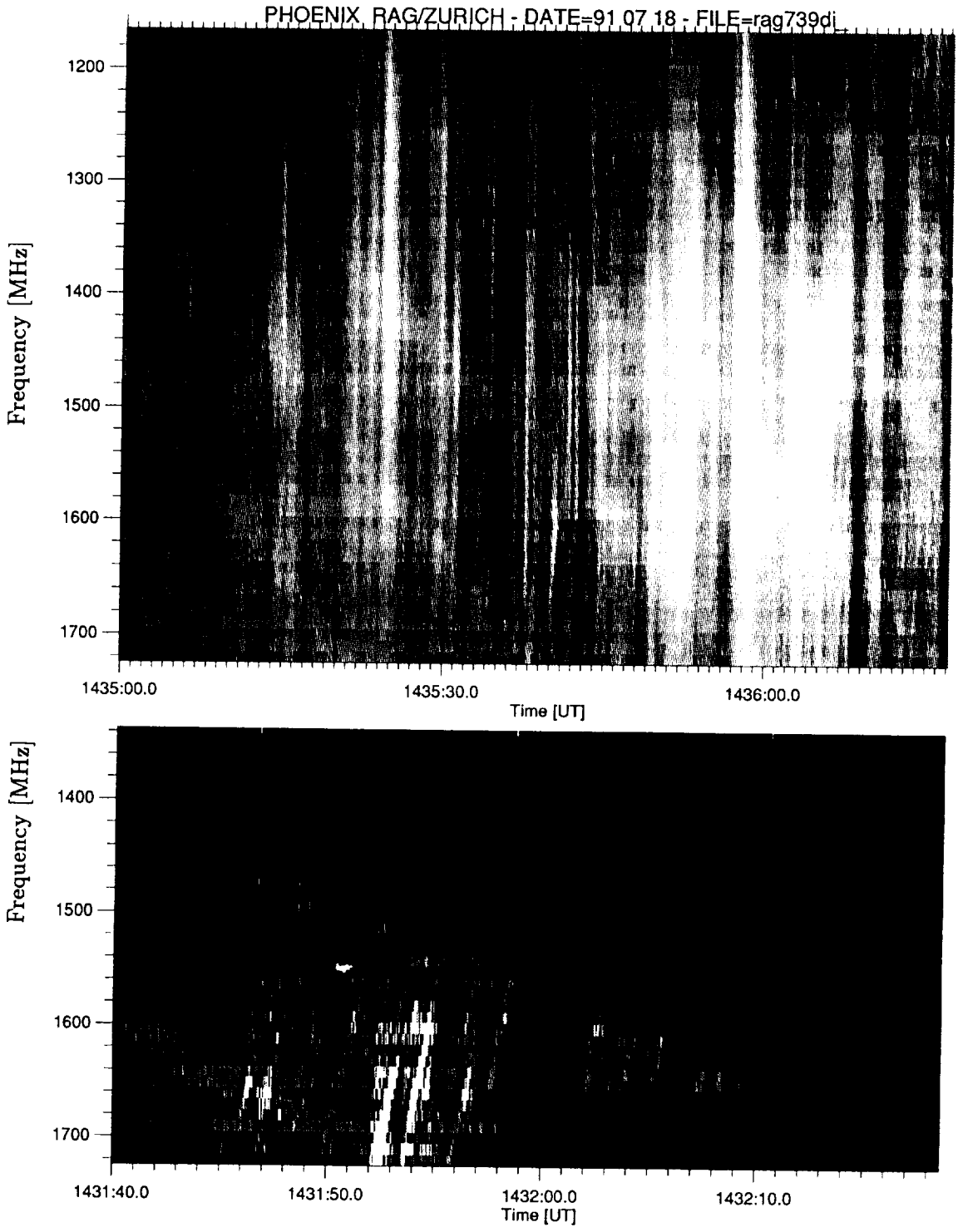

Fig. 5: *PHOENIX broadband observations at 1165-1725 MHz during the impulsive phase of the X1 flare. The white color in the grayscale indicates enhanced emission. The episode of "broadband quasi-periodic pulsations" at 1435-1437 UT is shown on top. Weak "intermediate drift bursts" are visible during 1431-1432 UT (bottom).*

3.1 Broadband, decimetric, quasi-periodic pulsations

The brightest radio emission at 20 cm occurs during 1435:00-1436:30 UT. While the VLA does not resolve many individual pulses, a total of about 80 pulses is identified in the PHOENIX record, with individual pulse durations of 1-2 s and frequency bandwidth of $\gtrsim 500$ MHz (Fig. 5). The frequency-time drift rate of these pulses has been measured with an automatic pattern recognition code, showing a symmetric distribution for positive and negative drift rates, where 80% of the pulses have a drift rate of $|d\nu/dt| \gtrsim 1000$ MHz/s. Monte-Carlo simulations of frequency-time drift rates with similar distributions have shown that the exciters of such radio emission originate in coronal structures with scale heights of $2 \cdot 10^3 - 2 \cdot 10^4$ km (Aschwanden and Benz, 1986). This is in good agreement with the spatial scale measured by the VLA, which is $\approx 7 \cdot 10^3$ km (10") for the half width of the 20 cm emission (Fig. 2, top) during the brightest pulses. This spatial scale probably corresponds to the transverse cross-section of large loops extending to heights of $\gtrsim 0.2 R_\odot$. Assuming plasma emission, the location of the 20 cm source corresponds to a density of $\gtrsim 10^{10}$ cm^{-3}. The time interval of the radio pulsation coincides roughly with the time of the steepest derivative in the soft X-ray time profile (Fig. 1), indicating the maximum heating rate during the flare, usually synchronized with the peak of hard X-ray emission. The characteristics of the pulsating radio time profile indicate the nonlinear dynamics of the underlying energy release mechanism (see review by Aschwanden, 1987); they cannot be explained by MHD eigen-modes which have much stricter periodicity.

3.2 Intermediate drift bursts

During the rise time of the impulsive flare phase we detected intermediate drift bursts with drift rates of ≈ -80 MHz/s (Fig 4,5). These bursts are detected for the first time in this high frequency range at 1.5-1.7 GHz. The normalized drift rate $(d\nu/dt)/\nu \approx 0.05$ is consistent with intermediate drift bursts found in the metric and decimetric range, also called "fibre" bursts. They represent a frequent fine structure of type IV bursts and can be used for diagnostics of the magnetic field. In current models they are interpreted in terms of Alfven wave solitons (Treumann et al. 1990) or whistler wave trains (Mann et al., 1987). 3D reconstruction of the magnetic field (using the Sakurai code) and the electron density (using the diagnostics from plasma emission of simultaneously localized type III bursts) should allow us for the first time to decide between the two theoretical models and to exploit their diagnostic potential.

Acknowledgements Solar radio and X-ray studies of the Sun at Tufts University are supported by NASA grant NAGW-2383 and by grant AFOSR-89-0147 with the Air Force Office of Scientific Research. The work at NASA/GSFC was performed under grant NAS5-30442 at USRA. The VLA is operated by Associated Universities, Inc., under contract with the National Science Foundation.

References

Aschwanden,M.J. 1987, Sol.Phys., 111, 113.
Aschwanden,M.J. and Benz, 1986, A&A, 158, 102.
Mann,G., Karlicky,M., and Motschmann,U. 1987, Sol.Phys., 110, 381.
Treumann,R.A., Güdel,M. and Benz,A.O. 1990, A&A, 236, 242.

Gamma-Ray and Microwave Emission from 1991 June Events

Shinzo Enome, Hiroshi Nakajima (NRO),
Hugh S. Hudson (UCSD), Richard Schwartz (GSFC)

ABSTRACT

The Sun showed unprecedented microwave activities in June 1991, which produced four major and numerous weaker bursts observed in Japan. Comparison is made between these microwave bursts and gamma-ray emission measured by the Gamma Ray Observatory.

The 1991 June 4 event shows a sharp maximum around 03:41 UT and weak emission a few minutes before the maximum in the gamma-ray record of the BATSE experiment, with a preliminary estimated energy of 5 MeV. Although the 80-GHz record also shows a similar time profile, 17-GHz and possibly 35-GHz records show more prominent emission in the pre-maximum stage. This strongly suggests the first observational evidence for gamma-ray and mm-wave emission from relativistic electrons.

Comparisons of other three major events on June 6 at 01:00 UT, June 9 at 01:34 UT, and June 11 at 01:51 UT between gamma-ray and microwave emission are also in progress, and results of analyses will be reported together, possibly, with statistics of transient emission of a wide range of sizes in both gamma rays and microwaves.

Flare γ-ray continuum emission from neutral pion decay

David Alexander and Alec L. MacKinnon
Department of Physics and Astronomy
University of Glasgow
Glasgow G12 8QT
Scotland, U.K.

Abstract

We investigate in detail the production of solar flare gamma ray emission above 10MeV via the interaction of high energy protons with the ambient solar atmosphere. We restrict our considerations to the broad-band gamma ray spectrum resulting from the decay of neutral pions produced in p-H reactions. Thick-target calculations are performed to determine the photon fluences. However, proton transport is not considered. Inferences about the form of the proton spectrum at 10-100MeV have already been drawn from de-excitation gamma ray lines. Our aim is to constrain the proton spectrum at higher energies. Thus the injected proton spectrum is assumed to have the form of a Bessel Function, characteristic of stochastic acceleration models, up to kinetic energies of a few hundred MeV, coupled to a power-law in proton kinetic energy at higher energies. The detailed shape of the gamma ray spectra around 100 MeV is found to have a strong dependence on the spectral index of the power-law and on the turnover energy (from Bessel function to power-law). As would be expected the harder the proton spectrum the wider the 100 MeV feature. The photon spectra are to be compared with observations and used to place limits upon the number of particles accelerated and to constrain acceleration models.

Gamma ray production

We require the production spectrum of γ-ray photons from the decay of secondary π^o produced in p-H collisions in solar flares. This is given by

$$F_{pH}(\varepsilon_\gamma) = \frac{2S}{R^2}\int_{\varepsilon_\gamma+\frac{m_\pi^2}{4\varepsilon_\gamma}}^{\infty}\frac{dE_\pi}{p_\pi}\int_{T_{p,min}}^{\infty}dT_p.j_p(T_p)\int_{T_{p,min}}^{T_p}\frac{d\sigma(T_p',T_\pi)}{dT_\pi}\frac{T_p'}{K}dT_p' \qquad (1)$$

where the integral over T_p' expresses the total number of pions per unit energy emitted by an average proton in time t, i.e. it allows for the proton spectrum to be modified by thick-target losses as the protons traverse the flaring loop; $j_p(T_p)$ [protons/cm^2/s/GeV] is the incident proton spectrum; $K = 2\pi e^4(m_p/m_e)\Lambda$ (Λ is the Coulomb logarithm relevant to protons); S is the flare area, typically 10^18cm^2; R=1AU; E_π/p_π are the total pion energy/momentum; T_p is the proton kinetic energy and $T_{p,min}$ is the minimum kinetic energy required by a proton in the lab. system to produce a pion of kinetic energy T_π. The differential cross-section for the production of a pion with energy T_p is given by

$$\frac{d\sigma(T_p,T_\pi)}{dT_\pi} = \langle\zeta\sigma(T_p)\rangle\frac{dN(T_p,T_\pi)}{dT_\pi} \qquad (2)$$

where $\langle\zeta\sigma(T_p)\rangle$ denotes the inclusive cross-section for the reaction $p+p \rightarrow \pi^o$+ anything and (dN/dT_π) is the normalised production spectrum of secondary π^o . We have ignored contributions from collisions of protons with alpha particles and heavier ions.

Pion production

The production mechanism for π^o from p-p collisions is dependent upon the kinetic energy of the incident protons. Comparison of the various models with accelerator data at various energies show that the production mechanism can be split into three distinct regions (Dermer 1986):

$T_p < 3GeV$: Isobar model (Stecker 1970)

- pion production mediated by excitation of the $\Delta(1232)$ isobar which decays into a proton and a neutral pion. The distribution of pions from this decay mechanism is effectively isotropic in the lab. system.

$$\frac{dN}{dT_\pi} = \omega_r(T_p) \int_{m_p+m_{\pi^o}}^{s^{1/2}-m_p} dm_\Delta . B(m_\Delta) . f(T_\pi; T_p, m_\Delta) \tag{3}$$

where

w_r is a normalisation factor.
B is the isobar mass distribution given by a Breit-Wigner distribution.
f is the normalised energy spectrum of pions in the laboratory system.
s is the total energy availbale in the centre-of-mass.

$T_p > 7GeV$: Scaling model (Stephens and Badhwar 1981)

- pion production obtained via scaling arguments which imply asymptotic forms for the differential cross-sections

$$\frac{dN}{dT_\pi} = \frac{2\pi p_\pi}{\langle \zeta \sigma(T_p) \rangle} \int_{cos\theta_{max}}^{1} dcos\theta \left(E^* \frac{d^3\sigma^*}{dp^{3*}} \right) \tag{4}$$

where $E^*(d^3\sigma^*/dp^{3*})$ is the invariant cross-section for neutral pion production in p-p collisions (the asterisk denotes centre-of-mass quantities) and $cos\theta_{max}$ may be obtained from kinematic limitations.

$3GeV < T_p < 7GeV$:

Between these two limiting energies neither of the above models fit the laboratory data very well and so we follow Dermer (1986) and extrapolate the normalised production spectrum linearly between these two limits.

Incident proton spectrum

Our choice of proton spectrum incident upon the target region is such that we have a Bessel function spectrum, characteristic of stochastic acceleration processes, up to some kinetic energy T_{p0} which is typically of the order of 100MeV since stochastic acceleration is only valid in the non-relativistic regime and a power-law spectrum at higher energies, viz.,

$$j_p(T_p) = A_N K_2[2(3p_p/m_p \alpha T)^{1/2}] \qquad T_p < T_{p0}$$

$$= A_N K_2[2(3p_{p0}/m_p \alpha T)^{1/2}](T_p/T_{p0})^{-\delta} \qquad T_p > T_{p0}$$

where

A_N is a normalisation factor to be determined from comparison with observations .
K_2 is the modified Bessel function (cf. Ramaty and Murphy 1987).
α is the acceleration efficiency.
T is the particle escape time from the acceleration region .
[typical value from fits to observations is $\alpha T = 0.02 - 0.04$]
T_{p0} is the turnover energy from Bessel function to power-law .

Results

In this section we display the form of our spectra for a variation of the spectral parameters, δ (the power-law spectral index) and αT (the hardness of the Bessel function spectrum), for a turnover energy equal to the threshold energy for pion production, $T_{p0} = 280MeV$, and the resulting photon spectra. We have also included the photon spectra obtained from a variation of T_{p0} with $\alpha T = 0.04$ and $\delta = -4$.

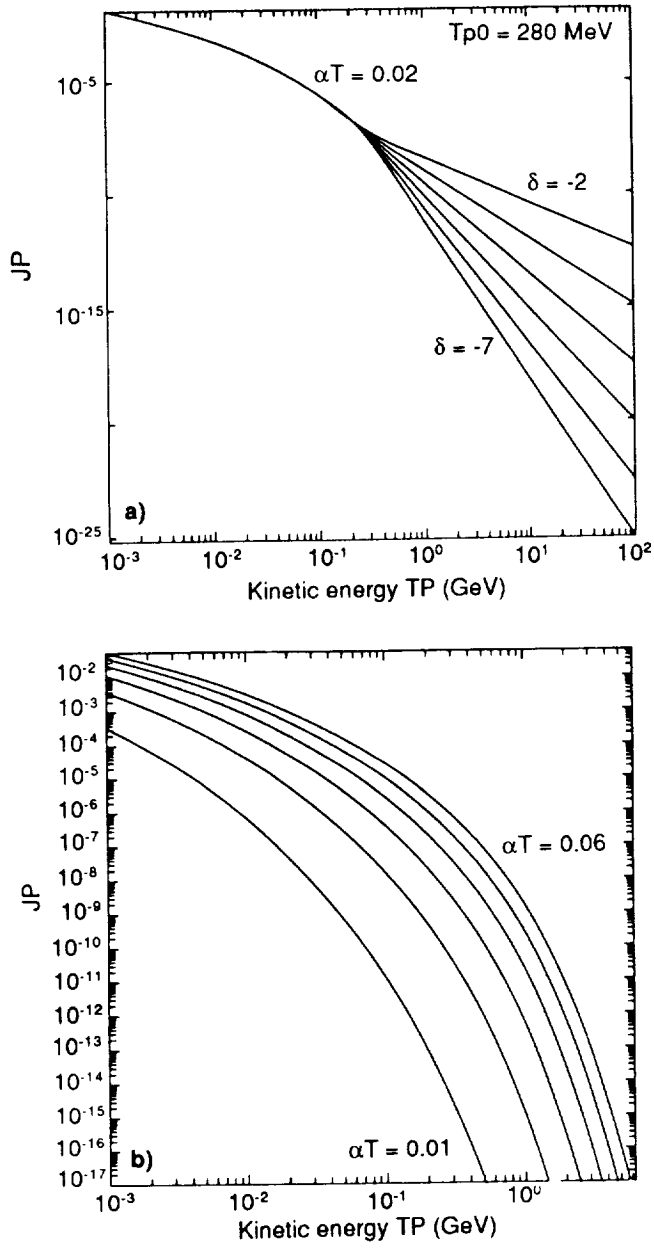

Figure 1: Injected proton spectra, J_p(protons/GeV/cm^2/s) **a)** Bessel function with $\alpha T = 0.02$ for $T_p < 280MeV$ (pion production threshold) and power-law of spectral index δ at higher energies. **b)** Bessel function spectra with range of spectral hardness αT (as **a** with turnover energy = ∞).

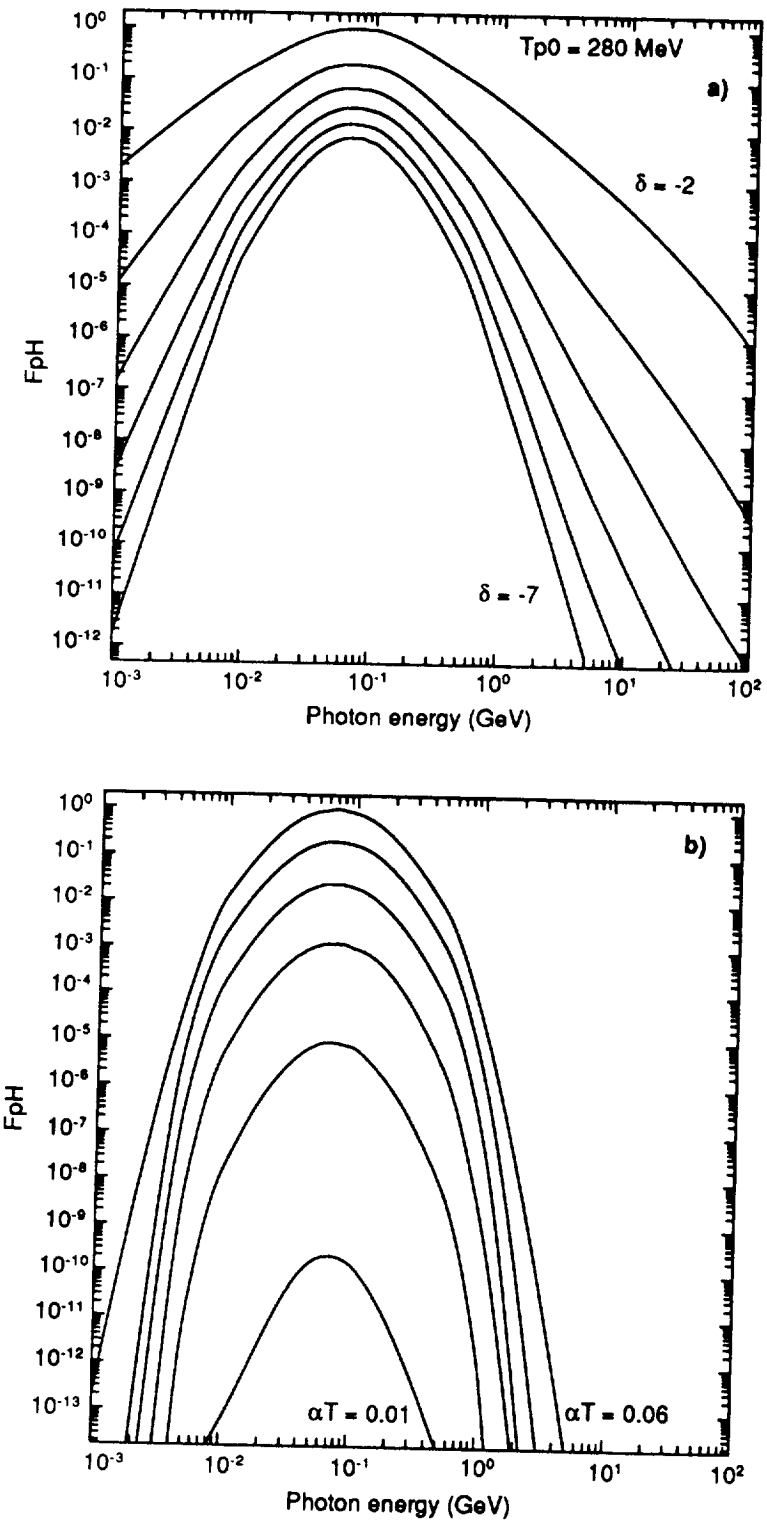

Figure 2: Gamma-ray spectra, FpH (photons/GeV/cm^2/s) resulting from the proton spectra shown in Figures 1. **a)** Bessel function/power-law spectra. **b)** Bessel function spectra.

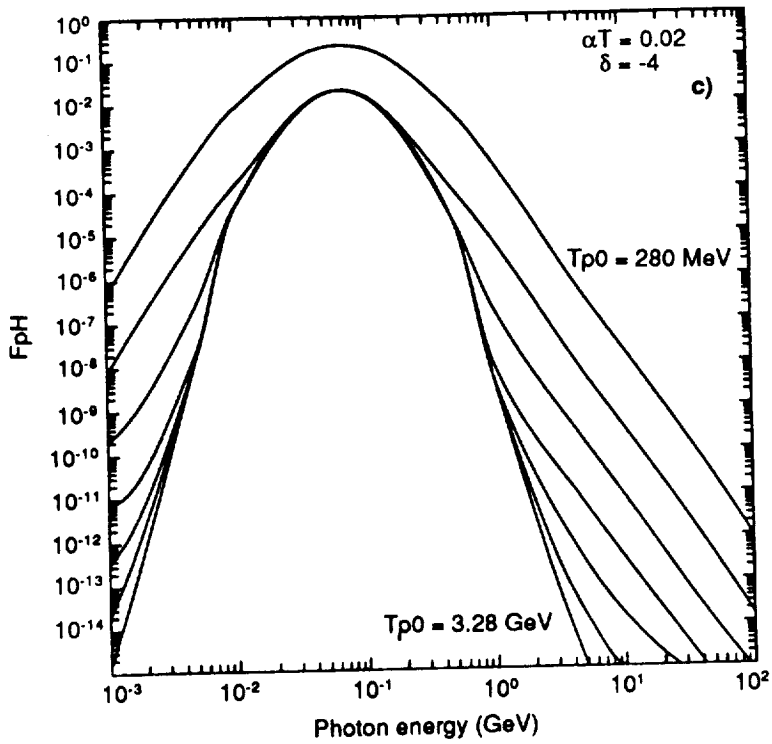

Figure 2c: Gamma-ray spectra, FpH (photons/GeV/cm^2/s) resulting from proton spectra similar to those of Figure 1a with a fixed $\delta = -4$ and $\alpha T = 0.02$ and the turnover energy T_{p0} allowed to vary.

Discussion and Conclusions

Our theoretical calculations show that the detailed structure of the 70MeV feature depends strongly upon the form of the accelerated proton spectrum at energies from 100MeV to a few GeV. The harder the proton spectra the wider the pion decay feature as one would expect. However, until a detailed comparison of our results are made with observation our conclusions are limited. There are a few observations which demonstrate a strong (possibly dominant) pion emission at energies of around 100MeV. Events such as the SMM event of June 3 1982 (studied in detail by Murphy et al. 1987) and possibly a couple of events from 1989 (Rieger - private communication) allow us some evidence for a neutral pion decay feature flattening the spectrum at ~70MeV. We intend to investigate these observations in more detail. Solar observations by the TASC spectrometer on The Compton Observatory should hopefully provide many more such data.

References

Dermer, C.D., 1986, *Astron. Astrophys.*, **157**, 223.
Murphy, R.J. et al., 1987, *Astrophys. J.*, **263**, 721.
Ramaty, R. and Murphy, R.J., 1987, *Space Science Rev.*, **45**, 213.
Stecker, F.W., 1970, *Astr. Space Science*, **6**, 377.
Stephens, S.A. and Badhwar, G.D., 1981, *Astr. Space Science*, **76**, 213.

Prompt Particle Acceleration around Moving X-point Magnetic Field during Impulsive Phase of Solar Flares

Jun-ichi Sakai
Laboratory for Plasma Astrophysics and Fusion Science
Department of Electronics and Information
Faculty of Engineering, Toyama University
Toyama 930 JAPAN

Abstract

We present a model for high-energy solar flares to explain prompt proton and electron acceleration, which occurs around moving X-point magnetic field during the implosion phase of the current sheet. We derive the electromagnetic fields during the strong implosion of the current sheet, which is driven by the converging flow toward the center of the magnetic arcade. We investigated test particle motion in the strong electromagnetic fields derived from the MHD equations. It is shown that both protons and electrons can be promptly(within 1 s) accelerated to ~ 70 MeV and ~ 200 MeV, respectively. This acceleration mechanism can be applicable for the impulsive phase of the gradual gamma ray and proton flares(gradual GR/P flare), which have been called *two-ribbon flares*.

1. Introduction

One of the important problems in high-energy solar flare physics is to understand the physical mechanism(s) of high energy particle acceleration during solar flares. From the observations by SMM and Hinotori satellites, it became clear that there are two classes of gamma-ray/proton(GR/P) flares- impulsive GR/P flares and gradual GR/P flares(see, for a review , Bai and Sturrock 1989). The GR/P flares refer to flares that produce nuclear gamma-rays and /or energetic interplanetary protons. Most short flares(< 100 s) corresponds to be impulsive GR/P flares, while most of the long-duration flares(> 200 s) corresponds to the gradual GR/P flares. In the impulsive GR/P flares there are two phases of particle acceleration : the first phase is that both electrons and protons are accelerated to ~ 10 MeV and to ~ 100 MeV energies , respectively, within 1 s (Kane et al. 1986; Riger 1989), and second phase is that electrons up to 100 MeV and protons up to GeV energies are accelerated within a few seconds to 100 s.

In order to explain the above prompt particle acceleration to relativistic energies, Sakai(1990) showed that during the 3D X-type current loop coalescence, where two crossed flux tubes interact in one point, both protons and electrons can be promptly(within less than 1 s) accelerated to ~ 100 GeV and ~ 100 MeV, respectively. De Jager and Sakai (1991) showed that the burst duration of elementary flare bursts(5-25 s) observed during the impulsive GR/P flares can be explained quantitatively by the mechanism of the 3D X-type current loop coalescence.

In the present paper we show a model for the long-duration gamma ray /proton flare(the gradual GR/P flares) to explain prompt proton and electron acceleration during the impulsive phase. These flares have been called *two-ribbon flares* and almost all gradual GR/P flares show impulsive behaviour in the beginning of the hard X-ray emission and gradual behaviour later on (Bai and Sturrock 1989). In most large two-ribbon flares with filament eruptions the filament begins to move up several minutes or more before the onset of the impulsive phase(Martin and Ramsey 1972; Kahler et al. 1988). Recently Sakai and Koide (1991) presented a theory of the filament eruption before the impulsive phase of solar flares. Figure 1 shows a schematic picture of the global magnetic field configuration and the filament which is located above the X-point magnetic configuration near the center of the magnetic arcade. Sakai and Koide (1991) showed that the upward motion of the X-point which may trace the filament eruption begins several minutes before the impulsive phase where the magnetic field, Bx produced by the current near the X-point can exceed the magnetic field, Bz along the filament. If the Bx exceeds the Bz, then the explosive magnetic reconnection (Tajima 1982; Sakai et al. 1984; Sakai and Ohsawa 1987) can be triggered in the current sheet. During the implosion phase of the current sheet, the strong electric field can be induced by the strong converging flow around the X-point.

In Section 2 we drive the electromagnetic fields during the implosion phase of the current sheet from the MHD equation. In Section 3 we investigate a test proton and electron motion under the electromagnetic fields derived in the previous section. We will show that both protons and electrons can be promptly accelerated within 1 s to ~ 70 MeV and ~ 200 MeV, respectively. In Section 4 we summarize our results.

2. Electromagnetic Fields around Moving X-point

2.1 MHD Equation and Energy Equation

In this section we present basic equations describing the dynamics of the current sheet near the magnetic X-point, which is located under the filament as shown in Figure 1. We assume that the filament is supported in the upper part of the X-type magnetic field along the z-direction, in which there exists the magnetic field, Bz. Following the gradual shearing motion at the footpoint of the magnetic arcade, the plasma upward motion can be induced, and the current near the X-point can be increased due to the converging flow near the current sheet. The current sheet continues to elongate to the vertical direction, and to become thin in the horizontal direction. We will focus on the dynamics of the plasma around the X-point to determine the electromagnetic fields during thinning of the current sheet. The x-axis is taken in the vertical direction, and the y-axis is in the horizontal direction. The current sheet is assumed to be homogeneous in the horizontal z-direction.
We begin from the following MHD equations including the gravity and Joule heating effect in the energy equation;

$$\frac{\partial \rho}{\partial t} + \nabla \cdot (\rho \mathbf{v}) = 0 \quad , \tag{1}$$

$$\rho\left(\frac{\partial \mathbf{v}}{\partial t} + \mathbf{v} \cdot \nabla \mathbf{v}\right) = -\nabla P + \frac{1}{4\pi}(\nabla \times \mathbf{B}) \times \mathbf{B} - \rho g \vec{e}_x \quad , \tag{2}$$

$$\frac{\partial \mathbf{B}}{\partial t} = \nabla \times (\mathbf{v} \times \mathbf{B}) + \frac{c^2}{4\pi\sigma}\Delta \mathbf{B} \quad , \tag{3}$$

$$\frac{\partial P}{\partial t} + (\mathbf{v} \cdot \nabla) P + \gamma P \nabla \cdot \mathbf{v} = (\gamma - 1)\frac{(\nabla \times \mathbf{B})^2}{16\pi^2 \sigma} \quad , \tag{4}$$

where r , v, P, B are the density, velocity, pressure, and magnetic field, respectively, and γ is the adiabatic constant. The gravitational acceleration is given by

$$g(x) = g_0\left(1 + \frac{x^2}{R^2}\right)^{-2} \quad , \tag{5}$$

where $R = R_S + r_0$ and $g_0 = GM_S R^{-2}$. M_S , R_S and r_0 are the solar mass, solar radius and distance to the origin of the coordinate from the solar surface, respectively. The right-hand side in Equation (4) shows the effect of the Joule heating.

2.2 Electromagnetic Fields around the Current Sheet

During the gradual shearing motion of the photosphere, the current near the magnetic X-point can increase due to horizontal plasma inflows from both sides. This horizontal plasma flow, v_y around the X-point can be approximately given by

$$v_y = \left(\frac{1}{a}\right)\left(\frac{da}{dt}\right)y \quad , \tag{6}$$

where a(t) is a time dependent scale factor. The scale factor a(t), which is determined later, characterizes continuous change of thickness of the current sheet due to the plasma inflows. The vertical flow, v_x is taken to be

$$v_x = v_{x0} + \left(\frac{1}{b}\frac{db}{dt}\right)x \quad , \tag{7}$$

where $v_{x0}(t)$ and another scale factor b(t) are determined self-consistently later.

The components of the magnetic field are taken as

$$B_x = B_{x0}(t)\frac{y}{\lambda} \quad , \tag{8}$$

$$B_y = B_n(t) + B_{y0}(t)\frac{x}{\lambda} \quad , \tag{9}$$

$$B_z = B_{z0}(t) \quad , \tag{10}$$

where λ is a characteristic scale-length of the current sheet, which can be considered to be the same as the radius of the filament located above the X-point. The magnetic field B_n in Equation (9) shows a role that the X-point can move during the evolution of the current sheet. Unknown functions, B_{x0}, B_n, B_{y0} and B_{z0} can be determined, self-consistently later.

Substituting Equations (6) and (7) into Equation (1), we find that the density $\rho(t)$ is only a function of time and given by

$$\rho(t) = \frac{\rho_0}{a(t)b(t)} \quad , \tag{11}$$

where ρ_0 is a constant.

From the induction equation (3), using the expression for the magnetic fields (8)-(10) and velocities (6) and (7), we find

$$B_{x0} = \frac{B_0}{a^2} \quad , \tag{12}$$

$$B_{y0} = \frac{B_0}{b^2} \quad , \tag{13}$$

$$B_{z0} = \frac{B_{00}}{ab} \quad , \tag{14}$$

$$\frac{dB_n}{dt} + \frac{v_{x0}}{\lambda}\frac{B_0}{b^2} + B_n\frac{1}{b}\left(\frac{db}{dt}\right) = 0 \quad , \tag{15}$$

where B_0 and B_{00} are constants.

We assume the pressure P(x,y,t) to be

$$P(x,y,t) = P_{00}(t) - P_0(t)\frac{x}{\lambda} - P_{x0}(t)\left(\frac{x}{\lambda}\right)^2 - P_{y0}(t)\left(\frac{y}{\lambda}\right)^2 \quad . \tag{16}$$

We here summarize normalized basic equations, which will be numerically solved in the next section,

$$\frac{d^2a}{dt^2} = \frac{\beta_p}{a^\gamma b^{\gamma-1}} + \left(\frac{1}{b} - \frac{b}{a^2}\right) , \tag{17}$$

$$\frac{d^2b}{dt^2} = \frac{\beta_p}{a^{\gamma-1}b^\gamma} - \left(\frac{a}{b^2} - \frac{1}{a}\right) + G_1 b , \tag{18}$$

$$\frac{dB_{n0}}{dt} = -\frac{v_{x0}}{b^2} - B_{n0}\frac{1}{b}\frac{db}{dt} , \tag{19}$$

$$\frac{dv_{x0}}{dt} = -v_{x0}\frac{1}{b}\frac{db}{dt} + \beta_p abP_0 - abB_{n0}\left(\frac{1}{b^2} - \frac{1}{a^2}\right) - G_2 , \tag{20}$$

$$\frac{dP_0}{dt} = -P_0\frac{1}{b}\frac{db}{dt} - \frac{2v_{x0}}{a^\gamma b^{\gamma+2}} - \gamma P_0\left(\frac{1}{a}\frac{da}{dt} + \frac{1}{b}\frac{db}{dt}\right) , \tag{21}$$

$$\frac{dP_{00}}{dt} = v_{x0}P_0 - \gamma P_{00}\left(\frac{1}{a}\frac{da}{dt} + \frac{1}{b}\frac{db}{dt}\right) + (\gamma-1)\frac{\beta_p}{S}\left(\frac{1}{b^2} - \frac{1}{a^2}\right)^2 , \tag{22}$$

where $\beta_p = c_s^2/v_{ap}^2$ is plasma beta-ratio, which is determined from the magnetic field, B_0 produced by the current induced near the X-point. The magnetic Reynolds number, S is $S = \tau_B/\tau_A$ ($\tau_B = 4\pi\sigma\lambda^2/c^2$). The parameters G_1 in Equation (18) and G_2 in Equation (20) are given as

$$G_1 = \frac{2g_0\tau_A^2}{R} , \tag{23}$$

$$G_2 = \frac{g_0\tau_A}{v_{ap}} . \tag{24}$$

In the above equations (17)-(22), the time , B_{n0}, v_{x0}, P_0, P_{00} are normalized by $\tau_A = \lambda / v_{ap}$, B_0, v_{ap}, Pa and Pa, respectively.

The normalized time-dependent part of the magnetic fields, Bx and Bz are given by

$$B_{xa} = \frac{1}{a^2} , \tag{25}$$

$$B_{za} = R_b\frac{1}{ab} , \tag{26}$$

where $R_b = B_{00}/B_0$ gives the initial ratio between Bz and By .

The electric field **E** induced by the change of the magnetic field **B**(eqs. [8]-[10]) can be determined from

$$\mathbf{E} = -\mathbf{v} \times \mathbf{B} / c . \tag{27}$$

By use of equations (6)-(10), we obtain the components of the inductive electric field;

$$E_x = -\frac{B_{z0}}{ca^2 b}\frac{da}{dt}y \quad , \tag{28}$$

$$E_y = \frac{B_{z0}}{cab^2}\frac{db}{dt}x + \frac{v_{x0}}{c}\frac{B_{z0}}{ab} \quad , \tag{29}$$

$$E_z = \frac{B_0}{c}\left[\frac{1}{a^3}\frac{da}{dt}\frac{y^2}{\lambda} - \frac{1}{b^3}\frac{db}{dt}\frac{x^2}{\lambda} - \frac{v_{x0}B_{n0}}{B_0} - \frac{v_{x0}}{b^2}\frac{x}{\lambda} - \frac{B_{n0}}{B_0}\frac{1}{b}\frac{db}{dt}\right] \quad . \tag{30}$$

We can obtain numerical results of the electromagnetic fields by solving the basic equations (17)-(20). The initial conditions are taken as a = 1, da/dt = -0.001, b = 2 , db/dt =0, B_n = 0.01, v_{x0} = 0.001, and other parameters are taken as G_1 = 0.01, G_2 = 0.27, S = 10^5, and $R_b = B_{00}/B_0$ = 100/10. The plasma beta-ratio β_p is 1.0 and the adiabatic ratio is γ = 5/3.

Some components of the inductive electric fields become explosively strong near the time 1.18 τ_A. The reason is due to the fact that near the implosion phase, the converging flow, v_y is increased by about 100 times and the magnetic field, B_{xa} is also increased by about 150 times through the current pinch. Therefore, the inductive electric field $E_x = v_y B_{x0}/c$ can be amplified to 1.5 x 10^4 times, compared with the initial values. This inductive electric field before the implosion is about 70 V/m , if we take v_{ap} = 7x 10^6 cm/s and B_0 = 10 G. The inductive electric field near the implosion can become $E_x \sim 10^6$ V/m. This strong electric field near the implosion is important for the high-energy particle acceleration. If we take $\lambda = 2x10^9$ cm, the Alfven transit time τ_A is $\tau_A = \lambda/v_{ap}$ = 300 s. Then the duration of implosion is about 0.01 τ_A = 3 s. As seen in the next section, the acceleration time for both protons and electrons is quite rapid compared with the duration of implosion , 3 s. Therefore we will investigate the motion of a test particle under the electromagnetic fields (28)-(30) in the next section.

3. Proton and Electron Acceleration

3.1 Equation of Motion

We consider the motion of a test proton under the electromagnetic fields given by equations (28)-(30)

$$\frac{d\tilde{\mathbf{P}}}{d\tilde{t}} = \left(\frac{v_{ap}}{c}\tilde{\mathbf{E}} + \frac{\tilde{\mathbf{P}}\times\tilde{\mathbf{B}}}{\Gamma_p}\right) \quad , \tag{31}$$

$$\frac{d\tilde{x}}{d\tilde{t}} = R_p\frac{\tilde{P}_x}{\Gamma_p} \quad , \tag{32}$$

$$\frac{d\tilde{y}}{d\tilde{t}} = R_p\frac{\tilde{P}_y}{\Gamma_p} \quad , \tag{33}$$

$$\frac{d\tilde{z}}{d\tilde{t}} = R_p\frac{\tilde{P}_z}{\Gamma_p} \quad , \tag{34}$$

where $\tilde{\mathbf{P}} = \mathbf{P}/m_p c$, $\tilde{\mathbf{E}} = \mathbf{E}/E_0$, $\tilde{\mathbf{B}} = \mathbf{B}/B_0$, $R_p = c/\omega_{cp}\lambda$, $\tilde{x} = x/\lambda$, $\tilde{y} = y/\lambda$, $\tilde{z} = z/\lambda$.
The time is normalized by the proton cyclotron period ω^{-1}_{cp} ($\tilde{t} = \omega_{cp} t$, $\omega_{cp} = eB_0/m_p c$).

3.2 Numerical Results for Proton Acceleration

The time-dependent amplitudes of the electromagnetic fields are assumed to be constant during the acceleration time, because the typical acceleration time to relativistic energy for the proton is about $10^5\,\omega^{-1}_{cp}$, which is about 1 s for B_0 = 10 G and is still within the duration of implosion , ~ $0.01\tau_A$ = 3 s. We investigate the motion of the proton at the time, t = 1.168 τ_A . The electromagnetic field amplitudes at the time, t = 1.168 τ_A are B_{xa} = 119.6, B_{ya} = 0.11, B_{za} = 37.0, B_n = -0.11, EX_1 = -2908.28, EY_0 = 35.5, EY_1 = 25.5, EZ_1 = 0.079, EZ_2 = -9391.1, EZ_0 = -0.113 and EZ_x = 0.029. We take $R_p = c/\omega_{cp}\lambda = 10^{-5}$ and v_{ap}/c = 1/ 4300. We show the results for the initial conditions with x(0)=y(0)=z(0)=0.5, P_x=P_y=P_z= 10^{-4}. Figure 2 shows the time history of the Lorentz factor $\Gamma = (1 + P^2)^{1/2}$ for the proton. Figure 3 shows the time history of the momentum for the proton. The proton can be accelerated to the x- and y-direction. As seen in Figure 3, the average value of the momentum P_x increases almost proportional to the time. Therefore we can evaluate the time dependency of the momentum P_x as

$$\tilde{P}_x = 2.5\times 10^{-4}\omega_{cp}t + 10^{-4} \quad , \qquad (35)$$

for y(0) = 0.5. Similarly, we find

$$\tilde{P}_x = 1.0\times 10^{-5}\omega_{cp}t + 10^{-4} \quad , \qquad (36)$$

for y(0) = 0.1 and

$$\tilde{P}_x = 4.0\times 10^{-6}\omega_{cp}t + 10^{-4} \quad , \qquad (37)$$

for y(0) = 0.05. These results are almost same for the initial momentum in the range of P(0) = 10^{-6} to 10^{-4} as well as for the other initial positions, x(0) and z(0). Therefore we conclude that within about one second of the implosion time the proton can be accelerated to ~ 70 MeV for protons with y(0)> 0.05.

3.3 Numerical Results for Electron Acceleration

In this section we present numerical results for electron acceleration by solving the following equations of motion for a test electron.

The time is normalized by the electron cyclotron period ω^{-1}_{ce} ($\tilde{t} = \omega_{ce}\,t$, $\omega_{ce} = eB_0/m_ec$). We take $R_e = 10^{-8}$ and v_{ap}/c = 1/ 4300. The initial conditions for the electron are x(0)=y(0)=z(0)=0.5, P_x=P_y=P_z= 10^{-4}. The electromagnetic fields are taken as the same one for the proton's case. Figure 4 shows the time history of the electron Lorentz factor Γ_e and P_x / m_ec. As seen in the lower part of Figure 4, the electron can be accelerated to the negative x-direction opposite the proton(see Figure 3). From the numerical calculation we find the time dependency of the average momentum P_x as

$$\left|\tilde{P}_x\right| = 2.5\times 10^{-4}\omega_{ce}t + 10^{-4} \quad , \qquad (38)$$

for y(0) = 0.5,

$$\left|\tilde{P}_x\right| = 1.0\times 10^{-5}\omega_{ce}t + 10^{-4} \quad , \qquad (39)$$

for y(0) = 0.1 and

$$\left|\tilde{P}_x\right| = 4.0\times 10^{-6}\omega_{ce}t + 10^{-4} \quad , \qquad (40)$$

for y(0) = 0.05. These results are almost same for the initial momentum in the range of P(0) = 10^{-6} to 10^{-4} as well as for the other initial positions, x(0) and z(0). As the electron cyclotron frequency is $\omega_{ce} = 10^8\ s^{-1}$ for B_0 = 10G,

we conclude from Equation (38) that within 1 s the electron with y(0)> 0.05 can be accelerated up to ~ 200 MeV.

4. Summary

In this paper, we presented a model for high-energy solar flares to explain prompt proton and electron acceleration, which occurs around moving X-point magnetic field. We derived the non-stationary electromagnetic fields during the strong implosion of the current sheet, which is driven by the converging flow toward the center of the magnetic arcade. We investigated a test particle motion in the electromagnetic fields derived from the MHD equations. It has been shown that both protons and electrons can be promptly(within 1 s) accelerated up to ~ 70 MeV and ~ 200 MeV, respectively. This acceleration process can be applicable for the impulsive phase of the gradual gamma ray and proton flares(gradual GR/P flare), which have been called *two-ribbon flares.*

Acknowlegements

The author would like to thank Mr. H. Ame of the ELCO Company for his scientific financial support. This work is supported in part by a Grant-in Aid for Scientific Research from the Ministry of Education (03640247).

References

Bai, T., and Sturrock, P. A. : 1989, *Ann. Rev. Astr. Astrophys.* 27, 421.
De Jager, C., and Sakai, J.-I. : 1991, Solar Phys. 133, 395.
Kahler, S.W., Moor, R.L., Kane, S.R., and Zirin, H.: 1988, Ap. J. 328, 824.
Kane, S. R. , Chupp, E. L., Forrest, D. J., Share, G. H., and Rieger, E. : 1986, Ap. J. (Letters) 300, L95.
Martin, S.F., and Ramsey, H.E.: 1972, in *Solar Activity Observations and Predictions*, ed. P.S. McIntosh and M. Dryer (Cambridge; M.I.T. Press), p.371.
Rieger, E. : 1989, Solar Phys. 121, 323.
Sakai, J.-I. : 1990, Ap. J. 365, 354.
Sakai, J.-I., and Koide, S. : 1991, *Research Report on Plasma Astrophysics and Fusion Science, PAFS-2,* June 1991 (Toyama University), to appear in Solar Physics.
Sakai, J.-I., and Ohsawa, Y.: 1987, Space Sci. Rev. 46, 143.
Sakai, J.-I., Tajima, T., and Brunel, F. : 1984, Solar Phys. 91, 103.
Tajima,T. : 1982, in *Fusion Energy-1981*, International Center for Theoretical Physics, Trieste, 1982, p.403.

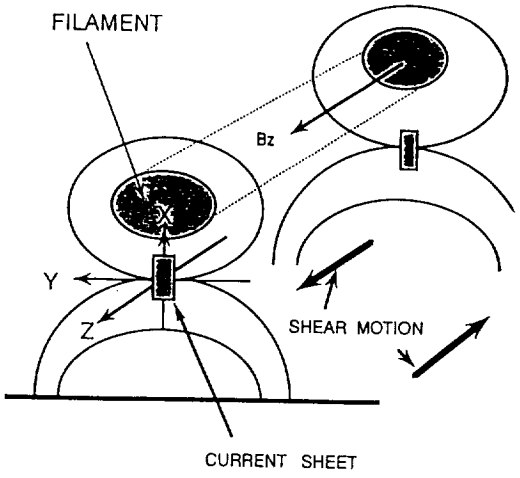

Fig.1 Schematic magnetic configuration and coordinate system.

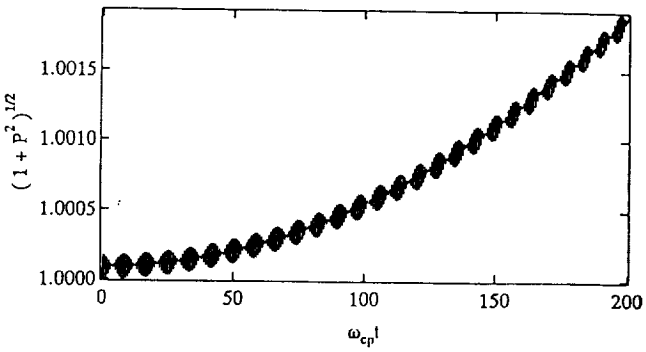

Fig.2 Time history of the proton's Lorentz factor.

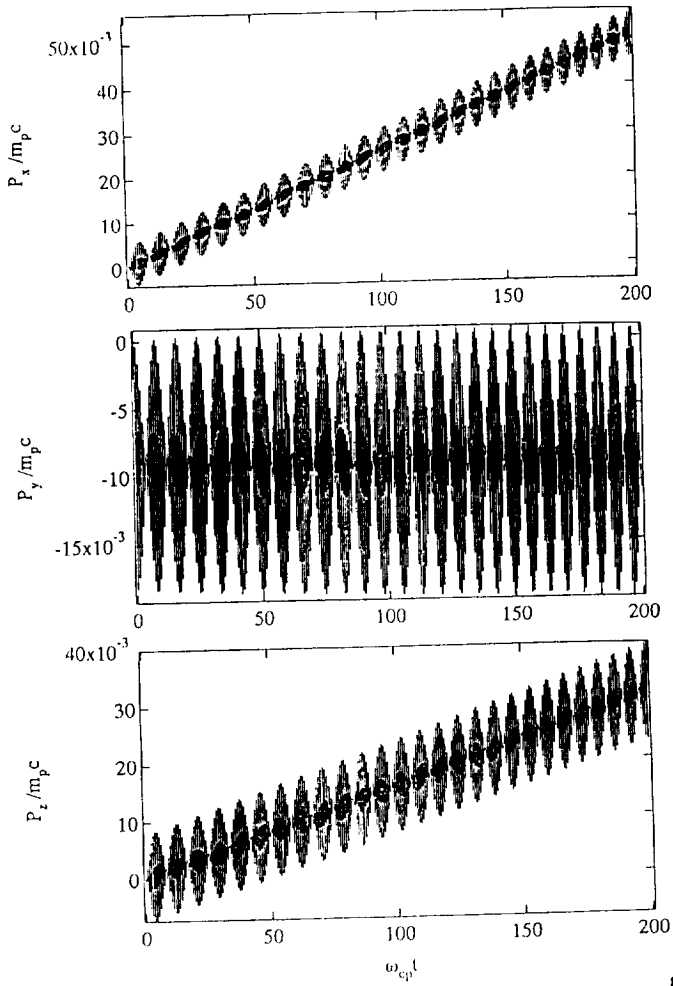

Fig.3 Time history of the proton's momentum.

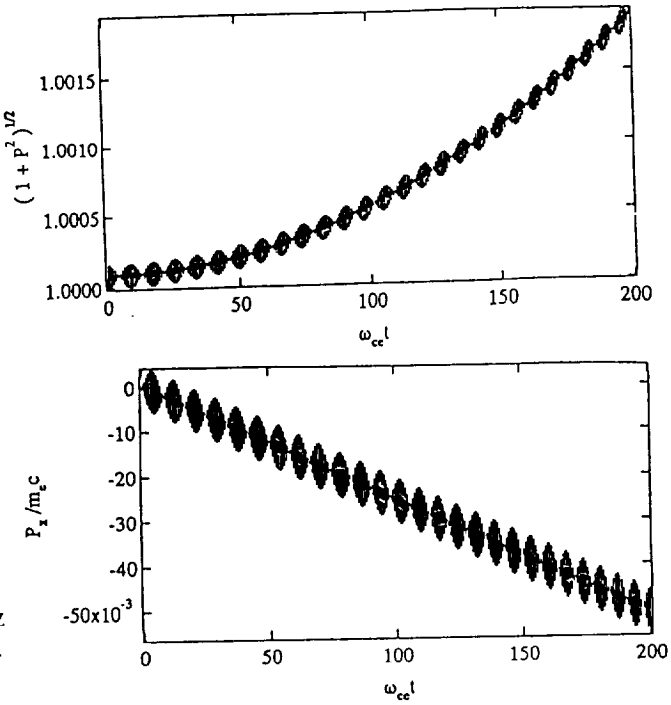

Fig.4 Time history of the electron's Lorentz factor(upper) and momentum P_x(lower).

Search for Evidence of Low Energy Protons in Solar Flares

Thomas R. Metcalf, Jean-Pierre Wülser, Richard C. Canfield, Hugh S. Hudson

Institute for Astronomy, University of Hawaii

Hénoux *et al.* (*Ap. J. Supp.*, **73**, 303, 1990) recently obtained observations of linear polarization in the Hα line during three solar flares, which they interpreted as impact polarization from a hecta-keV proton beam colliding with chromospheric hydrogen. They discuss several characteristics of impact polarization which allow its identification. First, for a vertical proton beam, the polarization should be directed towards the center of the solar disk and, second, the polarization should be strongest at the limb and weakest at disk center (for a truly vertical beam, the polarization would vanish at disk center). Hénoux *et al.* have identified the observed polarization as impact polarization based on its direction, which pointed along the line from the observation point to disk center in all three flares (to within ± 20 degrees).

We searched for linear polarization in the Hα line using the Stokes Polarimeter at Mees Solar Observatory (Mickey, *Solar Phys.*, **97**, 223, 1985) and present observations of a flare from NOAA active region 6659 which began at 01:30 UT on June 14, 1991. The Stokes Polarimeter has significantly better sensitivity to the polarization than Hénoux's instrument, but it does not have as large a field-of-view. Our dataset also includes Hα spectra from the Mees CCD (MCCD) imaging spectrograph (Penn et al, *Solar Phys.*, in press, 1991), as well as hard X-ray observations from the BATSE instrument on board GRO (Fishman et al., in *Proceedings of the Gamma Ray Observatory Science Workshop*, ed. W. N. Johnson, 1989). Hénoux *et al.* did not have Hα spectra or hard X-ray observations.

The polarimeter scanned a 40″ by 40″ field-of-view using 16 raster points in a 4×4 grid. Each scan took about 30 seconds with 2 seconds at each raster point. The polarimeter stepped 8.5″ between raster points and each point covered a 6″ region. This sparse sampling increased the total field-of-view without reducing the temporal cadence. At each raster point, an Hα spectrum with 20 mÅ spectral sampling is obtained covering 2.6Å centered on Hα line center.

Figure 1 shows, as a function of time, the Hα linear polarization averaged over a 0.4Å band centered on the Hα line. In this figure, the polarization is also averaged over all raster points in the 40″ by 40″ field-of-view. Since the direction of the polarization is an important diagnostic, we broke the polarization down into two components: one directed towards disk center (solid line) and one directed perpendicular to this (dotted line). The solid horizontal line is three times the standard deviation of the preflare polarization (01:15 - 01:30 UT) and indicates the significance of the observation. The figure ends at 01:40 UT since no data was obtained after that time. During the flare, the disk-center component of the polarization appears to increase preferentially as predicted by the impact polarization hypothesis.

In an alternative representation of the directionality of the polarization, **Figure 2** is a histogram of the polarization direction throughout the observations. The histogram

includes polarization at all wavelength points between ±0.3Å from line center and from all pixels and all times when the polarization was greater than 2.5%. The histogram bins are 9 degrees wide and the dashed line shows the direction of disk center. The polarization is directed roughly 20 degrees off of the disk center direction, a reasonable value considering the possible inclination of the chromospheric magnetic field.

Figure 3 demonstrates the spatial relationship between the observed polarization and the Hα flare. The underlying image from the MCCD imaging spectrograph shows the difference between the spectroheliogram (SHG) obtained 1.8Å blueward of line center and the SHG obtained 3.6Å blueward of line center ar 01:32:54 UT. Since precipitating electrons give the Hα profiles broad Stark wings, this image indicates sites of non-thermal electron precipitation. The white line segments show the direction and strength of the fractional Hα linear polarization from the scan beginning at 01:32:28 UT; the polarization occurs near the region where electrons are precipitating. The co-alignment between the MCCD image and the polarization has an uncertainty of approximately one polarimeter raster point (8″).

Figure 4 displays the hard X-ray light curve observed by the BATSE LAD discriminators on GRO in the 25-50 keV channel. Comparing Figure 4 with Figure 1, we see that four of the five most significant peaks in the Hα polarization occurred over the same time interval as the peaks in the hard X-rays. This is consistent with a non-thermal origin of the Hα polarization.

Figure 5 shows the soft X-ray light curve from the GOES satellite, and **Figure 6** shows the line center Hα light curve integrated over the flare area as observed with the MCCD. Most of the Hα emission and all of the GOES emission are thermal, and the linear Hα polarization does *not* track these emissions, being impulsive in nature.

Preliminary Conclusions

- Significant linear Hα polarization was observed during the June 14 flare and was preferentially directed about 20 degrees from disk center, consistent with nearly vertical particle precipitation.
- The Hα polarization occurred near sites of non-thermal electron precipitation, as indicated by the Stark broadened Hα wings observed with the MCCD, however, there was no compelling spatial relationship between these sites and the Hα polarization.
- The Hα polarization peaked at the times of the hard X-ray peaks, but did not track the soft X-ray or the Hα light curves. This suggests that the linear polarization is caused by a non-thermal process.
- The angular, spatial and temporal character of the polarization is consistent with the predictions of impact polarization by approximately 100 keV protons.
- Assuming that the observed polarization is indeed the signature of 100 keV protons, these protons are temporally coincident with approximately 25-100 keV non-thermal electrons.

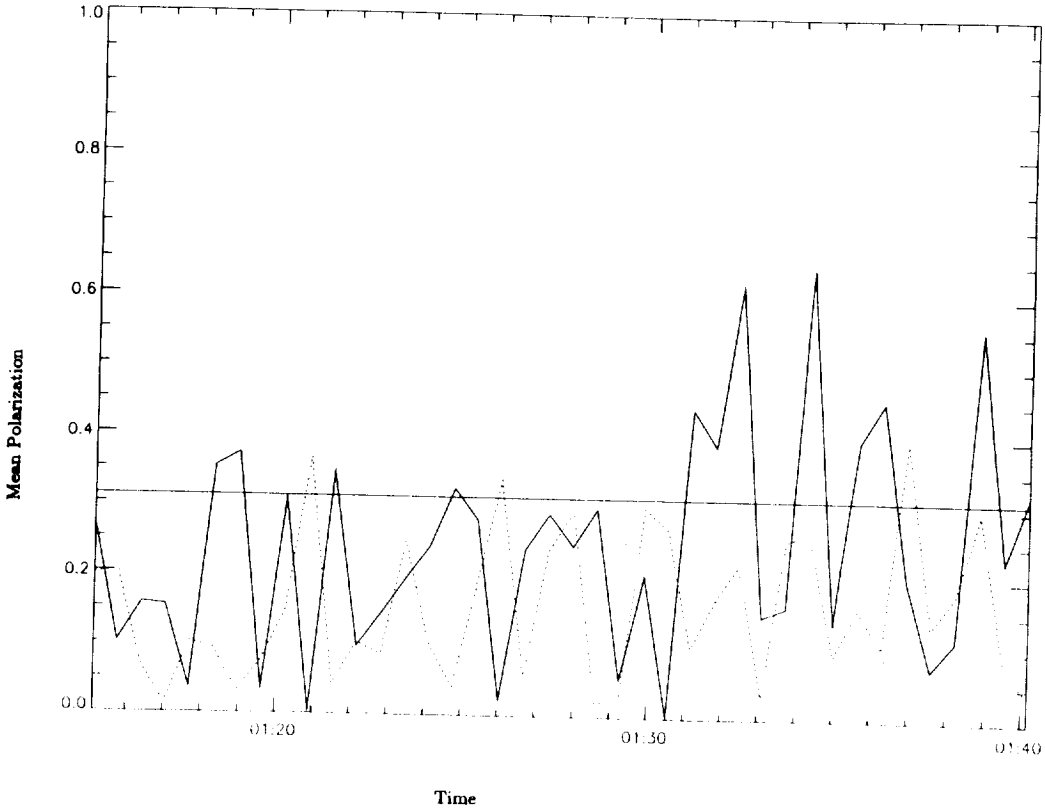

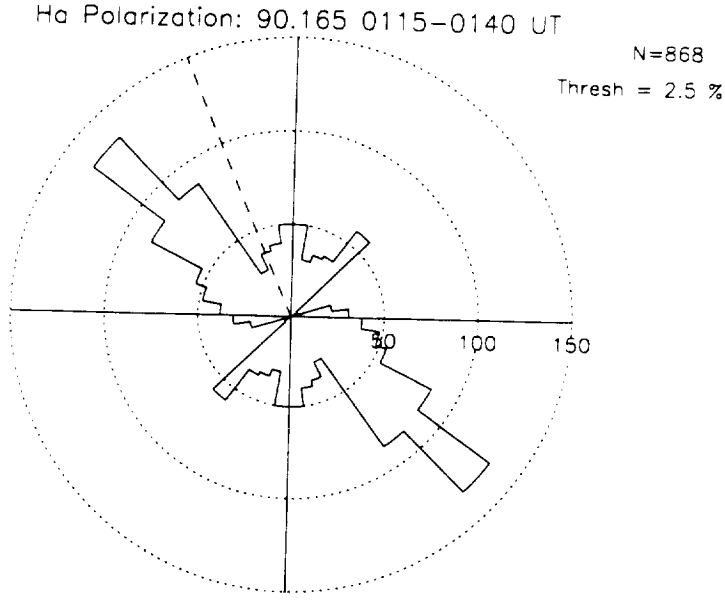

Figures 1 and 2

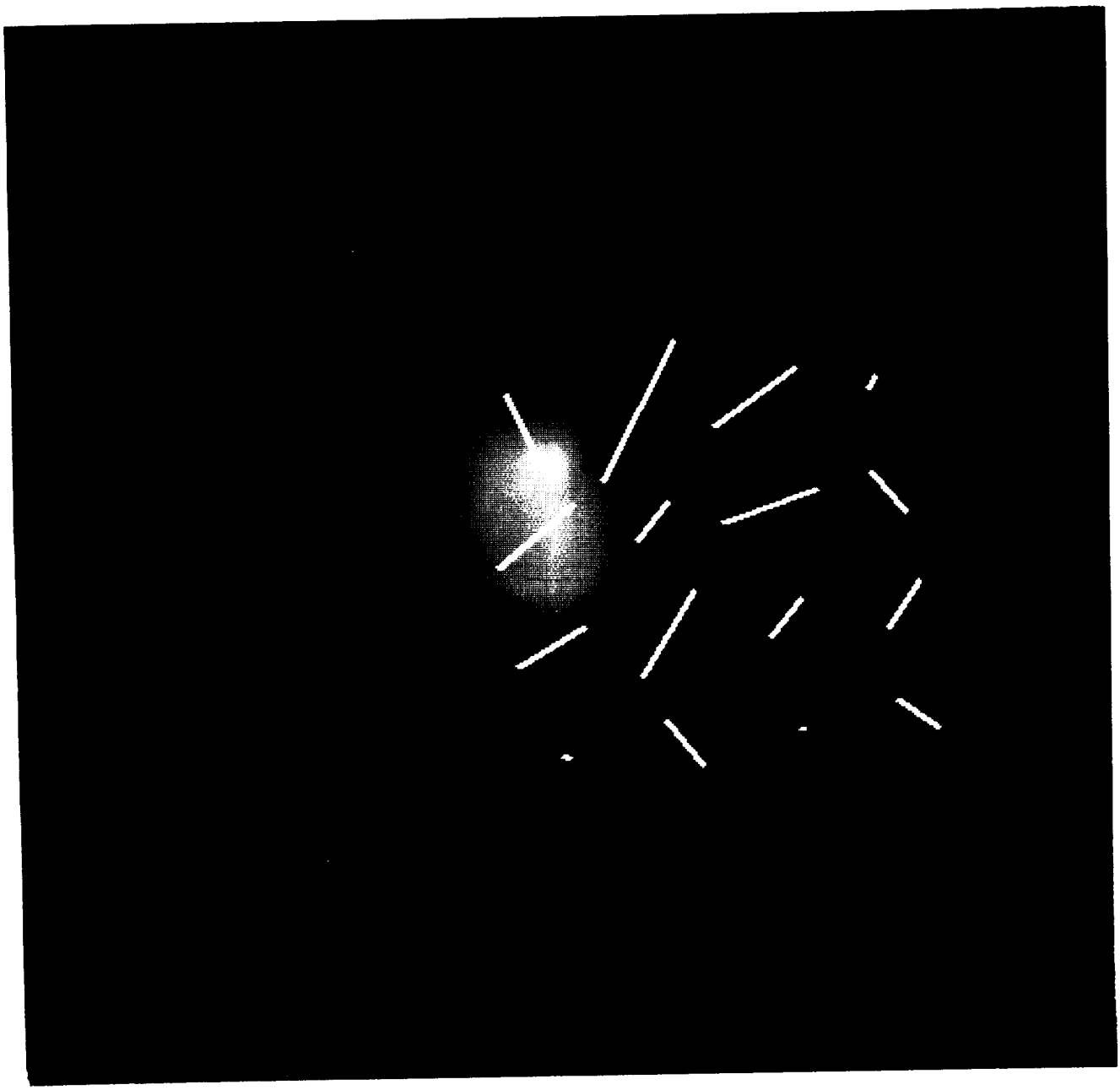

Figure 3

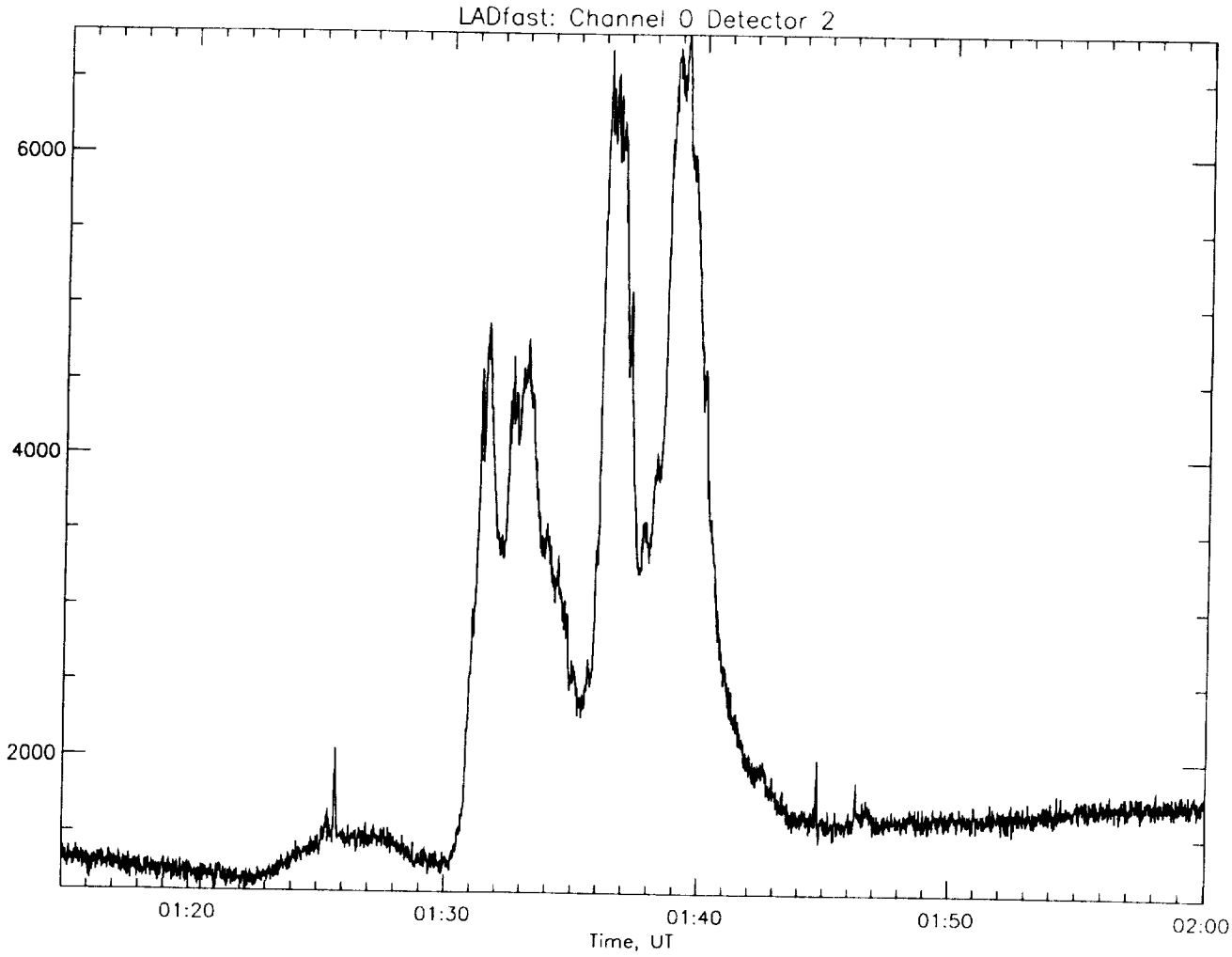
LADfast: Channel 0 Detector 2
6000
4000
2000
01:20
01:30
01:40
01:50
02:00
Time, UT

Figure 4

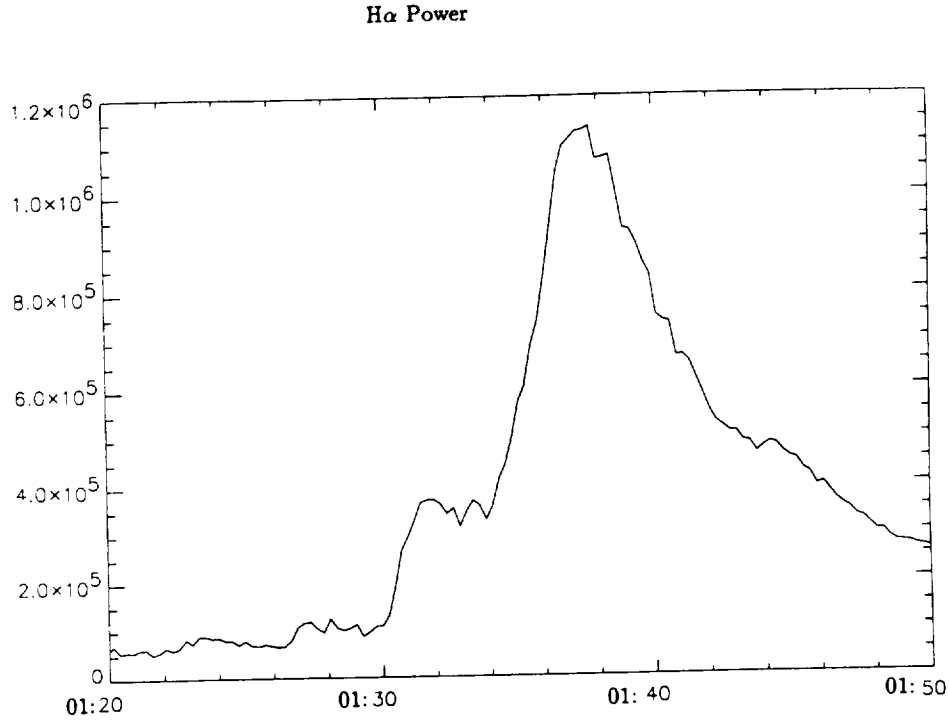

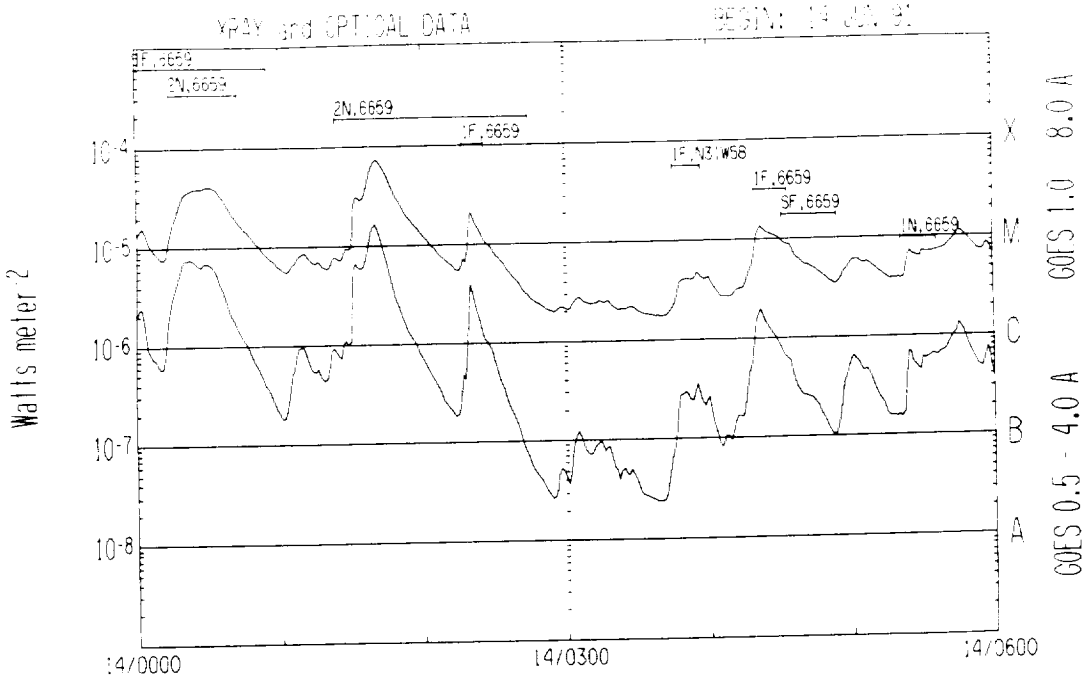

Figures 5 and 6

COSMIC RAY ALBEDO γ-RAYS FROM THE QUIET SUN

D. Seckel, T. Stanev and T.K. Gaisser
Bartol Research Institute, University of Delaware, Newark DE 19716

Abstract

We estimate the flux of gamma-rays that result from collisions of high energy galactic cosmic rays with the solar atmosphere. An important aspect of our model is the propagation of cosmic rays through the magnetic fields of the inner solar system. We use diffusion to model propagation down to the bottom of the corona. Below the corona we trace particle orbits through the photospheric fields to determine the location of cosmic ray interactions in the solar atmosphere and evolve the resultant cascades. For our nominal choice of parameters, we predict an integrated flux of gamma rays (at 1 AU) of $F(E_\gamma > 100 \text{ MeV}) \approx 5 \times 10^{-8} \text{ cm}^{-2} \text{ sec}^{-1}$. This can be an order of magnitude above the galactic background, and should be observable by EGRET.

Introduction

There are a number of reasons to study the sun as a source of γ-rays produced in cosmic ray cascades. First, there is the purely intellectual question of whether the γ-ray albedo is strong enough to be observed. Second, there is the practical issue of whether the sun could be a strong enough source of γ's to be a confusing background to other sources. Third, many of the same issues that occur in studying solar flares as γ-ray sources are likely to come into the calculation of the γ-ray albedo from cosmic ray interactions. These include the structure of the magnetic fields near the sun and charged particle propagation through those fields. The details of those issues will be different in the two cases, and so studying the γ-ray albedo may give one a new perspective on solar flare models. Finally, whereas models of other astrophysical γ-ray sources may be largely speculation, due to the sun's proximity models of the solar source may be directly tested in other ways. Successful modeling of the sun may lead to better models of other more remote sources.

In this contribution, we summarize a recent paper[1] in which we discuss a model for estimating the albedo γ-ray flux from cosmic ray cascades in the solar atmosphere. Our model explicitly includes several 'heliomagnetic' effects. A naive estimate might assume that the cosmic ray flux incident on the sun's surface equals the flux at Earth, and that the solar albedo, like the Earth's, might be quite small. We argue that the situation is just the reverse: interplanetary (IMF) and coronal magnetic fields suppress the flux reaching the solar surface, but photospheric magnetic fields result in an efficient albedo. These conclusions coupled with a Monte Carlo study of the photon production by cascades in the solar atmosphere lead to a prediction of a flux that is detectable by the EGRET[10] instrument on the Arthur H. Compton Gamma Ray Observatory (GRO). We raise and discuss some questions for future study.

Cosmic Ray Absorption by the Sun

Framework for Absorption. We write the absorption rate for cosmic rays of energy E as

$$\Gamma(E) = 4\pi r^2 j(E), \tag{1}$$

where j is the net radial flux of cosmic rays. For a simple model ignoring magnetic fields, charged particles travel in straight lines and j is given by $j_N = (R_\odot/2r)^2 f_\infty(E)\beta(E)c$, where $f_\infty(E)$ is the differential density of cosmic rays at $r = \infty$, βc is their velocity, and the subscript N indicates that this is the naive value for absorption on a sphere of radius $R_\odot$. We take $f_\infty(E) = f_\oplus(E)$, the observed density at Earth[2]. The naive absorption rate is then

$$\Gamma_N = \pi R_\odot^2 f_\oplus \beta. \tag{2}$$

More generally, we write the absorption rate as

$$\Gamma = \frac{A C_D \Gamma_N}{A + C_D - A C_D}, \tag{3}$$

where C_D is a correction factor to account for propagation through the IMF and corona, and A is the probability that a primary which reaches the photosphere will be absorbed there instead of being reflected back into the corona. The denominator arises from considering the possibility that a cosmic ray which was reflected back into the corona may diffuse back to the photosphere and be absorbed on the 2^{nd}, 3^{rd}, ... penetration of the photosphere before totally escaping the solar system.

Diffusion. We estimate C_D using a diffusion model for cosmic ray propagation in the inner solar system. Since the IMF is expected to be nearly radial inside the Earth's orbit[3], we take the diffusion problem to be spherically symmetric with a partially absorbing boundary condition at the photosphere. The inward flux is given by $j = -Df'$, which may be used in Eq. 1 to solve for Γ. For the diffusion 'constant' we consider the form,

$$D(E, r) = D_\oplus \, (r/r_\oplus)^\alpha \, (E/1 \text{ GeV})^\beta, \tag{4}$$

where D is normalized to $D_\oplus$, its value at $E = 1$ GeV and $r = r_\oplus$. Eq. 4 is subject to the constraint $D(E, r) < rc/8$, which is dictated by causality, *i.e.* the net flux j cannot exceed j_N. Our nominal choice of diffusion parameters[4] is $(D_\oplus, \alpha, \beta) = (0.03, 2, 1)$, where $D_\oplus$ is given in units of $c \times$ A.U. Unfortunately, the diffusion parameters are mostly based upon measurements by spacecraft in Earth orbit or the outer solar system, and this leads to uncertainty in our predictions. On the other hand, an observation of the signals we propose may provide a new way to probe the inner solar system.

The Absorption Coefficient, A. To determine the absorption probability we take an isotropic flux of cosmic rays at the bottom of the corona and propagate them inward including both magnetic effects and absorption by the ambient gas. For this part of our calculation we abandon diffusion and trace the particle orbits exactly. The small scale magnetic structure[5] used for this calculation is illustrated in Fig. 1. It consists of a loose network of flux tubes which penetrate the photosphere at the corners of convective cells, where the field is swept by the moving fluid. The tubes open up to a space filling 'canopy' at the bottom of the corona which we take to be 1250 km above the photosphere. We use field strengths within the tubes of 1500 G at the photosphere and 6.5 G at the bottom of the corona. We assume the flux tubes maintain pressure equilibrium with the gas, *i.e.* $B^2 \sim P_{gas}$. Due to the pinching of the flux tubes, most primaries are mirrored and return to the corona without interacting; however, there is a small loss cone where nearly vertical cosmic rays penetrate to sufficient depth to be absorbed. For the nominal parameters we find an absorption probability of $A = .0052$ for protons; and .0088 for ^{4}He.

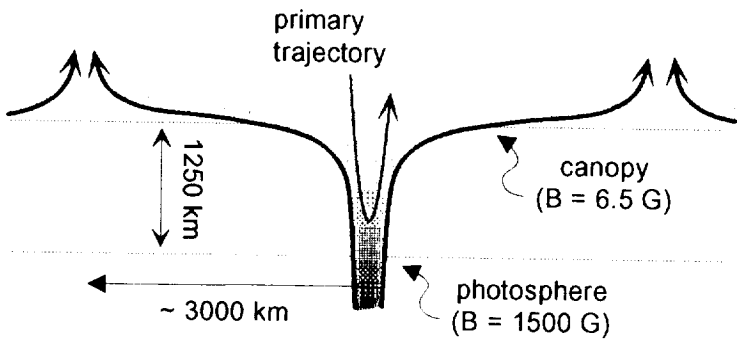

Figure 1: Model of magnetic fields near the photosphere. Shading increases with magnetic field intensity.

The discussion so far is valid only for relatively low energy primaries, which we argue will be trapped on field lines and necessarily enter the flux tubes. Higher energy primaries will not be trapped if their gyroradii are comparable to the distance bewteen flux tubes. We estimate the threshold for trapping to be $E_T \approx 3$ TeV, and take $A(E > E_T) = 1$. As cosmic rays with such high energies are relatively rare the uncertainty in E_T should not strongly affect our results.

Absorption Rates. We show our nominal absorption rate for protons as the bold curve in Fig. 2. We also show, as dashed lines, the results for a pessimistic $(D_\oplus, \alpha, \beta) = (0.01, 2, 0.5)$, and optimistic (0.1, 1.5, 2) choice of diffusion parameters; and, as light, solid curves, three different absorption coefficients ($A = 0.001, 0.01, 0.1$). We also show the naive flux from Eq. 2.

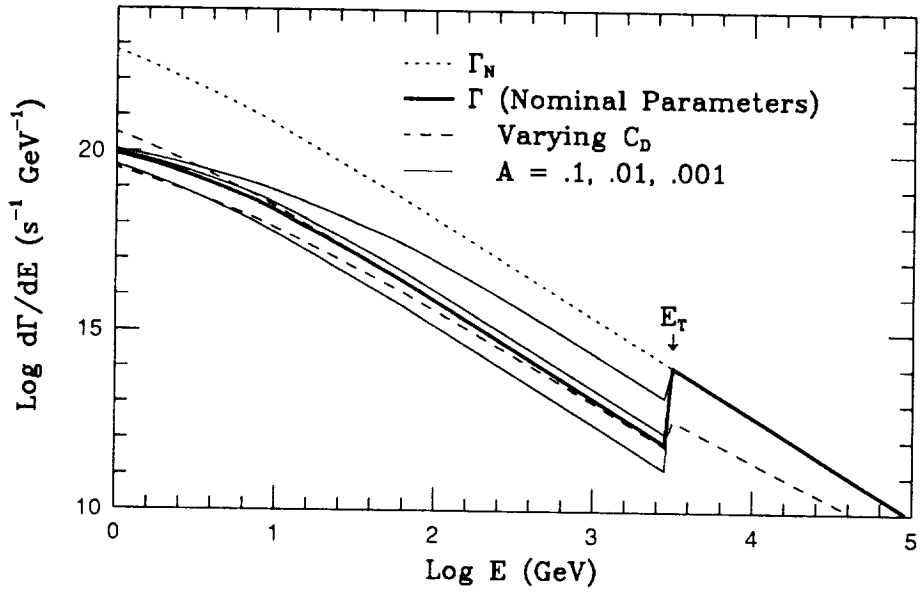

Figure 2: Absorption rate of cosmic ray protons by the sun. The bold curve is our nominal result. Varying the diffusion parameters results in the dashed curves. Varying the absorption coefficient yields the light, solid lines. The naive result (Eq. 2) is shown as a dotted curve for comparison.

The γ-ray Albedo

In calculating the γ-ray albedo we distinguish between two energy regimes; $E < E_T$ and $E > E_T$. As stated above, for $E > E_T$, cosmic rays are not trapped on flux lines and we may ignore local magnetic fields. The γ-ray albedo of these cascades will be very small, with contributions only from incident protons grazing the photosphere. Primaries with $E < E_T$, on the other hand, are assumed to stay within the flux tubes. Due to magnetic mirroring the albedo from these cascades may be significant.

Two Models for Cascade Propagation. Nearly vertical cosmic rays in the interior of the loss cone interact before being mirrored, *i.e.* while still having a downward velocity (Fig. 3a). At the boundary of the loss cone, however, is a region where protons may interact *after* being mirrored (Fig. 3b). These interactions will contribute to an upward flux of gamma-rays. We find that there is roughly a 25% chance that primary interactions will take place after the primary has been mirrored. Since γ-ray mean free paths are comparable to those for the primary hadrons, the albedo of the sun is considerable.

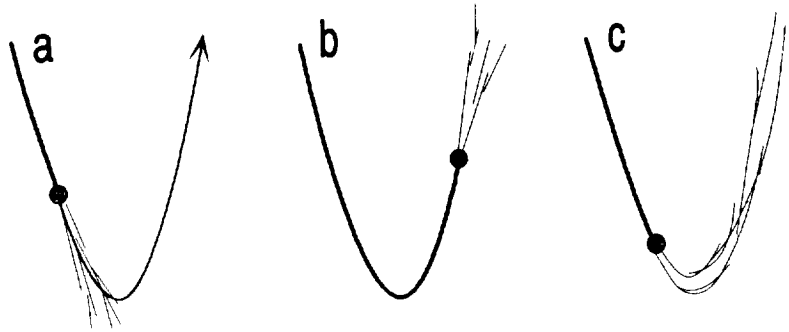

Figure 3: Cascade geometries for production of the γ-ray albedo. Shaded circles indicate interaction sites. Heavy lines show the primary trajectory before the interaction. The curved arrow in a) indicates the path the primary would take if no interaction occurred. a) Interaction occurs before the primary is mirrored. No albedo is produced if the cascade develops linearly. b) Interaction occurs after the primary is mirrored. This case contributes to the albedo. c) Interaction occurs early, but if the whole cascade is mirrored albedo photons may still result.

Another aspect of the low energy cascades is that the charged particles will follow the same trajectory the parent cosmic ray would have followed if it had not interacted; *i.e.* the whole cascade is to some extent mirrored (Fig. 3c), even though some of the cascade energy is neutral. To explore this effect we took two extreme models; one where the cascade developed along a constant zenith angle, and one where it developed along the path of a charged particle being mirrored out of the photosphere. In the first model photons can arise only from incident cosmic rays that interact after being mirrored, but in the second even cosmic rays which interact while moving downward can produce an upward flux of γ-rays.

Given these preliminaries, we calculate the γ-ray albedo by evolving 'atmospheric' cascades from the point where the primary cosmic ray interacts, through the solar material, to the surface. In the first model, the path length distribution is given by the slant depth from the interaction site. Cascades from primaries which interact before being mirrored are given infinite

path lengths and produce no albedo γ-rays. In the second model the path lengths are computed as if all particles are charged, in which case all cascades may in principle produce albedo γ-rays.

γ-ray Production. The γ-ray flux at Earth is given by

$$\phi(E_\gamma) = \frac{1}{4\pi r_{\oplus}^2} \frac{dL_\gamma}{dE_\gamma}, \tag{5}$$

where the γ-ray luminosity of the sun is given by

$$\frac{dL_\gamma}{dE_\gamma}(E_\gamma) = \sum_i \int_E^\infty Y_i(E_\gamma, E_i)\Gamma_i(E_i)dE_i. \tag{6}$$

The sum over i includes both p and ^{4}He primaries, and Γ_i is given by Eq. 3. The γ-ray yield per absorbed primary of energy E is given by averaging over the path length distribution

$$Y_i(E_\gamma, E_i) = \int y_i(E_\gamma, E_i, x)\frac{dP_i}{dx}dx, \tag{7}$$

where y_i is the yield of photons of energy E_γ that result from cascades with path length x initiated by primaries of energy E_i, and dP_i/dx is the probability that a primary of species i produces a cascade with path length x. In separating $P_i(x)$ and $\Gamma_i(E)$ we have ignored the slow energy dependence of the hadronic cross-section. The yields, y_i, are calculated using standard Monte Carlo techniques[6,7] including both hadronic and electromagnetic interactions. Note that the density is low enough that for primaries with $E < E_T$, all mesons decay before they are absorbed or stop.

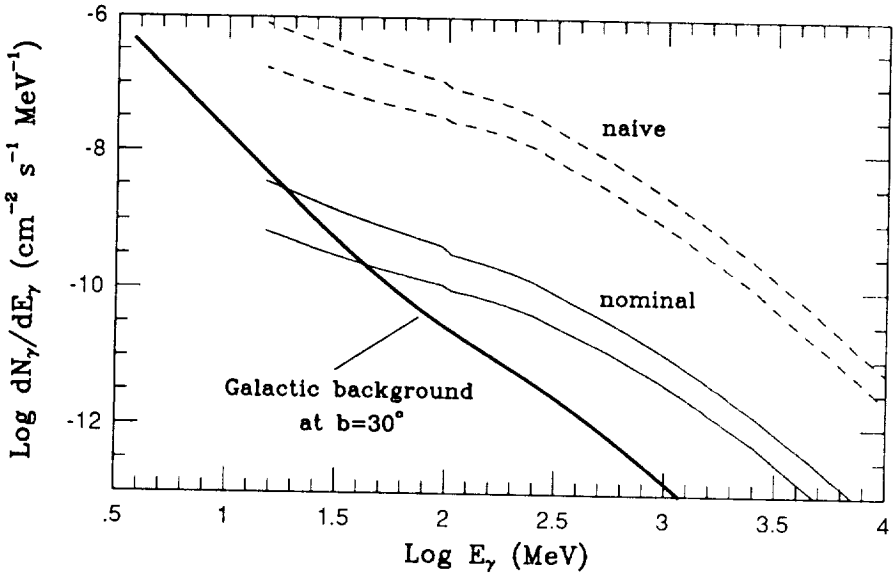

Figure 4: Photon flux at Earth. The solid (dashed) curves show results for the nominal (naive) absorption rate. In each pair, the upper curve shows a model where the cascades are mirrored, while the lower curve assumes the cascades follow straight trajectories. The heavy curve shows the galactic background at $b = 30°$.

Results. The results of our γ-ray calculations are illustrated in Fig. 4. The expected background is due to cosmic ray collisions with intergalactic gas[8], combined with observational data[9] below 200 MeV, and is shown for galactic latitude $b = 30°$. The background should scale as $1/\sin b$. Both signal and background are given for a solid angle equal to the solar disk. The signal is larger than the galactic background for reasonable assumptions about cosmic ray absorption.

Other Albedo Products

We have performed similar calculations[1] to estimate the albedos for other cascade products, which we summarize here.

Neutrons. From the perspective of the GRO the most interesting possibility is a quiet time flux of high energy neutrons from the sun. The primary production mechanisms for neutrons are spallation reactions of ^{4}He and charge exchange interactions between incident protons and target hadrons. Neutrons are unstable, so there is no galactic background to speak of, but as the distance to the sun is comparable to the neutron lifetime, neutrons produced on the sun may still reach the Earth before they decay.

The geometry of the neutron production mechanism is similar to that for photons - the albedo arises from cascades that are mirrored or for which the primary was mirrored before interacting. For neutron production we modified our Monte Carlo of the cascades to include explicit charge separation of protons and neutrons.

We estimate a quiet time neutron flux of $I_n(E_n > 100 \text{ MeV}) \simeq 5 \times 10^{-8} \text{ cm}^{-2} \text{ sec}^{-1}$, approximately a factor of 10^4 below the pre-GRO observational limits[12]. Both COMPTEL[13] and OSSE[14] have sensitivity to neutrons, as evidenced by their detection of neutrons during the June 1991 flares. However, their capabilities are not nearly good enough to detect our predicted quiet time flux. For example, COMPTEL's source sensitivity to photons is not quite $10^{-4} \text{ cm}^{-2} \text{ sec}^{-1}$, and it's neutron sensitivity is even less. It is interesting to note that the integrated neutron flux during the June 9 flare corresponds to ~ 30 yr of our predicted quiet time flux, albeit in a somewhat lower energy band.

Neutrinos. Neutrinos produced by solar cascades are potentially observable through their conversion to a flux of upward going underground muons. The calculation for neutrinos differs qualitatively from that for photons in that the high energy cascades dominate the signal. The relative importance of the high energy cascades arises since they are essentially unaffected by diffusion in the IMF and corona and because there is a roughly linear increase in both the muon production cross-section and range with E_ν. Also note that neutrinos (unlike photons) are not generally absorbed by the sun, and so there is no cutoff at $E > E_T$.

For the neutrino signal the principle background is the flux of neutrinos produced in *terrestrial* cascades[11]. For cascades with $E > 500$ GeV the sun is ~ 10 times more efficient at producing neutrinos than the Earth, due primarily to the larger scale height of the solar atmosphere. As a result if a neutrino telescope could resolve the sun, detection would be signal limited - not background limited. However, for our nominal model we calculate an underground muon flux of $I(E_\mu > 10 \text{ GeV}) \sim 5 \times 10^{-17} \text{ cm}^{-2} \text{ sec}^{-1}$, which is less than one event per year at any operational neutrino telescope, and so we conclude that the neutrino signal is currently unobservable.

Antimatter. Finally, we have considered antimatter signals, but do not find them promising. Antiprotons and positrons are charged, and so lack a directional signal. Antineutrons would be

difficult to distinguish from a much more copious neutron flux.

Future Directions

We have made a reasonable estimate of the γ-ray albedo from cosmic ray absorption by the sun; however, there are a number of issues that still need to be addressed.

Observing Strategies and Phase I EGRET Observations. The first question - is the signal really there? If the sun were resolved by EGRET then the source strength would be many times the galactic background. However, EGRET's point spread function δ is greater than the size of the sun[15] ($\delta = 1.4°$ for 150 MeV $< E <$ 500 MeV) and so it is important to reduce the background by observing the sun while it is at high galactic latitude. During the phase 1 observing program there are 29 scheduled 2 week observing periods (and several shorter ones), of which 4 (fortuitously) have the sun within EGRET's 20° HWHM field of view during part or all of the observing period. The three best of these (Oct. 3, 1991; Aug. 6, 1992; and April 2, 1992) have the sun's galactic latitude at $|b| > 44°$. It is therefore reasonable to estimate EGRET's exposure during the phase one viewing period as $\sim 1.8 \times 10^9$ cm^2 sec, which would give a yield of approximately 100 photons with $E > 100$ MeV. By comparison, the total number of galactic background photons detected within δ of the sun during the same exposure is expected to be ~ 240. A three sigma excess would then correspond to roughly 50 photons, and assuming our estimates of the signal are correct, the sun should be an observable source.

Improvements to the Calculations. In the event of a successful detection, there are a number of improvements that could be made without abandoning the basic structure of our model. We anticipate that some of these would increase our predicted flux if included and some would decrease it, but taken as a whole they would not change the results by an amount large compared to the uncertainty in a particular choice of diffusion and canopy parameters.

In no particular order - *a*) Eliminate the discontinuous treatment of absorption at E_T. This should not dramatically affect the flux estimates for E_γ in the range 100 MeV – 1 GeV since their parent primaries typically have $E \ll E_T$. *b*) Include an energy dependent leakage term in the calculation of the absorption rate. In the present model, a low energy primary which reaches the sun is either absorbed in a flux tube or eventually diffuses back out of the solar system. It is also possible that some fraction will leak across field lines to be absorbed in the space between flux tubes. Since these primaries and the resultant cascades would not be mirrored their contribution to the albedo would be suppressed. *c*) In the present Monte Carlo, charged particle secondaries that escape the sun were thrown away; however, it would be consistent with the treatment of non-absorbed primaries to assume that these charged secondaries eventually return to the sun and are absorbed, continuing the cascade after a 'pause'. We estimate that this would increase the γ-ray signal by a factor of 2-3. *d*) Include charge separation in the electromagnetic part of the cascade. *e*) Make the model of the flux tubes two dimensional to account for their finite radial extent, and to allow the magnetic field to have a horizontal component. *f*) Incorporate modulation by the solar wind into the incident flux calculations.

Phenomenological Considerations. Assuming that the signal is seen, there are various features of the γ-ray signal that may be useful either as diagnostics of the absorption model, or as indicators of transport phenomena around the sun. An obvious example is measuring the spectrum of the γ-ray flux and comparing it to the model predictions. Another possibility arises from noting that most of the interplanetary magnetic field is anchored to one of the polar regions of the

sun. If the primaries find it difficult to cross field lines (*i.e.* diffusion takes place parallel to but not perpendicular to the local magnetic field) then one might expect the polar caps to be significantly brighter in γ-rays than the equator. Although the diameter of the sun is smaller than EGRET's point spread function one might still hope to pick out a weak dipole pattern upon gathering sufficient data, especially at higher photon energies where EGRET's resolution is better.

This is not a complete list, but as these two examples indicate a study of the γ-ray flux from the sun can potentially provide useful information about γ-ray production mechanisms and cosmic ray transport in the solar system, and by extension to other sites in the Universe.

Acknowledgements

We thank J. Bieber, P. Evenson, D. Mullan, and R. Schaefer for helpful discussions. Work supported in part by NASA grants NAGW-1644 and NAGW 2076.

References

1. D. Seckel, T. Stanev, and T.K. Gaisser, *Astrophys. J.* **382**, in press. (1991)
2. D. Kniffen (chairman) *The Gamma-Ray Observatory Science Plan* (1988)
3. W. Webber and M. Potgieter, *Astrophys. J.* **344**, 779 (1989)
4. E.N. Parker, *Astrophys. J.* **128**, 664 (1958)
5. I.D. Palmer, *Rev. Geo. Sp. Phys.* **20**, 335 (1982)
6. E.R. Priest *Solar Magnetohydrodynamics*, D. Riedel Pub. Company, Dordrecht, Holland (1982)
7. T.K. Gaisser & T. Stanev, *Phys. Rev. Lett.* **54**, 2265 (1985)
8. T.K. Gaisser, *et al.*, *Phys. Rev.* **D38**, 85 (1988)
9. C.D. Dermer, *Astron. Astrophys.* **157**, 223 (1986)
10. C.E. Fichtel, *et al.*, *Astrophys. J.* **217**, L9 (1977)
11. J.A. Lockwood, *Space Science Reviews* **14**, 663 (1973)
12. J. Ryan, *These proceedings.*
13. R.J. Murphy, *These proceedings.*
14. L.V. Volkova *Yad. Fiz.* **31**, 1510 (1980) (*Sov. J. Nucl. Phys.* **31**, 384)
15. J.R. Mattox, *These proceedings.*

★U.S. GOVERNMENT PRINTING OFFICE: 1992 - 627 - 064/45019

REPORT DOCUMENTATION PAGE

Form Approved
OMB No. 0704-0188

1. AGENCY USE ONLY *(Leave blank)*	2. REPORT DATE	3. REPORT TYPE AND DATES COVERED
	February 1992	Conference Publication

4. TITLE AND SUBTITLE
The Compton Observatory Science Workshop

5. FUNDING NUMBERS

6. AUTHOR(S)
Chris R. Shrader, Neil Gehrels, and Brian Dennis, editors

7. PERFORMING ORGANIZATION NAME(S) AND ADDRESS(ES)
NASA-Goddard Space Flight Center
Greenbelt, Maryland 20771

8. PERFORMING ORGANIZATION REPORT NUMBER
92B00035

9. SPONSORING/MONITORING AGENCY NAME(S) AND ADDRESS(ES)
National Aeronautics and Space Administration
Washington, D.C. 20546-0001

10. SPONSORING/MONITORING AGENCY REPORT NUMBER
NASA CP-3137

11. SUPPLEMENTARY NOTES
Chris R. Shrader: Computer Sciences Corporation, Beltsville, Maryland 20705.
Neil Gehrels: NASA-GSFC, Code 661, Greenbelt, Maryland 20771.
Brian Dennis: NASA-GSFC, Code 682, Greenbelt, Maryland 20771.

12a. DISTRIBUTION/AVAILABILITY STATEMENT
Unclassified - Unlimited
Subject Category 90

12b. DISTRIBUTION CODE

13. ABSTRACT *(Maximum 200 words)*

The Compton Observatory Science Workshop was held in Annapolis, MD, on September 23-25, 1991. The primary purpose of the workshop was to provide a forum for the exchange of ideas and information among scientists with interests in various areas of high-energy astrophysics, with emphasis on the scientific capabilities of the Compton Observatory. Members of the Compton Observatory instrument development teams, as well as members of the guest investigator community were encouraged to participate. At the time of the workshop, the observatory had completed 5 months of successful in-orbit operations. Early scientific results, as well as reports on in-flight instrument performance and calibrations were presented. Additional reports describing guest investigator data products, analysis techniques and associated software as well as a report on the Phase-2 NASA Research Announcement were presented as an aid to prospective guest investigators. Theoretical papers, as well as papers describing results from other experiments were also presented. Scientific topics included active galaxies, cosmic gamma-ray bursts, solar physics, pulsars, novae, supernovae, galactic binary sources and diffuse galactic and extragalactic emission.

14. SUBJECT TERMS
Gamma-Ray Astronomy, High-Energy Astrophysics,
The Compton Observatory

15. NUMBER OF PAGES
556

16. PRICE CODE
A24

17. SECURITY CLASSIFICATION OF REPORT	18. SECURITY CLASSIFICATION OF THIS PAGE	19. SECURITY CLASSIFICATION OF ABSTRACT	20. LIMITATION OF ABSTRACT
Unclassified	Unclassified	Unclassified	